



TECHNICAL REPORT  
NATICK/TR-92/044

AD A 259 644

# PROCEEDINGS OF THE FOURTH NATICK SCIENCE SYMPOSIUM 9 - 10 JUNE 1992

*Editors*

**Matthew L. Herz**

**Thomas A. Sklarsky**

September 1992

---

---

---

Office of the Technical Director  
United States Army Natick Research, Development and Engineering Center  
Natick, Massachusetts  
01760-5002

APPROVED FOR PUBLIC RELEASE; DISTRIBUTION UNLIMITED

## **DISCLAIMERS**

The findings contained in this report are not to be construed as an official Department of the Army position unless so designated by other authorized documents.

Citation of trade names in this report does not constitute an official endorsement or approval of the use of such items.

## **DESTRUCTION NOTICE**

For Classified Documents:

Follow the procedures in DoD 5200.22-M, Industrial Security Manual, Section II-19 or DoD 5200.1-R, Information Security Program Regulation, Chapter IX.

For Unclassified/Limited Distribution Documents:

Destroy by any method that prevents disclosure of contents or reconstruction of the document.



# REPORT DOCUMENTATION PAGE

Form Approved  
OMB No. 0704-0188

Public reporting burden for this collection of information is estimated to average 1 hour per response, including the time for reviewing instructions, searching existing data sources, gathering and maintaining the data needed, and completing and reviewing the collection of information. Send comments regarding this burden estimate or any other aspect of this collection of information, including suggestions for reducing this burden, to Washington Headquarters Services, Directorate for Information Operations and Reports, 1215 Jefferson Davis Highway, Suite 1204, Arlington, VA 22202-4302, and to the Office of Management and Budget, Paperwork Reduction Project (0704-0188), Washington, DC 20503.

|   |  |  |  |   |  |
|---|--|--|--|---|--|
| 1. AGENCY USE ONLY (Leave blank)  |  | 2. REPORT DATE<br>September 1992                           |  | 3. REPORT TYPE AND DATES COVERED<br>Proceedings, 9-10 June 1992                 |  |
| 4. TITLE AND SUBTITLE<br>PROCEEDINGS OF THE FOURTH NATICK SCIENCE SYMPOSIUM,<br>9-10 JUNE 1992  |  |  |  | 5. FUNDING NUMBERS<br>Program Element No.:<br>62786<br><br>Project No.: CARRIER |  |
| 6. AUTHOR(S)<br>Matthew L. Herz<br>Thomas A. Sklarsky   |  |  |  |   |  |
| 7. PERFORMING ORGANIZATION NAME(S) AND ADDRESS(ES)<br>U.S. Army Natick Research, Development and Engineering<br>Center, ATTN: SATNC-T, Kansas Street, Natick, MA<br>01760-5002  |  |  |  | 8. PERFORMING ORGANIZATION<br>REPORT NUMBER<br><br>NATICK/TR-92/044             |  |
| 9. SPONSORING/MONITORING AGENCY NAME(S) AND ADDRESS(ES)   |  |  |  | 10. SPONSORING/MONITORING<br>AGENCY REPORT NUMBER                               |  |
| 11. SUPPLEMENTARY NOTES<br>Fourth Natick Science Symposium, 9-10 June 1992. Held at the U.S. Army Natick<br>RD&E Center, Natick, MA. Symposium Director: Dr. Robert W. Lewis, Technical<br>Director; (continued)  |  |  |  |   |  |
| 12a. DISTRIBUTION/AVAILABILITY STATEMENT<br>Approved for public release; distribution unlimited   |  |  |  | 12b. DISTRIBUTION CODE  |  |
| 13. ABSTRACT (Maximum 200 words)<br><br>This proceedings incorporates 25 papers presented at the Fourth Natick Science<br>Symposium, held 9-10 June 1992 at the U.S. Army Natick RD&E Center, Natick, MA.<br>The papers are included under the headings: Individual Survivability, Textiles,<br>Food Preservation and Characterization, Aerial Delivery, and Biotechnology. |  |  |  |   |  |
| 14. SUBJECT TERMS<br>Aerial Delivery                      Food<br>Biodegradation                      Food Preservation<br>Biotechnology                      Food Processing                      (continued)  |  |  |  | 15. NUMBER OF PAGES<br>468  |  |
| 17. SECURITY CLASSIFICATION<br>OF REPORT<br>Unclassified  |  |  |  | 16. PRICE CODE  |  |
| 18. SECURITY CLASSIFICATION<br>OF THIS PAGE<br>Unclassified   |  | 19. SECURITY CLASSIFICATION<br>OF ABSTRACT<br>Unclassified |  | 20. LIMITATION OF ABSTRACT<br>SAR   |  |

Report Documentation Page  
(continued)

11. Symposium Moderator: Dr. Matthew L. Herz, Associate  
Technical Director for Technology; Symposium Organizer:  
Mr. Thomas A. Sklarsky, Scientific and Technical Information  
Manager.

14. Food Storage  
Individual Protection  
Protection  
Rations  
Shelf Life  
Survivability  
Textiles  
Uniforms





REPLY TO  
ATTENTION OF

DEPARTMENT OF THE ARMY  
U.S. ARMY TROOP SUPPORT COMMAND  
NATICK RESEARCH, DEVELOPMENT AND ENGINEERING CENTER  
NATICK, MA

01760-5002



SATNC-T

June 1992

MEMORANDUM FOR SEE DISTRIBUTION

SUBJECT: Proceedings of the Fourth Natick Science Symposium,  
9-10 June 1992

1. The U.S. Army Natick Research, Development and Engineering Center held its fourth science symposium on 9-10 June 1992. Natick's programs emphasize a broad range of scientific and technical efforts to protect, sustain, and shelter the soldier on the battlefield. The papers in this volume represent the highlights of these programs that were presented at the symposium.

2. This year, 25 papers were presented by Natick scientists, engineers, and mathematicians. The general topical areas covered were:

Individual Survivability  
Textiles  
Food Preservation and Characterization  
Aerial Delivery  
Biotechnology

3. The Natick Science Symposium, established in 1986, has a threefold purpose:

- a. To recognize and encourage scientific and engineering talent.
- b. To demonstrate excellence in research and development.
- c. To stimulate the exchange of ideas among researchers at Natick, as well as among attendees from other Army commands and universities.

4. The symposium included papers and presenters from four Natick Directorates:

Aero-Mechanical Engineering  
Food Engineering  
Individual Protection  
Soldier Science


The symposium also included papers, coauthors, and presenters from universities. The papers represent the outstanding efforts of 79 researchers. This year's symposium was highly

SATNC-T

SUBJECT: Proceedings of the Fourth Natick Science Symposium,  
9-10 June 1992

successful and provided a lively scientific exchange among Natick researchers and numerous outside attendees. The Fifth Natick Science Symposium will be held in June 1994.

5. This volume is of value to attendees and other professionals interested in Natick's R&D efforts; it is approved for public release.

  
ROBERT W. LEWIS  
Technical Director

DISTRIBUTION:

Commander,  
U.S. Army Armament RD&E Center, ATTN: SMCAR-CO/SMCAR-TD,  
Dover, NJ 07801-5000  
U.S. Army Chemical RD&E Center, ATTN: SMCCR-TD, APG, MD  
21010-5423  
U.S. Army Communications-Electronics RD&E Center,  
ATTN: AMSEL-DCGD/AMSEL-TDD, Fort Monmouth, NJ 07703-5000  
U.S. Army Belvoir RD&E Center, ATTN: STRBE-Z/STRBE-ZT,  
Fort Belvoir, VA 21005-5066  
U.S. Army Aviation RD&E Center, ATTN: AMSAV-GRD/AMSAV-GTD,  
4300 Goodfellow Blvd, St. Louis, MO 63120-1798  
U.S. Army Atmospheric Sciences Laboratory, ATTN: SLCAS-D,  
White Sands Missile Range, NM 88002-5501  
U.S. Army Electronic Warfare Vulnerability Assessment  
Laboratory, ATTN: SLCEV-M-D, White Sands Missile Range, NM  
88002-5513  
U.S. Army Vulnerability Assessment Laboratory, ATTN: SLCVA-D,  
White Sands Missile Range, NM 88002-5513  
U.S. Army Missile RD&E Center, ATTN: AMSMI-R, Redstone Arsenal,  
AL 35898-5000  
U.S. Army Tank Automotive RD&E Center, ATTN: AMSTA-CF/AMSTA-CR,  
Warren, MI 48397-5000  
U.S. Army Ballistic Research Laboratory, ATTN: SLCBR-D, APG, MD  
21005-5066  
U.S. Army Electronics Technology and Devices Laboratory,  
ATTN: SLCEV-D, Fort Monmouth, NJ 07703-5302  
U.S. Army Harry Diamond Laboratories, ATTN: SLCHD-D,  
2800 Powder Mill Road, Adelphia, MD 20783-1145



SATNC-T

SUBJECT: Proceedings of the Fourth Natick Science Symposium,  
9-10 June 1992

DISTRIBUTION (CONT'D):

Commander,

U.S. Army Aviation and Troop Command, ATTN: AMSAT-G,  
4300 Goodfellow Blvd, St. Louis, MO 63120-1798

U.S. Army Materiel Command, ATTN: AMCDE,  
5001 Eisenhower Avenue, Alexandria, VA 22333-0001

U.S. Army Human Engineering Laboratory, ATTN: SLCHE-D, APG, MD  
21005-5001

U.S. Army Materials Technology Laboratory, ATTN: SLCMT-D,  
Watertown, MA 02172-0001

U.S. Army Materiel Systems Analysis Activity, ATTN: AMXSU-D,  
Aberdeen Proving Ground, MD 21005-5071

U.S. Army Armament, Munitions and Chemical Command,  
ATTN: AMSMC-CG, Rock Island, IL 61299-6000

U.S. Army Aviation Research and Technology Activity,  
ATTN: SAVDL-D, Ames Research Center, Moffett, CA 94035-1099

U.S. Army Laboratory Command, ATTN: AMSLC-TD/AMSLC-TP-PO,  
2800 Powder Mill Road, Adelphi, MD 20783-1145

U.S. Army Research Office, ATTN: SLCRO-ZC, Research Triangle  
Park, NC 27709-2211

U.S. Army Test and Evaluation Command, ATTN: AMSTE-TD,  
Aberdeen Proving Ground, MD 21005-5055

U.S. Army Cold Regions Research and Engineering Laboratory,  
ATTN: CECRL-TD, Hanover, NH 03755

U.S. Army Construction Engineering Laboratory, ATTN: CERL-ZT  
2902 Newmark Drive, Champaign, IL 61820

U.S. Army Engineer Topographic Laboratories, ATTN: CEETL-DC  
Fort Belvoir, VA 22060

CF:

Commander, U.S. Army Training and Doctrine Command Headquarters,  
ATTN: ATCG-S (Dr. Paul J. Berenson, Scientific Advisor to  
CG), Fort Monroe, VA 23651-5000

Commander, U. S. Army Materiel Command,  
ATTN: AMCSCI (Dr. Richard Chait, Chief Scientist),  
5001 Eisenhower Avenue, Alexandria, VA 22333-0001

Office of Assistant Secretary of the Army (Research, Development  
and Acquisition), The Pentagon, Room 3E510, ATTN: SARD-TC  
(Mr. Charles H. Church, Director, Advanced Concepts and  
Technology Assessment), Washington, DC 20310-0103

Commander, U. S. Army Materiel Command, Army Research Office,  
ATTN: SLCRO-MS (Dr. Andrew Crowson, Director, Materials  
Science Division), P. O. Box 12211, Research Triangle Park,  
NC 22709-2211

SATNC-T

SUBJECT: Proceedings of the Fourth Natick Science Symposium,  
9-10 June 1992

CF (CONT'D):

Office of Assistant Secretary of the Army (Research, Development  
and Acquisition), The Pentagon, Room 3E432, ATTN: SARD-ZR  
(Mr. Maurice R. Donnelly, Assistant Deputy for Plans and  
Programs), Washington, DC 20310-0103

Commander, U. S. Army Combined Arms Combat Development Activity  
(TRADOC), Mr. James F. Fox, Scientific Advisor,  
Fort Leavenworth, KS 66027

Commander, U. S. Army Materiel Command, ATTN: AMCDRA  
(Mr. Darold L. Griffin, Principal Assistant Deputy for RD&A),  
5001 Eisenhower Avenue, Alexandria, VA 22333-0001

Commander, U. S. Army Materiel Command, Army Research Office  
ATTN: SLCRO-D (Dr. Gerald J. Iafrate, Director), P. O. Box  
12211, 4300 S. Miami Blvd., Research Triangle Park, NC  
27709-2211

Office of Assistant Secretary of the Army (Research, Development  
and Acquisition) The Pentagon, Room 3E510,  
ATTN: Dr. Daphne Kamely, Director for Research & Laboratory  
Management, Washington, DC 20310-0103

Office of Assistant Secretary of the Army (Research, Development  
and Acquisition) The Pentagon, Room 3E479, ATTN: SARD-TR  
(Dr. A. Fenner Milton, Director for Technology), Washington,  
DC 20310-0103

Commander, U. S. Army Materiel Command, Army Research Office,  
ATTN: SLCRO-RT (Mr. George A. Neece, Director, Research &  
Technology Integration), P. O. Box 12211, Research Triangle  
Park, NC 27709-2211

Commander, U. S. Army Materiel Command, Army Research Office,  
ATTN: SLCRO-EG (Dr. Robert E. Singleton, Director,  
Engineering Sciences Division), P. O. Box 12211, Research  
Triangle Park, NC 27709-2211

Office of Assistant Secretary of the Army (Research, Development  
and Acquisition) The Pentagon, Room 3E374, ATTN: SARD-ZT,  
(Mr. George T. Singley, III, Deputy Assistant Secretary for  
Research and Technology), Washington, DC 20310-0103

Commander, U. S. Army Materiel Command, Laboratory Command,  
ATTN: AMSLC-DL (Mr. Richard Vitali, Technical Director),  
2800 Powder Mill Road, Adelphi, MD 20783-1145



## TABLE OF CONTENTS

### I. INDIVIDUAL SURVIVABILITY

|   |    |
|---|----|
| Chemical Structure and Liquid Crystallinity in Stilbene Polycarbonates,<br><i>Aaron L. Bluhm, Jeffery Carbeck, Peggy Cebe, Heidi L. Schreuder-Gibson,<br/>and Walter Yeomans</i>  | 1  |
| Synthesis and Characterization of Bioengineered Polymers with Nonlinear<br>Optical Properties, <i>Joseph A. Akkara, George Fischer, Francisco J. Aranda,<br/>David L. Kaplan, and D.V.G.L.N. Rao</i>  | 23 |
| Synthesis of Metallotetrabenzoporphyrins Possessing High Third-Order<br>Optical Nonlinearity for Military Laser Eye Protection,<br><i>Reginald A. Willingham, John H. Cornell, David M. Alabran, David E. Remy,<br/>Joseph F. Roach, and Masato Nakashima</i> | 33 |
| Phase Behavior of Chitosan/Nylon-4 Blends, <i>Jo Ann Ratto,<br/>Chien Chung Chen, Dong Young Kim, and Rita B. Blumstein</i>   | 41 |
| Fractal Surfaces and Reactivity, <i>Ronald A. Segars and Louis J. Piscitelle</i>  | 59 |
| Investigation of the Component Elements of Nonlinear (Chi-3) Effects,<br><i>Francisco J. Aranda, D.V.G.L.N. Rao, and Joseph F. Roach</i>  | 71 |

### II. TEXTILES

|   |     |
|---|-----|
| Numerical Simulation of the Ballistic Impact of Textile Structures,<br><i>Philip M. Cunniff</i>   | 87  |
| Deformations Near Axisymmetric Discontinuities in Inflated Fabric Tubes,<br><i>Thomas A. Godfrey</i>  | 103 |
| Comparative Adsorption of Agent and Simulant Vapor by Permeable<br>Fabrics Containing Activated Carbon, <i>Donald Rivin and Cyrus E. Kendrick</i> | 125 |

## CONTENTS

|   |     |
|---|-----|
| Effect of Crystallinity of Semicrystalline Polymer Matrices on Fiber Reinforced Ballistic Protective Composites, <i>John W. Song, Phillip W. Gibson, and Stuart R. Barlow</i> | 143 |
| 3D Analysis of Transient Thermal Transport Through Uniforms, <i>Barry S. DeCristofano, Gerald J. Caldarella, and Joseph F. Roach</i>  | 163 |
| Heat and Water Vapor Transfer Through Clothing Materials: Three Studies, <i>Phillip W. Gibson</i>   | 179 |

## III. FOOD PRESERVATION AND CHARACTERIZATION

|  |     |
|--|-----|
| Use of Acetate and Lactate for the Control of Pathogenic <i>Listeria</i> in Foods, <i>R. Victor Lachica and Chester T. Roskey</i>  | 219 |
| Antimicrobial Activity of Sucrose Laurate, EDTA, and BHA Alone and in Combination, <i>Anthony Sikes and Steve Whitfield</i>  | 237 |
| Contrast in Relative Effectiveness of Antioxidants in Bulk Versus Dispersed Lipid Systems: Validation of the Polar Paradox in Choice of Appropriate Antioxidants, <i>William L. Porter and Edward D. Black</i>             | 251 |
| Stability of Beta-Galactosidase and Immobilization on an Ultrafiltration Membrane for the Continuous Processing of Low Lactose Milk, <i>Andre G. Senecal and Arthur G. Rand</i>  | 277 |
| Structural Investigation of the Intrinsic Chemical Markers Formed in Aseptically Processed Particulate Foods, <i>Hie-Joon Kim, Irwin A. Taub, Michelle J. Richardson, Walter Yeomans, and Kenneth Kustin</i>               | 293 |
| Determining the Influence of Moisture and Humectants on the Staling of Long Shelf-Life Bread Using Dynamic Mechanical Analyzer and Nuclear Magnetic Resonance, <i>Pavinee Chinachoti, Yang Kou, and Linnea M. Hallberg</i> | 309 |
| Fourier and Fractal Analysis for the Textural Characterization of Porous Foods, <i>Ann Barrett, Mark Normand, Micha Peleg, and Edward Ross</i>   | 329 |



## CONTENTS

|  |     |
|--|-----|
| Kinetic Model for Predicting Bacterial Destruction from Intrinsic Chemical Marker Formation in Thermally Processed Foods*, <i>Edward Ross, Hie-Joon Kim, Irwin A. Taub, Kenneth Kustin, and Edgar Shattuck</i> | 345 |
|--|-----|

## IV. AERIAL DELIVERY

|   |     |
|---|-----|
| Bifurcation Analysis of Divergence and Flutter of an Aerodynamic Decelerator, <i>Louis J. Piscitelle</i>            | 359 |
| An Investigation of Parachute Aerodynamic Characteristics Using Computational Fluid Dynamics, <i>Keith R. Stein</i> | 385 |

## V. BIOTECHNOLOGY

|   |     |
|---|-----|
| Molecular Modeling Studies on Silk Peptides, <i>Stephen A. Fossey, George Nemethy, Kenneth D. Gibson, David L. Kaplan, and Harold A. Scheraga</i>   | 401 |
| Biodegradable Polymers for Packaging, <i>Jean M. Mayer, Joseph E. McCassie, Derek H. Ball, Robert E. Stote, James R. Wright, Ashley E. Shupe, Peter J. Stenhouse, Paul A. Dell, Mark J. Hepfinger, Elizabeth A. Costa, Elwyn T. Reese, and David L. Kaplan</i>        | 417 |
| Dynamic Optical Camouflage Systems Based on Orientated Streptavidin Conjugated Phycoerythrin Protein in Monolayers, <i>Lynne A. Samuelson, Pascal Miller, Diane M. Galotti, Rupmoni Sarma, Kenneth A. Marx, Jayant Kumar, Sukant K. Tripathy, and David L. Kaplan</i> | 431 |
| Characterization of Mollusc Shell Matrix Proteins -- Development of a Model for Biomimetic Ceramics, <i>Julia Keith, Scott Stockwell, Derek H. Ball, Kelly Napier, and Wayne Muller</i>   | 443 |

\* supplemental paper not presented at the symposium

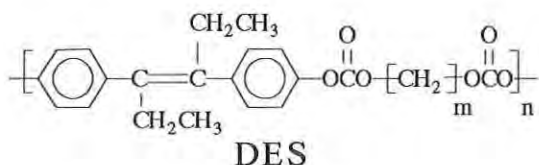
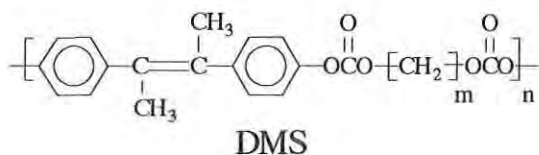
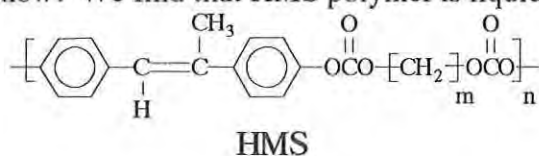


BLUHM, et al.

TITLE: Chemical Structure and Liquid Crystallinity in Stilbene Polycarbonates  
Aaron Bluhm, Dr., Jeffery Carbeck, Mr., Peggy Cebe, Dr., Heidi  
Schreuder-Gibson, Dr., and Walter Yeomans, Mr.

ABSTRACT: High performance polymers and fibers are necessary in a wide variety of clothing and equipment that protect and sustain the soldier. The current work explores the relationship between molecular structure and physical properties of liquid crystalline polymer precursors to high strength fibers, films and composites. We have been evaluating stilbene polymers that are liquid crystalline within reasonable processing temperature ranges. Not all stilbene polymers are liquid crystalline. Liquid crystallinity depends upon the chemical structure of the stilbene mesogen. Flexible spacer groups connecting the stiff stilbene mesogens also influence liquid crystalline properties.

Three variations of a liquid crystalline stilbene polycarbonate have been synthesized. Of these variations, DMS polymer has never been made or characterized by any group before now. We find that HMS polymer is liquid crystalline and that DES polymer is amorphous.



Thermal, microscopic and x-ray evidence will be presented to show the influence of these three chemical structures upon the presence of liquid crystallinity. Apparently, the size of the allylic substituent affects chain packing during crystallization. Plans for synthesizing additional variations will be presented along with synthetic methods for accomplishing this study.

BIOGRAPHY OF PRESENTER: Heidi  
L. Schreuder-Gibson

PRESENT ASSIGNMENT: Research  
Chemist, Soldier Science Directorate, U.S.  
Army Natick Research, Development and  
Engineering Center

PAST EXPERIENCE: Research Chemist, Solid Propulsion Division, U.S. Air Force  
Astronautics Laboratory

DEGREES HELD: B.S. Chemistry, University of California, Irvine; Ph.D. Polymer  
Science, The University of Akron

Chemical Structure and Liquid Crystallinity  
in Stilbene Polycarbonates

Aaron Bluhm, Dr., Jeffery Carbeck\*, Mr., Peggy Cebe\*, Dr.,  
Heidi Schreuder-Gibson, Dr., and Walter Yeomans, Mr.  
U.S. Army Natick Research, Development  
and Engineering Center, Natick, MA 01760

INTRODUCTION

The development of liquid crystallinity in polymers has advanced the properties of fibers and composites significantly since the early 1970s.<sup>1</sup> The current family of high strength aramid fibers (e.g. Kevlar®) are formed from the solution ordering of liquid crystalline polymers, called lyotropics. Recent research on polymer liquid crystals has produced a second family that are called thermotropics of promising fiber-forming nature and are processed simply from the molten state without the aid of solvents.

A fiber-to-fiber comparison of tensile modulus, breaking strength and elongation shows that lyotropic fibers and thermotropic fibers possess high stiffness and strength, Table 1. The thermotropic class is a viable and promising family of polymers for the production of high performance fibers.

Table 1. Fiber Properties

| <u>Fiber</u>                        | <u>Young's Modulus</u><br><u>(GPa)</u> | <u>Tensile Strength</u><br><u>(GPa)</u> | <u>Breaking Strain</u><br><u>(%)</u> | <u>Density</u><br><u>(g/cc)</u> |
|-------------------------------------|--|---|--------------------------------------|---------------------------------|
| <u>POLYETHYLENE</u>                 | 240 (Theoretical)                      |   |                                      |                                 |
| Spectra® 900                        | 117                                    | 2.5                                     | 3.5                                  | 0.97                            |
| Spectra® 1000                       | 172                                    | 3.0                                     | 2.7                                  | 0.97                            |
| <u>LYOTROPICS</u>                   |  |   |                                      |                                 |
| Kevlar® 29                          | 74                                     | 2.9                                     | 3.5                                  | 1.4                             |
| Kevlar® 49                          | 113                                    | 2.8                                     | 2.4                                  | 1.4                             |
| Kevlar® 129                         | 95                                     | 3.4                                     | 3.3                                  | 1.4                             |
| PBZT                                | 281                                    | 4.1                                     |                                      | 1.6                             |
| <u>THERMOTROPICS</u>                |  |   |                                      |                                 |
| Vectran®-HS                         | 65                                     | 2.8                                     | 3.3                                  | 1.4                             |
| Vectran®-M                          | 52                                     | 1.1                                     | 2.0                                  | 1.4                             |
| <u>HIGH TENACITY THERMOPLASTICS</u> |  |   |                                      |                                 |
| Nylon 6,6                           | 12.5                                   | 1.0                                     | 17.0                                 | 1.1                             |
| Polyester                           | 18.5                                   | 1.4                                     | 20.0                                 | 1.6                             |

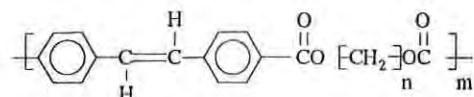
\*Materials Science and Engineering Department, Massachusetts Institute of Technology, Cambridge, MA 02139



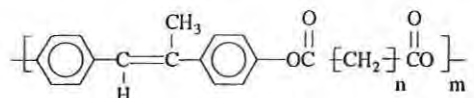
Thermotropics are a newer technology (1970s) than lyotropics (1960s). Chemical structural optimization and processing variables have recently begun to produce commercially available fibers.<sup>2</sup> Resulting from the efforts to optimize thermotropics, relationships between chemical structural features and liquid crystalline (LC) ordering have been established. The LC state produces the high degree of chain alignment considered necessary for high-strength fibers. However, these polymer molecules are rigid and elongated, and crystallization can be more favorable than liquid crystal formation. Chain rigidity can entirely prevent crystallization as well; such polymers do not melt at all below the temperature of decomposition. Rigid polymer chains can be modified to lower the melting point, or even produce liquid crystallinity through the inclusion of flexible links, chemical kinks along the backbone, random substitution, or random copolymerization.

Such chemical features can be easily incorporated into thermotropic LC polymers, melt processed, and tested. Stilbene based polymers have been used for such studies and have been reported to develop liquid crystallinity when copolymerized with flexible spacers.

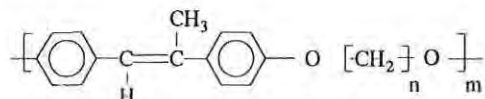
Unsubstituted stilbene polyesters<sup>3</sup>



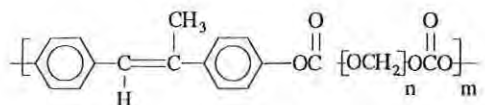
Methyl substituted stilbene polyesters<sup>4</sup>



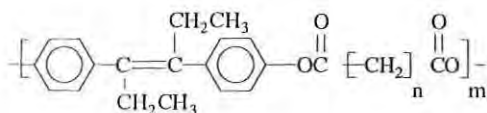
Methyl substituted stilbene polyethers<sup>5</sup>



Methyl substituted stilbene polycarbonates<sup>6</sup>



Diethyl substituted stilbene polyesters<sup>7</sup>

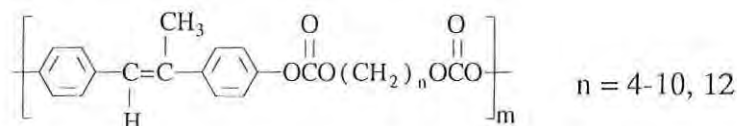


Diethyl substituted stilbene polymers have been reported to be amorphous by one source,<sup>4</sup> but liquid crystalline by another.<sup>7</sup>

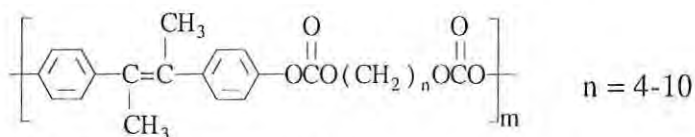
Our work has focused on the understanding of structure development using an easily synthesized series of thermotropic polycarbonates that contain the rigid (mesogen) stilbene monomer. Through modification of the stilbene unit, we have been able to study the influence of mesogen "bulkiness" on the development of order, and ultimately strength, in these polymers.

## EXPERIMENTAL

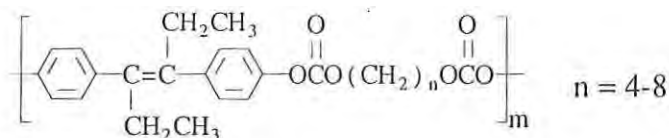
The following polymers were prepared by condensation reaction of diols with diphenylcarbonates:



HMS (Hydroxy- $\alpha$ -Methyl Stilbene) Polymer



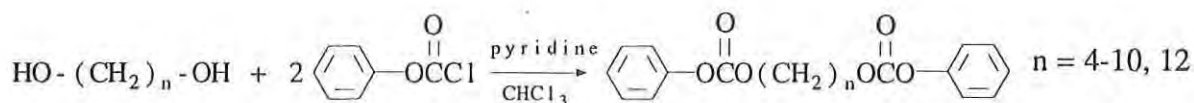
DMS (Dimethyl Stilbene) Polymer



DES (Diethyl Stilbene) Polymer

Variable lengths of the flexible methylene spacer units were copolymerized stoichiometrically, regularly alternating with the stilbene monomers. This was accomplished by first preparing alkylene diphenyl carbonates, according to the procedure of Sato et al.<sup>8</sup>

BLUHM, et al.

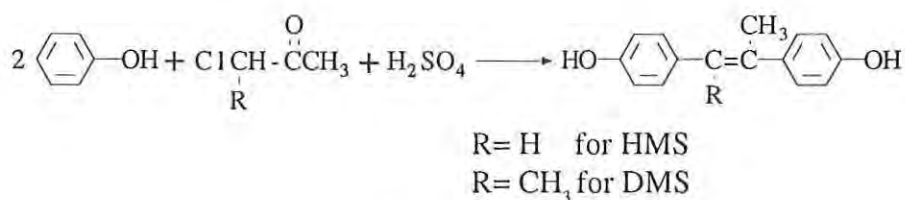


Crude yields from this reaction were usually 90% or better, and the resulting diphenyl carbonates were recrystallized from methanol.

Table 2. Alkylene (n) Diphenyl Carbonate Melting Points

| <u>m</u> | <u>T<sub>m</sub> (°C)</u> |
|----------|---------------------------|
| 4        | 84-85                     |
| 5        | 44.5-45.5                 |
| 6        | 85.5-86.5                 |
| 7        | 34-35                     |
| 8        | 71.5-72.5                 |
| 9        | 41.5-42.5                 |
| 10       | 78-79                     |
| 12       | 81-82                     |

4,4'-dihydroxy- $\alpha$ -methyl stilbene (HMS) and 4,4'-dihydroxy- $\alpha,\beta$ -dimethyl stilbene (DMS) were prepared by a procedure similar to that of Zaheer et al.<sup>9</sup>

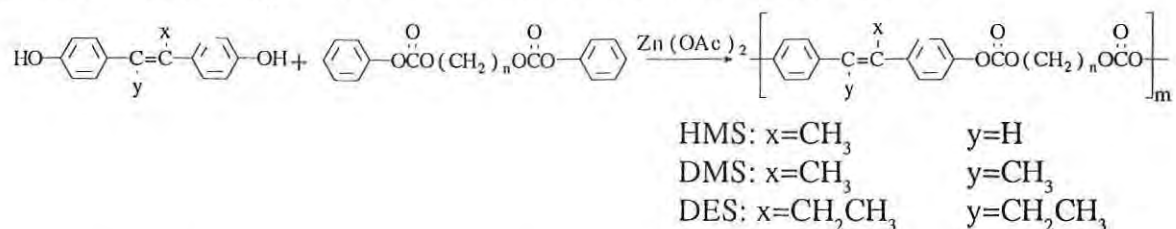


Condensation of phenol with the appropriate chloroketone produced HMS in 55% and DMS in 8% raw yields. The third mesogenic monomer, DES, is the commercially available hormone, diethylstilbestrol. Obtained from Aldrich, this monomer was recrystallized from toluene. HMS was purified by ethanol recrystallization followed by benzene extraction. DMS was purified by silica gel column chromatography with acetone/chloroform (5/95) eluent. Monomer purity, determined by thin layer chromatography and melting point, was essential to a successful polymerization reaction.

Table 3. Stilbene Diol Melting Points

| Monomer | Tm(°C)  | Lit. Value <sup>12</sup> (°C) |
|---------|---------|-------------------------------|
| HMS     | 183-185 | 181-182                       |
| DMS     | 193-195 | 193-194                       |
| DES     | 171-174 | 171                           |

In the polymer synthesis,<sup>8</sup> equimolar amounts of each monomer were combined with catalyst and heated without stirring to 190-200°C for 2-4 hours under N<sub>2</sub>. Pressure was then reduced and temperature increased to 210-220°C for 2-4 more hours.



The final brown glassy solid products recrystallized from chloroform to produce a powdery, sometimes fibrous polymer for HMS and DMS, in yields of 40-60% for HMS polymers and DMS polymers. Yields of 40-70% for DES polymers were achieved, but only soft rubbery or resinous product was isolated from the chloroform workup.

Elemental analysis of the HMS polymer series shows that the expected products were achieved. Chemical structure for HMS, DMS, and DES polymers were verified by proton NMR and IR as well.

Table 4. Elemental Analysis of HMS Polymers

| Sample | Calculated % |      |       | Actual % |      |       |
|--------|--------------|------|-------|----------|------|-------|
|        | C            | H    | O     | C        | H    | O     |
| HMS-4  | 68.47        | 5.47 | 26.05 | 68.58    | 5.48 | 26.05 |
| HMS-5  | 69.10        | 5.80 | 25.10 | 69.04    | 5.85 | 25.16 |
| HMS-6  | 69.68        | 6.10 | 24.21 | 69.54    | 6.09 | 24.43 |
| HMS-7  | 70.23        | 6.38 | 23.39 | 69.98    | 6.37 | 23.29 |
| HMS-8  | 70.74        | 6.65 | 22.61 | 70.65    | 6.65 | 22.86 |
| HMS-9  | 71.21        | 6.90 | 21.89 | 71.24    | 6.97 | 21.75 |
| HMS-10 | 71.66        | 7.13 | 21.21 | 71.35    | 7.24 | 21.62 |
| HMS-12 | 72.48        | 7.55 | 19.97 | 72.78    | 7.64 | 19.32 |



Polymer molecular weights were found to be mainly within the expected range for a polycondensation reaction. Both free radical (simple termination) and condensation reactions produce polymers of molar mass dispersions of around 2. Size exclusion chromatography was used to determine molecular weights for the chloroform-soluble polymers. Polycarbonate broad standards were used to calibrate the runs. Data variability due to baseline problems is reported below for two of the samples, HMS-4 and HMS-5.

Table 5. Polymer Molecular Weights

| <u>Sample</u> | <u>Mn</u> | <u>Mw</u> | <u>Mw/Mn</u> |
|---------------|-----------|-----------|--------------|
| HMS-4         | 6,786     | 40,059    | 5.9          |
| HMS-5         | 5,289     | 13,056    | 2.5          |
| HMS-6         | 3,400     | 7,700     | 2.3          |
| HMS-7         | 7,400     | 29,100    | 3.9          |
| HMS-8         | 6,000     | 15,100    | 2.5          |
| HMS-9         | 4,700     | 7,600     | 1.6          |
| HMS-10        | 6,200     | 13,300    | 2.1          |
| HMS-12        | 3,500     | 27,300    | 7.7          |
| DES-5         | 2,038     | 6,319     | 3.1          |
| DES-6         | 4,766     | 7,002     | 2.9          |
| DES-7         | 4,946     | 7,350     | 1.5          |
| DES-8         | 6,823     | 13,412    | 2.0          |

## EXPERIMENTAL RESULTS

Thermal Characterization. Differential scanning calorimetry (DSC) studies of the stilbene polycarbonates indicated the presence of some liquid crystalline features. Not all of our polymers were liquid crystalline. Not all of them were crystalline.

In general, DSC measurements verify the presence of the following features of polymers: glass transition temperatures for amorphous polymers, or the amorphous fraction of semicrystalline polymers; crystal melting points and energy associated with melting; and liquid crystalline temperature ranges, existing between the melting of the three-dimensional crystalline structure and the melting of the less ordered, two-dimensional liquid crystalline structure.

Thermal transitions for HMS-5 through -12 are shown in figures 1 and 2. The scans shown in these figures are obtained from samples that have been heated to 200°C. The first cooling exotherms and the following melting endotherms are presented. These transitions appear as sharp exotherms during the first cooling cycle and as broad endotherms

during the second heating scan. These thermal transitions are reproducible after the first heating step. Typically, liquid crystalline transitions exist as sharp doublets for simple liquid crystals and as broader, less well defined doublets for polymeric liquid crystals. Such double melting transitions occur as a result of a lower temperature transition due to the crystal-to-liquid crystal transformation, and a higher temperature liquid crystal-to-liquid transition. Notable features in our HMS polymer series include the high temperature shoulder on the exotherms of HMS-5, -6, -7, -9, and -10, a double exotherm for HMS-12, and a hint of a double endotherm for HMS-5, -7, -8 and -12. It is expected that these semiflexible polymer chains require a significant amount of time to organize into the liquid crystalline state, which may not be realized in the rapid heating and cooling cycles performed by DSC rates of 10°C/min. Therefore, not all of these samples as tested show the features indicative of an intermediate mesophase between crystal melting and full isotropization.

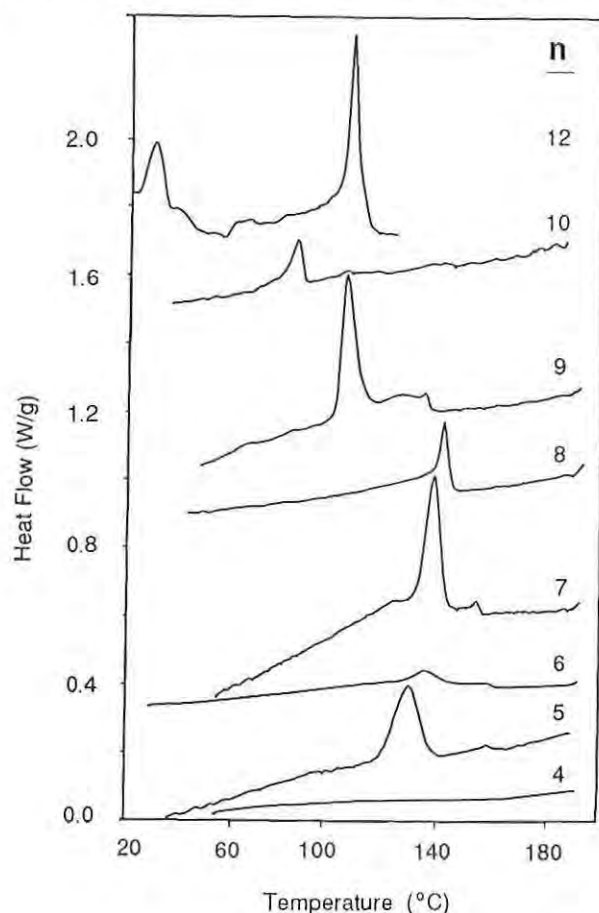


Figure 1. DSC exotherms for HMS-4 through -10 and -12. First cooling at -10°C/min. All scans plotted to scale and placed arbitrarily along ordinate.

Note: some scans contain large area factor differences.

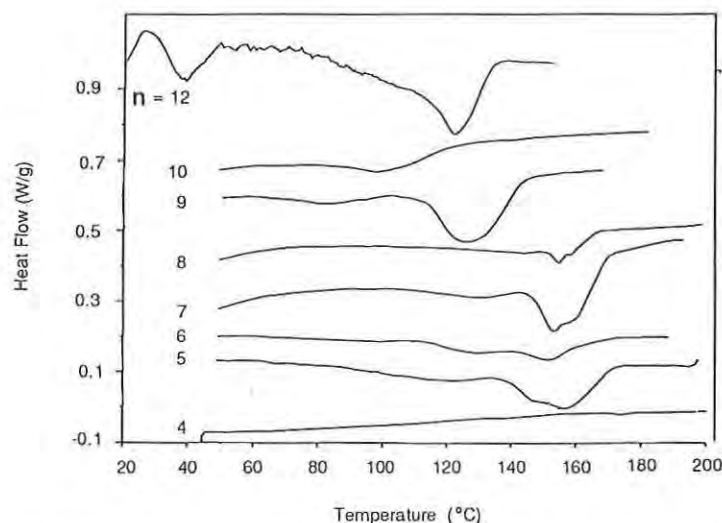


Figure 2. DSC endotherms for HMS-4 through -10 and -12. Second heating at 10°C/min.

Annealing studies verify the time dependence of the mesophase formation. Shown in figure 3, annealing of HMS-5, HMS-7, and HMS-8 produces multiple sharp endotherms, indicative of mesophase formation. Annealing temperatures were applied near the crystallization transition temperatures for these polymers for 15 minutes. Cooling to room temperature followed by heating produces a sharp endotherm for HMS-5 at 161°C, which is higher than the endotherm (156°C) without annealing. Similar sharpening and rising occurred for HMS-7 and -8. This means that the crystal perfection can be improved by just a short anneal. Minor exothermic departures occur at the annealing temperatures of 154°C for HMS-5, 154°C for HMS-7 and 144°C for HMS-8.

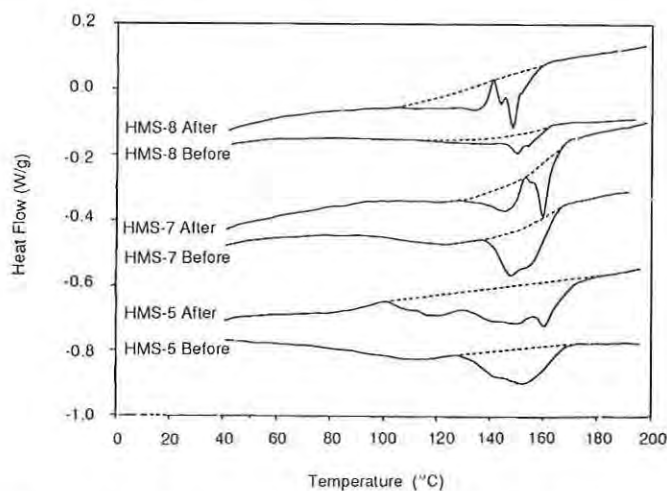


Figure 3. DSC heating curves of HMS-5, -7, and -8, before and after annealing treatment.

DMS polymers, featuring a disubstituted stilbene mesogen, show lower transition temperatures and broader peaks on cooling (figure 4) and on reheating (figure 5) than the HMS polymers. During the second heating of the samples, only the DMS-7 shows a double endotherm. Notably, DMS-5 exhibits no distinct transition temperatures, similar to the behavior of HMS-4. Apparently, a suppression of chain organization can be seen for the polymers of shorter alkyl spacer lengths, such as DMS-5 and HMS-4. The size of the alkyl spacer group is an important variable, since it enables positional ordering of the rigid stilbene mesogens. A flexible spacer can be too long to promote mesogen alignment above the crystalline melting temperature, or too short to allow mesogen orientation, resulting in an intractable solid with no melting or softening before decomposition.

This preliminary comparison of the HMS and DMS series shows that for both types of polymers, the exothermic response exists at lower temperatures than the endothermic response, an effect seen as melting point superheating. On the whole, HMS polymer melting superheats by roughly 20°C at the 10°C/minute heating and cooling rates. The DMS polymers of short alkyl spacer lengths of -6 and -7 superheat by 20-25°C. But longer spacer lengths of DMS develop considerable superheating (by 35 to 60°C) before melting occurs. The reference state for superheating is the previous cooling history. Superheating occurs when crystals melt at a temperature higher than the formation of the crystals. The more extensive superheating in the DMS polymers is an indication that the bulky, disubstituted mesogen is more difficult to order into a crystalline structure than the monosubstituted mesogen.

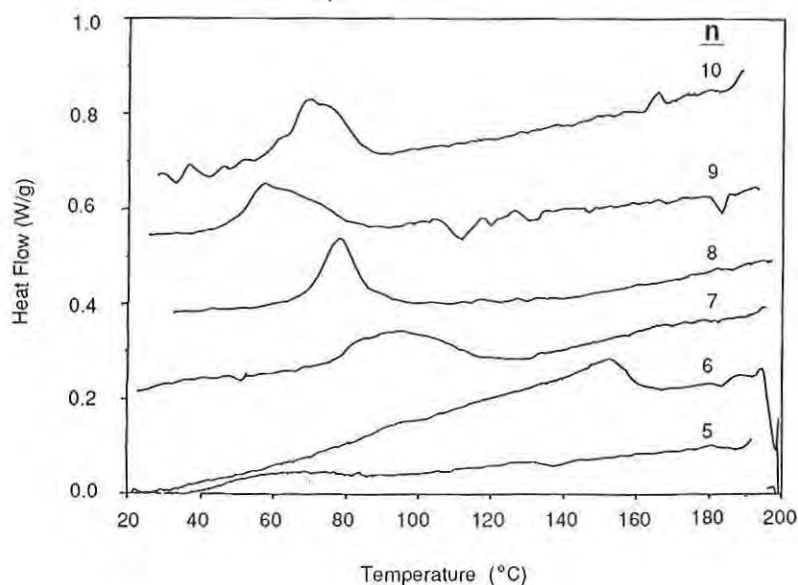


Figure 4. DSC exotherms for DMS-5 through -10. First cooling at -10°C/min.



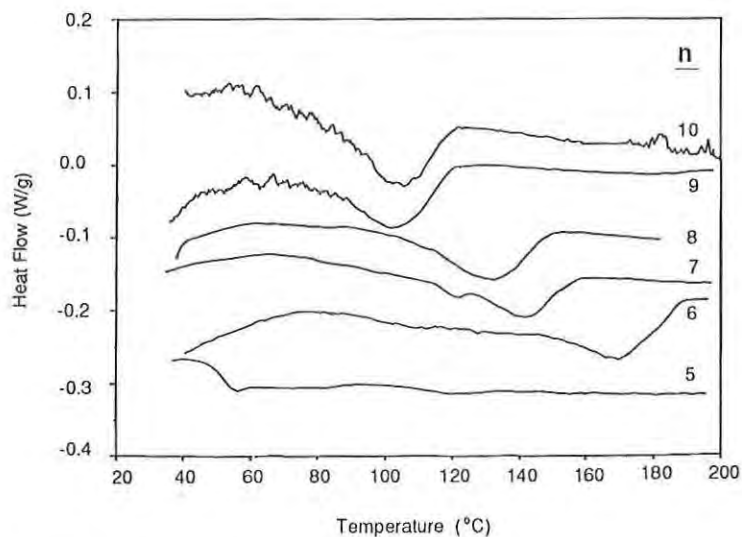


Figure 5. DSC endotherms for DMS-4 through -10. Second heating at 10°C/min.

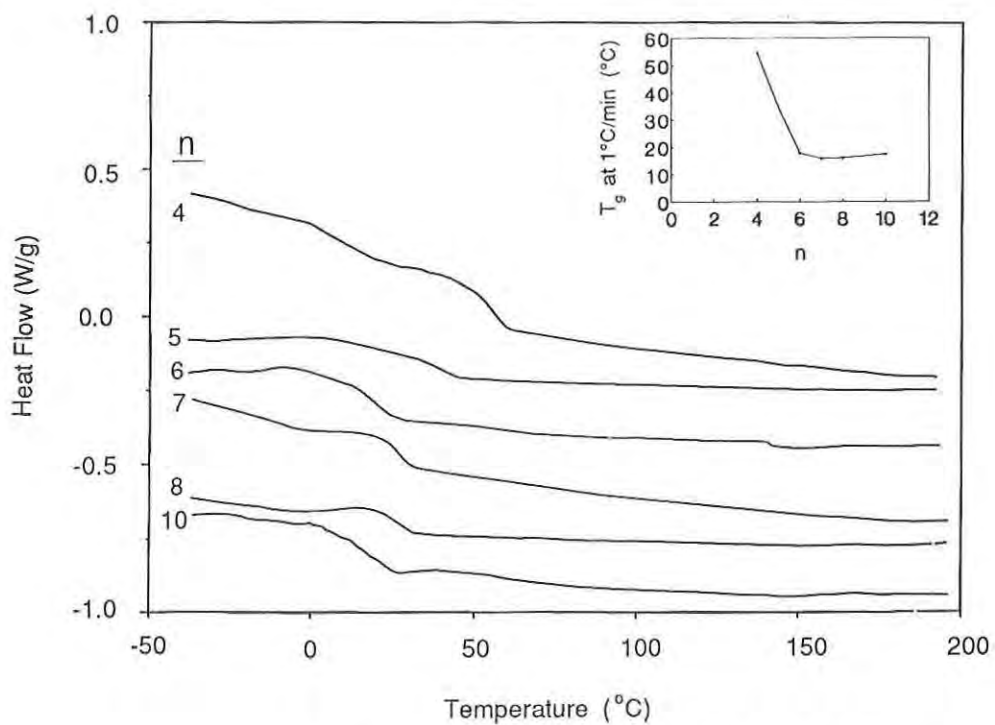


Figure 6. Glass transition temperatures of DES-4 through -8 and -10. Heating rate of 10°C/min that follows a cooling rate of -10°C/min.

Further comparison can be made in terms of the size of the stilbene substituent: methyl vs ethyl disubstitution. For our polymers, the DES mesogen cannot order into a crystalline structure at all. Clear glass transition temperatures are apparent, and are found to follow an expected trend. Building increased flexibility into the DES polymers via alkyl spacer lengths decreases the glass transition temperature as shown in figure 6. Presented here are the scans of the polymer glass transition temperatures obtained after a first heating to 200°C, a first cooling at -20°C/min, a second heating at 20°C/min, and a second cool at 10°C/min. Shown in the insert are the glass transitions extrapolated to an effective heating rate of 1°C/min from a set of scans at 20, 10 and 5°C/min for each polymer.

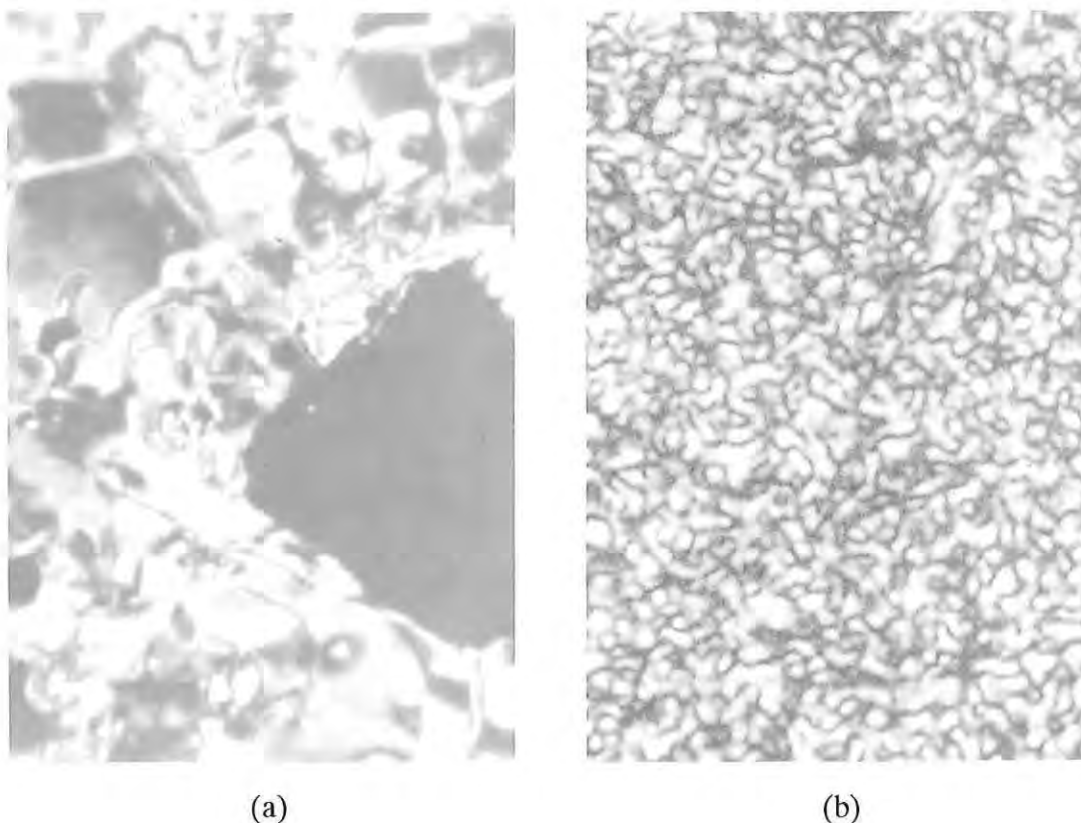


Figure 7. Polarized optical micrographs of a) para azoxy anisole heated to 119°C, magnification 190X; and b) HMS-5 cooled to 50°C from the melt, magnification 243X.

Polarizing Optical Microscopy can be used to confirm DSC evidence of liquid crystallinity. When a thin film of liquid crystalline polymer is observed between crossed polars, a nematic structure is seen to produce dark “threads” at extinction positions within the mesophase, resulting in a characteristic schlieren texture. For our polymers, thin films are produced by placing a drop of concentrated solution of polymer onto the microscope slide,

shearing the solution, and removing the solvent under vacuum. Shown in figure 7 are the patterns observed for a simple nematic liquid crystal prepared from the melt -- para azoxy anisole, and for our polymer, HMS-5, prepared by solvent casting. The scale of the textural pattern is very much smaller for polymers, which typically develop textures that are an order of magnitude smaller than simple LC textures.<sup>10</sup>

We found this scale of texture to be inconvenient for identifying crystal types and could not with certainty determine whether observed disclinations were caused by three-dimensional spherulite crystals or two-dimensional liquid crystallinity. It is likely that primary crystallization is superimposed onto a liquid crystalline texture. We observed in all polymer specimens a dense pattern of interference within the temperature ranges of the broad endotherms of the HMS polymers. The onset of a number of features seen under polarized light, such as melting of the original crystalline powder or semicrystalline film, isotropization (clearing), recrystallization upon cooling, and an unusual field color change, occurs in the appropriate ranges of thermal transitions, as measured by DSC at the same 10°C/minute scanning rate. In all samples, we found that upon melting a crystalline powder or solvent cast film, a melt formed film produced a fine grainy pattern that persisted below the clearing temperatures.

Evidence of primary crystallization was apparent for the HMS polymers when thin films of solvent-cast polymers were prepared and examined. Fibrillar structures occur in HMS-5, -6, -7, and -8 with HMS-5 and -6 having the larger-scale, coarser arrays of fibril clusters. HMS-4, -9, -10, and -12 had grainy birefringence and no fibrillar clusters; or if this higher order structure developed in these materials, they were too small to be resolved by this technique.

Upon cooling from the isotropic melt, a sample of HMS polymer would first develop a texture of black threads in a white field, but upon continued cooling, the white field would turn distinctly yellow. There was no pattern change corresponding to this effect. There are two possible reasons for a color change corresponding to longer wavelength: birefringence changes in the sample, or sample thickening as a function of temperature. A color change from white to yellow upon cooling indicates that the color change cannot be due to thickness increases, because the sample is certainly thinning as the polymer is cooled. The sample is changing in birefringence, possibly due to a crystallization event.

These optical observations are depicted for the HMS-5 sample in figure 8. The DSC heating and cooling cycle shows a very shallow endotherm between 90 and 130°C. Microscopic observations of HMS-5 place the onset of crystal melting at around 110°C. Nematic threads appear by 165°C. Clearing to the isotropic melt occurs at 182°C. Upon cooling, threads develop from the dark isotropic liquid at 158°C and increase in contrast as the field turns white and black. The field color changes to yellow at 140°C. This color with the black threaded pattern persists to room temperature and remains unchanged with time.

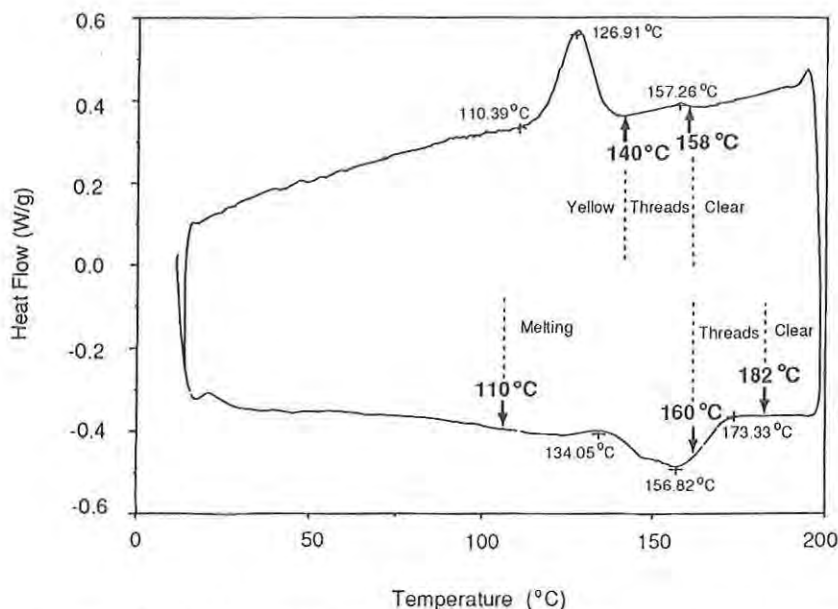


Figure 8. DSC scan of HMS-5, first cool followed by second heat at 10°C/min. Microscopic features noted.

Real-Time X-Ray Scattering was performed on the HMS polymers to elucidate the structures that might have produced the observations of high temperature shoulders on the cooling exotherms, the yellowing of the birefringent polymer films, and the general packing distances of the chains in the bulk.

X-ray scattering allows the determination of the packing arrangement and interchain distances of polymer chain segments. The wide angle scattering regime provides information on size scales ranging from 1Å to 20Å. Real time X-ray scattering was performed on HMS polymer samples as they were cooled so as to observe the development of structure from the isotropic melt state. In order to obtain information during crystallization, the detection time must be very short. This requires a high intensity source of X-radiation, and for our experiments we used the Brookhaven National Synchrotron Light Source, NSLS.

The X12B beam line at NSLS was used to obtain X-ray scattering data at high temperatures in beam *transmission* mode. The X-ray beam passed through a hot stage containing the sample film. HMS polymer films were prepared by sealing powder between two pieces of Kapton® tape, heating to the melt, then cooling at 5°C/min during the measurement.

Structure development was observed in these polymers using the scattering of 0.91Å wavelength X-rays. All HMS polymers show two strong scattering peaks, similar to those of HMS-8 in figure 9, which may have their origin in the separation distance for the packing of molecules with anisometric (possibly oval) cross-sections. These spacings are the correct size of interchain distances and are much smaller than the sizes of the monomer units along the chain. Some of the HMS polymers show additional peaks which are rather weak in comparison to the two major peaks. This structure is not very characteristic of isotropic



melt-crystallized thermoplastic polymers. Unoriented thermoplastics usually show broader and many more scattering peaks. Such sharp and sparse peaks are produced in highly oriented thermoplastic films and in the liquid crystal polymers, Vectra® and Xydar®. Based on additional scattering done in *reflection*, as described below, we find that the samples are not preferentially orienting in a monodomain so as to present only a few peaks. The two sharp reflections are strong indications of liquid crystallinity.

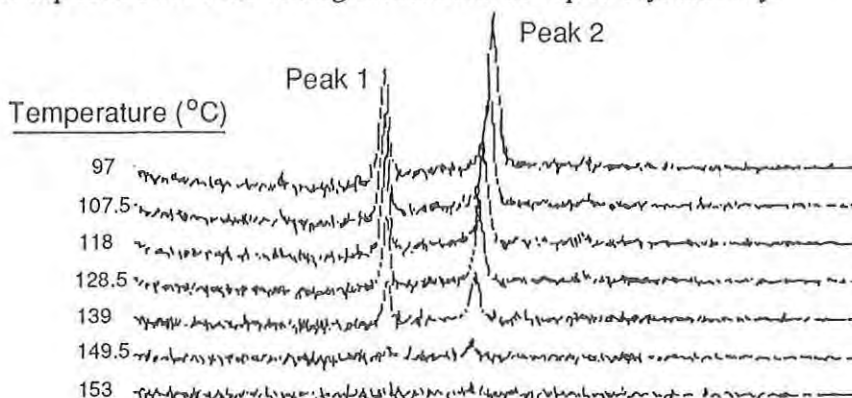


Figure 9. HMS-8 X-ray scattering peaks appear as the sample is cooled from 153°C at -5°C/min.

Wide Angle X-ray Scattering, described below, provided data which confirmed an odd-even alternation in properties for the HMS polymers. A weak odd-even effect was evident upon close examination of the DSC data. Plots of the melting points, figure 10, from DSC profiles of the HMS polymers of flexible spacer length,  $n$ , show that an alternation of melting temperatures occurs for polymers of  $n = 4-8$ . Other investigators report that even-numbered spacer lengths within the polymer backbone promote high temperature melting, while odd-numbered spacers result in low temperature melting stilbene polymer esters.<sup>11</sup>

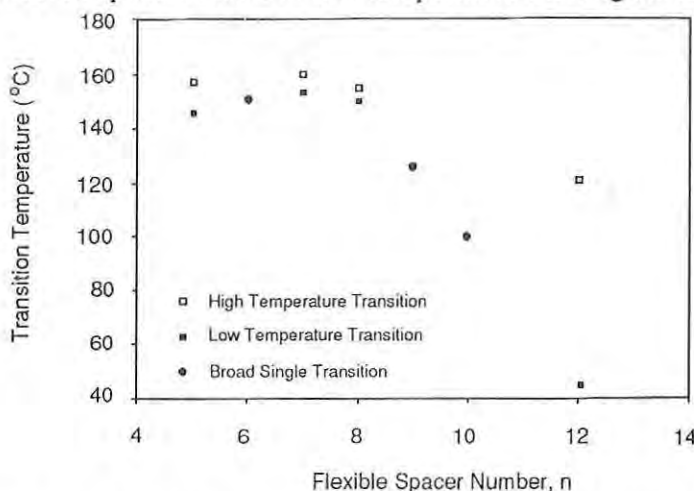


Figure 10. Melting points determined by DSC for HMS-4 through -10 and -12 at 10°C/min

Our stilbene polycarbonates show the reverse trend. This could signify a key difference between the ester and carbonate linkages. We also find that the stilbene polyesters melt at significantly higher temperatures than stilbene polycarbonates.

Wide angle X-ray measurements made at room temperature on melt-cast polymer films with a  $1.54\text{\AA}$  X-ray wavelength in the *reflection* mode produced d-spacings for each HMS polymer, shown in figure 11. These d-spacings, which are presumably the interchain distances, alternate regularly with the value  $n$  of the number of methylene units in the flexible spacer group. For HMS-5 through -8, d-spacings for even-numbered HMS polymers are larger than for odd-numbered polymers. Evidently, HMS-odd polymers have closer interchain packing than HMS-even polymers.

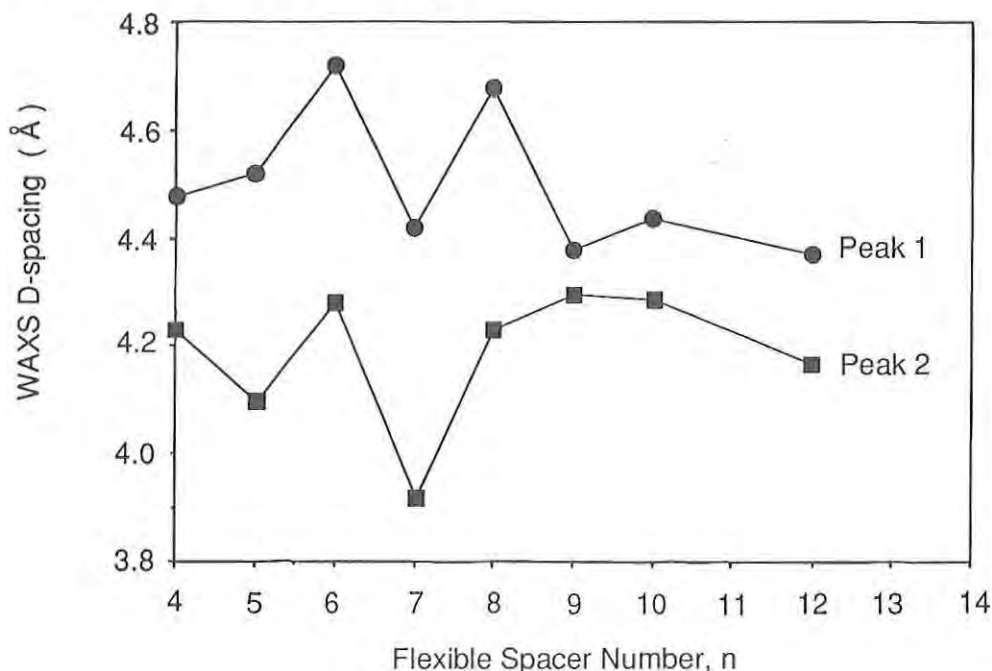


Figure 11. d-spacings for HMS polymers of alkyl chain length,  $n$ .

Molecular Modeling of HMS-5 polymer was used to confirm the X-ray measured interchain distances for lowest energy conformations of the backbone. Molecular mechanics calculations were performed using the Biosym molecular simulation program, Discover® and the Insight® molecular graphics package. Molecular fragments of stilbene, carbonate and pentane were constructed using Insight®, and then the structures were energy minimized using Discover®. The force field supplied by the software included nonbonded van der Waals and electrostatic interactions as well as the bond length, angle, and torsional parameters.

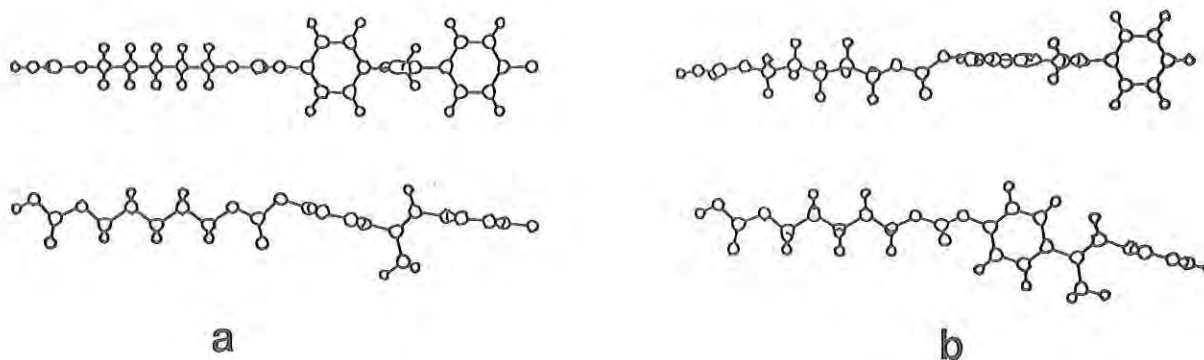


Figure 12. a) minimum and b) maximum energy conformations for single HMS-5 repeat unit.

It has been found that the HMS-5 fragments will accommodate an interchain distance on the order of  $4\text{\AA}$  in their minimum energy configuration, above in figure 12. This results in an interesting limitation, however. Within these interchain distances, stilbene phenyl ring rotation cannot occur without significant intermolecular interactions during the liquid crystalline phase. One possible reason for the mesogenic character of the stilbene monomer is the rotation of the phenyl rings in the structure, allowing favorable packing distances that promote the mesophase. Molecular modeling demonstrates that phenyl rotation is severely restricted: full ring rotation is energetically unfavorable. The steric interaction with the phenyl ring and the adjacent carbonate group results in significant rotational distortion of the carbonate group and the entire pentane group. Figure 13 shows the change in energy as the phenyl ring adjacent to the carbonate group is driven through the angle  $\phi$  from the minimum energy configuration.

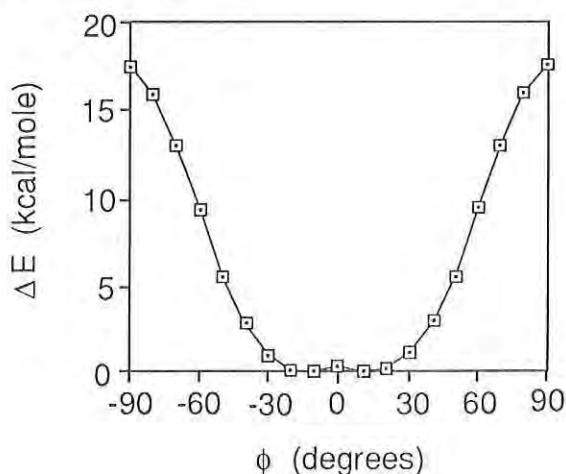


Figure 13. Rotational energy barrier for phenyl ring in stilbene carbonate.

The maximum energy for phenyl rotation in  $\alpha$ -methyl stilbene is 17.5 kcal/mole. In comparison, phenyl ring rotation results in calculated energy barriers on the order of 10.4 kcal/mole for glassy polycarbonate (bisphenol-A) and 3 kcal/mole for its amorphous state. For HMS polymers, intermolecular interactions would result in even higher barriers for ring rotation.

### SUMMARY

Polymers based on  $\alpha$ -methyl stilbene,  $\alpha,\beta$ -dimethyl stilbene and  $\alpha,\beta$ -diethyl stilbene have been synthesized with flexible spacer groups of methylene numbers,  $n = 4-10$  and 12.

Among these polymers, HMS-5 through -10 and -12 appear to be liquid crystalline, showing broad melting endotherms, which sharpen and multiply upon annealing. HMS-5, -7, and -8 have double endotherms, while HMS-5, -6, -7, -9, and -10 have double exotherms.

HMS-5 through -10 and -12 produce double peak reflections in X-ray diffraction. These reflections, related to interchain packing distances, alternate regularly with the length of the spacer group for HMS-5.

Microscopic examination of the HMS polymers shows the presence of fibrillar structure in HMS-5, -6, -7 and -8. A characteristic change in birefringence upon cooling from the melt indicates the presence of an unresolvable crystallization event.

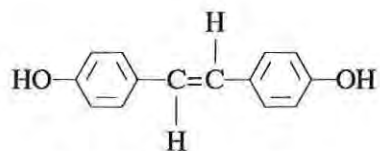
Molecular modeling suggests that the 4Å packing distances for HMS chains is reasonable. Phenyl ring rotation is calculated to be an unfavorable molecular motion for stilbenes (and for glassy polycarbonates).

The DMS series exhibit broad melting endotherms, but only DMS-7 shows a double endotherm. DMS exotherms are broad and no doublets or shoulders are present. A high degree of supercooling suggests that the DMS crystallization is hindered by a steric effect of the disubstituted mesogen. Liquid crystallinity in DMS polymers has not been confirmed yet.

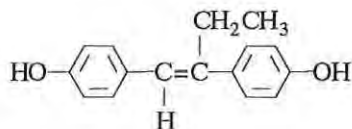
The DES polymer series are all amorphous in the temperature range of -50 to 200°C. In this case, the disubstituted ethyl groups appear to completely disrupt crystallinity. Glass transition temperatures for DES polymers range from 55°C to 16°C, decreasing with increasing spacer length.

## FUTURE DIRECTIONS

Synthesis of New Monomers. In an effort to elucidate the effect of the type of mesogen on the properties of thermotropic liquid crystalline polymers, our work on the synthesis of new stilbene monomers is underway. Stilbene structures needed to complete the study of substituent steric interference with liquid crystalline order include:

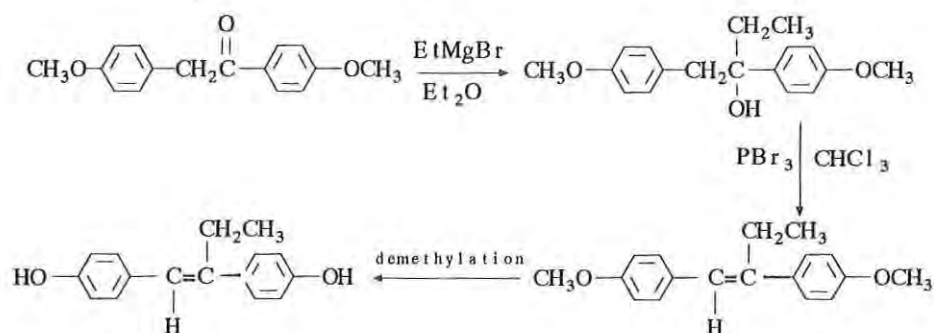


4,4'-dihydroxy stilbene



4,4'-dihydroxy  $\alpha$ -ethyl stilbene

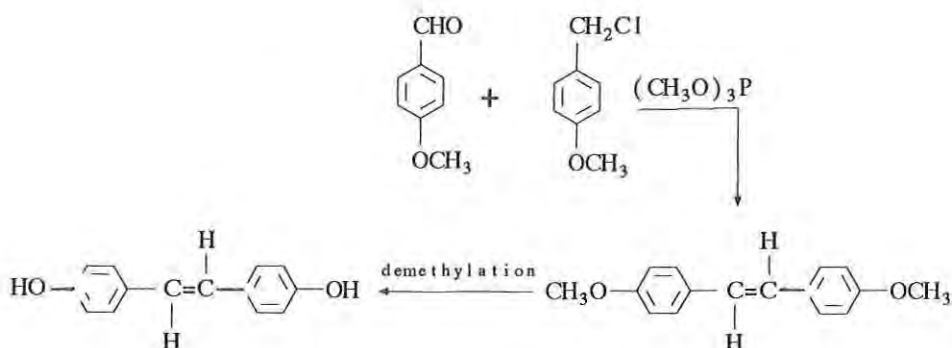
The 1939 procedure of Dodds et al.<sup>12</sup> is the commercial production method for DES. This reaction is as follows:





BLUHM, et al.

For the unsubstituted monomer,



#### ACKNOWLEDGEMENTS

This paper is dedicated to the memory of Dr. John Cornell (1923-1991), who supported our efforts in many significant ways through advice on synthesis, literature researching and creative ideas. The authors wish to acknowledge the assistance of Ms. Roslyn Kramer and Ms. Rosa Linda Bagalawis for chromatography, Ms. Nora Stackpole and Mr. Raymond Beauvais for synthesis, Ms. Wendy Russell for X-ray scattering at MIT, and Dr. Malcolm Capel for assistance with NSLS X-ray scattering.

#### REFERENCES

1. Jaffe, M., Calundann, G., and Yoon, H.-N., in "High Technology Fibers," Part B, Chapter 3, Lewin, M., and Preston, J., eds, Marcel Dekker, NY (1989).
2. Jackson, W.J., Mol. Cryst., Liq. Cryst., 169, 23(1989)
3. Jackson, W.J. and Morris, J.C., J. Applied Polym. Sci., Applied Polymer Symposium 41, 307(1985)
4. Blumstein, A., Polymer Journal, 17, No. 1, 277(1985)
5. Percec, V., Nava, H., Jonsson, H., J. Polym. Sci., Part A: Polym. Chem., 25, 1943(1987)

BLUHM, et al.

6. Roviello, A. and Sirigu, A., *Eur. Polym. J.*, 15, 423(1979)
7. Sato, M., *J. Polm. Sci., Part A: Polym. Chem.*, 26, 2613(1988)
8. Sato, M., et al., *Makromol. Chem., Rap. Comm.*, 7, 231(1986)
9. Zaheer, S.H., et al., *J. Chem. Soc.*, 3360(1954)
10. Viney, C., in "Liquid Crystalline Polymers," Weiss, R.A. and Ober, C.K., eds, ACS Symp. Ser. 435, 241(1990)
11. Jackson, W.J., Morris, J.C., in *Liquid-Crystalline Polymers*, ACS Symp. Ser. 435, 16(1990)
12. Dodds, E.C. et al., *Proc. Roy. Soc., London*, B127, 140(1939)
13. Wadsworth, W.S., Emmons, W.D., *J. Am. Chem. Soc.*, 83, 1733(1961)



AKKARA, et al.

**TITLE:** Synthesis and Characterization of Bioengineered Polymers with Nonlinear Optical Properties.

Joseph A. Akkara, Dr., G. Fischer, Mr., F. Aranda, Mr.,  
D. L. Kaplan, Dr., and D. V. G. L. N. Rao, Dr.

**ABSTRACT:** Bioengineered polymers and copolymers were synthesized from benzidine and para- substituted alkylphenols by horseradish peroxidase - catalyzed reactions in dioxane solutions with different amounts of buffer at pH 7.5. Polymers of different molecular weight were prepared from these solvent buffer solutions. Physical and chemical properties of the polymers were studied to determine functional groups, thermal properties, molecular weights, and nonlinear optical properties. Third-order nonlinear susceptibility  $\chi^{(3)}$  of these bioengineered polymers was measured in solution by degenerate four wave mixing using a frequency doubled Nd:YAG laser with 17 picosecond pulses at 532 nm. The molecular hyperpolarizability ( $\gamma$ ) was obtained from the polymer solution measurements, and the macroscopic value of the pure polymer was calculated.  $\chi^{(3)}$  values of polymers were in the range of  $10^{-9}$  to  $10^{-8}$  esu, and these values were four to six orders larger than those of monomers. Relative magnitude of the electronic and orientational contributions to the nonlinearity was determined by changing the probe polarization from parallel to perpendicular orientation with respect to the pump beams.

**BIOGRAPHY OF PRESENTER:** Joseph A. Akkara

**PRESENT ASSIGNMENT:** Biotechnology Division, Soldier Science Directorate, U. S. Army Natick Research, Development and Engineering Center, Natick, MA 01760-5020

**DEGREES HELD:** B. S., University of Kerala, India, 1958; Ph.D., University of Missouri, 1969.

Synthesis and Characterization of Bioengineered Polymers with  
Nonlinear Optical Properties.

Joseph A. Akkara, Dr., G. Fischer, Mr.\*, F. Aranda, Mr.\*,  
D. L. Kaplan, Dr., and D.V.G.L. N. Rao, Dr\*.

U.S. Army Natick Research Development and Engineering Center,  
Natick, MA 01760-5020.

\*University of Massachusetts,  
Boston, MA 02125.

## INTRODUCTION

This paper describes the synthesis and the determination of nonlinear optical properties of a group of bioengineered polymers. These polymers and copolymers were synthesized from aromatic amine and phenolic compounds by a horseradish peroxidase catalyzed reaction in an organic solvent solution containing buffer, with hydrogen peroxide as the oxidizing agent. Earlier studies have shown that polymers and copolymers of aromatic amines and substituted phenols with high molecular weight could be synthesized by these enzymatic reactions in organic solvents (1). These studies have also shown that reaction rate and the molecular weight of the polymer formed could be controlled by the amount of solvent in the reaction mixture. In addition, functional groups and thermal properties of these polymers and copolymers were also studied and are reported here.

Conjugated, one-dimensional  $\pi$ -electron delocalization associated with  $\pi$ -orbital overlap along linear, conjugated organic materials is suitable for third-order susceptibilities; whereas noncentrosymmetric charge transfer complexes with hydrogen bonds have high second-order nonlinear optical properties (2-6). Conducting conjugated polymers with very fast nonlinear responses should have low absorption loss i.e., transparent in selected regions of the optical spectrum. Low loss, and strong and fast response are some of the molecular requirements of nonlinear optical polymers.

In general, polymers with high third-order nonlinear optical properties are of interest for the following reasons: ultrafast and wide frequency response range, molecular structure adaptability, and high laser damage thresholds. Polymers have the well known fabrication advantages including molding and fiber forming by injection and extrusion, and thin-film fabrication by spin-coating or plasma deposition for possible applications in optical and electrooptical devices. In addition many of these polymers are compatible with a number of electronic and photo-electronic materials.



## MATERIALS AND METHODS

### Materials:

Horseradish peroxidase (Type II, 150-200 units/mg solid), hydrogen peroxide and buffers were purchased from Sigma Chemical Company (St. Louis, MO). Benzidine and alkyl substituted phenols were purchased from Aldrich Chemical Company (Milwaukee, WI). Solvents used were high performance liquid chromatography (HPLC) grade and were purchased from Caledon Laboratories (Ontario, Canada).

### Methods:

**Synthesis of Polymers:** We synthesized polymers and copolymers from benzidine and para-substituted alkylphenols by horseradish peroxidase catalyzed reaction in a solvent 1,4-dioxane with HEPES (N-[2-hydroxyethyl]-piperazine-N'-[ethanesulfonic acid]) buffer (0.1 M, pH 7.5) in the ratio of 85:15 (v/v). The synthesis was terminated after 18 hours incubation at room temperature. The polymer was isolated by centrifugation, washed twice with water followed by the solvent solution used for the synthesis of the polymer to remove residual buffer, enzyme, untreated monomers and low molecular weight oligomers. The prepared polymers and copolymers were air dried under vacuum. Figure 1 is a schematic of the experiment. Other details for the synthesis of these polymers and copolymers were described earlier (1).

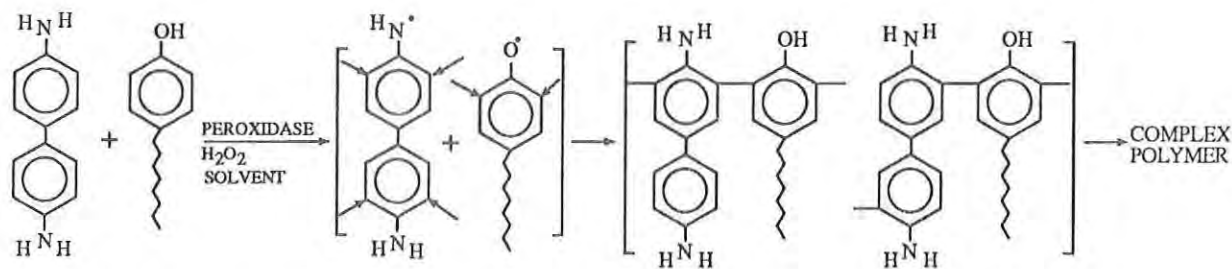


Figure 1. Schematic of the reaction for the synthesis of bioengineered polybenzidine with possible molecular structures of the polymers formed.

**Determination of Nonlinear Optical Properties:** Third-order nonlinear optical susceptibilities ( $\chi^{(3)}$ ) of the bioengineered polymers in solution were determined by two independent techniques - degenerate four wave mixing (DFWM) and self focusing - and the results obtained were compared. The polymer and copolymer solutions were prepared in a solvent mixture of dimethyl formamide and methanol in the ratio 4:1 (v/v) (DMF:MeOH 4:1) and at a concentration of 0.1% (w/v) for the DFWM

experiments. The solvent mixture DMF:MeOH (4:1) was used as a control.

Degenerate four wave mixing technique uses two intense counter propagating radiation fields interacting with a third probe beam in a polymer solution to produce the nonlinear polarization, which in turn produces a fourth beam (conjugate beam) parallel and opposite to the probe beam. The intensity of the conjugate beam is measured to determine the nonlinear susceptibility of the polymer solution. In this experiment a Quantel Nd:YAG laser of 1064 nm wavelength with a frequency doubled second harmonic generator crystal produced the radiation field. The vertically polarized output from the laser (a 17 picosecond pulse laser beam with an average energy of 25 mJ) at 532 nm was split into three beams, which overlapped (temporally and spatially) in the polymer solution contained in a cuvette. A silicon photodiode detector measured the intensity of the conjugate beam produced. Measurements under identical conditions with carbon disulfide as the reference standard reported a  $\chi^{(3)}$  value of  $6.8 \times 10^{-13}$  esu (7). Figure 2 is a schematic of the experimental arrangement. Other details of the DFWM technique and the theoretical calculations used for the determination of  $\chi^{(3)}$  of solutions appear in earlier descriptions (8).

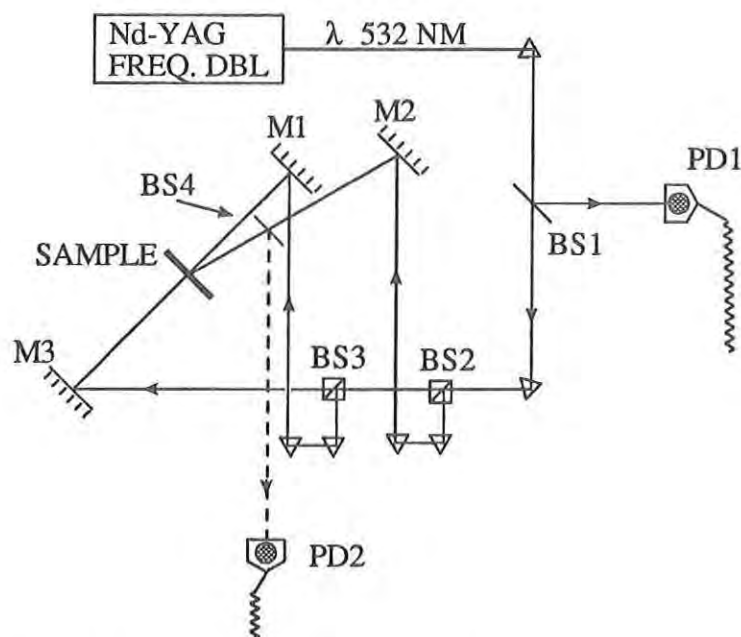


Figure 2. Schematic of the degenerate four wave mixing experiment. M1, M2, M3 - Mirrors; BS1, BS2, BS3, BS4, - Beam Splitters; PD1, PD2 - Photodiode Detectors.

The basis of self-focusing experiments for the measurement of  $\chi^{(3)}$  of polymer solutions is the optical field-induced refractive index changes with the intensity of the

light. The primary physical mechanism responsible for the field-induced refractive index changes is molecular reorientation and distortion of the electron clouds of the polymers in the solution. A laser beam pulse at a wavelength of 694 nm (width of 25 nanoseconds) from a single-mode ruby laser passively Q-switched with cryptocyanine in a methanol solution is used for the experiment. A pinhole with a diameter of 0.775 mm was introduced in front of the sample cell to ensure maximum spatial homogeneity of the laser beam. By studying the beam diameter at the exit end, we determined the threshold power for the onset of self-focusing as a function of incident power. The error in the absolute power of the laser is in the range of  $\pm 10\%$ , but relative values are more accurate. The schematic of the experimental setup is Figure 3. Other details of the experimental approach and the theoretical calculations used for the determination of  $\chi^{(3)}$  of polymers in solutions are in earlier descriptions (9,10).

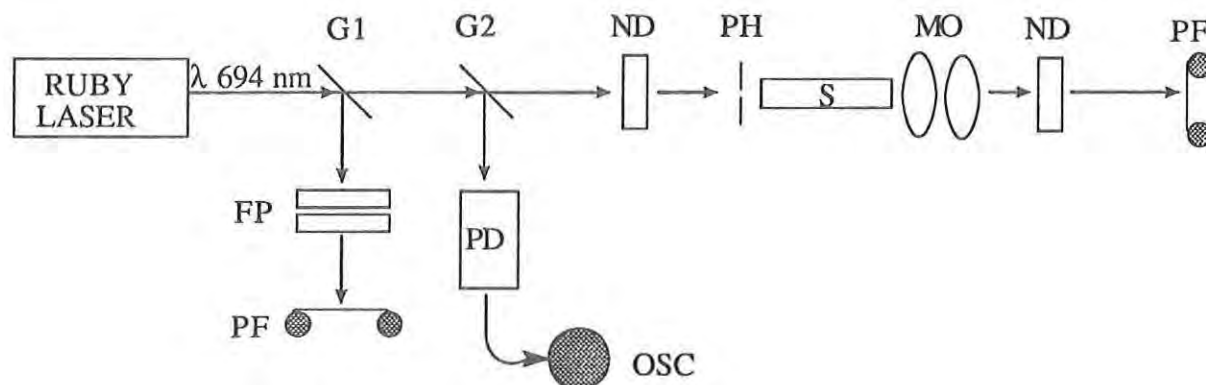


Figure 3 Experimental set up for self-focusing technique to determine  $\chi^{(3)}$  values.  
**G1, G2** - Beam Splitters; **ND** - Neutral Density Filters; **PH** - Pinhole Filter;  
**S.** - Sample Cell; **MO.** - Microscope Objective; **PF.** - Polaroid Film; **FP** - Fabry-Perot Interferometer; **PD** - Photodiode Detector; **OSC** - Oscilloscope

**UV/VIS Spectrum:** The UV/VIS spectra of the polymers (between 250 to 800 nm) were determined using a Spectrophotometer with a photodiode detector (Model DU 7500, Beckman Instruments Inc., Fullerton, CA)

## RESULTS AND DISCUSSION

Tables 1 and 2 show the  $\chi^{(3)}$  values of benzidine, para-phenylphenol, their polymers and copolymers, in a solvent mixture of DMF:MeOH (4:1) at a concentration of 0.1 % (w/v). Copolymers were prepared from benzidine and para- substituted

phenols in the ratio 1:1 and 1:2 and their nonlinear optical properties are reported in Tables 1 and 2, respectively. Nonlinear optical values of polymers were four to six orders of magnitude higher than the values obtained with monomers.  $\chi^{(3)}$  values of polymers and copolymers with a  $\pi$ -electron-delocalized carbon side chain had lower  $\chi^{(3)}$  values when compared with polymers and copolymers with alkyl side chains. Earlier studies had shown that conjugated, one-dimensional  $\pi$ -electron delocalization that is associated with  $\pi$ -orbital overlap along linear conjugated organic materials is suitable for fast third-order nonlinear susceptibilities. Our results indicate that conjugated organic materials with conjugated  $\pi$ -electron delocalization have significant  $\chi^{(3)}$  values (see Figure 1 for the structure of polymers synthesized). In addition, we have also observed that third-order nonlinear susceptibilities are decreased by the presence of  $\pi$ -electron delocalization in the side chain of these polymers and copolymers.

Table 1.  $\chi^3$  Values of polymers and copolymers by degenerate four wave mixing technique.

| POLYMERS                              | $\chi^3 (10^{-11})$ (esu) |
|---------------------------------------|---------------------------|
| Benzidine                             | 0.001                     |
| Polybenzidine                         | 1000.0                    |
| Poly(p-phenylphenol)                  | 2.5                       |
| Copolybenzidine-(p-phenylphenol)(1:1) | 305.0                     |
| Copolybenzidine-(p-ethylphenol)(1:1)  | 690.0                     |
| Copolybenzidine-(p-butylphenol)(1:1)  | 670.0                     |
| Copolybenzidine-(p-octylphenol)(1:1)  | 680.0                     |
| Copolybenzidine-(p-nonylphenol)(1:1)  | 410.0                     |

Table 2.  $\chi^3$  Values of polymers and copolymers by degenerate four wave mixing technique

| POLYMERS                              | $\chi^3 (10^{-11})$ (esu) |
|---------------------------------------|---------------------------|
| Benzidine                             | 0.001                     |
| Polybenzidine                         | 1000.0                    |
| Poly(p-phenylphenol)                  | 2.5                       |
| Copolybenzidine-(p-phenylphenol)(1:2) | 81.2                      |
| Copolybenzidine-(p-ethylphenol)(1:2)  | 158.0                     |
| Copolybenzidine-(p-butylphenol)(1:2)  | 125.0                     |
| Copolybenzidine-(p-nonylphenol)(1:2)  | 93.0                      |

Figures 4 and 5 show the UV/VIS spectra (in the range of 200 to 800 nm) of benzidine, polybenzidine and copolybenzidine-(p-ethylphenol)(1:1). There was a shift in the spectrum of benzidine to the visible range after polymerization of benzidine. The polymer solution had some optical absorption at 532 nm, the wavelength where the  $\chi^{(3)}$  determination was carried out. This optical absorption was decreased with the copolymer solutions of benzidine with alkyl phenols, thus decreasing the resonance contributions to  $\chi^{(3)}$  values (see Figure 5).

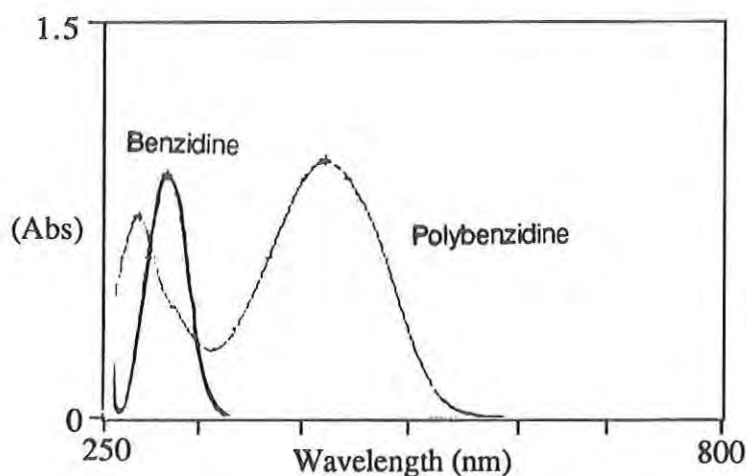


Figure 4. UV/VIS Spectra of benzidine and polybenzidine.

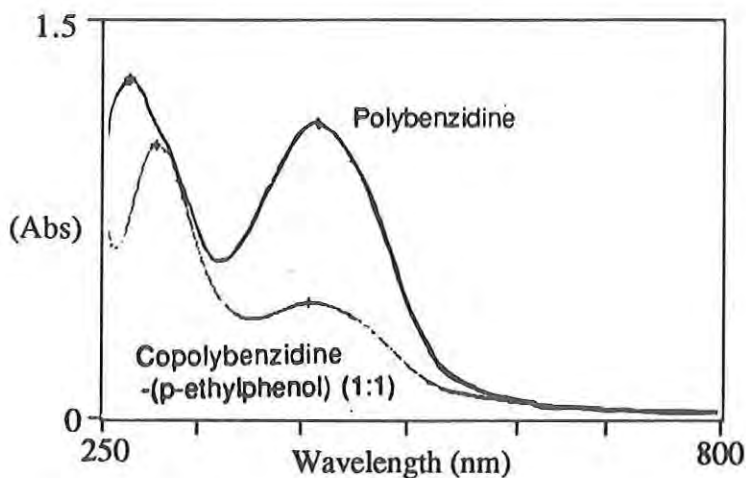


Figure 5. UV/VIS Spectra of polybenzidine and copolybenzidine(p-ethylphenol).



The time-resolved response of the polybenzidine solution is studied by observing the phase conjugate signal as a function of delay of the probe pulse with respect to the pump pulse to determine the relative contributions of the electronic and non-electronic nonlinear components to the  $\chi^{(3)}$  values of this polymer. This response was compared to that obtained with carbon disulfide reference (Figure 6). The results indicate that the dominant component, due to electronic nonlinearity, decays fast in a few picoseconds. In addition there is a slow component in the decay part of the spectrum and the origin of this may be due thermal, nuclear orientation or other related phenomena.

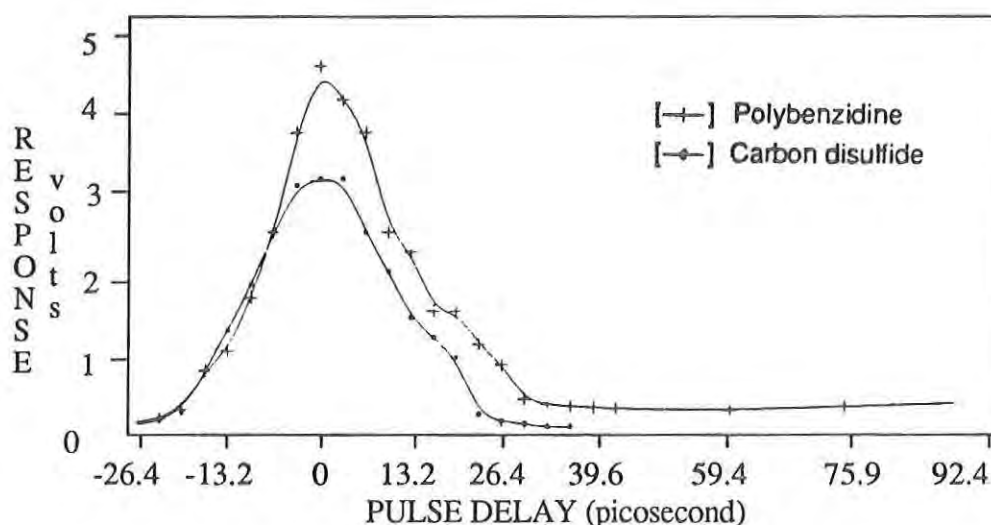


Figure 6. Time-resolved response of the polybenzidine solution with picosecond laser pulse at 532 nm.

Self-focusing experiments in bioengineered polymers were carried out to confirm the resonance contributions to  $\chi^{(3)}$  values of polybenzidine and copolymer of benzidine with substituted phenols. These experiments were carried out using a ruby laser at a wavelength of 694 nm. At this wavelength the bioengineered polymers were optically transparent. Experiments were carried out with sample cells of lengths 5, 10, 15, and 19 cm containing the polymer solution and the self-focusing threshold power was determined by studying the beam diameter at the exit end as a function of the incident power. The  $\chi^{(3)}$  values obtained by this method are given in Table 3. These values (measured at 694 nm) were lower than those obtained by degenerate four wave mixing technique carried out at 532 nm, indicating some contribution to the nonlinear optical properties when the measurements were carried out at 532 nm.

Table 3.  $\chi^3$  Values of polymers and copolymers by self-focusing technique.

| POLYMERS                              | $\chi^3 (10^{-11})$ (esu) |
|---------------------------------------|---------------------------|
| Polybenzidine                         | 160.0                     |
| Poly(p-phenylphenol)                  | low                       |
| Copolybenzidine-(p-phenylphenol)(1:1) | 220.0                     |
| Copolybenzidine-(p-butylphenol)(1:1)  | 140.0                     |
| Copolybenzidine-(p-octylphenol)(1:1)  | 68.0                      |

In summary, we synthesized and evaluated bioengineered polymers for third-order nonlinear optical properties and these values varied from  $1 \times 10^{-8}$  to  $1 \times 10^{-11}$  esu. We determined  $\chi^{(3)}$  values by two independent techniques and the values obtained with degenerate four wave mixing technique at 532 nm were higher than those obtained by the self-focusing technique at 694 nm. Based on the time-resolved nonlinear optical response of the polymer solutions to the laser pulse delay, we determined that the electronic nonlinearity is the major component of the  $\chi^{(3)}$  values observed. With a picosecond laser pulse, we determined the optical response of the polymers and copolymers in solution to be faster than 14 picoseconds.

## REFERENCES

- 1). J. A. Akkara, K. J. Senecal and D. L. Kaplan, J. Polymer Sci. Polymer Chem. Ed., **29**, 1561 -1574, 1991.
- 2). Y. R. Shen, *in* The Principles of Nonlinear Optics, John Wiley & Sons, New York, 1984
- 3). J. Zyss and D. S. Chemla *in* Nonlinear Optical Properties of Organic Molecules and Crystal, D. S. Chemla and J. Zyss eds., Academic Press, Orlando, Florida, 1987, pp 23-191.
- 4). J. Messier, *in* Nonlinear Optical Effects in Organic Polymers, J. Messier, F. Kajzar, P. Prasad and D. Ulrich, eds., NATO Advanced Science Institute Series E, Vol. 162, 1989, pp 47-60
- 5). P. N. Prasad, Nonlinear Optical Interactions *in* Polymer Thin Films, SPIE Proceedings Vol. 682, Molecular and Polymeric Optoelectronic Materials: Fundamentals and Applications, Washington, DC, 1987, pp 120-124.

AKKARA, et al.

- 6). L. R. Dalton *in* Nonlinear Optical Effects in Organic Polymers, J. Messier, F. Kajzar, P. Prasad and D. Ulrich, eds., NATO Advanced Science Institute Series E, Vol. 162, 1989, pp 123-141.
- 7). N. P. Xuan, J. L. Ferrier, J. Gaxengel and G. Rivoire, Opt. Comm. **51**, 433 1989.
- 8). D. V. G. L. N. Rao, F. J. Aranda, J. F. Roach and D. E. Remy, Appl. Phys. Lett. **58**, 1241-1243 1991.
- 9). D. V. G. L. N. Rao, J. H. Bickford, A. J. Shere and M. Muthukumar, J. Polymer Sci., Part C; Polymer Letters, **28**, 247-252, 1990.
- 10). G. L. Fischer, J. A. Akkara, F. J. Aranda, J. F. Roach, D. L. Kaplan, D. N. Ghosh Roy and D. V. G. L. N. Rao, Self-focusing in bioengineered polymers *in* Proceedings of Symposium on Optical Science and Engineering, Vol. 687, January 1992 (in press).

WILLINGHAM, et al.

**TITLE:** Synthesis of Metallotetrabenzporphyrins Possessing High Third-Order Optical Nonlinearity for Military Laser Eye Protection  
Reginald A. Willingham, Dr., John H. Cornell, Dr., David M. Alabran, Dr., David E. Remy, Dr., Joseph F. Roach, Mr., and Masato Nakashima, Dr.

**ABSTRACT:** . Metallotetrabenzporphyrins and homologs that possess a high degree of third-order optical nonlinearity,  $\chi(3)$ , have been investigated as part of an ongoing effort to develop laser eye protective devices for the soldier.

A series of metallotetrabenzporphyrins and a metallo-tetranaphthoporphyrin were prepared by reaction of the corresponding isoindole derivatives with an aldehyde and a metallic template ion, which is incorporated into the complex. These compounds were evaluated for third-order nonlinear optical susceptibility,  $\chi(3)$ , using a frequency-doubled (532 nm) Nd:YAG laser source and a degenerate four wave mixing technique. The measured  $\chi(3)$  values were in the range  $0.2\text{--}2.8 \times 10^{-8}$  esu, which are among the highest reported to date.

The electronic effect of substituents on the meso-phenyl moieties was also investigated. A plot of Hammett sigma values against  $\chi(3)$  exhibited two linear relations of opposite slopes for positive and negative sigma values, with a minimum at the unsubstituted meso-phenyl complex. The significance of these results is discussed with a view to designing porphyrin-based systems having higher third-order nonlinear optical activity values.

**BIOGRAPHY OF PRESENTER:** Reginald A. Willingham  
**PRESENT ASSIGNMENT:** Research Chemist, Soldier Science Directorate, U.S. Army Natick Research, Development and Engineering Center  
**PAST EXPERIENCE:** Research Chemist, Polymer Research Division, U.S. Army Materials Technology Laboratory, Watertown, MA  
**DEGREES HELD:** B.S. Chemistry, Morehouse College; Ph.D. Chemistry, Texas A&M University

WILLINGHAM, et al.

Synthesis of Metallotetrabenzporphyrins Possessing High Third-Order Optical Nonlinearity for Military Laser Eye Protection

Reginald A. Willingham, Dr., John H. Cornell, Dr., David M. Alabran, Dr., David E. Remy, Dr., Joseph F. Roach, Mr., and Masato Nakashima, Dr.

INTRODUCTION

A new threat to the soldier in the field has emerged through the potential use of tunable laser weapon systems. Laser range finders and target designators are already in use on the modern battlefield. Coherent radiation from laser sources even at low energy levels is capable of inflicting severe damage to the retina of the eye. One mode of protection against such laser threats is the use of nonlinear optical (NLO) media, which permit the transmission of visible light at low intensities but will reversibly block visible and near infrared radiation at intensities harmful to the eye. To be useful, the NLO media must have ultrafast response times.

The interaction of an electric field with a medium produces a separation of charges, resulting in a polarization in the medium. When the applied fields are weak, the induced polarization is linearly dependent on the applied field and the propagation behavior is determined by the linear susceptibility of the material,  $\chi(1)$ . At higher intensities the polarization includes a nonlinear dependence, which becomes increasingly more important, and the susceptibility must be defined by additional terms such as  $\chi(2)$  and  $\chi(3)$ . These terms represent second-order and third-order susceptibilities of the material and are determined by features at the molecular level, including electronic delocalization, molecular structure and overall molecular packing.  $\chi(3)$  is a property of a bulk material.

Enhanced third-order susceptibilities can arise from centrosymmetric and noncentrosymmetric molecular structures possessing extended pi-electron delocalization, such as in the porphyrin ring systems. When these molecules are immobilized in an applied electrical or optical field, third-order nonlinear processes can occur, such as third harmonic generation (THG) and self-focusing. A refractive index property change can result from these third-order nonlinear processes. If the refractive index change is of sufficient magnitude and has an ultrafast response time, an optical limiting effect can be effected as required for eye protection from incident laser irradiation.

This work focuses on the synthesis and measurement of third-order susceptibility,  $\chi(3)$ , of a class of compounds called metallotetrabenzporphyrins (TBP) that have recently demonstrated high  $\chi(3)$  values.<sup>1,2</sup>



## EXPERIMENTAL

The synthetic procedures for the preparation of the zinc tetrabenzoporphyrins and the zinc tetra-1,2-naphthoporphyrin followed standard methodologies reported previously<sup>3,4</sup>. A Varian XL-200 NMR Spectrometer was used for <sup>1</sup>H and <sup>13</sup>C analyses. Infrared spectroscopy was done on a Perkin-Elmer 1420 Ratio Recording Infrared Spectrometer. Mass spectrometry was done on a VG Quattro FAB with a ms/ms quadrupole mass analyzer. Elemental analyses on all compounds were done at Midwest Microlab. The technique of degenerate four-wave mixing (DFWM) with the frequency-doubled (532 nm) Nd:YAG laser source was done as previously described<sup>1,2</sup>.

## RESULTS AND DISCUSSION

A series of zinc tetrabenzoporphyrins (Table 1, Ia.-Ij.) were prepared as outlined in Figure 1. By varying the nature of the aldehyde, several different structural variations were accommodated in the "meso" or R position on the porphyrin ring system. The macrocyclic compound series consisted of aliphatic and aryl substituents at the meso position. One example with substitution on the benzo- portion of the molecule is included (Ib). Macrocycle, Ib, has a fully fluorinated tetrabenzo periphery. In all cases the metal coordinated at the center of the ring is zinc. Zinc tetra-1,2-naphthoporphyrin (II, R=H) was prepared as outlined in Figure 2.

The results of measurement of  $\chi(3)$  for the series of zinc tetrabenz- and a zinc tetranaphthoporphyrin are presented in Table 1. The effect on  $\chi(3)$  of electron delocalization over a larger ring system is shown by comparison of zinc tetrabenzoporphyrin (Ia) with zinc tetra-1,2- naphthoporphyrin (II). The annelation of an additional aromatic ring to the benzoporphyrin base structure has increased  $\chi(3)$  by a factor of three.

The introduction of electron donating groups into the meso-phenyl groups of the zinc tetrabenzoporphyrin series led to a progressive rise in the measured  $\chi(3)$  value as the relative electron donating of the substituent increased. Interestingly, as the electropositive character of the substituent increased, the value of  $\chi(3)$  also increased. These findings are consistent with the fact that greater polarization, whether emanating from electron withdrawal or electron donation, enhances  $\chi(3)$ .

Hammett linear free energy relationships have been traditionally developed to explain combined resonance and inductive effects on the reactivity of substituted aromatic systems. It is interesting to note, as shown in Figure 3, that a linear relationship is observed when  $\chi(3)$  values are plotted against the Hammett sigma constants. The plot shows a

WILLINGHAM, et al.

V-shape composed of two lines of opposite slope depending on whether the substituent is electron withdrawing or donating. As expected, the greater the absolute value of the sigma constant the greater is the polarization, and  $\chi(3)$  is increased proportionately.

Conjugated pi-electron systems such as in the porphyrin macrocycles are important to the manifest of the  $\chi(3)$  property. Apparently, the meso substituents contribute a resonance and inductive effect on the ring conjugated pi-electrons. A linear relationship was obtained when the meso-phenyl substituents' Hammett sigma constant values were plotted versus  $\chi(3)$ . These Hammett sigma constant values are based on combined resonance and inductive contributions of the respective substituents. Steric constraints in the porphyrin ring dictate that the meso-phenyl substituents will be almost orthogonal to the plane of the pi-electron conjugated porphyrinic ring. Thus, the meso substituents probably contribute a predominant inductive effect on the ring with the resonance contribution being a lesser contributor.

#### SUMMARY

A series of zinc tetrabenzoporphyrins and a zinc tetranaphthoporphyrin were synthesized for evaluation by a degenerative four-wave mixing technique. A high degree of third-order optical nonlinearity was found. The measured  $\chi(3)$  values were in the range of  $0.2\text{--}2.8 \times 10^{-8}$  esu, which are among the highest reported to date. The influence of the meso-substituents on the  $\chi(3)$  value was examined in relation to the Hammett sigma constant. Metallo-porphyrins incorporating variations in the ring systems will be prepared and evaluated to explore the impact of molecular design on the magnitude of third-order optical nonlinearity.

#### ACKNOWLEDGMENT

The authors would like to thank Joel Carlson of U.S. Army Natick RD&E Center for the mass spectrometric characterization of all the porphyrins we have reported in this paper.

#### REFERENCES

1. D.V.G.L.N. Rao, F.J. Aranda, J.F. Roach, and D.E. Remy, *Appl. Phys. Lett.*, 58(12), 1241 (1991).
2. S. Guha, K. Kang, P. Porter, J.F. Roach, D.E. Remy, F.J. Aranda, and D.V.G.L.N. Rao, *Optics Lett.*, 17(4), 264 (1992).
3. D.E. Remy, *Tetrahedron Lett.*, 24(14), 145 (1983).
4. D.E. Remy, G.C. Richard, and S.J. Weininger, U.S. Army Natick Technical Report NATICK/TR-87/029, AD A183957 (1987).

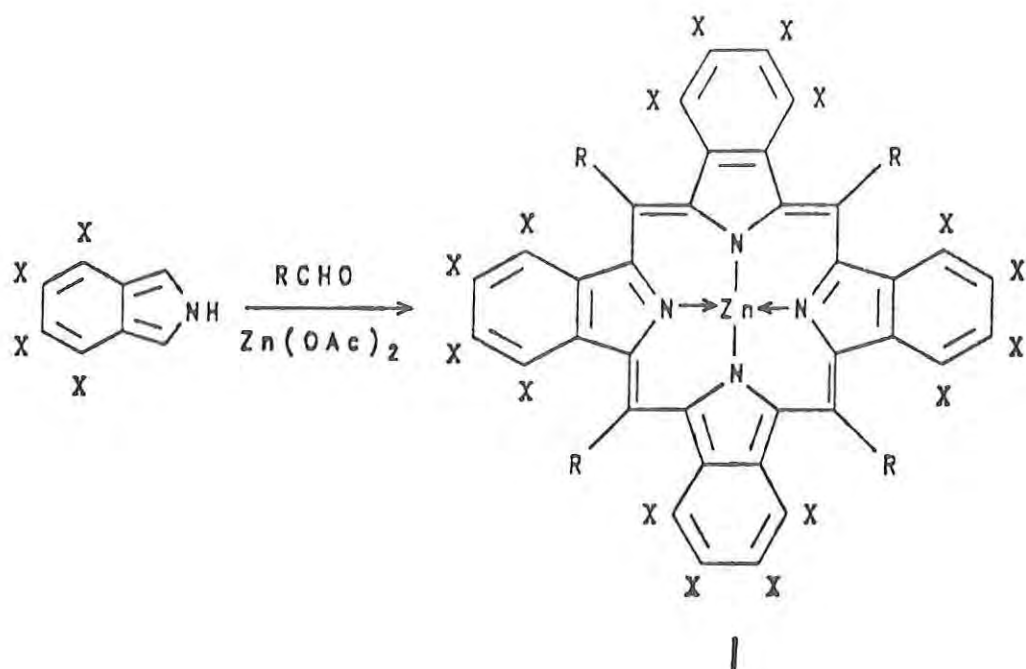


Figure 1  
Preparation of Tetrabenzporphyrins

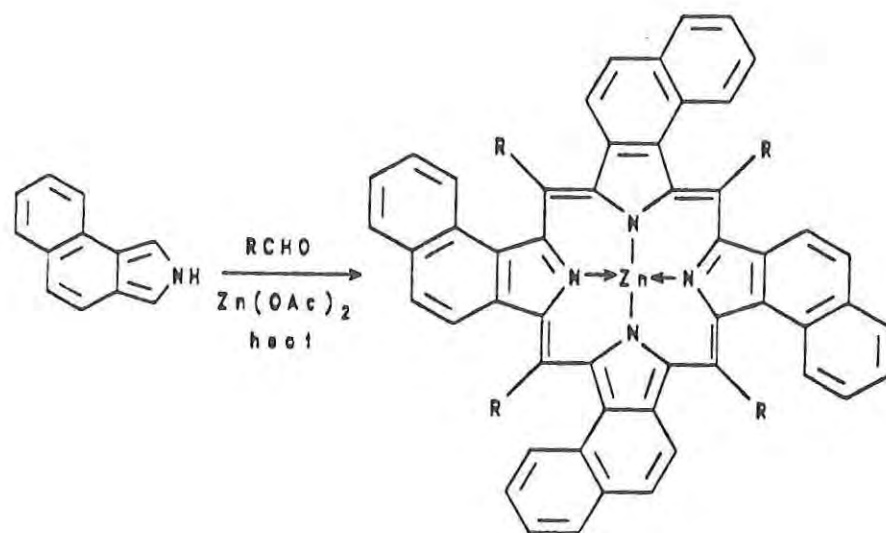


Figure 2  
Preparation of Tetranaphthoporphyrin

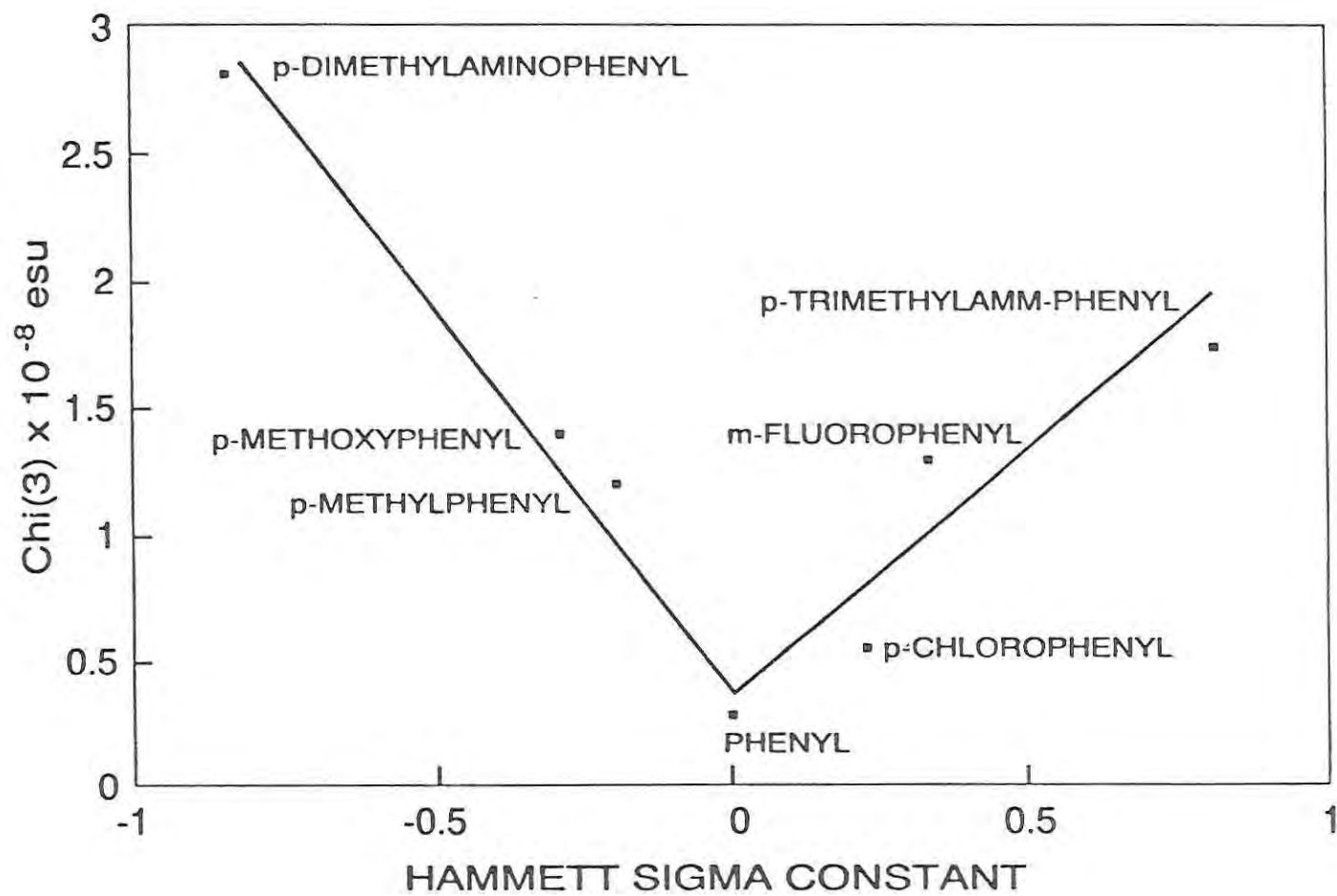


Figure 3  
Hammett Plot of  $\chi(3)$

Table 1. Values of  $\chi(3)$  for Porphyrins

| <u>ZnTBP (I)</u>                       | <u><math>\chi(3) \cdot 10^{-8} \text{esu}</math></u> |
|--|--|
| Ia. R = H, X = H                       | 0.3  |
| Ib. R = H, X = F                       | 0.2  |
| Ic. R = Me, X = H                      | 1.5  |
| Id. R = Ph, X = H                      | 0.3  |
| Ie. R = p-MePh, X = H                  | 1.2  |
| If. R = p-MeOPh, X = H                 | 1.4  |
| Ig. R = p-N(Me) <sub>2</sub> Ph, X = H | 2.8  |
| Ih. R = p-N(Me) <sub>3</sub> Ph, X = H | 1.8  |
| Ii. R = p-ClPh, X = H                  | 0.56   |
| Ij. R = m-FPh, X = H                   | 1.3  |
| <u>ZnTNP (II)</u>                      |  |
| II. R = H                              | 0.99   |



RATTO, et al.

**TITLE: PHASE BEHAVIOR OF CHITOSAN/NYLON-4 BLENDS**

Jo Ann Ratto, Ms., Chien Chung Chen, Mr.,  
Dong Young Kim, Dr., and Rita B. Blumstein, Dr.

**ABSTRACT:** To further enhance the properties of catalytic polymers for chemical agent detoxification, it is important to gain knowledge on the morphology and structure of blends and composites of conventional thermoplastic polymers with naturally occurring macromolecules. We describe here one such system, blends of nylon-4 (poly[imino(1-oxotrimethylene)]), with chitosan (the latter obtained by partial or total N-deacetylation of chitin (1), a naturally occurring linear polymer of acetyl amino-D- glucose). It has recently been observed that blends of chitosan with nylon-4 provide films with good mechanical properties and retain the excellent metal chelating abilities of chitosan that are necessary for catalysis and detoxification of chemical G-agents.

A differential scanning calorimetry (DSC) study was undertaken as part of an attempt to establish some fundamental morphological and structure-property correlations in these blends. In the blends, nylon-4 displays two melting peaks and the enthalpy of melt is linear with composition, indicating that the fraction of amorphous nylon-4 is independent of composition. Compositions containing 60-100% chitosan display two glass transition regions, corresponding to nylon-rich (lower T<sub>g</sub>) and chitosan-rich (higher T<sub>g</sub>) amorphous phases. Dynamic Mechanical Analysis (DMA) and Thermogravimetric Analysis (TGA) experiments were also performed and the results correlate well with the DSC data. All thermal analysis data suggests that water is present and has a significant role in the blends. Other nylon chitosan blends will be discussed and compared to the nylon-4 system.

**BIOGRAPHY OF PRESENTER:** Jo Ann Ratto

**PRESENT ASSIGNMENT:** Research Chemical Engineer, Soldier Science Directorate, U.S. Army Natick Research, Development and Engineering Center

**PAST EXPERIENCE:** Research Engineer, Centred'Etudes Nucleaires de Grenoble, Grenoble, France

**DEGREES HELD:** B.A. Chemistry, College of the Holy Cross; M.S. Plastics Engineering, University of Massachusetts, Lowell

## PHASE BEHAVIOR OF CHITOSAN/NYLON-4 BLENDS

Jo Ann Ratto, Ms.

U. S. Army Natick Research, Development and Engineering Center  
Natick, MA 01760

Chien Chung Chen, Mr., Dong Young Kim, Dr., and Rita B. Blumstein, Dr.  
Polymer Program, Chemistry Department  
University of Massachusetts, Lowell, MA 01854

## INTRODUCTION

Recently, blends of synthetic thermoplastic polymers with naturally occurring macromolecules, in particular cellulose, have been investigated for compatibility, phase behavior, morphology, mechanical properties, permeation, and adsorption properties.(1-4) However, there are very few studies on multicomponent systems involving chitosan.(5,6) Chitosan, a natural biopolymer, is produced by the deacetylation of chitin (a naturally occurring linear polymer of acetylamino- d-glucose), which is extracted from the outer shells of crustaceans and has unique solution, chemical, physical, and bioactive properties.(7) Blends of chitosan exhibit both enhanced permeability and mechanical properties.(8) In particular, chitosan and its blends with nylon provide films with good mechanical properties that retain the excellent metal chelating abilities of chitosan necessary for catalysis and detoxification of chemical agents.(9, 10)

Natural polymers such as chitosan are hydrophilic and water sorbed on these polymers significantly influences the physical properties.(11, 12) Molecular motions of water-polysaccharide systems have been studied by means of nuclear magnetic resonance (NMR), sorption isotherm techniques, dielectric measurements, and thermal analysis.(13, 14, 15)

In this study, we investigate chitosan with regard to its water sorption-desorption properties. In addition, we have studied blends of chitosan with semicrystalline and amorphous nylons by thermal analysis to establish some fundamental structure-property correlations that relate catalytic activity to the blends' morphology and water content.

## EXPERIMENTAL SECTION

### Materials

Chitosan was purified from Pronova B-MV chitosan glutamate, which was supplied by Protan Company. The degree of deacetylation was approximately 80%. The semi-crystalline nylon-4 was supplied by Barson Corporation and the inherent viscosity in 85% formic acid at 30°C was 0.54 dL/g. The amorphous copolymer of caprolactam and lauro lactam (CLL) was supplied by General Motors Research Laboratories. Structures and properties are shown in Figure 1 and Table 1, respectively.(16,17)

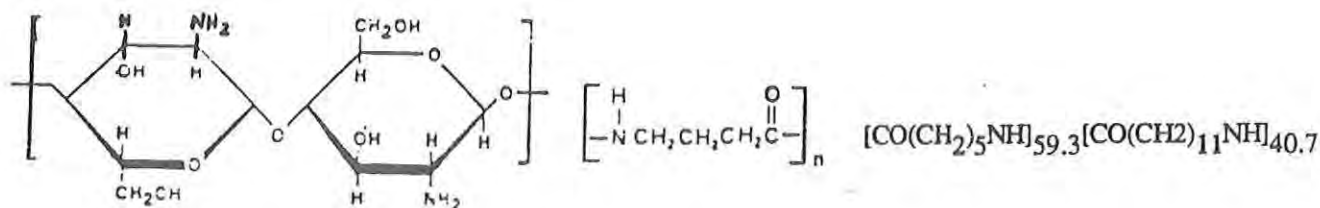


Figure 1. Structures of Chitosan, Nylon-4, and Caprolactam-Laurolactam Copolymer.

Table 1.  
Molecular Weights and Glass Transitions Temperatures (Tg)

|            | Chitosan           | Nylons             |                             |
|------------|--------------------|--------------------|-----------------------------|
|            |                    | Amorphous<br>CLL   | Semi-Crystalline<br>Nylon-4 |
| Mn (g/mol) | $1.45 \times 10^5$ | $24.4 \times 10^4$ | -                           |
| Mw (g/mol) | $2.35 \times 10^5$ | $76.8 \times 10^4$ | -                           |
| Tg (°C)    |                    | 33°C               | 60°C                        |

Films of the pure polymers and blends were cast from 1%(w/vol) solutions in 90% formic acid. The formic acid solutions were stirred for different mix times and then were allowed to evaporate at room temperature. Blends of various compositions ranging from 5-95% weight percent of chitosan were prepared. Some samples were used as formate salts while other films were converted to the neutral form by immersing the film in a bath of 2M sodium hydroxide and by washing with distilled water. The films were dried under vacuum for several days at either 40 or 100°C. Some chitosan samples (salt and neutral) were dried at 130°C under vacuum for several hours and then equilibrated at 59% humidity. The thickness of the films ranged from 0.02 to 0.08 mm.

### Methods

A Perkin Elmer 2C Differential Scanning Calorimeter (DSC) with a TADS data station and a TA 910 DSC was used to determine the melting, crystallization, and glass transition temperatures of the nylon and chitosan films. Each sample of 4 to 10 milligrams was run at a scanning rate of 20°C/minute in a nitrogen atmosphere. The blends were heated to the melt temperature of the nylon, quenched cooled, and then reheated.

A Dupont 951 Thermogravimetric Analyzer (TGA) with a 1091 Disk Memory Thermal Analyzer was used to obtain weight loss versus temperature graphs at a rate of 20°C/minute from room temperature to 200°C. TGA experiments were also performed isothermally at room temperature after different thermal treatment to obtain information on the sorption-desorption properties of chitosan. This method will be explained further in the results.

Dynamic Mechanical Analysis (DMA) experiments were performed on samples that were dried at 40°C under vacuum, but were exposed to the air during the loading of the sample. The dynamic storage modulus  $E'$ , loss modulus  $E''$ , and mechanical loss tangent ( $\tan \delta = E''/E'$ ) of the blends

RATTO et al.

were analyzed after drying the sample at 100°C or 120°C in the DMA chamber.  $E'$  and  $E''$  respectively represent a measure of energy stored and dissipated per cycle. A Seiko DMS-200 instrument was used with the following conditions: mode of deformation - auto-tension, strain amplitude - 30  $\mu\text{m}$ , base force - 10 g, initial force - 200 g, initial temperature - 150°C, heating rate - 4°C/min, frequency - 1 Hz, sample width - 5.5 mm, clamping distance - 10 mm.

Wide Angle X-ray Diffraction (WAXS) experiments were performed for the chitosan/nylon-4 salt and neutral blends using a Picker 4 circle diffractometer with a Model 210 Technology of Energy Corporation position sensitive proportional counter.

Fourier Transform Infrared Spectroscopy (FTIR) work was performed using the Perkin Elmer FTIR 1600 instrument. All films were scanned from 4000 to 450  $\text{cm}^{-1}$  as a function of temperature (25-180°C) with a heating cell and silver chloride plates. The conditions for the FTIR experiments were: resolution = 2, APOD = strong, mode = ratio, scans = 64.

## RESULTS AND DISCUSSION

### Chitosan

Figure 2 displays the X-ray diffraction pattern for the salt and neutral form of chitosan. Broad reflections are observed in the salt chitosan sample at  $2\theta = 12, 19,$  and  $23$ . The reflection at  $2\theta = 23$  is the most intense. The neutral form has much sharper and more intense reflections than the salt form at  $2\theta = 10, 20,$  and  $22$ . The reflection at  $2\theta = 20$  is over four times more intense than the strongest reflection ( $2\theta = 23$ ) for the salt form. We conclude from this data that the salt form diffraction pattern represents poorly developed crystals while the neutral chitosan diffraction patterns indicates some crystallinity. The X-ray patterns for both forms of chitosan are comparable with the results previously reported by Samuels.(18)

The water desorption characteristics for the salt and neutral chitosan equilibrated at 59% relative humidity are displayed in Figure 3. Figure 3 shows the TGA data that displays the percent water weight loss and the derivative of percent weight loss as a function of temperature. Two types of water are apparent; one which is easily removed (loosely bound), the second which is more difficult to remove (bound). The weight loss at room temperature until 110°C is loosely bound water which is compatible with the crystalline nature of neutral chitosan.(19) The higher temperature weight loss is bound water associated with the polymer. The neutral sample is essentially dehydrated at 110°C and has no apparent weight loss above this temperature. For the salt form, the water desorption is continuous over a broad temperature range (25 to 210°C). DSC curves for these samples which were placed in unsealed pans verifies the loss of water in the same temperature range as the TGA data. Typical TGA data of chitosan salt films dried at 40°C under vacuum is presented in Figure 4. The water loss is in two distinct stages (loosely bound and bound). There is a 13% weight loss of loosely bound water at 57°C and a 5% weight loss at 160°C of bound water. When a sample is thermally treated to 200°C and rerun on TGA, this second peak which we assigned as bound water, does not reappear. We observed from preliminary mass spectra data that water and carbon dioxide are being released almost simultaneously at 125°C and above. We can conclude that this peak cannot be attributed totally to

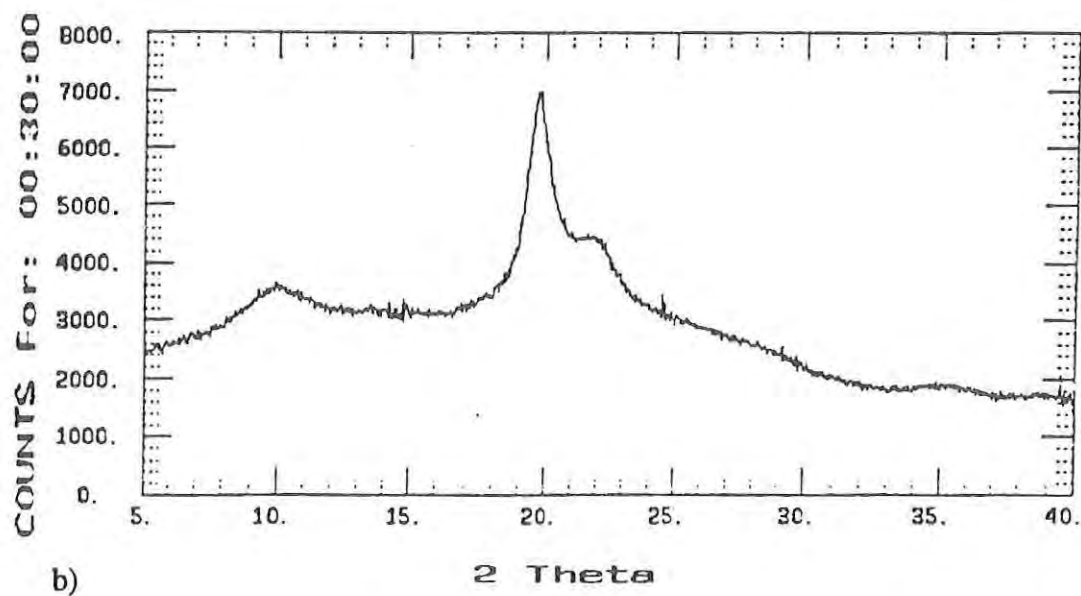
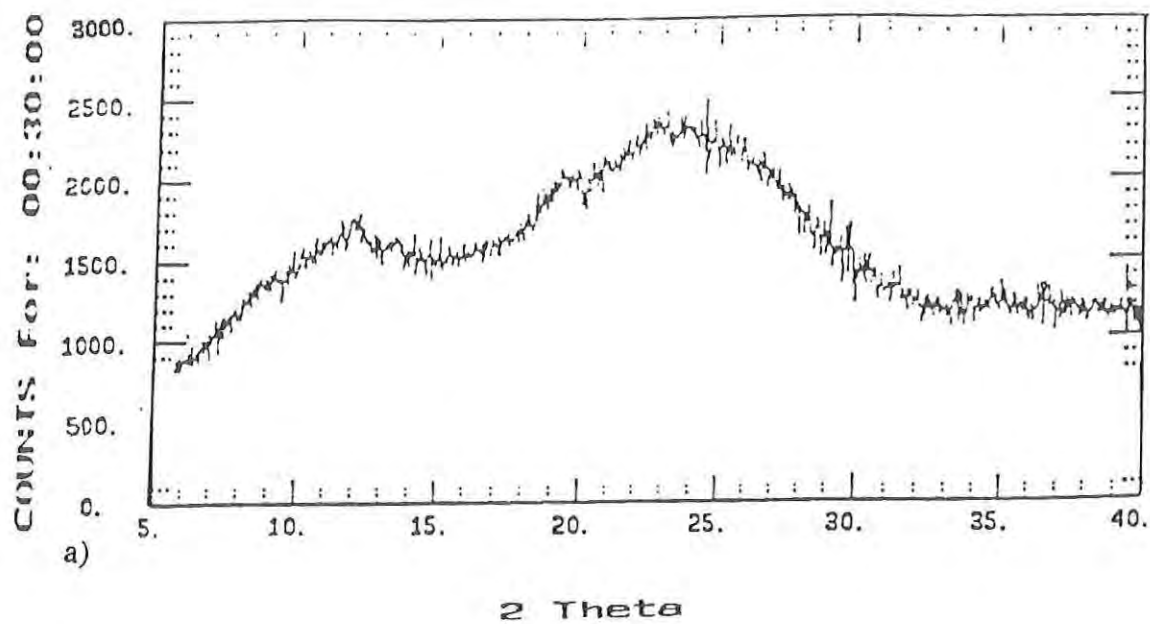


Figure 2. X-ray Diffraction Pattern of Chitosan.  
a.) salt form  
b.) neutral form



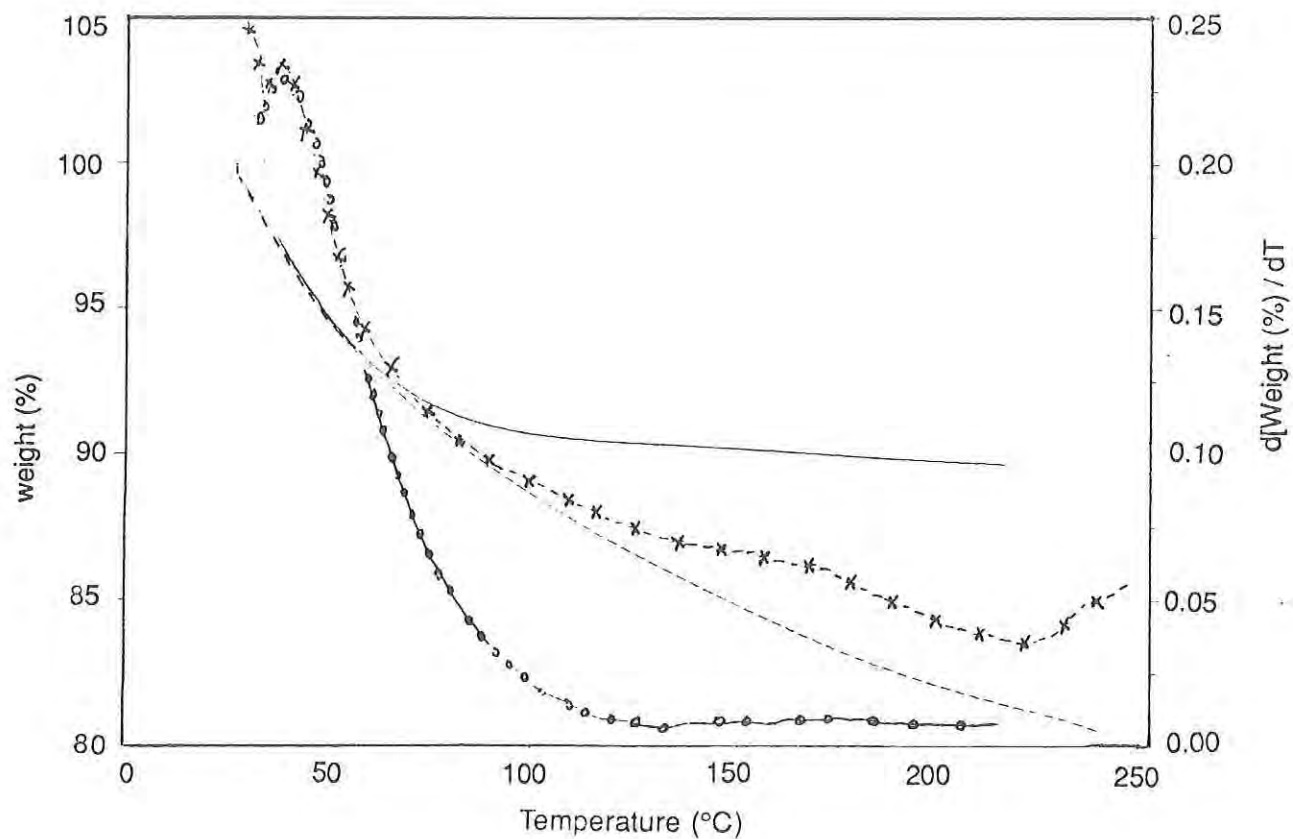


Figure 3. TGA Data For Chitosan Salt and Neutral Form Powders at 59% Humidity.

- neutral form (wt. %)
- neutral form (derivative wt. %)
- - - salt form (wt. %)
- x-x- salt form (derivative wt. %)



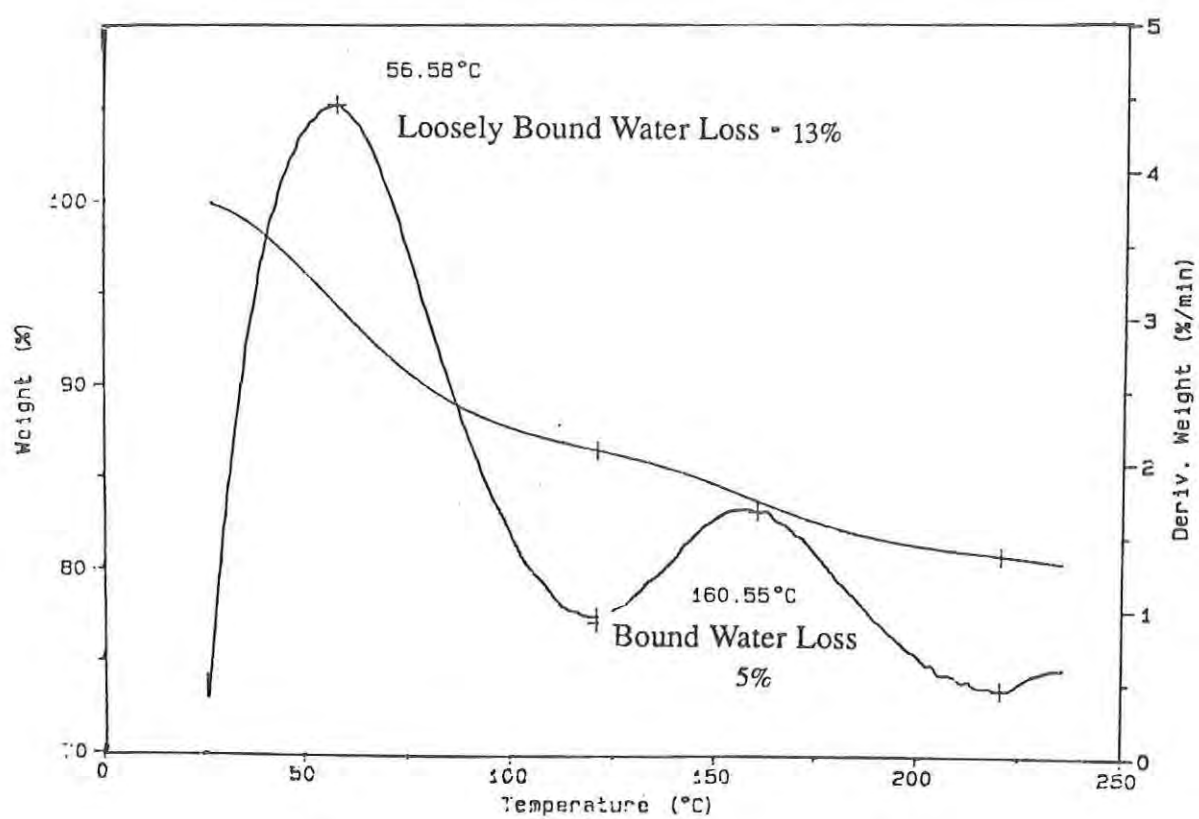


Figure 4. TGA Data of Chitosan Salt Form Dried at 40°C.

bound water; however, further experiments are in progress to confirm this fact.

Since chitosan samples are extremely hydrophilic, it is difficult to obtain a completely dry chitosan. Chitosan exposed to the ambient humidity always contains water. Sorption and desorption properties depend on the sample thermal history as illustrated by the following TGA experiment. Absorption curves presented in Figure 5 were obtained by taking a salt film which was dried at 40°C under vacuum and placed on the TGA microbalance. The sample was heated to 120°C and was held isothermally for 10 minutes and then the weight was recorded at room temperature and ambient humidity for 40 minutes. The same procedure was subsequently followed for another chitosan sample heated to 220°C. Figure 5a shows that within the first 10 minutes, chitosan absorbed 7.8% of water. The value levels off at approximately 13.3% after 30 minutes while the sample weight in Figure 4b has a weight gain of 7.0% after 10 minutes and then levels off at approximately 12%. Since this sample in Figure 5b was heated to 220°C, there is the possibility that some bound water was lost; however, it has absorbed only slightly less water than the sample in Figure 5a. Chemical changes in the samples from heat treatment are possible as was suggested for the data in Figure 4. Overall, the results illustrated in Figures 3, 4, and 5 indicate different permeation properties for different thermal histories. This water loss behavior can promote irreversible changes in morphological structure, permeation, self-association, and other properties.(6)

### Chitosan/Nylon Blends

Representative first heating DSC scans of the salt chitosan/nylon-4 blends dried at different temperatures are shown in Figure 6. In all the scans, melting of nylon-4 appears in the 250-260°C region, which is well above the water loss region and the decomposition temperature (220°C) of chitosan. For the pure nylon-4 sample, the T<sub>g</sub> is not visible on the DSC scans. Nylon-4 decomposes upon melting, therefore subsequent heating scans could not be performed.

Figure 6a shows DSC scans of the chitosan/nylon-4 salt blends dried at 40°C under vacuum. These preliminary DSC results suggested partial miscibility of amorphous regions with two T<sub>g</sub>s, the lower T<sub>g</sub> (50°C) corresponding to a nylon-rich amorphous region.(20) The possibility of a chitosan-rich upper T<sub>g</sub> (130 - 160°) is covered by a water loss endotherm, which limits the interpretation of the DSC data. Also, the lower T<sub>g</sub> may possibly be from water loss or some chitosan transition since this occurs in pure chitosan DSC data. The cold crystallization peak observed at approximately 100°C for the 40/60 and 60/40 samples is only present for the blends dried at 40°C, which is below the T<sub>g</sub> of nylon-4.

Figure 6b displays the scans for salt blends dried at 100°C under vacuum. The possible upper T<sub>g</sub> transition for chitosan in the blends is observed in a temperature region (140-210°C) significantly higher than the blends dried at 40°C under vacuum. At high nylon-4 contents (40-80%) the transition is very broad whereas at low nylon-4 contents and pure chitosan the upper T<sub>g</sub> transition is in a narrow temperature range and more enhanced. As mentioned previously for the data in Figure 6a, no conclusion can be made about the possible T<sub>g</sub>s because of the water loss. There are no visible cold crystallization peaks for these blends; however, the transition at 50°C is present. Multiple melting peaks for the nylon-4 are observed for the salt containing blends that were dried at 100°C. This is frequently associated with partial melting and recrystallization found in semicrystalline polymers.(21) These blends dried at higher temperatures undergo annealing which promotes crystallization and also the removal of water to a degree that is different than at

RATTO et al.

40°C drying.

DSC second heating scans are displayed in Figure 7 for the salt chitosan/CLL blends dried at 40°C under vacuum. Water has been removed from the chitosan/CLL blends upon heating the sample to 180°C and quench cooling the sample in liquid nitrogen before performing a second heating scan. This CLL amorphous nylon blended with the salt form of chitosan allows us to eliminate the effect of crystallinity that exists for the chitosan/nylon-4 system. Cold crystallization peaks are also observed at 70°C in the chitosan/CLL salt blends for the 80/20, 60/40, and 50/50 blends. Although the CLL polymer is essentially amorphous, melting endotherms with a peak maximum at approximately 125°C are observed for concentrations of 20 to 80% CLL. There appears to be a slight downward shift in the CLL Tg (35-30°C) for the chitosan/CLL blends as a function of increasing chitosan concentration. A possible explanation for this variable shift of the Tg is that the pure CLL has plasticized with residual water.

Although the DSC data could not conclude about the miscibility of the blends, the DMA data can confirm miscibility in the chitosan/nylon-4 blends. Table 2 displays the temperature of the peak maximum for the E'' and tan  $\delta$  for the wet and dry neutral samples. Dry samples were predried at 40°C under vacuum followed by an additional dry step at 100°C in the DMA chamber. Wet samples were predried at 40°C under vacuum, but then were exposed to ambient humidity in the DMA chamber. We observed that the temperatures of the peak maximum increases for the dry samples. The  $\beta$  transition, also known as the water dispersion for nylons and polysaccharides, appears to be associated with the prescence of water-polymer complexes and this transition's intensity increases with increasing moisture contents. (22) For these samples, the  $\beta$  transition has shifted to higher temperatures and has become a much weaker absorption indicating that there has been the removal of water. The Tg is referred to as the  $\alpha$  transition and is characterized by a large decrease in E' and a maximum in both the E'' and tan  $\delta$  curves near the inflection point of E'. The Tg of the blends is somewhat higher than the pure nylon-4, indicating partial miscibility.

Table 2.  
DMA Data for Neutral Chitosan/Nylon-4 Blends

| %Chitosan/Nylon-4 | E'' Peak Maximum (°C) |            | Tan $\delta$ Peak Maximum (°C) |            |
|-------------------|-----------------------|------------|--------------------------------|------------|
|                   | <u>Wet</u>            | <u>Dry</u> | <u>Wet</u>                     | <u>Dry</u> |
| 90/10             | 94                    | 109        | 106                            | 116        |
| 60/40             | 89                    | 126        | 106                            | 141        |
| 50/50             | 87                    | 103        |                                |            |
| 20/80             | 81                    | 87         | 109                            | 131        |
| 10/90             | 83                    | 87         | 107                            | 114        |
| 0/100             | 84                    | 86         |                                | 93         |

In the literature, there has been some disagreement involving the Tg of neutral chitosan. Ogura suggests that there is a Tg of dry chitosan at 140°C, which was obtained from DMA data (23). Recently, Pizzoli concluded from DMA and dielectric data that there was no certainty of a chitosan Tg because there is only a weak intensity peak and not a significant modulus drop in that region.(24) Kayim has investigated chitosan by thermomechanical analysis and found a Tg at -

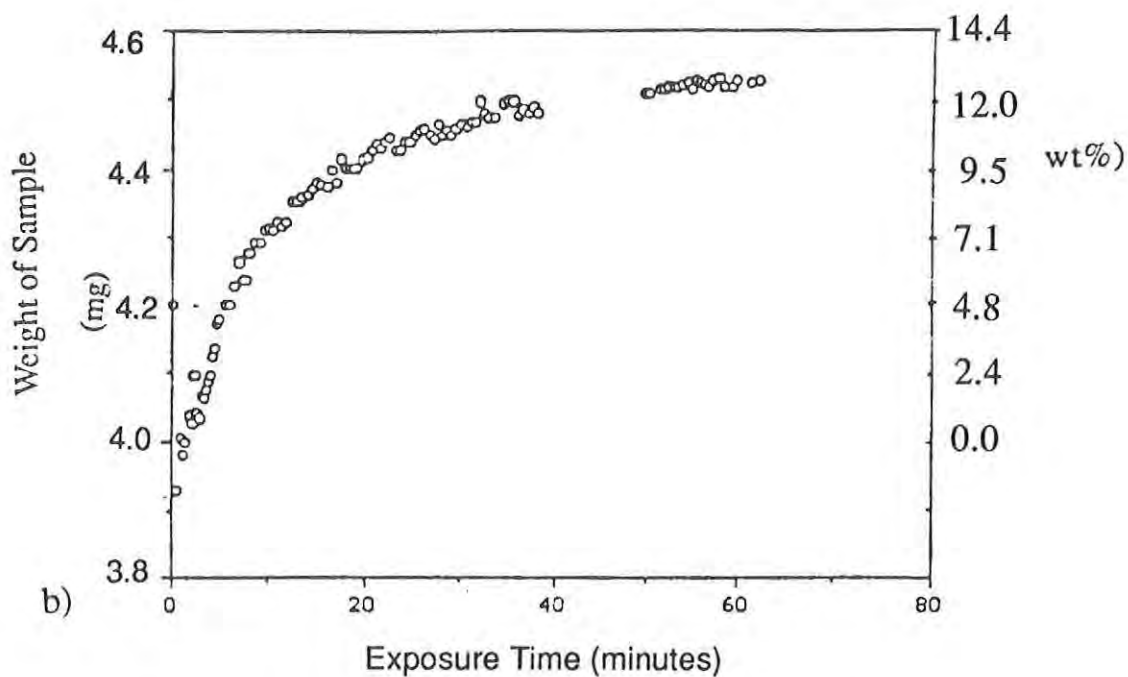
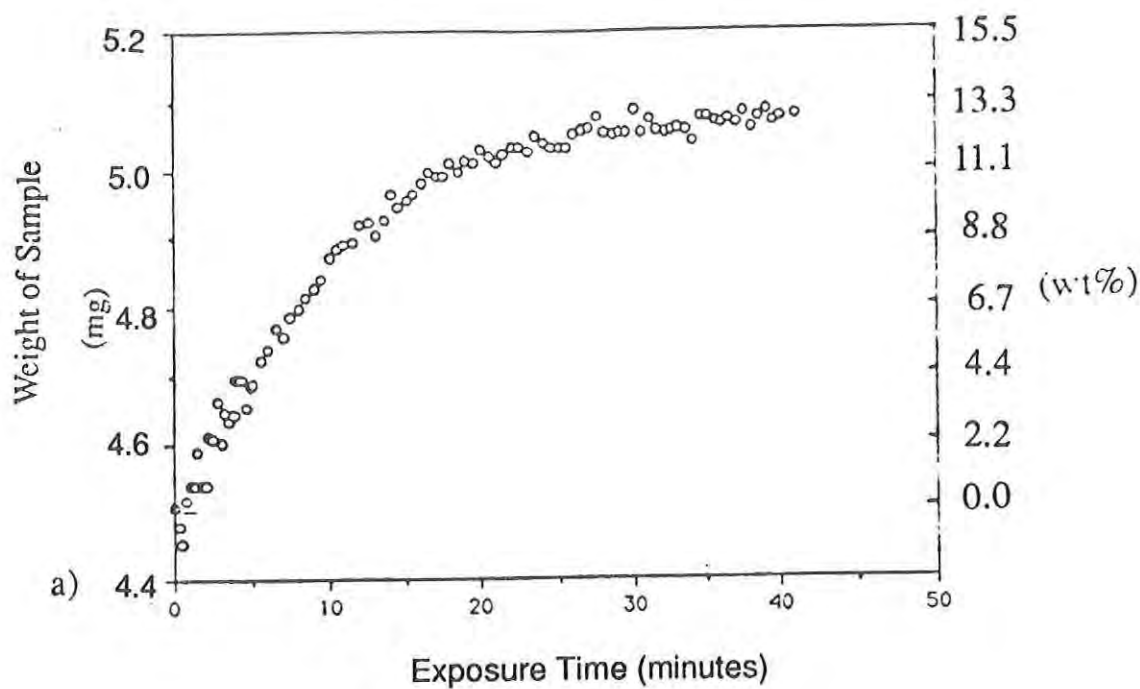


Figure 5. TGA Adsorption Curves of Chitosan (Salt Form)

a.) Heated to 120°C and exposed to air

b.) Heated to 220°C and exposed to air

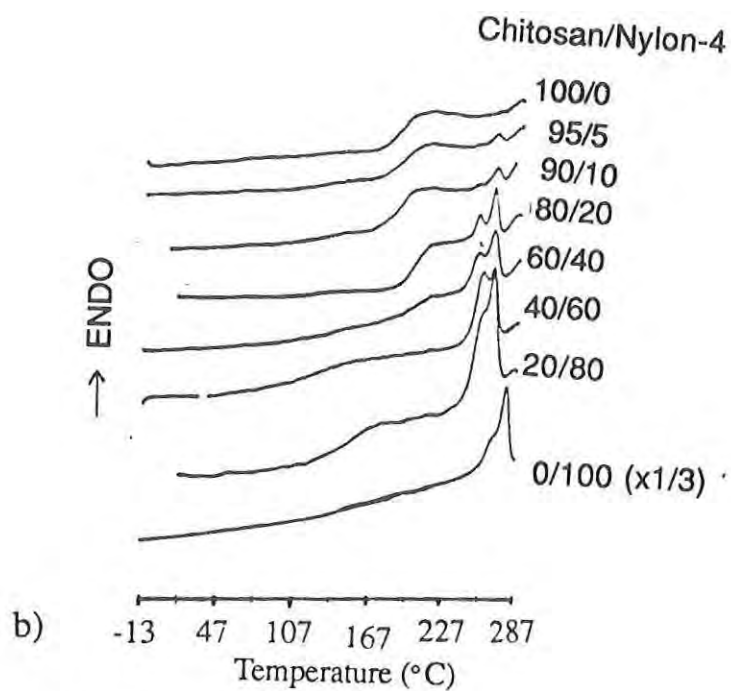
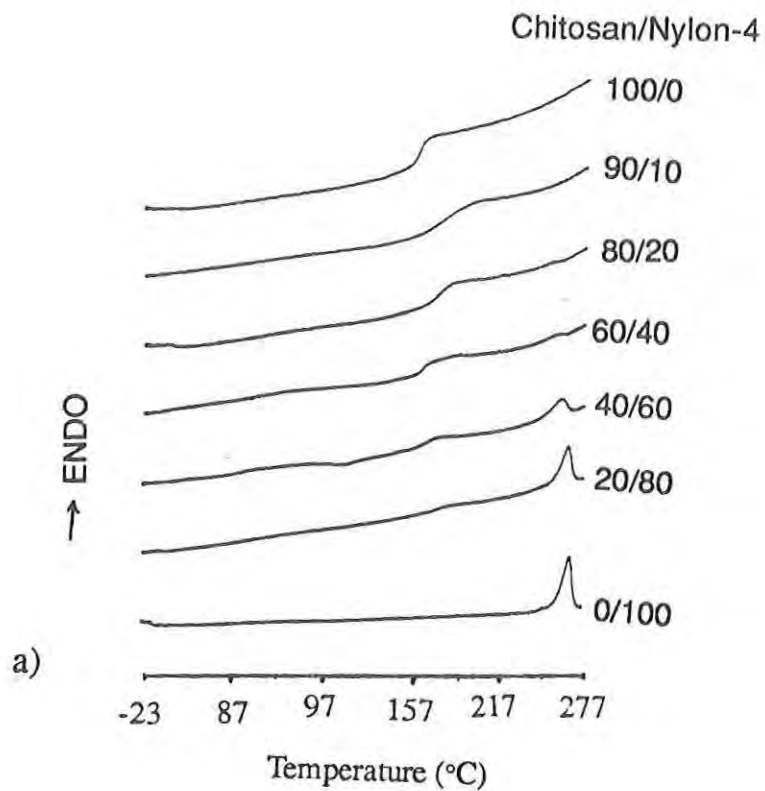


Figure 6. DSC Data of Chitosan/Nylon-4 Blends.  
 a.) Salt form dried at 40°C.  
 b.) Salt form dried at 100°C

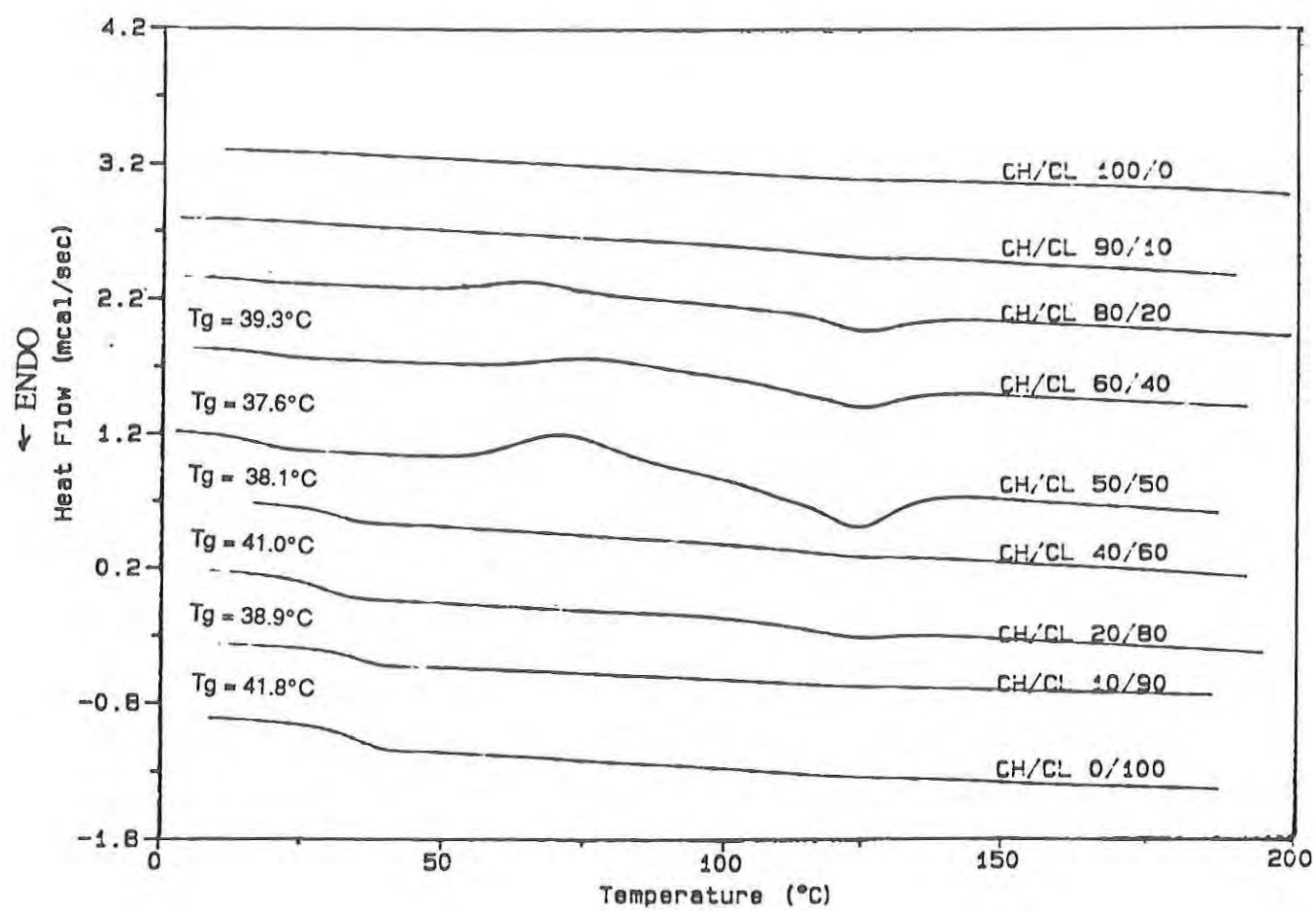


Figure 7. DSC of Salt Form Chitosan/CLL Blends



23°C (25). DMA data of a wet sample of neutral chitosan is found in Figure 8. This film was soaked in water before the DMA experiment was performed. There is a peak for  $E''$  and  $\tan \delta$  at approximately -105°C corresponding to the  $\gamma$  transition associated with end group rotations, crystalline defects, backbone chain motion of short segments, and/or phase separation of impurities. At approximately -45°C, we conclude that there is a  $\beta$  transition from water relaxation since Bradley and Carr have observed this  $\beta$  transition in several polysaccharides in the vicinity of -50°C. (26) The intense peaks at 4.7°C and 11.3°C for  $E''$  and  $\tan \delta$  respectively is not water loss, since there is a steep drop of  $E'$  in this temperature region. We speculate that this is a  $T_g$  of chitosan associated with water plasticization. The presence of a  $T_g$  in dry chitosan is under further investigation in our laboratory.

FTIR data does suggest molecular mobility in amorphous regions for neutral chitosan and for the blends. For polyamides, the Amide I peak at 1651  $\text{cm}^{-1}$  is a contribution from the C=O stretching, the C-N stretching, and the C-C-N deformation vibrations. As the temperature increases there is a shift to higher frequency. The Amide II peak at 1560  $\text{cm}^{-1}$  is a contribution from the N-H plane bending, C-N stretching, and the C-C stretching vibrations. This peak will decrease in frequency as the temperature increases. We notice from FTIR data the evolution of the Amide I peak and Amide II band region as a function of temperature, as shown in the data of Figure 9. Figure 9a shows that the evolution of the Amide bands in nylon-4 follows the usual behavior observed in normal semi-crystalline polyamides. (27) The intensity of the Amide I peak increases at temperatures above 140°C. In chitosan, the broad Amide II band suggests heterogeneity in bonding. There are profound changes in the spectra as a function of temperature suggesting changes in the interactions or rearrangements of the hydroxyl and glucosamine groups. This band changes progressively to several peaks as the temperature increases. The intensity decreased for both Amide peaks as the temperature increased, indicative of changes in the nature of hydrogen bonding and/or the stability of the interactions.

Figure 10 shows the enthalpy of nylon-4 melting versus composition for different preparation conditions for the chitosan/nylon-4 blends. Film preparation parameters included: mix time, dry temperature, salt, and neutral form. The mix time varied from several days to one week. The longer mix times (lm= long mix = one week) and the blends dried at 40°C give a nonlinear enthalpy relationship as a function of chitosan composition that indicates an interaction between the chitosan and nylon-4. Drying the films above the  $T_g$  of nylon-4 as well as mixing the solutions for a short time (12 hours) changes the morphology and interactions between the two polymers.

The blending of chitosan and nylon modifies the morphology and permeation properties depending on the water content. TGA data for the salt chitosan/nylon blends are displayed in Figures 11a and 11b. The total percent of water loss increases as the amount of chitosan increases in the blends. The chitosan/CLL blends contain more water overall since the CLL is amorphous, but the amount of bound water is almost equal to the chitosan/nylon-4 blends. This is observed in the bound water percent weight loss which becomes a constant value in high chitosan concentrations for the chitosan/CLL, but decreases in value for the .8-1.0 weight fraction of chitosan/nylon-4. The data suggest that there are high water contents bound to chitosan. We must note that for the chitosan/CLL blends, all the water is associated with the chitosan whereas in the chitosan/nylon-4 films there is a small portion of water (2.7%) associated with the nylon-4.

In summary, the results have shown how important water and preparation methods are in the investigation of the chitosan blends with the semicrystalline nylon-4 and the amorphous nylon. In

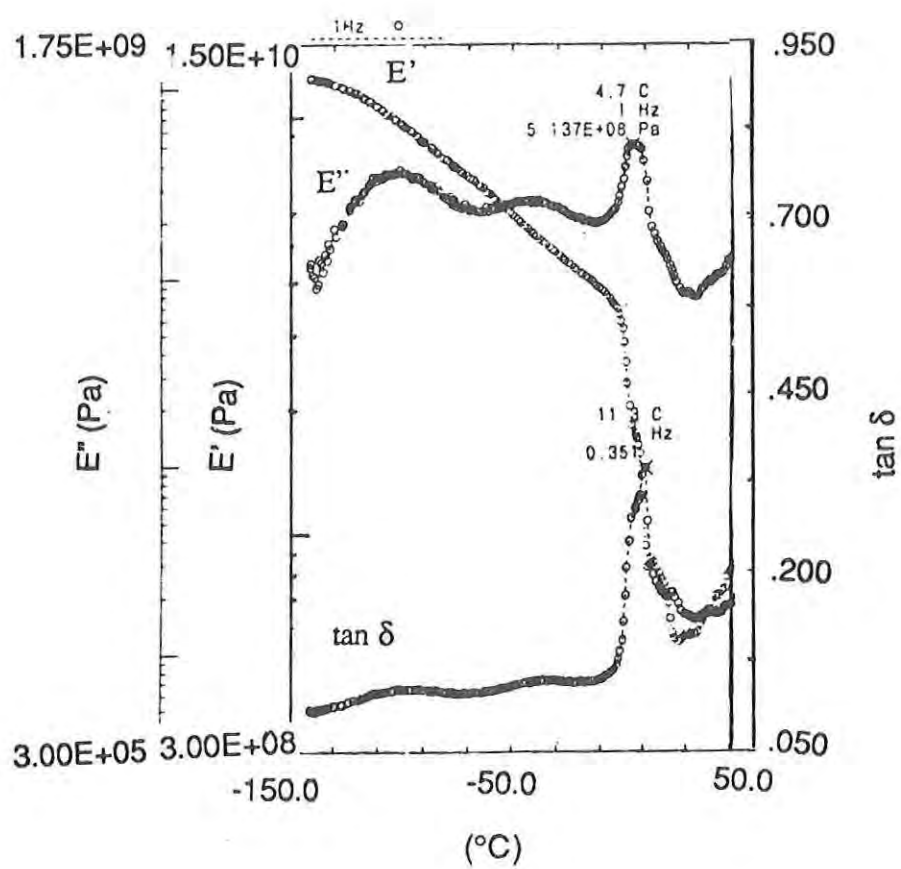


Figure 8. DMA Data for Wet Chitosan (Neutral Form)

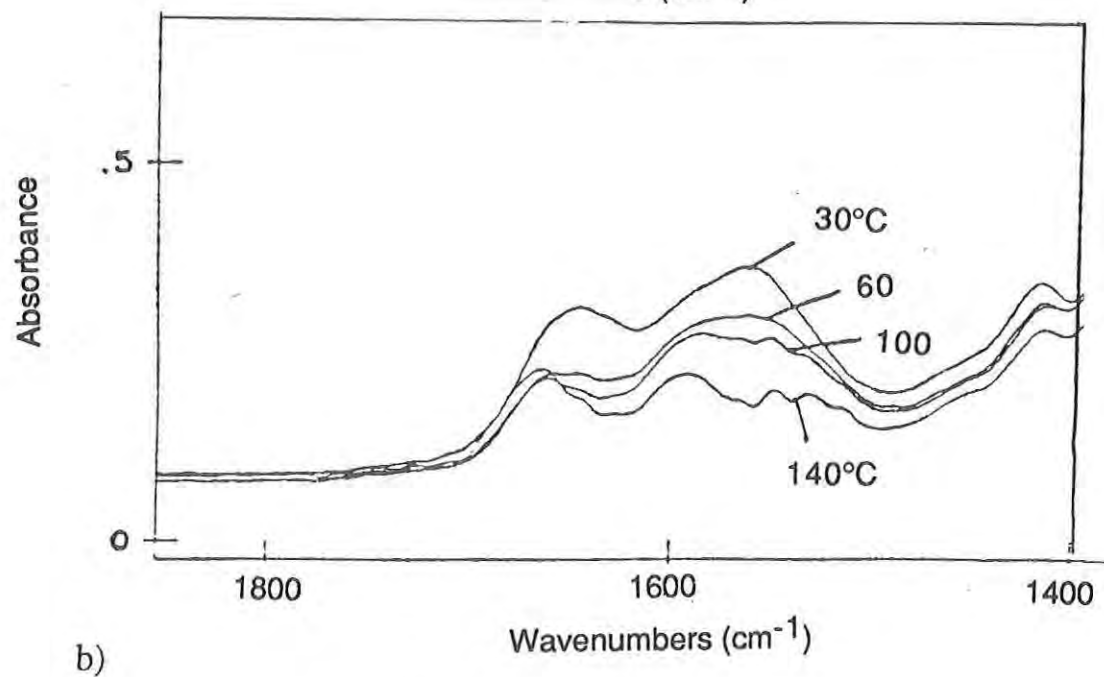
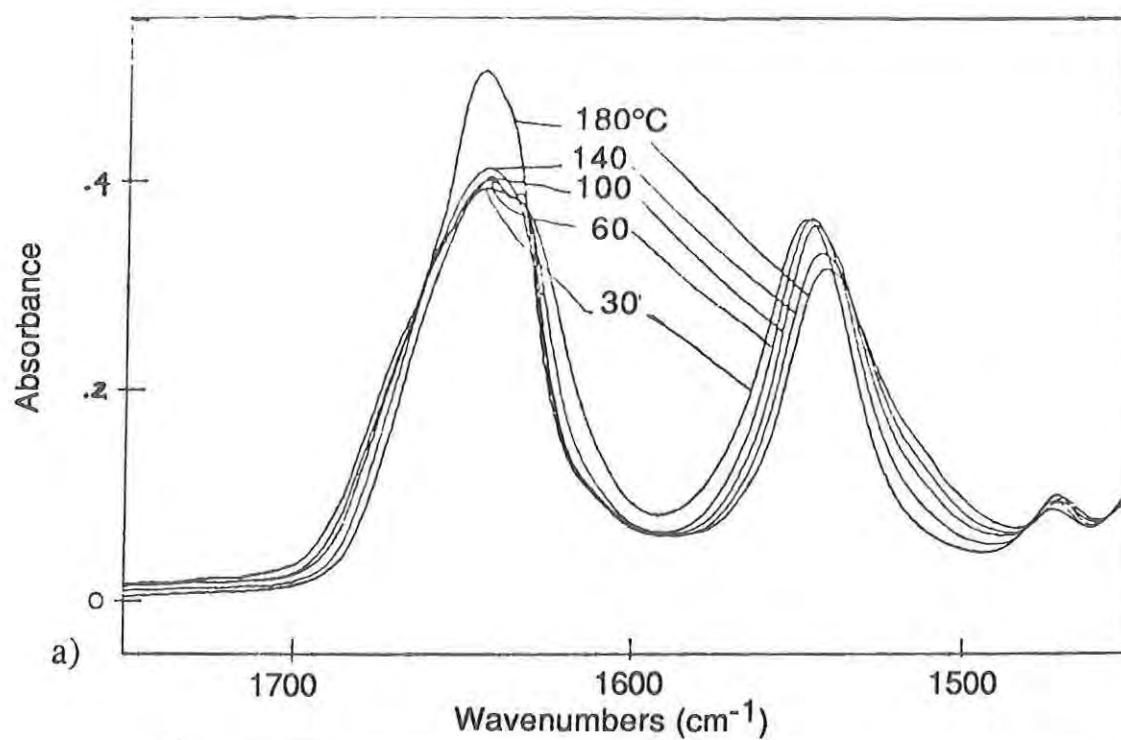


Figure 9. FTIR Data as a Function of Temperature.  
a.) Nylon-4  
b.) Chitosan (Neutral Form)

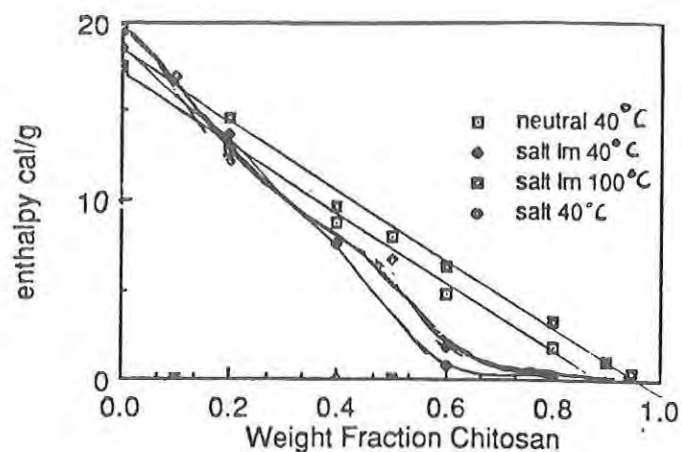


Figure 10. Enthalpy vs Weight Fraction of Chitosan.

- neutral dried 40° under vacuum
- ◆ salt long mix time (1 week) dried at 40° under vacuum
- ◻ salt long mix time (1 week) dried at 100° under vacuum
- salt dried 40° under vacuum

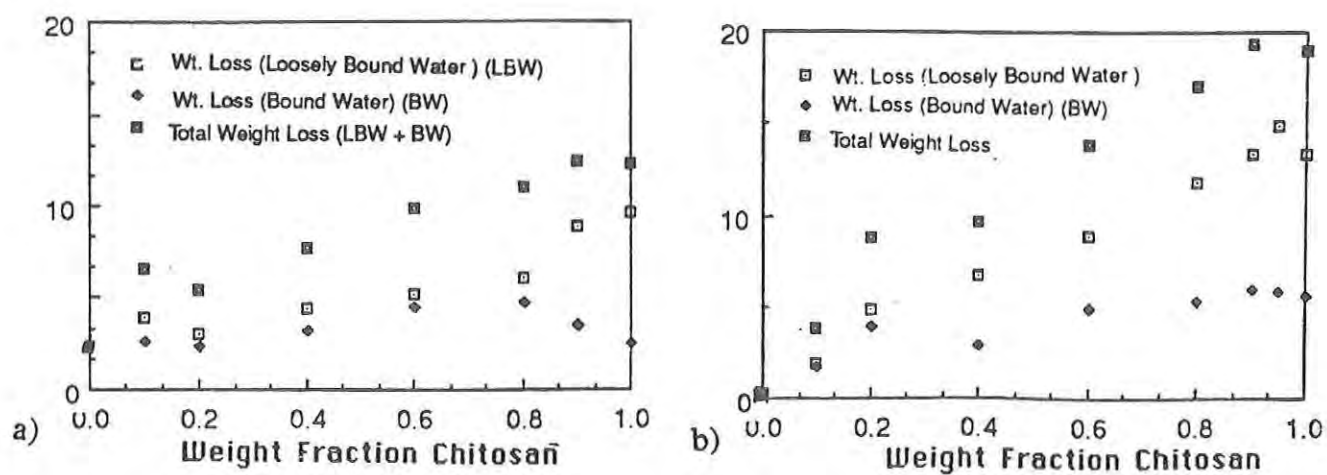


Figure 11. Percent Water Loss vs Weight Fraction Chitosan  
a.) Chitosan/Nylon-4 (Salt Form)  
b.) Chitosan/CLL (Salt Form)

blends exposed to ambient humidity, chitosan binds considerably more water than in the unblended state under the same conditions. The water content in the chitosan and the blends is influenced by the crystal structure of the chitosan (salt versus neutral form). This water absorption may explain the enhanced catalytic reactivity observed for these blends. Understanding why and how the water improves the catalytic activity in these blend systems will lead to better chemical protection for the soldier. Additional thermal experiments and reactivity tests are in progress to confirm these data as well as to complement these findings.

#### ACKNOWLEDGEMENTS

The authors would like to thank Dr. David Remy and Dr. Nathan Schneider for their helpful discussions throughout this research. We are also grateful to Captain Stuart Barlow for assisting with the X-ray experiments.

#### LITERATURE CITED

1. Masson, J. F., St. John Manley, R., *Macromolecules*, 24, 6670 (1991).
2. Nishio, Y., St. John Manley, R., *Polymer Engineering and Science*, 30(2), 71 (1990).
3. Nishio, Y., Haratani, T., Takahashi, T., St. John Manley, R., *Macromolecules*, 22, 2547 (1989).
4. Nishio, Y., St. John Manley, R. *Macromolecules*, 21, 1270 (1988).
5. Miya, M., Iwamoto, R., Mima, S., *J. of Polym. Sci.: Polym. Phys. Ed.*, 22, 1150 (1984).
6. Suzuki, F., Niizeki, H., Sen-I Gakaishi 42, 87 (1986).
7. Muzzarelli, R. A. A., ed., *Chitin in Nature and Technology*. Plenum Press, New York, (1986).
8. Chandy, T., Sharma, C. *J. of Appl. Polym. Sci.*, 44, 2146 (1992).
9. Walker, J., Robbins, F., Andreotti, R., Woodbury, C., Alabran, D., U. S. Army Natick RD&E Center Technical Report, NATICK/TR-91/015L (1990).
10. Peters, E., U. S. Army Natick RD&E Center Technical Report, in preparation.
11. Hatakeyama, T., Nakamura, K., Hatakeyama, H., *Thermochimica Acta*, 123, 153 (1988).
12. Hatakeyama, T., Nakamura, K., Yoshida, H., Hatakeyama, H., *Food Hydrocolloids*, 3, 301 (1989).
13. Hatakeyama, T., Iwata, H., Hatakeyama, H., in *Wood and Cellulosics: Industrial Utilization, Biotechnology, Structure and Properties*. 40 (1987).
14. Scandola, M., Ceccorulli, G., Pizzoli, M. *Int. J. Biol. Macromol.*, 13, 254 (1991).
15. Iwaki, T., Jilinek, H. H. G., *J. Colloid Interface Sci.*, 69, 17 (1979).
16. The molecular weights for chitosan were determined by size exclusion chromatography/light scattering and the experiments were performed by Dr. Rollins at Worcester Polytechnic Institute.
17. Ellis, T. S., *Polymer*, 31, 1059 (1990).
18. Samuels, R. J., *J. of Polym. Sci.*, 18, 1081 (1981).
19. Ogawa, K. *Macromolecules*, 17, 973 (1984).
20. Kim, D. Y., Ratto, J., Blumstein, R., *Polymer Preprints* 32(1), 12 (1991).
21. Todoki, M., Kawaguchi, T., *J. Polym. Sci., Polym. Phys. Ed.*, 15, 1067 (1977).
22. Hiltner, A. *Polymer Engineering and Science*. 19, 723 (1979).
23. Ogura, K., Kanamoto, T., Itoh, M., Miyashiro, H., Tanaka, K., *Polymer Bulletin*. 2, 303 (1980).
24. Pizzoli, M., Ceccorulli, G., Scandola, M., *Carbohydrate Research*, 222, 213 (1991).
25. Kayim, I., Ozolinya, G., Plisko, Y., *Polymer Science U.S.S.R.*, 22, 176 (1980).
26. Bradley, S. A., Carr, S. H. *Journal of Polymer Science: Polymer Physics Edition*, 14, 115 (1976).
27. Skrovanek, D., Howe, S., Painter, P., Coleman, M. *Macromolecules*. 18, 1677 (1985).





TITLE: Fractal Surfaces and Reactivity  
Ronald A. Segars and Louis J. Piscitelle

ABSTRACT: The surface areas of chitosan powders which differ only in their mean particle size and particle size distributions are measured using single gas Brunauer-Emmett-Teller (BET) adsorption. Plots of specific surface area,  $s$  (surface area per gram) vs mean particle size,  $d$ , clearly show the surfaces of these powders to be fractal. Fractal dimensions for the chitosan powders were found to range between 2.41 and 2.88 depending on their source and process history.

Nonlinear behavior was observed in the plots of experimental data from which the fractal dimension is obtained. Computer simulations of adsorption on both smooth and fractal surfaces demonstrate that the observed curvature in plots of  $\ln(s)$  vs  $\ln(d)$  can result from the particle size distribution. In particular, differences in the coefficient of variation between particle size groups not only produce nonlinearity, but in many cases lead to incorrect values for the fractal dimension. A mathematical model, which takes into account particle size distributions through inclusion of the coefficient of variation, is described. Validity of the model is demonstrated through computer simulations.

Reactivity or reaction rate is a function of the number of available sites on which the reaction can occur and hence, in many cases, on the total surface area. The surface properties as characterized by the fractal dimension and total surface area provide a measure of the available reaction sites and hence a measure of the reactivity. Limited data presently available show a linear relationship between the reactivity fractal dimension and the geometric fractal dimension. Increasing the "roughness" of the particle surface, i.e., increasing the geometric fractal dimension, at least within the scope of this work, increases the reactivity.

BIOGRAPHY OF PRESENTER: Ronald A. Segars

PRESENT ASSIGNMENT: Research Physicist, Soldier Science Directorate, U.S. Army Natick Research, Development and Engineering Center.

PAST EXPERIENCE: Research Physicist, Food Rheology, U.S. Army Natick Research, Development and Engineering Center.

DEGREES HELD: B.A. Physics, Bowdoin College, Brunswick, Maine.  
M.S. Physics, Northeastern University, Boston, Massachusetts.

### Fractal Surfaces and Reactivity

Ronald Segars, Mr.  
Soldier Science Directorate  
Louis Piscitelle, Dr.  
Aero-Mechanical Engineering Directorate  
U.S. Army Natick RD&E Center  
Natick, MA 01760-5020

### INTRODUCTION

Fractal concepts are now widely used to characterize the surfaces of powders, fractures, solids and porous media with applications appearing in chemistry<sup>1,2,3,4</sup>, pharmacology<sup>5,6</sup>, biology<sup>7</sup>, mechanics<sup>8,9</sup>, food science<sup>10,11</sup>, and other fields. In powder technology the fractal dimension,  $D$ , obtained by single gas BET adsorption on different-sized particles provides a measure of the surface roughness of the particles and serves as a link between total surface area, as determined by the size of the molecule used in the BET adsorption measurements, and (1) the area available for adsorption of other size molecules (2) area of successive molecular layers or (3) the number of sites available for chemical reactivity. Thus, the surface properties embodied in the geometric fractal dimension,  $D$ , reflect the total area in contact with a solvent or vapor and may determine the rates of dissolution, reaction rates and heats of adsorption/desorption, etc. of chemical reactions. Therefore, the fractal dimension is a surface parameter of considerable interest in the above-mentioned fields of science.

In a previous paper<sup>12</sup> the authors applied fractal measures to the natural polymer chitosan. Chitosan is derived from chitin, a natural polymer found in the shells of crustaceans. It is of interest primarily because of its chelating potential and interactions with other organic materials. Experimental results show that the surface of milled chitosan powders are indeed fractal and that the fractal dimension depends on the source of the chitin (crab vs shrimp) and on the temperature at which the chitosan was comminuted.

## EXPERIMENTAL METHODS

**MATERIAL:** Coarsely ground chitosan meal from shrimp and from crab was obtained from Protan Laboratories, Inc. Redmond, WA. The chitosan meals were further comminuted by milling at liquid nitrogen temperature (SPEX Industries freezer mill, model 6700) or by milling at ambient temperature using a standard ball mill. The milled powders were then passed through a series of standard sieves with mesh sizes ranging from  $44\mu\text{m}$  to  $297\mu\text{m}$ . For some runs, the finer powders were further divided by sonic sifting, which produced groups of 0-10, 10-20, 20-30, 30-38 and 38-44  $\mu\text{m}$  particles.

**SURFACE AREA:** The specific surface area, i.e., surface area per gram, of each group of particles was determined using a Micromeritics gas adsorption apparatus (model 2100E). Initial measurements were made using nitrogen gas as the adsorbate. However, the data points for the standard BET plots were very erratic and the expected linear behavior was seldom observed. This suggested insufficient sensitivity for this adsorbate-adsorbent pair. Switching to argon, a slightly smaller molecule ( $13.8$  vs  $16.2 \text{ \AA}^2$ ) with much lower saturation vapor pressure ( $189$  vs  $729 \text{ mmHg}$  at  $77 \text{ K}$ ), provided smooth and linear BET plots of volume adsorbed versus pressure. Fig.(1). The specific surface area of at least eight groups of particles with different average sizes was evaluated for each of the four treatments using argon as the adsorbate.

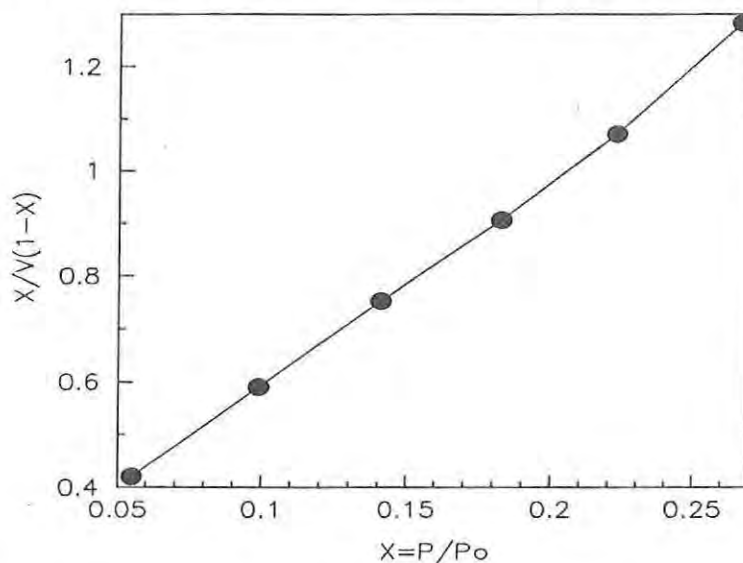


Figure 1. Plot of the linearized BET equation for a chitosan powder; argon is the adsorbate.

**REACTIVITY:** Several of the sieved particle groups were selected to determine their ability to hydrolyze the agent simulant diisopropyl fluorophosphate (DFP). The samples were treated as described by Andreotti et al.<sup>13</sup> and the reaction kinetics, i.e., the reaction rate constant,  $R$ , of each group of particles was obtained. The rate constant was determined by monitoring the release of the fluoride ion and fitting the amount of fluoride ion released versus time during the initial 20% of the reaction curve to a first order rate equation. The rate constant and the total fluoride ion released were obtained from the "least squares best fit" parameters. From the reaction rate constant,  $R$ , and the mean particle size,  $\bar{d}$ , a reactive dimension was obtained as described in the next section.

### DATA ANALYSIS

This section first outlines the standard approach to single gas BET determinations of the fractal dimension of powders where it is implied that the particles are monodispersed. A refinement of this approach is then presented, which shows how a particle size distribution can be incorporated into the analysis. Lastly, the rationale and the method for determining a reactive fractal dimension are described.

**STANDARD MODEL:** The surface area of a smooth spherical particle scales as  $d^2$ . If the particle surface is rough (but still in general spherical), the true surface area will no longer follow the  $d^2$  law but will actually be somewhat greater. We assume this surface area can be expressed as

$$S = k d^D \quad (1)$$

where  $D$  is called the fractal dimension and is expected to be a fractional number between 2 and 3. The mass of a rough-surfaced particle is assumed to scale the same as for a smooth surfaced particle, i.e.,  $m = k d^3$ . The specific surface area,  $s = S/m$ , as determined by gas adsorption methods becomes

$$s = k d^{(D-3)} \quad (2)$$

Taking the log of both sides gives

$$\ln(s) = \ln(k) + (D-3)\ln(d) \quad (3)$$

which shows that a log-log plot of surface area vs. particle size is linear and that the slope of the linear curve is equal to the fractal dimension minus 3. This is the working equation for obtaining the fractal dimension of powders when using the single gas BET approach. It provides all the experimental  $D$ -values in this study.

**NEW MODEL:** If we have a group of  $n$  smooth particles of diameters  $d_i$  then the surface area of the  $i^{\text{th}}$  particle is

$$S_i = k_1 d_i^2 \quad (4)$$

and for  $n$  such particles the total surface area becomes

$$S = k_1 \sum_{i=1}^n d_i^2 \quad (5)$$

The mass of the  $n$  particles is

$$m = k_2 \sum_{i=1}^n d_i^3 \quad (6)$$

and the specific surface can be written as

$$s = \frac{S}{m} = k \frac{\sum_{i=1}^n d_i^2}{\sum_{i=1}^n d_i^3} \quad (7)$$

If the particle diameters are expressed in terms of the mean diameter  $\bar{d}$  as  $d_i = \bar{d} + \sigma z_i$  where  $z$  is the standard normal random variable and  $\sigma$  is the standard deviation then

$$\sum_{d_i} d_i^3 = \sum_{z_i} (\bar{d} + \sigma z_i)^3 = \bar{d}^3 + 3\sigma^2 \bar{d} \quad (8)$$

and

$$\sum_{d_i} d_i^2 = \sum_{z_i} (\bar{d} + \sigma z_i)^2 = \bar{d}^2 + \sigma^2 \quad (9)$$

For a rough surface we need to approximate

$$\sum_{d_i} d_i^D = \sum_{z_i} (\bar{d} + \sigma z_i)^D \quad (10)$$

where  $2 \leq D \leq 3$ . It has been shown<sup>14</sup> that a suitable approximation can be found that when coupled with Eq.(7) yields

$$\ln(s) = \ln(C_1) + (D-3)\ln(\bar{d}) + \beta \quad (11)$$

where

$$\beta = \frac{3\sigma^2 \ln(3)}{\bar{d}^2 + 3\sigma^2} \quad (12)$$

This equation reduces to Eq.(3) for monodisperse particles where  $\sigma$  is zero, i.e.,  $\beta = 0$ .



REACTIVITY: The reactivity dimension,  $D_R$ , is determined in a manner analogous to that for the geometric fractal dimension,  $D$ . If the fluoride ion concentration, the experimental measure of the reaction taking place, is proportional to the number of reactive surface sites, then it is reasonable to assume that the fluoride ion concentration and its time dependence, from which the reaction rate constant,  $R$ , is determined, will also be proportional to the surface area. Since surface area for a rough surface scales as  $d^D$ , it is probable that the rate constant will scale as  $d^{D_R}$ . The surface area of particulate matter, e.g., powders, increases with the amount of material present. On a unit weight basis, since the mass of rough particles scales as  $d^3$ , the reaction rate constant,  $R$ , will scale as

$$R = kd^{D_R-3} \quad (13)$$

This is Eq.(2) with  $s$  replaced by  $R$  and  $D$  by  $D_R$ ; its linearized version is Eq.(3) with these same replacements.

## RESULTS AND DISCUSSION

Results of the gas adsorption measurements are shown in Fig.(2) where the natural log of the specific surface area,  $\ln(s)$  ( $s$  is the surface area in square meters per gram), is plotted against the natural log of the mean particle diameter. The four treatments, two products (crab and shrimp) milled at two temperatures (ambient and liquid nitrogen), are shown. The fractal dimension,  $D$ , varies between 2.41 and 2.88 for these products. The largest change in  $D$  occurs between the two temperatures, with ambient temperature milling producing the higher  $D$ -values. However, changes in the fractal dimension due to source (crab vs. shrimp) are also significant, especially when the raw products are milled at low temperatures. Shrimp chitosan shows the higher  $D$ -values. Higher  $D$ -values indicate an increase in surface roughness, that is, the surface has larger peaks and valleys or is more porous. As  $D \rightarrow 3$  the surface becomes "space filling". It is also clear from Fig.(2) that at higher  $D$ -values, the effect of particle size on the specific surface area becomes less pronounced. This is in accord with Eq.(3) which shows that at  $D=3$  the surface area becomes constant. Apparently, rough surfaces allow for a greater packing density of the adsorbate molecules so that the larger rough surface particles adsorb far more than their smooth surface counterparts. Adsorption on small particles remains limited whether or not their surface is rough.

The third observation that comes from Fig.(2) is the fact that the data plots for the three highest values of  $D$  are not strictly linear. The theory embodied in Eq.(3), however, shows that these plots of  $\ln(s)$  vs  $\ln(d)$  should be linear. For these three nonlinear cases, statistical analysis showed that a quadratic fit was significantly better than the linear fit. It was believed the cause of this nonlinearity could have significant implications (lack of sensitivity in some of the measurements, overly simplistic model, etc.) and a study was undertaken to determine the source of the nonlinearity.



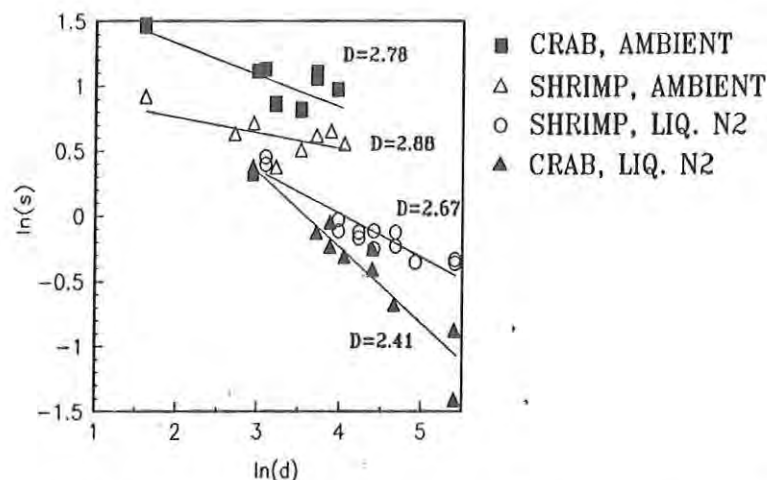


Figure 2. Plot of  $\ln(s)$  vs  $\ln(d)$  from Eq.(3). The fractal dimensions,  $D$ , for four chitosan products are shown in the figure.

Equation (3) incorrectly assumes that the particles within each group are all the same diameter, i.e. monodispersed. In fact, the diameter of the sieved particles evaluated in this study was shown to be normally distributed, Fig.(3). Thus, it seemed logical to investigate the relationship between particle size and the measured area of a powder.

It is easy to show using computer simulations that the total surface area of a group of monodispersed smooth particles of any given diameter can be increased or decreased by allowing a distribution of the particle diameters. The surface area can increase or decrease even though the mean diameter of the distribution is the same as the diameter of the monodispersed group. It is clear then that the observed curvature in the plots of  $\ln(s)$  vs.  $\ln(d)$  could be produced by particle size distributions within the particle groups used for the BET surface area determinations. Computer simulations carried out for both smooth and rough surfaces demonstrated that  $\ln(s)$  vs.  $\ln(d)$  plots, which are linear on the basis of mean particle diameter, can be nonlinear when the actual surface area is calculated from the known randomly chosen, normally distributed diameters.

Since the observed curvature in the plots used to obtain the fractal dimension can be attributed to particle size distributions, a mathematical model which takes into account such variations would be valuable. A brief derivation of a new model which corrects for size distribution effects was given in the previous section.

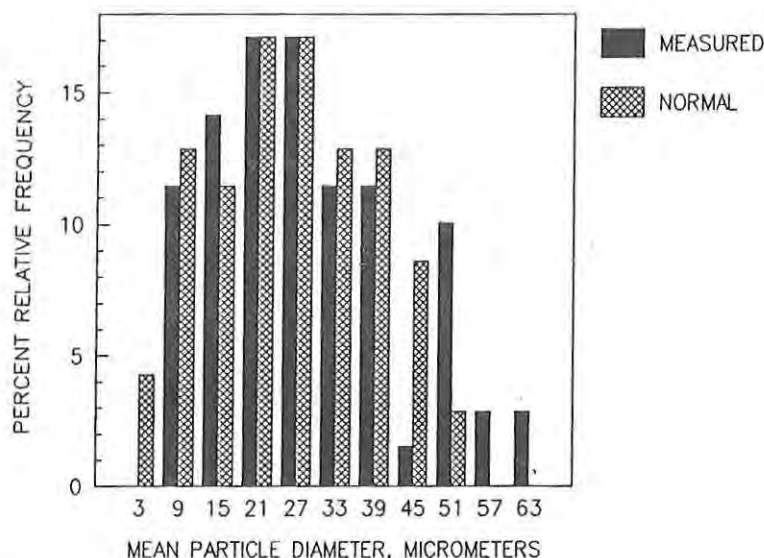


Figure 3. Particle size distribution for a group of 70 chitosan particles. A computer generated normal distribution of 70 particles is also shown.

Figure (4) shows the result of computer calculations obtained on computer simulated normally distributed-random-smooth particles. The particle diameters were generated using a random number generator in which the mean value and standard deviation of the distribution could be specified. By varying the coefficient of variation (% deviation) between groups of simulated particles, the nonlinear curves and the linear curves showing smooth particles to be fractal were calculated. Clearly then, particle size distributions can provide curvature in the standard  $\ln(s)$  vs.  $\ln(\bar{d})$  plots; other particle group distributions may generate linear plots but the fractal dimension obtained from them will be incorrect. Only if the coefficient of variation remains constant between groups of particles will the resulting plots be linear and of the proper slope to give the correct value of  $D$ .

Also shown in Fig.(4) are the results of applying the new model [Eq.(11)] described in the previous section which takes into account the particle size distributions. The linear curve showing smooth particles to have a fractal dimension of 2.3 is changed and now provides a fractal dimension of 1.93, which is much closer to the correct value of 2.0. Nonlinear plots have been linearized by the model and now provide the proper fractal dimension.

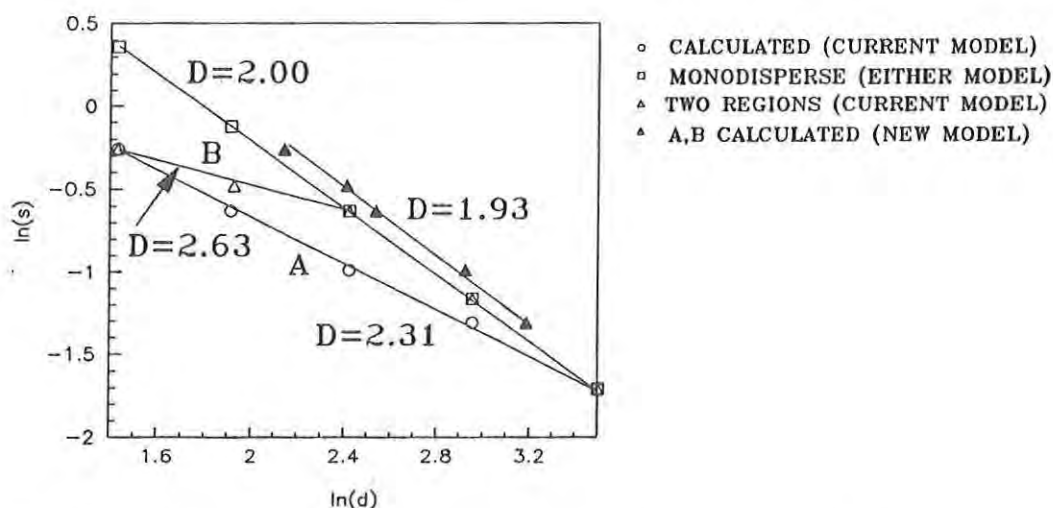


Figure 4. Plots of Eq.(3) (current model) and of Eq.(11) (new model) for computer generated particle size distributions. The particles are assumed smooth with fractal dimension  $D=2.0$ .

Figure (5) shows the results of a computer simulation for "rough" particles of fractal dimension 2.5. Again, particle size distributions can result in nonlinearities and incorrect values of  $D$ . Using the model to correct for size distributions linearizes the data plots and provides the correct value of  $D$ .

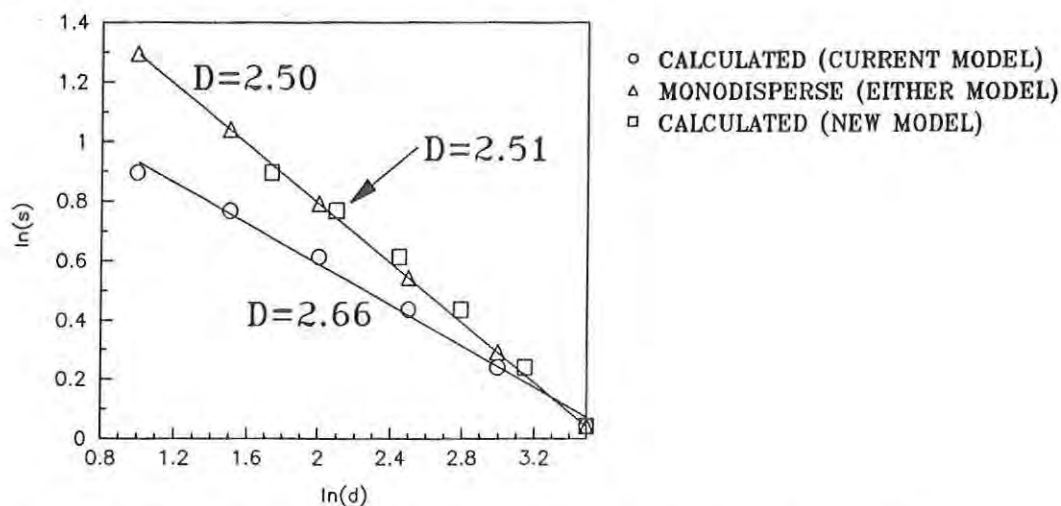


Figure 5. Plot of Eq.(3) (current model) and of Eq.(11) (new model) for computer generated particle size distributions. The particles are assumed rough with fractal dimension  $D=2.5$ .

Three particle size groups from each of three treatments (material from the fourth treatment, crab chitosan milled at liquid nitrogen temperature, was not available when reactivity measurements were being made) were submitted for a standard evaluation of their reactivity potential. The three groups selected covered the range of particle sizes available. The reaction rate constants provided by this analysis were used in place of the specific surface area, as suggested by Eq.(13), and plots of  $\ln(R)$  vs  $\ln(d)$  were used to obtain a reactive dimension  $D_R$ . Thus, the reactive dimension is a measure of the fraction of the surface, i.e., number of reactive sites per unit area, that is involved in the reaction. Figure (6) is a plot of the reactive dimension obtained as described above versus the geometric fractal dimension,  $D$ .

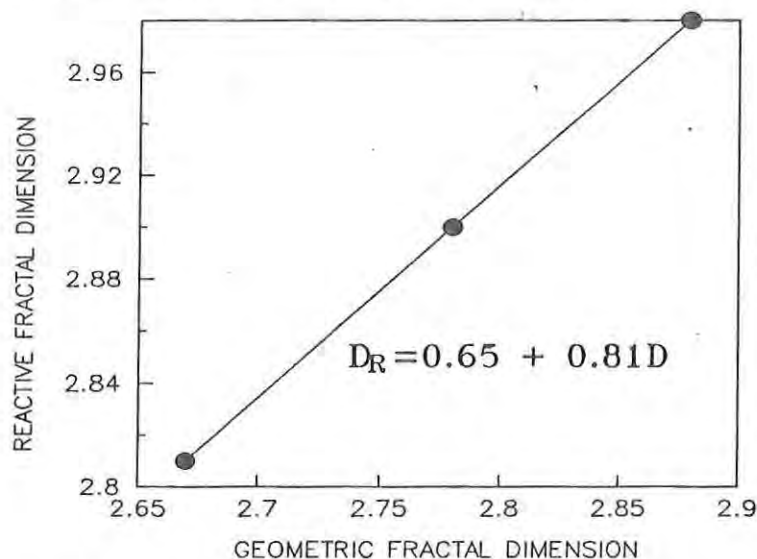


Figure 6. Plot of the reactive fractal dimension,  $D_R$ , vs the geometric fractal dimension,  $D$ , for the three chitosan products for which reactivity measurements could be made.

Although there are only three data points, one for each treatment evaluated for reactivity, the plot is perfectly linear. The additional data point for the fourth treatment could certainly strengthen this case, but in spite of this lacking, these initial results strongly indicate that the reactivity of chitosan powder can be predicted from its geometric properties as measured by the fractal dimension. This fact is perhaps not unexpected since, as mentioned in the derivation of  $D_R$ , it requires only a strong relationship between the total surface area and the number of reactive sites.

However, the strong linearity of these results indicate that the observed differences in the reaction rate constants for the various products evaluated are not due to inherent differences in the chitosan chemistry. Instead, it appears that the structure of the chitosan and the effect of milling operations on this structure control the reaction rates. All of the observed differences in the reaction rate constants, whether the products came from different size groups within a treatment or from different treatments, can be explained by geometric differences in the surface roughness.

### CONCLUSIONS

The surfaces of chitosan powders are fractal; the fractal dimension,  $D$ , ranged from 2.41 to 2.88 for the treatments studied. The value of  $D$  is affected by the temperature at which the powders are milled with ambient temperatures producing a rougher surface (higher  $D$ -values) than liquid nitrogen temperatures. The source of the chitosan powder also has some effect on the value of  $D$ . The chitosan obtained from shrimp had a rougher surface than the chitosan from crab at both milling temperatures.

Computer simulations show that particle size distributions can cause curvature in the standard  $\ln(s)$  vs  $\ln(\bar{d})$  plots used to obtain the fractal dimension,  $D$ , when single gas BET measurements are used to obtain the specific surface area. In addition to curvature, particle size distributions can produce incorrect values for the fractal dimension. A new mathematical model has been developed to correct these problems; computer simulations demonstrate the validity of this model.

The reactive fractal dimension,  $D_R$ , of chitosan powders, determined from the reaction rate constants of several groups of particles of different mean particle size, is a linear function of the geometric fractal dimension,  $D$ . This suggests that the inherent reaction rate of chitosan is constant across source (shrimp or crab) and milling temperature (ambient or liquid nitrogen); all observed differences in the reaction rate constants can be readily explained by geometric variations in surface roughness.

# REFERENCES

1. Avnir, David and Pfeifer, Peter, *Nouv. J. Chim.* 7, 71 (1983).
2. Schaefer, Dale W., *Science* 243, 1023 (1989).
3. Schaefer, Dale W., *MRS Bulletin*, 22 (Feb 1988).
4. Farin, Dina and Avnir, David, *J. Am. Chem. Soc.* 110, 2039 (1988).
5. Lewis, Mitchell and Rees, D.C., *Science* 230, 1163 (1985).
6. Thibert, R., Akbarieh, M., and Tawashi, R., *J. Pharm. Sci.* 77, 724 (1988).
7. Pfeifer, P., Welz, U., and Wippermann, H., *Chem. Phys. Lett.* 113, 535 (1985).
8. Hazlett, Randy Doyle, *J. Colloid Interface Sci.* 137, 527 (1990).
9. Mecholsky, J.J., Mackin, T.J., and Passoja, D.E., in Advances in ceramics 22: Fractography of Glasses and Ceramics, 127 (The American Ceramic Society 1988).
10. Nagai, T., and Yano, T., *J. Food Sci.*, 55, 1334 (1990).
11. Peleg, M., and Normand, M.D., *J. Food Sci.*, 50, 829 (1985).
12. Piscitelle, Louis, Segars, Ronald, Kramer, Roslyn, and Bagalawis, Rosa Linda, *Mat. Res. Soc. Extended Abstracts (EA-20)*, 115 (1989).
13. Andreotti, R.E., Robbins, F.M., Woodbury, C.T., Grady, P.M., and Connolly, J., *U.S. Army Natick RD&E Center Technical Report, NATICK/TR-91/015L* (1991).
14. Piscitelle, Louis, and Segars, Ronald, *J. Colloid Interface Sci.*, 149, 226 (1992).



ARANDA, et al.

TITLE: Investigation of the Component Elements of Nonlinear  
(Chi-3) Effects

Francisco J. Aranda, Mr., D.V.G.L.N. Rao, Dr.

Department of Physics, University of Massachusetts at Boston,  
Boston, MA 02125

and

Joseph F. Roach, Mr.

U.S. Army Natick RD&E Center, Natick, MA 01760-5020

ABSTRACT: The unraveling of the evolution of third-order nonlinear (Chi-3) effects in optical materials is an essential element in the development of materials for tunable laser eye protection. The processes by which nonlinearity contribute to laser eye protection are contained in the real and imaginary parts of Chi-3. The real part causes an intensity-dependent change in the phase of the interacting light (laser) and the imaginary part a change in the light intensity transmission. The real part has been measured using the Optical Kerr Gate technique. The imaginary part, intensity dependent transmission, can be characterized by two photon absorption, excited state absorption or a combination of the two. Using ultrashort laser pulses, we were able to differentiate between the two processes and hence determine the dominant mechanism affecting the nonlinearity. A simple theoretical model has been developed to include both kinds of effects.

In order to develop an effective nonlinear material for laser eye protection, the application (goggle configuration) must be specified. This will then determine the process to be maximized, i.e. phase change or intensity-dependent absorption. The techniques developed in this study will be used as a guide to design molecular structures with large nonlinearities in the most effective process mode.

BIOGRAPHY OF PRESENTER: Francisco J. Aranda

PRESENT ASSIGNMENT: Graduate Student at University of Massachusetts at Boston MA.

DEGREES HELD: B.S. Physics, University of Massachusetts at Boston,  
M.S. Physics, University of Massachusetts at Boston.

ARANDA, et al.

Investigation of the Component Elements of Nonlinear  
(Chi-3) Effects

Francisco J. Aranda, Mr., D.V.G.L.N. Rao, Dr.

Department of Physics, University of Massachusetts at Boston,  
Boston, MA 02125

and

Joseph F. Roach, Mr.

U.S. Army Natick RD&E Center, Natick, MA 01760-5020

INTRODUCTION

The interaction of an electric field with a material produces a separation of negative and positive charges, producing a polarization in the medium that varies according to the oscillations of the field. When the fields are weak, the induced polarization has a linear dependence on the field, which is described by equation (1).

$$D = \epsilon_0 E + P \quad (1)$$

At low field intensities, (E) the polarization (P) is characterized by a linear susceptibility  $\chi^{(1)}$  which determines its propagation properties in the material. At high field intensities we need to include a nonlinear polarization term  $P_{nl}$ , and so the overall polarization becomes

$$P = \epsilon_0 \chi^{(1)} E + P_{nl} \quad (2)$$

The nonlinear polarization is of the form

$$P_{nl} = \epsilon_0 (\chi^{(2)} E^2 + \chi^{(3)} E^3 + \dots) \quad (3)$$

where  $\chi^{(2)}$  and  $\chi^{(3)}$  represent the second-order and third-order susceptibilities. They represent the magnitudes of higher order interactions among the applied fields and are determined by features at the molecular level, including electronic delocalization, molecular structure and overall molecular packing. The parameter of special interest for this study is the third-order nonlinear effect as denoted by the third-order susceptibility  $\chi^{(3)}$ . It consists of a real part that describes a change in refractive index, and an imaginary part that is responsible for nonlinear absorption by excited state effects or by two-photon absorption or by a combination of both. The overall magnitude of the third-order susceptibility is obtained by degenerate four wave

mixing (DFWM) techniques. The magnitude of the real part is obtained from measurements of the Optical Kerr Gate effect and its sign by concentration-dependent DFWM values. Direct measurement of intensity-dependent total transmission of ultrashort pulses is one of the many ways of measuring the imaginary part of  $\chi^{(3)}$ . The relative contributions to the imaginary part from two-photon absorption or excited state absorption can be ascertained by performing intensity-dependent transmission experiments, monitoring the four wave mixing signal at different pump intensities for a wide range of concentrations, or by measuring the intensity transmitted straight through the sample as a function of different laser pulse widths.

Each of the mentioned effects is an essential element that properly assesses nonlinearity in relevant materials. The techniques developed in this study, as well as the values for materials tested, are essential factors in assessing the types of molecular structures with third-order nonlinearities. The intensity-dependent change in refractive index and the intensity-dependent absorption effects in materials are especially amenable to tunable laser eye protection schemes. This study will focus on these effects and on the magnitudes measured on selected samples.

## ANALYSES

### Measurement in Solutions

The experimental setup used for DFWM experiments is shown in Figure 1. The analysis of nonlinear measurements in solutions using this technique has been fully described elsewhere<sup>1</sup>, from which the following equation was derived based on the relationship of the second hyperpolarizability  $\chi^{(2)}$  to third-order macroscopic susceptibility.<sup>2</sup>

$$\chi_{solution}^{(3)} = \chi_{solvent}^{(3)} + \frac{L^4 \gamma_{solute} A C}{M} \quad (4)$$

where A is Avogadro's number, M the molecular weight of solute, C the concentration of solute in g/mL and  $L^4$  the local field correction factor. For low concentrations  $\chi^{(3)}$  of the solution follows a linear relationship with respect to the concentration of the solute. The plotted data will fall on a straight line whose slope is the value of the second hyperpolarizability of the solute. This is shown in Figure 2a.  $\chi^{(3)}$  can have both real and imaginary components originating from the solute as well as the solvent. The real part is responsible for the nonlinear refractive index and the imaginary part for nonlinear absorption. The real part can be either positive or negative. In the case of most organic solvents,  $\chi^{(3)}$  is real and positive and can be

ARANDA, et al.

expressed as a combination of the real and imaginary functions expressed by the relationship shown in equation 5.

$$|\chi^{(3)}| = \{(\chi_{\text{solvent}}^{(3)} + \text{Re}\chi_{\text{sample}}^{(3)})^2 + (\text{Im}\chi_{\text{sample}}^{(3)})^2\}^{\frac{1}{2}} \quad (5)$$

Thus by monitoring the concentration dependence of  $|\chi^{(3)}|$  the contribution from the solvent can be determined; it is the value shown at the intercept of the line describing the relationship in Figure 2. From the shapes of these curves, Figure 2, we can determine the sign of the real part and in qualitative terms whether the imaginary part is non-zero. Therefore, from DFWM experiments we are able to calculate the  $\chi^{(3)}$  values for the solvent and the solute and other relevant information. From Kerr Gate experiments we can measure the real part of  $\chi^{(3)}$  and by substituting into equation 5 determine the imaginary part. The elucidation of the components of the imaginary parts is further amplified by investigating intensity-dependent transmission experiments.

#### Kerr Gate Technique

The real part of  $\chi^{(3)}$  can be determined using the optical Kerr gate technique.<sup>3</sup> The experimental setup for making these types of measurements is shown in Figure 3. Two laser beams, one at 1064nm (the pump beam) and the other at 532nm (the probe beam) are directed into a sample by mirrors (M) with the probe beam temporally delayed by the delay line (DL). The probe beam is polarized at 45 degrees (P1) with respect to the pump beam. The probe beam experiences a phase retardation

$$\delta\phi(t) = \frac{L}{C} \omega_1 \delta n(t) \quad (6)$$

between its parallel and perpendicular components as it travels through the sample. This causes the polarization vector of the probe to change. Energy is then transmitted to the detector (D) through polarizer P2, which is oriented at 90 degrees to P1. The magnitude of the signal depends on the delay between the pump and probe beams and can be expressed as

$$S_p(\tau_D) = \frac{1}{S_1} \int_{-\infty}^{\infty} \langle E_{\omega_1}^2(t - \tau_D) \rangle \sin^2\left[\frac{\delta\phi(t)}{2}\right] dt \quad (7)$$

where  $S_1$  is the total signal of the probe beam when the two polarizers are oriented parallel to each other. The nonlinear index  $n_2$  is then calculated from the following equation

$$(8)$$

ARANDA, et al.

where:

$$B = \frac{4x^3}{(x^2-1)^2(x+2)} + \frac{4x^2}{(x^2-1)(1-x)(2x+1)} + \frac{2(1+x^2)}{3(1-x)^2(1+x)^2}$$

$$C = \frac{4x}{(x^2-1)(x+1)} + \frac{4}{3(1-x^2)} \quad x = \frac{\tau_0}{\tau_1}$$

Here  $\tau_1$  is the laser pulse width,  $i$  represents the  $i$ th solution,  $S_i(0)$  is the amplitude at zero time delay between pump and probe for the  $i$ th sample, and  $y$  is the fraction of the nonlinear refractive index arising from fast mechanisms. For samples for which the slow mechanisms cannot be resolved, the last term in the equation can be ignored. The relationship of the nonlinear index value with the third-order susceptibility is governed by

$$n_2(\omega) = 3\text{Re}\chi^{(3)}(-\omega; \omega, -\omega, \omega)/8n_0(\omega) \quad (9)$$

Positive  $\text{Re}\chi^{(3)}$  will lead to focusing of the beam and negative values to defocusing.

Intensity Dependent transmission

The equation for the intensity ( $I$ ) of a beam propagating through a material in which nonlinear absorption, two-photon absorption and excited-state absorption are occurring can be written as:

$$\frac{dI}{dz} = -\alpha I - \beta I^2 - \sigma NI \quad (10)$$

where  $\alpha$  is the linear absorption coefficient,  $\beta$  the two-photon absorption coefficient,  $\sigma$  the excited-state absorption cross section and  $N$  the population density of the excited-state created by the absorption process. The population density is described by the equation:

$$\frac{dN}{dt} = \frac{\alpha I}{h\nu} - \frac{N}{\tau} \quad (11)$$

where  $\tau$  is the decay time for the excited-state and  $h\nu$  is the energy of a laser photon. Solving equations 10 and 11 we can evaluate the total energy transmitted ( $T_E$ ) through the sample using the following expression



$$T_E = \frac{\int_0^\infty \int_{-\infty}^\infty I(1, r', t') dt' 2\pi r' dr'}{\int_0^\infty \int_{-\infty}^\infty I(0, r', t') dt' 2\pi r' dr'} \quad (12)$$

where  $I(0, r, t)$  is assumed to have Gaussian spatial and temporal profiles. The nonlinear transmission (the ratio of the total energy transmission,  $T_E$ , to the linear transmission) is measured as a function of the incident laser intensity. From an analysis of the data, the coefficients appearing in equation 10 can be ascertained and then related to the imaginary part of  $\chi^{(3)}$ .

### Experimental Results and Discussion

We have selected two organic compounds (Figure 5) for continued studies by determining the nonlinear absorption processes contributing to the overall  $\chi^{(3)}$  effects.  $\chi^{(3)}$  values were previously obtained for these compounds.<sup>1</sup> Intensity-dependent absorption measurements were performed using picosecond and nanosecond laser pulses. The nonlinear sample was placed at the focus of a lens (L) and the transmitted energy was measured as a function of the incident energy using silicon detectors (D1&D2). The setup for making these types of measurements is shown in Figure 4.

Figure 6 shows the dependence of the energy transmission through the samples as a function of incident intensity. If nonresonant two-photon absorption were the only mechanism contributing to the transmission decrease, we would expect the nanosecond and picosecond curves to be superimposed. The separation between the curves indicates other mechanisms are also contributing.

Figure 7 shows the dependence of the energy transmission through the sample as a function of incident fluence. The curves are essentially superimposed, indicating a fluence-dependent process such as excited-state absorption as the dominant nonlinear effect.

For both figures 6 and 7 the values of  $T_E$  (equation 12) were calculated and fitted to the experimental data to obtain the values of the parameters  $\beta$ ,  $\sigma$ , and  $\tau$  given in Table 1. These are shown as the dashed and dot-dashed lines for nanosecond and picosecond pulses, respectively. From the value of  $\beta$  obtained from the fit, we determined the imaginary part of  $\chi^{(3)}$  using the following relationship:

$$\beta = \frac{2\pi}{n^2 \epsilon_0 c \lambda} \text{Im} \chi^{(3)} \quad (13)$$

where  $n$  is the refractive index of the sample,  $c$  the speed of light,  $\epsilon_0$  the



ARANDA, et al.

vacuum permittivity and  $\lambda$  the wavelength of the laser light. For benzoporphyrin 2, only an upper limit for  $\beta$  could be determined because excited-state absorption dominated both the nanosecond and the picosecond behavior. The  $\beta$  of ZeSe is given in Table 1 for comparison. The real part of the nonlinearity was measured using the optical Kerr gate setup.

#### Summary

Techniques have been developed to provide insight into the origins of the nonlinear processes in materials. For laser eye protection schemes the nonlinear absorption effect will likely be the important operating mechanism. With this test and analysis method, we have successfully delineated and measured the real and imaginary parts of  $\chi^{(3)}$  for two benzoporphyrins that were originally synthesized as nonlinear materials for laser eye protection. The future success of providing protection against tunable lasers rests with providing materials with the right nonlinear properties in the right configuration. The techniques developed here will provide the necessary design information to intelligently provide the optimum protection.

#### REFERENCES

1. D.V.G.L.N. Rao, F.J. Aranda, J.F. Roach and D.E. Remy, Appl. Phys. Lett., 58(12), 1241 (1991)
2. M.T. Zhao, B.P. Singh and P.N. Prasad, J. Chem. Phys. 89, 5535 (1988)
3. P.P. Ho and R.R. Alfano, Phys. Rev. A20, 2170 (1979)



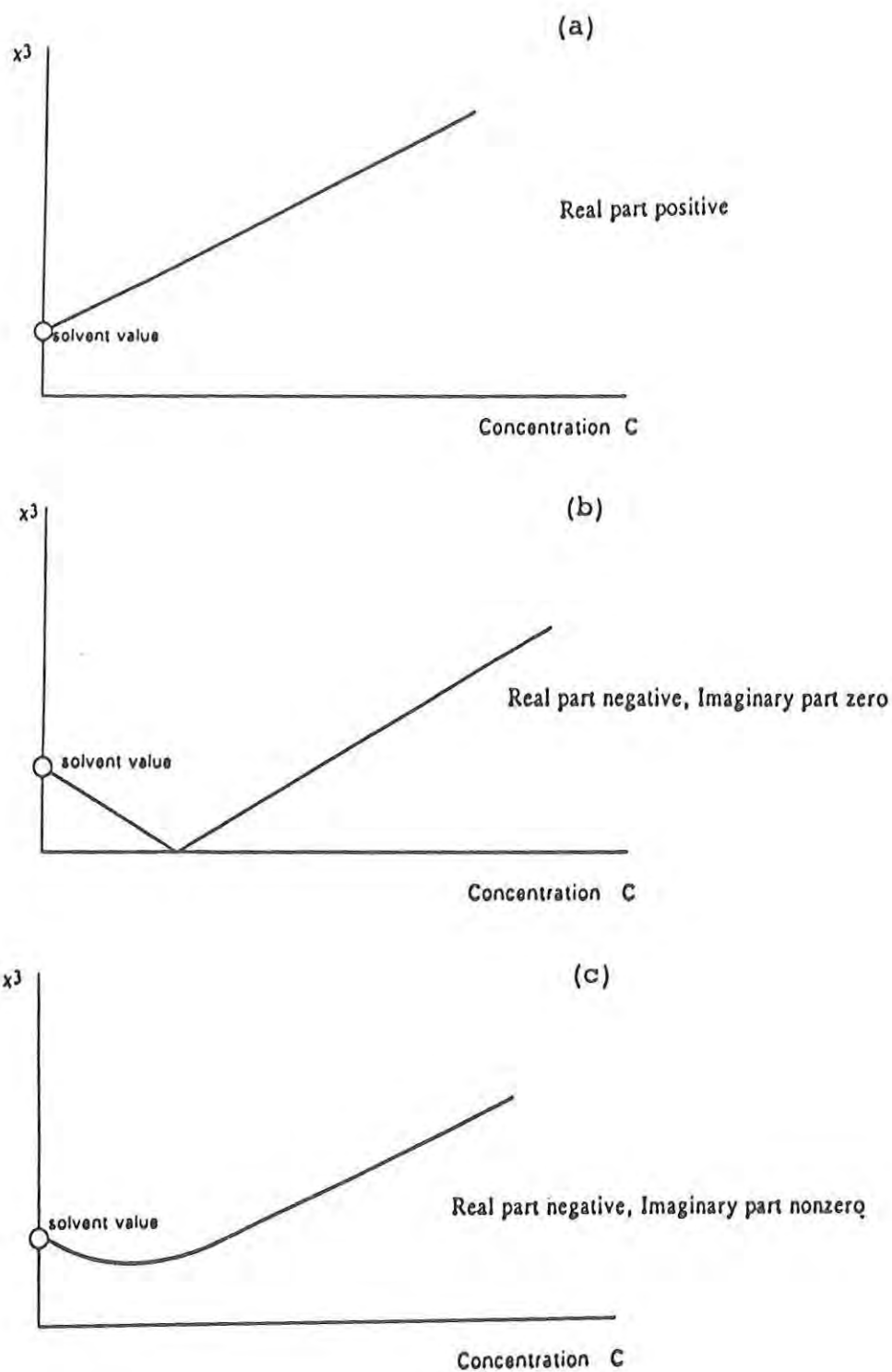


Figure 2. Examples of the variation of  $x^{(3)}$  with respect to sample concentration

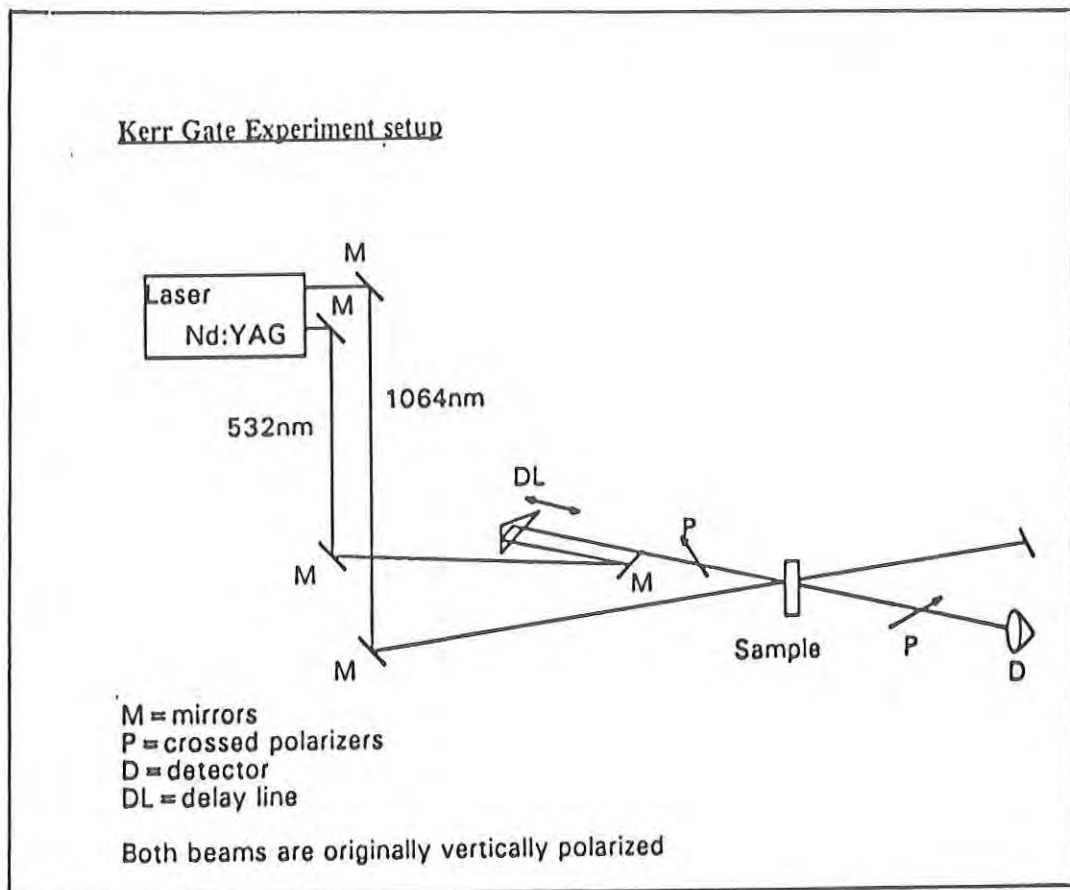


Figure 3. Experimental setup for measuring the Kerr gate effect

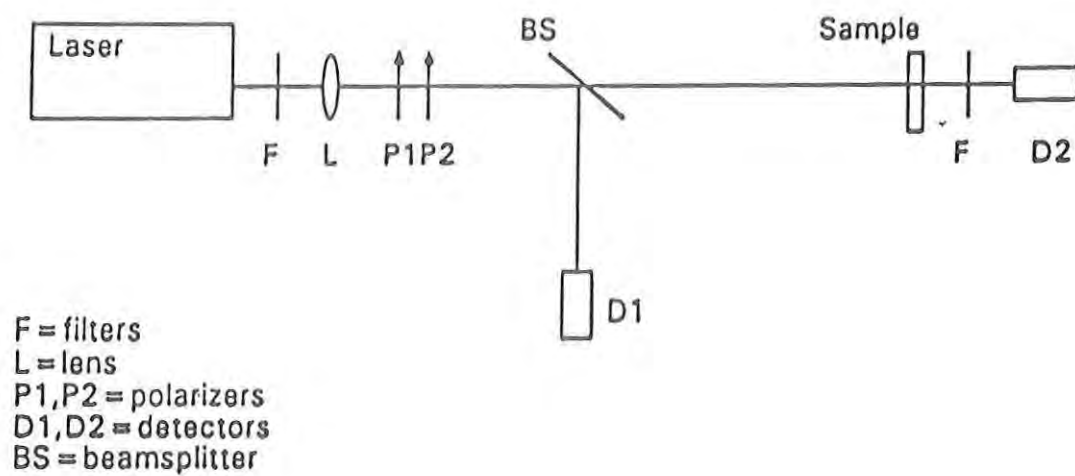
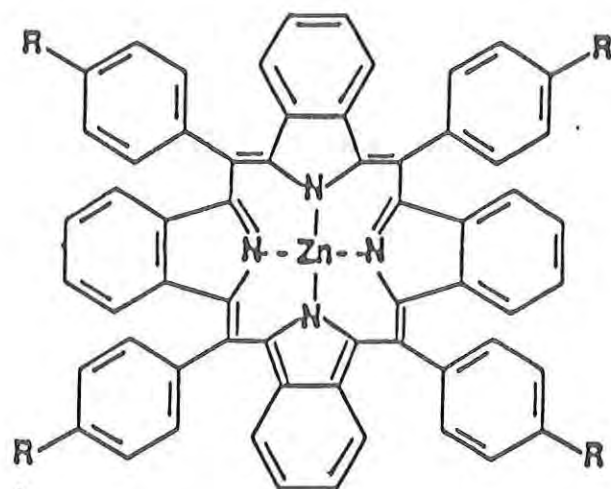


Figure 4. Experimental setup for intensity-dependent transmission measurements



**Benzoporphyrin 1: R = p-Methoxy**

**Benzoporphyrin 2: R = H**

Figure 5. The chemical structures of the benzoporphyrins used in this study



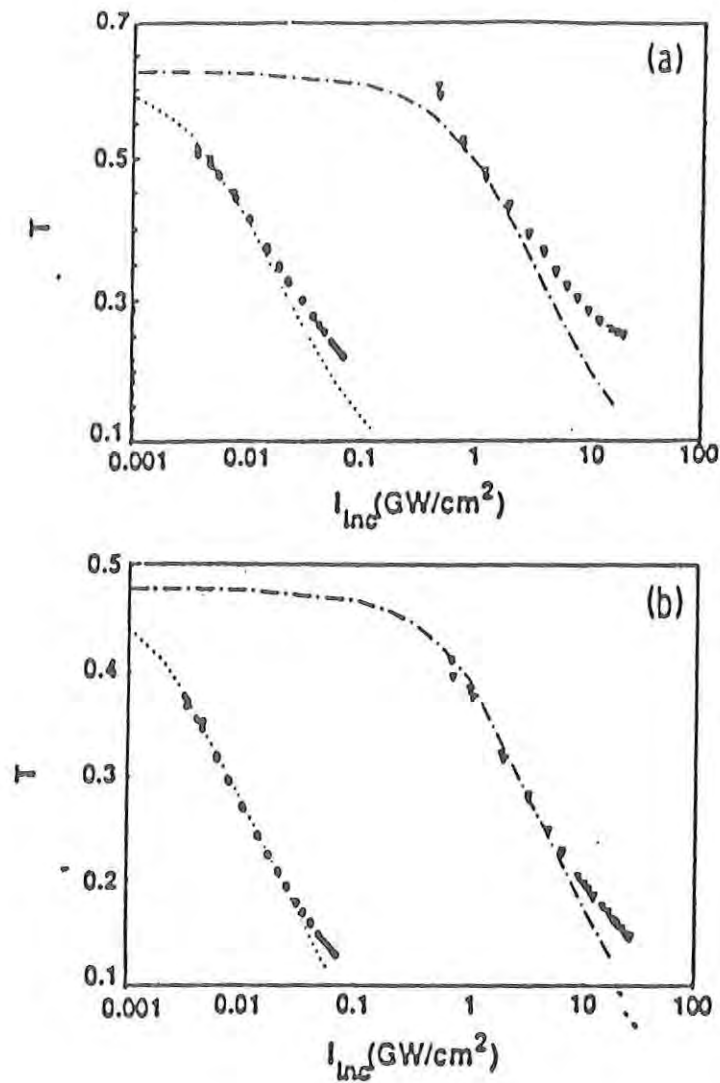


Figure 6. The energy transmission of the samples measured as a function of the incident intensity: a) benzoporphyrin 1, b) benzoporphyrin 2. The circles and the triangles represent the nanosecond and picosecond measurements, respectively. The dashed and dot-dashed lines are the best fit of the data to equation 12.

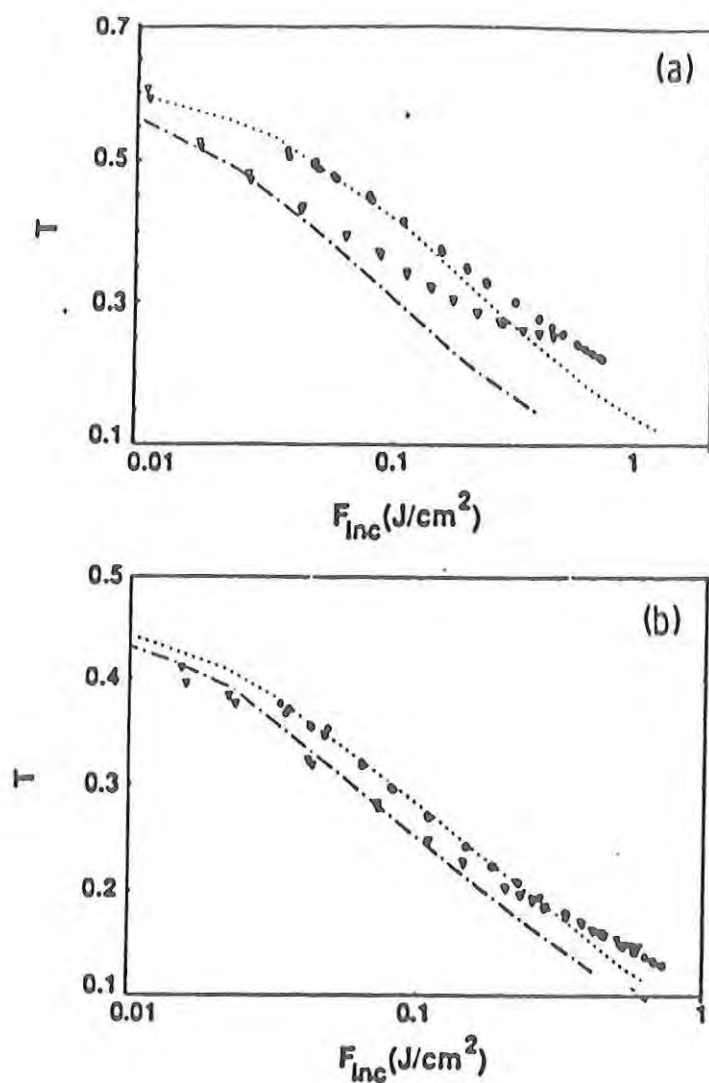


Figure 7. The energy transmission of the samples measured as a function of the incident fluence: a) benzoporphyrin 1, b) benzoporphyrin 2. The circles and the triangles represent the nanosecond and picosecond measurements, respectively. The dashed and dot-dashed lines are the best fit of the data to equation 12.

Table 1

Values of  $\beta$ ,  $\sigma$ , and  $\tau$  obtained from the best fits to  $T_E$ 

|  | Conc.<br>g/l | $\alpha$<br>$\text{cm}^{-1}$ | $\beta$<br>$\text{cm/GW}$ | $\sigma$<br>$10^{-17}\text{cm}^{-2}$ | $\tau$<br>ns | $\text{Im}(\chi^{(3)})$<br>$10^{-13}\text{esu}$ | $\text{Re}(\chi^{(3)})$<br>$10^{-14}\text{esu}$ |
|--|--------------|------------------------------|---------------------------|--------------------------------------|--------------|---|---|
| Benzo<br>Porphyrin 1                     | 0.46         | 2.4                          | 2.5                       | 3                                    | 15           | 9   | 7.8   |
| Benzo<br>Porphyrin 2                     | 0.46         | 3.8                          | $\leq 0.5$                | 3                                    | 15           | $\leq 1.8$                                      | 9.1   |
| $\beta(\text{ZnSe}) = 5.5 \text{ cm/GW}$ |              |                              |                           |                                      |              |   |   |



## **CUNNIFF**

**TITLE:** Numerical Simulation of Ballistic Impact of Textile Structures

Philip Cunniff, Mr.

**ABSTRACT:** A systematic examination of the simplifying assumptions used to enhance the computational efficiency of numerical models to predict the performance of body armor materials under ballistic impact has been conducted. The influence of different fabric-based armor construction and impact parameters was considered analytically using a direct analysis computational scheme. Model predictions of fabric deformation characteristics, and projectile striking and residual velocity properties of a series of Kevlar<sup>®</sup>, Spectra<sup>®</sup>, and nylon fabrics were compared to experimental data using high speed photography. In this paper, an overview of the experimentation performed and the capabilities of the model to predict the performance of orthogonally woven fabric body armor systems under normal (0-degree) impact by rigid (nondeforming) projectiles is provided.

Characteristics of fabric weave and of projectile geometry were found to be important factors in the characterization of the fabric deformation geometry and penetration resistance. Model predictions using a point impact approximation, while qualitatively correct, were found to lead to considerable discrepancies with the experimental data, particularly at projectile striking velocities near the ballistic limit of the system.

**BIOGRAPHY OF PRESENTER:** Philip Cunniff

**PRESENT ASSIGNMENT:** Research Mechanical Engineer, Materials Research and Engineering Division, Individual Protection Directorate, U.S. Army Natick Research, Development and Engineering Center, Natick, Massachusetts.

**PAST EXPERIENCE:** Electronics Engineer, Naval Undersea Warfare Engineering Station, Keyport Washington.

**DEGREES HELD:** B.S., Mechanical Engineering, University of Portland, OR

## **Numerical Simulation of Ballistic Impact of Textile Structures**

**Philip Cunniff**

**U.S. Army Natick Research, Development and Engineering Center  
Individual Protection Directorate  
Natick MA, 01760-5019**

The U.S. Army Natick Research, Development and Engineering Center (Natick) is the lead laboratory within the Department of the Army for the development of improved body armor systems. In that role, Natick has been aggressively active in obtaining and evaluating materials that may have potential to improve the performance of existing body armor systems. Those evaluations are intended to identify high potential materials and may be used to assist in the optimization of textile fibers for body armor applications. Textile materials are ideally suited for body armor applications, since the performance of these systems is not judged solely in terms of the impact performance; the weight, bulk, and comfort of the system also affect performance.

Under ballistic impact, textile fibers are subjected to intense axial tensile and lateral compressive stresses at extremely high strain rates. A precise definition of optimal fiber properties for applications where the loading placed on the fibers is due to ballistic impact must account for the energy absorption of systems of these fibers under conditions typical of ballistic impact. Conventional fiber test methods, however, are designed to determine material properties at strain rates decades below the rates typical of ballistic impact. Consequently, the optimization of textile fibers for body armor applications must rely on experimentation using test methods designed to approximate the loading conditions of ballistic impact, or use some alternative methodology. Numerical modeling of the impact event provides one such alternative methodology.

One possible path to optimization would be to produce fairly large quantities (10's of kilograms) of a number of processing variants of the subject fiber, weave these fibers into fabrics, and experimentally determine the impact performance of systems of these woven fabrics. This method has the disadvantages of being rather costly, time consuming, and inefficient. The use of numerical models in conjunction with experimental techniques enables



the fiber developer to estimate the performance of body armor systems under ballistic impact without producing large quantities of fiber.

The numerical model discussed in this paper takes experimentally determined material properties as input parameters and provides a prediction of the impact performance of systems of woven fabric. The main role of numerical models for the prediction of the impact response of body armor systems has been to determine the dominant failure and energy absorbing phenomena that occur during the impact event. Extension of the use of these models to include characterization of systems for which no experimental data exist implicitly includes many simplifying assumptions. However, to the extent that these assumptions are considered accurate and pertinent to the new system, experimentation may be reduced to the determination of fiber material properties at applicable strain rates.

This determination can be made using a single yarn ballistic impact test procedure<sup>1</sup>. The single yarn impact test is performed on yarns of sufficient thickness to be imaged on Polaroid<sup>®</sup> film during the impact event. A minimum of about one gram of material is required to conduct these tests.

While the accuracy of Natick's numerical models is considered to be quite good, the ultimate test of the performance of a body armor system is always determined from actual experiment. The availability of numerical models to predict the performance of body armor systems merely reduces the parameter space over which actual ballistic impact tests must be conducted to optimize a textile fiber. Perhaps of equal or greater importance, however, is the capacity of these models to elucidate the fundamental energy absorption and failure mechanisms that are active in body armor systems under ballistic impact.

This paper provides an overview of the capabilities of a numerical model to predict the performance of orthogonally woven fabric body armor systems under normal (0-degree) impact by rigid (nondeforming) projectiles. A more rigorous description of the model algorithm and performance characteristics, not considered appropriate for publication in this paper, will be presented later. The predictions of the model have been extensively compared to experimental data; an exhaustive description of that work is similarly deferred. This paper presents an overview of the scope of the testing performed, and some representative comparisons of the model predictions to the experimental data. Comparison of the model predictions to experimental data serves as a method of examining the simplifying assumptions used in developing the model. The consequences of making some of those assumptions are discussed in some detail in this paper.

## EXPERIMENTAL

Several special purpose ballistic impact tests were conducted to verify the model predictions. In the first series of tests, single ply systems of fabric were subjected to impact by 1.1 gram right circular cylindrical fragment simulators over a range of velocities from just below the ballistic limit of the system to several hundred meters per second above the ballistic

limit. The fabric systems tested in this work are tabulated in Table 1.

**Table 1: Fabrics Tested in Special Purpose Impact Tests**

| MATERIAL     | DENIER | FABRIC WEIGHT         |                      | ENDS/PICKS          | WEAVE      |
|--------------|--------|-----------------------|----------------------|---------------------|------------|
|              |        | (oz/yd <sup>2</sup> ) | (g/cm <sup>2</sup> ) | (cm <sup>-1</sup> ) |            |
| Kevlar 29    | 1500   | 14.0                  | 0.048                | 13.4 x 13.4         | 2X2 Basket |
| Kevlar 29    | 1000   | 8.7                   | 0.029                | 14.7 X 14.7         | Plain      |
| Kevlar 29    | 200    | 3.2                   | 0.011                | 25.2 X 25.8         | Plain      |
| Spectra 1000 | 650    | 6.5                   | 0.022                | 13.0 X 14.2         | Plain      |
| Spectra 1000 | 375    | 5.2                   | 0.018                | 19.7 X 22.0         | Plain      |
| Spectra 1000 | 200    | 3.3                   | 0.011                | 21.7 X 22.0         | Plain      |
| nylon        | 1500   | 14.0                  | 0.048                | 13.4 X 13.4         | 2X2 Basket |

The experimental procedure used to quantify the impact response of fabrics tested in this work is typical of other work<sup>2,3</sup>. Briefly, a compressed helium charge was used to propel a 0.558 cm diameter steel projectile onto fabric systems which were constrained in one of several different sample mounts. Projectile striking ( $V_s$ ) and residual velocities ( $V_r$ ) were monitored using light screens and counter timers. These velocities were corrected for air drag according to:

$$V_{corrected} = V_{uncorrected} \left( \frac{R - S}{R} \right)$$

where:

- $V_{uncorrected}$       Velocity as determined from the instrumentation
- $V_{corrected}$       Actual velocity.
- R                      Correction Constant. (R=55.4 for V in m/s)
- S                      1/2 the baseline distance + distance to the sample. Note the baseline distance is the distance between the light screens

In addition to the special purpose impact tests and available ballistics data, two types of high speed photographic techniques were used to verify the computational procedure. In each technique, the image of the deforming fabric was recorded on ASA 20,000 (Polaroid Type 57) film. When a photographic record of the impact event was required, the impact tests were conducted as discussed above for the special purpose impact tests except that a thin film piezoelectric transducer was mounted to the fabric at the impact point to allow for triggering of the photographic equipment. The photographic techniques required that the camera shutter be open during the impact test; just prior to firing the projectile, the room was darkened and the shutter of a camera was opened to expose the film to the target. Illumination for the photographs was supplied by either a EG&G Model 501 single microflash unit (single flash photographs), or an EG&G Model 502 multiple microflash unit (multiple microflash

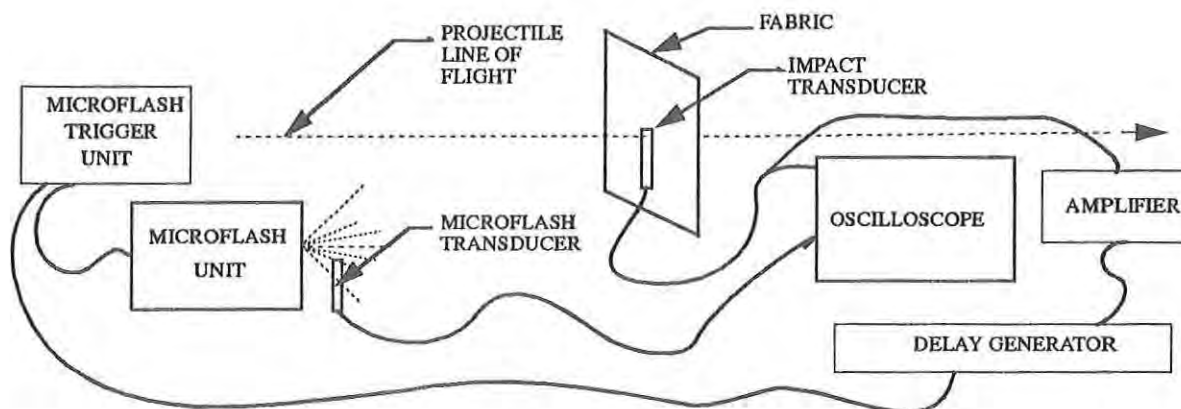


Figure 1. Instrumentation used in high speed photography.

photographs). These microflash units provide light pulses with a duration of about  $0.5\mu\text{s}$ ; the multiple microflash unit provides a series of up to 15 such pulses at a user-specified delay between pulses. The time of impact was determined by monitoring the response of a thin film piezoelectric transducer (Pennwalt Corp, Kynar Piezo Film Department) mounted at the impact point on the impact face of the fabric sample. Figure 1 illustrates the instrumentation associated with use of these transducers to determine timing during the impact event. The thin film piezoelectric transducers used in this work are relatively inexpensive (costing less than \$2.00 each), and were found to be reusable for up to 5 or 6 different impact tests. Since the projectile physically penetrated the transducer, the damaged part of the film was simply cut away with a pair of scissors and the transducer was reused. The response of the impact transducer was monitored on a multiple-channel digital oscilloscope (Norland Model 3001, minimum sample interval 100 ns).

The signal produced by the transducer was amplified and fed into a delay generator; after a user-specified delay, the delay generator triggered the light source. The exact time of the occurrence of the light pulse was determined by monitoring the response of another piezoelectric film transducer mounted on the reflective surface of the flash head. The response of this transducer was fed into a separate channel of the digital oscilloscope. The time after impact of the photograph was taken to be the difference in time between the rise of the respective signals of the impact transducer and the flash transducer.

In the more simple of the photographic techniques, single flash high speed photographs were taken of the fabric system during the impact event; a representative photograph using this technique is illustrated in Figure 2. The tent-shaped transverse deflection of the fabric is typical of deflection pattern in orthogonally woven fabrics under ballistic impact. The photographic clarity of the images produced by this method allowed for

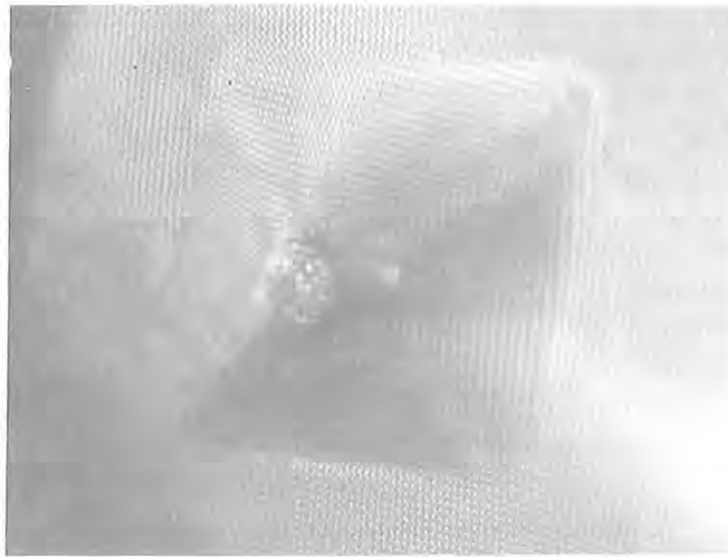


Figure 2. Single microflash photograph of a Kevlar<sup>®</sup> fabric under ballistic impact ( $V_s=259$  m/s; time after impact:  $34\mu s$ )

direct measurement of the base dimension of the transverse deflection from the photographs. A time history of the base dimension of the transverse deflection was made by photographing a series of impacts at the same impact velocity at different times after impact. This method had the advantage of allowing for the simultaneous recording of the transverse deflection in both the warp and weft yarns; in unbalanced fabrics, the deflection geometry may be strikingly asymmetric. The fabric under impact in the photograph of Figure 2 was a nearly balanced fabric; in such cases measurement of the base dimension of the transverse deflection was taken to be the average of the measurements made in the warp and weft directions.

Multiple microflash photographs of the deforming fabric were also obtained. This technique allowed for the observation of the transverse deflection of the fabric at up to four times after impact. The use of this technique provided equivalent data to up to four single flash photographs, but no information pertaining to differences in the transverse deflection in the warp and weft directions was recorded. The main advantage of the multiple microflash technique was that direct measurement of the out of plane deflection could be made from the photographs. The combination of the two techniques provided data pertaining to the three dimensional deflection of the fabric system as a function of time after impact. Figure 3 is a typical multiple microflash photograph of a single ply of  $3.2 \text{ oz/yd}^2$  Kevlar<sup>®</sup> fabric.

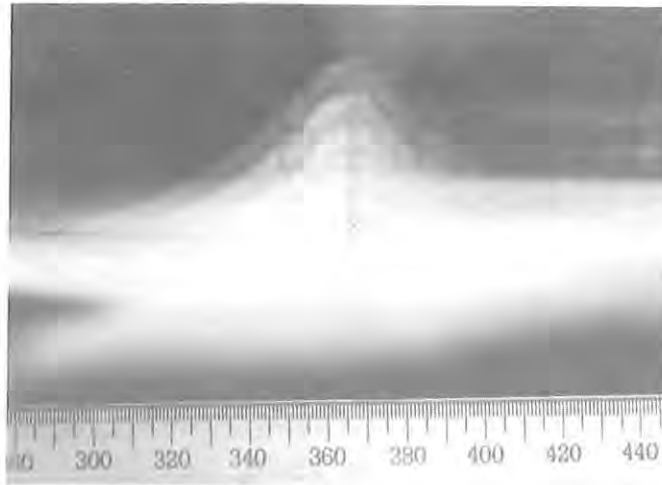


Figure 3. Multiple microflash photograph of a Kevlar fabric under ballistic impact ( $V_s \approx 259$  m/s).

## NUMERICAL

The model developed in this work provides a prediction of the time history of stress, strain, position, and velocity of a body armor material system under ballistic impact. The model is designed to continue with these predictions until either a user-specified time after impact is reached, or a user-specified failure criteria is exceeded. Table 2 summarizes the input parameters that are required of the user.

Table 2: User Supplied Input Parameters

|                              |   |
|------------------------------|---|
| Projectile striking velocity | Fabric constitutive properties                      |
| Projectile mass              | Fabric panel areal density                          |
| Projectile diameter          | Fabric panel dimensions                             |
| Boundary conditions          | Fabric crimp  |
| Model output parameters      | Model stability parameters (not currently required) |
| System failure criteria      | Maximum simulation time                             |

The basic numerical algorithm in the present numerical model is essentially unchanged from the algorithm reported by Roylance<sup>4-6</sup>; at each time increment of the simulation, the momentum, continuity, and strain compatibility equations are solved, and an "energy discrepancy" factor is calculated in lieu of the solution of an energy balance. Details of the implementation differ in that the code is now modular; the code allows for simulation of projectile geometry (the original implementation assumed point impact), and several new boundary conditions are possible. The code now allows for graphical output of field variables, and provides an automatic search capacity for the determination of ballistic limits.



It is of practical necessity to simplify the problem of ballistic impact onto woven fabric body armor; solution of the full field equations is exceedingly complex. On such simplification arises from the symmetry of the systems. Under normal (0-degree obliquity) impact, the response of a balanced weave fabric has three-fold symmetry; the response of one eighth of the system is representative of the response of the entire system. Using the symmetry argument reduces the number of model calculations without reducing the level of detail that the model is capable of providing.

As in other problems in solid mechanics, problems concerning wave propagation require the solution of the governing field equations, a set of appropriate boundary conditions, the constitutive equation, and a failure criteria to fully describe the response of the system. Computational procedures are usually designed to solve the governing equations over smaller domains. To accommodate the computational procedure, the domain of the problem is discretized, or divided into smaller sections.

The discretization of the domain of the problem was accomplished by assuming the fabric system could be modeled as a network of pin-jointed yarn elements. The yarn elements are assumed to have user-defined constitutive properties in the axial direction but are assumed to have zero shear and compressive stiffness. The grid spacing, or distance between parallel yarn elements is programmed as a user-defined input parameter. The user defines the length of the panel to be modeled, and the number of elements along one edge of the panel. The mass of the system is modeled as a uniform distribution of lumped masses over the system located at the points on intersection of crossing yarns.

It was recognized early in the development of the code that the allowable number of nodes over which a tractable solution of the impact problem could be accomplished would necessarily have to be fairly small (preferable less than 40,000 nodes). To accomplish that, the assumption that a multiple-ply system could be modeled as a single-ply system was explored<sup>7</sup>. The system effects that occur in multiple-ply systems were speculated to be due to the net increase in compressive stress that such systems are subjected to, and to a much lesser extent, to restrictions on the motion of the transverse deflection of the individual fabric plies by the other fabric plies within the system.

Since lateral compressive strain energy and shear strain energy are quite localized around the impact point, and therefore small in comparison to axial tensile strain energy, the contributions of these strains to the total deformation mechanics of the problem were assumed to be negligible. Strain energy stored within the fabric system was assumed to be in the form of axial tensile strain only. The resulting constitutive equations for materials where a linear elastic model was appropriate was therefore reduced to the familiar Hooke's Law.



An instantaneous failure criteria was selected for this work. Failure of the fabric systems is assumed to occur instantaneously whenever the parameter  $K$  defined by

$$K = \int_0^t (\sigma - \sigma_0)^\lambda dt$$

where:

|          |                                     |            |  |
|----------|-------------------------------------|------------|--|
| $\sigma$ | Stress                              | $\sigma_0$ | Stress level, below which no damage will occur   |
| $K$      | Material dependant damage parameter | $\lambda$  | Material dependent parameter chosen to fit data. |

exceeds a critical value. In the present study, the value of  $K$ ,  $\sigma$ , and  $\lambda$  were determined from regression analysis of the model predictions of the response of single ply fabric armor systems. Surfaces were generated to define the predicted values of strain in one of the yarns in contact with the projectile as a function of time after impact and as a function of projectile striking velocity.

The key assumption implicit in this approach is that the compressive stresses in single ply fabric systems under ballistic impact are negligible. In multiple ply systems, however, this is not the case<sup>7</sup>. Each fabric layer more distant from the impact point transfers a load through subsequent plies to the projectile. This loading of intermediate plies manifests itself as a localized lateral compressive stress in the fibers of those plies.

Among the simplifying approximations considered for use in the code was the idealization of the projectile. Examination of post-impact projectiles indicates that virtually no plastic deformation of the projectile (and hence no plastic work) occurs. The amount of elastic strain energy absorbed by the projectile is small in comparison the energy absorbed by the fabric system. For example, the elastic strain energy absorbed by a 17-grain body (e.g. munition fragment) at the yield point of the steel is less than 0.1 joule. It was therefore considered reasonable to consider the projectile as a rigid body.

A point impact approximation of the geometry of the projectile was initially considered. Using this approximation, the projectile is considered to impact at the intersection of two crossing yarns; the impulse imparted by these yarns to the projectile results in a decrease in the velocity of the projectile over time. The magnitude of the impulse is proportionate to the stress in the yarns, the fabric's deformed geometry, and the denier of the yarns. However, since the grid spacing is a user-selectable parameter, the denier of the modeled yarns may be continuously varied by the user. In addition to difficulties associated with the computational procedure, it is an experimental fact that the effect of projectile geometry on the performance of woven fabrics under impact is pronounced. Figure 4 illustrates the effect of projectile geometry on the energy absorption capacity of several actual fabric systems, including the current Personnel Armor System for Ground Troops (PASGT). The ordinate of Figure 4 represents the ratio of the energy absorbed by the system at the ballistic limit when the system is under impact by a right circular cylindrical steel fragment

(ES) to the energy of the same system under impact by a tungsten fragment (EW) of equal mass and length to diameter ratio. The performance of these fabric systems under impact by the high density tungsten projectiles is strikingly different from the performance against steel projectiles, particularly for the Kevlar<sup>®</sup> materials. An increase in the ratio of projectile diameters of approximately 30% appears to lead to an increase in fabric energy absorption at the ballistic limit of 20 - 200%.

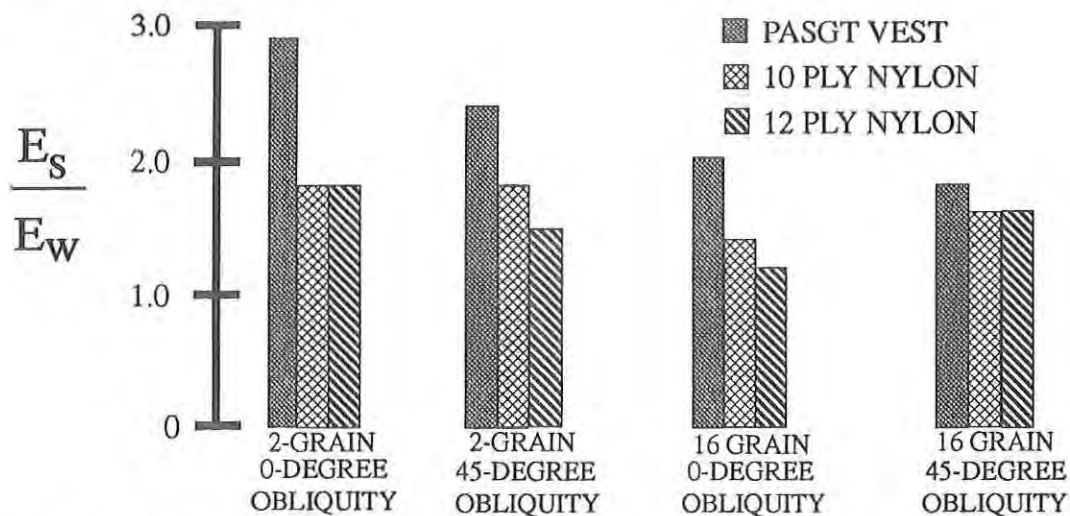


Figure 4. Ratio of the energy absorbed by the system at the ballistic limit when the system is under impact by a steel fragment (ES) to the energy of the same system under impact by a tungsten fragment (EW) of equal mass and length to diameter ratio.

The profound sensitivity of body armor system energy absorption capacity on the projectile's presented area necessitated some accounting for this parameter. However, in keeping with the general simplicity of the model, the modifications to the code to account for projectile geometry were kept simple. Projectiles were modeled as nondeformable platelets of zero-thickness and user supplied diameter and mass.

## RESULTS

Typical results of the computational procedure are illustrated in Figure 5. Figure 5 is a time series of output plots for both fabric displacement and fabric strain from the model. In this case, the fabric modeled was a 3.2 oz/yd<sup>2</sup> Kevlar<sup>®</sup> fabric under impact by a 1.1-gram right circular cylindrical projectile; the velocity of the projectile was 259 m/s. Only a small portion of the fabric was modeled; however, the boundary condition used in the model simulated an infinite fabric length. This condition sets the energy efflux rate at the edge of the panel to a constant. The strain profiles illustrated in Figure 5, therefore, represent the strain that would be developed in an effectively infinite fabric panel at the respective times after impact.

Note that the impact condition simulated in Figure 5 is similar to the impact condition of Figure 2. The plots in the left hand column of Figure 5 are displacement plots; those on the right are strain plots. As illustrated in Figure 5, at short times after impact, the strain developed in the fabric is concentrated in the yarns in contact with the projectile. As the impact event progresses in time, material not in direct contact with the projectile is placed under strain. As alluded to previously<sup>7</sup>, the transverse deflection of yarns in contact with the projectile produces an effective impact condition in neighboring yarns not in contact with the projectile.

## DISCUSSION

The predictions of the model for fabric strain indicate that fabrics perform as a collection of yarns with fairly weak coupling between the yarns. The predicted strain profiles illustrate the strongly anisotropic response of the fabric systems. It is anticipated that the response of composite materials to ballistic impact will show a somewhat more uniform stress response, due to the ability of these materials to transfer loads through shear stress in the resin system to adjacent parallel yarns.

The model predictions of strain as a function of distance from the impact point along individual yarns within the fabric indicate an oscillatory behavior as evidenced by the waviness of the lines in the strain plots of Figure 5. This oscillatory behavior is thought to be a numerical artifact. Presumably, the strain in adjacent sections of a single yarn is more smoothly varying than the model predictions indicate. The computer code developed in this work was designed to be relatively easy to modify. This was done to a certain extent at the expense of computational efficiency. These conveniences, together with the relative simplicity of the model, are thought to have led to these (small) discrepancies.

The pronounced peaks near the periphery of the projectile are thought to be an accurate representation of the behavior of woven fabrics under ballistic impact. Examination of the collection of over 300 photographs obtained during the experimental portion of this work indicates the failure of fabrics under ballistic impact is initiated at the edge of the projectile, approximately in the position indicated in the strain plots of Figure 5. Close examination of a number of photographs such as the one in Figure 2 indicates the initiation of such a failure.

The model assumes a pin-jointed connection between orthogonal yarn elements; no slippage within the fabric is accounted for. This assumption is largely borne out by experiment; yarn to yarn slippage is observed only after the initiation of failure of yarns at the periphery of the projectile. The assumption of a pin jointed connection between orthogonal yarns manifests itself in several ways in the predictions of the model, including effects relating to the load sharing between orthogonal yarn elements.

The strain profiles of Figure 5 indicate a trough, or depression in strain, in yarns that pass over the center of the projectile relative to the magnitude of strain in yarns that pass

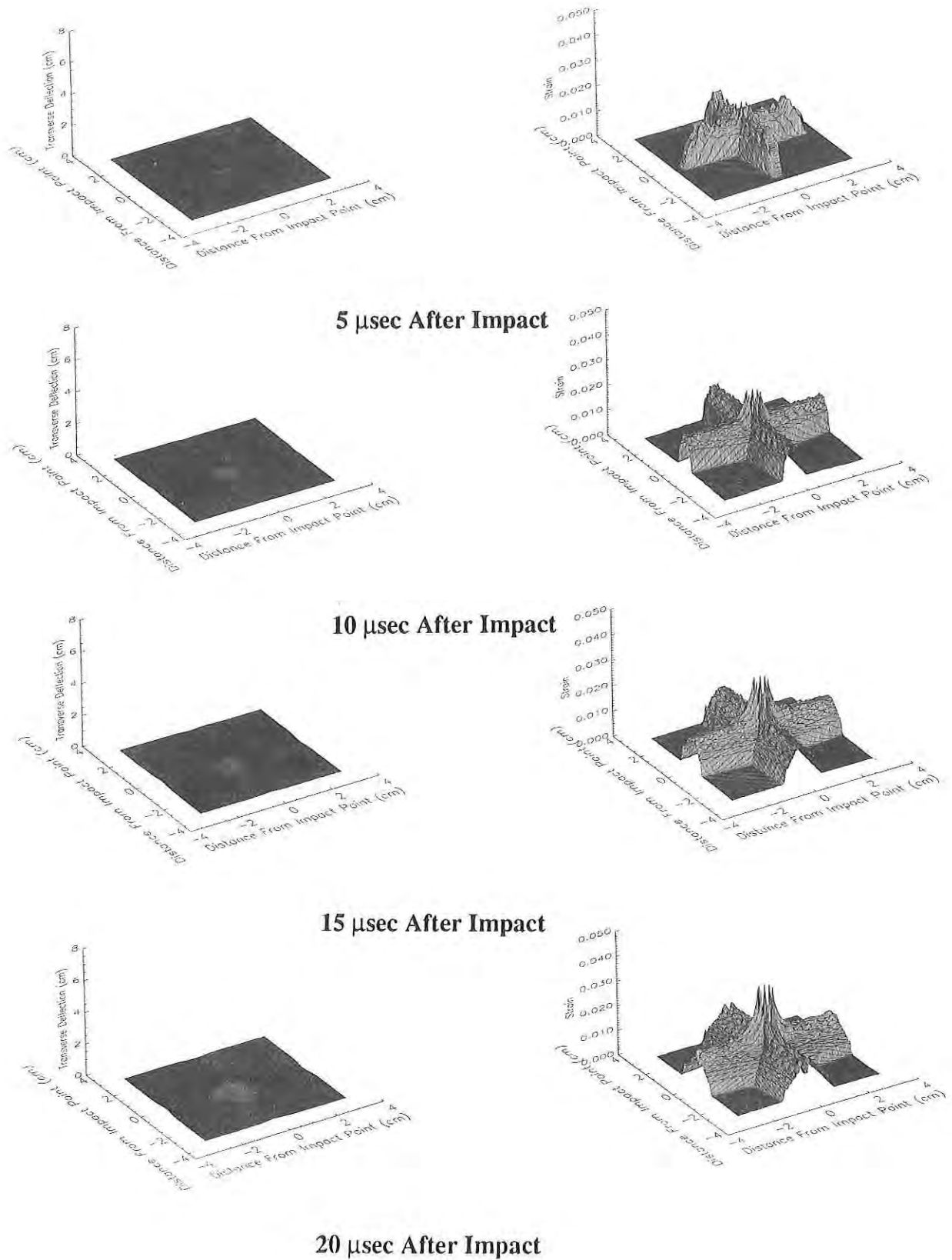
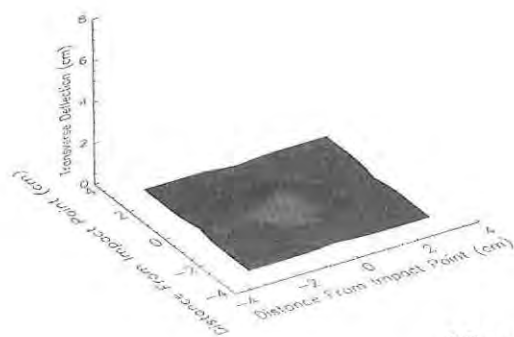
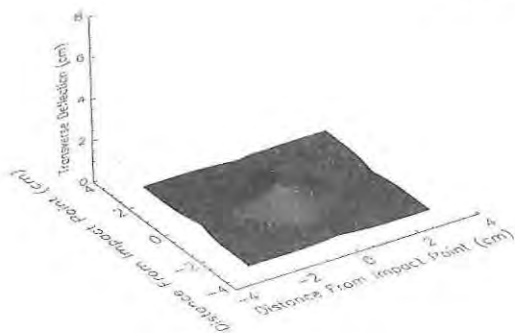
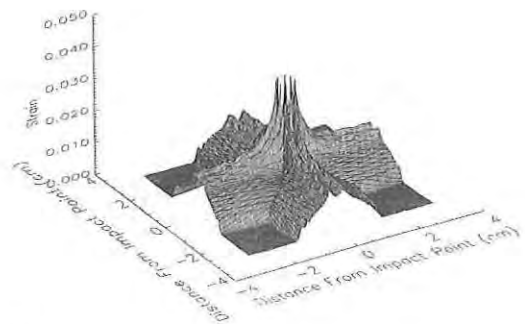


**Figure 5.** Fabric Geometry at 5 microsecond Intervals After Impact (left column); Strain in Fabric at 5 microsecond Intervals After Impact (right column), 3.2 oz/yd<sup>2</sup> Kevlar 29 Fabric Under Impact by 17-grain Fragment.

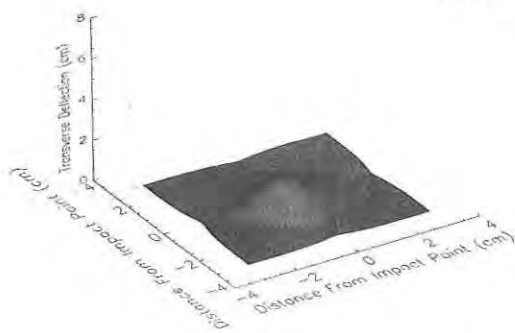
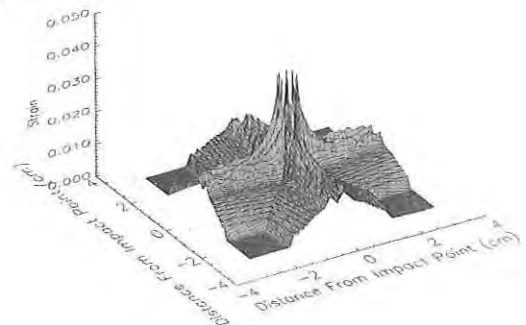
(Continued)



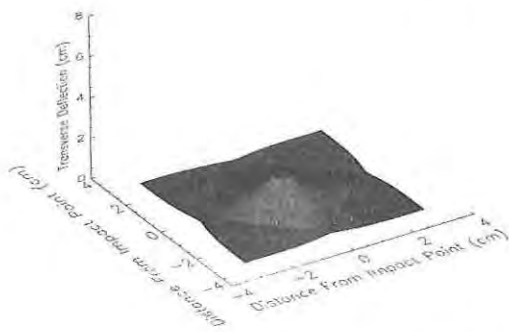
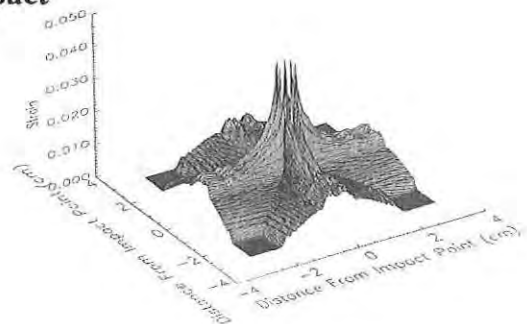
25  $\mu$ sec After Impact



30  $\mu$ sec After Impact



35  $\mu$ sec After Impact



40  $\mu$ sec After Impact

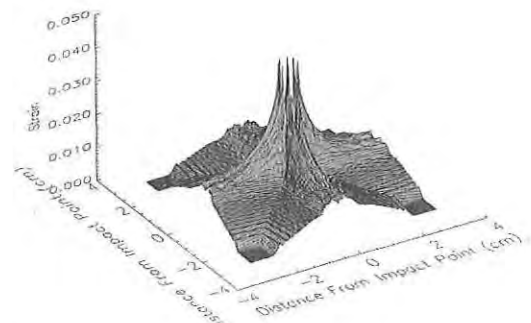


**Figure 5.** Fabric Geometry at 5 microsecond Intervals After Impact (left column); Strain in Fabric at 5 microsecond Intervals After Impact (right column). 3.2 oz/yd<sup>2</sup> Kevlar 29 Fabric Under Impact by 17-grain Fragment.



over the edge of the projectile. Apparently, very little load sharing is accomplished between parallel yarns. Under the pin-jointed approximation, load sharing is accomplished by distension of orthogonal yarns that connect neighboring parallel yarns. In actual fabrics, bending of the yarns also acts as a mechanism of load transfer between parallel yarns. It is recognized that yarns do possess a (small) bending stiffness. The bending stiffness of the yarns, which is proportionate to the moment of inertia of the filaments, is small because the filaments within the yarns are very slender. The moment of inertia of the filaments is proportionate to the fourth power of the filament diameter.

In the present development, yarn bending is ignored. This notwithstanding, the predictions of the model indicate that at least a marginal performance improvement may be obtained by increasing the load sharing between parallel yarns. One possible path to this performance improvement may be to increase the denier per filament of the fibers of the system (thereby consequently increasing the bending stiffness of the yarns). There is usually a price to pay for increasing filament denier; however, the fiber strength may be adversely affected by these variations. Since the performance improvement anticipated by increasing denier per filament is expected to be relatively small, an associated decrease in fiber strength may have an overall deleterious effect on the impact performance of the system. The modifications required to adapt the model to investigate these trade-offs are relatively simple, and will be considered in the future.

## SUMMARY

A numerical model capable of predicting the performance trade-off associated with altering the mechanical properties of textile fibers intended for use in body armor systems has been implemented. The model may be used to assist in the optimization of fibers for improved body armor systems by using it in conjunction with other experimental techniques to determine the high strain rate constitutive properties of textile fibers.

While the predictions of the model are considered to be quite accurate, the model merely represents another tool that may be used in the optimization process. This statement is not intended to diminish the importance of the models, or denigrate the utility of the models; it is intended simply to place the use of these models in a proper perspective.

The algorithm for models developed under this work is relatively simple; this feature allows use of the models in the evaluation of large numbers of impact situations. However, the simplicity of the algorithm also has certain drawbacks; critical issues pertinent to the penetration of textile armor systems such as fiber melting, shear failure, and compressive failure have been completely ignored or only peripherally addressed. The model was developed to be fairly easy to modify; incorporation of many of these enhancements should be fairly straightforward.



## REFERENCES

- 1 Cunniff, P., Constitutive Equations for Liquid Crystalline Polymers Under Ballistic Impact. Army Symposium on Solid Mechanics, Newport, RI, May 1989
- 2 Niemi, S. R., and Cunniff, P., The Performance of Quilted Body Armor Systems Under Ballistic Impact by Right Circular Cylinders. U.S. Army Natick Research, Development and Engineering Center, Natick, MA, Technical Note TN-92/002, Jan. 1992
- 3 Niemi, S. R., and Cunniff, P., The Performance of Modern Body Armor Systems Under Ballistic Impact by Various Fragment Simulators. U.S. Army Natick Research, Development and Engineering Center, Natick, MA, to be published, Technical Note 1992
- 4 Houghton, W., and Roylance, D.K., Improved Flexible Armor Design, Advanced Composites Laboratories Report, August 1989
- 5 Roylance, D.K., Penetration Mechanics of Textile Structures, U.S. Army Natick Research, Development and Engineering Center, Natick, MA, Technical Report TR-80/021, June 1979
- 6 Roylance, D.K., communications (1988-1992)
- 7 Cunniff, P., An Analysis of the System Effects in Woven Fabrics Under Ballistic Impact, accepted for publication, TRJ, 1992



GODFREY

TITLE: Deformations Near Axisymmetric Discontinuities In  
Inflated Fabric Tubes  
Thomas A. Godfrey, Mr.

ABSTRACT: Air-inflated fabric arches are being developed to provide lightweight, easily erected support frames for high mobility Army tents. These inflated tubular structures exhibit noticeable variations in their inflated shapes in boundary layer regions around discontinuities in their construction. In this work, the boundary layer behavior of inflated fabric tubes is investigated through numerical solution of the equations of nonlinear membrane theory for boundary value problems corresponding to two types of axisymmetric discontinuities: a boundary with a reinforced fabric and a boundary with a rigid collar. The analysis includes constitutive relations obtained experimentally for a particular fabric using a biaxial testing apparatus. The implications of the results with respect to design of air-inflated fabric arches is discussed.

BIOGRAPHY OF PRESENTER: Thomas A. Godfrey

PRESENT ASSIGNMENT: General Engineer, Engineering Technology  
Division, Aero-Mechanical Engineering Directorate, U.S. Army  
Natick Research, Development and Engineering Center, Natick, MA  
01760-5017

DEGREES HELD: B.S. in Mechanical Engineering, Rensselaer  
Polytechnic Institute (1983), M.S. in Mechanical Engineering,  
Mechanics Concentration, Northeastern University (1991)

GODFREY

Deformations near Axisymmetric Discontinuities in  
Inflated Fabric Tubes

Thomas A. Godfrey  
US Army Natick R,D&E Center  
Natick, MA 01760-5017

**Introduction**

Pressure-stabilized fabric arches are being developed to provide lightweight, easily erected support frames for high mobility Army tents. Pressurized arches or ribs consist of fabric tubes curved to assume an arch shape on inflation. When pretensioned by air inflation, these structures develop significant stiffness and load-carrying capability.

Pressure-stabilized arches exhibit visually noticeable distortions in their inflated shapes near discontinuities in their construction. In two prototype arches ruptures originating at the distorted region near a reinforced zipper discontinuity suggest that stress concentration effects may be important. To investigate these effects and aid in the development of future arches, an analytical model is sought to represent the deformation of cylindrical inflated fabric structures near boundaries and discontinuities where moderate changes in the shape of the structure are expected.

In this work, the structural behavior of inflated arch tubes in the vicinity of discontinuities is investigated through application of a nonlinear membrane theory. The theory idealizes the fabric as a two-dimensional continuum that can support direct tensile stress resultants in a tangent plane, but the continuum has vanishing bending stiffness. The global curvature of the tube is neglected because the segment of the tube under study is small compared to the radius of curvature. Furthermore, for simplicity, only axisymmetric problems will be addressed.

The theory of nonlinear axisymmetric membranes is given by Green and Adkins<sup>1</sup>. Equilibrium is satisfied by two nonlinear ordinary differential equations, one of which is integrable. When the undeformed geometry of the membrane is cylindrical, Pipkin<sup>2</sup> and Wu<sup>3</sup> show that integrals can be obtained for both equilibrium equations. Fortunately, arch tubes with discontinuities in construction, such as doubler patches and

GODFREY

strapped seams, are cylindrical in their original geometry. Following the approach given by Wu, the deformed geometry, extension ratios, and stress resultants in the membrane can be determined by evaluating constants of integration particular to the problem, and performing quadratures.

The goal of this work is to investigate the behavior of inflated fabric tubes as completely and generally as practicable. The nonlinear theory applied is valid for quite severe changes in geometry, such as the distortion of a cylindrical tube into an annulus<sup>4</sup>. Equally important, the constitutive relation between stress and strain in the fabric must be modelled in order to achieve meaningful results. Fabric stress versus strain behavior under biaxial loading is complex. Power law relationships have been used with success<sup>5</sup>. Model # 5 from Steeves' work will be used here.

A biaxial fabric test device<sup>6</sup> employing a cylindrical specimen under axial load and internal pressure was used to obtain the empirical data modelled in Steeves' work. The device has been rebuilt to support this project. At the time of this writing, however, the project has not progressed to the point that constitutive relations are available from the current effort.

Two representative problems are considered that relate to construction discontinuities: a rigid collar fitted over a fabric tube at some point, and an interface between two long regions of tube with significantly different stiffnesses. The second problem will be investigated using a linear stress-strain relationship.

The following notation will be used in the analysis:

|                   |   |
|-------------------|---|
| $\epsilon_1$      | Meridional strain   |
| $\epsilon_2$      | Circumferential strain  |
| $\lambda_1$       | Meridional extension ratio, $ds/dS$ , $\epsilon_1+1$            |
| $\lambda_2$       | Circumferential extension ratio, $r/R$ , $\epsilon_2+1$         |
| $\omega$          | Strain energy density function                                  |
| $\phi$            | Tangent angle of deformed membrane                              |
| $C$               | Meridian curve generating middle surface of undeformed membrane |
| $c$               | Meridian curve generating middle surface of deformed membrane   |
| $P(R, \theta, Z)$ | Point on undeformed membrane                                    |

GODFREY

|                 |  |
|-----------------|--|
| $p(r,\theta,z)$ | Point to which P is carried by deformation   |
| $q$             | Internal pressure  |
| $S$             | Arclength of meridian curve generating the undeformed middle surface of the membrane                               |
| $s$             | Arclength of meridian curve generating the deformed middle surface of the membrane                                 |
| $t_1$           | Meridional stress resultant referred to the deformed geometry, $(\partial\omega/\partial\lambda_1)/\lambda_2$      |
| $t_2$           | Circumferential stress resultant referred to the deformed geometry, $(\partial\omega/\partial\lambda_2)/\lambda_1$ |
| $T_1$           | Meridional stress resultant referred to the undeformed geometry, $\partial\omega/\partial\lambda_1$                |
| $T_2$           | Circumferential stress resultant referred to the undeformed geometry, $\partial\omega/\partial\lambda_2$           |

A cylindrical coordinate system,  $(R,\theta,Z)$ , is used with the  $Z$  axis coinciding with the axis of symmetry of the membrane. Figure 1 shows an axisymmetric membrane with deformed meridian curve  $c$ . A point  $P$  with coordinates  $R,\theta,Z$  on the undeformed membrane is carried to point  $p$  with coordinates  $r,\theta,z$  on the deformed membrane.

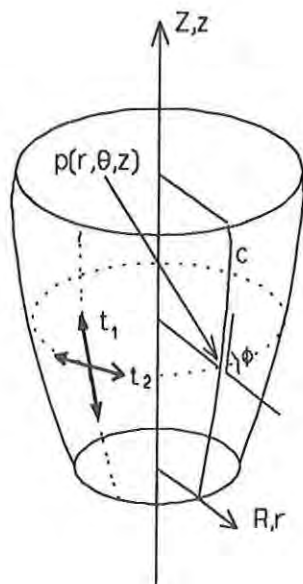


Figure 1 Axisymmetric membrane coordinate system and deformed meridian curve.



GODFREY

### Solution of initially cylindrical axisymmetric membrane problems

The equilibrium equations for axisymmetric nonlinear membranes are<sup>3</sup>:

$$\frac{d(rt_1)}{ds} = t_2 \frac{dr}{ds} \quad (1)$$

$$\frac{d\phi}{ds} t_1 + \frac{\sin\phi}{r} t_2 = q \quad (2)$$

Equation (1) can also be written as<sup>7</sup>:

$$\frac{dt_1}{dr} + \frac{1}{r} (t_1 - t_2) = 0 \quad (3)$$

In (2),  $d\phi/ds$  and  $(\sin\phi)/r$  are the principal curvatures in the meridional and normal directions. For circular cylindrical tubes of undeformed radius  $R=1$ , the principal curvatures can be written in terms of the principal extension ratios<sup>7</sup>,  $\lambda_1$ ,  $r=\lambda_2$ :

$$\frac{d\phi}{ds} = \frac{r'\lambda_1' - \lambda_1 r''}{\lambda_1^2 (\lambda_1^2 - r'^2)^{1/2}} \quad (4)$$

$$\frac{\sin\phi}{r} = \frac{(\lambda_1^2 - r'^2)^{1/2}}{\lambda_1 r} \quad (5)$$

where the prime denotes differentiation with respect to  $Z$ .

Since  $t_1$  is a function of  $\lambda_1$  and  $r$ , (3) can be written as:

$$\frac{\partial t_1}{\partial r} + \frac{\partial t_1}{\partial \lambda_1} \frac{d\lambda_1}{dr} + \frac{1}{r} (t_1 - t_2) = 0 \quad (6)$$

Making the substitution  $d\lambda_1/dr = \lambda_1'/r'$  yields:

GODFREY

$$\frac{\partial t_1}{\partial r} + \frac{\partial t_1}{\partial \lambda_1} \frac{\lambda_1'}{r'} + \frac{1}{r} (t_1 - t_2) = 0 \quad (7)$$

Inspection of (2), (4), (5) and (7) reveals that the two equilibrium equations consist of one that is second order in  $r$  and one that is first order in  $\lambda_1$  and  $r$ . Therefore, three boundary conditions are required, and these may be of the form  $\lambda_1 = \text{constant}$ ,  $r = \text{constant}$ , or  $r' = \text{constant}$  on a boundary.

For membranes with circular cylindrical undeformed middle surfaces generated by a meridian curve  $C: R=1, Z=S, 0 \leq S \leq L < \infty$ , equilibrium equations (1) and (2) can be integrated to obtain<sup>3</sup>:

$$\omega - \lambda_1 \frac{\partial \omega}{\partial \lambda_1} = a \quad (8)$$

$$r t_1 \sin(\phi) = \int q(r) r \, dr + b \quad (9)$$

where  $a$  and  $b$  are constants of integration, and  $\omega$  is the strain energy density function for the material.

For both problems considered here,  $r$  is prescribed at  $Z=0$ . Let  $r=r_0$  at  $Z=0$ . Equation (9) can then be written:

$$r t_1 \sin \phi = \int_{r_0}^r q(r_1) r_1 \, dr_1 + b \quad (10)$$

To obtain a solution for a particular problem requires three appropriate boundary conditions. The three boundary conditions are applied to determine the three constants  $a$ ,  $b$ , and  $r_0$  occurring in (8) and (10).

Evaluating (10) at  $Z=0$  gives:

$$r_0 t_1 \sin \phi|_{Z=0} = b \quad (11)$$

Our problems involve uniform internal pressure, therefore  $q$  is a constant. In addition, there is no load applied other

GODFREY

than the internal pressure. If we recognize that  $t_1 \sin \phi$  is the axial component of the meridional stress resultant, axial equilibrium of the membrane at  $z=0$  allows the constant  $b$  to be written as:

$$b = r_0 t_1 \sin \phi|_{z=0} = r_0 \frac{q \pi r_0^2}{2 \pi r_0} = \frac{q r_0^2}{2} \quad (12)$$

Carrying out the integration, we can now write (10) as:

$$r t_1 \sin \phi = \frac{q(r^2 - r_0^2)}{2} + \frac{q r_0^2}{2} = \frac{q r^2}{2} \quad (13)$$

The tangent angle  $\phi$  is therefore:

$$\phi = \sin^{-1} \left( \frac{q r}{2 t_1} \right) \quad (14)$$

At this point, two of the constants,  $b$  and  $r_0$  have been determined. The third constant,  $a$ , will allow the solution to be completed. Equation (8) is evaluated with the remaining boundary conditions to determine  $a$ . Generally,  $\omega$  is expressed as  $\omega(\lambda_1, r)$ , and (8) is used with the known  $a$  to express or tabulate  $\lambda_1$  as a function of  $r$ . Constitutive relations are subsequently used to tabulate  $t_1$  and  $t_2$  as functions of  $r$ . Our fabric stress-strain relations give strains explicitly from stresses, so it is more convenient to use (8) to obtain a stress as a function of  $r$ . The deformed geometry,  $z(r)$ , is finally determined using<sup>3</sup>:

$$z = \int_{r_0}^r \tan \phi(r_1) dr_1 \quad (15)$$

where  $\phi$  is obtained from (14)

The steps in solving a particular initially cylindrical axisymmetric membrane problem are first determining  $a$ ,  $b$ , and  $r_0$  to satisfy the boundary conditions. Second, the algebraic equations consisting of (8) and the two stress-strain relations are used to tabulate  $\lambda_1$ ,  $t_1$ , and  $t_2$  as functions of  $r$ . Third, the quadrature of (15) is carried out to determine the deformed geometry.

It should be noted that (11) indicates that the constant  $b$

GODFREY

would be used to apply an additional axial load at  $z=0$ . In our problems, all axial load is due to internal pressure.

### Stress-strain relations and strain energy density function for fabric

The following empirical power law model for the biaxial stress-strain behavior of a fabric is assumed<sup>5</sup>:

$$\epsilon_1 = C_{11} T_1^{P_1} + C_{12} T_2^{P_2} \quad (16)$$

$$\epsilon_2 = C_{21} T_1^{P_3} + C_{22} T_2^{P_4} \quad (17)$$

For evaluation of (8), however, a strain energy density function is required. If we use the fact that the strain energy density function must act as a stress potential function, the stress-strain relations can be used to derive the strain energy density function. The strain energy density function is obtained by integration of the differential work done in stretching the fabric from its natural state to its final state of biaxial stress:

$$d\omega = \frac{\partial \omega}{\partial \epsilon_1} d\epsilon_1 + \frac{\partial \omega}{\partial \epsilon_2} d\epsilon_2 \quad (18)$$

$$d\omega = T_1(\epsilon_1, \epsilon_2) d\epsilon_1 + T_2(\epsilon_1, \epsilon_2) d\epsilon_2 \quad (19)$$

$$d\epsilon_1 = \frac{\partial \epsilon_1}{\partial T_1} dT_1 + \frac{\partial \epsilon_1}{\partial T_2} dT_2 \quad (20)$$

$$d\epsilon_2 = \frac{\partial \epsilon_2}{\partial T_1} dT_1 + \frac{\partial \epsilon_2}{\partial T_2} dT_2 \quad (21)$$

Since the fabric is assumed to be elastic,  $\omega(T_1, T_2)$  can be obtained by integration of (19) along any path. Realistically, fabrics are not perfectly elastic, and integration would be path

GODFREY

dependent. The biaxial test device used to collect stress-strain data loads the specimen up in a test format that holds the axial and circumferential stress resultants in a constant ratio. For convenience, integration of (19) will be along a path of constant stress ratio, thus:

$$T_2 = K T_1 \quad (22)$$

where K is a constant.

Equations (16), (17), (19), (20), (21) & (22) can be used to express the differential of the strain energy density function in terms of  $T_1$ :

$$d\omega = C_{11} P_1 T_1^{P_1} dT_1 + C_{12} P_2 K^{P_2} T_1^{P_2} dT_1 + C_{21} P_3 K T_1^{P_3} dT_1 + C_{22} P_4 K^{P_4+1} T_1^{P_4} dT_1 \quad (23)$$

Integration from the natural unstressed state to a biaxial state of stress  $T_1, K T_1$  yields:

$$\omega = \frac{C_{11} P_1}{P_1 + 1} T_1^{P_1+1} + \frac{K^{P_2} C_{12} P_2}{P_2 + 1} T_1^{P_2+1} + \frac{K C_{21} P_3}{P_3 + 1} T_1^{P_3+1} + \frac{K^{P_4+1} C_{22} P_4}{P_4 + 1} T_1^{P_4+1} \quad (24)$$

### Rigid collar problem

Consider a rigid collar of radius 1 fastened at  $Z=0$  to a long tube of undeformed radius  $R=1$ . The tube is then inflated to a certain internal pressure. At  $z=\infty$  the geometry of the tube is that of an inflated cylinder unaffected by the boundary condition  $r_0=1$ . Let the subscript  $\infty$  denote evaluation at  $z=\infty$ . Consider for the moment  $T_{1\infty}$  to represent the intensity of the inflation. The boundary conditions for this problem are:

$$\begin{array}{ll} Z=0: & r=r_0=1 \\ Z=\infty: & \lambda_1=\lambda_{1\infty}, \quad r=r_\infty=\lambda_{2\infty} \end{array} \quad (25)$$

Two of the three constants required have already been determined. The constant b is given by (12) and  $r_0=1$ . To evaluate the constant a requires that the extension ratios  $(\lambda_{1\infty}, \lambda_{2\infty})$  in an inflated fabric circular cylinder be determined. These are the boundary conditions at  $z=\infty$ .

GODFREY

The stress resultants at  $z=\infty$  are related by:

$$t_{2\infty} = 2t_{1\infty} \quad (26)$$

Since the stress resultants in the deformed and undeformed geometries are related by:

$$t_1 = T_1 / \lambda_2 \quad (27)$$

$$t_2 = T_2 / \lambda_1 \quad (28)$$

the stress resultants in the undeformed geometries at  $z=\infty$  are related by:

$$T_{2\infty} = \frac{2\lambda_{1\infty}}{\lambda_{2\infty}} T_{1\infty} \quad (29)$$

Substituting (29) in the constitutive relations, (16) & (17), gives two nonlinear equations for the extension ratios at  $z=\infty$ :

$$\lambda_{1\infty} - C_{11} T_{1\infty}^{P_1} - C_{12} \left( \frac{2\lambda_{1\infty}}{\lambda_{2\infty}} T_{1\infty} \right)^{P_2} - 1 = 0 \quad (30)$$

$$\lambda_{2\infty} - C_{21} T_{1\infty}^{P_3} - C_{22} \left( \frac{2\lambda_{1\infty}}{\lambda_{2\infty}} T_{1\infty} \right)^{P_4} - 1 = 0 \quad (31)$$

The system of (30) & (31) can be solved numerically to obtain  $\lambda_{1\infty}$  and  $\lambda_{2\infty}$  for a given  $T_{1\infty}$ .

With the boundary conditions at  $z=\infty$  numerically determined, the third integration constant  $a$  from (8) can be evaluated. Equation (8) is evaluated at  $z=\infty$  using (8), (16), (22), (24) & (29):



GODFREY

$$\frac{-C_{11}}{P_1+1} T_{1\infty}^{P_1+1} + \frac{-K_{\infty}^{P_2} C_{12}}{P_2+1} T_{1\infty}^{P_2+1} + \frac{K_{\infty} C_{21} P_3}{P_3+1} T_{1\infty}^{P_3+1} + \frac{K_{\infty}^{P_4+1} C_{22} P_4}{P_4+1} T_{1\infty}^{P_4+1} - T_{1\infty} = a \quad (32)$$

where  $K_{\infty}$  is evaluated numerically using the boundary conditions  $\lambda_{1\infty}$  and  $\lambda_{2\infty}$ .

With the constant  $a$  obtained,  $T_1$  can be determined as a function of  $r$  using (8), (16), (17), (22) & (24). Note that  $r=\lambda_2$  since  $R=1$ :

$$\frac{-C_{11}}{P_1+1} T_1^{P_1+1} + \frac{-K^{P_2} C_{12}}{P_2+1} T_1^{P_2+1} + \frac{K C_{21} P_3}{P_3+1} T_1^{P_3+1} + \frac{K^{P_4+1} C_{22} P_4}{P_4+1} T_1^{P_4+1} - T_1 - a = 0 \quad (33)$$

$$K = \left[ \frac{r-1}{C_{22} T_1^{P_4}} - \frac{C_{21}}{C_{22}} T_1^{P_3-P_4} \right]^{1/P_4} \quad (34)$$

Substituting (34) in (33) gives a nonlinear equation in  $T_1$  that can be solved numerically. In this manner, the extension ratios and stress resultants can be tabulated at any number of points by determining  $T_1(r)$ , then  $T_2=KT_1$ , and  $\lambda_1$  from the constitutive relation. The deformed geometry of the tube,  $z(r)$ , is determined by quadrature using (14) & (15).

For practical applications it is useful to know the internal pressure causing the deformation. This is given by the classical strength of materials result<sup>8</sup>:

$$q = \frac{2 t_{1\infty}}{\lambda_{2\infty}} = \frac{2 T_{1\infty}}{\lambda_{2\infty}^2} \quad (35)$$

Calculations were performed for the rigid collar problem using Steeves' parameter estimates for model 5 from data set FD21-2<sup>5</sup>. The fabric used to generate data set FD21-2 was a polyurethane coated nylon fabric with base fabric weight of 41 g/m<sup>2</sup> and coated weight of 112 g/m<sup>2</sup>. The fabric was plain weave with 72 ends/cm and 44 picks/cm. Crimp was 0.7 % in the warp and 2.3 % in the fill. For the rigid collar problem, the fabric fill

GODFREY

direction coincides with the meridional direction, and the warp direction coincides with the circumferential direction.

The numerical calculations were performed using a computer program coded in FORTRAN 77. The nonlinear equation solver, DNSQE, revision date 5 April 1984, written by K. L. Hiebert, was used to solve the system (30) & (31). The secant method was used to solve the nonlinear equation indicated by (33) & (34). The quadrature of (15) was performed using the subroutine DQAGSE, revision date 18 May 1983, written by Robert Piessens and Elise De Doncker. Both DNSQE and DQAGSE are part of the Slatec software package obtained from the National Energy Software Center, Argonne National Laboratory, Argonne, IL.

#### Interface between tubes of differing stiffness

Consider two long tubes of the same undeformed radius  $R=1$ , made from fabrics of significantly different stiffnesses, joined together end to end at  $z=0$ . The composite tube and coordinate system are shown in Figure 2. The composite tube is then inflated to some internal pressure and assumes an inflated shape like that shown in Figure 3. At  $z=\infty$  the right-hand tube assumes the geometry of an inflated cylinder, unaffected by the boundary conditions at  $z=0$ . Likewise at  $z=-\infty$  the left-hand tube assumes the geometry of an inflated cylinder, unaffected by the boundary at  $z=0$ . If the left-hand tube is the stiffer, the left-hand tube will curve outward with positive curvature approaching  $z=0$  from  $z=-\infty$ . The right-hand tube will curve outward with negative curvature as  $z=\infty$  is approached from  $z=0$ .

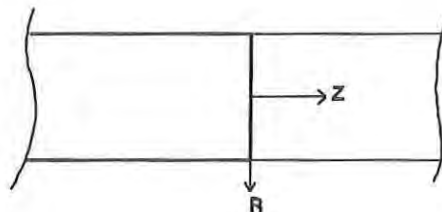


Figure 2 Interface between tubes of different stiffnesses.

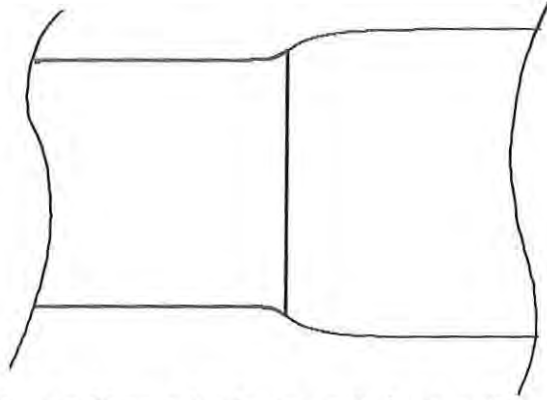


Figure 3 Inflated shape of interface between tubes.

The solution to this problem will be discussed only briefly to conserve space. The boundary conditions at  $z=+\infty$  and  $-\infty$  are the same as in the rigid collar problem. Equation (8) is evaluated for the left-hand tube (subscript LH) and the right-hand tube (subscript RH), to determine the constant  $a$  that applies in each region:

$$[\omega_{LH} - \lambda_1 \frac{\partial \omega_{LH}}{\partial \lambda_1}] \big|_{z=-\infty} = a_{LH} \quad (36)$$

$$[\omega_{RH} - \lambda_1 \frac{\partial \omega_{RH}}{\partial \lambda_1}] \big|_{z=+\infty} = a_{RH} \quad (37)$$

The boundary conditions at  $z=0$  are that  $r$  and  $t_1$  in each tube match. Using the  $a$  for each tube region, the matching conditions for  $t_1$  and  $r$  can be satisfied by numerical solution of a nonlinear equation in  $r$ :

$$[t_1 (LH) (r, a_{LH}) - t_1 (RH) (r, a_{RH})] \big|_{z=0} = 0 \quad (38)$$

The solution of (38) is  $r|_{z=0} = r_0$ . The extension ratios, stress resultants, and deformed geometry of each tube region can

then be calculated over the range  $r_{\infty}$  to  $r_0$  for the left-hand tube and  $r_0$  to  $r_{\infty}$  for the right-hand tube.

### Results for rigid collar problem

The extension ratios and stress resultants in the fabric tube with the rigid collar at  $z=0$  are given in Figures 4 through 7. Since the undeformed radius of the tube is, for convenience, one cm, Figure 5 can also be taken as the deformed geometry,  $r(z)$ , of the tube. The meridional stress resultant,  $t_1$  (Figure 6) is plotted nondimensionalized by  $t_{1\infty}$  to show the small variations in  $t_1$  in more detail. Calculations were performed for three inflation intensities:  $T_{1\infty}=5, 10$  and  $15$  N/cm. Results at the tube boundaries are in Table 1.

Table 1 Results at boundaries for rigid collar problem

| $T_{1\infty}$ , N/cm,<br>Pressure,<br>kPa | $z$      | $\lambda_1$ | $\lambda_2$ | $t_1$ ,<br>N/cm | $t_2$ ,<br>N/cm | $\phi$  |
|---|----------|-------------|-------------|-----------------|-----------------|---------|
| 5, 94.4                                   | 0        | 1.0446      | 1.0000      | 4.83            | 2.64            | 1.3527  |
|   | $\infty$ | 1.0352      | 1.0295      | 4.86            | 9.71            | $\pi/2$ |
| 10, 180.0                                 | 0        | 1.0712      | 1.0000      | 9.43            | 3.98            | 1.2683  |
|   | $\infty$ | 1.0580      | 1.0539      | 9.49            | 18.98           | $\pi/2$ |
| 15, 259.2                                 | 0        | 1.0926      | 1.0000      | 13.86           | 5.01            | 1.2091  |
|   | $\infty$ | 1.0772      | 1.0758      | 13.94           | 27.9            | $\pi/2$ |

The calculations show that stress resultants are lower near the rigid collar than they are in the fully inflated region. The circumferential stress resultant, Figure 7, varies considerably, being a minimum at the collar. At higher inflation pressures the variation in the circumferential stress resultant is increased. The meridional stress resultant, Figure 6, is nearly constant. Variation in the meridional stress resultant is less than 2% even at the highest inflation pressure.

The circumferential extension ratio, Figure 5, increases monotonically from the collar to the fully inflated region. The

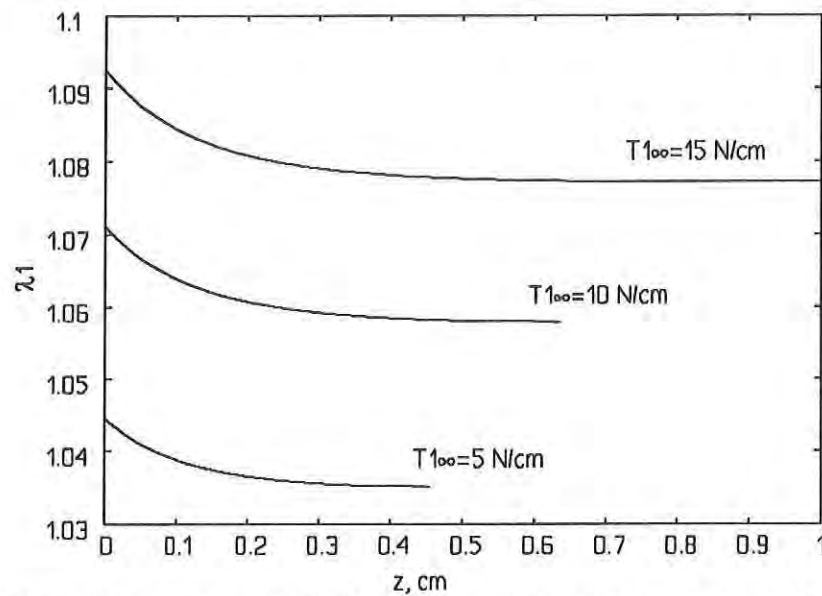


Figure 4 Meridional extension for rigid collar problem

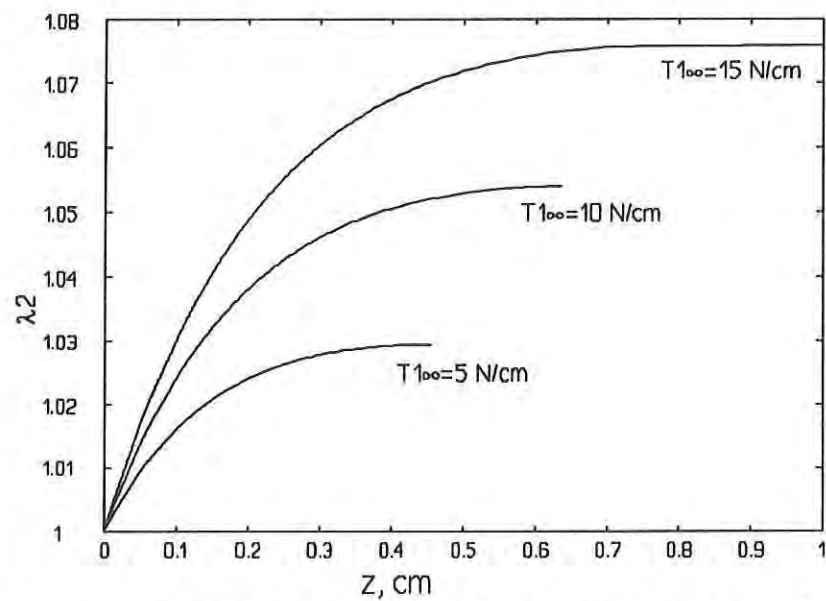


Figure 5 Circumferential extension for rigid collar problem.

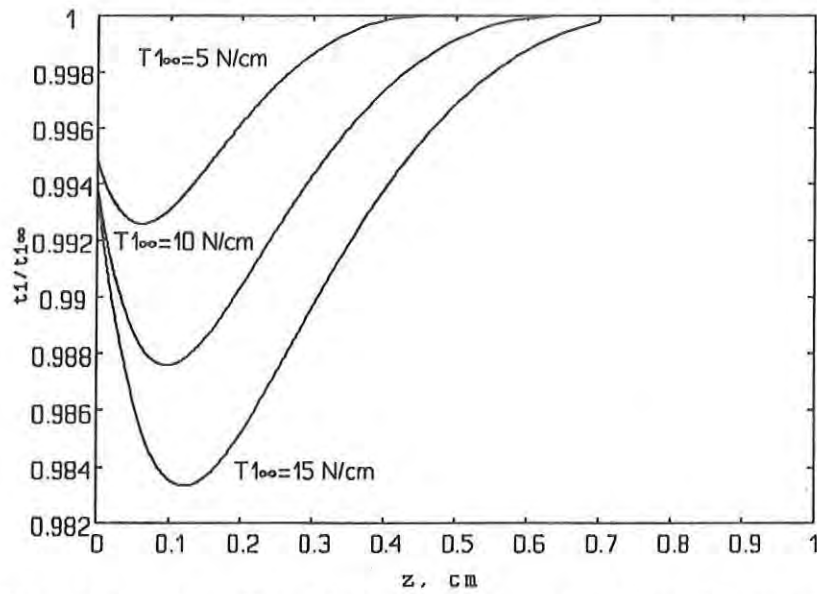


Figure 6 Meridional stress resultant for rigid collar problem.

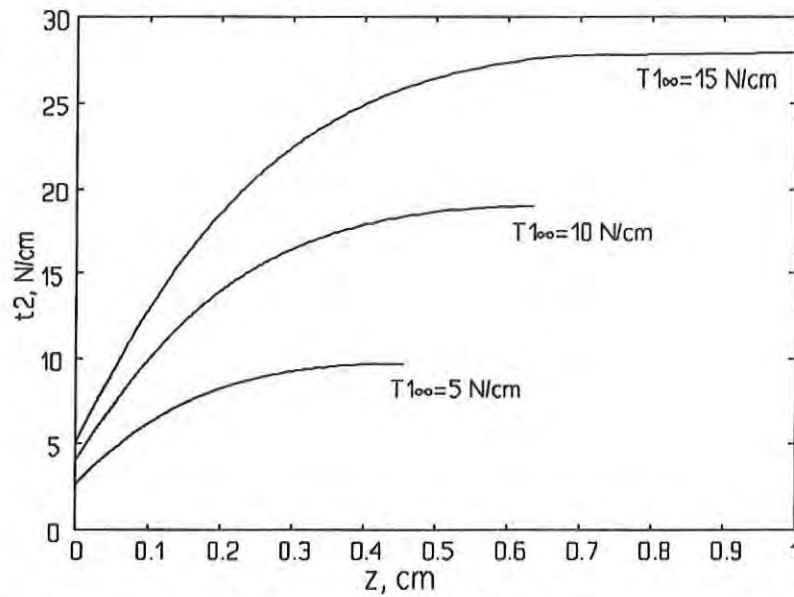


Figure 7 Circumferential stress resultant for rigid collar problem.



meridional extension ratio, Figure 4, is a maximum at the collar and decreases monotonically to the fully inflated region. The change in the inflated shape of the tube caused by the collar discontinuity is evident within an axial distance of three quarters of the tube radius from the rigid collar.

Some reservations are noted about the application of the stress-strain relation to this problem. Data set FD21-2 contains data collected only up to about 20 N/cm in stress. The  $T_{100}=15$  N/cm calculation is an extrapolation based on the parameters estimated for the constants in (16) and (17). The results near the rigid boundary are suspect because the warp (circumferential) to fill (meridional) stress ratio ranges from one third to one half and the stress level is relatively low. Under these conditions, the data set indicates that strain contractions in the warp direction will occur<sup>5</sup>, a situation that model #5 models poorly. Such a strain contraction is not physically reasonable for this problem because it would require the tube to shrink away from the rigid collar boundary.

The rigid collar problem is important because it represents an extreme case of a stiffness discontinuity in the tube. The behavior of an interface between tubes of different stiffnesses should approach that of the rigid collar problem as the stiffness of the stiffer of the tubes is increased.

### Results for interface problem

Some preliminary results for the problem of an interface between tubes of different stiffnesses are shown in Figures 8 and 9. Because of the lack of constitutive relations for fabrics at the time of the work, the calculations were performed using linear stress-strain relations of the following form:

$$t_1 = \frac{1}{\lambda_2} [C_{11}(\lambda_1 - 1) + C_{12}(\lambda_2 - 1)] \quad (39)$$

$$t_2 = \frac{1}{\lambda_1} [C_{12}(\lambda_1 - 1) + C_{22}(\lambda_2 - 1)] \quad (40)$$

For the calculations shown, the less stiff or unreinforced tube has nondimensional stiffness constants  $C_{11}=1$ ,  $C_{12}=0.3$ , and

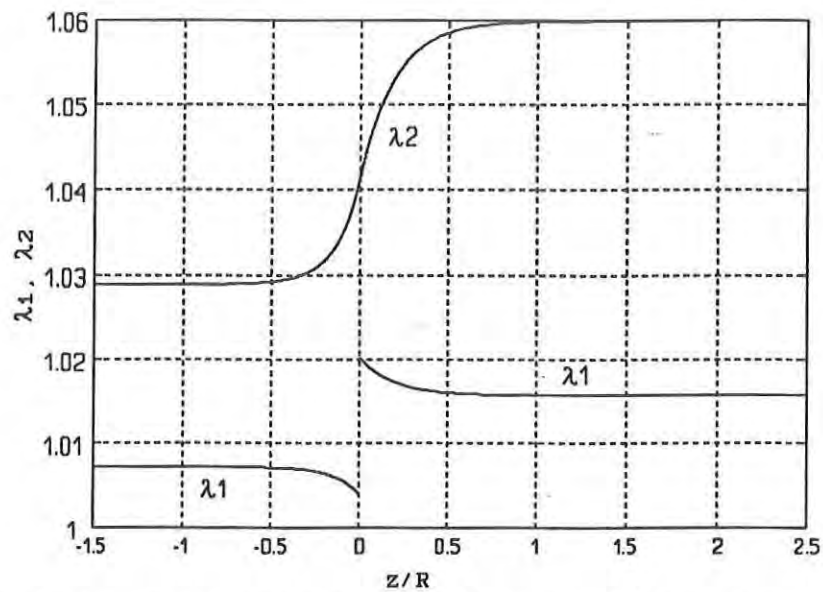


Figure 8 Extension ratios in interface.

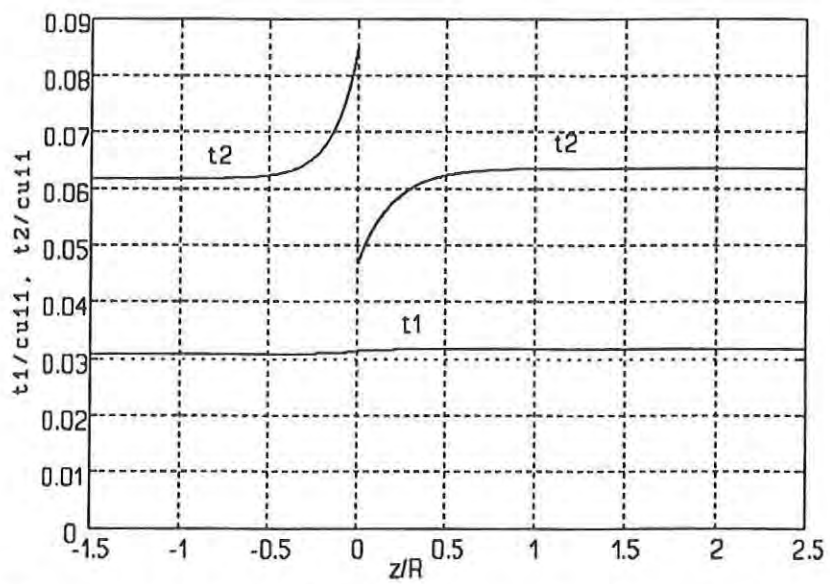


Figure 9 Stress resultants in interface.

## GODFREY

$C_{22}=1$ . The stiffer or reinforced tube has nondimensional stiffness constants relative to the unreinforced tube of  $C_{11}=2$ ,  $C_{12}=0.6$ , and  $C_{22}=2$ . The composite tube is inflated to a nondimensional pressure,  $qR/cu_{11}$ , of 0.06. The constant  $cu_{11}$  is the dimensional stiffness constant associated with  $\lambda_1$  term for  $t_1$  in the unreinforced tube. The stress resultants in Figure 9 have been nondimensionalized by  $cu_{11}$ .

As in the rigid collar problem, the meridional stress resultant changes little. The circumferential stress resultant is lower near the boundary for the unreinforced tube. For the reinforced tube, however, the circumferential stress resultant reaches a peak at the boundary.

The circumferential extension ratio smoothly progresses from the reinforced tube into the unreinforced tube, indicating a trumpet-like flaring of the reinforced tube near the boundary. The meridional extension ratio decreases near the boundary for the reinforced tube, and increases near the boundary for the unreinforced tube.

### Concluding remarks

To address the effect of construction discontinuities in pressurized fabric arches, a method for solving axisymmetric nonlinear membrane problems was applied to two representative situations: a boundary with a rigid collar and an interface between arch tubes of different stiffnesses. The rigid collar problem was solved using empirically derived stress-strain relations for a particular fabric. The interface problem was solved for hypothetical linear membrane materials.

For the rigid collar problem, both principal stress resultants are lower in the region adjacent to the rigid collar than in the remainder of the tube. The circumferential stress resultant is significantly lower, and the meridional stress resultant is slightly lower near the collar.

Results for the interface problem indicate that circumferential stress resultants are significantly increased in the interface region of the reinforced tube and decreased in the interface region of the unreinforced tube. There are discontinuities in the circumferential stress resultants and meridional extension ratios across the interface between the

tubes. Meridional stress resultants are nearly constant throughout the reinforced and unreinforced tubes.

In both problems an increasing circumferential extension ratio in a given region was accompanied by a decreasing meridional extension ratio, and similarly a decreasing circumferential extension ratio was accompanied by an increasing meridional extension ratio. The effect of the discontinuity was confined to well within one tube radius of the boundary for all calculations.

The inadequacy of the fabric constitutive relation used to properly model strain contractions occurring at high stress ratios and low stresses is a concern. A more sophisticated model, designated model #11<sup>5</sup>, will be applied in the future to address this concern.

The lack of any stress concentration effect in the rigid collar problem should not be misinterpreted as indicating that there is no strength problem associated with a rigid collar discontinuity. Little scientific work has been done concerning the biaxial strength of fabrics. Indications are that the strength of a fabric under biaxial loads is significantly different than any familiar uniaxial strength result. At this time information is lacking to develop the strength envelop of a particular fabric over a variety of biaxial stress and strain conditions.

Although this work addresses only axisymmetric situations, most realistic arch construction discontinuities are not axisymmetric. It is these nonaxisymmetric problems that will most likely generate critical stress states through the introduction of shear stresses in the fabric. The current effort provides a key step to these more complicated problems.

GODFREY

### References

1. Green, A. E., Adkins, J. E., Large Elastic Deformations, Clarendon Press, Oxford, 1960.
2. Pipkin, Allen C., Integration of an equation in membrane theory, Z. Angew. Math. Phys., 19 (1968), pp. 818-819.
3. Wu, Chien-Heng, On certain integrable nonlinear membrane solutions, Quart. Appl. Math., 28 (1970), pp. 81-90.
4. Wu, Chien-Heng, Tube to annulus--an exact nonlinear membrane solution, Quart. Appl. Math., 27 (1970), pp. 489-496.
5. Steeves, Earl C., Mathematical Modeling of the Biaxial Stress-Strain Behavior of Fabrics, U.S. Army Natick R&D Laboratories Technical Report, NATICK/TR-82/009, March 1982 (AD A115 058)
6. Monego, Constantin J., Pilsworth, Jr., Malcolm N., Development of an Apparatus for Biaxial and Shear Stress-Strain Testing of Fabrics and Films, U.S. Army Natick R&D Command Technical Report, NATICK/TR-80/028, October 1980 (AD A094 270)
7. Yang, W. H., Feng, W. W., On axisymmetrical deformations of nonlinear membranes, Journal of Applied Mechanics, December 1970, pp. 1002-1011.
8. Singer, Ferdinand L., Pytel, Andrew, Strength of Materials, Harper & Row, New York, 1980.





RIVIN & KENDRICK

TITLE: COMPARATIVE ADSORPTION OF AGENT AND SIMULANT VAPOR BY  
PERMEABLE FABRICS CONTAINING ACTIVATED CARBON  
Donald Rivin, Dr. and Cyrus E. Kendrick, Mr.

ABSTRACT: Vapor challenge testing of carbon-loaded fabric swatches provides adsorption data which can be used to determine relative protection levels, and to predict field performance when interpreted in the context of an holistic model. Fundamental chemical and physical parameters which control adsorption/desorption of organic vapors by adsorbent fabric are described, and applied to a comparison of the interaction of CW agents and simulants with carbon-impregnated Type III foam laminate. Parallel thermodynamic and kinetic adsorption measurements demonstrate that the dynamic adsorption capacity approaches the equilibrium capacity as an upper limit. Often these capacities agree to within ten percent, attesting to the correlatability of breakthrough data for organic compounds of widely disparate volatility.

Dynamic testing with simulant vapor under standard challenge conditions is well-suited to evaluating fabric adsorption for quality assurance, acceptance, stockpile surveillance, and development of adsorbent materials. Conversely, current vapor challenge tests using either agent or simulant are not suitable for predicting performance in the field because they do not provide information about sensitivity of the adsorption process to ambient exposure conditions (e.g., vapor concentration profile, temperature, air pollutants, and relative humidity). The role of these environmental variables is illustrated in this study through their effect on the adsorption of HD and simulant vapors by Type III fabric. Meaningful performance projections could be obtained from a model which combines these functional dependencies with field exposure scenarios, including data for agent distribution and wind-driven permeation.

BIOGRAPHY OF PRESENTER: Donald Rivin

PRESENT ASSIGNMENT: Chief, Materials Section, Materials Research and Engineering Division, Individual Protection Directorate, U.S. Army Natick Research Development and Engineering Center, Natick, MA

PAST EXPERIENCE: Corporate Research Fellow, Cabot Corporation, Billerica, MA

DEGREES HELD: B.A., M.A., Ph.D. (Chemistry), Columbia University, New York, NY

COMPARATIVE ADSORPTION OF AGENT AND SIMULANT VAPOR BY PERMEABLE  
FABRICS CONTAINING ACTIVATED CARBON

Donald Rivin, Dr., and Cyrus E. Kendrick, Mr.  
U. S. Army Natick Research, Development and Engineering Center  
Natick MA 01760

## 1. INTRODUCTION

Protective clothing based on permeable fabrics provides an effective barrier against toxic organic vapors with relatively little reduction in the transmission of air and water vapor. Although a variety of fabric compositions and designs are employed worldwide, all contain some form of activated carbon as the vapor protective component. This material is used universally because it combines high capacity with low selectivity, providing maximum protection against a wide range of percutaneous toxins. In order to understand how activated carbons function in protective fabrics it is useful to examine the structure of these solids, and the mechanism of the adsorption process responsible for their barrier properties.

Active carbons are produced by pyrolysis of carbonaceous precursors, such as coal, petroleum derivatives or botanical materials, followed by controlled oxidation (activation) to develop a complex network of internal pores. High resolution electron microscopy<sup>1</sup> and small angle X-ray scattering (SAXS)<sup>2</sup> reveal a disordered structure consisting of a twisted array of defective graphitic layers crosslinked by short aliphatic carbon bridges. From the schema of active carbon in Fig. 1<sup>3</sup> it follows that interlaminar spaces and occlusions associated with bent aromatic sheets can be treated as slit-shaped pores. To a good approximation, these pores are classified in three size ranges<sup>4</sup>: micropores (<2nm pore width), mesopores (2-50nm), and macropores (>50nm).



Fig. 1. Schematic representation of the internal structure of active carbon. From Ref. 3

Adsorption of gases or vapors at low pressure occurs mainly in micropores due to the increased potential arising from overlap of the adsorption forces generated by proximate opposing walls<sup>5</sup>. For this reason, carbons of interest for military applications are predominantly microporous, with lesser amounts of wider pores which influence internal mass transfer rates. All carbon adsorbents also contain heteroatoms (e.g., H, O, S, N) covalently bound as organic functional groups at edge and defect sites on the aromatic layers<sup>6</sup>. Except for C-H, these groups interact strongly with dipolar molecules causing enhanced adsorption of polar vapors. Localized interaction is of secondary importance for current chemical agents, which are generally of low to moderate polarity, and interact with the carbon through nonspecific van der Waals dispersion forces. However, likely contaminants, e.g., cigarette smoke constituents, and water vapor, are strongly adsorbed at polar sites. Water vapor adsorbs as clusters surrounding polar nucleating sites at low relative humidity (RH) on acidic and basic carbons but does not adsorb until very high RH on carbons with few heteroatoms<sup>7</sup>.

## 2. ROLE OF LABORATORY VAPOR SORPTION TESTS

In the laboratory, vapor challenge with agents or simulants is performed with fabric swatches in order to determine protective properties, or on complete garments or "systems" to evaluate design and construction parameters. In the case of swatch tests, it is not possible to assess protection levels in the field based on either agent or simulant exposure under a single set of conditions, in the absence of information regarding the sensitivity of the adsorption process to contaminants (e.g., water) and environmental variables (e.g., temperature, toxic vapor concentration, flowrate, and exposure profile). In principle, however, laboratory studies covering a suitable range of conditions can be used to predict end-use performance provided that an appropriate model is available to describe exposure conditions in the field. It will be shown that although adsorption characteristics are dependent on both the challenge vapor (adsorptive) and the carbon/fabric (adsorbent), reliable methods are available for equating adsorptives, and thus evaluating agent protection from laboratory experiments with faster, safer, less expensive, and more convenient simulant tests.

## 3. EQUILIBRIUM ADSORPTION

Nonporous carbon adsorbents usually retain organic molecules by reversible surface adsorption, whereas microporous carbons also act reversibly but primarily by accumulation of liquified adsorptive (adsorbate) in micropores. Adsorption at constant temperature is represented by an adsorption isotherm, which gives the amount of adsorbate at equilibrium as a function of adsorptive relative pressure ( $P/P_0$ , where  $P_0$  is the saturated vapor pressure of liquid adsorptive). A number of theoretical models have been proposed to describe the adsorption process in order to quantitatively characterize adsorbents, and to generalize adsorptive-adsorbent interactions<sup>8,9</sup>. Of these, Dubinin's Theory of Volume Filling of Micropores (TVFM)<sup>10</sup> has been most broadly applied to studies of microporous carbon. The TVFM is derived from the Polanyi mechanism, in which the differential free energy of adsorption, or adsorption potential,  $\epsilon$ , at the initiation of vapor condensation on the surface is given by

$$\epsilon = RT \ln(P_0/P) \quad (1)$$

where  $R$  is the universal gas constant, and  $T$  is the absolute temperature. Based on the Polanyi characteristic curve (amount adsorbed vs.  $\epsilon$ ), the TVFM is expressed as

$$V/V_0 = \exp[(\epsilon/\beta E_0)^n] \quad (2)$$

where  $V$  is the volume of adsorbate per gram of carbon,  $V_0$  is the total micropore volume,  $E_0$  is a structural energy constant arising from the pore size distribution of the adsorbent, and  $\beta$  is an affinity coefficient which depends on the interaction energy and facilitates superimposition of the characteristic curves for different adsorptives. The exponent  $n$  varies from 3 for homogeneous molecular sieve carbons to a minimum of 1.5 for carbons having a very broad micropore size distribution<sup>11</sup>. When  $n = 2$ , eq. 2 is the Dubinin - Radushkevich (D-R) equation which accurately describes the adsorption behavior of most commercial active carbons at low to moderate pressures<sup>12</sup>. Both adjustable parameters in the D-R equation,  $\beta$  and  $E_0$ , can be estimated from independent properties of the system. From SAXS and molecular probe adsorption studies,  $E_0$  is found to depend inversely on the mean pore width,  $L$ , of the carbon in the range  $0.4\text{nm} < L < 2\text{nm}$  according to the empirical equation<sup>13</sup>

$$E_0 \text{ (kJ/mol)} = (10.8/L) + 11.4 \quad (3)$$

The affinity coefficient can be estimated from molecular properties related to the strength of interaction of an adsorptive with the electronic field of the adsorbent. Dispersion forces play a dominant role in the adsorption of organic vapors by carbon, except for very polar molecules having permanent dipole moments  $> 4D$  where electrostatic interactions are also important. Total molecular polarizability is closely related to the magnitude of the dispersion force in that it is a measure of the instantaneous dipole moment induced by interaction with the electronic field of the adsorbent. To a good approximation, total polarizability is represented by the electronic polarizability,  $P_e$ , given by the Lorenz - Lorentz equation

$$P_e = [(n^2 - 1)/(n^2 + 2)][M/\sigma] \quad (3a)$$

where  $n$  is refractive index at the sodium D wavelength,  $M$  is molecular weight, and  $\sigma$  is liquid density. Alternatively,  $\beta$  can be estimated from the molar volume,  $M/\sigma$ , or the molar parachor, which is the molar volume corrected to constant internal pressure. Affinity coefficients calculated by the three methods were compared to experimental results for adsorption of 10 organic vapors by a beaded active carbon<sup>9</sup>. All agreed well with the experimental data, giving a mean error of  $\leq 4\%$ . In addition, equilibrium adsorption capacities ( $A_e$ , g/g) measured for two adsorptives over a temperature range of 25 - 60C showed comparable agreement to values predicted from relative molar volume. A similar comparison was carried out for 15 nonpolar and polar adsorptives on BPL carbon<sup>14</sup>, a granular active carbon produced from coal but otherwise possessing adsorption properties akin to those of the powdered carbon used in Type III fabric. Applying relative  $P_e$  to estimate  $\beta$ , this study yielded an internally consistent  $E_0$  ( $16.9 \pm 0.3$  kJ/mol), and total micropore volume of  $0.42 \text{ cm}^3/\text{g}$ . Using the D-R equation, these adsorbent parameters with predicted  $\beta$ 's ( $\text{CHCl}_3 = 1$ ) yield adsorption capacities which are compared in Table 1 to agent and simulant vapor adsorption data for BPL carbon reported by Jonas<sup>15</sup>. Agreement between calculated and observed parameters are within the experimental error, attesting to the efficacy of the TVFM approach.

TABLE 1

PREDICTED vs. OBSERVED ADSORPTION PROPERTIES FOR BPL CARBON AT 25C

| VAPOR <sup>3</sup> | MOL WT. | $\sigma^{25}, \text{g}/\text{cm}^3$ | $n$   | $\beta^1$ |       | $w(0.1)^2$ |      |      |
|--------------------|---------|-------------------------------------|-------|-----------|-------|------------|------|------|
|                    |         |                                     |       | $V_m$     | $P_e$ | Obs        | Pred | Obs  |
| $\text{CHCl}_3$    | 119.4   | 1.48                                | 1.443 | 1         | 1     | 1          | 0.56 | 0.60 |
| $\text{CCl}_4$     | 153.8   | 1.59                                | 1.460 | 1.20      | 1.24  | 1.15       | 0.62 | 0.65 |
| MS                 | 152.1   | 1.18                                | 1.536 | 1.60      | 1.88  | -          | 0.48 | -    |
| HD                 | 159.1   | 1.27                                | 1.531 | 1.55      | 1.81  | 1.66       | 0.52 | 0.54 |
| DMMP               | 124.1   | 1.15                                | 1.434 | 1.34      | 1.31  | 1.22       | 0.45 | 0.48 |
| GA                 | 162.3   | 1.07                                | 1.422 | 1.88      | 1.80  | 2.07       | 0.43 | 0.45 |
| GB                 | 140.1   | 1.09                                | 1.381 | 1.59      | 1.39  | 1.26       | 0.43 | 0.45 |
| GF                 | 180.2   | 1.13                                | 1.434 | 1.98      | 1.95  | 2.16       | 0.46 | 0.48 |

1. Calculated from molar volume ( $V_m$ ), and polarizability ( $P_e$ ).

2. Adsorption capacity(g/g) at  $P/P_0 = 0.1$ ; Pred using eq. 2 with  $\beta$  from  $P_e$ ,

$V_0 = 0.42 \text{ cm}^3/\text{g}$ , and  $E_0 = 16.9 \text{ kJ/mol}$ . Obs is from Ref. 15.

3. MS = methyl salicylate, HD = bis(2-chloroethyl)sulfide, GA = Tabun, GB = Sarin, DMMP = 0,0-dimethylmethylphosphonate, and GF = 0-cyclohexylmethylphosphonofluoridate.



## 4. WATER ADSORPTION ISOTHERM

Water vapor is adsorbed by active carbon via a mechanism which differs substantially from that for organic vapors. Water interacts weakly with the electronic field at the conjugated basal layer of carbon, but readily forms hydrogen bonds at oxygenated functional groups. Little adsorption occurs at low relative humidity (RH) until sufficient vapor pressure is attained to initiate rapid growth of water clusters associated with hydrated polar sites. At higher RH, micropore filling dominates, such that similar total pore volumes are obtained for water and organic vapors on many active carbons<sup>16</sup>. Desorption of water is also qualitatively different from that of organic adsorptives, in that water exhibits marked hysteresis over almost the entire RH range<sup>17</sup>, whereas organic vapor isotherms are mainly reversible with minor hysteresis limited to the mesopore region ( $P/P_0$  ca. 0.2-0.5). At high RH or when preadsorbed, water competes effectively with organic adsorptives for available pore volume but not on dry carbons at low RH<sup>18</sup>. This fundamental contrast in isotherm behavior is illustrated in Fig. 2 for cyclohexane and water vapor on BPL carbon<sup>19</sup>.

Fig. 2. Adsorption - desorption isotherms on BPL carbon. Water adsorption(□) and desorption(■), cyclohexane(▲) adsorption and desorption. From Ref. 19

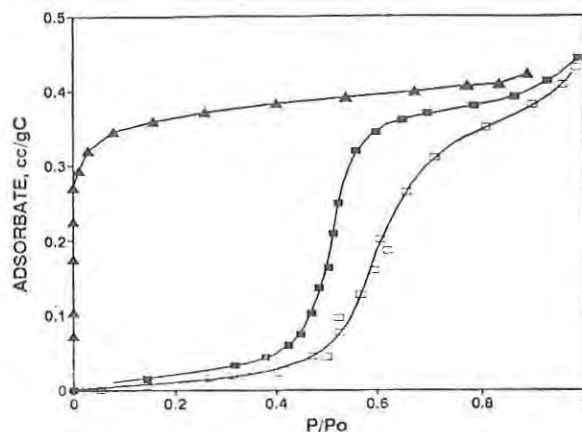
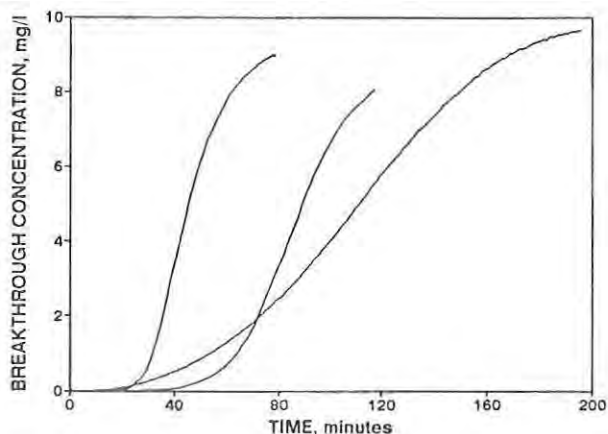


Fig. 3. BTC ( $\text{CCl}_4$  @ 10mg/L) for diverse active carbon fabrics at 32.2C

## 5. DYNAMIC ADSORPTION

Performance of an adsorbent in military applications is dependent on kinetic factors as well as adsorption capacity at equilibrium. Mass transfer is rate determining over a wide range of environmental conditions, emphasising the importance of particle size, spatial distribution, and access to internal porosity, in addition to temperature, adsorptive diffusivity and concentration, and flowrate. Standard evaluation of vapor challenge protection is thus carried out in a dynamic rather than static mode.<sup>20,21</sup> Test conditions specified for agent<sup>22</sup> and simulant<sup>23,24</sup> vapor challenge of permeable protective fabric are summarized in Table 2, for 100cm<sup>2</sup> swatches at 90F(32.2C) in a carrier stream of dry air or nitrogen at a face velocity of 10 cm/minute.

TABLE 2

## STANDARD VAPOR CHALLENGE CONDITIONS FOR PERMEABLE FABRICS

| Vapor          | Conc. $\mu\text{g/L}$ | %RH | Penetration, $\mu\text{g/cm}^2$ |
|----------------|-----------------------|-----|---------------------------------|
| $\text{CCl}_4$ | 5000                  | 0   | 50 (1800 adsorption)            |
| HD             | 20                    | 80  | 4                               |
| GD             | 10                    | 80  | 10                              |

Passage of a gas stream carrying a vapor adsorptive through a bed of granular adsorbent or layer of adsorbent fabric produces a characteristic breakthrough curve (BTC) of effluent vapor concentration against time. Representative BTC's for carbon tetrachloride vapor challenge at 32.2C of adsorbent fabrics containing dissimilar active carbons are illustrated in Fig.3. Although mathematical descriptions of the sigmoid BTC can yield rate and capacity information required for estimation of potential performance in the field, current standard evaluation tests give only a cumulative breakthrough endpoint and do not define the BTC.

Of the many published methods proposed for quantitative analysis of the BTC, those based on the modified Wheeler equation have been used most frequently<sup>21</sup>. This study employs the Site Depletion Model (eq. 4) which combines elements of the Wheeler algorithm and the Method of Statistical Moments<sup>24</sup>.

$$t = [A_d/C_0 Q] [W - \sigma Q \ln((C_0/C) - 1)/k\tau^a] \quad (4)$$

$$\text{at } C_0/C = 2; \quad t = t_{1/2} = A_d W/C_0 Q \quad (5)$$

where  $t$  is adsorption time(min),  $C$  is the corresponding effluent vapor concentration(g/L),  $W$  is adsorbent weight(g),  $C_0$  is challenge concentration(g/L),  $Q$  is volumetric flowrate(L/min),  $\sigma$  is adsorbent bed density(g/L),  $\tau = t/t_{1/2}$ ,  $a$  is an empirical curve fitting constant which compensates for a negative deviation from the sigmoid curve at  $\tau > 1$ ,  $A_d$  is the dynamic adsorption capacity(g/g), and  $k$  is the pseudo first order rate constant( $\text{min}^{-1}$ ) for the overall net adsorption process. Rearranging eqs. 4 and 5, and substituting  $C_f$  for  $((C_0/C) - 1)$ , and  $\delta$ (min) for  $W/\sigma Q$ , gives the following expressions for dynamic adsorption capacity, and the apparent rate constant at any point on the breakthrough curve. Note that  $\delta$  is the average time required for nonadsorbed molecules to traverse the bed.

$$A_d = t_{1/2} C_0 Q / W \quad (6)$$

$$k_v = k\tau^a = \ln C_f / \delta(1 - \tau) \quad (7)$$

Calculated values for  $A_d$ , and  $k_v$  at both 3% and 50% breakthrough are listed in Table 3 for foam laminates containing equivalent loadings of different active carbons but with lower polymeric binder levels than Type III fabric. Also included in Table 3 are equilibrium adsorption capacities for these adsorbent fabrics obtained at the same relative pressure<sup>25</sup>. Characteristic of these fabrics are the similarity between static and dynamic adsorption capacities, and the temporal decrease in adsorption rate after breakthrough. A 10 to 20 percent decrease in adsorption capacity is observed relative to that for the corresponding unincorporated powdered active carbon, which is attributed to partial blocking of the pore volume by components of the acrylic binder formulation used in the fabric process. This same phenomenon was observed for adsorption of the agent GB by composite fabrics prepared by spray coating a nonwoven substrate with a mixture of active carbon and acrylic latex binder<sup>26</sup>.



TABLE 3

## DYNAMIC ADSORPTION OF CARBON TETRACHLORIDE BY ADSORBENT FABRICS

| Carbon      | $C_0$ , mg/L | $k_v$ , min <sup>-1</sup> |     | $A_d$ , g/g | $P/P_0 \times 10^3$ | $A_e$ , g/g | $A_d/A_e$ , % |
|-------------|--------------|---------------------------|-----|-------------|---------------------|-------------|---------------|
|             |              | 3%                        | 50% |             |                     |             |               |
| PCB-G       | 10.0         | 441                       | 246 | 0.33        | 8.0                 | 0.43        | 77            |
| AX-21       | 5.0          | 430                       | 320 | 0.54        | 4.0                 | 0.61        | 89            |
| MAXSORB 300 | 5.0          | 532                       | 320 | 0.62        | 4.0                 | 0.73        | 85            |
| RENOVES M40 | 9.9          | 235                       | 120 | 0.77        | 7.9                 | 0.79        | 97            |

## 6. CORRELATION OF AGENT AND SIMULANT VAPOR CHALLENGE TESTS

There are few reported studies comparing vapor adsorption of agents and simulants on comparable fabric samples (e.g., adjacent areas from a garment or swatch), and none for replicate tests of the same specimen. To compare test data, it is usually assumed that breaktimes for different adsorptives can be normalized to a single reference challenge concentration, provided that other experimental conditions are constant. This comparison procedure is valid for a given adsorbent fabric based on eq.4 and the TVFM (eq.2), if the following conditions are met; 1) challenge concentrations correspond to the same relative pressure, predicated on the similarity of  $A_e$  and  $A_d$ , 2) adsorbate volumes rather than weights are compared, and 3)  $k_v$  is relatively insensitive to the properties of the adsorptive. In practice, only the third condition is satisfied in most cases. For example, at 32.2C the relative pressure corresponding to the standard vapor challenge concentration for HD (20 $\mu$ g/L) is 0.012, and for CCl<sub>4</sub> (5mg/L) it is 0.004. Furthermore, because test challenge levels sometimes differ significantly from the nominal challenge concentration, it is customary to adjust adsorption results using a linear concentration correction. This adjustment introduces an error if test concentrations fall in a strongly concentration dependent region of the isotherm having a rapidly changing slope. Often this is the case for agent challenge levels, as illustrated in Fig.4 for HD adsorption by Merck 2514, a

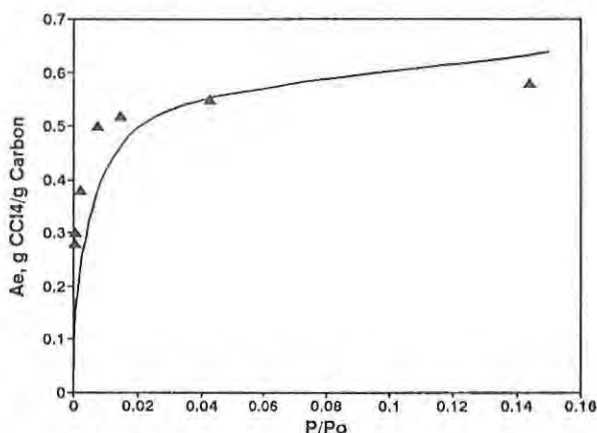


Fig. 4. Vapor adsorption isotherms. HD/Merck 2514 carbon @ 30C (—), CCl<sub>4</sub>/PCB-G carbon @ 32.2C ( $\Delta$ ).

microporous activated charcoal similar in surface area to BPL and PCB-G<sup>27</sup>. The standard challenge level for the simulant, CCl<sub>4</sub>, also falls in a region of high slope as shown by the isotherm points for adsorption of CCl<sub>4</sub> by PCB-G superimposed on the HD isotherm in Fig. 4. However, as predicted by TVFM, there is a close correspondence between the isotherms for these very different adsorptives with similar adsorbents. Further confirmation of the merit of this approach is shown by the almost identical isotherms obtained for adsorption of HD and dipropyl sulfide vapor on DH-30 carbon, the active carbon used in the Chinese M-82 permeable chemical suit<sup>28</sup>. A small displacement between the HD and

dipropyl sulfide isotherms is reflected in a 15% lower value of  $\beta$  for HD. These authors also found good agreement between the dynamic and equilibrium adsorption capacities for dipropyl sulfide on the DH-30 in the acrylic-coated flannel fabric of the M-82 suit.

Irrespective of the above caveats, it is possible to demonstrate a linear correlation (albeit with high variance) between alternative challenge tests, although satisfying all conditions is required for absolute equivalence. An extensive agent - simulant correlation is shown in Fig. 5 for  $\text{CCl}_4$  and HD vapor challenge of Type I fabric (MIL-C-43858) swatches from unworn, chemical protective overgarments<sup>29</sup>. Employing concentration normalization (i.e.,  $\text{CCl}_4$  breaktime adjusted for HD concentration), this statistical study yields a linear regression equation for adsorptive breaktime of the form

$$\text{HD (hours)} = 116.8 + 0.35(\text{CCl}_4 \text{ equivalent hours}) \quad (9)$$

Several earlier attempts to correlate swatch tests with these adsorptives also produced linear regression equations, but with little statistical significance due to inadequate sample size (<20).

An additional confounding factor in comparing agent and simulant vapor challenge tests is that agent adsorption is performed at 80%RH whereas dry carrier gas is standard for simulants such as  $\text{CCl}_4$ . The decrease in adsorption associated with this high humidity is approximately 30-40%, as reported for HD on carbon loaded foam laminate fabric<sup>30</sup>.

The present study is an attempt to resolve uncertainties regarding the proper use of agent and simulant vapor challenge tests of adsorbent fabric, via application of modern theory and experimental techniques.

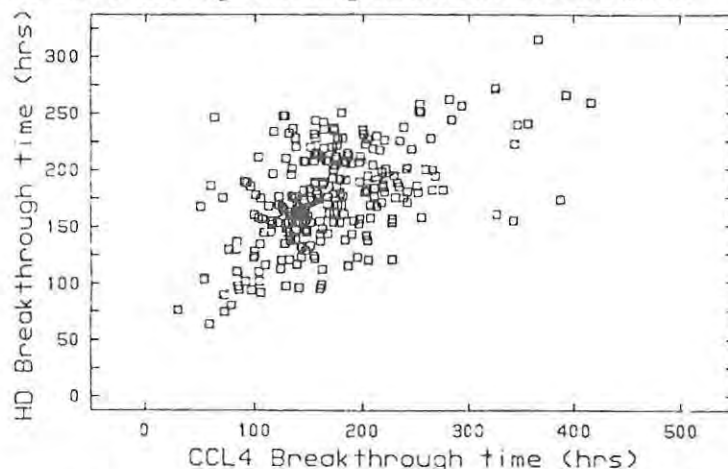


Fig. 5. Correlation of HD and  $\text{CCl}_4$  vapor challenge tests of Type I fabric. From Ref. 29.

## 7. EXPERIMENTAL

**7.1 Materials** - Type III chemical protective fabric (MIL-C-43858) swatches from jackets and trousers of stockpiled, unworn Battledress Overgarments were die-cut into 14cm disks for dynamic adsorption experiments, and 2cm X 5cm strips for measurement of equilibrium adsorption. Type III adsorbent fabric is composed of open-cell polyester polyurethane foam laminated to nylon tricot, and impregnated with Calgon PCB-G active carbon in an acrylic binder formulation. PCB-G powdered (90% <40 $\mu\text{m}$ ) carbon produced by steam activation of coconut shell char has an  $\text{N}_2$  BET surface area of 1150-1250 $\text{m}^2/\text{g}$ , and a total pore volume of 0.72 $\text{cm}^3/\text{g}$ . Type III fabric has an average thickness of 0.23cm, and a nominal carbon loading density of 0.05 $\text{g}/\text{cm}^3$ . Mean carbon loading for the forty fabric samples in this study is 0.053 $\text{g}/\text{cm}^3$ , ranging from 0.028 $\text{g}/\text{cm}^3$  to 0.075 $\text{g}/\text{cm}^3$ . Swatches were dried/regenerated for at least three hours in a forced draft oven at 95C before adsorption.

Carbon tetrachloride, Certified A.C.S. Spectranalyzed grade, lot C199-4, and methyl salicylate, Reagent grade, lot C-3695, adsorptives were obtained from Fisher Scientific and used without further purification.

**7.2 Equilibrium Adsorption of Simulant** - Strips of Type III fabric suspended by a platinum wire from the weighing arm of a Cahn Model D200 Digital Recording Microbalance are exposed to adsorptive vapor in dry nitrogen gas flowing down a vertical Pyrex tube (4cm diam. X 56cm). A thermocouple probe immediately below the suspended specimen provides thermal regulation at  $32.2 \pm 0.1^\circ\text{C}$  via a temperature controller (Cole Parmer cat.# BA-2155-50) connected to heating tape wound around the exterior of the tube, and covered with an outer winding of Zircar Products Inc. Silica Alumina RS tape insulation. Nitrogen gas from a liquid nitrogen tank is split into a diluent and a vapor carrier stream, each maintained at a selected flow rate by an appropriate range Matheson Model 8270 mass flow controller. The carrier stream passes through a sintered glass diffusion tube into liquid MS or  $\text{CCl}_4$  held at  $0^\circ\text{C}$  in an ice bath. Nitrogen saturated with challenge vapor, and diluent nitrogen are combined in the ratio required to achieve a vapor concentration corresponding to the desired adsorption vapor pressure calculated from the Ideal Gas Law [at 760torr;  $P, \text{mm} = 0.06236(T, \text{K})(C_0, \text{mg/L})/(\text{MW})$ ]. Digitized output from the microbalance is converted into weight vs. time data in a 286 PC equipped with Cahn proprietary software. A schematic of the equilibrium adsorption system is shown in Fig. 6.

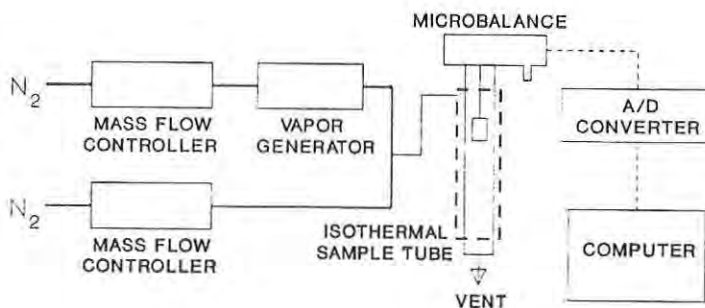


Fig. 6. Equilibrium Adsorption System

**7.3 Dynamic Adsorption of Simulant** - Two independent dynamic vapor challenge systems were used for studies with  $\text{CCl}_4$ . The specification method described in MIL-C-43858 gives a single cumulative breakthrough endpoint, whereas the research method produces a complete BTC. Vapor generation in the research method is identical to that of the equilibrium adsorption system, except that a humidifier and associated bypass valves are incorporated in the diluent gas flow loop to accommodate experiments at known RH. As illustrated in Fig.7, the diluted challenge passes through a specimen holder thermostated at  $32.2 \pm 0.1^\circ\text{C}$ . Effluent vapor is sampled automatically at one minute intervals by a Microsensor Technology Inc. M200 dual column thermal conductivity gas chromatograph, with breakthrough concentration vs. time data obtained from a 286 PC with resident EZ Chrom® software. A tube filled with Drierite® dessicant is inserted between the sample cell and detector for tests at 80% RH to eliminate interference caused by water vapor. Control experiments with  $\text{CCl}_4$  indicate that in-line drying effects only a minor shift in BTC, which is disregarded in the calculations.

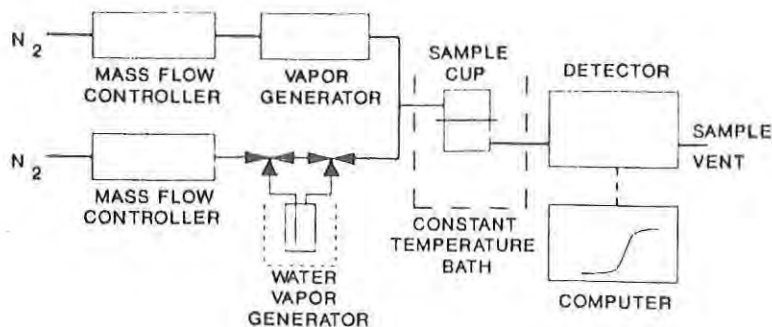


Fig. 7. Dynamic (Research) Adsorption System

In both methods, the specimen is held in a stainless steel "Dawson cup" as depicted in MIL-C-43858, which exposes a fabric area of  $100\text{cm}^2$  to the challenge vapor in dry nitrogen gas carrier. The single point cumulative endpoint of the specification method represents the same total adsorption as occurs at 1% effluent breakthrough in the research method, as determined by quantitative comparison of these methods using identical Type III fabric specimens (20) under standard conditions ( $T = 32.2^\circ\text{C}$ ,  $C_0 = 10\text{mg/L}$ ,  $Q = 1\text{L/min}$ ). Unless otherwise noted the research method is used in this study, and adsorption at 1% breakthrough is reported for comparison to the specification method. Dynamic adsorption of MS is carried out in a separate research method apparatus with effluent detection by an HNU Systems, Inc. Model PI-101, photoionization detector (PID) with a  $10.2\text{eV}$  lamp. Substitution of the PID for the gas chromatograph is necessitated by the high sensitivity required to monitor the very low MS concentration at breakthrough.

**7.4 Dynamic Adsorption of HD** - Agent vapor challenge testing of Type III fabric samples was performed at Midwest Research Institute, and at GEOMET Technologies, Inc. using a test system similar to the specification apparatus<sup>20</sup>. Samples were conditioned for 16 hours in air at  $90\pm 2^\circ\text{F}$  ( $32.2^\circ\text{C}$ ) and  $80\pm 2\%$  RH before exposure to  $20\mu\text{g/L}$  HD in air at  $1.0\pm 0.1\text{L/min}$  and the same temperature and humidity. Fabric swatches tested at Midwest Research Institute were taken from unseamed areas of overgarments adjacent to those tested with  $\text{CCl}_4$ . Fabric specimens sent to Geomet Corporation were subjected to at least six challenge and regeneration cycles with  $\text{CCl}_4$  before submission for testing with HD.

## 8. RESULTS

**8.1 Equilibrium Adsorption of Simulant** - Isotherms at  $32.2^\circ\text{C}$  for MS and  $\text{CCl}_4$  on representative samples of Type III fabric are displayed in Fig. 8. Equilibrium adsorption is attained more slowly with MS than with  $\text{CCl}_4$  at all vapor pressures, as for example, at  $P/P_0 = 0.06$  where maximum adsorption is achieved in less than two hours for  $\text{CCl}_4$  and almost five days for MS. Characteristic adsorption parameters from D-R plots (eq. 2) of the MS and  $\text{CCl}_4$  isotherms in Fig. 9 are respectively,  $V_0 = 0.34$  and  $0.31\text{cm}^3/\text{g}$ , and  $\beta E_0 = 34.7$  and  $20.2\text{kJ/mol}$ . These latter values yield a  $\beta$  ratio of 1.72, in fair agreement with the ratio of 1.52 from relative  $P_e$  (see Table 1). Conversely,  $E_0 = 17.4\pm 1.1\text{kJ/mol}$  for PCB-G based on relative  $P_e$  is slightly greater than  $E_0$  for BPL carbon, and corresponds to a mean micropore diameter of  $1.8\text{nm}$  (eq. 3).

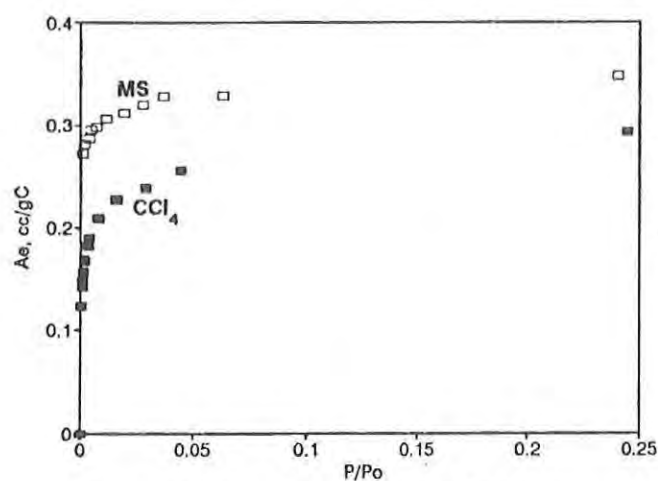


Figure 8. Isotherms at 32.2C for TYPE III fabric

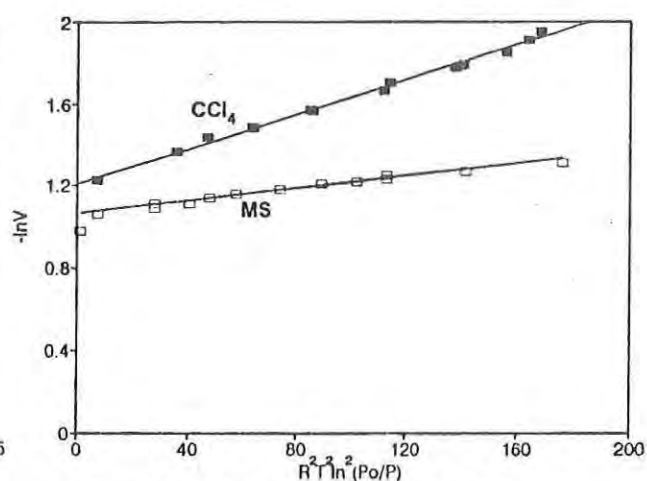


Figure 9. D-R Plots for Isotherms in Fig. 8

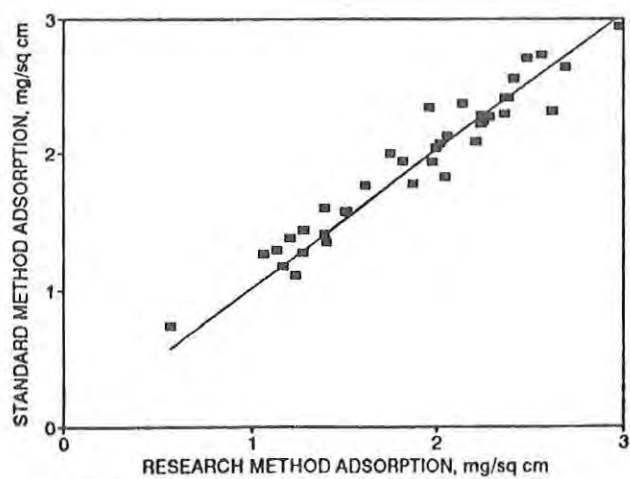


Figure 10. Research vs Specification: all samples

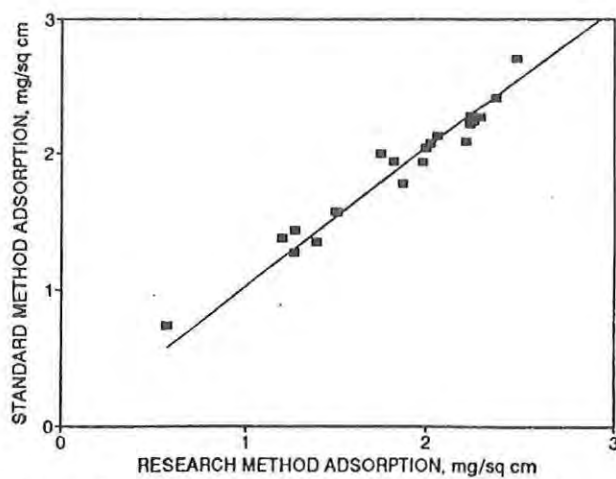


Figure 11. Research vs Specification: selected samples



The 10% greater micropore volume for Type III fabric derived from the MS isotherm could be due to either enhanced accessibility to micropores or to a specific interaction with the polymeric binder. The former appears unlikely from inspection of the molecular dimensions of these adsorptives as summarized in Table 4<sup>31</sup>. Except in the Z direction, dimensions of MS are greater than those of symmetric  $\text{CCl}_4$ ; both molecules, however, are large enough to experience measurable exclusion if the micropore size distribution is broad. In general, there is not a sufficient difference between the dimensions of the three adsorptives to expect significant selectivity due to molecular sieve phenomena.

TABLE 4  
CALCULATED MOLECULAR DIMENSIONS

| Adsorptive     | Maximum Dimension, nm |       |       | Volume, nm <sup>3</sup> |
|----------------|-----------------------|-------|-------|-------------------------|
|                | X                     | Y     | Z     |                         |
| $\text{CCl}_4$ | 0.626                 | 0.626 | 0.626 | 0.091                   |
| MS             | 1.066                 | 0.751 | 0.597 | 0.131                   |
| HD             | 1.081                 | 0.495 | 0.450 | 0.133                   |

To test for possible polymer interaction effects, partial isotherms were obtained at 32.2°C for MS and  $\text{CCl}_4$  on pure PCB-G powder. Equilibrium is attained more slowly for the powder bed than for carbon distributed within a foam matrix, requiring 4 hours with  $\text{CCl}_4$  and 16 days with MS, at  $P/P_0 = 0.06$ . For both adsorptives, maximum adsorption for the carbon powder is about 10-15% above the corresponding point on the carbon/fabric isotherm. This finding agrees with previous observations, which indicate slight blockage of pore entrances, but does not support the occurrence of specific interactions with the polymeric binder.

8.2 Sequential and Factorial Design Simulant Experiments - Forty fabric disks were challenged with  $\text{CCl}_4$  in the specification apparatus then retested successively in either the specification or research apparatus. Specimens were regenerated by heating before each test. Sample identification, weight, and sequential adsorption capacity at breakthrough are summarized in Table 5. A subset of 22 samples listed in the last column of Table 5, which exhibit the smallest variation in simulant adsorption capacity, were subsequently tested with HD vapor at 80%RH. A linear regression of  $\text{CCl}_4$  breakthrough capacity in the specification vs. research ( $C/C_0 = 0.01$ ) apparatus is shown in Fig.10 for all samples, and in Fig.11 for the subset selected for agent testing. Excellent linear correlation is demonstrated for the entire class ( $m = 1.01$ ,  $R^2 = 0.93$ ), and also for the subset ( $m = 1.02$ ,  $R^2 = 0.96$ ), confirming equivalence of the sorption analyses. Apparent adsorption capacity at breakthrough is estimated from mean areal fabric adsorption for each specimen using eq. 10, assuming impregnant is 78% active carbon and the foam substrate weighs 2.59g per 153cm<sup>2</sup> fabric disk.

$$\text{Ads., g/g} = \text{Areal ads., mg/cm}^2 / [5.10(\text{Specimen wt., g}) - 13.2\text{g}] \quad (10)$$

Individual fabric samples displayed a wide range in adsorption (0.13 - 0.32g $\text{CCl}_4$ /gPCB-G), with most samples clustered near the mean of  $0.21 \pm 0.04$ g/g which is only 66% of the maximum adsorption capacity at a concentration of 10mg/L ( $P/P_0 = 0.00796$ ) from the  $\text{CCl}_4$  isotherm. It follows that partial adsorption is a result of the short time to breakthrough (10 to 30min) in the sequential test series, whereas, full attainment of equilibrium requires more than one hour exposure in the gravimetric system. In support of this hypothesis,  $A_d$  calculated from  $t_{1/2}$  is close to  $A_e$  in most cases.



TABLE 5  
Sequential CCl<sub>4</sub> Dynamic Adsorption Tests of Type III Fabric\*

| SAMPL<br>ID | Specimen<br>wgt. g | BREAKTHROUGH ADSORPTION, mg/sq. cm |     |      |     |     |     |          | HD  |
|-------------|--------------------|------------------------------------|-----|------|-----|-----|-----|----------|-----|
|             |                    | S1                                 | R2  | S3   | S4  | R5  | S6  | MEAN     |     |
| 1           | 4.289              | 2.2                                | 1.6 | 1.6  | 1.9 | 1.5 | 1.4 | 1.7      |     |
| 2           | 4.454              | 2.7                                | 1.7 | 1.8  | 1.6 |     | 1.9 | 1.9      | 2.5 |
| 3           | 4.640              | 1.8                                | 2.0 | 2.2  | 2.1 |     | 1.7 | 1.9      | 1.4 |
| 4           | 5.145              | 3.0                                | 2.0 | 2.3  | 2.1 | 2.1 | 2.0 | 2.2      |     |
| 5           | 4.170              | 2.2**                              | 1.3 | 1.1  | 1.4 |     | 1.3 | 1.2(1.5) | 1.1 |
| 6           | 3.912              | 2.9**                              | 1.1 | 1.4  | 1.1 | 1.0 | 1.3 | 1.2(1.5) |     |
| 7           | 4.005              | 2.9                                | 2.4 | 2.0  | 2.1 | 2.2 | 2.3 | 2.3      |     |
| 8           | 3.952              | 2.3**                              | 1.2 | 0.7  | 1.2 | 1.1 | 1.7 | 1.2(1.4) |     |
| 9           | 4.566              | 4.3**                              | 2.7 | 2.3  | 3.0 | 2.9 | 2.6 | 2.7(3.0) |     |
| 10          | 3.836              | 3.9**                              | 2.0 | 1.7  | 2.0 | 1.8 | 1.7 | 1.9(2.2) |     |
| 11          | 3.709              | 1.9**                              | 1.2 | 1.1  | 0.9 | 0.9 | 1.3 | 1.1(1.2) |     |
| 12          | 4.839              | 1.8                                | 2.4 | 2.8  | 2.4 | 2.2 | 2.8 | 2.4      |     |
| 13          | 5.095              | 3.3                                | 2.6 | 2.4  | 2.3 | 2.5 | 3.0 | 2.7      |     |
| 14          | 5.038              | 2.7                                | 2.6 | 2.3  | 2.1 | 2.4 | 2.1 | 2.4      |     |
| 15          | 5.045              | 3.0                                | 2.5 | 2.8  | 2.4 |     | 2.7 | 2.7      | 3.0 |
| 16          | 4.582              | 2.2                                | 2.0 | 2.0  | 1.9 |     | 2.1 | 2.0      | 1.7 |
| 17          | 4.841              | 3.6**                              | 2.1 | 2.3  | 2.6 | 1.9 | 2.2 | 2.2(2.5) |     |
| 18          | 4.380              | 3.4**                              | 1.4 | 1.6  | 1.8 | 1.3 | 1.5 | 1.5(1.8) |     |
| 19          | 4.466              | 3.3**                              | 1.5 | 1.6  | 1.6 |     | 1.4 | 1.6(1.9) | 1.8 |
| 20          | 4.149              | 3.1**                              | 2.3 | 2.3  | 2.5 |     | 2.0 | 2.3(2.4) | 1.9 |
| 21          | 4.387              | 2.6                                | 2.2 | 2.4  | 2.1 |     | 1.8 | 2.2      | 2.6 |
| 22          | 4.516              | 2.3                                | 2.3 | 2.3  | 2.2 | 2.2 |     | 2.2      | 2.1 |
| 23          | 4.325              | 2.2                                | 2.2 | 2.1  | 2.2 |     | 1.9 | 2.1      | 2.3 |
| 24          | 4.407              | 1.3                                | 1.1 | 1.4  | 1.4 | 1.1 | 1.1 | 1.2      |     |
| 25          | 5.049              | 3.1                                | 3.0 | 2.9  | 3.1 | 2.8 |     | 3.0      | 2.2 |
| 26          | 4.133              | 1.5                                | 1.5 | 1.8  | 1.5 |     | 1.5 | 1.6      | 2.2 |
| 27          | 4.569              | 1.9                                | 1.9 | 2.1  | 1.5 |     | 1.7 | 1.8      | 1.9 |
| 28          | 4.448              | 2.0                                | 2.0 | 2.4  | 1.8 |     | 2.2 | 2.1      | 1.4 |
| 29          | 4.577              | 2.9                                | 2.4 | 2.8  | 2.4 | 2.3 | 2.1 | 2.5      |     |
| 30          | 4.595              | 2.2                                | 2.2 | 2.4  | 2.3 | 2.1 |     | 2.2      | 2.5 |
| 31          | 4.268              | 1.5                                | 1.4 | 1.9  | 1.1 | 1.3 | 1.2 | 1.4      |     |
| 32          | 4.073              | 1.3                                | 1.3 | 1.8  | 1.5 |     | 1.2 | 1.4      | 1.1 |
| 33          | 4.775              | 2.7                                | 2.4 | 2.6  | 2.1 |     | 2.3 | 2.4      | 2.4 |
| 34          | 4.372              | 1.9                                | 1.8 | 2.0  | 1.9 | 1.7 |     | 1.9      | 2.3 |
| 35          | 3.513              | 1.4                                | 1.4 | 1.3  | 1.6 |     | 1.0 | 1.4      | 1.8 |
| 36          | 4.982              | 2.0                                | 2.1 | 2.5  | 2.0 |     | 2.0 | 2.1      | 1.5 |
| 37          | 5.439              | 3.4                                | 3.0 | 2.6  | 3.2 | 3.1 | 2.5 | 3.0      |     |
| 38          | 4.725              | 3.0                                | 3.2 | 5.0* | 3.0 | 3.2 | 2.6 | 3.0(3.3) |     |
| 39          | 4.163              | 1.3                                | 1.2 | 1.6  | 1.3 |     | 1.4 | 1.3      | 0.9 |
| 40          | 3.329              | 0.6                                | 0.6 | 1.0  | 0.6 |     | 0.8 | 0.7      | 0.5 |

\* Sequential tests of 153 sq. cm fabric disks using specification (S) or Research (R) method.

\*\* Values greater than 50% from the average are not used in calculation of mean  
Parenthetical means include \*\* values in calculation

Table 6  
Adsorption Factorial Experiments

| Temp | Hum | Conc | Flow | CCI4/Sample #9 |        |              | CCI4 separate samples |      |        |              | MS/separate samples |      |
|------|-----|------|------|----------------|--------|--------------|-----------------------|------|--------|--------------|---------------------|------|
|      |     |      |      | Ar             | Ad g/g | 1% Kv, 1/min | ID #                  | Ar   | Ad g/g | 1% Kv, 1/min | ID #                | Ar   |
| L    | L   | L    | L    | 1.14           | 0.477  | 471          | 18                    | 1.11 | 0.263  | 459          | 18                  | 1.63 |
| H    | L   | L    | L    | 0.74           | 0.351  | 415          | 10                    | 0.57 | 0.255  | 436          | 10                  | 1.16 |
| L    | H   | L    | L    | 0.65           | 0.278  | 434          | 24                    | 0.74 | 0.165  | 374          |                     |      |
| H    | H   | L    | L    | 0.23           | 0.175  | 306          | 14                    | 0.04 | 0.128  | 234          | 11                  | 0.65 |
| L    | L   | H    | L    | 1.31           | 0.466  | 552          | 6                     | 1.22 | 0.276  | 457          |                     |      |
| H    | L   | H    | L    | 0.97           | 0.381  | 472          | 12                    | 0.75 | 0.358  | 362          | 12                  | 1.51 |
| L    | H   | H    | L    | 0.82           | 0.347  | 454          | 7                     | 0.90 | 0.346  | 583          | 7                   | 1.31 |
| H    | H   | H    | L    | 0.44           | 0.250  | 353          | 37                    | 0.48 | 0.250  | 327          |                     |      |
| L    | L   | L    | H    | 0.67           | 0.347  | 736          | 13                    | 0.79 | 0.233  | 921          | 13                  | 0.65 |
| H    | L   | L    | H    | 0.49           | 0.278  | 696          | 11                    | 0.40 | 0.198  | 627          |                     |      |
| L    | H   | L    | H    | 0.47           | 0.257  | 722          | 29                    | 0.59 | 0.278  | 747          | 29                  | 0.54 |
| H    | H   | L    | H    | 0.21           | 0.183  | 586          | 31                    | 0.10 | 0.123  | 454          |                     |      |
| L    | L   | H    | H    | 1.03           | 0.438  | 807          | 8                     | 0.84 | 0.279  | 722          |                     |      |
| H    | L   | H    | H    | 0.68           | 0.344  | 766          | 17                    | 0.62 | 0.197  | 840          | 17                  | 0.58 |
| L    | H   | H    | H    | 0.64           | 0.312  | 753          | 1                     | 0.32 | 0.169  | 606          | 1                   | 1.09 |
| H    | H   | H    | H    | 0.04           | 0.100  | 400          | 4                     | 0.07 | 0.100  | 450          | 24                  | 0.78 |

Table 7  
Estimate of Factor Effects  
Dynamic Adsorption of CCl<sub>4</sub> by Type III Fabric

|  | Ar     |          | Ad     |          | 1% Kv  |          |
|--|--------|----------|--------|----------|--------|----------|
|  | Single | Multiple | Single | Multiple | Single | Multiple |
| Average Response                             | 0.658  | 0.595    | 0.312  | 0.226    | 558    | 537      |
| Relative Factor Effect<br>% average response |        |          |        |          |        |          |
| Temperature                                  | -56    | -74      | -35    | -22      | -21    | -26      |
| Humidity                                     | -67    | -65      | -47    | -28      | -20    | -24      |
| Concentration                                | 25     | 18       | 12     | 18       | 4      | 2        |
| Flow Rate                                    | -39    | -43      | -19    | -26      | 45     | 50       |

Remaining samples from this sequential test were assigned to two groups for determination of the effect of challenge concentration, flow rate, temperature, and relative humidity on the dynamic adsorption of  $\text{CCl}_4$ . In a full factorial experiment (FFE), each variable was tested at two levels on separate samples, and on a single sample regenerated between tests. Factor levels are: temperature -  $0/32.2^\circ\text{C}$ , humidity -  $0/80\%\text{RH}$ , challenge -  $5/20\text{mg/L}$ , and flowrate -  $1/2\text{L/min}$ . Table 6 gives the FFE matrix and responses for areal adsorption at breakthrough ( $A_b$ ) for the trial relative to mean adsorption for the same sample in Table 1,  $A_e$ , and  $k_v$  at 1% breakthrough. Main factor effects derived from the FFE are listed in Table 7, second and higher order interaction effects are much smaller than the primary factor effects and are not included in the Table. The reasonably consistent responses from both single and multiple sample trials indicate that the dynamic adsorption process is sensitive to all of the tested environmental factors. Accumulated adsorption at breakthrough increases with challenge concentration but is strongly reduced by increasing temperature, humidity and flowrate. The origin of these effects can be deduced from behavior of the derived capacity and rate parameters;  $A_b$  exhibits a parallel but lesser dependence on all factors, whereas, as expected,  $k_v$ , which is strongly influenced by external mass transfer, increases with flow and is almost independent of challenge concentration. These effects are consistent with the arguments in Sections 3 & 4, and eqs. 4 - 7 in Section 5, but cover too limited a range in factor level to yield a quantitative response profile. A more extensive FFE is planned.

To determine whether MS behaves similarly, a two-level, 10 trial, fractional factorial design was carried out on separate samples only. Specimens were not regenerated due to the extremely slow desorption of MS at temperatures ( $<110^\circ\text{C}$ ) which do not degrade the fabric. Factor levels are the same as for  $\text{CCl}_4$ , except for vapor concentrations of  $0.03$  and  $0.15\text{mg/L}$  which represent about the same range of relative pressure as used for  $\text{CCl}_4$  (i.e.,  $P/P_0$  limits for  $\text{CCl}_4$  and MS are; at  $32.2^\circ\text{C}$  -  $0.004$  and  $0.016$ , at  $0^\circ\text{C}$  -  $0.066$  and  $1.0$ ). As a consequence of the low challenge concentration required for MS, breakthrough time is more than 150-fold longer than for  $\text{CCl}_4$ . For example, under the same conditions at low concentration, breakthrough occurs at 40min. for  $\text{CCl}_4$  and at over 130h for MS. Responses for MS in Table 6 parallel those for  $\text{CCl}_4$ , except for a greater inverse dependence on flowrate, and lower sensitivity to relative humidity. The latter is a direct result of the high affinity coefficient ( $\beta$ ) for MS which is similar to that for HD, in contrast to the strong preference for adsorption of water in the presence of a lower  $\beta$  adsorptive, such as  $\text{CCl}_4$ .

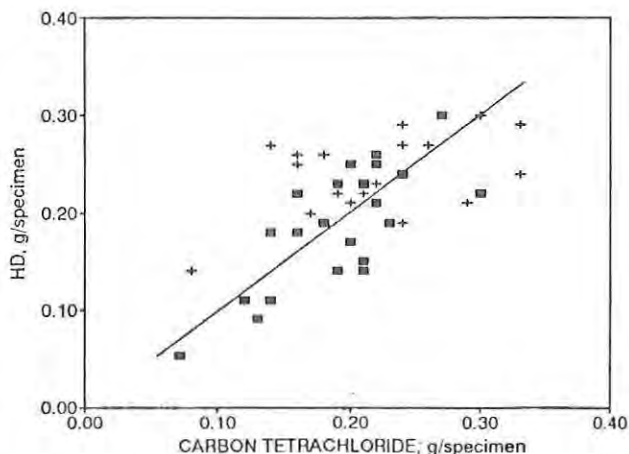


Fig. 12. Comparison of agent and simulant adsorption (CTQ) for Type III Fabric. Regenerated(■) and adjacent(+) swatches.

8.3 Correlation of HD and CCl<sub>4</sub> vapor challenge tests - Although HD and CCl<sub>4</sub> vapor challenge tests are carried out at the same flowrate and temperature, enhanced adsorption of HD at breakthrough is expected due to isotherm considerations, such as the use of higher relative pressure and the greater affinity coefficient for HD. Compensating for these effects is the moderate reduction in adsorption at high relative humidity noted previously with HD, and also observed in this study with MS. Overall, the maximum deviation in cumulative adsorption of HD and CCl<sub>4</sub> at breakthrough should not exceed 30 percent due to individual factors, and together their net effect should be much smaller. To test this premise, agent and simulant vapor challenge of Type III fabric is compared in Fig. 12 for adsorbed CTQ ([vapor concentration][time][flowrate] rather than the customary hours to breakthrough. CTQ is a direct measure of protection level, which eliminates the need to correct exposure time for disparate challenge concentrations. Results from separate tests of adjacent and regenerated (Table 5) swatches cluster around the 1:1 equivalence line shown in Fig. 12. Linear regression analyses of the individual test groups and the combined data set are listed below, with CTQ's denoted as [HD] and [CCl<sub>4</sub>].

Adjacent swatches;  $[HD]/[CCl_4] = 1.03 \pm 0.07$ ,  $R^2 = 0.22$   
 Regenerated swatches;  $[HD]/[CCl_4] = 0.97 \pm 0.04$ ,  $R^2 = 0.56$   
 All swatches;  $[HD]/[CCl_4] = 1.00 \pm 0.04$ ,  $R^2 = 0.23$

Although a linear correlation is expected on theoretical grounds the near absolute equivalence between the adsorptives is due to a fortuitous counterbalance of opposing factors. Manifest scatter in the data is reflected in the coefficient of determination ( $R^2$ ), which indicates a poor fit to the linear model, even for the carefully selected regenerated samples. It follows that most of the variance can be attributed to the HD vapor test with a lesser contribution from imprecision in simulant adsorption, and fabric heterogeneity in the case of adjacent swatches. Approximate equivalence between [HD] and [CCl<sub>4</sub>] also was reported for Type I foam laminate fabric<sup>30</sup>.

## 9. CONCLUSIONS

It is demonstrated that a good theoretical foundation is available for evaluating adsorption characteristics of permeable protective fabrics containing active carbon. Vapor breakthrough in dynamic challenge tests can be estimated from equilibrium adsorption capacities for adsorbent fabrics and adsorptive vapors, which in turn, are derived from molecular parameters. Breakthrough also depends on environmental conditions such as vapor concentration, temperature, flowrate, and humidity as predicted by the Site Depletion Model and the adsorption competition with ambient water vapor.

Since adsorptives are virtually interchangeable, vapor challenge tests using chemical surety agents are rarely justified. Simulants are the most appropriate choice for evaluation of developmental materials, acceptance testing, and whenever relative adsorbent properties are of interest. A linear correlation is confirmed for adsorption of agent and simulant vapor by adsorbent fabric, albeit with high variance associated mainly with the agent test. A single simulant vapor challenge test should be implemented for routine testing of all adsorbent fabrics.

Extensive response profiles are required for agents and selected simulants to enable transition of laboratory vapor challenge data into information applicable to field exposure scenarios. This study represents a step in that direction.

ACKNOWLEDGMENTS

We thank Ms. M. Bonanca for able execution of a portion of the  $\text{CCl}_4$  FFE series, and Mr. J. Jarboe and Dr. P. Angelini for coordination of HD tests. Ms. E. Klemperer is thanked for helpful suggestions regarding this manuscript.

REFERENCES

1. M. Huttepain and A. Oberlin, *Carbon*, 28, 103 (1990)
2. A. Janosi and H.F. Stoeckli, *Carbon*, 17, 465 (1979)
3. H.F. Stoeckli, *Carbon*, 28, 1 (1990)
4. K.S.W. Sing, D.H. Everett, R.A.W. Haul, L. Moscou, R.A. Pierroti, J. Rouquerol, and T. Siemienewska, *Pure Appl. Chem.*, 57, 603 (1985)
5. P.J.M. Carrott, and K.S.W. Sing, *Chem. Ind.*, 360, (1986)
6. D. Rivin, *Rubber Chem. Technol.*, 44, 307, (1971)
7. J.R. Dacey, J.C. Cluney, and D.G. Thomas, *Trans. Far. Soc.*, 54, 250 (1958)
8. M. Jaroniec, R. Madey, J. Choma, B. McEnaney, and T.J. Mays, *Carbon*, 27, 77 (1989)
9. K.E. Noll, D. Wang, and T. Shen, *Carbon*, 27, 239 (1989)
10. M.M. Dubinin, in *Chemistry and Physics of Carbon*, Vol. 2 (Edited by P.L. Walker, Jr.) Marcel Dekker, Inc., New York, pp 51-120, 1966
11. M.M. Dubinin and H.F. Stoeckli, *J. Coll. Interf. Sci.*, 75, 34 (1980)
12. B. McEnaney, *Carbon*, 26, 267 (1988)
13. H.F. Stoeckli, P. Rebstein, and L. Ballerini, *Carbon*, 28, 907 (1990)
14. P.J. Reucroft, W.H. Simpson, and L.A. Jonas, *J. Phys., Chem.*, 75, 3526 (1971)
15. L.A. Jonas, Edgewood Arsenal Technical Report EATR 4578, July 1971
16. S.S. Barton, M.J.B. Evans, and J.A.F. MacDonald, *Carbon*, 29, 1099 (1991)
17. J.J. Mahle and D.K. Friday, *Carbon*, 27, 835 (1989)
18. M.M. Dubinin, *Carbon*, 18, 355 (1980).
19. S.S. Barton, M.J.B. Evans, J. Holland, and J.E. Koresh, *Carbon*, 22, 265 (1984)
20. P.B. Dawson and M.F. Gilcrist, Edgewood Arsenal Technical Memorandum EATM 311-3, December 1967



RIVIN & KENDRICK

21. D.W. Hall, Dugway Proving Ground Technical Report DPG-TR-91-401, December 1990
22. M.J. Waters, Chemical Research and Development Center Special Publication CRDC-SP-84010, June 1984
23. Military Specification MIL-C-43858, Cloth, Laminated, Nylon Tricot Knit, Polyurethane Foam Laminate, Chemical Protective and Flame Resistant
24. D. Rivin, C. Kendrick, C. Capone, and J. Gaul, Paper presented at the Scientific Conference on Chemical Defense Research, Aberdeen Proving Ground, November 14, 1990
25. D. Rivin and C. Kendrick, Paper presented at the Scientific Conference on Chemical Defense Research, Aberdeen Proving Ground, November 19, 1991
26. D.W. Jones and P. Watts, Performance of Protective Clothing: Second Symposium, ASTM STP 989, S. Z. Mansdorf, R. Sager, and A.P. Nielsen, Eds., American Society For Testing Materials, Philadelphia, 1988, pp. 832-846
27. K. Schoene, J. Steinhanses, and U. Wienand, J. Coll. Interf. Sci., 91, 595 (1983)
28. G. Fang, H. Dingmao, L. Jiangge, and B. Yi, Third Scandinavian Symposium on Protective Clothing Against Chemicals and Other Health Risks, Gausdal Norway, September 1989
29. B.W. Paris, Interim Note R-192, U. S. Army Analysis Activity, Aberdeen Proving Ground, MD, June 1989
30. E. Klemperer, Proceedings of the Third International Simulant Workshop, CRDEC-SP-011, pp. 145-153, November 1989
31. Personal communication from Dr. G. R. Famini, U.S.Army Chemical Research, Development, and Engineering Center, Aberdeen Proving Ground, MD



SONG, et al.

**TITLE:** Effect of Crystallinity of Semicrystalline Polymer Matrices on Fiber-Reinforced Ballistic Protective Composites

John W. Song, Mr., Phillip W. Gibson, Mr., and Stuart R. Barlow, CPT

**ABSTRACT:** The effect of cooling rate on the crystallization behavior of nylon-66 and polyetherether ketone (PEEK) matrices was observed and correlated to the mechanical properties of composites using the differential scanning calorimetry (DSC) and dynamic mechanical analysis (DMA) techniques. Microscopic studies and preliminary ballistic evaluations were also performed. Kevlar®-29, 2x2 basket weave fabric was used as a fiber reinforcement for all composites.

Based on the findings of this evaluation, crystal formation was significantly affected by varying the cooling rate from the melt state of the polymers. From the correlation between DSC and DMA analyses, it appears that more perfect crystals formed at slower cooling rates than at higher cooling rates. At the same time the degree of crystallinity showed a slight increase with slower cooling rates.

Relative crystallinity was estimated from flexural storage moduli data obtained from DMA analysis of composites. The observed relative crystallinities upon completion of melt crystallization were in agreement with the degree of crystallinity obtained from DSC endotherms of neat resins. This indicates that the fiber influence on the degree of crystallinity is minimal in composites. Behavior of crystal formation observed in polarized microscope analysis also agreed well with DSC data.

The ballistic limit values obtained were reasonable for the composite samples as molded. It was found that the processing conditions need to be improved to achieve optimum ballistic performance. Scanning Electron Microscope (SEM) analysis revealed the possibility of thermal degradation of the Kevlar/PEEK composites.

**BIOGRAPHY OF PRESENTER:** John W. Song

**PRESENT ASSIGNMENT:** Materials Research Engineer, Materials Research and Engineering Division, Individual Protection Directorate, U.S. Army Natick Research, Development and Engineering Center, Natick, Massachusetts.

**PAST EXPERIENCE:** Textile Engineer, Dai-nong Textile Company, Seoul, Korea.

**DEGREES HELD:** Master of Science, Polymers, Massachusetts Institute of Technology; Master of Science, Textiles, Georgia Institute of Technology; Bachelor of Engineering, Textile Engineering, Yeung Nam University.

Effect of Crystallinity of Semicrystalline Polymer Matrices on  
Fiber-Reinforced Ballistic Protective Composites

John W. Song, Mr., Phillip W. Gibson, Mr., Stuart R. Barlow, CPT  
U.S. Army Natick Research, Development and Engineering Center  
Natick, MA 01760-5019

**Introduction**

Thermoplastic composites offer significant improvements in terms of increased durability and reduced processing costs over conventional thermoset resin matrices. Thermoplastic composites have undergone intense technology development over the past decade for a variety of military and civilian applications. The inherent toughness and chemical resistance of these polymers make them well suited for composites which must maintain high strength under harsh environments. Since thermoplastics are melt processable, they offer potential ease of fabrication and field repair, since the resin can be remelted.

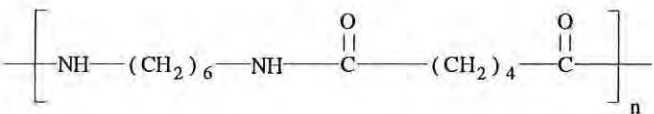
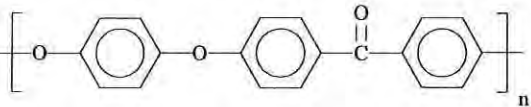
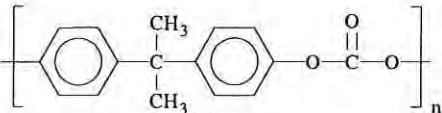
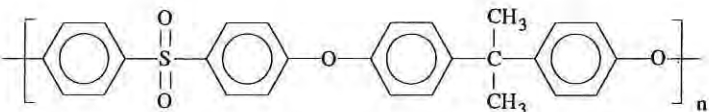
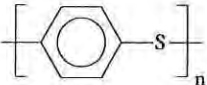
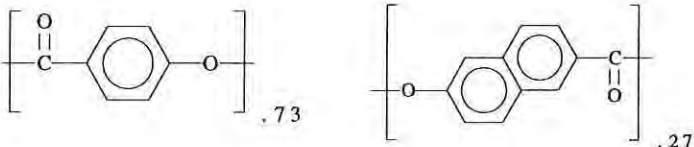
The properties of thermoplastic resins lend themselves well to ballistic composite applications. The wide variety of high temperature thermoplastics that have become available over the past decade make it feasible to consider using thermoplastic resins in many military ballistic composite applications. This new generation of thermoplastics, with their improved creep resistance and insensitivity to hot/wet conditions, offer the potential for rugged ballistic armor for soldiers' helmets, aircraft armor, and tank armor.

Our evaluation of thermoplastic composites for ballistic protection applications encompasses both semicrystalline(SC) and amorphous(A) thermoplastic resins. The resins used to manufacture ballistic test panels are shown in Table 1. These resins include both traditional polyamide engineering resins and some of the more recently developed higher performance thermoplastics.

Under normal fabrication conditions, amorphous polymers do not develop crystals upon cooling, but are frozen into the glassy state. However, semicrystalline polymers develop their crystals during the cooling stage of fabrication. The physical and mechanical properties of the semicrystalline polymers are highly dependent on their crystal morphology which is mainly governed by the processing history. This paper examines the effect of cooling rate on the

morphological parameters of nylon-66 and PEEK resins and composites. This study will assist in the optimization of processing conditions of thermoplastic composites for ballistic protective applications.

**Table 1: Thermoplastic Resins**

| Generic Name<br>Trade Name<br>Manufacturer                              | Types | Structure  |
|---|-------|--|
| Nylon-66<br>Zytel®<br>DuPont  | (SC)  |    |
| Polyetherether Ketone (PEEK)<br>Vitrex®<br>ICI                          | (SC)  |   |
| Polycarbonate<br>Lexan®<br>General Electric                             | (A)   |  |
| Polysulfone<br>Udel®<br>Union Carbide                                   | (A)   |  |
| Polyphenylene Sulfide (PPS)<br>Fortron®<br>Hoechst-Celanese             | (SC)  |   |
| Copolyester<br>(Liquid Crystalline)<br>Vectra® A900<br>Hoechst-Celanese | (SC)  |  |

### Background

When semicrystalline polymers are cooled from the melt or annealed at a certain temperature, they crystallize. Crystallization occurs between the melting temperature ( $T_m$ ) and the glass transition temperature ( $T_g$ ). Crystallization of semicrystalline materials is a result of nucleation and growth of crystallites.

Crystallization behavior and nucleation mechanisms are often analyzed using the Avrami equation [1] which is based on the laws of expanding spheres and circles.

$$\alpha = 1 - \exp(-kt^n) \quad (1)$$

Here  $\alpha$  is fractional conversion from melt state to crystal state at time  $t$ ,  $k$  is a crystallization rate constant which is a function of temperature,  $n$  is the Avrami exponent which contains information on the number of dimensions in which the growth take place and the order of the time dependence of the nucleation process. For normal crystallization, where crystal growth initiates from nuclei appearing sporadically in time and the radial rate of growth is constant,  $n$  is 4. For rod-like or disk-like crystals (i.e., 1 or 2 dimensional) growth, the values of  $n$  are less than 4.

For melt crystallization, nylon-66 and polyetheretherketone (PEEK) crystallize in at least two stages [2-7]. The first stage mainly involves rapid 3 dimensional (3D) spherulite growth from the nuclei. As spherulites grow bigger, they impinge on each other and begin to restrict each other's growth. After spherulite impingement, the second stage takes over with a slower restricted one or two dimensional growth process. Therefore, values of  $n$  for first stage growth are expected to be larger than for second stage growth. As implied in equation 1, the Avrami equation describes well first stage growth where the 3D growth predominates, but does not adequately describe the second stage of crystallization [2,3].

The values of the Avrami exponent  $n$  are also affected by melt temperature [2,4,8], crystallization temperature [2,9,10], fiber type [4,5,6,11], and molecular weight [4]. Reported  $n$  values of spherulitic growth for nylon-66 and PEEK are approximately 2 [8] and 3 [4] respectively. Velisaris and Seferis [3] developed a dual crystallization model through modification of the Avrami equation and obtained values for  $n$  of 2.5 for the first stage crystallization process and 1.5 for the second stage crystallization process of PEEK.

This study examines the crystallization behavior of nylon-66 and PEEK resins and composites using differential scanning calorimetry (DSC) and dynamic mechanical analysis (DMA) techniques. These techniques allow correlation of the crystallization behavior to mechanical properties such as modulus. To closely simulate the actual processing conditions during composite fabrication, dynamic scanning was applied, rather than isothermal, for both

techniques. Ballistic evaluations of the laminated composite samples were also performed.

## Experimental

### Materials

The matrix materials used in the experiments were 12 mil thick nylon-66 (Zytel-101) film, manufactured by E. I. duPont deNerous & Co., Inc., and PEEK (Vitrex) pellet, manufactured by ICI Advanced Materials, Ltd.

A Kevlar®-29, 2x2 basket weave fabric, 14oz/yd<sup>2</sup>, manufactured from 1500 denier yarn was the reinforcement material for the laminates.

### Fabrication process

Laminates were prepared using a heated hydraulic press. Platens were heated to the resin melting temperatures (i.e., Kevlar/nylon-66 laminates (280°C), Kevlar/PEEK laminates (360°C)). The nylon-66 laminates were prepared by alternating layers of fabric and film, and heating the layered sample to above the resin melting temperature at a pressure of 70 psi. This first stage of heating the sample up above the resin melt temperature took approximately 45 to 60 minutes. Once the sample reached 280°C the pressure was increased to 1400 psi for 10 to 20 minutes to squeeze out excess resin. Two cooling rates were used to vary the crystallinity of the Kevlar/nylon-66 composite sample. Cold water circulated through the plates provided a fairly fast cooling rate of approximately 60°C/min. A slower cooling rate of approximately 1.5°C/min was achieved by simply turning off the power to the heated platens.

Kevlar/PEEK laminates were prepared by using electrostatically coated powder prepreg stacked in layers. The prepreg was placed in the preheated platens under 350 psi for 10 minutes to consolidate the laminate. The PEEK samples were then cooled at the rate of 60°C/min.

For the ballistic evaluations, one- to five-layer laminates were prepared. Resin contents for Kevlar/nylon-66 laminates and Kevlar/PEEK laminates were approximately 30 and 25%, respectively.

### DSC and DMA Characterization

A TA Instrument 912 DSC cell calibrated using an indium standard was used to obtain the heat of crystallization upon cooling through dynamic DSC experiments. Both nylon-66 film and PEEK powder samples were heated at 10°C/min until well above the melting temperatures



(280°C for nylon-66 and 380°C for PEEK). Samples were held at that temperature for 5 minutes to eliminate any remaining thermal history. These molten polymers were then cooled at four different cooling rates (1, 5, 10, 20°C/min). After each cooling cycle, samples were heated again at the 10°C/min rate to the melting temperature to observe the changes in melting behavior.

Dynamic mechanical analyses were performed using a TA983 DMA. One-layer of Kevlar/nylon-66 or Kevlar/PEEK laminate was used for the DMA evaluations. The heating rate used for dynamic mechanical analyses, after the various rates of cooling experiments, was 2°C/min. Isothermal temperatures and cooling rates for the molten polymers in the laminates were the same as in the DSC experiments. Samples of approximately 15x12x0.6mm size were tested in flexural mode at a frequency of 1 Hz. The flexural amplitude was 0.5mm for the nylon-66 laminates and 0.8mm for PEEK laminates.

A Mettler hot stage with an Olympus polarized microscope was used to observe crystal formation in the polymers. Due to the temperature limitations of the hot stage, observations were performed only on nylon-66 samples.

#### Ballistic Evaluation

Kinetic energy absorbed by laminates during ballistic penetration was measured using a high speed impact apparatus described in reference 12. The projectile used for all ballistic testing was a 17-grain, 22 caliber fragment simulator.

### **Results and Discussions**

#### DSC Analyses of Neat Resins

Figure 1 and Table 2 are the DSC thermograms of crystallization from the polymer melt at various cooling rates. In all cases the heat of crystallization,  $\Delta H_c$ , increased with increasing cooling rate, and the crystallization peak temperature,  $T_c$ , decreased with increasing cooling rate. These relationships indicate that nuclei formation starts earlier at higher temperatures with slower cooling rates. In other words, the degree of supercooling,  $\Delta T$  (which was obtained from the difference between melt temperature of the polymers where the cooling starts (i. e., 280°C for nylon-66 and 380°C for PEEK in this study) and temperature of crystallization initiation from DSC experiment) for nuclei initiation increases with increasing rate of cooling, as indicated in Figure 2. However, as shown in the schematic representation in Figure 3, the nucleation rate and rate of crystallization increases very rapidly with decreasing crystallization temperature until it reaches a maximum, whereupon the rate of crystallization starts to decrease. We see this effect in the DSC exotherm ( $\Delta H_c$ ) which increases with increasing cooling rate as demonstrated in Figure 2. Dependence of supercooling on nucleation or crystallization rate has been reported by many workers [4,13,14].



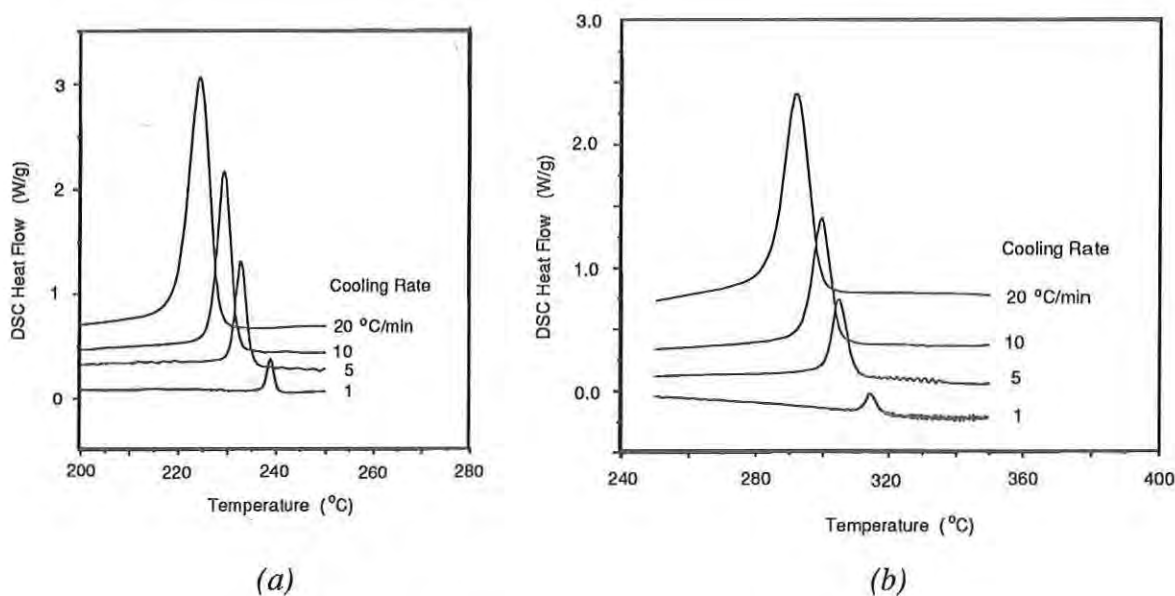


Figure 1. DSC Thermograms for Heat of Crystallization at Cooling Rates of 1,5,10, and 20°C/min. a) Nylon-66; b) PEEK.

Table 2: Summary of DSC data for nylon-66 and PEEK polymers with various cooling rates,  $\phi$ . (Crystallization temperature,  $T_c$ , Crystallization Initiation temperature,  $T_i$ , Supercool,  $\Delta T$ , Heat of crystallization,  $\Delta H_c$ , Melting temperatures,  $T_{m1}$  and  $T_{m2}$ , Heat of melting,  $\Delta H_m$  and Degree of crystallinity,  $X_c$ )

| Sample   | $\phi$<br>(°C/min) | $T_c$<br>(°C) | $T_i$<br>(°C) | $\Delta T$<br>(°C) | $\Delta H_c$<br>(J/g) | $T_{m1}$<br>(°C) | $T_{m2}$<br>(°C) | $\Delta H_m$<br>(J/g) | $X_c$<br>(%) |
|----------|--------------------|---------------|---------------|--------------------|-----------------------|------------------|------------------|-----------------------|--------------|
| Nylon 66 | 20                 | 224.30        | 232.00        | 48.0               | 45.38                 | 250.70           | 260.87           | 68.70                 | 35.51        |
|          | 10                 | 229.40        | 235.60        | 44.4               | 40.46                 | 251.89           | 260.74           | 66.69                 | 34.03        |
|          | 5                  | 232.74        | 237.60        | 42.4               | 33.98                 | 252.39           | 260.71           | 72.93                 | 37.21        |
|          | 1                  | 238.72        | 241.70        | 38.3               | 32.88                 | 253.77           | 260.54           | 79.58                 | 40.60        |
| PEEK     | 20                 | 292.10        | 305.40        | 74.6               | 54.95                 |                  | 342.42           | 33.49                 | 25.76        |
|          | 10                 | 299.39        | 310.50        | 69.5               | 51.34                 |                  | 343.58           | 38.55                 | 29.65        |
|          | 5                  | 304.88        | 316.10        | 63.9               | 48.80                 |                  | 344.10           | 34.81                 | 26.78        |
|          | 1                  | 314.06        | 322.20        | 57.8               | 36.58                 |                  | 346.31           | 41.05                 | 31.58        |

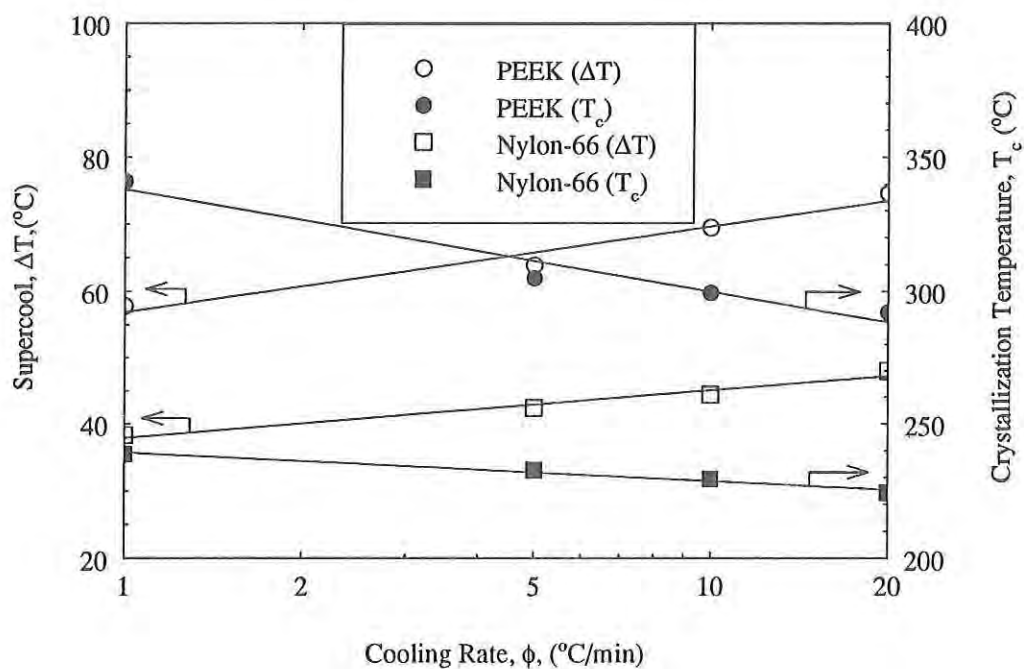


Figure 2. Supercool,  $\Delta T$ , and Crystallization Temperature,  $T_c$ , as a Function of Cooling Rate,  $\phi$ .

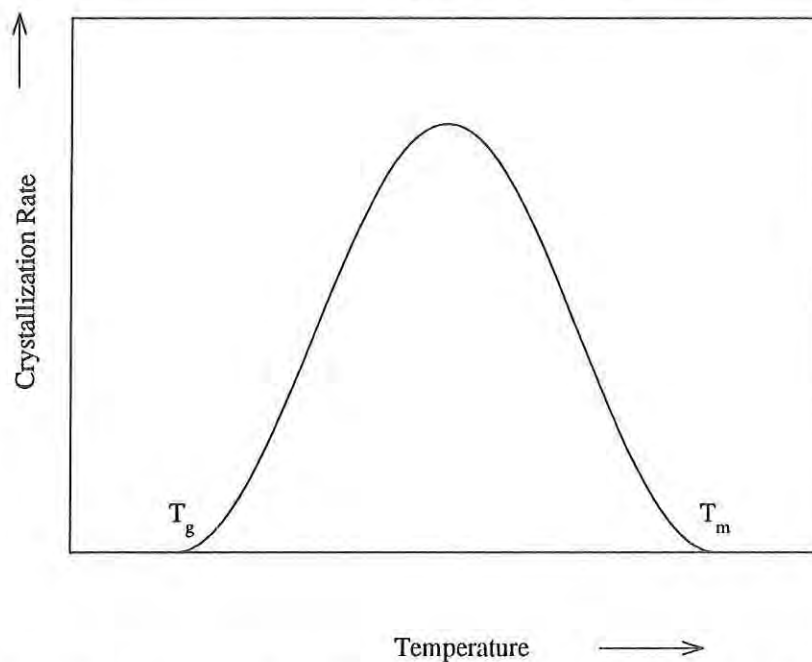


Figure 3. Schematic Representation of General Polymer Crystallization Rate as a Function of Temperature. Crystallization Rate Reaches Maximum Between  $T_m$  and  $T_g$ .

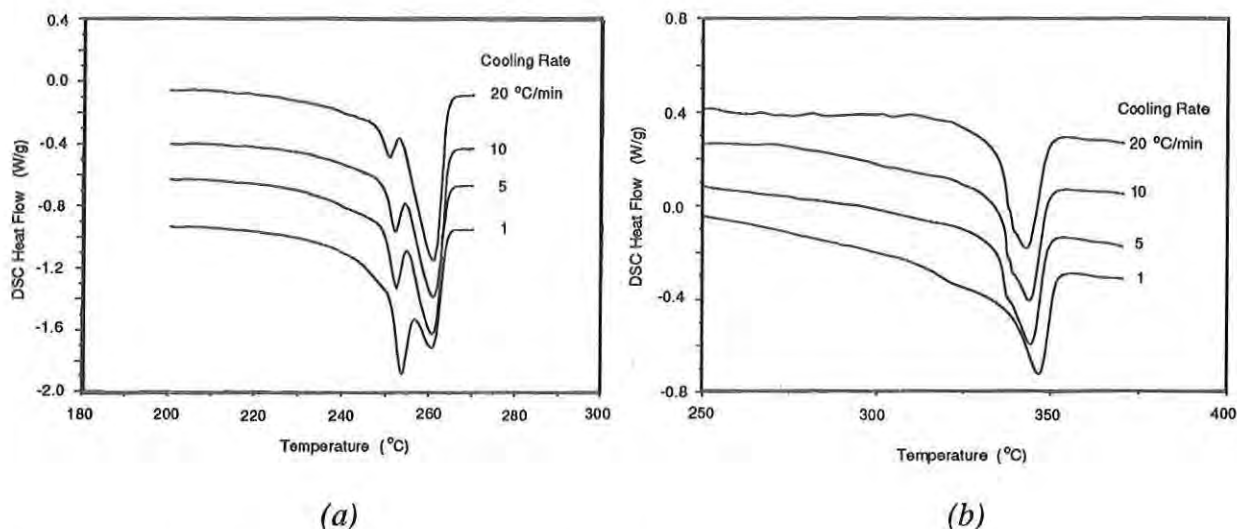


Figure 4. DSC Thermogram for Heat of Melting After 1, 5, 10 and 20 °C/min Cooling.  
a) Nylon-66; b) PEEK.

Figures 4a and 4b show the melting of nylon-66 and PEEK after melt crystallization. In nylon-66, two melting transitions were observed. Signs of low temperature melting were also observed in PEEK. This double melting behavior may be explained as a recrystallization - remelting phenomenon [15] or the formation of different types or sizes of crystals. With the conditions used in this study, PEEK did not clearly show lower-temperature melting peaks, whereas to others [5,11,16] they were apparent. As shown in Figure 4a and Table 2, the higher melting peak of nylon-66 does not show a significant dependence on rate of cooling. However, the lower melting peak shifted to the higher temperatures as the cooling rate decreases.

Also shown in Table 2 is that the heat of melting,  $\Delta H_m$ , increased with decreasing cooling rate. Assuming the heats of fusion for 100% crystallinity,  $\Delta H_f$ , for nylon-66 and PEEK are 196 [13] and 130 J/g [17] respectively, the degree of crystallinity from the endotherms, which is the ratio of  $\Delta H_m$  to  $\Delta H_f$ , were calculated and listed in Table 2.

At lower cooling rates, first stage crystallization occurs earlier at higher temperatures. Since at higher temperatures the nucleation rate is slow, spherulites will grow more freely and take a longer time to impinge upon adjacent spherulites. This increases the time before the crystallization process changes to the second stage. For a nonisothermal crystallization kinetic study of PEEK, Cebe [4] observed that the time to change over from rapid first stage crystal growth to slower second stage growth increased with decreasing cooling rate and that the relative crystallinity at that time was also slightly higher at a lower cooling rate. With similar reasoning, it is reasonable to expect to increase crystallinity with more perfect crystals at lower cooling rates or a higher  $T_c$ . This is shown in Figure 5.

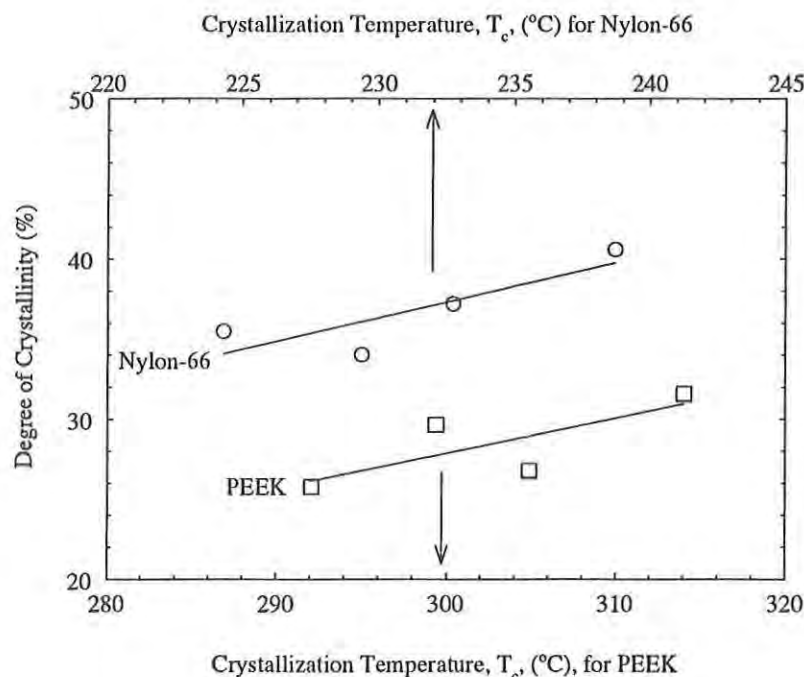


Figure 5. Degree of Crystallinity of Nylon-66 (○) and PEEK(□) as a Function of Crystallization Temperature.

#### DMA Analyses of Laminates

Since the temperature range examined in this study is significantly lower than the Kevlar decomposition temperature, which is above 450°C, it is assumed that the behavior observed in the DMA study is mainly resin matrix behavior.

As described earlier, in semicrystalline polymers, crystalline morphology will greatly influence the mechanical properties such as modulus. Figures 6 and 7 are flexural storage modulus ( $E'$ ) and loss modulus ( $E''$ ) scans obtained during cooling. As discussed in the DSC analysis section of this paper, when crystallization occurs at higher temperatures (i.e., low supercooling temperature), which is the consequence of the slower cooling rate, formed crystals may be more perfect than crystals from a faster cooling rate. More perfect crystals should show higher stiffness at higher temperatures. This is well demonstrated in Figures 6a and 6b which are the cooling scans of  $E'$ . The initial steep slope portions of the curve (stiff material) correspond to the first stage of crystallization. The second stage of crystallization follows with a lower slope (less stiff material). The  $E''$  scans shown in Figures 7a and 7b somewhat resemble the corresponding DSC scans. As the cooling rate decreases the  $E''$  peaks become smaller and sharper, which is another indication of improving crystal perfection.

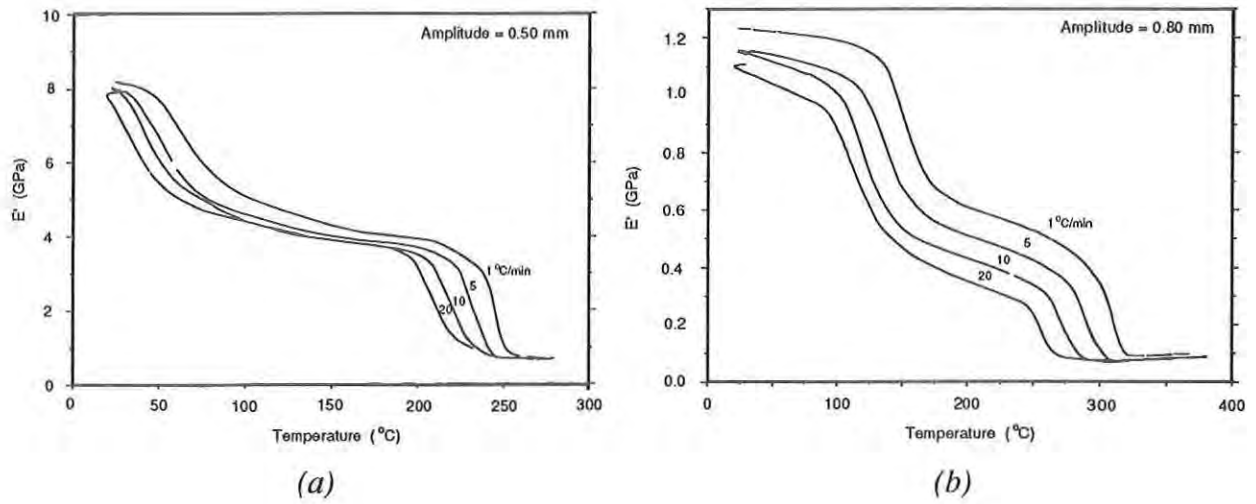


Figure 6. Flexural Storage Modulus ( $E'$ ) as a Function of Temperature. a) Kevlar/Nylon-66; b) Kevlar/PEEK. Laminate Samples Were Cooled From Polymer Melt Temperature at 1, 5, 10 and 20  $^{\circ}\text{C}/\text{min}$  Cooling Rate.

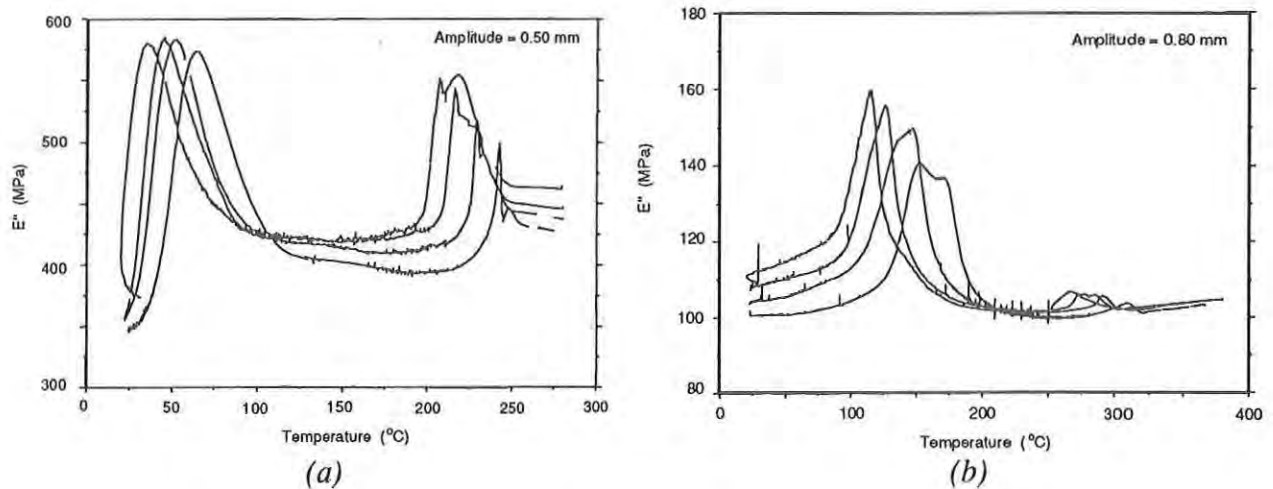


Figure 7. Flexural Loss Modulus ( $E''$ ) as a Function of Temperature. a) Kevlar/Nylon-66; b) Kevlar/PEEK. Laminate Samples Were Cooled From Polymer Melt Temperature at 1, 5, 10 and 20  $^{\circ}\text{C}/\text{min}$  Cooling Rate.

As can be seen in Figures 6 and 7, DMA cooling scans show not only the melt crystallization behavior but also allow detailed observation of the entire polymer hardening process. The transition observed at a much lower temperature (see Figures 7a and 7b) is the glass transition temperature due to the free volume reduction upon cooling ( $T_{gc}$ ). As shown in Figure 8 and Table 3, as cooling rate decreases,  $T_{gc}$  approaches  $T_g$  which is observed from 2°C/min heating. From these observations, it is obvious that after melt crystallization the amorphous region continues to harden. As for melt crystallization, this transition occurs earlier at higher temperatures when the material is cooled at a slower rate.

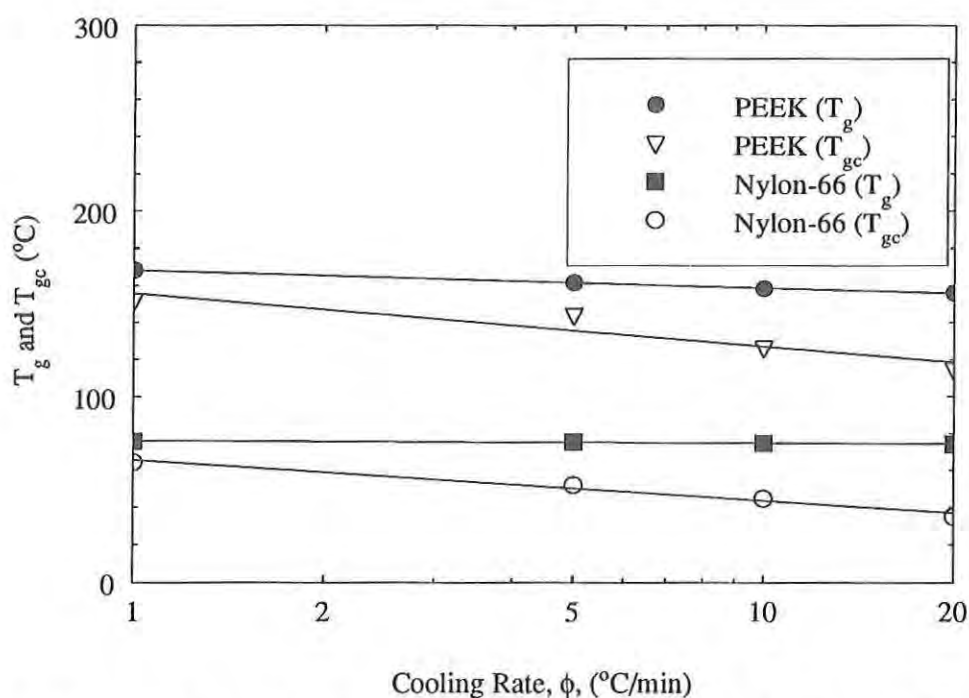


Figure 8.  $T_g$  Obtained During Cooling,  $T_{gc}$ , and  $T_g$  Obtained During Heating After Cooling for Kevlar/Nylon-66 and Kevlar/PEEK Laminates. Cooling Rates are 1, 5, 10 and 20 °C/min.



**Table 3: Summary of DMA data. All temperature readings are E'' peak values.**

| Sample              | $\phi$<br>(°C/min) | $T_c$<br>(°C) | $T_{gc}$<br>(°C) | $T_g$<br>(°C) | $E_m'$<br>(GPa) | $X_{RC}$<br>(%) |
|---------------------|--------------------|---------------|------------------|---------------|-----------------|-----------------|
| Kevlar/<br>Nylon-66 | 20                 | 206.7         | 34.85            | 74.14         | 7.848           | 38.6            |
|                     | 10                 | 216.4         | 44.58            | 74.64         | 8.029           | 37.8            |
|                     | 5                  | 229.5         | 51.89            | 75.36         | 8.057           | 40.2            |
|                     | 1                  | 242.4         | 64.38            | 75.8          | 8.205           | 40.8            |
| Kevlar/<br>PEEK     | 20                 | 266.1         | 114.4            | 155.9         | 1.104           | 20.6            |
|                     | 10                 | 283.8         | 126.5            | 158.2         | 1.151           | 24.2            |
|                     | 5                  | 290.4         | 144.1            | 161.6         | 1.157           | 28.4            |
|                     | 1                  | 308.1         | 151.9            | 168.3         | 1.233           | 32.5            |

From Figures 6a and 6b, relative crystallinity,  $X_T$ , in the melt crystallization region can be estimated as

$$X_T = (E_T' - E_o') / (E_m' - E_o') \quad (2)$$

where  $E_T'$  is  $E'$  at a given temperature,  $E_o'$  is the lowest modulus of the polymer melt and  $E_m'$  is the maximum obtainable modulus ( $E'$  values at 20°C were used). The results of equation 2 were plotted in Figure 9a and 9b. As shown in Table 3, just after the completion of melt crystallization, determined from  $E'$  and  $E''$  data, the relative crystallinities,  $X_{RC}$ , ranged from 39 to 41% and 21 to 33% for Kevlar/nylon-66 and Kevlar/PEEK laminates, with slightly higher value for slow-cooled samples. These values are very similar to the degree of crystallinities of the neat resins calculated from the heat of fusion of the polymer (see Table 2). These results confirm the close relationship between crystal morphology and mechanical properties and that this morphology can be controlled through cooling rate. The close agreement between the degree of crystallinity,  $X_c$ , from the neat polymer and the relative crystallinity,  $X_{RC}$ , from the laminate indicates that the influence of the fiber on degree of crystallinity is minimal as assumed earlier. These results also show that the sensitivity of crystal morphology to cooling rate is somewhat greater for PEEK than for nylon-66 laminates.

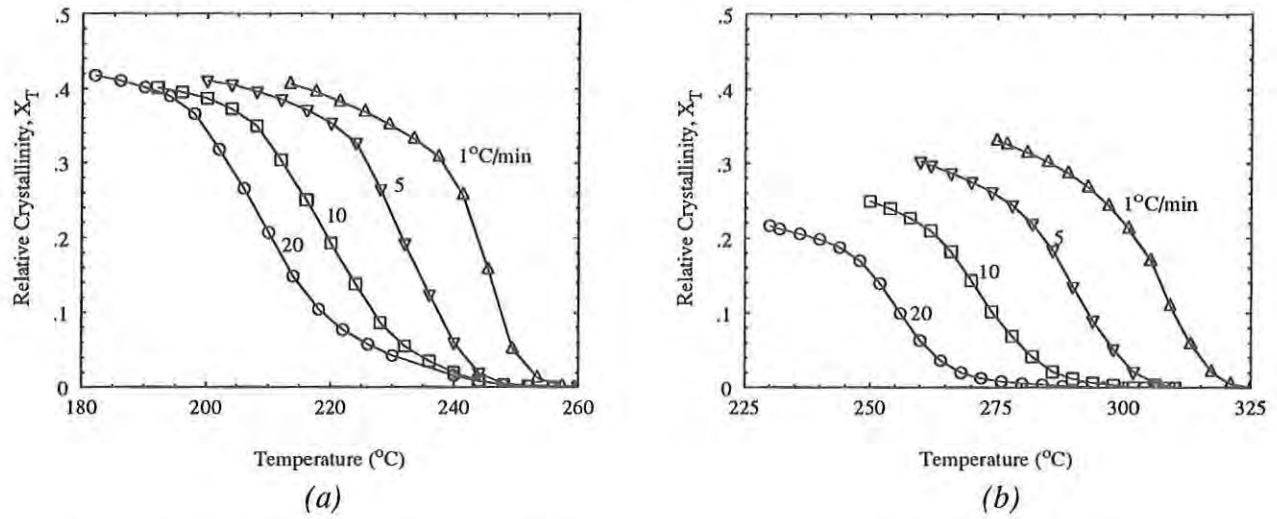


Figure 9. Relative Crystallinity as a Function of Temperature as Indicated at Various Cooling Rates. a) Kevlar/Nylon-66 Laminate; b) Kevlar/PEEK Laminate

Figure 10 is a plot of the maximum obtainable flexural storage modulus,  $E_m'$ , as a function of cooling rate. Although the differences are small,  $E_m'$  is greater at slower rates of cooling. These crystallization studies of Kevlar composite samples confirm that slow cooling rates in the mold will produce higher modulus composite samples.

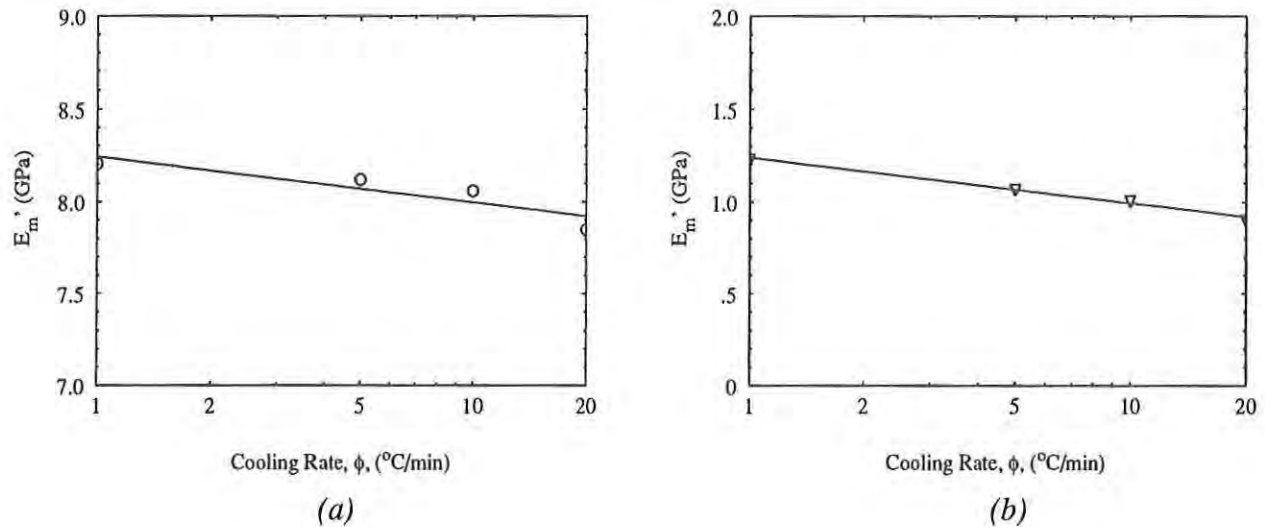


Figure 10. Maximum Obtainable Flexural Storage Modulus Obtained at 20 $^{\circ}\text{C}$  ( $E_m'$ ) as a Function of Cooling Rate. a) Kevlar/Nylon-66 Laminate; b) Kevlar/PEEK Laminate

### Microscopic Analysis

Crystal formation was observed using a Mettler hot stage with an Olympus polarized microscope. Due to the temperature limitations of the hot stage, observations for PEEK were not possible. Observations were made only on 1°C/min and 20°C/min cooling rates. The scans of a strip chart which was connected to the microscope were used to observe the progress of crystal formation. The scans of this strip chart (not shown) are the results of the light intensity differences due to the crystal formation upon cooling.

From the examinations of the chart scans, it was observed that for a 20°C/min cooling rate, the first stage crystallization started at around 230°C and ended at around 225°C and, for a 1°C/min cooling rate, nucleation started at around 244°C and the first stage of the process ended at 241°C. Therefore, at a 20°C/min cooling rate, the primary crystal formation period lasted only 15 seconds, while at 1°C/min rate, the period lasted 3 minutes, which is 12 times longer than the higher cooling rate.

Although the primary crystal formation region for 1°C/min cooling is shifted to the higher temperatures than the same region observed in DSC experiments (see Figure 1a and Table 2), ranges for the primary crystal formation regions for both cooling rates agreed reasonably well with DSC data. In Table 2, the differences between crystallization initiation temperature,  $T_i$ , and crystallization exotherm peak,  $T_c$ , are 7.7 °C for 20°C/min cooling rate and 3°C for 1°C/min cooling rate, which correspond to 23 seconds and 3 minutes, respectively.

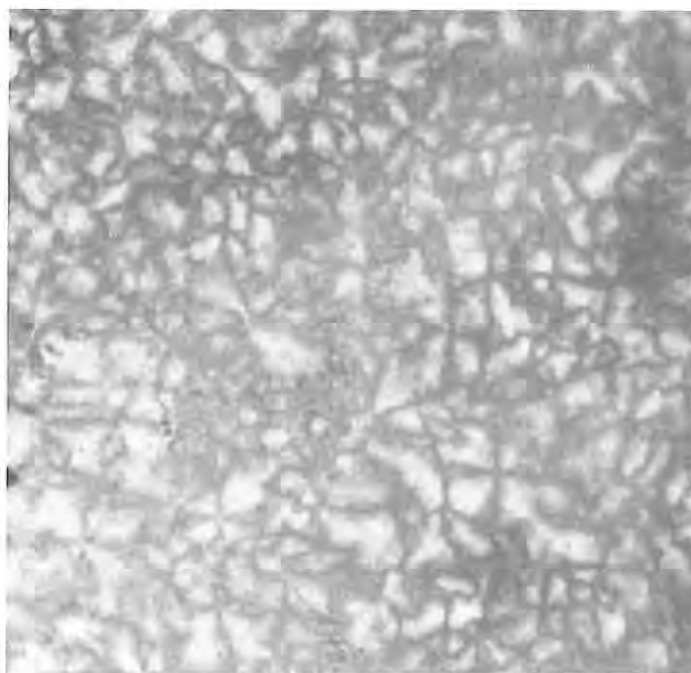


*Figure 11. Spherulites Formed in a Nylon-66 Air Bubble.  
Picture was made at room temperature.*

During the 1°C/min cooling, it was somewhat easier to identify initiation of nucleation than for the 20°C/min cooling rate, but it was still a very fast process. After completion of crystallization, it was difficult to distinguish the differences in spherulite size between the two different rates. However, in the bubbles, generated during the cooling process, where the nucleating sites are minimal, grown spherulites are reasonably large and stay the same size. Figure 11 shows spherulites formed in a bubble of nylon-66.

### Ballistic Evaluation

Figure 12 is a plot of ballistic limit as a function of areal density of the laminates. The ballistic limit was obtained from the energy absorption of the laminate as described in reference 12. Curves for Kevlar/Polyvinylbutyral + Phenol formaldehyde (PVB+PH) and S-2 Glass/PVB+PH are also from reference 12 and plotted for comparison purpose. As shown, ballistic limits of the thermoplastic laminates fabricated during this study are somewhat lower than Kevlar/PVB+PH, which is the current Army helmet material, and slightly better than S-2 Glass/PVB+PH laminates.

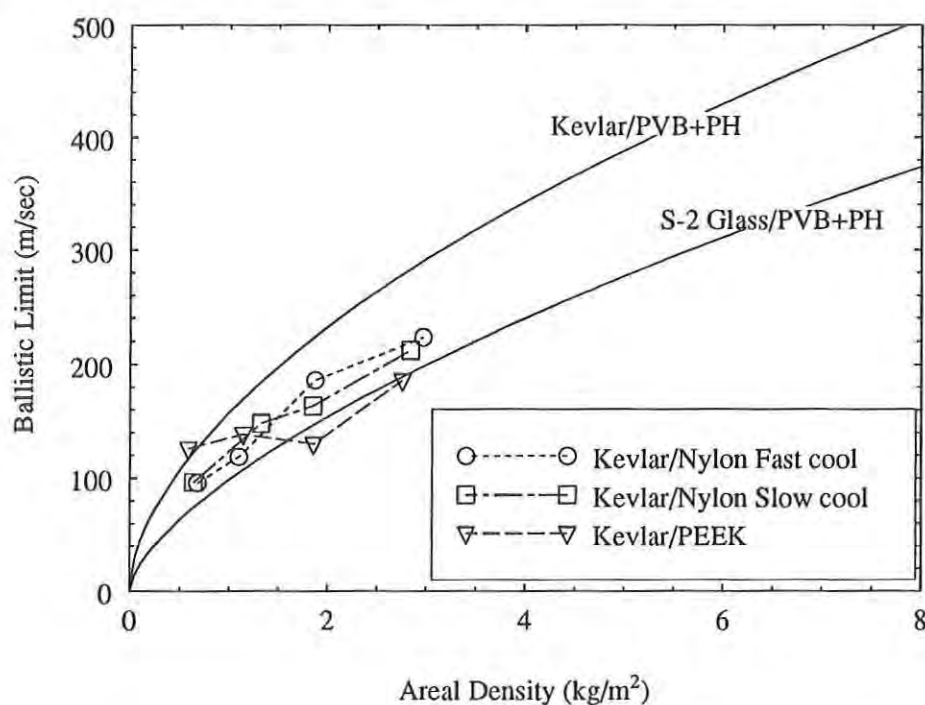


Figure 12. Ballistic Limits of Kevlar/Nylon-66 and Kevlar/PEEK Laminates as a Function of Areal Density. Curves for Kevlar/PVB+PH and S-2 Glass/PVB+PH are from Reference 12.

It must be noted that the processing conditions of the laminates fabricated during this study were not optimized due to the limitations on equipment and lack of experience. For example, we feel that in some cases, laminates were kept in the mold too long at high pressure. The high pressure forced the molten polymer into the interfiber spaces within the Kevlar yarns. This probably resulted in restricting the fiber mobility during ballistic impact. It has been shown that out-of-plane deformation of the Kevlar fabric is necessary for good ballistic impact resistance, and that composite laminates which are optimized for properties such as flexural modulus do not provide good ballistic impact resistance [18]. The function of the resin in a Kevlar ballistic protective composite is mainly to provide structural integrity. A resin which interferes too much with the motion of the Kevlar fabric during ballistic impact will decrease the composite's ballistic impact resistance.

In the Kevlar/PEEK laminates, it was noticed that the Kevlar fabric changed color from light gold to brown, which may be an indication of thermal degradation. The Scanning Electron Micrographs in Figures 13a and 13b reveal the degradation of Kevlar fiber in Kevlar/PEEK laminates. In both pictures, typical Kevlar fibrillation upon ballistic impact was observed. However, fibrillation in Kevlar/PEEK laminate was very localized at the impact area, whereas fibrillation observed in Kevlar/nylon-66 laminate extended to considerably longer distances from the impact point. These observations led us to believe that the Kevlar fiber in Kevlar/PEEK laminates is weakened from thermal degradation and resulted in the localized fibrillation in the impact area during ballistic impact. Figure 14 shows the unusual mode of nylon-66 matrix cracking.



*Figure 13. Scanning Electron Micrographs of a) Kevlar/Nylon-66 and b) Kevlar/PEEK Laminates After Ballistic Impact. Kevlar/PEEK Laminate Shows Localized Fibrillation Whereas Kevlar/Nylon-66 Laminate Shows the Fibrillation Extended a Much Longer Distance.*



*Figure 14. Unusual Matrix Cracking After Ballistic Impact Observed on Kevlar/Nylon-66 Laminate.*

### Conclusions

From the observations of crystallization behavior of nylon-66 and PEEK neat resin and their laminates for various cooling rates, it was found that the cooling rate influenced the crystallization behavior significantly. At lower cooling rates more perfect primary crystals are formed and this fact results in higher crystallinity and higher modulus.

The relative crystallinity calculated from storage flexural moduli of the laminates in the melt crystallization region agreed well with the degree of crystallinity obtained from the neat resin melting endotherm. This agreement indicates that the influence of fiber on degree of crystallinity on laminates is minimal.

From the DMA cooling scan, it was found that after the completion of melt crystallization, amorphous hardening continued. Another transition at a much lower temperature was also observed. This is clearly due to the free volume reduction upon cooling and is probably due mainly to the amorphous region behavior. At a very slow cooling rate, this transition will merge to the  $T_g$ .



Crystal formation in nylon-66 observed via a polarized microscope with hot stage agreed reasonably well with DSC data. Times spent for primary crystal formation for the observed cooling rates (1 and 20°C/min) were similar in DSC and in a polarizing microscope with hot stage.

For the samples as molded, ballistic limit values obtained during this study are reasonable. It was believed that in some cases high molding pressures and other conditions forced resin into the interior of yarns, thereby lowering the ballistic impact resistance of the composites.

SEM photos revealed the possible thermal degradation of Kevlar fibers in the Kevlar/PEEK laminate fabricated in this study.

### Acknowledgements

The authors would like to express their thanks to M. Auerbach for the SEM preparations and helpful discussions.

### References

1. Avrami, M., *J. Chem. Phys.*, 8, 212 (1940)
2. Inoue, M., *J. Poly. Sci.*, 55, 753 (1961)
3. Velisaris, C. N., and Seferis, J. C., *Poly. Eng. & Sci.*, 26, No.22, 1574 (1986)
4. Cebe, P., *Polymer Composites*, 2, No4, 271 (1988)
5. Ma, C. and Yur, S., *Antec'89*, 1422 (1989)
6. Hartness, J. T., *SAMPE J.*, 26 (1984)
7. Sharples, A., *Introduction to Polymer Crystallization*, St. Martin's Press, NY (1966)
8. Allen, P. W., *Trans. Faraday Soc.*, 48, 1178 (1952)
9. Inoue, M. and Takayanagi, T., *J. Poly. Sci.*, 47, 498 (1960)
10. Cebe, P. and S. Hong, *Polymer*, 27, 1183 (1986)
11. Lee, Y. and Porter, R. S., *Poly. Eng. Sci.*, 26, 633 (1986)

SONG, et al.

12. Song, J. W. and Egglestone, G. T., Proc. 19th SAMPE International Technical Conference, Closed Session, 108 (1987)
13. Inoue, M., *J. Poly. Sci.*, Part A, 1, 2697 (1963)
14. Flory, P. J. and McIntyre, A. D., *J. Poly. Sci.*, 18, 592 (1955)
15. Lee, Y. and Porter, R. S., *Macromol.* 20, 1336 (1987)
16. McHugh, E., Spagnuolo, D. and Chin, A., *Antec'91, 2008* (1991)
17. Blundell, D. J. and Osborn, B. N., *Polymer*, 24, 953 (1983)
18. Lastnik, A. and Karageorgis, C., U.S. Army Natick Research, Development and Engineering Center Technical Report, *NATICK/TR-84/030* (1982)

DeCRISTOFANO, et al.

TITLE: 3D Analysis of Transient Thermal Transport  
Through Uniforms

Barry S. DeCristofano, Gerald J. Caldarella  
and Joseph F. Roach

ABSTRACT: An advanced thermal response data acquisition system has been custom designed and built by Natick to provide state-of-the-art collection and analysis of the effects of thermal insults from a variety of sources on military uniform systems, items and fabrics. Data can be recorded in a laboratory setting or sent for miles on a single coaxial cable, fiber optic cable or FM frequency. Using software tailored to the system, the researcher acquires data to be displayed in real time or stored for analysis of burn-severity predictions at any future time convenient. The software used in this process has been written by Natick specifically for thermal response investigations. The data recorded from the experiment are used to generate two- and three-dimensional representations of the extent of skin burns predicted from skin simulant recordings. The three-dimensional manikin display is capable of showing the progression of skin damage as it changes with time. The software is linked to models used by equipment design engineers to allow projection of certain articles of equipment onto the image. This system is a complete package, which gives researchers the tools required to study accurately and comprehensively the effects of thermal radiation on existing and potential uniform materials and systems.

BIOGRAPHY OF THE PRESENTER: Barry S. DeCristofano

PRESENT ASSIGNMENT: Physics and Engineering Group, Physical  
Science Division, Soldier Science Directorate

PAST EXPERIENCE: Research and development of microclimate  
cooling systems.

DEGREES HELD: B.S. Chemical Engineering, Lafayette College,  
M.S. Chemical Engineering, Northeastern University.

### 3D ANALYSIS OF TRANSIENT THERMAL TRANSPORT THROUGH UNIFORMS

Barry S. DeCristofano, Gerald J. Caldarella  
and Joseph F. Roach  
U.S. Army Natick RD & E Center

#### 1.0 INTRODUCTION

Since 1950, compelled largely by the prospect of nuclear weapons use, a number of investigators have studied the possibility of using simulants that mimic the response of skin tissue as a substitute for animals in thermal injury studies (refs. 1-6). Major efforts to develop techniques to simplify and standardize experimental investigations of skin tissue damage from flame and nuclear thermal insults were conducted at the laboratories of the University of Rochester, Massachusetts Institute of Technology, the U.S. Naval Material Laboratory and the U.S. Army Natick Quatermaster Research and Engineering Command (later the U.S. Army Natick Research, Development and Engineering Center).

#### 2.0 PRIOR TECHNOLOGIES

One of the first successful methods of recording surface temperatures in thermal radiation research was the temperature indicating tape. Tapes of black paper coated with organic compounds of various melting points were used to record the surface temperature attained beneath fabrics (Fig. 1). These compounds formed an opaque, white spot when deposited on the tape and when melted were absorbed by the paper allowing the paper to become visible. When conducting an experiment, a series of these tapes was affixed to a manikin in several locations. The highest surface temperature attained at any site was indicated by the color change of the tapes placed there. This technology is still marketed today (Fig. 2) and is useful in applications where there exists a limiting temperature beyond which materials or components can become damaged or ineffective.

A hypothesis advanced by Henriques (ref. 7) is that in burned skin, cellular death follows the thermal inactivation of a critical fraction of the sensitive protein molecules in the skin. While a correlation between skin surface temperature and skin tissue damage has been determined, a more precise predictor of tissue damage can be achieved by knowing the increase in temperature at the dermis-epidermis boundary (approximately 80  $\mu\text{m}$  beneath the skin surface) as a function of time. The index used by Henriques to indicate the severity of a burn was  $\omega$ ,  $\Omega$  (Eqn. 1).

$$\Omega = 3.1 \times 10^{98} \int_0^t e^{(75000 / (T + 273))} dt \quad (1)$$

where,

$\Omega$  is the index of burn severity (an omega value of 1 indicates a second degree burn)

T is the sensor temperature in degrees Celsius  
and t is the time in seconds

The temperature-versus-time relationship is required to calculate this parameter. To this end, sensors were constructed to simulate the thermal properties of skin tissue and correlate burn severity with the temperature history at a known depth beneath the skin surface. Derksen et al., at the Naval Material Laboratory (NML) (ref. 5) experimented with various proportions of thermosetting resins and fillers to form a material that had the same thermal response characteristics as human skin tissue.

The result was a mixture of urea-formaldehyde and silica compression molded into a disc, 3.8 cm-diameter and 1.3 cm-thick that was curved on one face. A 0.01 cm thick, Type T (copper-constantan) thermocouple embedded 0.05 cm beneath the curved surface provided a temperature history of the simulant's response to a thermal source (Fig. 3). The response of the sensor closely matched that of skin tissue (Fig. 4). In 1973, the Air Force bought an instrumented manikin that was designed for field testing in aircraft fuel fires (ref. 8). The manikin had a network of 124 sensors that were similar in design to the NML sensors. This manikin (Fig. 5) was obtained by Natick shortly thereafter and used in testing garment materials at a flame pit located at Natick's annex facility in Maynard, MA.

The collection and analysis of the data from these sensors, though sophisticated at the time, seem quite cumbersome by today's standards. Thermocouple voltages were scanned three times each second and the data were recorded on a tape cassette recorder located in the torso of the manikin with the multiplexing hardware, referred to as the Manikin Data Acquisition System (MDAS). This equipment was powered by a lead dioxide battery (also in the torso), which had to be recharged prior to each run to ensure proper operation. The Manikin Support System (MSS) was used at the beginning and end of each experiment. Before a test, the MSS was used to charge the battery of the MDAS, perform a check-out of the manikin sensors, and initialize the MDAS for the test. At the conclusion of the experiment, the data were transferred from the cassette in the manikin to a separate data reduction unit where it was reformatted and stored on another cassette. The reformatted data were then transcribed to a tape reel compatible with a digital computer (ref. 9). Upon returning from the test site, the data on the tape reel were down-loaded to the UNIVAC 1106 computer located at Natick and the data reduced (usually overnight). The program converted the data to skin burn

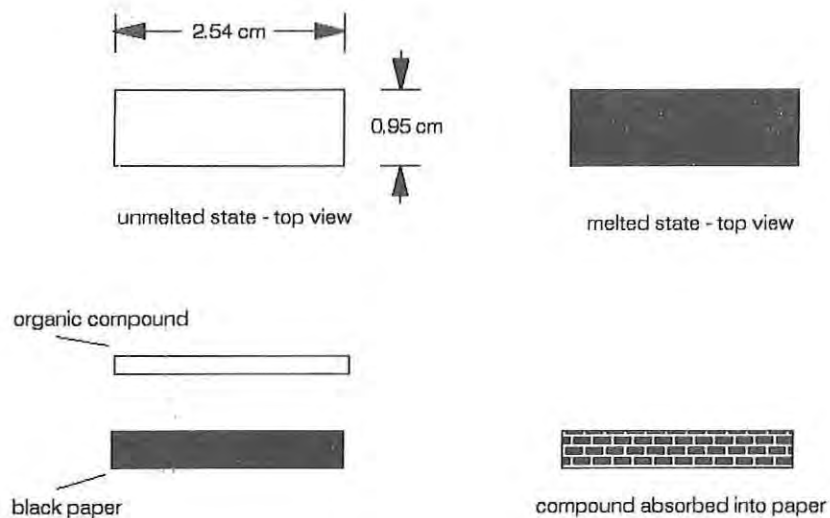


Figure 1. Schematic of an early temperature tape design.

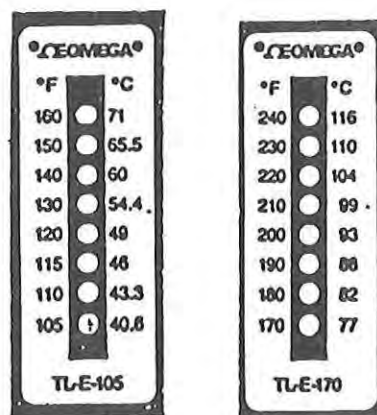


Figure 2. Representative temperature tapes currently marketed.



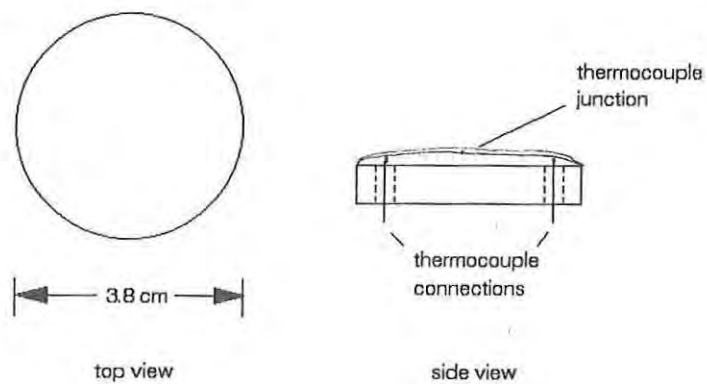


Figure 3. Schematic of the NML skin simulant.

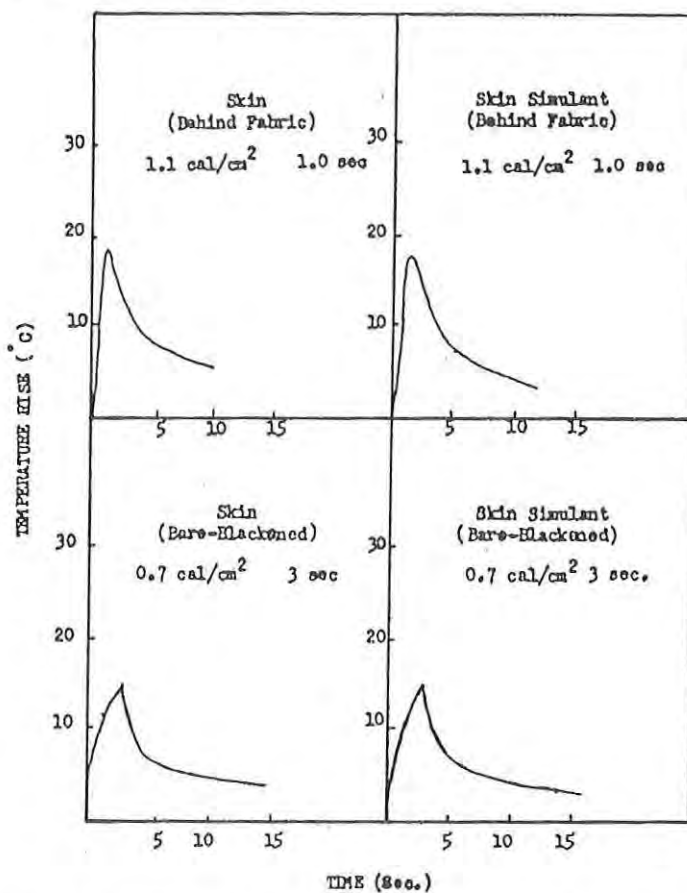


Figure 4. A comparison of the NML skin simulant response to that of skin (ref. 2).

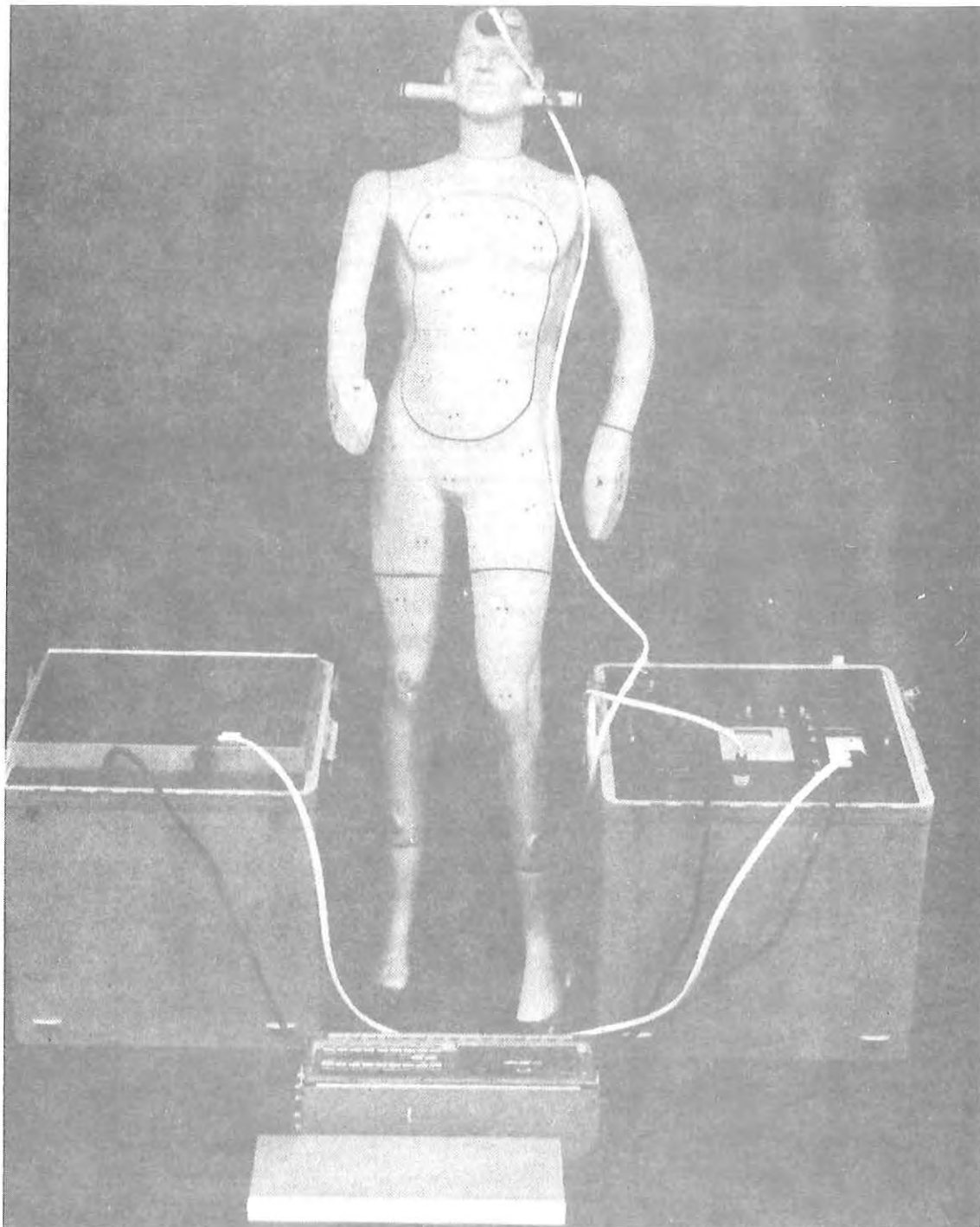


Figure 5. Manikin and support system (circa 1973) consisting of the manikin (center rear), the MDAS (center front), and the MSS (left, right).

DeCRISTOFANO, et al.

damage criteria. The program also provided a body-regional analysis of the simulated skin damage and a two-dimensional representation of the affected areas (Fig. 9). The data processing hardware external to the manikin was bulky, heavy, and sensitive to shock and temperature.

The problems with handling the data in this manner were two-fold. First, the accumulated noise generated by recording and re-recording the data caused data to become muddled and lost at times. Second, the lengthy turnaround time needed before researchers saw the data meant equipment problems went undetected. This sometimes required that some multiple, costly experimental runs had to be repeated.

With the advent of personal computers, it became possible to handle the large quantity of data generated by the manikin's 124 sensors rapidly and on-site. The tape recorder and multiplexing circuitry mounted inside the manikin were replaced by eight circuit boards (Fig. 10). The multiplexors on these boards allowed the thermocouple voltages to be measured 10 times each second. This three-fold increase in data provided a more accurate determination of each sensor's temperature response as a function of time. The multiplexor sequencing and a/d conversion were controlled by commercial software (Labtech Notebook) running on a portable computer (Compaq Portable 386). The system allowed for an evaluation of the status of all sensors immediately prior to and after each experiment.

Final processing of the data resulting in the calculation of skin tissue damage and two-dimensional plotting of the body areas affected required under 30 minutes and could be accomplished on-site if desired (Fig. 11). These calculations were also carried out on a portable computer using software developed at Natick (program MANBURN.BAS).

This system too, though representing a marked improvement over its predecessor, had significant limitations. With the ability to record only 124 channels, the system was limited to the use of one manikin. This system did not take full advantage of extended target area ( $33 \text{ m}^2$ ) available at the Thermal Radiation Source (TRS). When more than one manikin was used in an experiment, such as in the bi-annual high-explosive tests, the additional manikins were equipped with paper tapes, described above. Also, the hard-wiring of the manikin to the computer via a 10-twisted-pair cable (necessary for multiplexor control and data exchange) limited the distance the computer could be located away from the manikin. This restriction would have made fire-pit experiments more difficult to execute and complicated the use of the manikin in combat vehicle crew compartments. Finally, the two-dimensional representation of the predicted skin tissue damage area could not give a true impression of the extent of damage due to foreshortening of the areas on the sides of the manikin.

To extend the capabilities of researchers to collect and analyze the response of fabrics and uniform systems to varied thermal insults and

# DeCRISTOFANO, et al.

RUN NUMBER 018 SUIT NUMBER 112 MANIKIN NUMBER 2 DAY 229 OF YEAR 1972

## SUMMARY OF BURN DAMAGE TO THE TOTAL\* BODY

\*(COVERAGE LIMITED TO 78 PERCENT OF BODY SURFACE)

| PERCENTAGE OF BODY SURFACE BURN DAMAGE BY CLASS            | BASED ON        |                                   |
|--|-----------------|-----------------------------------|
|  | TOTAL BODY AREA | TOTAL AREA COVERED BY FLIGHT SUIT |
| CLASS A (NO DAMAGE, OMEGA LESS THAN 0.53 AT 100 MICRONS)   | 39.68           | 50.88                             |
| CLASS B (OMEGA BETWEEN 0.53 AND 1.0 AT 100 MICRONS)        | 5.47            | 7.02                              |
| CLASS C (OMEGA EQUAL TO 1.0 BETWEEN 100 AND 2000* MICRONS) | 21.21           | 27.19                             |
| CLASS D (OMEGA GREATER THAN 1.0 AT 2000 MICRONS)           | 11.63           | 14.91                             |
| TOTAL  | 78.00           | 100.00                            |
| TOTAL CLASS C AND D  | 32.84           | 42.11                             |

THE ABOVE PERCENTAGES ARE BASED ON THE COVERAGE BY OPERATIONAL SENSORS OF 78.00 PERCENT OF THE BODY SURFACE AREA.  
MALFUNCTIONING SENSORS COVERED 0.00PERCENT. 22 PERCENT OF BODY SURFACE (HEAD, FEET, HANDS) IS NOT COVERED BY SENSORS.

\*\*\*\*\*

## SUMMARY OF HEAT FLUX DATA

TOTAL INTEGRATED HEATING  
BTU/FT2 (CAL/CM2)

|                  | LEFT HAND        | RIGHT HAND       | BACK            |
|------------------|------------------|------------------|-----------------|
| CALORIMETER REAR | 46.243 ( 12.532) | 38.436 ( 10.416) | 19.313 ( 5.234) |
| FRONT            | 28.471 ( 7.716)  | 35.560 ( 9.637)  |                 |
| SIDE             | 29.766 ( 8.067)  | 50.017 ( 13.555) |                 |
| AVERAGE          | 34.827 ( 9.438)  | 41.338 ( 11.203) |                 |
| RADIOMETER       | 40.939 ( 11.094) | 51.081 ( 13.843) | 14.651 ( 3.970) |

AVERAGE FIRE LEVEL  
(AVERAGE OF ALL HAND CALORIMETERS)

38.082 ( 10.320)

Figure 9a. Text output using MDAS data (ref 10).

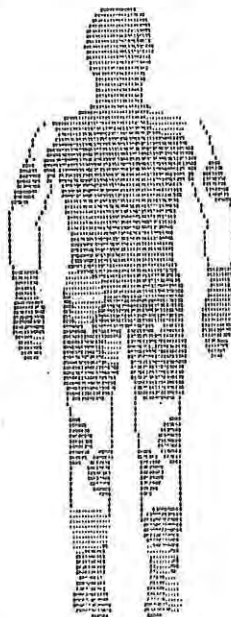


Figure 9b. Graphics output using MDAS data (shaded areas represent severity of burn).

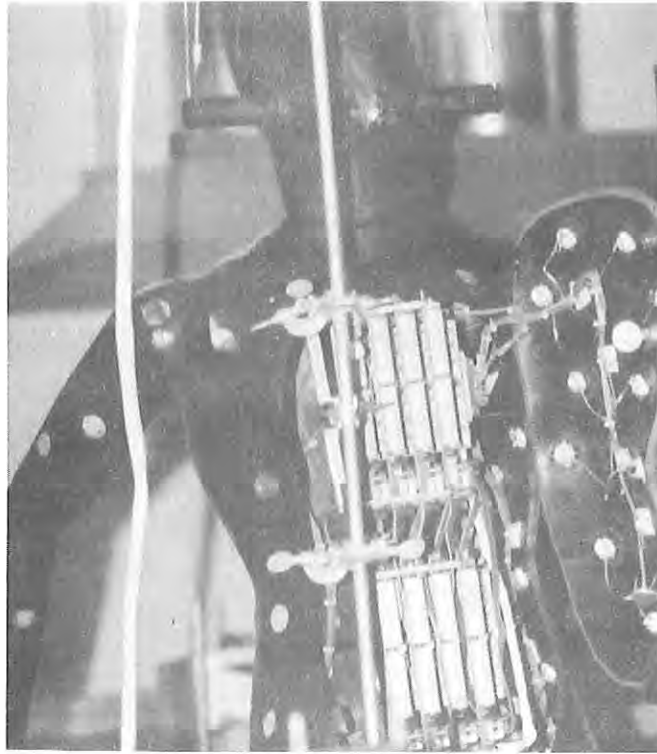


Figure 10. Circuit boards located in manikin.

Today's date is: 08-08-1990  
Experiment name: AUID-5 (20 cal/cm2)  
Experiment date: 2-16-1990

|       |          |          |          |          |          |          |          |          |
|-------|----------|----------|----------|----------|----------|----------|----------|----------|
| TC #  | 1        | 2        | 3        | 4        | 5        | 6        | 7        | 0        |
| Omega | 0.12E-22 | 0.37E-26 | 0.14E-26 | 0.22E-27 | 0.23E-26 | 0.52E-24 | 0.42E-22 | 0.00E+00 |
| TC #  | 8        | 9        | 10       | 11       | 12       | 13       | 14       | 0        |
| Omega | 0.95E-15 | 0.74E-15 | 0.42E-13 | 0.11E-11 | 0.23E+00 | 0.20E+00 | 0.10E-05 | 0.00E+00 |
| TC #  | 15       | 16       | 17       | 18       | 19       | 20       | 21       | 0        |
| Omega | 0.45E+00 | 0.17E+02 | 0.85E+03 | 0.12E+04 | 0.13E+05 | 0.19E+05 | 0.33E+05 | 0.00E+00 |
| TC #  | 22       | 23       | 24       | 25       | 26       | 27       | 28       | 0        |
| Omega | 0.50E+06 | 0.53E+05 | 0.21E+09 | 0.11E+06 | 0.32E+05 | 0.14E+04 | 0.33E+03 | 0.00E+00 |
| TC #  | 29       | 30       | 31       | 32       | 33       | 34       | 35       | 36       |
| Omega | 0.12E+02 | 0.12E+01 | 0.83E-02 | 0.42E-04 | 0.25E-06 | 0.17E-06 | 0.22E-10 | 0.46E-13 |
| TC #  | 37       | 38       | 39       | 40       | 41       | 42       | 43       | 44       |
| Omega | 0.12E-15 | 0.14E-17 | 0.98E-20 | 0.53E-22 | 0.00E+00 | 0.48E-24 | 0.39E-24 | 0.15E-24 |
| TC #  | 45       | 46       | 47       | 48       | 49       | 50       | 51       | 52       |
| Omega | 0.36E-25 | 0.16E-23 | 0.63E-21 | 0.42E-18 | 0.16E-15 | 0.22E-13 | 0.94E-11 | 0.29E-08 |
| TC #  | 53       | 54       | 55       | 56       | 57       | 58       | 59       | 60       |
| Omega | 0.37E-06 | 0.27E-04 | 0.26E-02 | 0.21E+00 | 0.81E+01 | 0.17E+03 | 0.30E+04 | 0.23E+05 |
| TC #  | 61       | 62       | 63       | 64       | 65       | 66       | 67       | 68       |
| Omega | 0.27E+06 | 0.35E+07 | 0.44E+07 | 0.10E+08 | 0.00E+00 | 0.62E+07 | 0.33E+07 | 0.50E+06 |
| TC #  | 69       | 70       | 71       | 72       | 73       | 74       | 75       | 76       |
| Omega | 0.48E+05 | 0.24E+04 | 0.98E+02 | 0.97E+00 | 0.94E-02 | 0.53E-01 | 0.20E-04 | 0.97E-07 |
| TC #  | 77       | 78       | 79       | 80       | 81       | 82       | 83       | 84       |
| Omega | 0.16E-09 | 0.17E-12 | 0.18E-15 | 0.44E-18 | 0.14E-20 | 0.37E-18 | 0.13E-19 | 0.13E-25 |
| TC #  | 85       | 86       | 87       | 88       | 89       | 90       | 91       | 92       |
| Omega | 0.15E-24 | 0.25E-20 | 0.48E-24 | 0.15E-22 | 0.44E-22 | 0.52E-19 | 0.17E-15 | 0.31E-13 |
| TC #  | 93       | 94       | 95       | 96       | 97       | 98       | 99       | 100      |
| Omega | 0.88E-11 | 0.60E-09 | 0.44E-07 | 0.61E-05 | 0.12E-02 | 0.00E+00 | 0.14E+01 | 0.15E+02 |
| TC #  | 101      | 102      | 103      | 104      | 105      | 106      | 107      | 108      |
| Omega | 0.25E+04 | 0.00E+00 | 0.19E+06 | 0.50E+06 | 0.19E+07 | 0.26E+07 | 0.28E+07 | 0.70E+07 |
| TC #  | 109      | 110      | 111      | 112      | 113      | 114      | 115      | 116      |
| Omega | 0.55E+09 | 0.29E+06 | 0.20E+06 | 0.37E+04 | 0.86E+03 | 0.27E+02 | 0.36E+00 | 0.88E-05 |
| TC #  | 117      | 118      | 119      | 120      | 121      | 122      | 123      | 124      |
| Omega | 0.14E+00 | 0.14E-06 | 0.86E-08 | 0.36E-11 | 0.25E-12 | 0.13E-14 | 0.22E-17 | 0.37E-24 |

Figure 11a. Output from MANBURN.BAS, omega values.

Today's date is: 08-08-1990  
 Experiment name: AUIB-5 (20 cal/cm2)  
 Experiment date: 2-16-1990

| % of SENSOR area with 2nd degree burns or greater   |  |  |  | % of BODY area with 2nd degree burns or greater   |  |  |  |
|---|--|--|--|---|--|--|--|
| WHOLE BODY: 40.3<br>FRONT: 39.3      BACK: 41.1   |  |  |  | WHOLE BODY: 35.5<br>FRONT: 33.9      BACK: 37.1   |  |  |  |
| HANDS: 49.9<br>FRONT: 50.0      BACK: 49.9<br>RIGHT: 100.0      LEFT: 0.0<br>RF: 100.0      RB: 100.0      LF: 0.0      LB: 0.0 |  |  |  | HANDS: 46.5<br>FRONT: 46.6      BACK: 46.4<br>RIGHT: 93.1      LEFT: 0.0<br>RF: 93.3      RB: 92.9      LF: 0.0      LB: 0.0  |  |  |  |
| ARMS: 42.0<br>FRONT: 43.9      BACK: 40.4<br>RIGHT: 84.3      LEFT: 0.0<br>RF: 83.6      RB: 85.1      LF: 0.0      LB: 0.0     |  |  |  | ARMS: 34.8<br>FRONT: 34.0      BACK: 35.6<br>RIGHT: 69.7      LEFT: 0.0<br>RF: 68.0      RB: 71.4      LF: 0.0      LB: 0.0   |  |  |  |
| LEGS: 16.7<br>FRONT: 16.8      BACK: 16.5<br>RIGHT: 20.3      LEFT: 13.1<br>RF: 16.0      RB: 25.4      LF: 17.7      LB: 7.8   |  |  |  | LEGS: 15.8<br>FRONT: 16.1      BACK: 15.5<br>RIGHT: 19.3      LEFT: 12.4<br>RF: 15.3      RB: 23.7      LF: 16.9      LB: 7.4 |  |  |  |
| TORSO: 61.8<br>FRONT: 63.4      BACK: 60.5  |  |  |  | TORSO: 53.1<br>FRONT: 51.9      BACK: 54.2  |  |  |  |

Figure 11b. Output from MANBURN.BAS, body-region analysis.

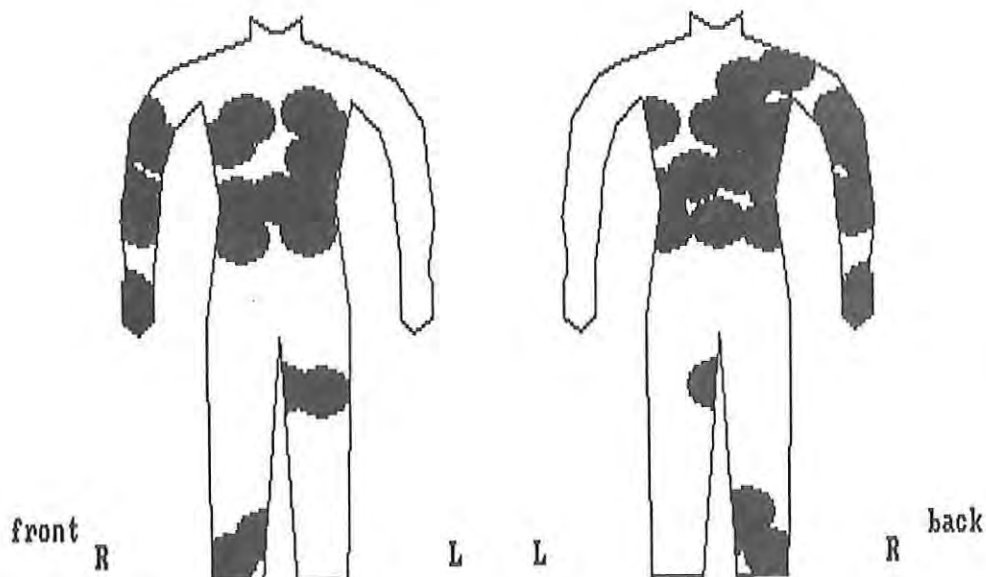


Figure 11c. Output from MANBURN.BAS, graphics.



DeCRISTOFANO, et al.

enhance understanding of the pattern(s) and mechanism(s) of energy transfer through and within materials, a design was needed which used reliable, lightweight, compact, and user-friendly instrumentation. To this end, the Advanced Thermal Response Data Acquisition and Analysis System (ATRES/DAAS) was designed.

### 3.0 DESCRIPTION OF THE ATRES/DAAS

The system consists of the following components: 1) remote data collection units, 2) main data controller unit, 3) data processing and storage unit, and 4) graphical analysis and presentation unit. The relationship between the first three components is illustrated in Figure 12. Each of these units is described in detail below.

#### 1) REMOTE DATA COLLECTION SITES:

A data collection site consists of a manikin, skin sensors, and electronic hardware. There are four manikin data acquisition sites in the ATRES/DAAS. The manikins may be used together or each of the manikins can be fielded separately, providing the ability to tailor the system to the scope of the research investigation.

The manikin shells constructed for previous investigations (ref. 11) have been reused. The manikins are constructed of epoxy-coated fiberglass mat molded into the shape of a size 40-regular male and the manikin surfaces are coated with polytetrafluoroethylene. The sensors used to simulate the response of skin tissue have been improved. The resin formulation developed earlier to mimic the thermal response of skin tissue has been retained as have the dimensions, but the method of temperature measurement has been changed. Each sensor is a 1.09 cm-thick, 2.70 cm-diameter disk fabricated of a mixture of  $\alpha$ -cellulose-filled urea formaldehyde and silica. The type T thermocouples (copper/constantan) used in the original sensors were replaced with thermistors. Use of thermistors allows for measurement of a larger signal (volts instead of microvolts) and better interpolation of the corresponding temperatures because they are more linear over the short range of temperature values involved. The thermistors are however, more expensive and more fragile (the glass beads surrounding the semiconductor are 0.0127 cm in diameter and the leads are 0.002 cm in diameter).

Data from the sensors are fed into a single data acquisition board mounted in the chest cavity of the manikin. The board is custom-designed to accept the feed from 124 analog input channels. The board contains integrated circuits providing multiplexing, amplification, analog-to-digital conversion, DC-to-DC conversion, and monitoring functions as well as buffers and line drivers to pass the data on to the main controller unit.

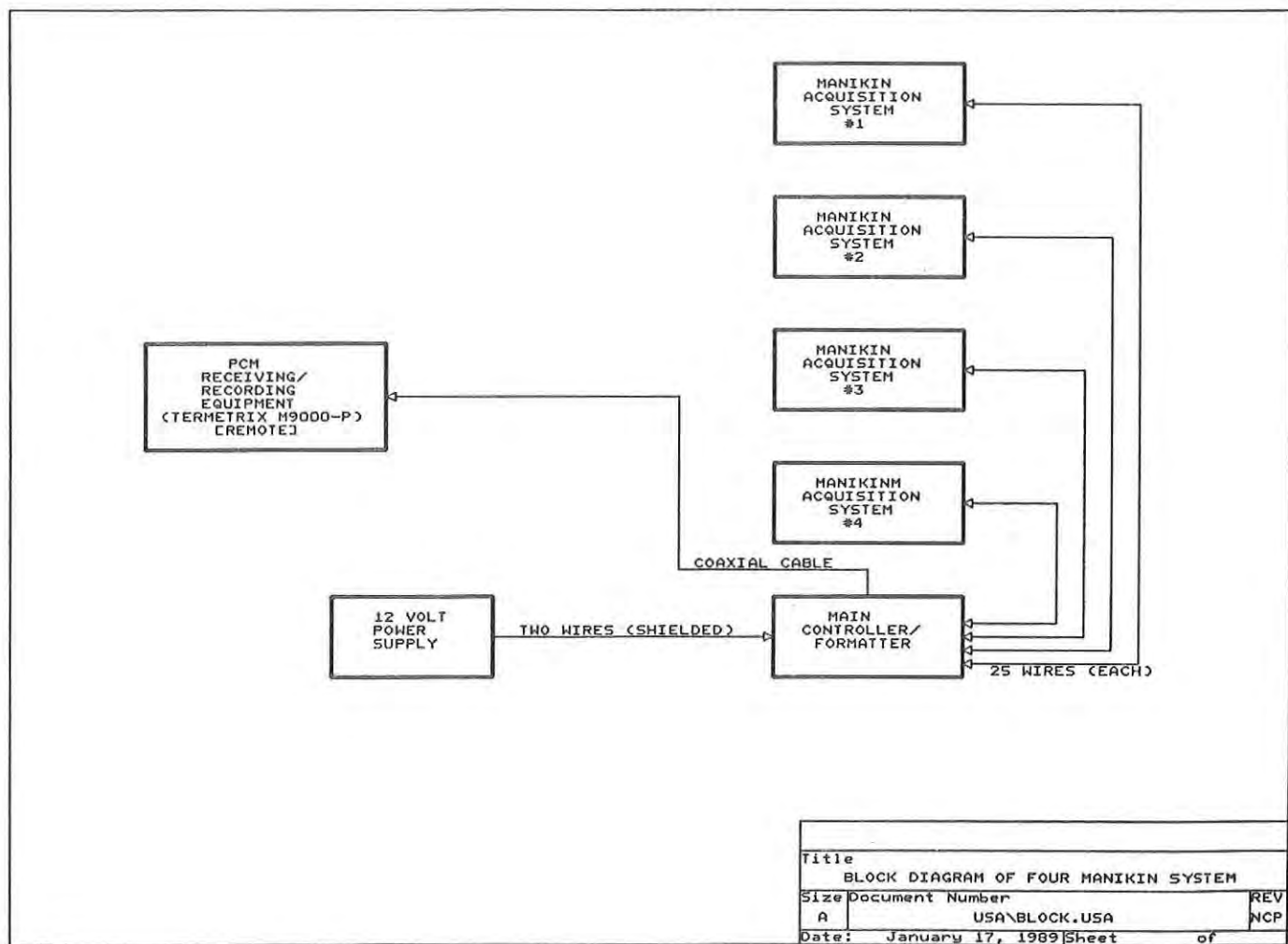


Figure 12. Schematic of the ATRES/DAAS.

2) MAIN FORMATTER AND ACQUISITION CONTROL UNIT:

The main controller receives input from each of the remote data sites ( $4 \times 124 = 496$  data channels). It is a versatile, custom-designed assembly, which selects each site in turn and conditions the signals for storage. Data from each of the 496 sensors are received every 50 ms. This translates to 9,920 pieces of data each second. The controller addresses the sites, performs parallel-to-serial conversion of the digital data, generates code for use by the data processing software, and outputs the signal to the data processor and storage unit. This unit also has the capacity to handle an additional 25 channels of data beyond those from the four manikins. This capability provides the flexibility to field an additional sensor array of any configuration as well as to use the system in a laboratory environment. Located with the main controller is a compact 12-volt DC battery for power distribution to each of the remote sites.

3) DATA PROCESSING AND STORAGE UNIT:

The coded data from the main controller unit is sent via a single coaxial cable or by telemetry using a radio frequency (RF) to an 80386 microcomputer. The direct, coaxial link can be miles long and the RF link can be used to transmit at extreme ranges. Here, using software tailored to the ATRES/DAAS, the data is stored for analysis at any future time, convenient for the researcher. If the experimenter has access to the unit during the test, the data may be displayed in real-time. Upon completion of the thermal exposure, this unit performs the conversion of the raw data from the remote collection sites into burn-severity evaluations. The control of signal timing, a/d-d/a conversions (including thermistor calibration prior to each experiment), real-time system status, and numerical and graphical displays are performed using Micro-TLM (TM) by Terametrix.

4) GRAPHICAL ANALYSIS AND PRESENTATION UNIT:

At the conclusion of an experiment, conversion of the temperature-versus-time data into calculations of omega values is accomplished by a FORTRAN program, MANBURN.F. The output from this program becomes the input to a routine (program BURNMAP) that generates three-dimensional views of the predicted tissue-damage areas of each manikin (Fig. 13). This software was written using SuperSyntax, a graphics manipulation language incorporated into the MEDUSA (TM) computer-aided-design package marketed by PRIME Computers, Inc. MANBURN.F also produces a tabular analysis of the predicted skin tissue damage including area affected as a percentage of total manikin area and by manikin regions, identical to the output of MANBURN.BAS. The output of a two-dimensional projection of predicted damage can still be generated using BURNMAP.BAS.

#### 4.0 APPLICATIONS

The ATRES/DAAS is a complete package which gives researchers the tools required to study accurately and comprehensively the effects of

DeCRISTOFANO, et al.

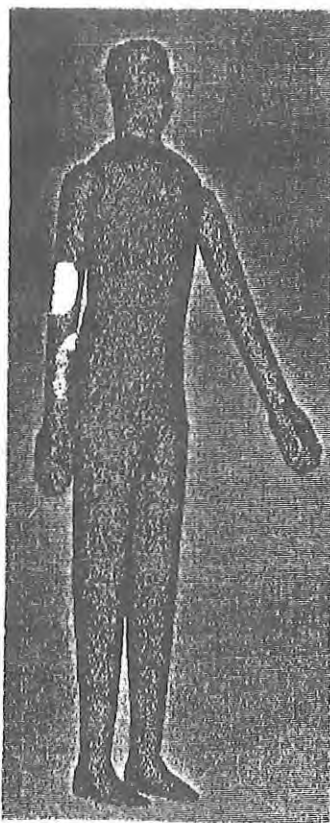


Figure 13a. Graphics output from BURNMAP.

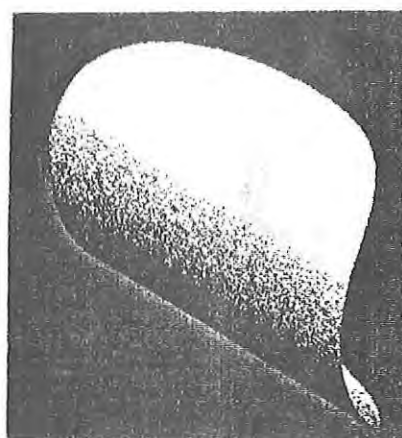


Figure 13b. A representative sensor area from BURNMAP.

DeCRISTOFANO, et al.

thermal radiation on existing and potential uniform materials, whenever and wherever required.

In the field of nuclear-thermal and nuclear-thermal/blast synergy research, the new system takes full advantage of the large test area available with current simulators. We can utilize four instrumented manikins in front of the source rather than just one. This provides a greater degree of control in an experiment because environmental conditions and source characteristics vary slightly from test to test as well as from location to location on the testbed. This added control over experimental conditions increases the confidence-level in the statistical analysis of the data. The capability to target four manikins at once also reduces the cost and time required to perform these experiments.

Investigations of fires in and around combat vehicles can also be conducted with the ATRES/DAAS. Since the data from the manikin sensors can be transferred to the computer by telemetry, the computer may be located safely away from the flame environment. Telemetry also eliminates the need to run a cable out of the test area. Using all four manikins, an entire crew may be realistically placed in a vehicle or a vehicle mock-up at one time.

Data from these investigations will aid in the development of enhanced protective clothing as well as improve our understanding of the underlying energy transport phenomena involved. An increased understanding of the energy transfer mechanisms will allow better mathematical modelling and simulation of material response to thermal insults.

## 5.0 FUTURE WORK

Further refinements of the Advanced Thermal Response Data Acquisition and Analysis System have already been planned. The manikins used in the system have separable hands, feet, arms, legs, and head. These rigid fittings will be replaced with movable joints to allow articulation of the manikins into more realistic postures as required for mounted as well as dismounted combat soldiers. Also, the graphics software will be modified to allow models of clothing and equipment to be superimposed over the burn-prediction profiles in order to facilitate the analysis of the energy transfer to the manikin by relating the damaged areas to specific components of the combat ensemble. The documented computer codes used in the manipulation and presentation of the ATRES/DAAS data will be released in a future publication.



DeCRISTOAFNO, et al.

## 6.0 LIST OF REFERENCES

1. J.D. Loconti, S.L. Knesbach, E.D. Weil, "Temperature Indicator Papers" Quartermaster Research and Development Laboratories, Research Service Test Report No. GC-30, 1 October 1951.
2. R.C. Maggio, "A Molded Skin Simulant Material With Thermal and Optical Constants Approximating Those of Human Skin" Naval Material Laboratory, Final Report NS 081-001, 23 August 1956.
3. N.Y. Chen and W.P. Jensen, "Skin Simulants With Depth Magnification" Fuels Research Laboratory, Massachusetts Institute of Technology, Project DSR 7666, Technical Report No. 5, 15 March 1957.
4. A. Levine, "The Use of QM Paper Thermometers in Radiant Energy Calorimetry" Quartermaster Research and Engineering Command, Report T-20, 21 January 1958.
5. W.L. Derksen, G.P. Delhery, T.I. Monahan, "Thermal and Optical Properties of the NML Skin Simulant" Naval Material Laboratory, Final Report SF-001-05-11, 18 January 1960.
6. Skin Simulants for Studies of Protection Against Intense Thermal Radiation" The Review of Scientific Instruments, Vol. 41, No. 7, pp. 1040-1049, July 1970.
7. F.C. Henriques, "Studies of Thermal Injury. V. The Predictability and the Significance of Thermally Induced Rate Processes Leading to Irreversible Epidermal Injury" Archives of Pathology, Vol. 43, pp. 489-502, 1947.
8. J. Wheatley, "Manikin Data Acquisition and Support System" EG & G Inc., AL-797, 31 May 1972.
9. W. Elkins and J.G. Thompson, "Research on Instrumented Manikins" Air Force Systems Command, ASD-TR-73-33, Vol. 1, July 1973.
10. H.L. Morse and J.R. Swan, "Manikin Code for the Reduction and Analysis of Data from the Thermally Instrumented Manikin" Air Force Systems Command, Aerotherm Report UM-72-32, 15 January 1973.
11. B.S. DeCristofano, G.J. Caldarella, C.J. Fitzgerald, and J.F. Roach, "Effects of Thermal Radiation on Army Clothing: Fabric Damage and Extent of Burn Incidence" NATICK/TR-90/009L, December 1989.



GIBSON

**TITLE:** Heat and Water Vapor Transfer Through Clothing Materials: Three Studies  
Phillip W. Gibson, Mr.

**ABSTRACT:** Military uniform materials vary widely in their heat transfer and water vapor transport characteristics. Several techniques exist to evaluate the water vapor transport characteristics of clothing materials. The most common techniques include guarded hot plate sweating skin simulants and cup-type moisture vapor transmission rate (MVTR) tests. Theoretically, all such tests measure an identical property, water vapor resistance, but the results between different types of tests rarely agree. The reasons for the discrepancies are due to the different conditions present in each test; in some cases the intrinsic properties of the materials are altered by the test conditions. The results of three studies illustrate important factors to be considered when evaluating the thermal and moisture vapor transport properties of textile materials

The first study showed that MVTR and sweating skin simulant water vapor resistances correlate quite well for permeable materials. Semipermeable membranes divide neatly into two types of behavior. Hydrophobic membranes show good correlation between MVTR and sweating skin simulant tests, but hydrophilic membranes show poor agreement between the two types of tests. The scatter is accounted for by noting the different vapor pressure gradients present in the two types of tests. When combined with the different levels of water present in the hydrophilic membranes, these different gradients drastically alter the intrinsic transport characteristics of these hydrophilic membranes. The implications for materials screening testing are discussed.

In the second study a variety of experimental and standard textile materials were evaluated for thermal properties, water vapor resistance, and air permeability. The materials included permeable and impermeable types tested as single layers, laminates, and layered composites. The permeable materials were evaluated under a variety of air flow conditions, including varying the direction of air flow over the sample and the inclusion of an air space between the sample and the sweating skin simulant surface. The effect of these different air flow conditions on the ranking of materials can be significant. Air permeability becomes particularly important in the case of an air space between the fabric and the sweating skin simulant surface.

A third study determined the agreement between several different guarded hot plate sweating skin simulant test methods. The comparison included the Hohenstein Skin Model, which has become the standard apparatus used in Europe. Test results between the different types of equipment compare well as long as the differences in air velocity over the sample are taken into account. In general, air velocities of at least one to two meters/second minimize the contributions of radiant heat transfer and boundary air layer resistances, which tend to obscure intrinsic textile sample properties.

**BIOGRAPHY OF PRESENTER:** Phillip W. Gibson

**PRESENT ASSIGNMENT:** Materials Research Engineer, Materials Research and Engineering Division, Individual Protection Directorate, U.S. Army Natick Research, Development and Engineering Center, Natick, Massachusetts.

**PAST EXPERIENCE:** Senior Rocket Propulsion Engineer, U.S. Air Force Astronautics Laboratory, Edwards AFB, California.

**DEGREES HELD:** M.S. Mechanical Engineering, University of Washington; M.S. Systems Management (R&D), University of Southern California; B.S. Engineering Science and Mechanics, Tennessee Tech.

## Heat and Water Vapor Transfer Through Clothing Materials: Three Studies

Phillip W. Gibson

U.S. Army Natick Research, Development and Engineering Center  
Natick, MA 01760-5019

### Introduction

The water vapor permeability of clothing materials is a critical property for clothing systems that must maintain thermal equilibrium for the wearer. Clothing materials with high water vapor permeability allow the human body to take advantage of its ability to provide cooling due to sweat production and evaporation. High water vapor permeability is also important in cold environments to prevent or minimize water buildup in clothing.

A variety of laboratory methods are available to determine the heat and mass transfer characteristics of clothing materials. These laboratory tests are usually performed using small pieces of fabric ranging in area from 0.4 m<sup>2</sup> to 0.006 m<sup>2</sup>. These small-scale test methods, which use flat samples, are convenient for comparative material property testing, but neglect many factors important to actual clothing systems. Factors such as garment fit and design, influenced by the geometry of the human body, are often more important to the performance of a clothing system than the clothing material properties. The importance of these other factors must be assessed by test methods such as heated mannikins or human chamber trials.

The work presented here summarizes the results of three separate studies concerned with the laboratory measurement of heat and water vapor transfer through clothing materials. Each study concentrated on one particular aspect of problems encountered in measuring relative performance of these materials. The first study involves an experimental correlation between two types of water vapor permeability tests. The second study looks at the influence of air permeability on heat and water vapor transport through woven and nonwoven fabrics. The final study determines the agreement between several different guarded hot plate (sweating skin simulant) test methods, which differ mainly in the air velocity over the test samples. Each study will be presented in a separate section of this paper.

### Study 1. Comparison of Sweating Guarded Hot Plate and Upright Cup Methods of Measuring Water Vapor Permeability

#### Background

The water vapor permeability of clothing materials can be measured in a variety of ways. Two common methods are cup/dish tests and sweating hot plate devices.

In general, the cup/dish methods are easy to perform and use simple and inexpensive equipment. Sweating hot plate methods require much more elaborate equipment and need much larger sample sizes. Sweating guarded hot plate measurements of moisture vapor permeability are often preferred over cup/dish methods since it is thought that the sweating guarded hot plate simulates the heat and mass transfer conditions of the human body fairly accurately.

The objective of the work presented here is to obtain an experimental correlation of these two methods using a wide variety of clothing materials. The materials include a variety of single layer woven and nonwoven fabrics, layered woven and nonwoven fabrics, and semipermeable membrane laminates from different manufacturers.

The basic equation for diffusion of one substance through another is given by Fick's law<sup>1</sup>:

$$\frac{\dot{m}}{A} = \frac{D(\Delta c)}{R}$$

$\dot{m}$  = mass flux  
 $A$  = area  
 $D$  = diffusion coefficient  
 $\Delta c$  = concentration difference  
 $R$  = resistance to diffusion

For most woven or nonwoven permeable clothing materials, the diffusion constant  $D$  in Fick's law is simply that of moisture vapor in air. The pathway of moisture vapor diffusion is through the air spaces in the fabric, and the measured resistance to water vapor transfer  $R$  is independent of the average water vapor concentration in the sample. The water vapor concentration in the sample is proportional to the average of the relative humidities on both sides of the sample. In most cases, the uptake of water by the textile fibers themselves can be ignored<sup>2</sup>. Exceptions to this would be if excessive swelling of fibers and yarns significantly reduces the free air volume within the fabric, or if one is interested in nonequilibrium water vapor transport, where the initial transport behavior is influenced by fiber water vapor absorption and desorption.<sup>3,4</sup>

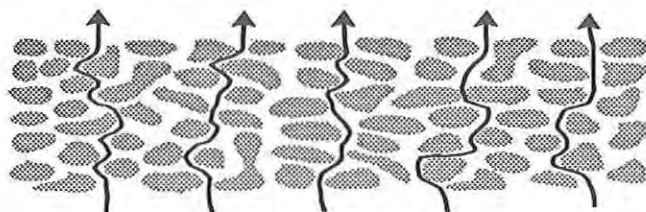


Figure 1. Diffusion Through Most Permeable Materials Is a Result of Mass Transfer Through Air Spaces.

There should be good agreement between the relative rankings of all water vapor permeability test methods for permeable clothing materials. There should also be good correlations between the resistances measured by any water vapor permeability test method for these types of permeable clothing materials.

Many so-called "semipermeable" membrane laminates also depend on moisture vapor diffusion through tiny interconnected pores in a membrane<sup>5-7</sup>. The polymers in these membranes are usually hydrophobic to prevent liquid water from wetting the surface and entering the pores. The measured resistances are again independent of the water vapor concentration in the membrane, and there is good correlation between the measurements done by different methods. Porous membrane laminates and woven and nonwoven permeable fabrics exhibit similar behavior, as shown in Figure 2.

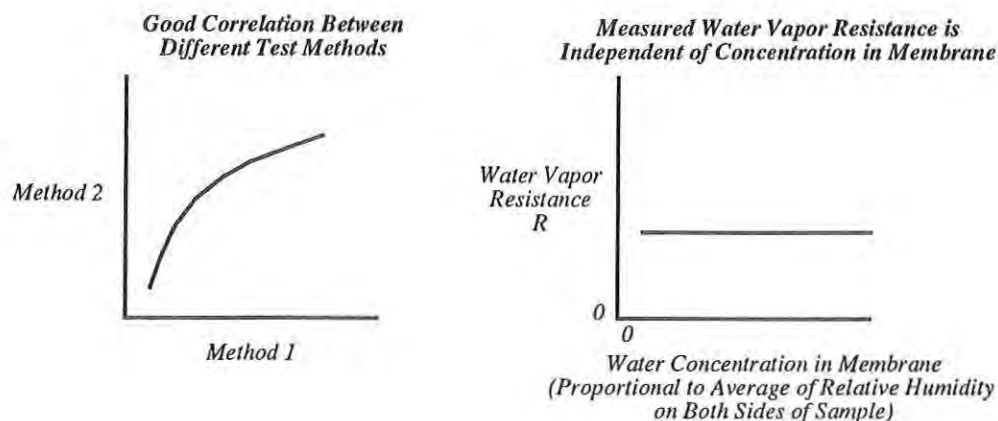


Figure 2. Diffusion Behavior Dominated by Air Spaces in Fabric.

There is a whole class of materials that cannot be assumed to have measured resistances independent of the water vapor concentration. These materials incorporate hydrophilic polymers to continuously coat fabrics or semipermeable membrane laminates<sup>8-11</sup>. The resulting materials include a monolithic layer, yet still have high moisture vapor transport rates.

The concentration dependence of the diffusion constant in high molecular weight polymers can be very pronounced<sup>12</sup>. Fick's law must be modified so that the expression for the diffusion constant becomes a function of the diffusant concentration:

$$D = D_0 \{1 + f(c)\} \quad , \quad \text{where } c \text{ is average concentration of water in the membrane.}$$

In most moisture vapor permeability tests the concentration in the membrane is related to the relative humidity on both sides of the membrane.

Fick's first law thus becomes:

$$\frac{\dot{m}}{A} = \frac{D_0 \{1 + f(c)\} (\Delta c)}{R}$$

Materials which incorporate hydrophilic membranes behave much differently than materials which depend only on transport through fixed air spaces, as shown in Figure 3. There is poor agreement between various test methods which do not produce similar water concentration levels in the material. The measured water vapor resistance of these materials is a function of the average relative humidity in the test.

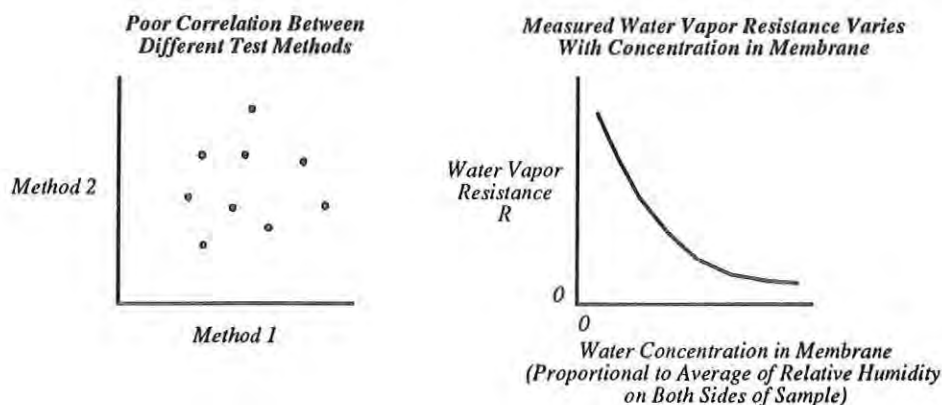


Figure 3. Diffusion Behavior Influenced by Hydrophilic Membranes.

This concentration-dependent diffusion behavior has been noticed in several studies, most notably by Oczevski and Dolhan<sup>13</sup>, and Farnworth, Lotens, and Wittgen<sup>14</sup>. The Farnworth, Lotens, and Wittgen study, in particular, nicely illustrates the differences between hydrophobic microporous films and monolithic hydrophilic films.

Figure 4 is adapted from the Farnworth, Lotens and Wittgen study. It illustrates that indeed there is a marked concentration dependence of the measured value of water vapor resistance for materials which incorporate nonporous hydrophilic polymers.

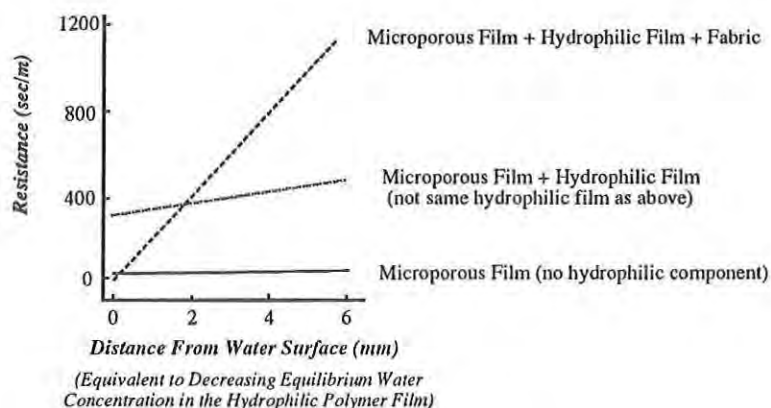


Figure 4. Variation in Water Vapor Resistance as a Function of Distance From Sample to Water Surface.  
(Adapted from Reference 14)

Most textile materials should thus fall into two distinct classes. Materials which depend on diffusion of water vapor through air spaces should show good correlations between all moisture vapor transmission test methods. The measured water vapor resistance values should also be independent of the conditions used in the test. Materials which incorporate nonporous hydrophilic polymer films should show a poor correlation between different water vapor transmission test methods, and the measured water vapor resistance will be dependent upon test conditions such as relative humidity.



## Methods and Materials

Descriptions of the two types of water vapor permeability tests (cup/dish and sweating guarded hot plate) follow. These test methods are in routine use at the U.S. Army Natick Research, Development and Engineering Center (Natick). Descriptions of the various materials used for this study are also included in this section.

### ASTM E96-80, Procedure B, Upright Cup

The American Society for Testing and Materials (ASTM) publishes standard test methods for water vapor transmission properties of materials. The standard condition used most extensively at Natick is Procedure B - Water Method at 23°C (73.4°F) of ASTM E96-80<sup>15</sup>. A schematic of this test method is shown below.

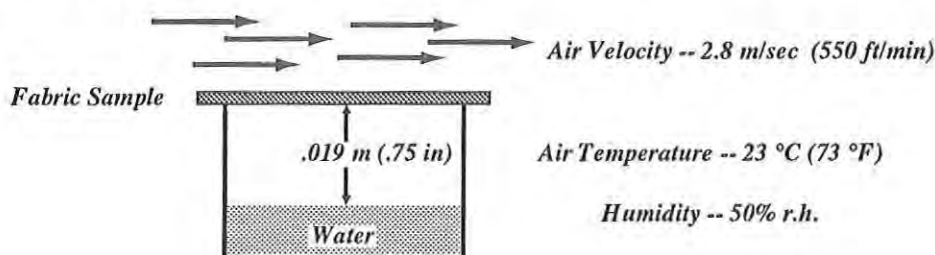


Figure 5. Sample Arrangement for ASTM Method E96-80, Procedure B, Upright Cup Method for Determining Water Vapor Transmission of Materials.

The reported quantity from this test is the Moisture Vapor Transmission Rate (MVTR), in  $\text{g/m}^2/24 \text{ hr}$ , which is determined from periodic weighings of the sample dish. Although the ASTM Method E96-80 calls for reporting units of  $\text{g/m}^2/\text{hr}$ , it is standard practice at Natick to use the longer time period of 24 hours.

This particular ASTM Method E96-80, Procedure B, although widely used, has some inherent problems. Most importantly, the still air layer between the fabric sample and the water surface has a high resistance to moisture vapor transmission. This still air layer often has a higher water vapor resistance than the fabric itself. There are a variety of other methods, well documented in the literature, which are perhaps more appropriate for determining the water vapor resistance of textile materials. These methods may be found in references 16-23. The ASTM Method E96-80 is most suitable for materials which have high water vapor resistances. The ASTM Method E96-80 continues to be used for textiles, however, because of its widespread acceptability, convenience, and large existing database of previous results.

The MVTR values generated with ASTM E96-80 Procedure B include the effect of the resistances of the air layers both above and below the sample. However, these resistances are not subtracted out in the reported data. It is desirable to determine the intrinsic properties of the textile material alone, by accounting for the existence of the air layers in some way. In order to accomplish this, it is possible to convert the MVTR values obtained from the ASTM E96-80 test to water vapor resistance values, which are independent of test conditions for porous materials. Resistance values are convenient since they may be added in series to determine the overall properties of layers of materials.

The next two sections deal with establishing an upper limit for the MVTR values in the ASTM E-96-80 Procedure B test, and with developing a simple way to convert MVTR values to resistance units.



### Limiting Moisture Vapor Transmission Rate Due to Still Air Layer in Cup

The ASTM E96-80 Procedure B test includes a layer of still air under the fabric sample. This still air layer of 1.9 cm (0.75 inch) imposes an upper limit on the measurable moisture vapor transport rate. For fabrics that prevent significant air penetration into the cup, the air layers remain stagnant, and the limiting moisture vapor transmission rate as determined by this still air layer may be calculated.

The air layer between the surface of the water and the fabric is thin enough so that convective mass transfer is suppressed. Convection at this temperature would not occur until the air layer thickness is appreciably greater than 2 centimeters<sup>24</sup>. Mass transfer through this still air layer is assumed to proceed by pure diffusion.

Diffusion through a stagnant air layer is well understood. The isothermal evaporation of water and diffusion through a stagnant air layer can be described by Stefan's law<sup>25</sup>, and is illustrated in Figure 6.

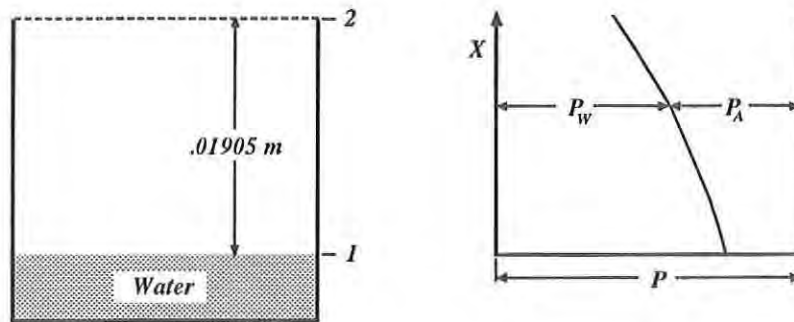


Figure 6. Diffusion of Water Vapor Through a Stagnant Air Layer (adapted from Reference 25).

$$\dot{m}_{total} = - \left( \frac{DM_w A}{R_0 T} \right) \left( \frac{p}{p - p_w} \right) \left( \frac{dp_w}{dx} \right)$$

$\dot{m}_{total}$  = total mass flow of water vapor through air layer of thickness  $dx$

$D$  = diffusion coefficient of water in air (0.256 cm<sup>2</sup>/sec)

$p$  = absolute air pressure (1.01326 × 10<sup>5</sup> N/m<sup>2</sup>)

$M_w$  = molecular weight of water (18 g/mole)

$A$  = area (m<sup>2</sup>)

$R_0$  = universal gas constant (8315 N-m/kg-mole-K)

$T$  = temperature in degrees K

$p_w$  = partial pressure of the water vapor

$p_A$  = partial air pressure

$dx$  = air layer thickness

Stefan's law may be integrated to obtain the total mass flux of water between the water surface and the top of the cup:

$$\dot{m}_{wtotal} = \int_{p_{w1}}^{p_{w2}} - \left( \frac{DM_w A}{R_0 T} \right) \left( \frac{p}{p - p_w} \right) \left( \frac{dp_w}{dx} \right)$$

$$\dot{m}_{wtotal} = \frac{DpM_w A}{R_0 T(x_2 - x_1)} \ln \frac{p - p_{w2}}{p - p_{w1}} = \frac{DpM_w A}{R_0 T(x_2 - x_1)} \ln \frac{p_{A2}}{p_{A1}}$$

$\dot{m}_{wtotal}$  = total water mass flux between water surface and top of cup  
 $x_2 - x_1$  = distance from water surface to top of cup (0.01905 m)  
 $p_{w1}$  = saturated water vapor pressure at water surface ( $0.0028366 \times 10^6$  N/m<sup>2</sup>)  
 $p_{w2}$  = partial water vapor pressure at the top of the cup =  $\phi p_{w1}$ ,  
 where  $\phi$  is relative humidity (0.50), so  $p_{w2} = 0.0014183 \times 10^6$  N/m<sup>2</sup>  
 $p_{A1} = p - p_{w1}$  ( $9.848 \times 10^4$  N/m<sup>2</sup>)  
 $p_{A2} = p - p_{w2}$  ( $9.991 \times 10^4$  N/m<sup>2</sup>)

$$\frac{\dot{m}_{wtotal}}{m^2} = \frac{(0.256 \times 10^{-4} \text{ m}^2 / \text{sec})(1.013 \times 10^5 \text{ N/m}^2)(18 \text{ g/mole})}{(296 \text{ K})(8315 \text{ N} \cdot \text{m} / \text{kg} \cdot \text{mole} \cdot \text{K})(0.01905 \text{ m})} \left[ \ln \frac{9.99 \times 10^4 \text{ N/m}^2}{9.84 \times 10^4 \text{ N/m}^2} \right]$$

$$\frac{\dot{m}_{wtotal}}{m^2} = 1.425 \times 10^{-5} \text{ kg/m}^2 / \text{sec} = 1231 \text{ g/m}^2 / 24 \text{ hr}$$

$$MVTR = 1230 \text{ g/m}^2 / 24 \text{ hr}$$

This is the highest moisture vapor transport rate possible (assuming still air conditions underneath the fabric) in the ASTM E96-80 Procedure B test. As will be shown later, the assumption of still air conditions is a good one for fabrics with low to moderate air permeability values. The still air assumption is not valid for fabrics with very high air permeability since the external air flow begins to penetrate through the fabric into the cup.

#### Conversion of MVTR Values to Resistance Units

The moisture vapor transmission rate measured in the ASTM E96-80 Procedure B Method is a result of the sum of three resistances, as shown in Figure 7.

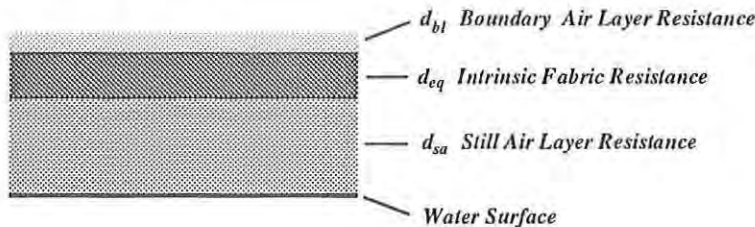


Figure 7. Three Resistances to Moisture Vapor Transfer in ASTM E96-80 Procedure B.

One can define the intrinsic resistance of the material in terms of the equivalent thickness of still air. This works well as long as the transport properties are dependent on diffusion of water vapor through air spaces in the material.

Fick's law may be written as:

$$d_{total} = \left( \frac{1}{\dot{m}} \right) D (\Delta c) A$$

$d_{total}$  = total resistance of the system ( $d_{sa} + d_{eq} + d_{bl}$ ) in cm of still air

$\dot{m}$  = mass flux of water vapor, g / sec

$D$  = diffusion coefficient of water vapor in air,  $\text{cm}^2 / \text{sec}$

$\Delta c$  = concentration difference,  $\text{g} / \text{cm}^3$

$A$  = Area,  $\text{cm}^2$

As noted by Fourt and Harris<sup>17</sup>, the concentration difference  $\Delta c$  can be obtained from the relation:

$$\Delta c = \Delta p M_w / RT = (2.89 \times 10^{-4}) (\Delta p / T)$$

$\Delta c$  = concentration difference ( $\text{g}/\text{cm}^3$ )

$\Delta p$  = vapor pressure difference (mmHg)

$M_w$  = molecular weight of water (18 g/mole)

$R$  = gas constant

$T$  = absolute temperature (K)

The equation for the intrinsic fabric resistance becomes for ASTM E96-80, Procedure B:

$$d_{eq} = \left( \frac{1}{\dot{m}} \right) D (2.89 \times 10^{-4}) \left( \frac{\Delta p}{T} \right) A - d_{sa} - d_{bl}$$

The resistance of the still air layer underneath the fabric is found simply from its thickness in cm, so for the ASTM E96-80, Procedure B:

$$d_{sa} = 1.905 \text{ cm.}$$

Finding the resistance of the outer air layer presents a more difficult problem. Turl<sup>16</sup> determined the equivalent resistance as a function of air flow velocity, but the boundary layer thickness  $d_{bl}$  is greatly affected by the flow conditions, which are not the same as in Turl's study. Because the ASTM E96-80 Procedure B method uses an air flow of 2.8 m/sec (550 ft/min), the equivalent thickness of the outer boundary air layer should be quite small (less than 0.3 cm). It will not be accounted for explicitly, but is included in the value for  $d_{eq}$ . This outer boundary air layer resistance, which is highly sensitive to air velocity and direction, is an obvious source of data scatter.

For the ASTM E96-80 Procedure B test, the appropriate values for the variables in the equation for intrinsic fabric resistance are:

$$\begin{aligned} D &= 0.256 \text{ cm}^2/\text{sec} \\ \Delta p &= 10.65 \text{ mmHg} \\ T &= 296 \text{ K} \\ d_{sa} &= 1.905 \text{ cm} \end{aligned}$$

The equation for the equivalent air resistance of the fabric alone can be expressed in terms of the measured MVTR and the air layer resistances as:

$$d_{eq} = \left( \frac{2300}{MVTR} \right) - d_{sa} \quad \text{or equivalently,} \quad d_{eq} = \left( \frac{2300}{MVTR} \right) - 1.9$$

$d_{eq}$  = intrinsic fabric moisture vapor resistance, expressed in cm of still air (includes boundary layer,  $d_{bl}$ )  
 MVTR = moisture vapor transmission rate, g/m<sup>2</sup>/24 hr, ASTM E96-80, Procedure B

The intrinsic fabric resistance  $R_f$  may also be expressed in resistance units of sec/cm through the relation:

$$R_f = \frac{d_{eq}}{D}$$

#### Sweating Guarded Hot Plate Method

The general principles of a guarded hot plate apparatus may be found in Reference 26. The guarded hot plate measures the power required to maintain a flat isothermal area at a constant temperature. When the plate is covered with a test material, the amount of power required to maintain the plate at a given temperature can be related back to the dry thermal resistance of the test material. If the plate is saturated with water, then the amount of power required to maintain the plate at a given temperature is related to the rate at which water evaporates from the surface of the plate and diffuses through the material.

Since this method must account for both heat and mass transfer effects, it is necessary to determine the dry thermal resistance of the material first. Then the plate is saturated with water and the material is tested again to determine its moisture vapor transmission properties. Figure 8 shows a schematic of the sweating guarded hot plate apparatus.

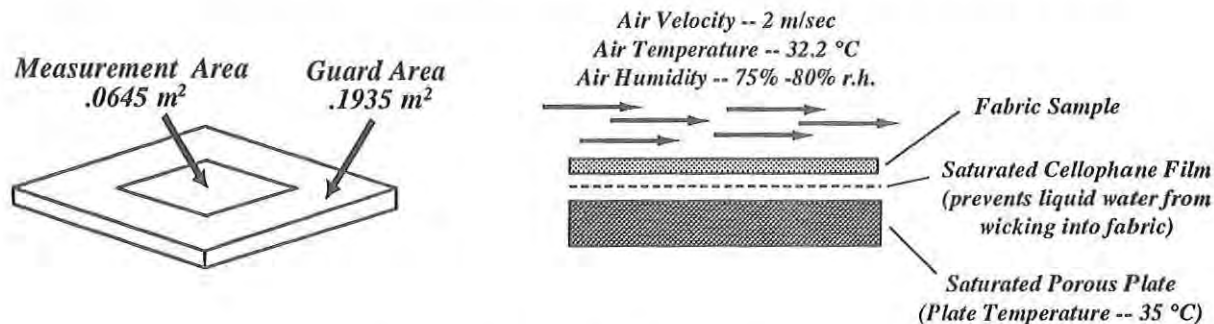


Figure 8. Sweating Guarded Hot Plate.

A general description of each of the two types of tests follows.

### Dry Thermal Resistance

Dry thermal resistance is calculated by measuring the temperature difference between the surface of the heated measurement area of the guarded hot plate and the temperature of the ambient air away from the plate. It is this temperature difference which drives heat transfer through the fabric. The equation used for calculating the thermal resistance is:

$$R_{total} = \frac{A(T_{plate} - T_{air})}{Q}$$

- $R_{total}$  = Thermal resistivity of material plus the boundary air layer
- $A$  = Surface area of guarded plate measurement area
- $T_{plate}$  = Temperature of the plate surface
- $T_{air}$  = Temperature of the ambient air
- $Q$  = Power required to maintain a constant plate surface temperature

The units used in this paper are :

- $R_{total}$  given in clo (clo is a unit of thermal resistance and is equal to 0.155 °C-m<sup>2</sup>/watt)
- $A$  given in m<sup>2</sup>
- $T_{plate}$  and  $T_{air}$  given in °C
- $Q$  given in watts

The total thermal resistance  $R_{total}$  includes the apparent thermal resistance of the boundary air layer above the fabric material surface. The thermal resistance of this boundary air layer can be measured by performing a test on the bare plate without a fabric sample. The value of  $R$  thus obtained for the bare plate is designated  $R_0$ .

$R_0$  decreases as the air speed sweeping over the surface of the guarded hot plate increases. Increased air movement reduces the thickness of the boundary air layer over the plate and enhances heat transfer. It is assumed that the boundary air layer over the bare plate is identical to the boundary air layer over the fabric. This assumption may introduce errors if the surface characteristics of the fabric are extremely different from those of the bare plate. The intrinsic thermal resistance  $R_i$  of the fabric may be obtained by subtracting out the thermal resistance of the overlying boundary air layer:

$$R_i = R_{total} - R_0$$

$R_{total}$  is very sensitive to the effect of air speed, while  $R_i$  should be much less sensitive and is more of an intrinsic material property.  $R_i$  may also be affected by wind penetration into or through the fabric, particularly for materials with high air permeability. This effect can become very important if the wind direction is perpendicular to the plate, or if there is an air space between the fabric and the plate.

### Water Vapor Permeability

Water vapor permeability of materials can be measured with a guarded hot plate by saturating the plate surface with water. The power required to maintain the surface at a given temperature is related to the rate at which water evaporates from the surface of the plate and diffuses through the material. The thermal resistance of the material to convective heat transfer must be known before it is possible to extract the vapor permeability coefficient. Woodcock<sup>27</sup> developed a moisture vapor permeability index, known as  $i_m$ , which serves as a very convenient relative measure of the moisture vapor permeability of materials.

$$i_m = \frac{\left\{ \frac{(Q)(R_{total})}{A} \right\} - (T_{plate} - T_{air})}{S(p_s - \phi p_a)}$$

- $i_m$  = Moisture vapor permeability index
- $R_{total}$  = Thermal resistivity of the fabric plus the boundary air layer
- $A$  = Surface area of guarded plate measurement area
- $T_{plate}$  = Temperature of the saturated plate surface
- $T_{air}$  = Temperature of the ambient air
- $Q$  = Power required to maintain a constant saturated plate surface temperature
- $S$  = Lewis relation between evaporative mass transfer coefficient and convective heat transfer coefficient
- $p_s$  = Saturated water vapor pressure at the plate surface
- $p_a$  = Saturated water vapor pressure of the ambient air
- $\phi$  = Relative humidity of ambient air

The units used in this paper are :

- $R_{total}$  given in clo
- $A$  given in m<sup>2</sup>
- $T_{plate}$  and  $T_{air}$  given in °C
- $Q$  given in watts
- $S$  given as 2.2 °C/mmHg
- $p_a$  and  $p_s$  given in mmHg
- $\phi$  given in fractional relative humidity (not %)

The  $i_m$  value is a relative measure of the permeability of the material to the passage of water vapor. The  $i_m$  index should vary between 0 (for completely impermeable materials), and 1 (for completely permeable materials). In practice, the value of 1 as an upper limit is not approached until the wind speed over the plate becomes great enough to minimize the contribution of radiative heat transfer.

The moisture vapor permeability index,  $i_m$ , may be combined with the total dry thermal resistance,  $R_{total}$ , to yield a quantity which takes into account both convective and evaporative heat transfer. In this study  $R_{total}$  is given in clo units, so the term becomes  $i_m/clo$ . The term  $i_m/clo$  provides a good ranking measure between materials if one is interested in materials which minimize the potential for heat stress.



The importance of the term  $i_m/clo$  is illustrated if the equations for dry heat transfer ( $E_{dry}$ ), and evaporative heat transfer ( $E_{evap}$ ), are written:

$$E_{dry} \text{ (watts / m}^2\text{)} = \left( \frac{6.45}{clo} \right) (\Delta T)$$

$$E_{evaporative} \text{ (watts / m}^2\text{)} = 14.2 \left( \frac{i_m}{clo} \right) (\Delta p)$$

$$\text{Total Heat Transfer (watts / m}^2\text{)} = \left( \frac{6.45}{clo} \right) (\Delta T) + 14.2 \left( \frac{i_m}{clo} \right) (\Delta p)$$

$\Delta T$  = temperature difference, °C

$\Delta p$  = vapor pressure difference, mmHg

$clo = R_{total}$  in clo units

The higher the value for  $i_m/clo$ , the easier it is for heat to be dissipated through the materials via both evaporative cooling and convective heat transfer. However, when the ambient humidity is high and wind speed is low, evaporative cooling becomes less important, and the dry thermal resistance (clo) is the most important property.

Note that these values include the effects of the boundary air layer over the sample. It is desirable to obtain intrinsic properties of the materials, such as intrinsic thermal resistance and intrinsic water vapor resistance. Such a system of intrinsic units is available in the draft standard German Deutsches Institut für Normung (DIN) Standard 54-101<sup>28</sup>, and is also described in a NATO publication<sup>29</sup>.

The intrinsic unit  $R_{et}$  for fabric water vapor resistance can be found from the values of  $R_{total}$  (clo) and  $i_m$  as shown below:

$$R_{et} = .0928 \left\{ \frac{1}{(i_m / clo)} - \frac{1}{(i_{m0} / R_0)} \right\}$$

$R_{et}$  = intrinsic water vapor resistance, watt-m<sup>2</sup>/mbar

$i_{m0}$  = bare plate  $i_m$  value

$R_0$  = bare plate thermal resistance, clo units

This intrinsic resistance,  $R_{et}$ , is analogous to the intrinsic resistance obtained in the previous section on the ASTM E96-80, Procedure B, Upright Cup Method.

A moisture vapor transmission rate may also be defined for the sweating guarded hot plate<sup>30</sup>.

$$WVT = \frac{1}{(R_{et} + R_{et0})(\Delta H_{vap})}$$

- $R_{et}$  = intrinsic water vapor resistance, watt-m<sup>2</sup>/mbar  
 $R_{et0}$  = water vapor resistance of boundary layer on bare plate, watt-m<sup>2</sup>/mbar  
 $\Delta H_{vap}$  = latent heat of vaporization at sweating guarded plate temperature (35°C)  
 = .672 watt-hr/g  
 $WVT$  = water vapor transmission, g/m<sup>2</sup>-hr-mbar

For a water vapor pressure difference  $\Delta p$  between the plate surface and the ambient atmosphere, the MVTR as measured with the plate is given by:

$$MVTR_{plate} = (WVT)(24 \text{ hr})(\Delta p), \text{ in units of g/m}^2/24 \text{ hr}$$

The test conditions used in this study resulted in a  $\Delta p$  of 17.7 mbar:

$$MVTR_{plate} = 424.8(WVT)$$

In terms of  $i_m/clo$ , the moisture vapor transmission rate may be written as:

$$MVTR_{plate} = 6806 \left( \frac{i_m}{clo} \right), \text{ in units of g/m}^2/24 \text{ hr}$$

## Materials

The materials chosen for this study can be divided into four classes: 1) Permeable, 2) Hydrophilic membrane laminates, 3) Hydrophobic membrane laminates, and 4) Impermeable. Many of these materials are under development for military applications and are not commercially available. Applicable military specification identifications for several standard fabrics are included in the references. Further information on many of the semipermeable membranes, such as manufacturer and physical property data, may be found in reference 7.

### Permeable Materials

The permeable materials include both woven and nonwoven materials. Some of the materials are multilayer laminates either adhesively bonded or laid over the top of each other.

Table 1. Permeable Materials

| Sample # | Configuration    | Materials   |
|----------|------------------|---|
| 1        | Single Layer     | Water-Repellent Treated Nylon/Cotton Woven Fabric <sup>31</sup>       |
| 2        | Single Layer     | Water-Repellent Treated Nylon/Cotton Twill Woven Fabric <sup>32</sup> |
| 3        | Single Layer     | Nonwoven Fabric Coated with Activated Carbon, Scrim Backing           |
| 4        | 2 Layer Laminate | Carbon-Loaded Polyurethane Foam Laminate (90 mil thick) <sup>33</sup> |
| 5        | 2 Layer Laminate | Carbon-Loaded Polyurethane Foam Laminate (50 mil thick)               |
| 6        | 3 Layer Laminate | Kevlar® Shell, Activated Carbon Cloth, Nomex® Liner Fabric            |
| 7        | 2 Layers         | Sample #1 and Sample #5 Combined                                      |
| 8        | 2 Layers         | Sample #2 and Sample #5 Combined                                      |
| 9        | 2 Layers         | Sample #1 and Sample #4 Combined                                      |
| 10       | 2 Layers         | Sample #2 and Sample #4 Combined                                      |

**Hydrophobic Membrane Laminates**

These materials, often termed "semipermeable" membranes, are made of a hydrophobic polymer containing tiny interconnected pores which allow water vapor to diffuse through the membrane. Most of these membranes have been laminated to a shell fabric, and are often also laminated to an inner liner fabric.

**Table 2. Hydrophobic Membrane Laminates**

| <b>Sample #</b> | <b>Configuration</b> | <b>Materials</b>  |
|-----------------|----------------------|---|
| 11              | 2 Layer Laminate     | Nylon/Cotton Shell<br><b>Plastolon® Membrane</b> (polytetrafluoroethylene--PTFE)                          |
| 12              | 2 Layer Laminate     | Nylon Taffeta Shell<br><b>Tetratex® Membrane</b> (PTFE)   |
| 13              | 2 Layer Laminate     | Nomex® Shell<br><b>Empore® Membrane</b> (carbon-loaded PTFE)  |
| 14              | 3 Layer Laminate     | Nylon Taslan® Shell<br><b>Plastolon® Membrane</b> (PTFE)<br>Nylon Tricot Knit Liner                       |
| 15              | 3 Layer Laminate     | Nylon Taslan® Liner<br><b>Celgard® 2500 Membrane</b> (isotactic polypropylene)<br>Nylon Tricot Knit Liner |
| 16              | 3 Layer Laminate     | Nylon Taslan® Shell<br><b>Repel® Membrane</b> (acrylic fluoropolymer)<br>Nylon Tricot Knit Liner          |
| 17              | 3 Layer Laminate     | Nomex® Shell<br><b>Repel® Membrane</b> (acrylic fluoropolymer)<br>Nylon Tricot Knit Liner                 |
| 18              | 3 Layer Laminate     | Nylon/Cotton Shell<br><b>Repel® Membrane</b> (acrylic fluoropolymer)<br>Nylon Tricot Knit Liner           |
| 19              | 3 Layer Laminate     | Nylon Taslan® Shell<br><b>Empore® Membrane</b> (carbon-loaded PTFE)<br>Nylon Tricot Knit Liner            |

**Hydrophilic Membrane Laminates**

These membranes contain a monolithic hydrophilic polymer coating or layer. They may also contain a porous hydrophobic membrane as a support for the hydrophilic layer.

**Table 3. Hydrophilic Membrane Laminates**

| <b>Sample #</b> | <b>Configuration</b> | <b>Materials</b>   |
|-----------------|----------------------|--|
| 20              | 2 Layer Laminate     | Nomex® Shell<br><b>Hyperm® Membrane</b> (coextruded polyether/polyester)   |
| 21              | 3 Layer Laminate     | Taslan® Nylon Shell<br><b>Thintech® Membrane</b> (polyethylene/polyurethane)<br>Nylon Tricot Knit Liner                  |
| 22              | 3 Layer Laminate     | Nomex® Shell<br><b>Sympatex® Membrane</b> (co-polyether-polyester)<br>Nomex® Jersey Knit Liner                           |
| 23              | 3 Layer Laminate     | Taslan® Nylon Shell<br><b>Sympatex® Membrane</b> (co-polyether-polyester)<br>Nylon Tricot Knit Liner                     |
| 24              | 3 Layer Laminate     | Nomex® Shell<br><b>Gore-Tex® II Membrane</b><br>(PTFE/polyurethane/polyalkylene oxide)<br>Nomex® Jersey Knit             |
| 25              | 3 Layer Laminate     | Nomex® III Shell<br><b>Gore-Tex® II Membrane</b><br>(PTFE/polyurethane/polyalkylene oxide)<br>Nomex® Jersey Knit         |
| 26              | 3 Layer Laminate     | Taslan® Nylon Shell<br><b>Gore-Tex® II Membrane</b><br>(PTFE/polyurethane/polyalkylene oxide)<br>Nylon Tricot Knit Liner |
| 27              | 3 Layer Laminate     | Taslan® Nylon Shell<br><b>Gore-Tex® II Membrane</b><br>(PTFE/polyurethane/polyalkylene oxide)<br>Nylon Tricot Knit Liner |

**Impermeable Material**

One impermeable material is included to illustrate the full range of material behavior.

**Table 4. Impermeable Material**

| <b>Sample #</b> | <b>Configuration</b> | <b>Materials</b>                       |
|-----------------|----------------------|--|
| 28              | Single Layer         | Butyl-Coated Nylon Cloth <sup>34</sup> |

### Correlation of Upright Cup and Sweating Guarded Hot Plate

A general correlation between the upright cup and the guarded sweating hot plate is shown in Figure 9. The two measurements shown are the Moisture Vapor Transmission Rate (for the upright cup method) and the  $i_m/clo$  values (for the sweating guarded hot plate). The additional upper horizontal axis shows the corresponding moisture vapor transmission rate calculated for the guarded sweating hot plate.

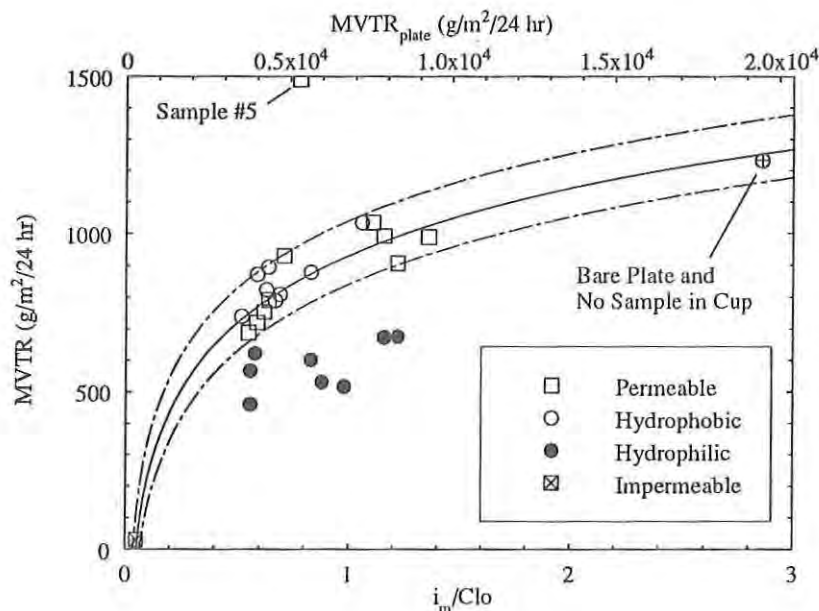


Figure 9. Experimental Correlation Between ASTM Method E96-80, Procedure B, and Guarded Sweating Hot Plate.

It is clear that there is a fairly good correlation between the two test methods for materials whose properties depend on water vapor diffusion through air passages in the structure. Nearly all the permeable and hydrophobic membrane laminates lie within the 95% confidence limits shown in Figure 9. The lone exception is Sample #5, which has an anomalously high  $MVTR$  value. It will be shown later that the very high air permeability of this particular material allows the 550 ft/min air flow over the cup to begin penetrating through the fabric into the cup, disturbing the still air diffusion conditions, and enhancing the moisture vapor transfer rate.

Figure 9 also shows that all the hydrophilic membrane laminates show no correlation between the two test methods. The hydrophilic materials exhibit much better water vapor transmission properties in the sweating guarded hot plate test than they do in the upright cup test. As discussed in the Background section of this paper, the test conditions in the guarded sweating hot plate test result in a much higher equilibrium water content in the hydrophilic polymer layer, which changes the polymer's permeability, greatly increasing the water vapor transport rate through the membrane.

The quantities shown in Figure 9 are both essentially measurements of the mass flux of water vapor which passes through the material. Both the  $MVTR$  values and the  $i_m/clo$  values include the various air layer resistances present in the two tests.

The Methods section derived relations which allow the intrinsic water vapor resistance to be calculated from  $MVTR$  and  $i_m/clo$  measurements. Intrinsic fabric water vapor resistances are convenient since they may be added in series to determine the overall resistance of combined layers of fabrics, using only the measured resistances of the individual layers. The intrinsic water vapor resistance of a material is also closer to being a fundamental material property than quantities such as  $MVTR$  or  $i_m/clo$ , which are both highly dependent on the test conditions.

There should also be a direct linear correlation between the intrinsic fabric resistances as measured by the two methods, except for materials with concentration-dependent diffusion constants. Intrinsic fabric water vapor resistances calculated from the results of the two test methods are shown in Figure 10.

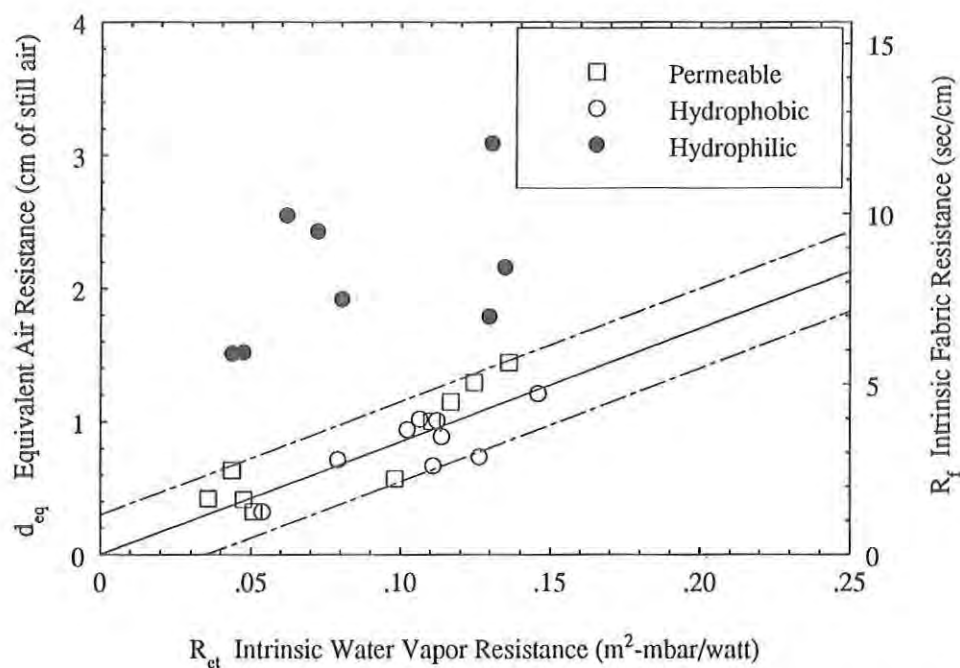


Figure 10. Correlation of Intrinsic Water Vapor Resistance Values for ASTM Method E96-80, Procedure B, and Guarded Sweating Hot Plate.

The measured intrinsic water vapor resistances correlate in a linear fashion for the permeable and hydrophobic membrane laminates. Again, the hydrophilic membrane laminates show a much lower resistance to water vapor transport in the guarded sweating hot plate apparatus, due to the much greater water concentration in the hydrophilic polymer layer.

Figures 9 and 10 indicate that the ASTM E96-80, Procedure B upright cup method is adequate for screening most materials dependent upon water vapor diffusing through the air spaces in their structure. However, the upright cup method gives anomalous results for materials which incorporate monolithic hydrophilic polymer layers, and for materials with high air permeability. Both cases are discussed in the next two sections.



### Effect of High Air Permeability on ASTM E96-80, Procedure B Measurements

Materials with high air permeability may allow the external air flow to penetrate through the sample and disturb the still air layer between the water surface and the sample. Whether penetration occurs is not just a function of air permeability, but also depends on factors such as average diameter of the pores, the material's thickness, and the tortuosity of the passages through the material. Some of these effects are shown schematically in Figure 11.

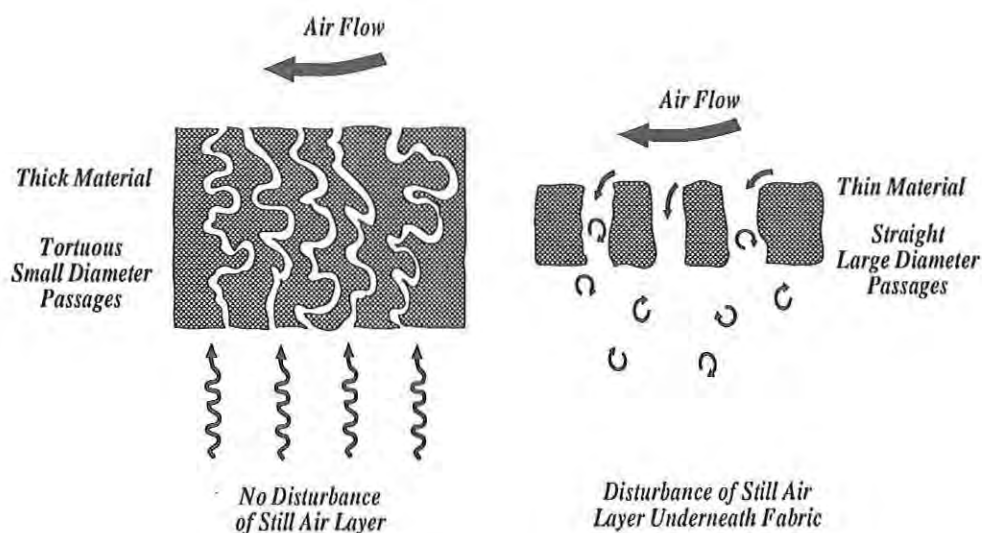


Figure 11. Factors Influencing Anomalous MVTR Values for Two Materials with Identical Air Permeability.

The disturbance of the still air layer means that the nature of the test has changed. Since the upper limit of *MVTR* allowed by the still air layer is approximately  $1200 \text{ g/m}^2/24 \text{ hr}$  in the ASTM E96-80, Procedure B test, it's clear that the resistance of the air layer within the cup is changing in some undefined way. In fact, if one calculates the intrinsic fabric resistance ( $d_{eq}$  or  $R_f$ ) of sample #5, it turns out to be a negative number, which is clearly unreasonable.

Sample #5, which exhibited this type of behavior, was also tested in combination with two different cover fabrics (samples #7 and #8). The cover fabrics eliminated the air penetration into the still air layer, and the results for samples #7 and #8 fall onto the expected curves in Figures 9 and 10. If Sample #5 really did have some fundamentally different water vapor transport mechanism, it would also be evident in the results for samples #7 and #8.

Materials with ASTM E96-80, Procedure B, *MVTR* values greater than  $1200 \text{ g/m}^2/24 \text{ hr}$  should be regarded with skepticism. Such high values indicate air flow penetration into the still air layer under the fabric, making it difficult to compare results between different materials, since intrinsic fabric properties are no longer being measured.

### ASTM E96-80, Procedure BW, Inverted Water Method

The deficiencies of the upright cup method for hydrophilic membranes have been recognized for some time. An alternate procedure BW in ASTM E96-80 inverts the cup so that the water is in direct contact with the sample. A schematic of Procedure BW is given in Figure 12.

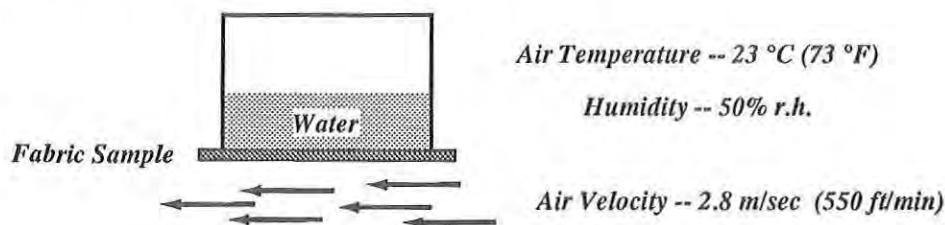


Figure 12. ASTM E96-80, Procedure BW, Inverted Water Method.

Procedure BW results in a much higher equilibrium water content in the hydrophilic polymer layer. The diffusion constant changes, dramatically lowering the measured water vapor resistance. In addition, the still air layer resistance underneath the fabric is eliminated.

The intrinsic fabric water vapor resistance  $d_{eq}$  can be calculated for both Procedure B and BW and plotted as a function of distance from the water surface.

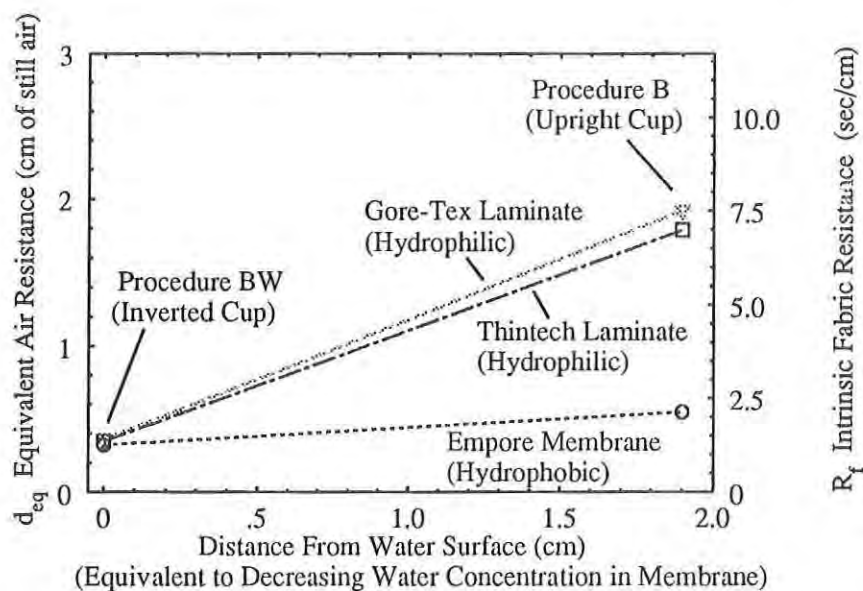


Figure 13. Water Vapor Resistances Derived from ASTM E96-80, Procedures B and BW Moisture Vapor Transmission Rates.

This figure is essentially identical to Figure 4, which shows results from the Farnworth, Lotens, and Wittgen study<sup>14</sup>. The hydrophobic membrane's properties change very little between Procedure B and BW. The resistance values of the two hydrophilic membrane laminates, which are approximately the same as the hydrophobic membrane in Procedure BW, become four times larger when measured under the conditions present in Procedure B. Note that neither Procedure B or BW is representative of actual use conditions. Procedure B tests hydrophilic membranes in fairly dry conditions, which makes them look disproportionately poor compared to other materials. Procedure BW tests the membrane in contact with liquid water and under a pressure head due to the weight of water in the cup. Procedure BW tends to make the hydrophilic membranes look a little better than they really are, since actual use conditions do not allow liquid water under pressure to come in contact with the inner surface of clothing.

### **Evaluation and Ranking Techniques for Hydrophilic Membrane Laminates**

Minimum moisture vapor transmission rates (ASTM E96-80, Procedures B and BW) are incorporated into the military specifications for components of several U.S. Army uniforms and equipment systems<sup>35-39</sup> which include semipermeable membranes. These measurements are used for quality control purposes. The two measurements give a good indication if a particular lot of material will provide equivalent water vapor permeability as compared to another lot of material.

For many materials, ASTM E96-80, Procedure B and BW, will also be sufficient to rank the water vapor permeability of new candidate materials with respect to standard materials used in present uniform and equipment items. Procedures B and BW represent the two environmental extremes for semipermeable membrane laminates, particularly for monolithic hydrophilic membranes. Procedure BW, the inverted cup method, represents the condition of having a high average water concentration in the membrane. Procedure B, the upright cup method, represents the condition of a low average water concentration in the membrane.

As long as one semipermeable membrane laminate exhibits a higher MVTR in both the inverted and upright cup tests, it is safe to say that the material will have a higher moisture vapor permeability over the range of actual use conditions present in a clothing system.

Unfortunately, when materials are compared to each other using both Procedure B and BW, the ranking of materials can flip-flop. That is, a material with the higher MVTR in the inverted cup can have the lowest MVTR in the upright cup test. One must then decide which test is more representative of actual field use conditions, or whether another test condition would be more representative of actual field use conditions.

Figure 14 illustrates how the degree of concentration dependence of the water vapor resistance of a semipermeable membrane can complicate the evaluation or ranking of one material compared to another. Figure 14 shows the intrinsic water vapor resistance as a function of distance from the water surface for three different semipermeable membranes.

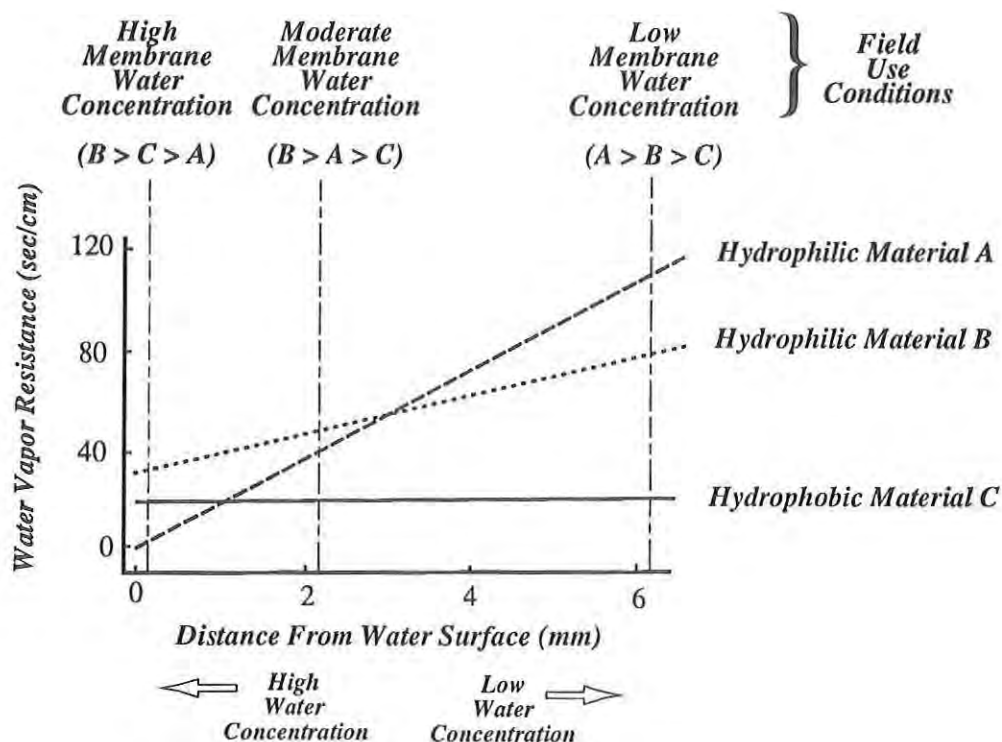


Figure 14. Variation of Water Vapor Resistance with Average Water Concentration in Membrane.

It's clear that the choice of test conditions can greatly influence the rankings of candidate materials. At the extreme of high membrane water concentration, hydrophilic membrane A has the lowest water vapor resistance and would appear to have the best water vapor transport properties. At the other extreme of low membrane water concentration, hydrophobic membrane C appears to be much better than the other materials, and hydrophilic membrane A is clearly the worst performing material. At moderate membrane water concentration levels, which are more representative of conditions which might be found in a clothing system, one could pick test conditions such that either membrane A or C is rated superior, and the relative ranking of membranes A and B can reverse depending on which test conditions are used.

In the case illustrated by Figure 14, it would be prudent to evaluate and rank the water vapor permeability of candidate membrane laminates on a device such as a guarded sweating hot plate, which more accurately simulates the heat and mass transfer conditions present for the skin/clothing system. The use of ASTM E96-80, Procedures B and BW, to evaluate and rank semipermeable membrane laminates against each other would be justified only if one material consistently exhibits higher water vapor permeability in both Procedure B and Procedure BW.

### Comments on Multilayer Clothing Systems Incorporating Hydrophilic Membranes

The water vapor transport behavior of hydrophilic membrane laminates is highly dependent on the water concentration in the membrane. This means the effectiveness of the membrane is influenced by both the microclimate underneath clothing and the environment outside the clothing system. The extremes in microclimate underneath the clothing are: 1) a low human work rate where little sweat is being produced and the humidity is about the same as the outside environment, and 2) a high human work rate, where a large amount of sweat is being produced and the water vapor pressure underneath the clothing approaches saturation vapor pressure. The extremes of the outside environment are simply low or high ambient humidity. The temperature differences between the skin and the outside air, and condensation/accumulation of sweat in clothing layers are complicating factors that will not be addressed here.

The intrinsic water vapor resistance of permeable materials and hydrophobic membrane laminates would not be affected much by the ambient humidity or human sweating rate. In contrast, the intrinsic water vapor resistance of monolithic hydrophilic membrane laminates would be affected by both ambient humidity and the human sweating rate, i.e. the average water concentration in the hydrophilic membrane. This difference between the two classes of materials is illustrated schematically in Figure 15.

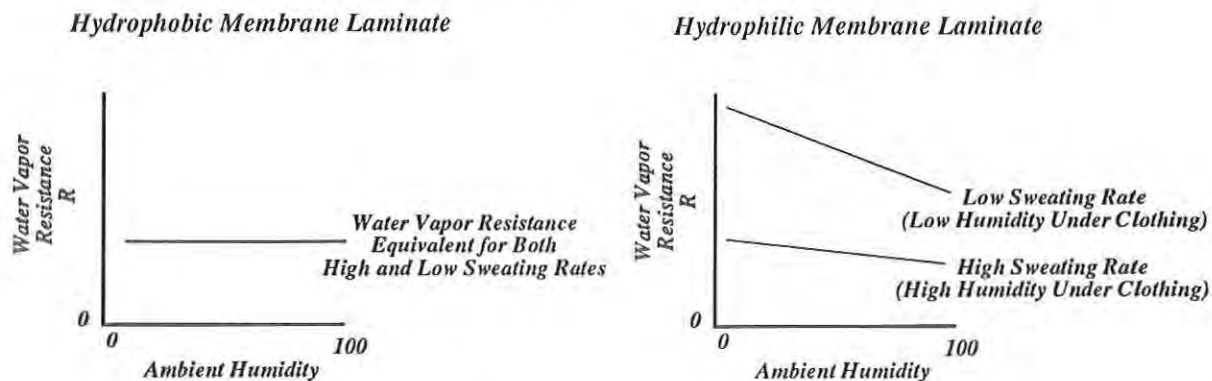


Figure 15. Water Vapor Resistance of Hydrophilic Membrane Laminates Depends on Ambient Humidity and Human Sweating Rate

The main point of Figure 15 is that the water vapor transport behavior of hydrophilic semipermeable membranes is greatly influenced by the amount of water dissolved in them. The moisture vapor transmission rate of hydrophilic membranes "adapts" to use conditions. That is, the intrinsic water vapor resistance of these materials decreases under precisely those conditions where increased water vapor transport is desired: high human sweating rates and/or high ambient humidity.

The water vapor resistance of a multilayer hydrophilic clothing system may also be altered by changing the configuration of the layers. If a hydrophilic membrane laminate is incorporated in the inner layer as opposed to the outer layer of a clothing system, the equilibrium water concentration of the hydrophilic layer will again be dependent on the relative humidity it is exposed to. This is illustrated in Figure 16, where it is assumed that the microclimate next to the skin is saturated due to sweat production at high human work rates.



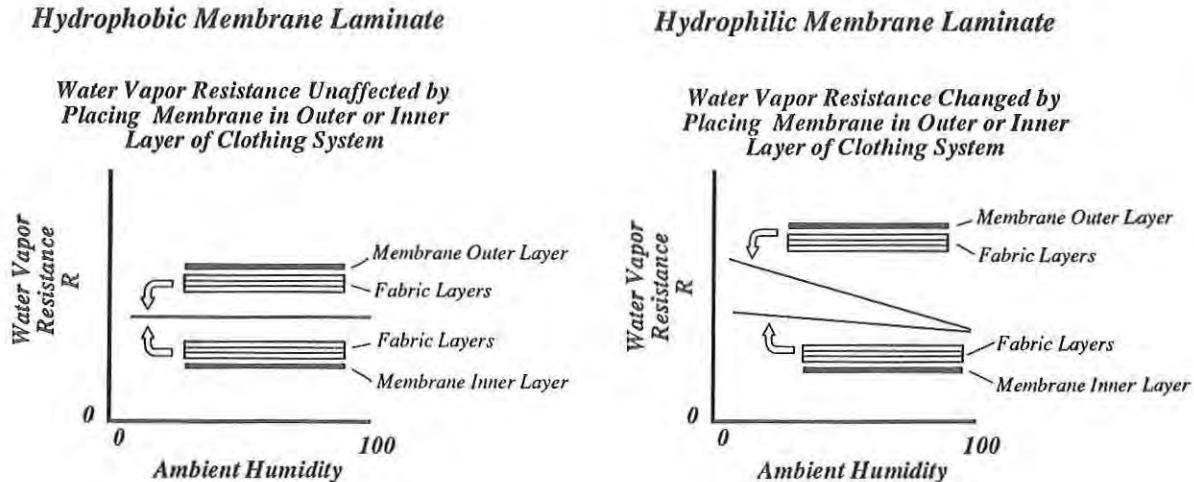


Figure 16. Placement of Hydrophilic Membrane Laminate Affects Water Vapor Resistance of Multilayer Clothing System (High Human Sweating Rate Assumed).

If the hydrophilic polymer layer is next to the skin, water vapor is concentrated within the clothing, and the membrane has a higher equilibrium water content than if it was the outermost layer and exposed to a low ambient humidity. At conditions of high humidity, the relative difference between the performance of the hydrophilic membranes incorporated into the outermost layer versus the innermost layer becomes much less important.

The above discussion ignores many important factors, such as the role of temperature differences within the clothing system, and the condensation/accumulation of sweat in various clothing layers. A numerical model developed by Farnworth<sup>40</sup> was successful in modeling both heat and water vapor transfer through multilayer clothing systems while taking into account all the complicating factors just mentioned. Although the model did not incorporate concentration-dependent water vapor resistances, the system of equations is amenable to incorporating such a modification. The importance of factors such as configuration to the performance of a multilayer clothing system incorporating hydrophilic membrane laminates could be assessed with Farnworth's modified model.

## Study 2. Influence of Air Permeability on Heat and Water Vapor Transfer Through Permeable Materials

### Background

Most laboratory test methods for measuring heat and mass transfer properties of clothing materials produce little air flow through the fabric. These test methods measure the rate at which heat or water vapor diffuses through the material unassisted by any significant air flow penetration through the sample. When air flow through the fabric does occur, both the measured heat and mass transfer increase greatly.



Air flow past a human body and penetration through permeable layers of a clothing system are highly dependent on body geometry, air velocity, and spacing between the layers of the clothing system. The most successful efforts to determine the interaction between fabric air permeability and heat transfer properties have focused on cylindrical test devices such as those used by Fonseca and Breckenridge<sup>41</sup> and Lamb and Yoneda<sup>42</sup>. Their studies illustrate the extremely complicated interactions between air speed, fabric air permeability, and cylinder size and geometry. The modeling of Lamb and Yoneda<sup>42</sup> and Stuart and Denby<sup>43</sup> also approximate the human body as cylinders of various sizes covered by fabric with an air space between the cylinder surface and the covering. Although cylindrical geometries are most appropriate for studies of this type, a qualitative assessment of the interplay between fabric air permeability and thermal properties is obtained by using the simpler guarded hot plate apparatus.

### Methods and Materials

The materials shown previously in Table 1 and Table 4 were used for the air permeability study. The Frazier air permeability<sup>44</sup> of these materials ranged from 0 ft<sup>3</sup>/min/ft<sup>2</sup> to 170 ft<sup>3</sup>/min/ft<sup>2</sup>.

Each material was tested on both the dry and sweating guarded hot plate under three separate test conditions. The three test conditions approximated actual use conditions which might be present in a typical clothing system, and are shown in Figure 17.

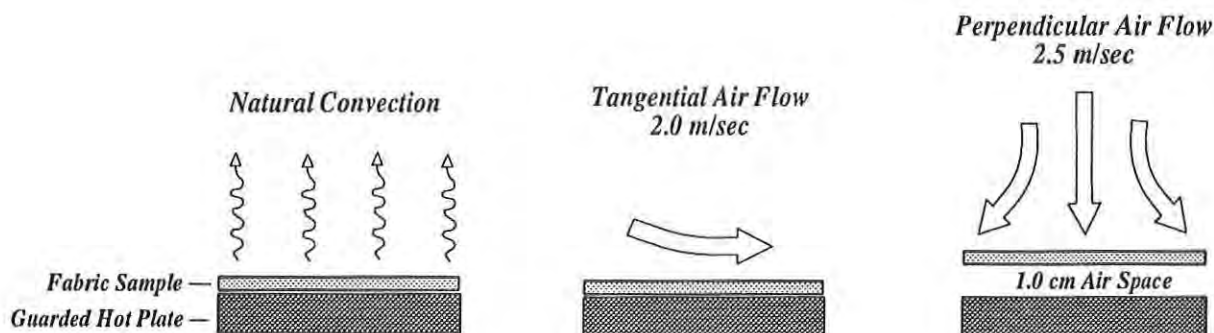


Figure 17. Three Test Conditions for Assessing Influence of Frazier Air Permeability Values on Thermal and Evaporative Resistance of Permeable Fabrics

The test condition expected to show the greatest effect due to air permeability is where an air space is included under the fabric, which allows the perpendicular air flow to penetrate through the fabric and enhance heat and mass transfer from the guarded hot plate surface. For this test condition, the apparatus was modified to seal the edges of the fabric both at the guard heater perimeter and measurement heater section perimeter, as well as to prevent the fabric from sagging into the air space.

The approach of including an air space between the guarded hot plate and the fabric has also been used by Niven<sup>45</sup> and Hatch, et. al.<sup>46</sup>, to study the influence of air penetration on measured thermal properties. This study extends the method to a wider variety of fabric types which have a greater range of air permeability values.

## Results and Discussion

The  $i_m$  index for the test materials is shown for each of the three test conditions in Figure 18.

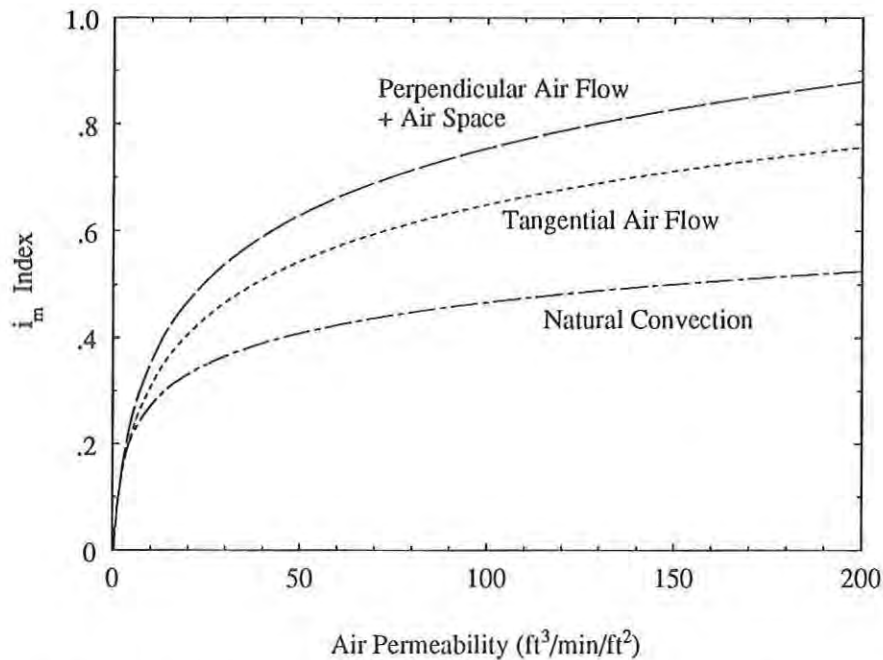


Figure 18. Influence of Frazier Air Permeability on  $i_m$  Index of Fabrics Measured Under Three Air Flow Conditions

Figure 18 shows that the test condition which includes perpendicular air flow onto fabric suspended above the heated plate shows the highest  $i_m$  index. The relative difference between the two test conditions which include no air space between the fabric and the plate is due entirely to the boundary air layer resistance, which is included in the  $i_m$  index. If the thermal and water vapor resistance of the boundary air layer is accounted for, the intrinsic water vapor resistance curves for the tangential air flow and natural convection test conditions are identical.

Figure 18 also shows that changing air permeability has the most effect on measured  $i_m$  values for fabrics with Frazier air permeability between 0 and 50 ft³/min/ft². Above the value of 50 ft³/min/ft² the fabrics are so open that they all begin to approach the thermal and water vapor resistance values of their respective boundary air layers.

The influence of fabric air permeability on fabric intrinsic thermal resistance ( $R_{ct}$ ) and intrinsic water vapor resistance ( $R_{et}$ ) may be illustrated by subtracting out the resistances of the external air boundary layer for each material. For the perpendicular air flow/air space test condition, the intrinsic resistances also include the resistance of the air layer underneath the fabric. As the fabric air permeability increases, more air penetrates through the fabric, which increases the forced convection heat transfer through the air layer. The other two test conditions do not include an air space so they are relatively unaffected by air flow penetration through their structure.

The air flow penetration through the fabric to the underlying air space can be illustrated by calculating the difference between the perpendicular flow/air space conditions and the other two conditions where:

$$\text{Relative Difference in Measured Intrinsic Resistance } (R_{ct} \text{ or } R_{et}) = \Delta R = R_3 - R_{1,2}$$

$R_3$  (i or et) = measured intrinsic resistance, perpendicular air flow/air space test condition

$R_1$  (i or et) = measured intrinsic resistance, natural convection test condition

$R_2$  (i or et) = measured intrinsic resistance, tangential air flow test condition

If the quantity  $\Delta R$  is plotted versus Frazier air permeability it is noticed that the thicker fabrics and fabric combinations are displaced quite a bit from the general experimental data curve. A variety of analytical functions relating air permeability to fabric structural parameters such as thickness, contained in references 2 and 47, were examined to attempt to reduce this data scatter. It was found that simply using the quantity (Air Permeability) $\times$ (Thickness) worked just about as well as any of the more complicated relations in reducing data scatter (although the data are still very scattered). No simple explanation for the success of the quantity (Air Permeability) $\times$ (Thickness) is available. In fact, if thickness were independent of air permeability (which it's not) one would expect  $\Delta R$  to be proportional to air permeability divided by thickness.

The relative difference in measured intrinsic resistance is shown in Figures 19 and 20.

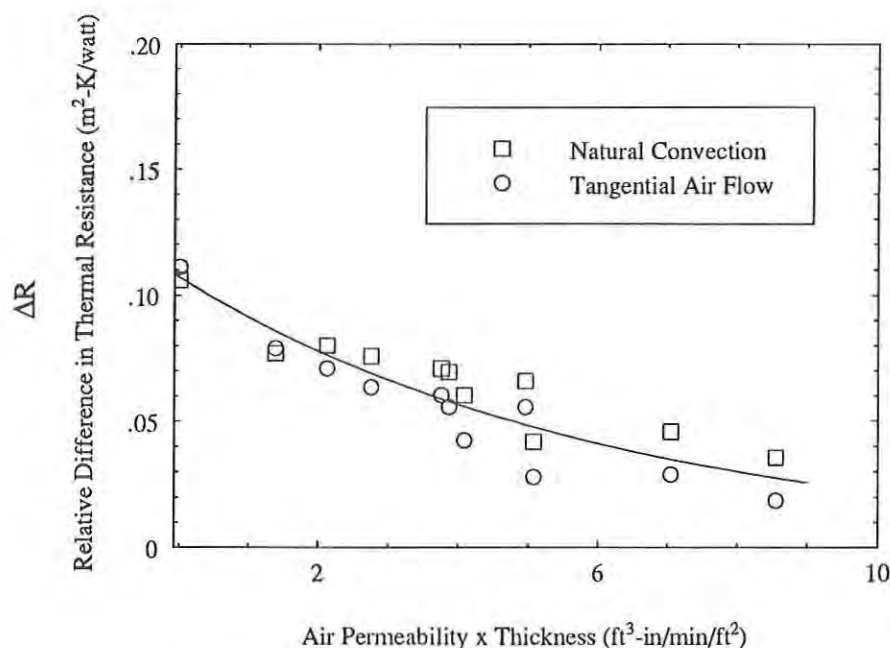


Figure 19. Relative Difference in Measured Intrinsic Thermal Resistance of Fabric/Air Space Combination Due to Penetration of Air Flow Through the Fabric

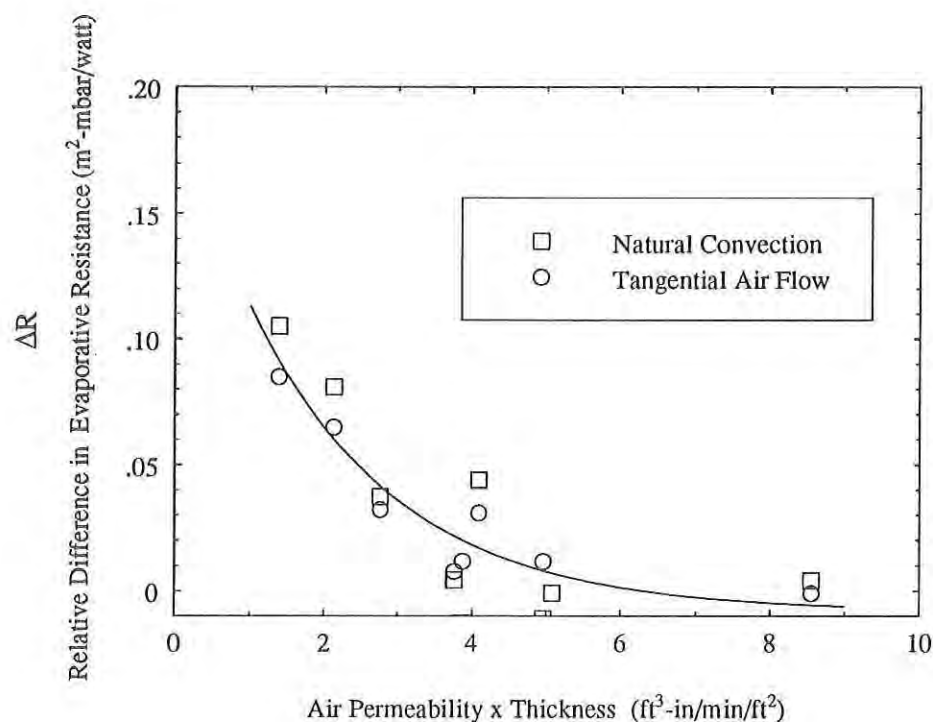


Figure 20. Relative Difference in Measured Intrinsic Water Vapor Resistance of Fabric/Air Space Combination Due to Penetration of Air Flow Through the Fabric

Figures 19 and 20 show that air penetration through the fabric is greatly increased by including an air space between the fabric and the heated plate surface. Figure 19 includes data for an impermeable fabric, which illustrates the highest thermal resistance of the still air layer, undisturbed by air penetration, which is gradually reduced as fabric air permeability increases. The impermeable data points are not shown on Figure 20, since an evaporation/condensation/dripping cycle occurred with the impermeable fabric.

The perpendicular air flow was 2.5 m/sec (5.6 miles/hour). If a higher air flow velocity had been used, then it is possible that the  $\Delta R$  for many of the highly permeable fabrics could have been less than zero, since the increasing air motion in the underlying air layer will greatly enhance heat and mass transfer from the plate, and the intrinsic resistance of the fabric itself will become very small due to the high air flow through the fabric.

There are a great many combinations of air flow conditions and fabric/plate spacings which could be examined to explore some of these effects. However, this would probably not be worth the effort since geometric effects are so important to studies of this type. The effects of air permeability on heat and water vapor transfer are more appropriately studied using cylindrical test devices or thermal mannikins. Some of the qualitative observations made in this study are useful for questions concerning the effect of air flow velocity on guarded hot plate measurements, which is discussed in the next section.

### **Study 3. Comparative Study of Heat Transfer and Water Vapor Permeability at Three Laboratories**

Three organizations on-site at Natick routinely determine the thermal properties of materials in the laboratory. These organizations are the Individual Protection Directorate (IPD) of Natick, the U.S. Army Research Institute of Environmental Medicine (USARIEM), and the U.S. Navy Clothing and Textile Research Facility (NCTRF). All three organizations determine the thermal and water vapor transport properties of materials and evaluate these materials for their intended use.

Each facility conducts laboratory tests based on the same concepts and principles, but which differ in the actual test conditions. Occasionally the need arises to compare materials tested at one laboratory with materials tested at another facility. Because of the differences in test procedures among the three laboratories, this comparison can be very difficult.

The intent of this study was not to standardize test procedures, although that may come about at some point, but rather to observe how the differences in standard practice at each laboratory influence material property results obtained with these test methods. Further information on individual test methods is available in reference 48.

#### **Materials**

Each laboratory was asked to determine the thermal and water vapor transport properties of two different materials. Three samples of each material were provided.

The first material was a nylon/cotton blend fabric used in the U.S. Army's Battle Dress Uniform<sup>49</sup>. This material is a 50% nylon, 50% cotton fabric printed with a Woodland camouflage pattern.

The second material was a carbon-impregnated polyurethane foam, which is used as the inner liner of the Battle Dress Overgarment<sup>33</sup> (BDO). It is composed of a nylon tricot knit fabric laminated together with a polyurethane foam, which incorporates activated carbon particles in an acrylic binder for chemical agent adsorption.

#### **Methods**

Each facility uses a guarded hot plate apparatus to determine dry thermal resistance and water vapor permeability of materials. The most important difference between the test methods used by IPD, NCTRF, and USARIEM is the velocity of the air flowing over the guarded hot plate. NCTRF conducts both dry thermal resistance and water vapor permeability testing according to air flow conditions as set forth in ASTM Method D-1518<sup>26</sup>. USARIEM and IPD normally conduct tests where the air flow rate is much higher than called for in the ASTM standard. It should be noted that the ASTM standard applies only to dry thermal testing and that there is no ASTM standard for this type of water vapor permeability testing. USARIEM tests are conducted according to draft DIN Standard 54-101<sup>28</sup>, using the Hohenstein Skin Model, which has become the standard sweating guarded hot plate apparatus used in Europe.

To provide a full range of test conditions IPD repeated all the thermal tests under conditions of natural convection, where there was no air flow over the plate. This provided a wide range of air flow velocities.



### Bare Plate Results

Each laboratory tests materials under different air flow conditions. As the air velocity over the plate increases, the evaporation rate from the plate surface also increases, until the  $i_m$  value approaches the limiting value of 1.0 for high air flow velocities. This effect of air velocity on the measured value of  $i_m$  is well known, and agrees with data obtained by Woodcock during the original development of the concept of the  $i_m$  index. Figure 21 shows data obtained by Woodcock<sup>27</sup> plotted along with the data from the three laboratories. The variation in  $i_m$  with wind speed is due to radiative heat transfer, which becomes an appreciable portion of the total heat transfer at very low air speeds, when the thermal and mass transfer resistance of the boundary air layer greatly increases. The variation in  $i_m$  with wind speed is not due to changes in the Lewis relation  $S$ , although Spencer-Smith<sup>50</sup> proposed that  $S$  does show a slight dependence on both wind speed and the geometry of the heated isothermal surface.

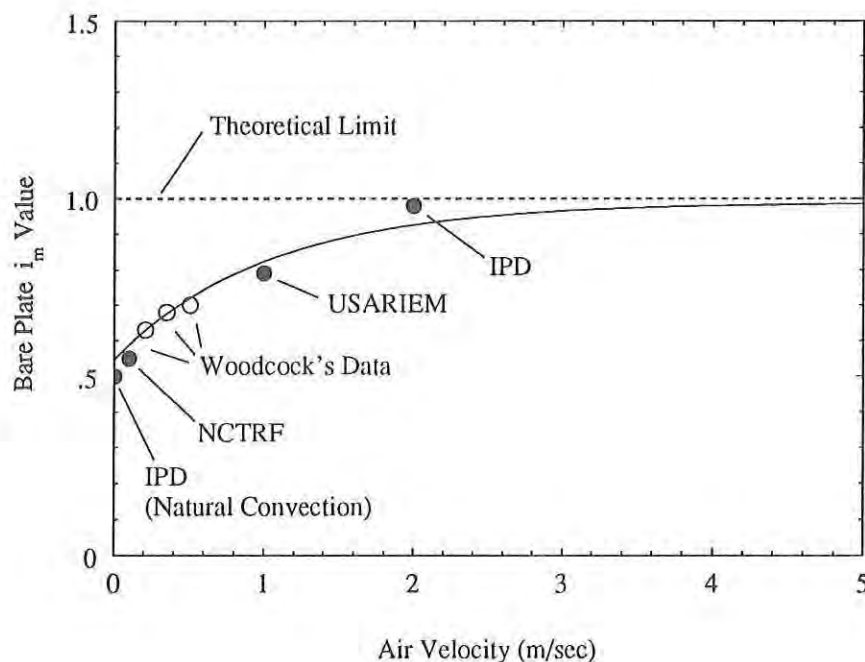


Figure 21. Bare Plate  $i_m$  as a Function of Air Velocity, Including Woodcock's Data

The equation for  $i_m$ , as developed by Woodcock, incorporates the Lewis relation  $S$ , which is the relation between the coefficients of convective heat transfer and evaporative heat transfer. This relation is very useful since for air and water the Lewis relation remains essentially constant as long as atmospheric pressure remains the same. The validity of the Lewis relation is based on the Chilton-Colburn analogy between heat transfer and mass transfer<sup>51</sup>. Because both convective heat transfer and evaporative heat transfer develop similar gradient profiles, one can infer diffusion parameters from measured convective coefficients<sup>52</sup>. Since it is often easier to measure heat transfer coefficients than diffusion coefficients, this approach is commonly used to obtain diffusion properties. Furthermore, it has been found that if the Lewis number ( $Le$ ) is close to 1.0, then the convective behavior and diffusive behavior are essentially identical for a wide range of conditions<sup>53</sup>.



Note that the Lewis *number* ( $Le$ ) is not the same as the Lewis *relation* ( $S$ ). The Lewis number is a dimensionless group similar to the Reynolds number or Prandtl number. The Lewis number relates the thermal diffusivity  $\alpha$  to the diffusion coefficient  $D$ :

$$Le = \frac{\alpha}{D}$$

For air at 35°C, the thermal diffusivity<sup>54</sup>  $\alpha \approx 0.22 \text{ cm}^2/\text{sec}$ , and the diffusion coefficient of water vapor in air<sup>55</sup>  $D \approx 0.26 \text{ cm}^2/\text{sec}$ . Thus  $Le \approx 1$ , and the temperature and water vapor concentration profiles are identical.

The actual value of the Lewis relation  $S$  has been shown analytically<sup>56</sup> and experimentally<sup>57</sup> to be about 2.2 °C/mmHg. An example calculation of the Lewis relation  $S$  is shown below.

The Lewis relation  $S$  is the ratio of the convective heat transfer coefficient  $h_c$  and the mass transfer coefficient  $h_m$ . The Lewis relation  $S$  can also be shown to be defined by<sup>58</sup>:

$$S = \frac{h_c}{h_m} = \rho c_p \left( \frac{Sc}{Pr} \right)^{2/3}$$

$\rho$  = density of air  
 $c_p$  = heat capacity of air  
 $Sc$  = Schmidt number of water vapor diffusing in air  
 $Pr$  = Prandtl number of air

For an air temperature of 65 °F,  $Sc$  is 0.6,  $Pr$  is 0.7,  $\rho$  is 0.0756 lb/ft<sup>3</sup>, and  $c_p$  is 0.24 Btu/lb-°F; this yields a value of approximately 12.6 psi/°F (or 2.2 °C/mmHg) for the Lewis relation  $S$ .

The same relations that apply to the ratio between convective and evaporative heat transfer from the flat saturated guarded hot plate also apply to a wet-bulb thermometer. Experimentally it is known that the temperature depression of a wet-bulb thermometer is constant over a wide range of air velocities once a certain critical air velocity is reached. Normally, the air speed over the wet bulb is recommended to be not less than 3.5 to 4 meters/second<sup>59</sup>. Below this critical air velocity the bulb configuration and air velocity begin to affect the reading<sup>60</sup>. The reason for the inaccuracy of wet-bulb thermometers at the low air velocities is that the Lewis relation neglects radiative heat transfer. At very low air velocities, or under natural convection conditions, the proportion of heat lost by radiation is a significant fraction of the total heat loss or gain.

When there is no air movement over the guarded hot plate, both heat and mass transfer proceed by natural convection. As the air flow rate across the plate increases, the boundary layers over the plate become thinner, and the temperature and concentration gradients through the layers increase. Finally, a point is reached where the heat loss due to radiation can be neglected since it is so small in comparison to the convective and evaporative losses. This behavior is apparent in the bare plate results obtained by each laboratory, as illustrated in Figure 21. The  $i_m$  value steadily rises from a value of 0.5 under natural convection conditions, until  $i_m$  approaches its theoretical value of 1.0 at 2 meters/second air velocity.

It should also be clear that the  $i_m$  value for the bare plate can only approach 1.0, since there will always be a radiative component of heat loss from the plate.

Figure 21 also provides justification for performing water vapor permeability testing with a significant air velocity across the plate. The purpose of the guarded hot plate testing is to rank materials with respect to their intrinsic thermal properties. Tests which are performed under natural convection conditions, or at very low air speeds, are mostly measuring the properties of the boundary air layer over the plate. The fabric properties are usually a small portion of the total resistance to heat and vapor transfer at low air speeds. Testing at higher air speeds can also help distinguish between similar materials, since the range of the measurement is expanded.

In addition, at low air speeds, the radiative heat loss becomes more important. Differences in the emissivity of two fabrics may lead to a large difference in total heat transfer due not to higher permeability, but due to the fact that one fabric may simply be of a different color (different emissivity). Testing at high air velocities minimizes the contribution of radiant heat loss to the guarded hot plate measurement.

Besides the differences in air flow velocity over the guarded hot plate, each laboratory also tests at different plate temperatures and ambient humidities. These variables have little effect on measured  $i_m$  values. Giblo<sup>61</sup> showed that the measured bare plate  $i_m$  value does not change appreciably over a wide range of temperature and humidity conditions as long as the air flow conditions remain the same. Unpublished data from IPD for a narrower range of conditions also show no change in bare plate  $i_m$  values as the plate temperature, air temperature, and the air relative humidity are varied.

### Fabric Results

The influence of air flow velocity over the guarded hot plate upon measured fabric properties becomes clear if the data from each lab are plotted as a function of air flow. Figures 22 and 23 show the  $i_m$  and  $i_m/clo$  values obtained for the two materials as a function of air velocity over the guarded hot plate.

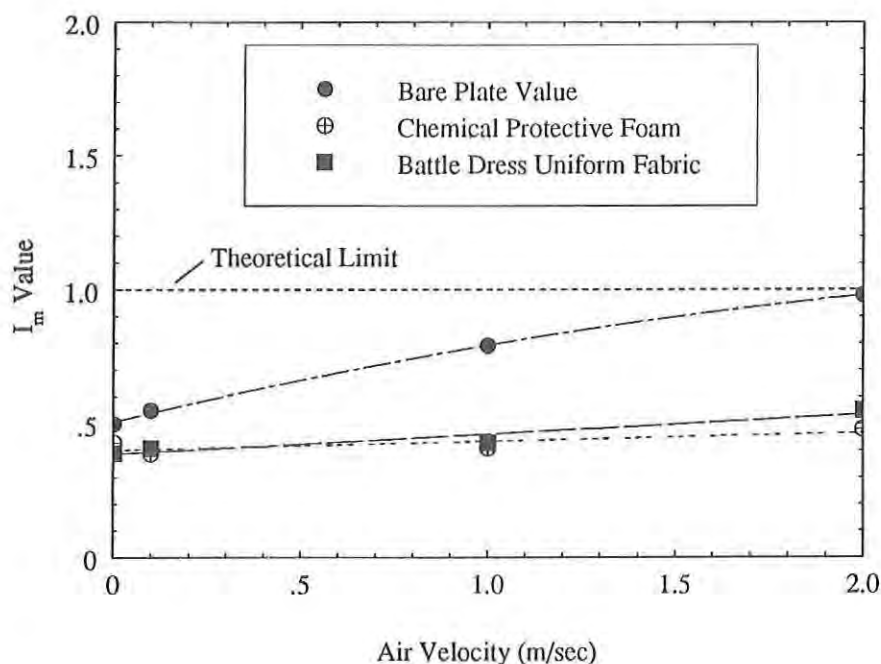


Figure 22. Water Vapor Permeability Index of the Battle Dress Uniform Fabric and the Chemical Protective Foam Determined Under Several Air Flow Conditions

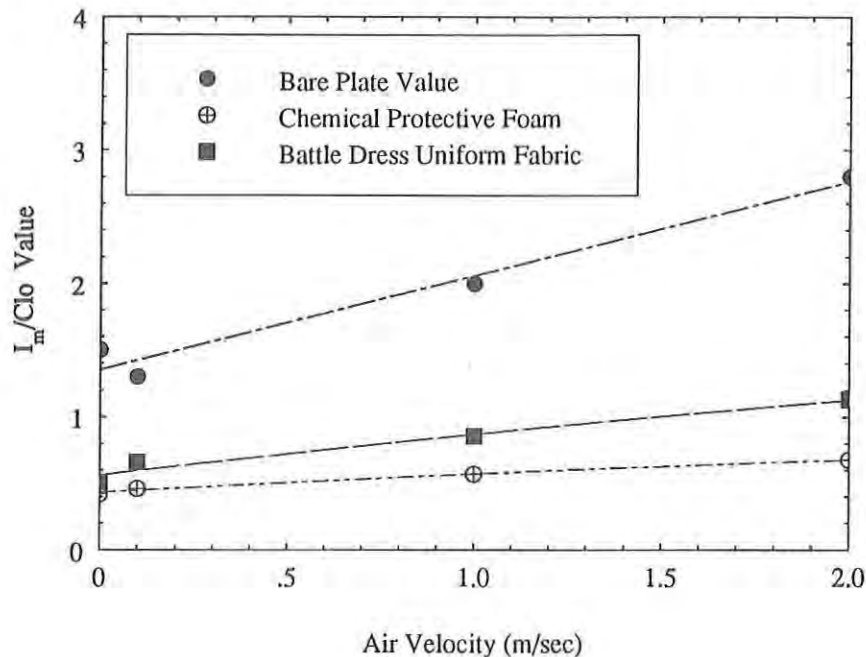


Figure 23.  $I_m/Clo$  Values of the Battle Dress Uniform Fabric and the Chemical Protective Foam Determined Under Several Air Flow Conditions

The two materials follow the same trends as the bare plate results. The normal test procedures for all three laboratories show that the BDU fabric has better water vapor transmission characteristics ( $i_m$ ) and more potential for heat stress reduction ( $i_m/clo$ ) than the CP foam. For the still air condition only, the relative  $i_m$  ranking between the two materials is reversed, although it is also clear from Figure 22 that the still air  $i_m$  values for these two materials are essentially identical. It is also interesting to note that the relative differences between materials are much more pronounced at the higher air flow velocities. This makes distinguishing differences between materials much easier, which is, after all, the reason for performing guarded hot plate tests in the first place.

The slope of the regression-fit line for each material differs. This variation is in line with previous experience obtained with thermal heated mannikins, which shows that thermal properties of different clothing ensembles are proportional to different powers of the air velocity<sup>62</sup>.

Unfortunately, the different slope of the regression lines for each material means that it is not possible to normalize data from the three laboratories based on a simple correction factor. It is encouraging that even though the BDU fabric and the CP foam material are very different in composition and structure, they seem to follow the same trend. One should be able to estimate the proper slope for a different material and be able to determine the properties which would be measured at each laboratory, given the results generated at another laboratory.

### Variability of Intrinsic Fabric Properties

The measurements of  $i_m$  and  $i_m/clo$  include the boundary air layer above the plate. This makes direct comparison of the values reported by IPD, USARIEM, and NCTRF difficult. It is easier to compare the true variability of results by subtracting out the influence of the air layer and comparing the intrinsic properties of the materials.

Figures 24 and 25 show the calculated values for  $R_{ct}$  and  $R_{et}$  plotted along with the sample coefficient of variance (error bars) for each laboratory. The error bars were calculated based on the three samples of each material supplied to each laboratory. A reference line which shows the average value calculated using the data from all four test conditions is also shown on these figures. Each laboratory has a comparable sample-to-sample variability. The repeatability of measurement is excellent for the normal test procedures of the three laboratories.

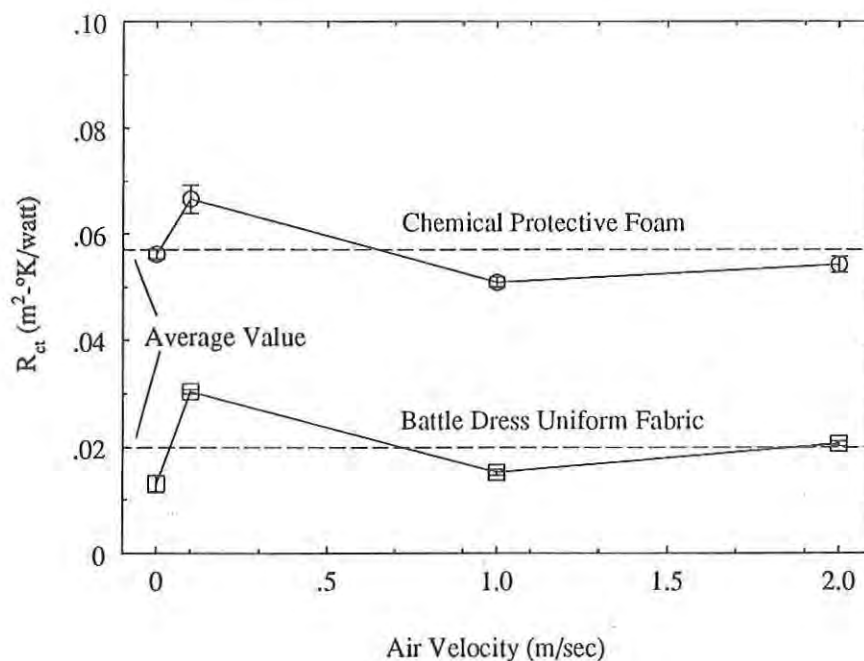


Figure 24. Interlaboratory Variation in Intrinsic Thermal Resistance  $R_{ct}$  for the Battle Dress Uniform Fabric and the Chemical Protective Foam

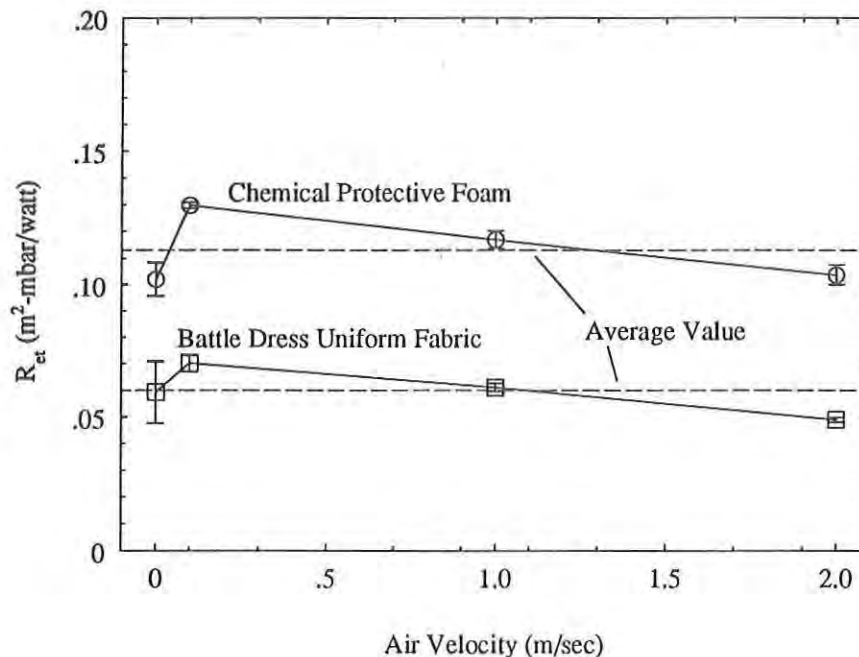


Figure 25. Interlaboratory Variation in Intrinsic Water Vapor Resistance  $R_{et}$  for the Battle Dress Uniform Fabric and the Chemical Protective Foam

There is a definite bias in the intrinsic properties reported by each laboratory. Both Figure 24 and 25 show a similar pattern of interlaboratory variation. The differences are not very large, but they are real.

For all test conditions, the coefficient of variance of all four average value of  $R_{ct}$  and  $R_{et}$  is approximately 10%, except for the intrinsic thermal resistance  $R_{ct}$  of the Battle Dress Uniform fabric, where the interlaboratory coefficient of variation is approximately 30%.

## Conclusions and Recommendations

### Conclusions

- Guarded sweating hot plate and ASTM E96-80, Procedure B, water vapor permeability test methods correlate quite well for a wide variety of woven and nonwoven permeable fabrics, and hydrophobic microporous semipermeable membrane laminates.
- Hydrophilic monolithic semipermeable membrane laminates show no correlation between the sweating guarded hot plate and the ASTM E96-80, Procedure B, upright cup test. This is due to the concentration-dependent water vapor resistance of the hydrophilic polymer layer, and the fact that the two types of tests result in different equilibrium water concentrations in test samples.

- Guarded hot plate thermal and water vapor transport data generated by the Hohenstein Skin Model and other types of guarded hot plate devices agree well if the variation in air speed over the plate is taken into account.
- A small bias between sweating guarded hot plate results generated by different facilities does exist. NCTRF consistently measured a higher intrinsic thermal resistance, while IPD measured the lowest value of intrinsic thermal resistance. NCTRF also reported the highest values of water vapor resistance, while USARIEM (Hohenstein Skin Model) measured the lowest values. The bias is not significant for most materials. Measured intrinsic thermal and mass transfer properties should agree within 10% for all the laboratories. Better agreement is probably possible only if identical test conditions are used.

### Recommendations

- Water vapor permeability screening tests on hydrophilic membranes and laminates should be done under the range of conditions which approximate the actual use conditions. The ranking of various materials will change dramatically according to the water concentration in the hydrophilic polymer layer.
- ASTM E96-80, Procedure B and Procedure BW, may be used together to rank the water vapor permeability of candidate materials only if one material shows better water vapor transport properties in both test methods. If the rankings change between Procedure B and BW, then some other method, such as the sweating guarded hot plate, should be used to rank the materials.
- Materials with ASTM E96-80, Procedure B, *MVTR* values greater than  $1200 \text{ g/m}^2/24 \text{ hours}$  are influenced by air penetration through the fabric, since the limiting *MVTR* for the still air layer is  $1230 \text{ g/m}^2/24 \text{ hours}$ . Unless the fabric will actually be used as a single layer, it is better practice to perform comparison tests with other materials using a cover fabric with low water vapor resistance.
- Farnworth's numerical model<sup>40</sup> of heat and moisture transfer through multilayer clothing systems should be adapted to incorporate concentration-dependent water vapor resistances of monolithic hydrophilic polymer layers. The optimum placement of the hydrophilic membrane could be determined for a variety of human work rates and external environmental conditions.
- Laboratories should always report test conditions, especially air speed over the plate, along with thermal property and water vapor transport data. The lack of accepted test methods for sweating guarded hot plate testing makes comparing test results generated by different apparatus difficult. The inclusion of bare plate wet and dry calibration values in reported data allows the calculation of intrinsic textile properties  $R_{ct}$  and  $R_{et}$ . These intrinsic properties should be directly comparable between apparatus used in different laboratories, unlike the  $i_m$  index, which is highly dependent on the boundary air layer properties.
- Test conditions which produce a bare plate  $i_m$  value approaching the limit of 1.0 make it easier to distinguish differences between similar materials. Air velocities of at least 1.0 meter/second, and preferably higher, should be used during moisture vapor permeability testing.



## References

1. Crank, J., *The Mathematics of Diffusion*, 2nd ed., Oxford University Press, London, 1975, p. 2.
2. Yoon, H.N., Buckley, A., "Improved Comfort Polyester - Part I: Transport Properties and Thermal Comfort of Polyester/Cotton Blend Fabrics," *Textile Research Journal*, May 1984, pp. 289-298.
3. Wehner, J.A., Miller, B., Rebenfeld, L., "Dynamics of Water Vapor Transmission Through Fabric Barriers," *Textile Research Journal*, October 1988, pp. 581-592.
4. Wang, J.H., Yasuda, H., "Dynamic Water Vapor and Heat Transport Through Layered Fabrics, Part I: Effect of Surface Modification," *Textile Research Journal*, January 1991, pp. 10-20.
5. Buchek, D.J., "Comfortable Clothes Through Chemistry," *Chemtech*, March 1991, pp. 142-147.
6. Keighley, J.H., "Breathable Fabrics and Comfort in Clothing," *Journal of Coated Fabrics*, Vol. 15, October, 1985, pp. 89-104.
7. Truong, Q.C., Laible, R.C., "Testing and Evaluation of Waterproof/Breathable Materials for Chemical Protective Clothing Applications," U.S. Army Natick Research, Development and Engineering Center Technical Report, *NATICK/TR-88/016L*, October 1987.
8. Lomax, G. R., "The Design of Waterproof, Water Vapour-Permeable Fabrics," *Journal of Coated Fabrics*, Vol 115, July 1985, pp. 40-66.
9. Gohlke, D.J., "Improved Analysis of Comfort Performance in Coated Fabrics," *Journal of Coated Fabrics*, Vol. 10, January 1981, pp. 209-224.
10. Lomax R.G., "Hydrophilic Polyurethane Coatings," *Journal of Coated Fabrics*, Vol. 20, October, 1990, pp. 89-107.
11. Reagan, E., "The Weather Warriors," *Outside Business*, April, 1991, p. 37-45.
12. Crank, J., "Diffusion in Fibre-Forming Substances," in *Moisture in Textiles*, J.Hearle and R. Peters, eds., Butterworths Scientific Publications (1960).
13. Osczevski, R.J., Dolhan, P.A., "Anomalous Diffusion in a Water Vapour Permeable, Waterproof Coating," *Journal of Coated Fabrics*, Vol. 18, April 1989, pp. 255-258.
14. Farnworth, B., Lotens, W.A., Wittgen, P.P.M.M., "Variation of Water Vapor Resistance of Microporous and Hydrophilic Films with Relative Humidity," *Textile Research Journal*, January, 1990, pp. 50-53.
15. American Society for Testing and Materials (ASTM) E96-80, Standard Test Methods for Water Vapor Transmission of Materials (1984).
16. Whelan, M.E., MacHattie, L.E., Goodings, A.C., Turl, L.H., "The Diffusion of Water Vapor Through Laminae with Particular Reference to Textile Fabrics," *Textile Research Journal*, Vol. 25, No. 3, March, 1955, pp. 197-223.

17. Fourt, L., Harris, M., "Diffusion of Water Vapor Through Textiles," *Textile Research Journal*, Vol. 17, May 1947, pp. 256-263.
18. Weiner, L. I., "The Relationship of Moisture Vapor Transmission to the Structure of Textile Fabrics," *Textile Chemist and Colorist*, Vol. 2, No. 22, 1970, p. 378-385.
19. Watkins, D., Slater, R., "The Moisture-Vapour Permeability of Textile Fabrics," *Journal of the Textile Institute*, no. 1, 1981, pp. 11-18.
20. Dolhan, P., "A Comparison of Apparatus Used to Measure Water Vapor Resistance," *Journal of Coated Fabrics*, 10, (October, 1987) p. 96.
21. Miller, B., Design Criteria for Effective Chemical Protective Clothing with Asymmetric Transport Properties," U.S. Army Natick Research, Development and Engineering Center Technical Report, NATICK/TR-87/036L, August, 1987, pp. 37-42.
22. Van Best, C.A., Wittgen, P.P.M.M., "A Simple Apparatus to Measure Water Vapor Resistance of Textiles," *Textile Research Journal*, 56, (1986), p. 566.
23. Farnworth, B., Dolhan, P., "Apparatus to Measure the Water Vapour Resistance of Textiles," *Journal of the Textile Institute*, 75, 1985, pp. 142-145.
24. Langmuir, I., Schaeffer, J.J., "Rates of Evaporation of Water Through Compressed Monolayers on Water," *Journal of the Franklin Institute*, Vol. 235, 1943, p. 126-128.
25. Holman, J.P., *Heat Transfer*, 5th ed., McGraw-Hill, Inc., New York, 1981, pp. 486-491.
26. ASTM D1518-77, Standard Test Method for Thermal Transmittance of Textile Materials Between Guarded Hot-Plate and Cool Atmosphere (1977).
27. Woodcock, A.H., "Moisture Transfer in Textile Systems," *Textile Research Journal*, 32, 1962, pp. 622-633.
28. Deutsches Institut für Normung (DIN) Standard 54-101 (Draft), Measurement of Stationary Thermal and Water Vapour Resistance by Means of a Thermoregulatory Model of Human Skin (1984).
29. North Atlantic Treaty Organization (NATO) ACCP-1, "Heat Transfer and Physiological Evaluation of Clothing," NATO Unclassified Document AC/301-D/277, April 1984.
30. Mecheels, J.H., Demeler, R.M., Kachel, E., "Moisture Transfer Through Chemically Treated Cotton Fabrics," *Textile Research Journal*, April, 1966, pp. 375-384.
31. Military Specification, MIL-C-44031D, Cloth, Camouflage Pattern: Woodland, Cotton and Nylon, Class 2 - Camouflage Printed and Quarpel Treated, 22 Aug 1989.
32. Military Specification, MIL-C-43892A, Cloth, Twill: Cotton and Nylon, Water Repellent Treated, 21 Dec 1984.

33. Military Specification, MIL-C-43858B(GL) Cloth, Laminated, Nylon Tricot Knit, Polyurethane Foam Laminate, Chemical Protective and Flame Resistant, Type III, 16 Jan 1986.
34. Military Specification, MIL-S-12189, Cloth, Coated: Butyl Coated, Toxicological Agents Protective.
35. Military Specification, MIL-C-44187B, Cloth, Laminate, Waterproof and Moisture Vapor Permeable.
36. Military Specification, MIL-P-44189, Parka, Extended Cold Weather Camouflage
37. Military Specification, MIL-C-44356, Coat and Trousers, Chemical Protective, Aircrew, Flame Resistant (i.e. Aircrew Uniform, Integrated Battlefield, AUIB)
38. Military Specification, MIL-C-44307, Bivy Cover, Sleeping Bag System, Extreme Cold Weather
39. Military Specification, MIL-G-44419, Glove Shell, Intermediate Cold/Wet Glove System
40. Farnworth, B., "A Numerical Model of the Combined Diffusion of Heat and Water Vapor Through Clothing," *Textile Research Journal*, 56, vol 11, November 1986, pp. 653-663.
41. Fonseca, G., Breckenridge, J., "Wind Penetration Through Fabric Systems, Part I," *Textile Research Journal*, 35, pp. 95-103; Part II, *Textile Research Journal*, 35, pp. 221-227.
42. Lamb, G., Yoneda, M., "Heat Loss from a Ventilated Clothed Body" *Textile Research Journal*, July, 1990, pp. 378-383
43. Stuart, I., Denby, E., "Wind Induced Transfer of Water Vapor and Heat Through Clothing," *Textile Research Journal*, November, 1983, pp. 655-660.
44. Permeability to Air; Cloth; Calibrated Orifice Method, Method 5450, Federal Test Method Standard Number 191A, 20 July, 1978.
45. Niven, C., "The Heat Transmission of Fabrics in Wind," *Textile Research Journal*, October, 1957, pp. 808-811.
46. Hatch, K., Woo, S., Barker, R., Radhakrishnaiah, P., Markee, N., Maibach, H., "In Vivo Cutaneous and Perceived Comfort Response to Fabric - Part I: Thermophysiological Comfort Determinations for Three Experimental Knit Fabrics," *Textile Research Journal*, July, 1990, pp. 405-412.
47. Hoke, L., Segars, R., Cohen, S., King, A., Johnson, E., "Low Speed Air-Flow Characterization of Military Fabrics," U.S. Army Natick Research, Development and Engineering Center Technical Report, *NATICK/TR-89/013*, October 1988.
48. Gibson, P., Endrusick, T., Giblo, J., "Comparative Study of Heat Transfer and Water Vapor Permeability at Three Laboratories," *NATICK/TR-91/029*, May 1991.
49. Military Specification, MIL-C-44031D, Cloth, Camouflage Pattern: Woodland, Cotton and Nylon, Class 1, 22 Aug 1989.

50. Spencer-Smith, J.L., "The Limitations of Woodcock's 'Moisture Permeability Index' ", *Textile Research Journal*, March 1975, p. 220-222.
51. Kays, W.M., Crawford M.E., *Convective Heat and Mass Transfer*, McGraw-Hill Publishing Co., New York, 1987, pp. 365-371.
52. Lewis, W.R., "The Evaporation of a Liquid into a Gas", *ASME Transactions*, 4, 1922, pp. 325-335.
53. Holman, J.P., *Heat Transfer*, 5th ed., McGraw-Hill, Inc., New York, 1981, p. 493.
54. National Bureau of Standards (U.S.) Circular 564, 1955.
55. Perry, J.H., *Chemical Engineers Handbook*, 4th ed., McGraw-Hill Book Company, New York, 1963.
56. Sibbons, J.L.H., "Coefficients of Evaporative Heat Transfer", *International Symposium on Physiological and Behavioral Temperature Regulation*, Hardy, J.D., editor, Charles C Thomas, Springfield, Illinois, 1968, pp. 109-112.
57. Nishi, Y., Gagge, A.P., "Moisture Permeation of Clothing - A Factor Governing Thermal Equilibrium and Comfort", *ASHRAE Transactions*, 76, 1970, pp. 137-145.
58. Simonson, J.R., *An Introduction to Engineering Heat Transfer*, McGraw-Hill, New York, 1967, pp. 152-153.
59. *ASHRAE Handbook--1985 Fundamentals*, American Society of Heating, Refrigeration, and Air-Conditioning Engineers, Atlanta, Georgia, p. 13.23.
60. Reynolds, W.C., Perkins, H.C., *Engineering Thermodynamics*, McGraw Hill, New York, 1977, pp. 398-399.
61. Giblo, J., Pimental, N., "The Effect of Ambient Temperature on the Measurement of  $Clo$  and  $I_m$ ", Final Report for Project 62330-01, U.S. Navy Clothing and Textile Research Facility, Natick, Massachusetts, September, 1988.
62. Breckenridge, J.R., Goldman, R.F., "Effect of Clothing on Bodily Resistance Against Meteorological Stimuli", *Progress in Biometeorology*, Vol I, Part II, Swets and Zeitlinger, N.V. Amsterdam and Lisse, 1977, pp. 194-208.

Note: Military Specifications are available on order from:

Standardization Document Order Desk  
 700 Robbins Avenue  
 Building 4D  
 Philadelphia, PA 19111-5094

LACHICA & ROSKEY

TITLE: Use of Acetate and Lactate for the Control of Pathogenic *Listeria* in Foods

R. Victor Lachica, Dr., and Chester T. Roskey, Dr.

ABSTRACT: *Listeria monocytogenes* (IM) has been recognized recently as a foodborne pathogen. It is widely distributed in the environment and therefore not easily kept away from our food supply. The risk of listeriosis is especially high from refrigerated, ready-to-eat foods, since the pathogen can grow at refrigeration temperatures. The increasing use of such foods both by military food service and the commercial marketplace may put increasing numbers of people at risk. Exposure of these foods to abuse temperatures exacerbates the problem. This study addresses the need for an additional barrier to control growth of the cold-tolerant pathogen in foods. The approach involves adding organic acids or their salts to foods at levels that are organoleptically acceptable while maintaining their pH values at  $\geq 5.0$ . Using a liquid nutrient medium as a model, IM was shown to be inhibited throughout the 40 days of observation even at a high storage temperature of  $35^{\circ}\text{C}$  at pH 5.6 in the presence of 0.5% sodium acetate or 3.0% sodium lactate. The presence of 1.0% sodium acetate was required for complete inhibition of IM in chicken or beef slurry at pH 5.0 when stored at temperatures no higher than  $15^{\circ}\text{C}$ . Our results demonstrate that the risk of listeriosis from consumption of refrigerated meat items can be prevented by minor reformulation of these items.

BIOGRAPHY OF PRESENTER: R. Victor Lachica

PRESENT ASSIGNMENT: Research Microbiologist, Food Engineering Directorate.

PAST EXPERIENCE: Chief, Microbiology Branch, Food Control Division, Institute of Nutrition, Guatemala City, Guatemala.

DEGREES HELD: B.A., Wartburg College, Ph.D., Iowa State University.



Use of Acetate and Lactate for the Control of Pathogenic  
*Listeria* in Foods

Dr. R. Victor Lachica  
Food Engineering Directorate, U.S. Army Natick  
Research Development and Engineering Center  
Natick, MA 01760-5018

Dr. Chester T. Roskey  
Biology Department, Framingham State College  
Framingham, MA

INTRODUCTION

*Listeria monocytogenes* (IM) is presently considered an important food-borne pathogen. Listeriosis may well be the leading fatal food-borne infection in the United States (11). Outbreaks of listeriosis have been attributed to the consumption of raw vegetables and post-process contaminated dairy products (18) as well as *Listeria*-contaminated poultry products (2,4). The incidence of listeriosis appears to be increasing along with an increase in the susceptible population and the numbers and types of foods in which IM is able to survive and grow (7). Work in our laboratory revealed that IM survived but did not grow in ground pork when stored at 4.5°, 10°, or 20°C. However, IM survived and grew well in pork breakfast sausage (15). In view of the ubiquitous presence of IM in foods and its potential to cause fatal illness, efforts need to be made to develop acceptable means to control its replication in foods.

Organic acids, particularly lipophilic organic acids, exhibit antimicrobial activity (3). Studies of the effect of acidulants on IM in broth showed that at equal pH values the order of antimicrobial activity of organic acids is acetic > lactic > citric > malic (17,8). Ahamad and Marth (1) reported that 0.05% acetic acid slightly inhibited the growth of IM in broth. Other workers (5, 6, 10, 13, 14, 16) have shown that acetic and/or lactic acid may be useful in the control of IM as well as Gram negative spoilage flora. The effect of the addition of sodium acetate or sodium lactate under conditions of controlled pH and temperature on the growth of IM has not been reported.

The present study examines the effect of organoleptically acceptable levels of sodium lactate and sodium acetate on the growth of IM in foods during storage at normal and abusive conditions.

EXPERIMENTAL

Effect of temperature, pH and sodium salts of lactate or acetate in brain heart infusion (BHI) broth. BHI broth was initially used as a model to determine the combined effect of storage temperature, pH and sodium salts on lactate or acetate in the inhibition of three strains of IM.



Three milliliter aliquots of pH 5.6, 6.0, and 6.5 adjusted BHI containing either 0.25%, 0.5%, 1.0%, 2.0% sodium acetate or 1%, 2%, 3%, 6% sodium lactate were each inoculated with 20 uL of a  $10^{-4}$  dilution of an active overnight culture of IM (NA-1), IM (NA-2) or IM (NA-16) from the Natick culture collection and then incubated at 10°, 15°, 20°, 30°, and 35°C. Growth of the bacteria in each culture tube was monitored for 40 days by daily determinations of optical density at 686 nanometers.

The effect of concentration of sodium acetate on the growth of IM in BHI at pH 5.6, 6.0, and 6.5 during incubation at 15°C is shown in Figure 1. The pH of the media had little effect on the growth of IM in control samples. The population of IM in control BHI, without sodium acetate, doubled approximately every 6.5 hours regardless of pH. At pH 5.6 even the lowest concentration of sodium acetate, 0.25%, significantly inhibited the growth of IM. When the media contained 0.25% sodium acetate the population of IM barely increased by one log cycle during the 8 day storage period at 15°C. Higher concentrations resulted in complete inhibition of IM at pH 5.6. The recovery of approximately the same number of cells after eight days as were present at the time of inoculation indicates that at this pH concentrations from 0.5% to 2.0% have a static rather than cidal effect on IM. Increasing the pH decreased the effectiveness of sodium acetate in controlling IM. However, these results indicate that 1% and 3% sodium acetate in BHI at pH 6.0 and 6.5, respectively, can effectively inhibit the growth of IM at 15°C. These results are in accord with Ahamad and Marth (1) who reported that acetic acid suppressed the growth of IM in tryptose broth. However, these workers did not control the pH of the broth and inhibition could be expected due to low pH (3.8 - 4.6) as well as toxicity of the undissociated acetic acid molecule.

The effect of 0.5% to 6.0% sodium lactate on the growth of IM in BHI at pH 5.6, 6.0 and 6.5 during incubation at 15°C is shown in Figure 2. At pH 5.6 the growth of IM was effectively controlled by 2% sodium lactate. The growth of IM in BHI containing less than 2% sodium lactate, although inhibited, does not appear to be significantly different from the growth of IM in control BHI. At pH 6.0 the generation time of IM increased with increasing concentration of sodium lactate in the media. At 1.0% the IM population doubled in approximately 7 hours while 7.5 hours and 13.5 hours were required when the concentration of sodium lactate was 2% and 3%, respectively. At pH 6.5, 6% sodium lactate was required to obtain the same degree of inhibition as was observed by 3% at pH 6.0. Since complete inhibition of IM in BHI occurred only when 3% sodium lactate was present at pH 5.6, the use of sodium lactate to control the growth of IM in food may be limited. Sensory evaluation of sodium lactate in turkey meat revealed that 3.5% sodium lactate was organoleptically unacceptable. (14)

The combined effect of storage temperature, pH, and concentration of sodium acetate on three serovars of IM was examined. An analysis of the ability of IM to grow under varying conditions of temperature, pH and sodium acetate concentration is depicted in Figure 3. The three serovars of IM (3b, 1/2a, and 4b) behaved similarly. At pH 5.6 when the media contained 0.25% sodium acetate there was no evidence of growth by spectrophotometric determination even after forty days incubation at 10° and at 15°C. Incubation at the higher temperatures of 20°, 30° and 35°C allowed the listeria to overcome the inhibitory activity of sodium acetate. At pH 6.0 complete inhibition occurred when the media contained 1.0% sodium acetate and incubation was at 10° and 15°C. Increasing the sodium acetate to 2% prevented the growth of IM even at 20° and 30°C. At pH 6.5, 2% sodium acetate still completely prevented growth of listeria at 10° and 15°C. These results are in accord with other workers who also reported that the efficacy of organic acids increases as pH and temperature decrease. (12, 1, 9, 6).

An analysis of the ability of IM to grow under varying conditions of temperature, pH and sodium lactate concentration is depicted in Figure 4. The three serovars of IM behaved similarly. At pH 5.6 when the media contained 3% sodium lactate there was no evidence of growth of IM even after forty days of storage at 10°, 15°, 20°, 30° or 35°C. At pH 6.0 and 6.5 sodium lactate was ineffective in preventing the growth of IM even at the lowest storage temperature.

These results provided convincing evidence that sodium lactate had limited potential as an antilisterial agent and that sodium acetate may be an effective, organoleptically acceptable control agent. Further experiments were performed to ascertain the effectiveness of sodium acetate against high population density of IM and its activity in controlling the growth of IM in two food systems, baby food chicken and baby food beef.

The effect of a high initial population of IM on inhibition by sodium acetate is shown in Figure 5. Baird-Parker (3) reported that organic acids are usually ineffective as microbial inhibitors when initial levels of microorganisms are high. The results of this investigation revealed that sodium acetate was as effective when the initial microbial load was high (log 5.6 CFU/mL) as when the initial microbial load was low (log 1.5 CFU/mL). When the BHI (pH 5.6) contained log 5.6 CFU/mL, the addition of 0.5% sodium acetate completely inhibited the growth of IM. These results again demonstrate the stasis-inducing activity of sodium acetate against IM. It was possible to recover nearly the same number of IM after 8 days incubation at 15°C as were present at the time of inoculation. There was no difference in the behavior of IM when the media contained 1% sodium acetate.

Effect of various environmental factors in the inhibition of IM in slurries of chicken and beef. Jars of Gerber baby food, "second food chicken" and "second food beef", were purchased from a local supermarket. The pH of the chicken was 6.5 and the pH of the beef was 6.0. Approximately 120-g portions of chicken or beef were transferred to large stomacher bags. Appropriate amounts of a stock 40% solution of sodium acetate were added to some portions to obtain concentrations of 0.5% and 1.0% sodium acetate. The samples were pummeled for two minutes to obtain homogeneity. The pH of the acetate supplemented meat was then adjusted to pH 5.0 and 5.6 by the dropwise addition of 1N or 0.1N HCL. Controls without sodium acetate and controls with neither pH adjustment nor acetate fortification were similarly prepared. Bag contents were transferred to 250 mL glass beakers, covered with aluminum foil and sterilized by autoclaving. After autoclaving the sterile meat was again transferred to large stomacher bags and then inoculated with 1 mL of a  $10^{-4}$  dilution of an overnight BHI culture of IM (NA-2). The inoculated meat was pummeled for two minutes to achieve thorough dispersal of the bacteria. The inoculated meat was then aseptically distributed in ca. 30 g portions to smaller stomacher bags and stored at 5°, 10°, 15° and 25°C. At intervals the bags were removed from storage, pummeled for two minutes, and five to 10 gram aliquots aseptically removed, diluted, and blended in 0.1% peptone and the number of viable cells determined by spread plate on BHIA.

The effect of sodium acetate on inhibition of IM in chicken at pH 5.0 and stored at 10°, 15° and 25°C is shown in Figure 7. The pH of baby food chicken was found to be 6.5. The growth rate of IM in chicken adjusted to pH 5.0 with 1N HCL was significantly slower than its growth in chicken at pH 6.5 when the chicken was stored at either 10° or 15°C. The generation time at pH 6.5 was ca. 7 hours at both 10° and 15°C while the generation time in chicken adjusted to pH 5.0 was ca. 36 hours at 10°C and 7 hours at 15°C. IM was able to overcome the inhibitory effect of the low pH when storage was at 25°C. The effect of sodium acetate on the growth of IM in chicken was similar to the effect observed in BHI. A low concentration, 0.5%, was effective in completely inhibiting the growth of IM in chicken at pH 5.0 during storage at 10° and 15°C. At 25°C 1% sodium acetate was required to achieve complete inhibition.

The effect of sodium acetate on inhibition of IM in chicken at pH 5.6 and stored at 7°, 10°, 15° and 25°C is shown in Figure 8. IM grew as well at pH 5.6 as it did at pH 6.5 at each storage temperature. 0.5% sodium acetate greatly inhibited the growth of IM at 7°C. However, cells remained viable and growth did occur. Plate counts after 22 days storage at 7°C revealed the presence of ca.  $\log 5.5$  CFU/g. There was no increase in the population of viable IM even after 22 days storage when the chicken contained 1% sodium acetate. At 10°C the behavior of IM in the presence of 0.5% and 1.0% sodium acetate in chicken was similar to that observed at 7°C. 1.0% sodium acetate was effective in controlling growth of IM at 10°C but was ineffective at 25°C.

The effect of sodium acetate on inhibition of IM in beef at pH 5.0 and 5.6 during storage at various temperature is shown in Figures 9 and Figure 10, respectively. Growth suppression of IM by sodium acetate was greater in beef than in chicken at both pH 5.0 and 5.6. IM grew well in chicken containing 0.5% sodium acetate at pH 5.0 during storage at 25°C but was unable to grow in beef under the same conditions. Similarly IM grew well in chicken containing 1% sodium acetate at pH 5.6 during storage at 25°C but grew poorly in beef under the same conditions. These results are in agreement with those of Shelef and Yang (16) who reported that growth suppression of IM by lactate was greater in beef than in chicken. These workers attributed the sensitivity in beef to the protective effect of fat, which is higher in chicken than in beef.

#### SUMMARY AND CONCLUSIONS

The growth of IM in broth was effectively suppressed by 0.25% to 0.5% sodium acetate. Higher concentrations (2% to 3%) sodium lactate were necessary to achieve listeristatic activity in broth. Effectiveness of both sodium acetate and sodium lactate increases as both storage temperature and pH decrease. At pH 5.6 growth of IM at 10°, 15°, 20°, 30° and 35°C could be suppressed by either 0.5% sodium acetate or 3% sodium lactate. The three serovars tested behaved similarly in their response to sodium acetate and sodium lactate.

Sodium acetate was nearly as effective in controlling the growth of IM in food as it was in broth. The results of these investigations suggest that the growth of IM in food can be controlled by the addition of as little as 0.5% sodium acetate if the pH of the acetate fortified food is adjusted to between 5.0 and 5.6 and the food is stored under normal refrigeration conditions (0-10°C). Control can be achieved even under conditions of temperature abuse (15-25°C) by the addition of 1% sodium acetate.

Additional studies need to be done to determine the efficacy and limitations of sodium acetate in other foods as well as organoleptic evaluation and acceptability of sodium acetate fortified food.



BIBLIOGRAPHY

1. Ahamad, N. and E.M. Marth. Behavior of Listeria monocytogenes at 7, 13, 21, and 35°C in tryptose broth acidified with acetic, citric, or lactic acid. J. Food Prot. 52:688-695.
2. Anonymous. 1989. Listeriosis associated with consumption of turkey franks. Morbid. Mortal. Weekly Rep. 38:266-268.
3. Baird-Parker, A.C. 1980. Organic Acids. In Microbial Ecology of Foods. Vol. 1. 126-133.
4. Breer, C. and G. Breer. 1988. The isolation of Listeria spp. in meat and meat products. Proc. 34th Inter. Congress. Meat Science Technol. B:520-521.
5. Brocklehurst, T.F. and B. M. Lund. 1988. The effect of pH on the initiation of growth of cottage cheese spoilage bacteria. Int. J. of Food Microbiol. 6:43-49.
6. de Wit and F.M. Rombouts. 1990. Antimicrobial activity of sodium lactate. Food Microbiology. 7:113-120.
7. Farber, J.M. and P.I. Peterkin. 1991. Listeria monocytogenes, a food-borne pathogen. Microbiol. Rev. 55:476-511.
8. Farber, J.M., G.W. Sanders, S. Dunfield, and R. Prescott. 1989. The effect of various acidulants on the growth of Listeria monocytogenes. Letters in Appl. Microbiol. 9:181-183.
9. George, A.E. and P.N. Levett. 1990. Effect of temperature and pH on survival of Listeria monocytogenes in coleslaw. Int. J. of Food Microbiol. 11:345-350.
10. Gill C.O. and K.G. Newton. 1982. Effect of lactic acid concentration on meat of gram-negative psychrotrophs from a meatworks. Appl. Environ. Microbiol. 43:284-288.
11. Gellin, B.G., C.V. Broome, W.F. Bibb, R.E. Weaver, S. Gaventa, L. Mascola, and the Listeriosis Study Group. 1991. The epidemiology of Listerioses in the United States-1986. Am. J. Epidemiol. 133:392-401.
12. Harmayani, E., J.N. Sofos, and G.R. Schmidt. 1991. Effect of sodium lactate, calcium lactate and sodium alginate on bacterial growth and aminopeptidase activity. J. Food Safety. 11:269-283.
13. Lamkey, J.W., F.W. Leak, W.B. Tuley, D.D. Johnson, and R.L. West. 1991. J. Food Science. 56:220-223.

14. Maas, M.R., K.A. Glass, and M.P. Doyle. 1989. Sodium lactate delays toxin production by Clostridium botulinum in cook-in-bag turkey products. Appl. Environ. Microbiol. 55:2226-2229.
15. Roskey, C.T. 1990. Growth and control of Listeria monocytogenes in ground pork and in pork breakfast sausage. Report submitted to U.S. Army Natick RD & E Center under contract no. DAAL03-86-D-0001.
16. Shelef, L.A. and Q. Yang. 1991. Growth suppression of Listeria monocytogenes by lactates in broth, chicken, and beef. J. Food Prot. 54:283-287.
17. Sorrells, K.M., D.C. Enigl, and J.R. Hatfield. 1989. Effect of pH, acidulant, time and temperature on the growth and survival of Listeria monocytogenes. J. Food Prot. 52:571-573.
18. World Health Organization. 1988. Foodborne listeriosis. Report of WHO informal working group. World Health Organization, Geneva.



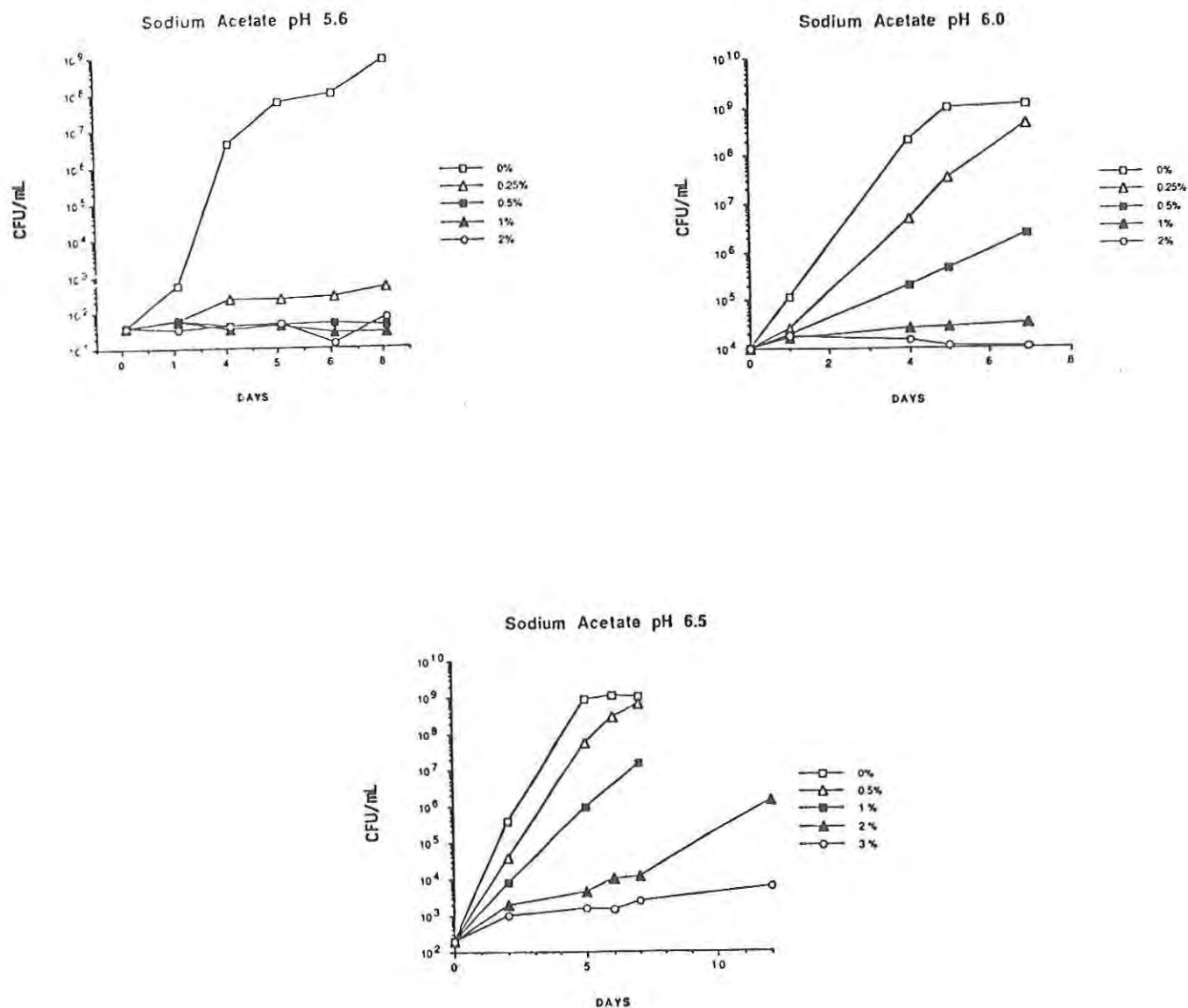


Fig. 1. Effect of concentration of sodium acetate on growth of LM in BHI at pH 5.6, pH 6.0 and pH 6.5 during incubation at 15°C.

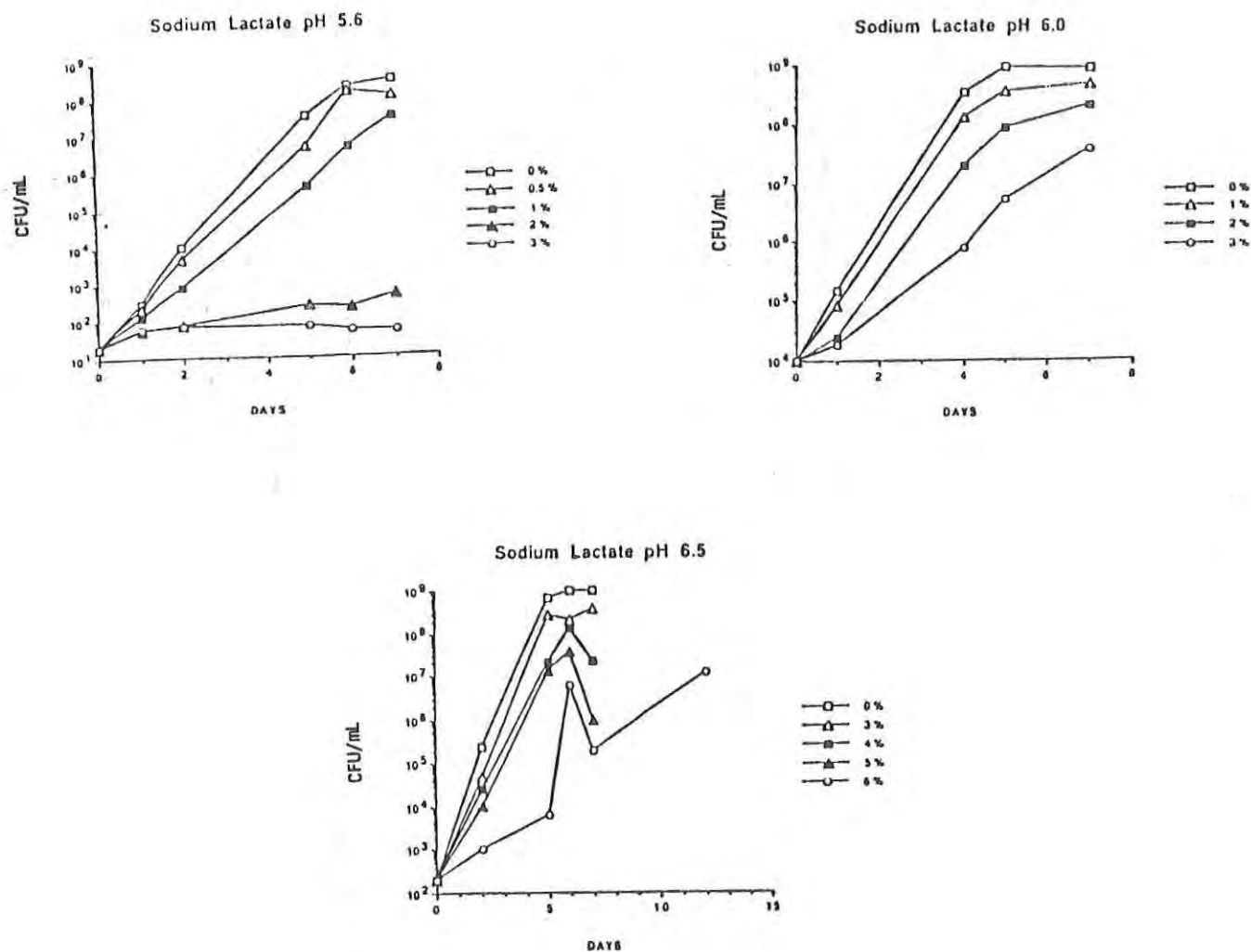


Fig. 2. Effect of concentration of sodium lactate on growth of LM in BHI at pH 5.6, pH 6.0, and pH 6.5 during storage at 15°C.

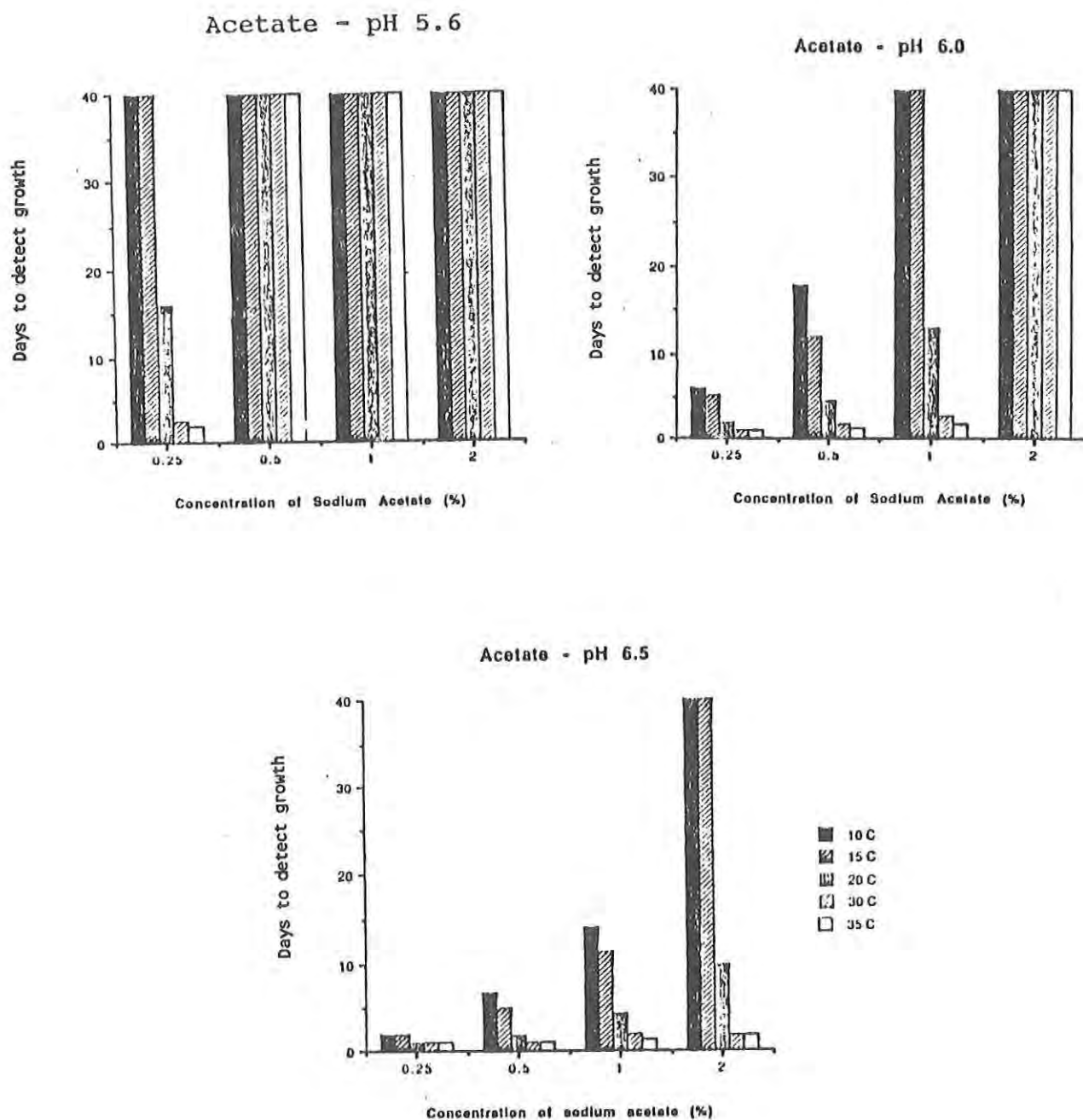


Fig. 3. Effect of storage temperature, pH, and concentration of sodium acetate on inhibition of LM.

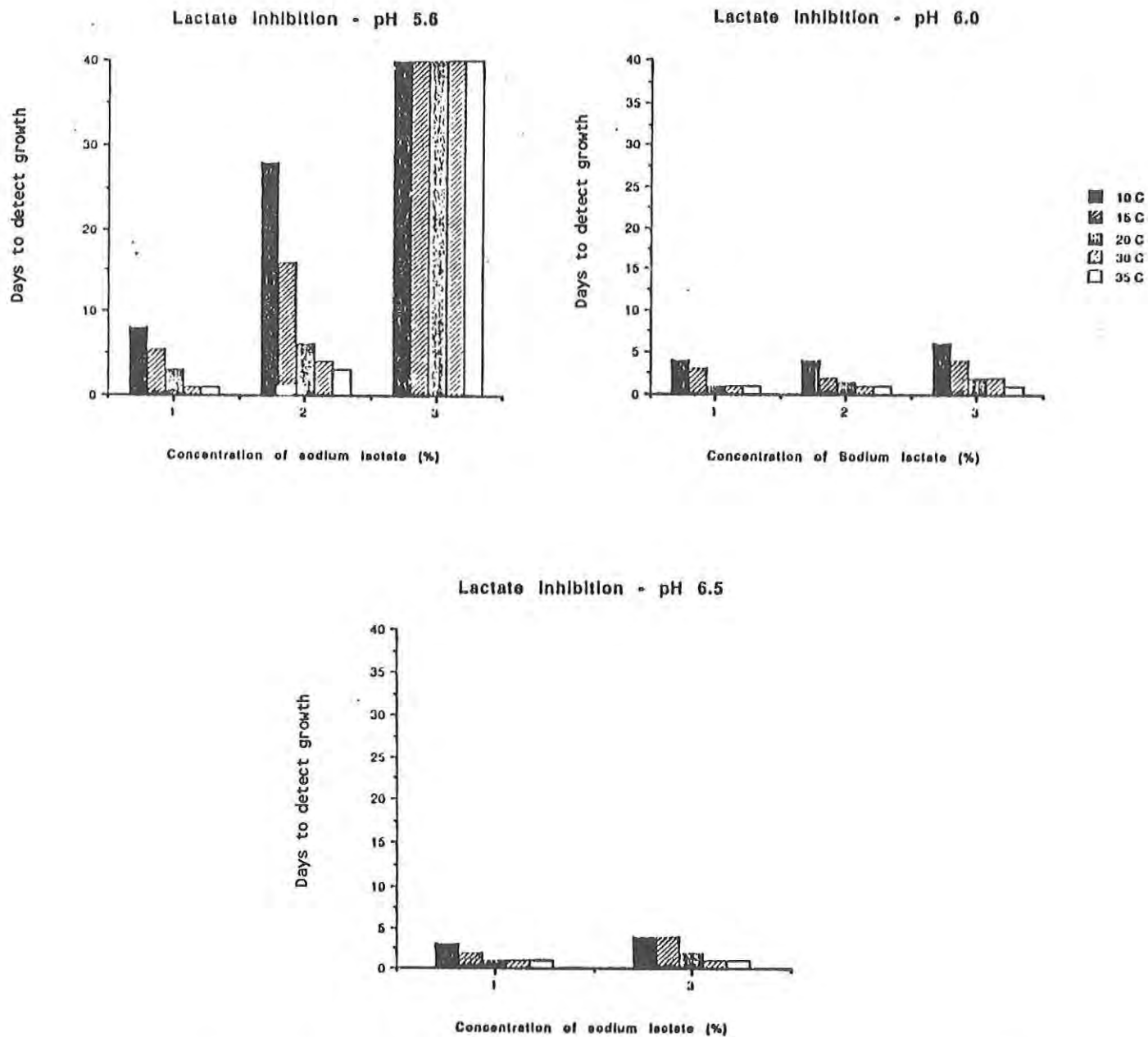


Fig. 4. Effect of storage temperature, pH, and concentration of sodium lactate on inhibition of LM.

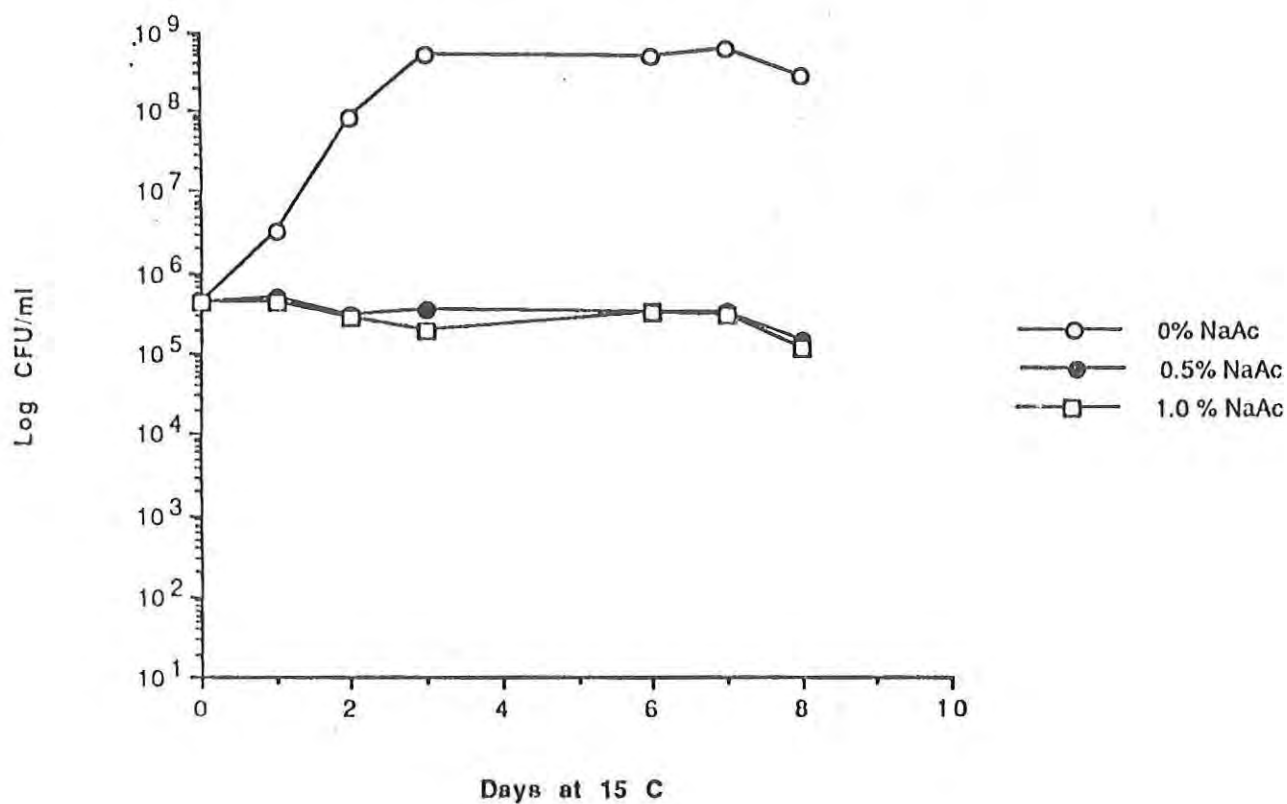


Fig. 5. Effect of high inoculum level on inhibition of LM in BHI by 0.5% and 1.0% sodium acetate at pH 5.6 and 15°C.

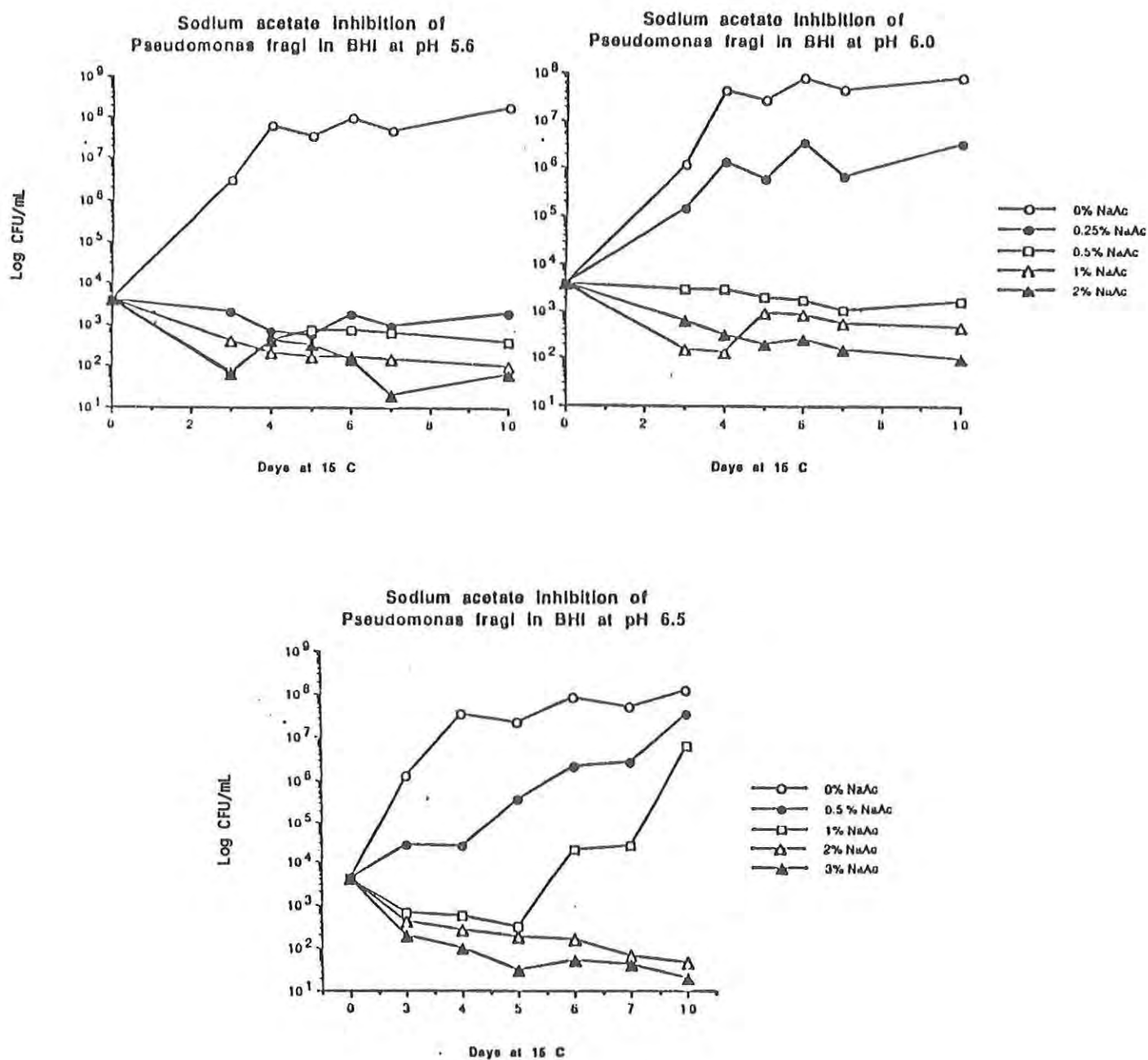


Fig. 6. Effect of sodium acetate on inhibition of *Pseudomonas fragi* in BHI at pH 5.6, 6.0 and 6.5 during incubation at 15°C.



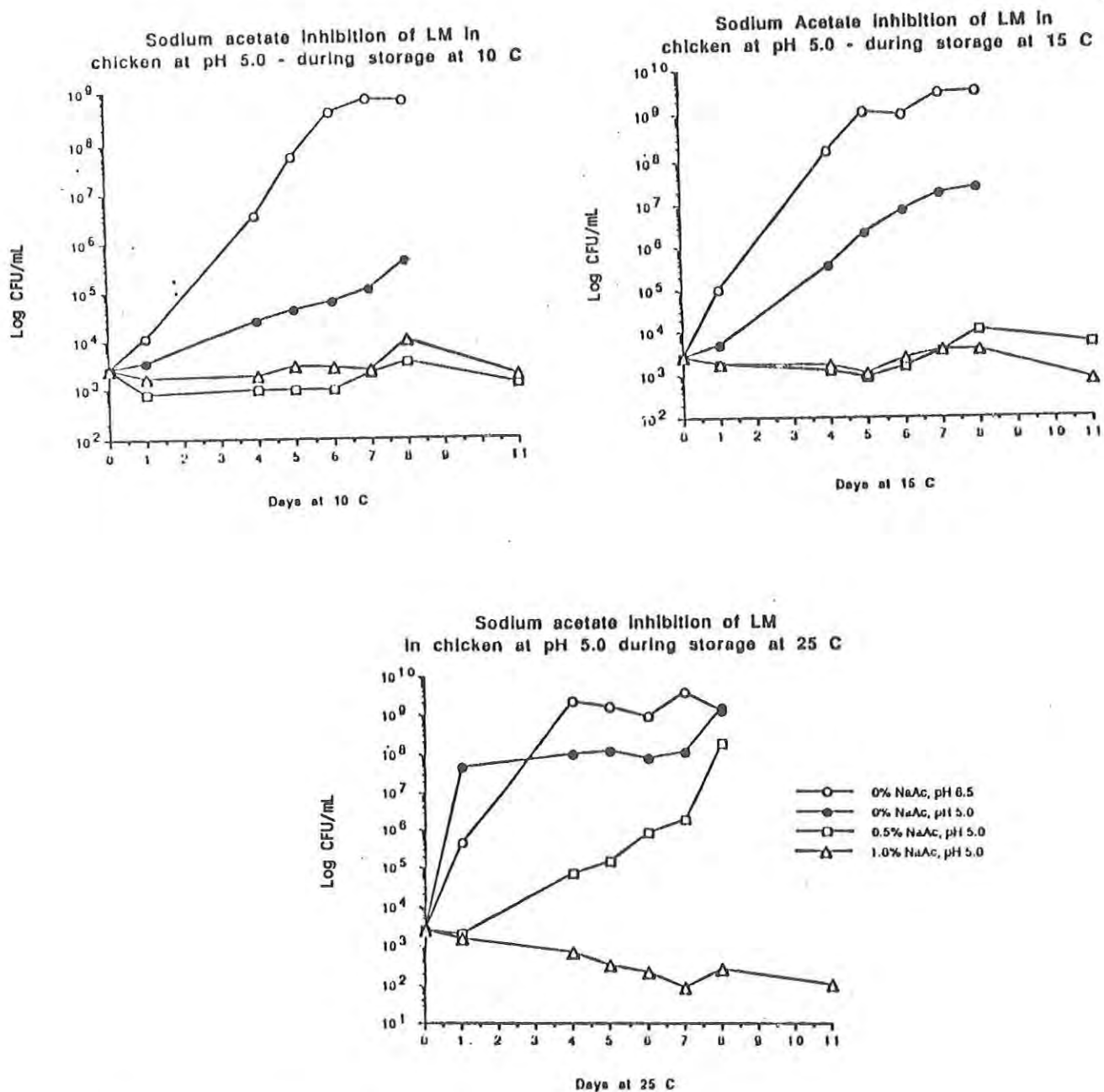


Fig. 7. Effect of sodium acetate on inhibition of LM in chicken at pH 5.0 and stored at 10°, 15°, and 25°C.

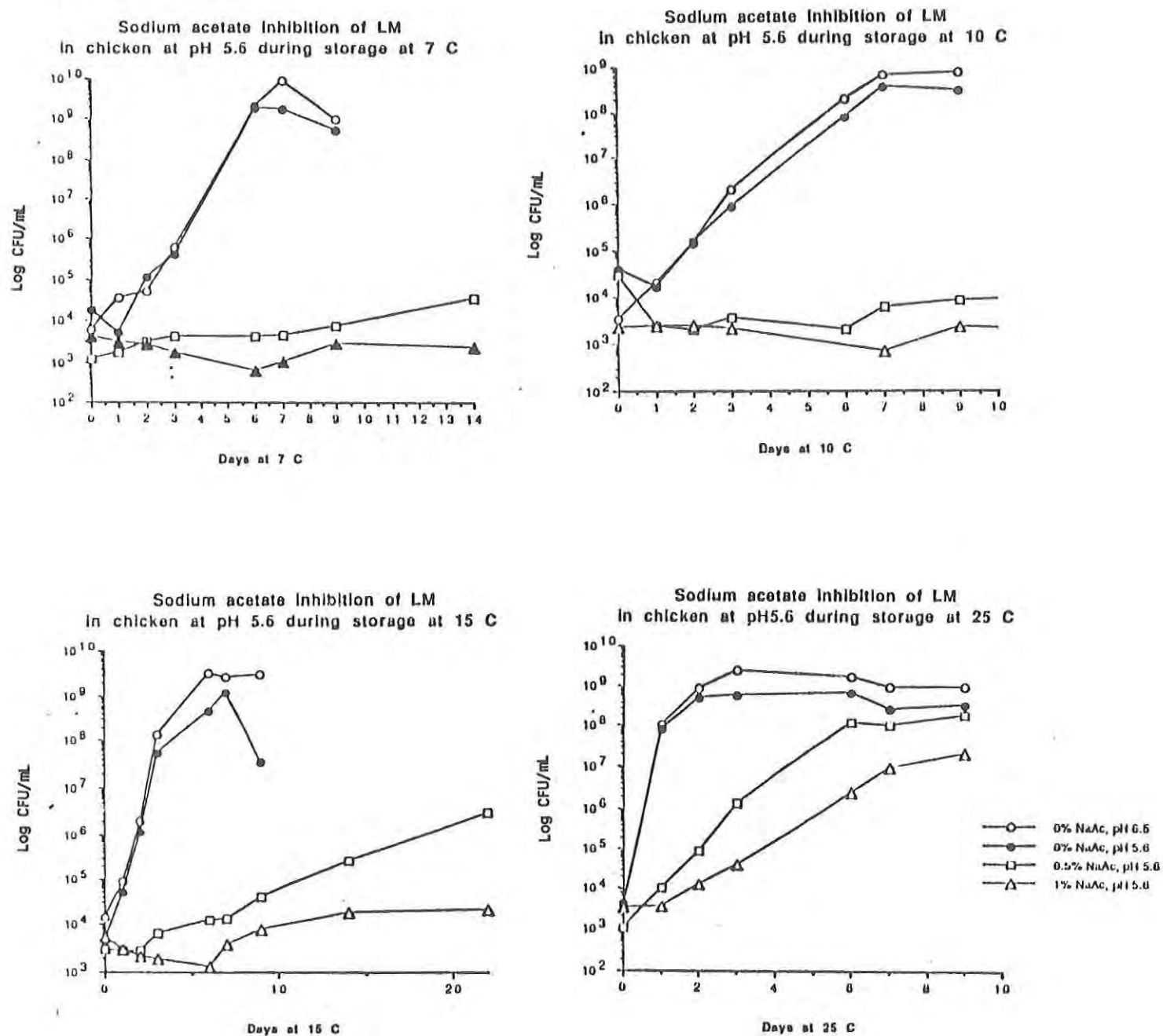


Fig. 8. Effect of sodium acetate on inhibition of LM in chicken at pH 5.6 and stored at 7°, 10°, 15°, and 25°C.

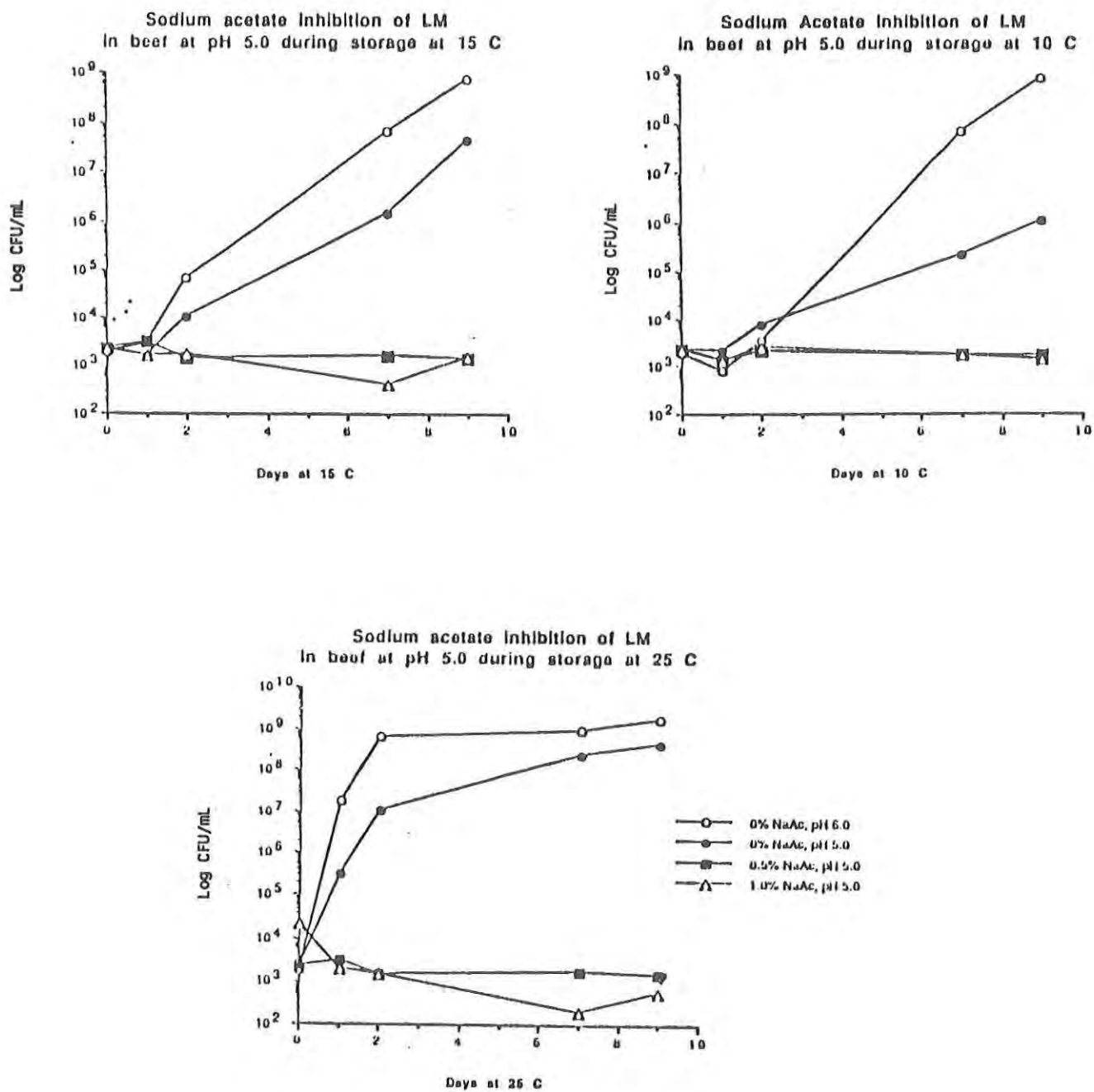


Fig. 9. Effect of sodium acetate on inhibition of LM in beef at pH 5.0 and stored at 10°, 15°, and 25°C.

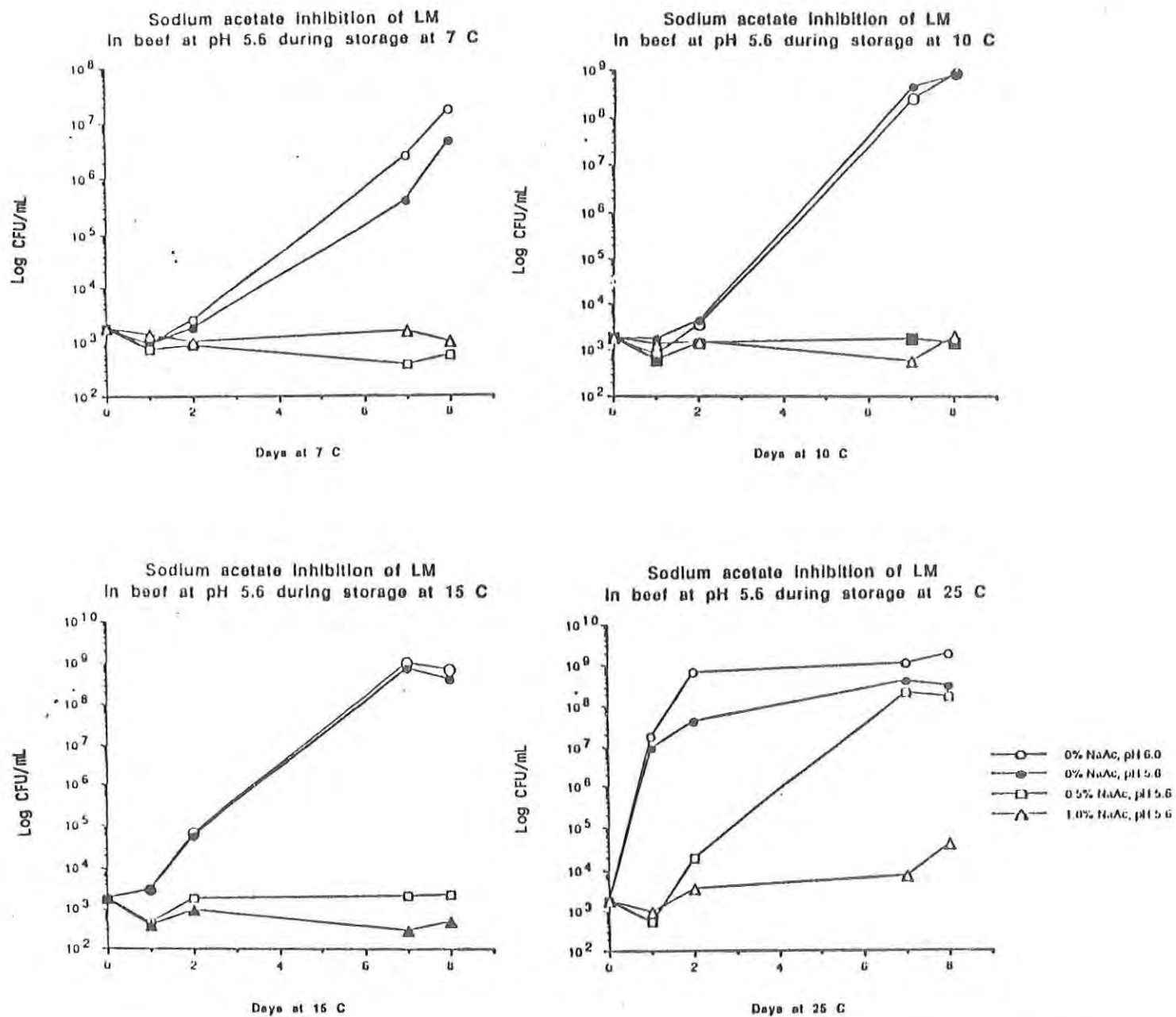


Fig. 10. Effect of sodium acetate on inhibition of LM in beef at pH 5.6 and stored at 7°, 10°, 15°, and 25°C.

TITLE: Antimicrobial Activity of Sucrose Laurate, EDTA, and  
BHA Alone and in Combination

Anthony Sikes, Dr. , Steve Whitfield, Mr.

ABSTRACT: The progressive use of new processing and packaging technologies for home-cooked-type ration items requires new approaches to microbial preservation of these types of foods. The antibacterial effects of sucrose laurate (SL), ethylenediaminetetraacetate (EDTA) and tert-butylated hydroxyanisole (BHA) were evaluated alone and in combination at several concentrations in trypticase soy broth (TSB), TSB+fat (1-5%, w/v) and skim milk. Results indicated that the inhibitory properties of SL+EDTA+BHA (SLEB) were greater than SL or BHA. In broth (TSB) containing up to 0.1% (v/v) SLEB, *Staphylococcus aureus* and *Listeria monocytogenes* did not grow during 20 days of storage at 10 and 25°C, respectively. At a lower concentration of SLEB (0.05%, v/v), *Salmonella typhimurium* was inhibited during 24 h of storage at 25°C. In two model food systems, skim milk and TSB with added fat, SLEB (0.1%) effectively controlled the growth activities of *L. monocytogenes* in skim milk; viable cell counts decreased 10 fold during a 20-day storage period at 25°C. In TSB containing 1-5% fat, *L. monocytogenes* overcame the initial inhibitory effects of SLEB and grew after a 12-15 day lag at 25°C. Results from this study demonstrated that a systems approach and combination strategy to prevent food spoilage may have more flexibility and utility than the use of single inhibitors. Such combinations of food preservatives may then be used together with physical processes (e.g., pressurized CO<sub>2</sub>, heat, microwave) to produce more fresh-like but shelf-stable ration components.

BIOGRAPHY OF PRESENTER: Anthony Sikes, Ph.D.

PRESENT ASSIGNMENT: Research Microbiologist, Food Engineering Directorate

PAST EXPERIENCE: Assistant Prof., Dept. of Food Sci. & Animal Industries, Alabama A&M Univ., Huntsville, AL

DEGREES HELD: B.S., Biology, Lane College; M.S., Biology, Ill. Institute of Technology; Ph.D., Food Sci. & Technology, Univ. of Nebraska

ANTIMICROBIAL ACTIVITY OF SUCROSE LAURATE, EDTA  
AND BHA ALONE AND IN COMBINATION

Anthony Sikes, Dr. , Steve Whitfield, Mr.  
U. S. Army Natick RD&E Center  
Natick, MA 01760

INTRODUCTION

The concept of using combinations of multifunctional food-grade inhibitors to control microbial activity in food, i.e., "systems approach", was first proposed by Kabara (1981). The basic idea of the systems approach to food preservation is the creation of a microbially hostile environment which precludes the proliferation of undesirable microorganisms (Kabara, 1979). The advantage of the systems approach is that presently approved multifunctional food materials, which are either approved food additives or Generally Recognized As Safe (GRAS), e.g., parabens, sorbic acid, etc., can be used to design preservation systems that will meet specific microbiological needs.

In the system described by Kabara (1979), three food-grade substances were used: a fatty acid (monolaurin), food-grade phenolic antioxidants (BHA/BHT) and chelator (EDTA). Each component of the triad has a specific effect on the microbial cell. Monolaurin is effective against gram-positive bacteria and yeast (15-200 ppm), and BHA/BHT inhibits both gram-negative and gram-positive bacteria (Jay, 1986). It is believed that lipophilic agents (fatty acids and phenolics) prevent microbial growth by inhibiting the transport of substrate molecules into the cell (Freese et al., 1973). The third component of the triad is EDTA, which has minimal antimicrobial activity but is proposed to function by enhancing the germicidal activity of the two lipophilic substances (perhaps by competing with cell membranes for stabilizing calcium ions).

In the present investigation, a modified version of Kabara's combination preservation system was evaluated. Multifunctional sucrose laurate (SL) was substituted for monolaurin while the other two components remained unchanged. Studies have shown that SL inhibits both gram-negative and gram-positive bacteria (Conley and Kabara, 1973; Kato and Arima, 1971).

The objective of this investigation was to evaluate the antimicrobial activity of sucrose laurate, EDTA and BHA as a combination and as individual components in laboratory media and model food systems.



## METHODS

Preparation of cultures

Cultures of *Listeria monocytogenes* (Scott A), *Staphylococcus aureus* (A-100) and *Salmonella typhimurium* were all obtained from the culture collection of the Microbiology section, U.S. Army RD&E Center, Natick, MA. Cultures were maintained on trypticase soy agar (TSA; Difco, Detroit, MI) slants and stored at 1-4°C. Bimonthly transfers were made to maintain viably active cultures. Before each experiment, cultures were activated by transferring a loopful of the stock culture to freshly prepared trypticase soy broth (TSB) and grown quiescently for 24 h at 30°C. This procedure was repeated twice before cells were harvested.

Inocula were prepared by harvesting cells from growth media (centrifuged at 3,000 x g for 15 min at 10 °C; TSB), washing (3x) with 0.1% peptone water (Difco) and resuspending cells in 0.1% peptone water to the original growth media volume (100 ml). Subsequently, the culture density was determined by measuring the absorbance at a wavelength of 600 nm and relating it to a previously prepared standard curve.

Additives

Stock solutions of sucrose laurate (L-1695; Mitsubishi-Kasei America Inc., White Plains, NY) and EDTA (disodium ethylenediaminetetraacetate; Fisher Scientific Co., Fair Lawn, NJ) were prepared by suspending 1 g in 10 ml of distilled H<sub>2</sub>O (10 %, w/v). BHA (2[3]-t-butyl-4-hydroxyanisole; Sigma Chemical Company, St. Louis, MO) was prepared by suspending 1 g in 10 ml of absolute ethyl alcohol (Quantum Chemical Corp., Tuscola, IL). After preparation, all samples were stored in tightly capped screw-cap tubes at 1-4°C until used.

Preparation of growth media

Trypticase soy broth (Difco) was the basic growth media for all antimicrobial testing except when skim milk was used as the test medium. To each flask (250 ml screw-cap Erlenmeyer flasks) containing 100 ml of media (TSB), an appropriate volume of additive(s) was added, pH was adjusted to 6.8-6.9 and sterilized at 121°C for 15 min. When experiments were done with BHA, all control samples received a volume of ethyl alcohol equivalent to the volume used in the test sample(s).

The preparation of TSB with fat was similar to the preparation of TSB+antimicrobial (described above) except three levels of fat (1, 2.5 and 5% Mazola<sup>TM</sup> corn oil) and 0.5% Tween<sup>TM</sup> 80 [polyoxyethylene (20) sorbitan monooleate; Fisher Scientific Co., Fair Lawn, NJ] was added as a dispersing agent before sterilizing at 121°C for 15 minutes. Similarly, control samples received an equivalent amount of Tween 80 before sterilizing.

## SIKES & WHITFIELD

Bacto-skim milk (Difco) was prepared according to the directions given by Difco. SL+EDTA+BHA (SLEB) was the only additive used in skim milk. The pH of skim milk (6.4) was not adjusted before sterilizing.

### Bacterial growth

In screw-cap flasks (Erlenmeyer, 250 ml) containing 100 ml of growth media (TSB, TSB+fat or skim milk) plus additive(s), 1 ml of the washed cell suspension of the test organism was added ( $\sim 10^2$ - $10^3$  cfu/ml). Samples were incubated quiescently in a Hotpack incubator (Hotpack Corp., Philadelphia, PA) at 25°C for 0-24 h. Growth was monitored by removing an appropriate aliquot (1 ml) at 2 or 3 h intervals, serially diluting in 9 ml blanks of sterile 0.1% peptone water and surface plated (bent glass rod) on TSA. Inoculated plates were incubated at 30°C for 24 h before colonies were counted.

### Minimum inhibitory concentrations (MIC) of SLEB

The procedure used to determine the amount of SLEB required to inhibit *S. typhimurium*, *S. aureus* and *L. monocytogenes* was similar to the procedure described by Bargiota et al. (1987). Washed and resuspended (0.1% peptone water) cells of the test organisms were serially diluted through  $10^{-8}$ , and 0.1 ml portions of the  $10^{-3}$  and  $10^{-6}$  dilutions were spread-plated on TSA plates in triplicates. TSA-SLEB plates were prepared by adding 1 ml of a 10% stock solution of SLEB (1:1:1, w/v) to 200 ml of melted TSA media and sterilizing at 121°C for 15 min. SLEB concentrations ranged from 50-500 ppm.

### Statistical analysis

Differences in microbiological counts were examined for significance by analysis of variance using the Statgraphics program (Statistical Graphics Corp., Rockville, MD). Data presented are the mean  $\log_{10}$  colony-forming units of two replications with duplicate subsamples. Significant differences ( $p < 0.05$ ) among treatment means were separated by Duncan's multiple-range test.

## RESULTS AND DISCUSSION

Results indicated that the minimum inhibitory concentrations (MICs) of SLEB (sucrose laurate+EDTA+BHA, 1:1:1) required to prevent the growth of *S. aureus*, *L. monocytogenes* and *S. typhimurium* on TSA plates at 30°C and pH 7.0 were 200, 200 and 350 ppm, respectively. Although the MICs of individual components of SLEB were not determined in this study, it has been shown by other investigators that the MICs of BHA necessary to inhibit the growth of *L. monocytogenes* were 128-400 ppm (Chang and Branen, 1975; Payne et al., 1989), 100-400 ppm for *S. aureus* (Ayaz et al., 1980; Stern et al., 1979) and >400 ppm for *S. typhimurium* (Chang and Branen, 1975; Pierson et al., 1980). Limited data are available on the MICs of sucrose laurate (SL) required to inhibit vegetative cell growth; however, Beuchat (1980) found that sucrose esters of lauric acid at 100 ppm were ineffective against *Vibrio parahaemolyticus*. EDTA has no biocidal capability by itself but functions as a

potentiator in combination preservation systems (Kabara, 1981).

In trypticase soy broth (Difco, pH 6.9), 1000 ppm of SLEB totally inhibited the growth of *L. monocytogenes* at 25 °C for 12 days. However, at the same concentration (1000 ppm), SL was not inhibitory but did reduce the growth rate and increase the lag period. At 500 ppm (0.05%), SL exhibited no inhibitory activity against *L. monocytogenes*, but did reduce the growth rate during the 12-day storage period (Fig. 1). The difference between the growth of *L. monocytogenes* in TSB containing two concentrations of SL (500 and 1000 ppm) was not significant ( $p > 0.05$ ) but was significantly different from growth in SLEB ( $p < 0.05$ ).

The growth of *L. monocytogenes* in two model food systems containing 1000 ppm SLEB, skim milk (pH 6.4) and TSB with 1-5% fat (pH 6.9), was evaluated. During 20-day storage at 25°C, results indicated that in skim milk *L. monocytogenes* lost cell viability,  $10^3$  to  $10^{2.5}$  cfu/ml (Fig. 2). During a comparable storage period at 25°C, *L. monocytogenes* was totally inhibited when grown in the presence of 1000 ppm of SLEB; however, in the presence of increasing concentrations of fat (1, 2.5 and 5% corn oil), SLEB, at all levels, caused slight decreases in cell viability during the first 12 days of storage ( $< 1$  log reduction). After this initial period, growth began in the sample containing the highest fat level (5%), followed by growth in the 2.5% and 1% fat-containing samples at 15 days of storage (Fig. 3). The difference between growth in the presence of the three fat levels was not significant ( $p > 0.05$ ), but growth in the presence of SLEB was significantly different ( $p < 0.05$ ) from the growth in media containing fat.

It was demonstrated in this study that the MIC of SLEB required to inhibit *S. typhimurium* was 350 ppm (0.035%, Table 1). In TSB containing 250 ppm of SLEB (pH 6.9), *S. typhimurium* was partially inhibited (Fig. 4). Initially, cell viability decreased during the first 4 h of storage at 25°C ( $10^7$  to  $10^4$  cfu/ml) but increased rapidly to  $> 10^7$  cfu/ml during the next 20 h of storage; however, in the presence of 500 ppm of SLEB, cell growth was totally inhibited (Fig. 4). In the presence of a similar concentration of BHA (500 ppm), *S. typhimurium* grew during the first 4 h of storage (25 °C) to  $> 10^8$  cfu/ml; but, during the next 4 h, cell viability decreased to  $10^6$  cfu/ml, then, at 10 h, began an accelerated-growth period over the next 16 h. The difference between the growth of *S. typhimurium* in media containing 250 ppm of SLEB and 500 ppm of BHA was not significant ( $p > 0.05$ ). Both differed significantly from growth in media containing 500 ppm of SLEB ( $p < 0.05$ ).

## *L. monocytogenes*

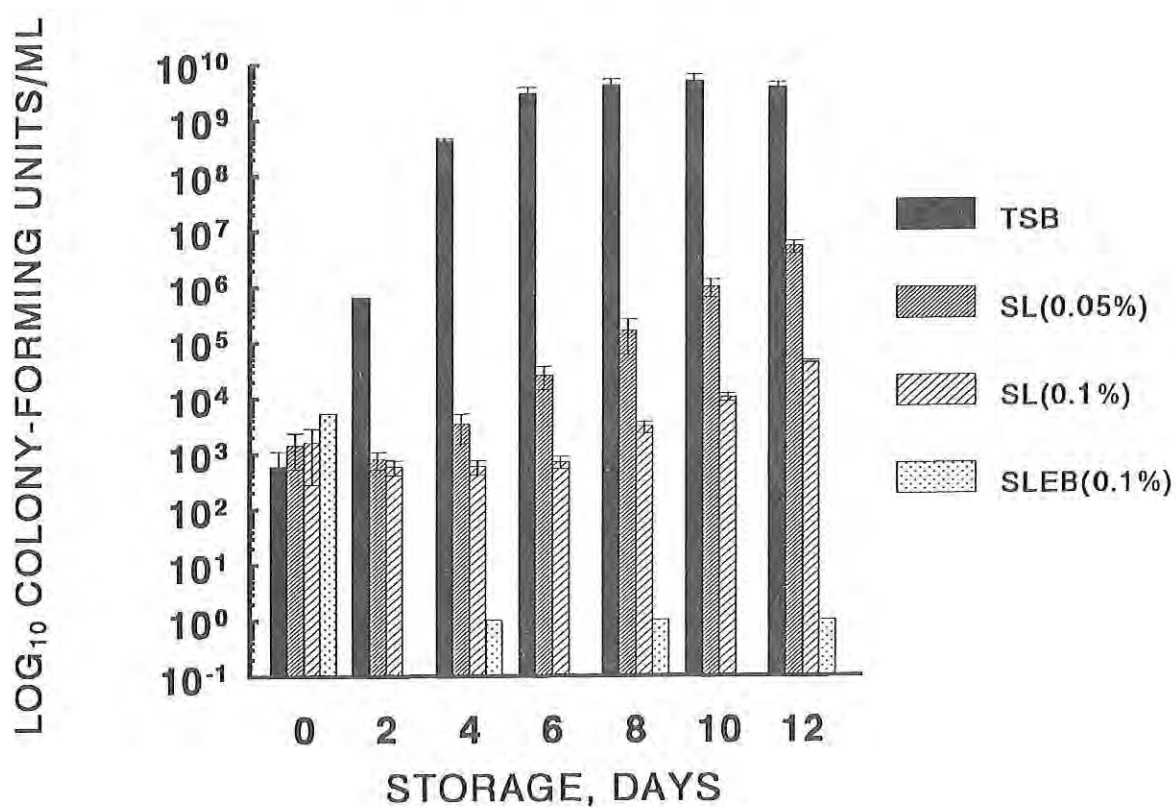


Figure 1. Growth of *L. monocytogenes* in TSB, TSB+0.05 and 0.1% SL (sucrose laurate,v/v) and TSB+0.1% SLEB (sucrose laurate+EDTA+BHA, v/v) at 25°C and pH 6.9. Bar heights represent the mean of two experiments (with duplicate subsamples). Error bars represent the standard deviation of four experimental values.

*L. monocytogenes*

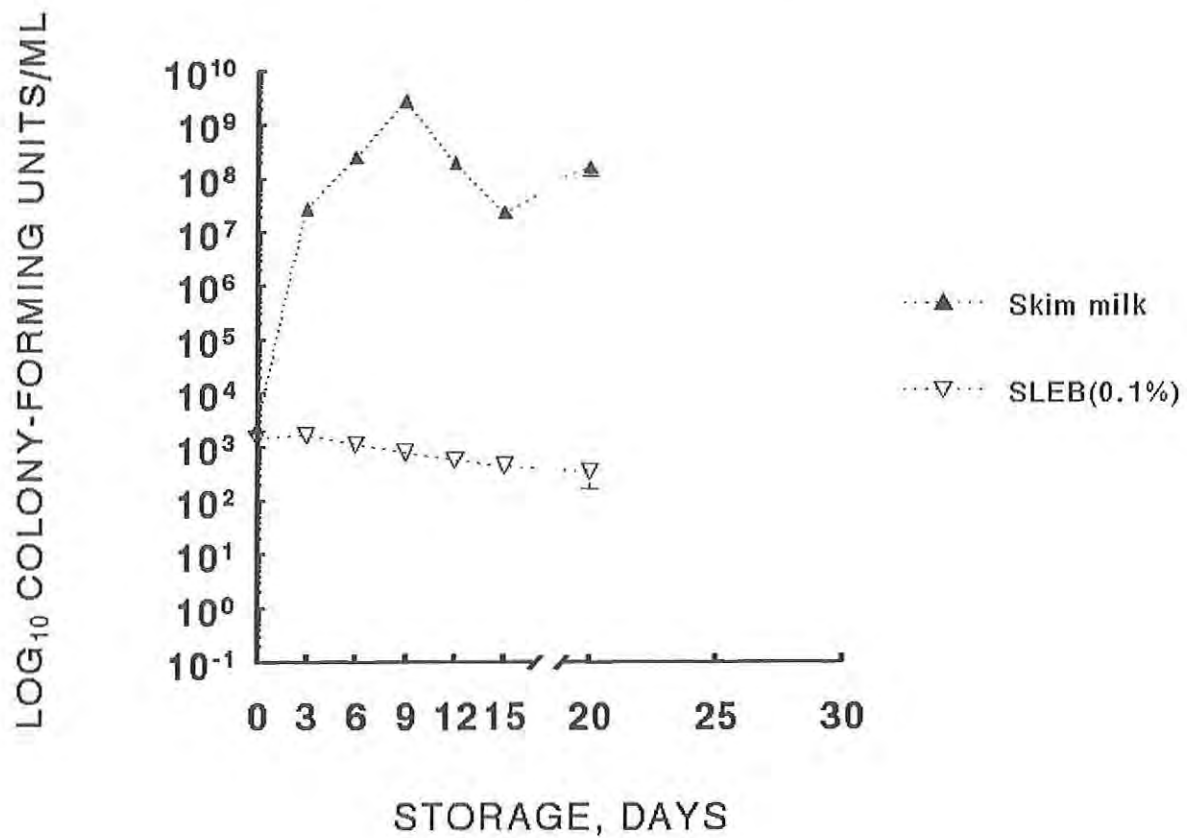


Figure 2. Growth of *L. monocytogenes* in skim milk and skim milk containing 0.1% SLEB (v/v) at 25 C and pH 6.4. Data points represent mean values from two experiments (with duplicate subsamples). Error bars indicate the standard deviation of four experimental values.



## *L. monocytogenes*

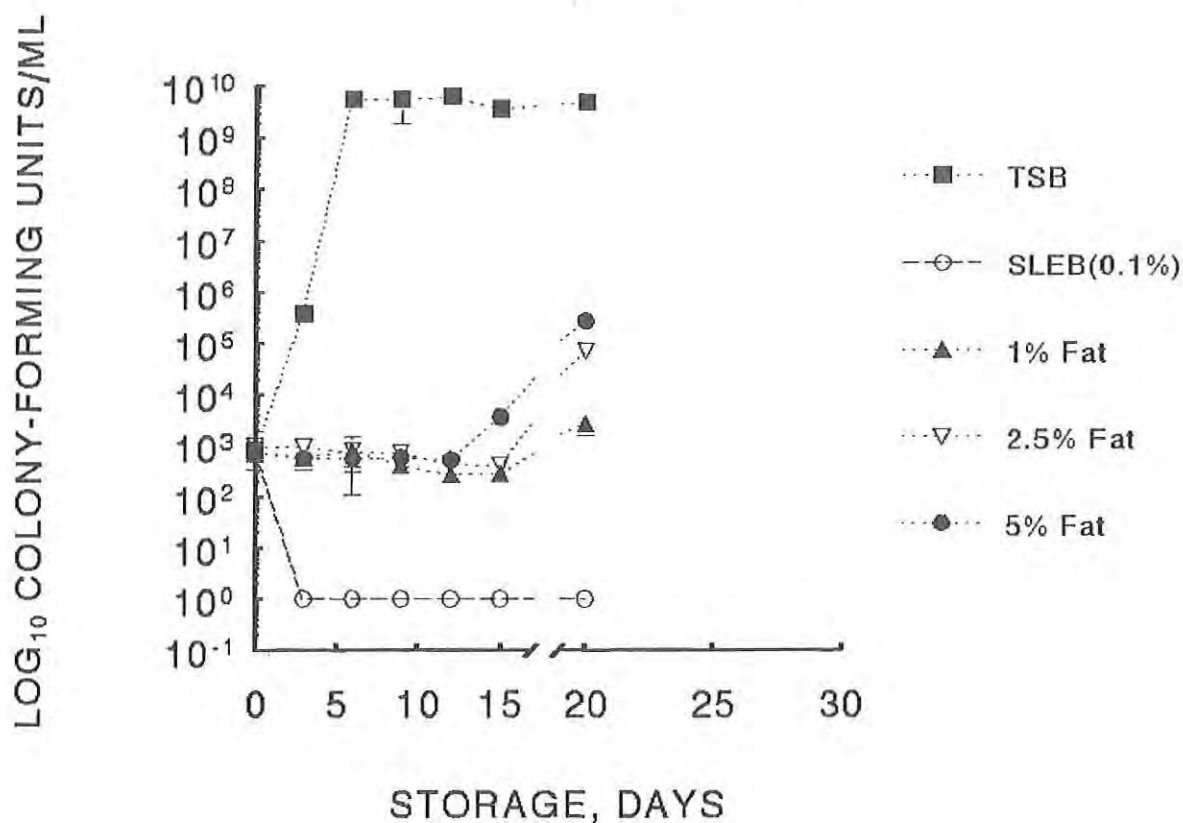


Figure 3. Growth of *L. monocytogenes* in TSB, TSB+SLEB (0.1%, v/v) and TSB+SLEB (0.1%, v/v)+1, 2.5 and 5% corn oil (w/v) at 25°C and pH 6.9. Data points represent mean values from two experiments (with duplicate sub-samples). Error bars indicate the standard deviation of four experimental values.



TABLE 1 . Minimum inhibitory concentrations<sup>a</sup> (MIC) of sucrose laurate+ EDTA+BHA (SLEB)<sup>b</sup> required to prevent the growth of three foodborne bacteria in trypticase soy broth media

| ORGANISM                | MIC <sup>c</sup> (ppm) |
|-------------------------|------------------------|
| <i>S. aureus</i>        | >200 (0.02%)           |
| <i>L. monocytogenes</i> | >200 (0.02%)           |
| <i>S. typhimurium</i>   | >350 (0.035%)          |

<sup>a</sup> Minimum inhibitory concentration was the lowest concentration of SLEB required to inhibit the growth of the specified organism for 48 h at 30°C

<sup>b</sup> SL+EDTA+BHA, 1:1:1 (w/v)

<sup>c</sup> Values shown represent the average MIC (ppm) of three tests

# *S. typhimurium*

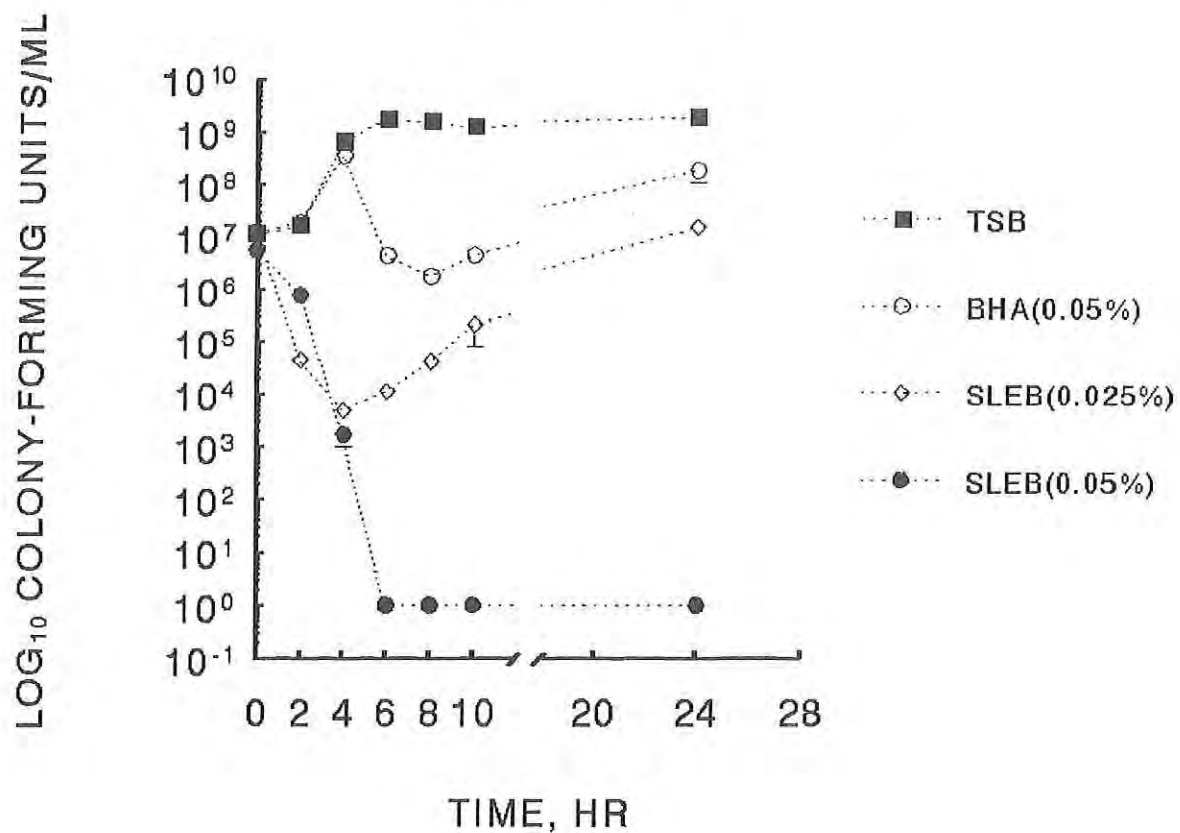


Figure 4. Growth of *S. typhimurium* in TSB, TSB+BHA (0.05%, v/v) and SLEB (0.025 and 0.05%, v/v) at 25 C and pH 6.9. Data points represent mean values from two experiments (with duplicate subsamples). Error bars indicate the standard deviation of four experimental values.

# *S. aureus*

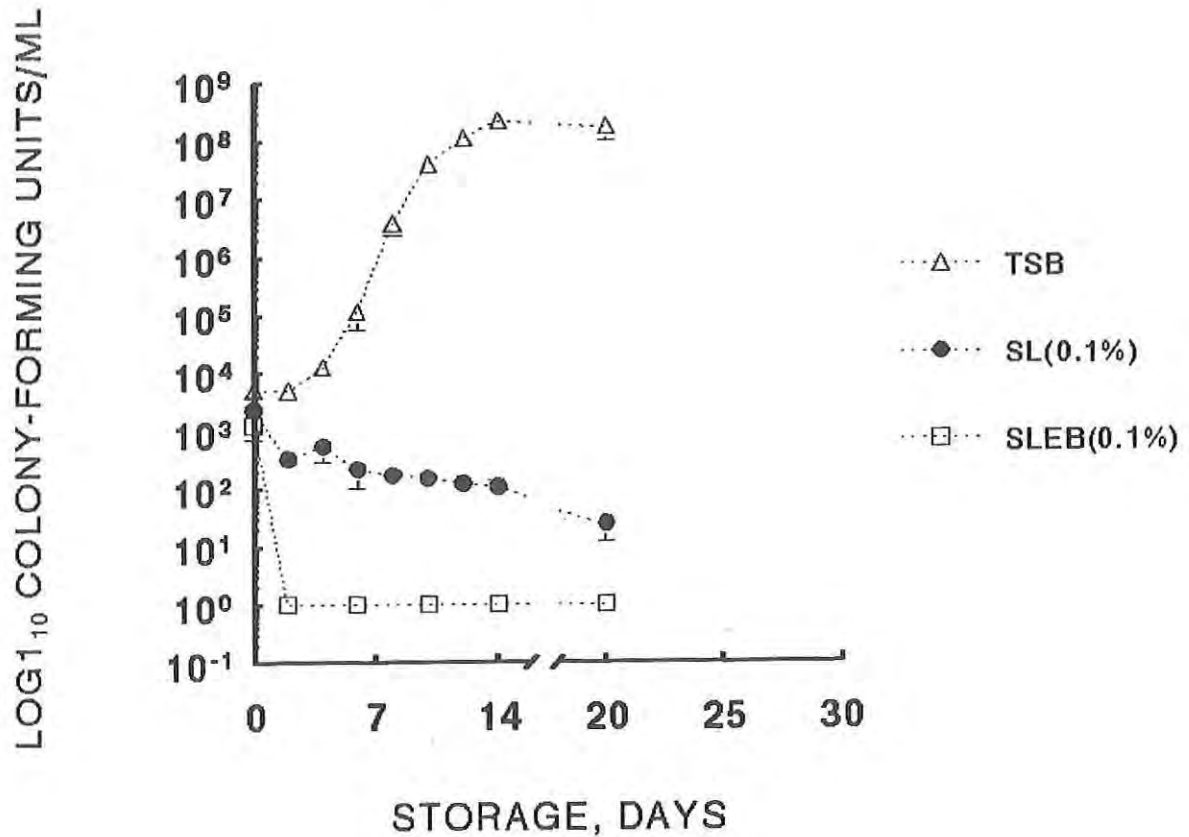


Figure 5. Effect of SL (sucrose laurate, 0.1%; v/v) and SLEB (sucrose laurate+EDTA+BHA, 0.1%; v/v) on the growth of *S. aureus* in TSB at 10°C and pH 6.9. Data points represent mean values from two experiments (with duplicate subsamples). Error bars indicate the standard deviation of four experimental values.

During 20 days of storage (10°C, pH 6.9) in TSB containing 1000 ppm of SLEB (0.1%), *S. aureus* was totally inhibited (Fig. 5). Under the same culture and storage conditions, it was also observed that sucrose laurate (SL), at a concentration 1000 ppm, caused a gradual decrease in cell viability of *S. aureus* ( $10^3$  to  $<10^2$  cfu/ml). Growth of *S. aureus* in TSB containing SLEB and SL was significantly different ( $p < 0.05$ ).

Future military ration items may include highly perishable, minimally processed, refrigerated food products ("new generation foods"), which are food products that receive less than the full commercial sterility treatment; thus new approaches must be considered to assure product safety. Unlike traditional refrigerated foods, such as ready-to-eat meats and raw meats, minimally processed (partially processed) products, such as fresh salads and refrigerated cooked meat, may not have a preservative system other than refrigeration (Corlett, 1989). If products are temperature abused or the refrigeration system fails, products could become susceptible to the growth of foodborne pathogens. Incorporation of multiple barriers (e.g., combination preservative systems, reduced  $A_w$ , modified atmospheres, etc.) into the formulation of minimally processed food products, will minimize microbial activity and increase microbiological safety (NFPA, 1988)

### CONCLUSIONS

This study demonstrated that the combination preservative system of SLEB was more inhibitory against the test organisms used in this study than the single inhibitory substances, sucrose laurate (SL) or BHA. Results also suggested that additional inhibitory advantages could be gained from a combination preservation system by creating a more hostile microenvironment through chemical or physical manipulations, such as, pH,  $A_w$ , thermal processing, refrigeration and modified atmospheres.

## REFERENCES

- Ayaz, M., L. O. Luedecke, and A. L. Branen. 1980. Antimicrobial effect of BHA and BHT on *Staphylococcus aureus*. J. Food Prot. 43: 4-6.
- Bargiota, E., E. Rico-Munoz, and P. M. Davidson. 1987. Lethal effect of methyl and propyl parabens as related to *Staphylococcus aureus* lipid composition. Intl. J. Food Microbiol. 4: 257-266.
- Beuchat, L. R. 1980. Comparison of anti-vibrio activities of potassium sorbate, sodium benzoate and sucrose esters of fatty acids. Appl. Environ. Microbiol. 39: 1178-1182.
- Chang, H. C. and A. L. Branen. 1975. Antimicrobial effects of butylated hydroxyanisole (BHA). J. Food Sci. 40: 349-351.
- Conely, A. J. and J. J. Kabara. 1973. Antimicrobial action of esters of polyhydric alcohols. Antimicrob. Agents Chemother. 4: 501-506.
- Corlett, D. A., Jr. 1989. Refrigerated foods and use of hazard analysis and critical control point principles. Food Tech. 43: 91-94.
- Freese, E., C. W. Sheu and E. Galliers. 1973. Function of lipophilic acids as antimicrobial food additives. Nature. 241: 321-325.
- Jay, J. M. 1986. Food preservation with chemicals. In: *Modern food microbiology*. New York: Van Nostrand Reinhold Company Inc: 1986: 259-296.
- Kabara, J. J. 1979. Multi-functional food-grade preservatives in cosmetics. Drug and Cosmetic Ind., Oct., pp., 60-145.
- Kabara, J. J. 1981. Food-grade chemicals for use in designing food preservation systems. J. Food Prot. 44: 633-647.
- Kato, A. and K. Arima. 1971. Inhibitory effect of sucrose ester of lauric acid on the growth of *Escherichia coli*. Biochem. Biophys. Res. Comm., 42(4): 596-601.
- NFPA/RFMCC. 1988. Safety considerations for new generation refrigerated foods. Dairy and Food Sanit. 8(1): 5-7.

SIKES & WHITFIELD

Payne, K. D., E. Rico-Munoz, P. M. Davidson. 1989. The antimicrobial activity of phenolic compounds against *Listeria monocytogenes* and their effectiveness in a model milk system. J. Food Prot. 52:151-153.

Pierson, M. D., L. A. Smoot, and K. R. Vantassel. 1980. Inhibition of *Salmonella typhimurium* and *Staphylococcus aureus* by BHA and propyl ester of p-hydroxybenzoic acid. J. Food Prot. 43: 191-194,

Stern, N. J., L. A. Smoot, and M. D. Pierson. 1979. Inhibition of *Staphylococcus aureus* growth by combinations of butylated hydroxyanisole, sodium chloride and pH. J. Food Sci. 44(3): 710-712.



**TITLE:** Contrast in Relative Effectiveness of Antioxidants in Bulk Versus Dispersed Lipid Systems: Validation of the Polar Paradox in Choice of Appropriate Antioxidants  
William L. Porter, Dr. and Black, E. D., Dr.

**ABSTRACT:** The change in emphasis in autooxidation protection from bulk fats and oils as military ration components to the highly dispersed lipids in the emulsions and membranes of pre-processed "fast" foods has made obsolete the mere empirical selection of antioxidants. We have evolved broad, scientifically based principles for choice of antioxidants appropriate to the state of dispersion of the lipid. We report here on further validation of these principles, first developed for synthetic antioxidants in soybean oil and soy lecithin emulsions, in the areas of phenolic acids, tannins, flavonoids, tocopherols and ascorbic acid derivatives in the substrates freeze-dried milk and synthetic liposomes.

Briefly summarized, the polar paradox principle states that other things being equal, dry bulk (neat) oils and fats of the cooking and salad types have a low surface to volume ratio and are best protected by polar or hydrophilic antioxidants. Emulsions and membranes with a high surface to volume ratio require lipophilic, non-polar, or amphiphilic antioxidants with a low hydrophilic-lipophilic balance number.

This paradoxical reciprocal rule now has been shown to apply equally to synthetic and so-called natural occurring compounds with demonstrated antioxidant potential, including the tocopherols and ascorbic acid derivatives. Unfortunately, except for the tocopherols and carotenoids, naturally occurring antioxidant compounds tend preponderantly to be polar, and thus inappropriate to the current fast foods with dispersed lipids. This lack of lipophilic natural antioxidants is frustrating in the current "all-natural" consumer climate.

**BIOGRAPHY OF PRESENTER:** William L. Porter

**PRESENT ASSIGNMENT:** Research Chemist at the U.S. Army Natick Research, Development and Engineering Center, Food Engineering Directorate.

**PAST EXPERIENCE:** Meteorologist/Climatologist with Environmental Protection Research Division, Natick Laboratories from 1953-1962.

**DEGREES HELD:** PhD in Plant Biochemistry, Harvard University, 1962.  
Meteorologist, U.S. Army Air Force Aviation Cadet School, 1943.

Contrast in Relative Effectiveness of Food Antioxidants in  
Bulk Versus Dispersed Lipid Systems: Validation of the Polar  
Paradox In Choice of Appropriate Antioxidants

William L. Porter, Dr.  
Edward D. Black, Dr.  
U.S. Army Natick RD&E Center  
Natick, MA. 01760

What kind of antioxidant should a food scientist choose to protect one of the wide variety of military lipid-containing foods?

We report here on further validation of a rationale first advanced in 1980<sup>1</sup> and amplified in 1989<sup>2</sup> and 1991<sup>3</sup>, concerning choice of food antioxidants appropriate, on the one hand, to bulk oils and fats (low surface to volume ratio or LSV) or, in contrast, to the highly dispersed lipids in emulsions, or the membranes and fat cells of whole tissue foods (high surface to volume or HSV).

In brief, this rationale, the so-called polar paradox principle, states that, other things being equal, dry bulk (neat) oils and fats of the cooking and salad types (LSV) are best protected by more polar or hydrophilic antioxidants. Emulsions and membranes (HSV), whether in the liquid or dehydrated state, are better stabilized by lipophilic, nonpolar, or amphiphilic antioxidants with a low hydrophilic-lipophilic balance number (HLB). The principle, which was first hypothesized in the area of synthetic antioxidants, is now shown to apply to tannins, flavonoids, and to the tocopherols and ascorbic acid and their derivatives.

Autoxidation of lipids, whether enzymatically, photo-, or metal catalyzed, even with inert atmospheres and highly impermeable packaging, remains a problem in shelf life of military rations. The relative effectiveness of antioxidants in delaying this process varies widely, in a manner that our experiments and those of others suggests is a strong function of lipid dispersion and antioxidant polarity, among other parameters. The advent of more permeable biodegradable or recyclable plastics, such as might be used in the proposed polymeric container for TrayPack ration items, increases the need for viable antioxidants.

Food lipid exposures in the military have a wide range: storage of cooking and salad oils, frying with oils and fats, storage and use of mayonnaise and salad dressing emulsions, comminuted and reformed meats, baked goods, spray-dried milks and freeze-dried items. Many of the military ration items are similar to the convenience or "fast" foods in current domestic use. These often contain dispersed lipids predisposed by comminution and pre-cooking to autoxidation. Performance of antioxidants in this mode is often radically different from that in bulk oils and fats.

Historically, food scientists have developed much of the relative effectiveness data using bulk oils and fats.

This is because before the mid-Fifties, in the civilian sector, most of the food lipid was purchased and stored in bulk for subsequent use in cooking. In addition, antioxidant testing is simpler and faster in bulk exposures. Very often these results have been extrapolated uncritically from LSV to HSV situations like emulsions, micelles and membranes in whole tissue foods.

Certain definitions and explanations are needed for clarification.

Antioxidant. For the purpose of this paper an antioxidant will be considered as any acidic compound (thus embracing both phenols and ascorbic acid) which is usable in foods and can readily donate an electron or hydrogen atom to a peroxy or aryloxy radical to terminate a lipid peroxidation chain reaction or to regenerate a phenolic compound.

Antioxidant Effectiveness. Figures 1 and 2 show the essential features of the initiation and propagation of the chain reaction of autoxidation in an unsaturated lipid and its termination by an antioxidant, whose regeneration by a second antioxidant is also indicated. Tests to determine the relative effectiveness of antioxidants in bulk oils include, among others, the Active Oxygen Method, the Schaal Oven Test (45-60°C), and room temperature tests. In the first, oxygen is bubbled into an oil heated to 100°C; in the second and third, oils or foods are left open to air at the stated temperatures. Endpoint may be peroxide value or UV absorption at 234 nm, the wavelength of conjugated diene hydroperoxide. Results of these have shown sufficient agreement in rating relative antioxidant effectiveness that they will be cited without special identification<sup>4-6</sup>. Similarly, details of tests used in dispersed systems can be found in the cited references. A brief description of tests used by the writers will be furnished.

## LIPID AUTOXIDATION - INITIATION

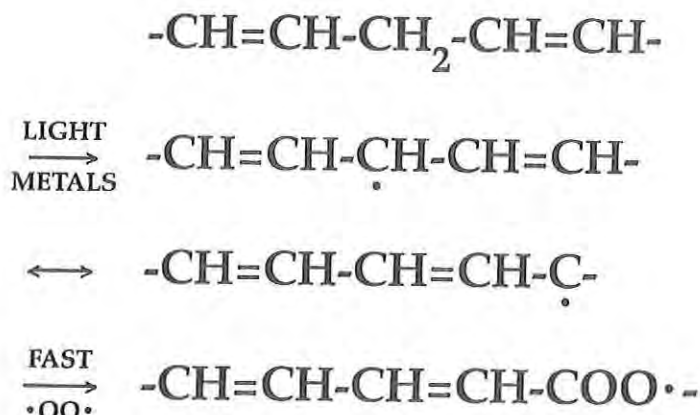
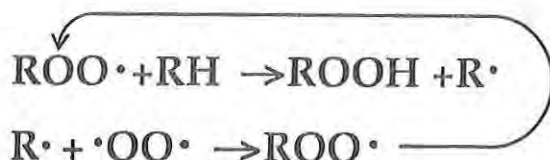


Figure 1. Lipid Autoxidation - Initiation.

## LIPID AUTOXIDATION - CHAIN PROPAGATION



## ANTIOXIDANT CHAIN TERMINATION



## ANTIOXIDANT SYNERGISTIC REGENERATION

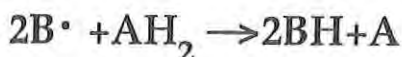


Figure 2. Lipid Autoxidation - Chain Propagation.

### Early Work With Dispersed Systems

This laboratory became aware of the paradoxical behavior of antioxidants during the Sixties when we first began working with lipid systems of high surface area to model synthetic and natural membrane protection by antioxidants<sup>7,8,9</sup>. Bishov and Henick worked with a freeze-dried carboxymethylcellulose system holding thin layers of stripped corn oil and focussed their attention on natural antioxidants from spices and on protein hydrolysates, following oxygen uptake with gas partition chromatography of the headspace gas<sup>7</sup>. Porter initially worked with linoleic acid monolayers on silica gel, again using gas partition chromatography<sup>8</sup>. Later he focussed on freeze-dried red blood cell membranes, again using gas partition. It became clear that the relative effectiveness of antioxidants was greatly different in the HSV array from that in the ISV configuration as in bulk oils.

### Liposomes and Polyamide Fluorescence

Vesicles and emulsions formed from dispersed phospholipids have been used as membrane models for pro- and antioxidant testing<sup>10-17</sup>. In assaying the relative effectiveness of antioxidants in dry oils and lecithin liposomes and emulsions, we have used a front-face fluorescence method, which measures a fluorophore formed on polyamide powder films coated on glass or plastic supports when exposed to the volatiles from oxidizing lipids<sup>18-20</sup>.



Polyamide fluorescence has been used in the work reported here to assay the relative effectiveness of antioxidants in cobalt-accelerated soy lecithin emulsions. Results are contrasted with those in bulk vegetable oils reported in the literature.

#### MATERIALS AND METHODS

Details of procurement and purification of soy lecithin and antioxidants have been reported elsewhere, as have the methods of oxidation and its assessment<sup>2</sup>. Antioxidants were tested for purity and lipophilic solvent mobility by melting point and thin-layer chromatography (TLC). The latter was carried out on heat-activated silica with solvent systems (1) chloroform (2) chloroform/methanol (19/1), and (3) chloroform, methanol, acetic acid (19/1/0.1).

In brief, crude soybean lecithin, double-bleached with hydrogen peroxide and benzoyl peroxide (which we showed destroyed most endogenous tocopherols) and containing about 35% triglyceride, was sonicated after dispersion in deionized water buffer (13 mM phosphate, pH 5.5). Sonication was carried out at maximum power for 20 minutes under a stream of nitrogen. Two mL of a hematin solution in KOH was added at zero time to give a phosphatide/hematin ratio of 100/1. Final pH was 5.5-5.6 and concentration of lecithin was 3 mg/mL.

Antioxidant tests were conducted in 9 x 1 cm Pyrex<sup>(R)</sup> petri dishes; to the undersurface of the dishes' lids polyamide-coated terephthalate plastic plates were attached powder side down by double-faced transparent tape. The plates, 2 x 3 cm, were cut from standard 20 x 20 cm thin-layer chromatography plates. In the typical procedure, 50 mL of the lecithin dispersion was treated with 0.5 mL of ethanol containing 0.15 mg of antioxidant. Controls were 50 mL of dispersion and 0.5 mL of ethanol. The dispersions were bubbled with glass-filtered air for 30 minutes after antioxidant addition. Hematin was added at zero time and 25 mL of the mixture was placed in each petri dish. Incubation was in a 65°C draft oven, from which the covered dishes, with attached polyamide strip, were sampled every 30 minutes by removing each dish to a room temperature dark cupboard, substituting a labeled petri lid for the test lid, and measuring the fluorophore intensity in a Hitachi solid sample attachment for an MPF-2A Hitachi Perkin-Elmer fluorescence spectrophotometer. The Baird Atomic Model SF-1 and the Spex Fluorolog instruments have also been used and are equally satisfactory.

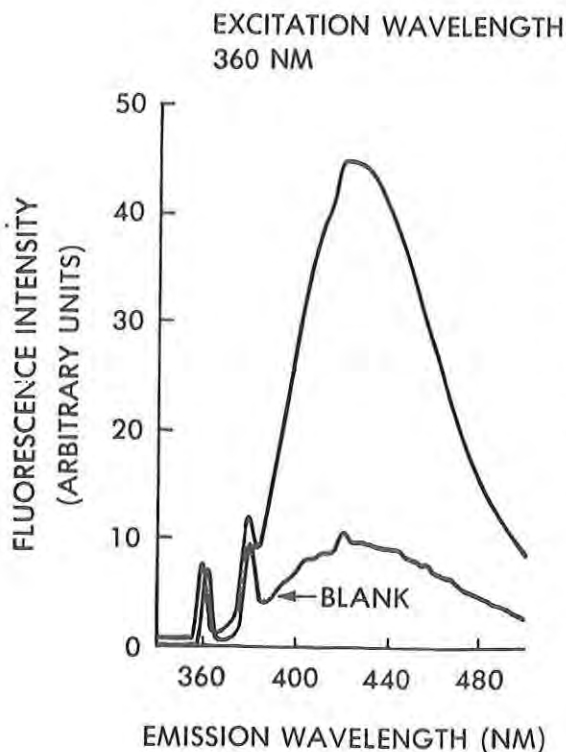


Figure 3. Oxidative polyamide fluorescence spectrum of oxidized soy lecithin emulsions 65°C (Reproduced with permission from Ref. 2).

Figure 3 shows a typical front-face polyamide plate fluorescence spectrum from an oxidized soy lecithin dispersion at pH 5.6 and 65°C. The blank is the spectrum from a plate exposed similarly but without lipid. A 390 nm filter is used in the emission light path, and the spectrum is scanned through the excitation wavelength, 360 nm. The residual scatter peak at 360 nm is used as an internal reference and the fluorescence index (FI) is the ratio  $I(\text{emission})/I(\text{scatter at 360 nm})$ . Ratio methods of expressing intensity are always more dependable in front face fluorescence measurements than simple intensity, even though the instrument is repeatedly calibrated with 1 ppm quinine sulfate in 0.1N  $\text{H}_2\text{SO}_4$ . Fluorescence indices are measured at every sampling period for the blank, the control without antioxidant, and the treated sample. Relative mean deviation of two replicates (after repositioning the plate) is  $\pm 5\%$ .

## RESULTS

### Antioxidant Evaluation in Soy Lecithin Emulsions

Figure 4 illustrates the kinetics of fluorescence index development for soy lecithin emulsions with added quercetin, a polar flavonol, and Figure 5, with added nonpolar BHA (butylated hydroxyanisole), both at 0.1%. Shown in both is the typical autooxidative induction period, however short, which occurs with or without added antioxidant. It is noteworthy that quercetin is a much more effective inhibitor of autooxidation than BHA in dry vegetable oils, a nonpolar medium. The situation is clearly reversed here.

For quantification, a protective index was used, called relative effectiveness (REFF). It is defined as  $(IP_A/IP_C) - 1$ , where  $IP_A$  is induction period with added antioxidant and  $IP_C$  that without. Induction



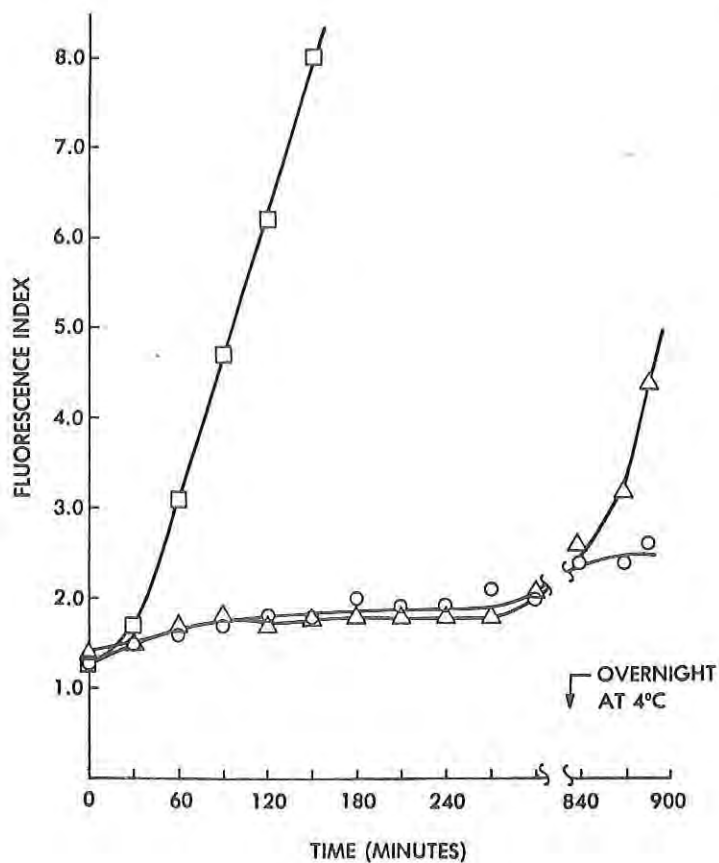
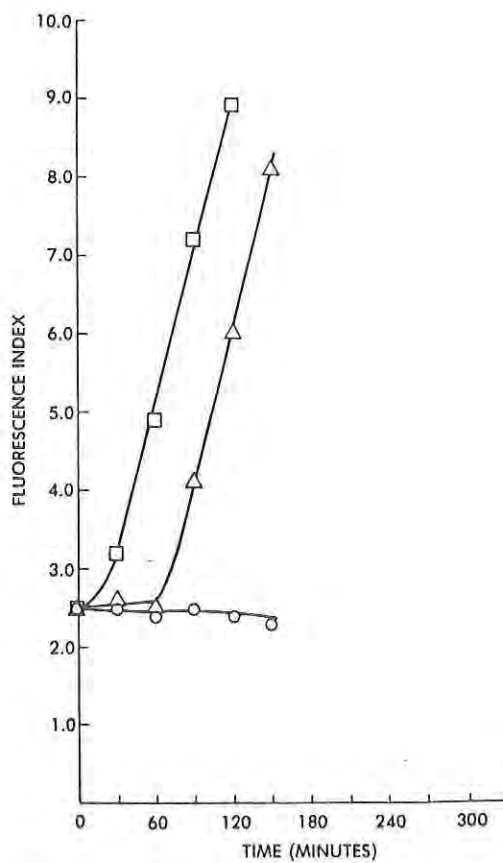


Figure 4. Antioxidant evaluation by oxidative polyamide fluorescence from soy lecithin emulsions - (o) blank; (□) lecithin plus hematin; (Δ) lecithin-hematin plus 0.1% quercetin, 65°C (Reproduced with permission from Ref. 2).

Figure 5. Antioxidant evaluation by oxidative polyamide fluorescence from soy lecithin emulsions - (o) blank; (□) lecithin plus hematin; (Δ) lecithin-hematin plus 0.1% BHA, 65°C (Reproduced with permission from Ref. 2).



period was defined graphically as the number of minutes between zero time and the intersection of the tangent to the linear portion of the curve corresponding to rapid phase fluorescence development with the curve for the blank.

In the work reported here we have evaluated 16 antioxidants, both in individual experiments and, alternatively, with a common repeated control substance like BHA. Total number of tests was 71. The average number for a given antioxidant was 5, was always greater than 3 and as high as 12 for critical compounds, or those with high variability. Table 1 shows mean REFF and standard deviation for the eight most effective antioxidants in soy lecithin dispersions, and Table 2 the same for the eight least effective ones, based on the highest three values. REFF for the tables is  $IP_A/IP_C$ . The high coefficient of variation for some of the alkyl gallates, topanol and TBHQ is unexplained.

Table 1. Relative Effectiveness of Most Effective Antioxidants in Soy Lecithin Emulsions.  $REFF = IP_A/IP_C$ .

| Compound             | Mean <sup>a</sup> | Standard Deviation | Coefficient Of Variation |
|----------------------|-------------------|--------------------|--------------------------|
| BHA                  | 32                | ±7.8               | 0.24                     |
| BHT                  | 21                | 8.1                | 0.39                     |
| ETHOXYQUIN (SAN)     | 13                | 5.6                | 0.43                     |
| PROPYL GALLATE (PG)  | 11                | 3.8                | 0.35                     |
| OCTYL GALLATE (OG)   | 11                | 7.9                | 0.72                     |
| DODECYL GALLATE (DG) | 10                | 6.0                | 0.60                     |
| TOPANOL (TOP)        | 10                | 6.3                | 0.63                     |
| ETHYL GALLATE (EG)   | 7                 | 5.8                | 0.78                     |

<sup>a</sup>Highest three values

Table 2. Relative Effectiveness of Least Effective Antioxidants in Soy Lecithin Emulsions.  $REFF = IP_A/IP_C$ .

| Compound                        | Mean <sup>a</sup> | Standard Deviation | Coefficient Of Variation |
|---------------------------------|-------------------|--------------------|--------------------------|
| TBHQ                            | 4.9               | ±4.4               | 0.90                     |
| QUERCETIN (Q)                   | 4.1               | 1.7                | 0.41                     |
| METHYL GALLATE (MG)             | 3.2               | 0.4                | 0.13                     |
| HYDROQUINONE (HQ)               | 3.2               | 0.9                | 0.28                     |
| GALLIC ACID (GA)                | 1.4               | 0.3                | 0.21                     |
| CAFFEIC ACID (CA)               | 1.4               | 0.2                | 0.14                     |
| CHLOROGENIC ACID (CHLA)         | 1.4               | 0.1                | 0.14                     |
| POLY AO <sup>TM</sup> 79 (POLY) | 1.1               | 0.2                | 0.18                     |

<sup>a</sup>Highest three values

Figure 6 shows the mean REFF of all available trials for the tested antioxidants in soy lecithin dispersions, as opposed to that of the three highest values shown in the tables. REFF is here defined as  $(IP_A/IP_C)-1$ , in contrast to the definition for the tables. Also shown are REFFs based on the AOM in dry oils, largely derived from vegetable sources. Table 3 indicates the literature sources consulted for the latter values.

Clearly shown in Figure 6 is the roughly reciprocal relationship for a series of compounds between their effectiveness in polar (dispersion) versus nonpolar (dry oil) environments.

In Figure 7, the REFF in lecithin dispersions is plotted against a rough measure of polarity, the  $R_f$  value in silica gel TLC chromatography using a lipophilic solvent, chloroform/methanol/acetic acid (19/1/0.5). As before, the relationship is not rigidly linear, but, in general, the compounds with high  $R_f$  (less polar) tend to be more effective in dispersions. A notable exception is Poly AO 79, a polymeric antioxidant, which shows high mobility in TLC and has no activity in our dispersions.

Table 3. Literature Sources Consulted for Values of Antioxidant Relative Effectiveness in Bulk Dry Oils

| <u>Antioxidant<sup>a</sup></u> | <u>Substrate</u>                                     | <u>Source Reference</u> |
|--------------------------------|--|-------------------------|
| BHT                            | Safflower oil  | 5                       |
| BHT                            | Lard, cottonseed oil,<br>hydrogenated cottonseed oil | 34                      |
| SAN                            | Safflower oil  | 5                       |
| BHA                            | Safflower oil  | 5                       |
| BHA                            | Lard, cottonseed oil,<br>hydrogenated cottonseed oil | 34                      |
| TOP                            | Sunflower seed oil                                   | 21                      |
| DG, OG, PG                     | Cottonseed oil                                       | 26                      |
| PG                             | Safflower oil  | 5                       |
| PG                             | Lard, cottonseed oil,<br>hydrogenated cottonseed oil | 34                      |
| PG                             | Oat oil  | 29                      |
| Q                              | Ethyl linoleate                                      | 22                      |
| TBHQ                           | Safflower oil  | 5                       |
| HQ                             | Safflower oil  | 5                       |
| HQ                             | Lard, cottonseed oil,<br>hydrogenated cottonseed oil | 34                      |
| CA                             | Oat oil  | 29                      |
| GA                             | Safflower oil  | 5                       |
| POLY                           | Cottonseed, soybean oil blend                        | 23                      |

<sup>a</sup>See Table 1 for full name

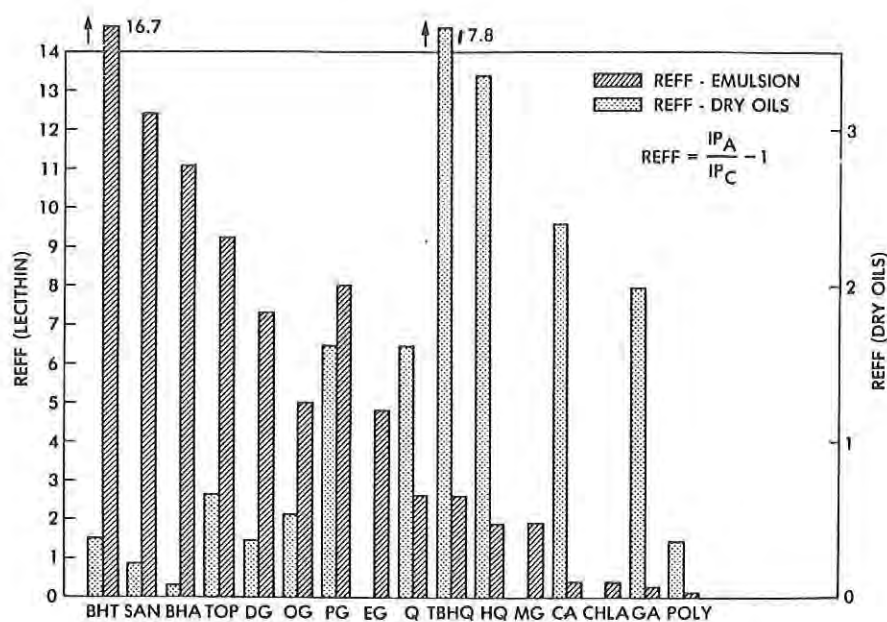


Figure 6. Relative effectiveness (REFF) of antioxidants in soy lecithin and dry vegetable oils - SAN - Santoquin; TOP - Topanol; DG - dodecyl gallate; OG - octyl gallate; PG - propyl gallate; EG - ethyl gallate; Q - quercetin; HQ - hydroquinone; MG - methyl gallate; CA - caffeic acid; CHLA - chlorogenic acid; GA - gallic acid; POLY - polymeric antioxidant. Values shown are means of all trials (reproduced with permission from Ref. 2).

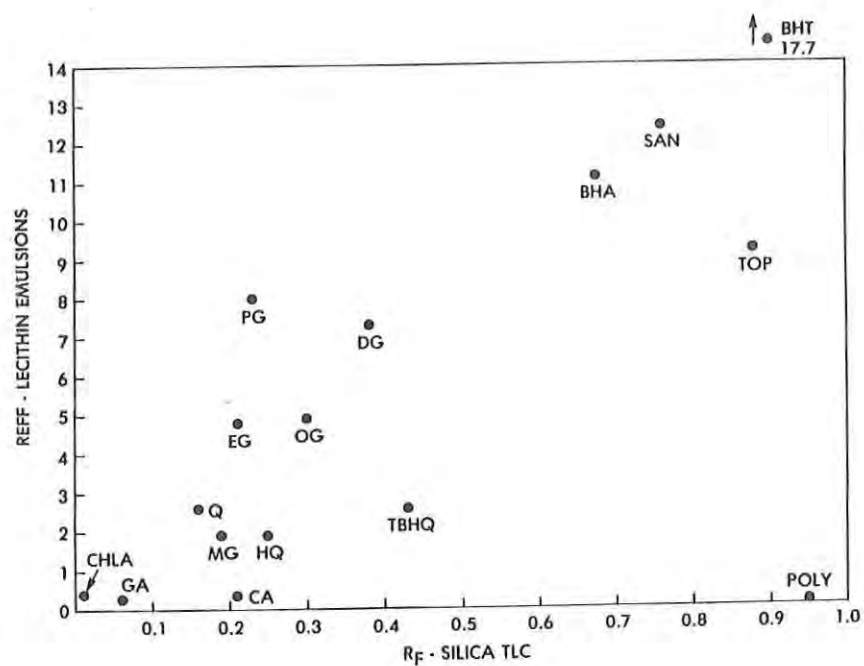


Figure 7. Relative effectiveness (REFF) of antioxidants in soy lecithin emulsions versus TLC mobility.  $R_f$  measured on silica in chloroform/methanol/acetic acid (19/1/0.5). (Reproduced with permission from Ref. 2.)



### Subsequent Studies

In addition to the lecithin evaluations, we have also studied effectiveness of many of the above-mentioned antioxidants in both a freeze-dried energy-dense corn oil-soy lecithin model<sup>24</sup> and in freeze-dried whole milk<sup>25</sup> both accelerated with cobaltous chloride. The energy-dense system used was corn oil, soy lecithin-based with the following formulation in percent: stripped corn oil, 35; stripped soy lecithin, 1.5; sodium caseinate, 15; lactose, 35; starch, 5; assorted additives, 8.5<sup>24</sup>. Results are too detailed to report here, but noteworthy is the fact that in both dispersed systems, whether compressed or uncompressed, the lipophilic dodecyl gallate was nearly twice as effective as the much more polar propyl gallate. In addition, condensed rosemary extract (Herbalox<sup>(R)</sup>) containing the active ingredient carnosol, a lipophilic species, is as effective as the higher alkyl gallates in these dispersions and is a GRAS (generally regarded as safe) substance to the FDA. The lipophilic rosemary extract is known to be ineffective in dry vegetable oil as predicted by the polar paradox rationale.

### DISCUSSION

Our work and that of others has demonstrated that the polar paradox rationale appears to apply to both synthetic antioxidants and so-called "natural" antioxidants. Of the 16 antioxidants we evaluated, five were naturally occurring compounds, and these were uniformly polar and of low activity in dispersions, but high in dry oils. Only the tocopherols and ascorbic acid appear to function in nature as membrane and fat cell antioxidants in the sense defined in this paper (although carotenoids are antioxygenic in the sense of singlet oxygen quenching). Other "natural" antioxidants are designated in this paper as incidental antioxidants, i. e., they have been shown to function as antioxidants in bulk oil or dispersed test systems, but have no comparable natural function. The applicability of the polar paradox rationale will be discussed for three main classes: synthetic antioxidants, the true natural antioxidants (the tocopherols and ascorbic acid) and incidental antioxidants.

### Synthetic Antioxidants

Tables 4<sup>5,26</sup> and 5<sup>5</sup> show the detrimental effect of increasing lipophilicity on antioxidant effectiveness in bulk oils in a homologous series of synthetic compounds. In these vegetable oils modification by increasing the alkyl chain length of either gallic acid esters or alkylated hydroquinones progressively decreases antioxidant effectiveness in bulk oils. Increasing hydroquinone ring methylation beyond one methyl group shows similar effects, as Table 6<sup>5</sup> demonstrates. Similar effects in bulk oils are shown for the caffeate

and ferulate esters<sup>29,30</sup>, and in the flavonoids, where the most polar member is the most effective antioxidant<sup>31,32</sup>. For the food-approved synthetic compounds the ascending order of lipophilia is Propyl Gallate, TBHQ, BHA, BHT<sup>33</sup>. Although the compounds differ in other respects, it is worthy of note that BHA and BHT are nearly completely ineffective in vegetable oils while Propyl Gallate and TBHQ are very effective in ascending order<sup>5</sup>. The latter two are also more effective than BHA and BHT in the same order in lard<sup>34</sup>.

Table 4. Effect of Increasing Length of Alkyl Chain on Antioxidant Activity of Gallic Acid Esters

| Antioxidant Treatment of Oil (% by Wt) | AOM Stability of Vegetable Oil (Hours to PV 70) |     |         |                        |     |         |
|--|---|-----|---------|------------------------|-----|---------|
|  | Cotton Seed <sup>a</sup>                        |     |         | Safflower <sup>b</sup> |     |         |
|  | Wt %  | AOM | Control | Wt %                   | AOM | Control |
| Gallic Acid                            | -   | -   | -       | 0.05                   | 27  | 9       |
| Propyl Gallate                         | 0.01  | 19  | 9       | 0.05                   | 24  | 9       |
| Hexyl Gallate                          | -   | -   | -       | 0.05                   | 22  | 9       |
| Octyl Gallate                          | 0.01  | 11  | 8       | -                      | -   | -       |
| Dodecyl Gallate                        | 0.01  | 10  | 8       | -                      | -   | -       |

<sup>a</sup>Sherwin (1976)<sup>26</sup>

<sup>b</sup>Thompson and Sherwin (1966)<sup>5</sup>

Table 5. Effect of Increasing Alkyl Chain Length on Antioxidant Activity of Substituted Hydroquinones<sup>a</sup>

| Antioxidant (0.05<br>Wt % in Safflower Oil) | Oil Life (Time to PV 70) <sup>b</sup> |                          |
|---|---------------------------------------|--------------------------|
|   | AOM at 210°F<br>Hours                 | Storage at 110°F<br>Days |
| None (Control)                              | 9                                     | 21                       |
| Hydroquinone                                | 39                                    | 191                      |
| Methylhydroquinone                          | 69                                    | 330                      |
| Pentylhydroquinone                          | 50                                    | 203                      |
| Octylhydroquinone                           | 46                                    | 208                      |
| Dodecylhydroquinone                         | 34                                    | 162                      |

<sup>a</sup>Thompson and Sherwin (1966)<sup>5</sup><sup>b</sup>Meq. peroxide/kg oil

Table 6. Effect of Ring Methyl Substituents on Antioxidant Activity, Reduction Potential and Solubility of Substituted Hydroquinones<sup>a</sup>

| Antioxidant (0.05 Wt % in Safflower Oil) | Oil Life (Hours to PV 70) AOM at 210°F | Reduction Potential <sup>b</sup> | Solubility <sup>c</sup> |           |
|--|--|----------------------------------|-------------------------|-----------|
|  |  |                                  | Water                   | Benzene   |
| None (Control)                           | 9                                      | -                                | -                       | -         |
| Hydroquinone                             | 39                                     | 0.681                            | Soluble                 | Insoluble |
| Methylhydroquinone                       | 69                                     | 0.623                            | Very Sol.               | Slightly  |
| 2,3-Dimethylhydroquinone                 | 36                                     | -                                | Soluble                 | -         |
| 2,5-Dimethylhydroquinone                 | 36                                     | 0.582                            | Sol. Hot                | Slightly  |
| 2,3,5-Trimethylhydroquinone              | 19                                     | -                                | Slightly                | Very Sol. |
| Tetramethylhydroquinone                  | 9                                      | 0.480                            | -                       | -         |

<sup>a</sup>Thompson and Sherwin (1966)<sup>5</sup>

<sup>b</sup>Volts. Latimer (1938)<sup>27</sup>. Standard oxidation-reduction potential.

<sup>c</sup>CRC Handbook of Chem. and Phys. 1978<sup>28</sup>.

#### The Tocopherols and Ascorbic Acid

As noted above, the tocopherols (Figure 8), especially alpha tocopherol (Vitamin E), and ascorbic acid (Vitamin C), acting in concert have been solidly established as the true natural membrane, organelle and adipocyte or oil droplet antioxidants. Dispersions, not bulk monophases, are the way lipids are displayed in natural tissue. Supporting the tocopherols is the reductive glutathione-ascorbic acid cascade (Figure 9), whose energy finally derives from glucose oxidation.

Figure 8 shows three of the common tocopherols. It has been well established that relative effectiveness of tocopherol in bulk oils is in the descending order delta, gamma, beta, alpha<sup>35</sup>. This is contrary to what might be predicted from relative reduction potential (alpha -0.273, beta, -0.343, gamma -0.348, and delta -0.405, pH 7 basis, where the less negative number corresponds to greater tendency to donate hydrogen atoms or electrons<sup>36</sup>. Observed relative tendency to be autoxidized is consistent with the reduction potentials<sup>37,38</sup>. Relative steric hindrance would appear to decrease from alpha through delta. Such increased methyl substitution normally stabilizes the aryloxy radical and increases effectiveness.

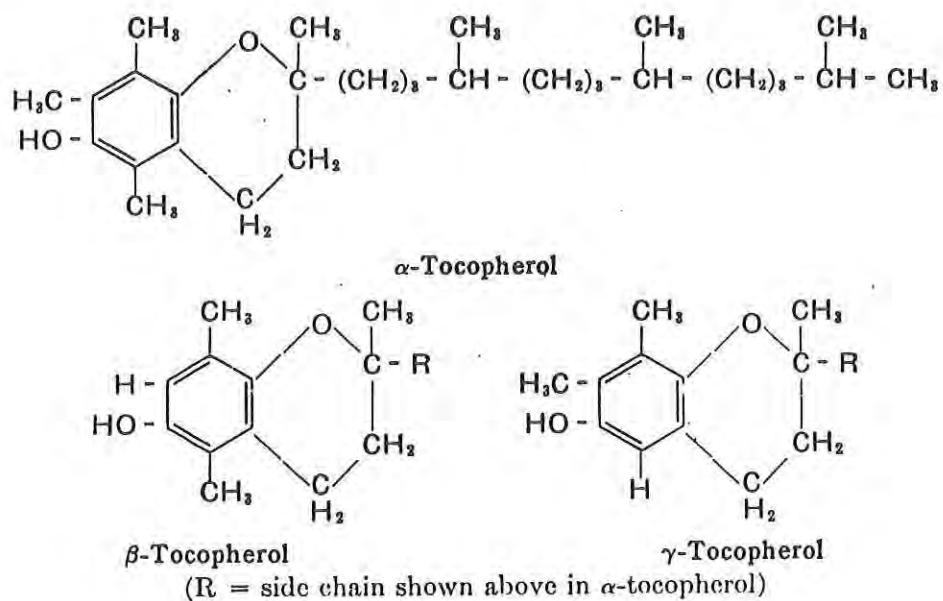


Figure 8. Three naturally occurring tocopherols.  
(Reproduced with permission from Ref. 53.)

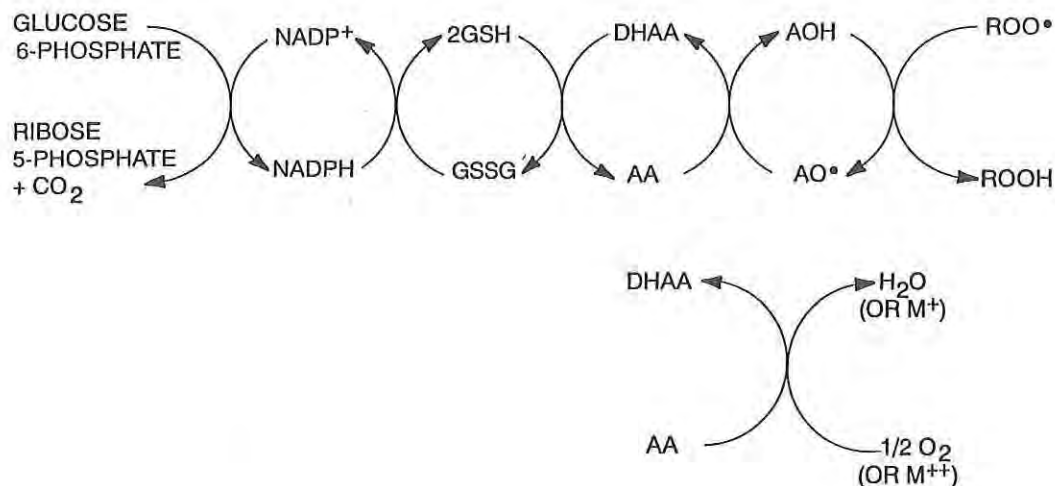


Figure 9. Hexose monophosphate shunt and regeneration of antioxidants.

In contrast, the relative effectiveness of the tocopherols in dispersed systems<sup>39,40</sup> and liposomes<sup>41</sup> is in the opposite order, alpha being notably the most effective. The order is alpha>>beta>gamma>>delta. Judging by their elution behavior in chromatographic systems<sup>37,42</sup>, the order of decreasing lipophilicity is alpha, beta, gamma, delta, corresponding to the effectiveness in dispersed systems.

Similarly correlated with the state of dispersion of the oxidizing lipid and the polarity of its environment is the antagonism of tocopherols to other lipophilic antioxidants in bulk oils, including a self-antagonism commencing at concentrations of over 1000 ppm. The bulk oil tocopherol antagonism for BHA and ethoxyquin (6-ethoxy-2,2,4-trimethyl-1,2-dihydroquinoline), both highly lipophilic and effective antioxidants in dispersions, is manifest at concentrations of alpha-tocopherol as low as 20 ppm and becomes nearly total at 500 ppm<sup>43</sup>, a typical concentration in vegetable oils.

Interestingly, the tocopherol self-antagonism is relieved in dispersed lipids such as the dispersed lard of crackers, pastry and potato chips, in contrast to bulk lard<sup>44</sup>. In addition, in the same items, the tocopherol antagonism for BHA manifest in bulk lard is changed to a pronounced positive synergism. It is also noteworthy that BHA is virtually without antioxidant effect in bulk soybean vegetable oil containing high levels of tocopherols, but in the dispersed phase in soybean oil-based salad dressings, it becomes an effective antioxidant<sup>45</sup>.

Ascorbic acid and its derivatives also obey the polar paradox rationale. Ascorbic acid may be esterified with palmitic acid at the 6 position to change its strongly hydrophilic to moderately lipophilic behavior, although no derivative is easily soluble in fats and oils. The change adds little to its effectiveness in bulk oils, but in dispersed systems, ascorbyl palmitate is much more effective than ascorbic acid<sup>4,46</sup>. It is noteworthy that the antioxidant effectiveness of ascorbic acid is dependent on the presence of tocopherol, which it continuously and stoichiometrically regenerates<sup>47</sup>. Thus, ascorbic acid is very effective when added alone to vegetable oils, but not in lard, which is very low in tocopherols.

#### Incidental Antioxidants

In the natural world, there is an abundance of polar di- and tri-phenols, which are often esterified or in glycosidic linkage with even more polar sugars<sup>48</sup>. Tea, wine, vegetables and fruits have an abundance of phenolic acids, hydrolyzable and condensed tannins and flavonoids. Catecholamines (which rapidly autoxidize) occur in animal tissue. These are usually very effective antioxidants in dry bulk oils, their activity, other things being equal, seeming to increase with every added ortho or para polar OH group. However, as was shown with several examples



(quercetin, hydroquinone, caffeic acid, chlorogenic acid and gallic acid<sup>2</sup>), these are relatively ineffective in HSV situations like emulsions and membranes, providing they are present at comparable concentrations to lipophilic antioxidants.

#### Disadvantages of Most Polar Antioxidants.

The ubiquitous polar incidental antioxidants found in many plants and animals also often have drawbacks for their use in foods<sup>49</sup>. They often taste bitter or astringent. They tend to form colored complexes with trace metals and complexes with proteins, even in the unoxidized state. The quinones resulting from their oxidation, which is usually enzymic, are toxic and aggressively react with amine or sulfhydryl groups of amino acids, proteins and phospholipids to form dark, insoluble melanins. They are also antagonistic to thiamine, which can result in deficiency in the tea-drinking cultures of Southeast Asia.

#### Scarcity of Lipophilic Antioxidants in Nature.

The increased demand for antioxidants in the vulnerable preprocessed convenience foods with dispersed rather than bulk lipids together with the consumer suspicion of synthetic antioxidants has resulted recently in an unprecedented search for appropriate antioxidants from natural sources<sup>50</sup>. Unfortunately, except for the tocopherols, there are not many lipophiles suitable for dispersed lipids. Seed oils and bran of oats and sesame, rice bran hulls and oils, and the spices thyme (paramethoxythymol), turmeric (curcumin), cloves (eugenol), vanilla (vanillin), red pepper (capsaicin), ginger (zingiberone), and rosemary and sage (carnosol and rosmaridiphenol) are among the few candidates<sup>51</sup>, if one excludes urushiol, the active principle of poison ivy. Most of the spice (incidental) antioxidants are highly flavored or colored. The lipophilic rosemary antioxidants, true to the polar paradox, show little activity in vegetable oils, are only moderately effective in animal fats, but quite effective in emulsions. Bilirubin, the bile pigment, is highly lipophilic and has been shown to be antioxidant, but probably only incidentally to its main function as part of the breakdown pathway for hemoglobin. It also conforms to the polar paradox rationale, since it is much more effective in lecithin liposomes than it is in homogeneous solution<sup>52</sup>. Porphyrins like chlorophyll or pheophytin are antioxidant in the dark but pro-oxidant in light, a paradoxical behavior traceable to the photoactivated formation of singlet oxygen<sup>51</sup>.

#### Impact of the Polar Paradox on Ration Formulation.

It is evident from the above discussion that the disparate effectiveness of antioxidants in bulk versus dispersed systems must bear on the choice of antioxidants for protection of lipids in military rations. In salad and cooking oils, for example, the more lipophilic

antioxidants like BHA, BHT and eugenol are counterindicated, both because of low inherent effectiveness in this milieu and because, in vegetable oils, there is very strong antagonism from the more lipophilic tocopherols, such as alpha tocopherol (Vitamin E). The predominantly polar natural incidental antioxidants, on the other hand, like those from tea and vegetables, together with ascorbic acid, achieve good protection when mechanically dispersed in bulk oils, even when, as with ascorbic acid, they are virtually insoluble in the medium. In this connection, it should be recalled that the presence of tocopherol is essential for the regenerant action of ascorbic acid which is very ineffective without an additional primary antioxidant.

In dispersed systems, however, which are the typical conditions in many military ration items, lipophilic antioxidants at equal concentration are very much more effective than polar compounds. In the tocopherol series, the effectiveness is  $\alpha > \beta > \gamma > \delta$  in such dispersions, whereas the reverse is true in bulk oils. In addition, tocopherols in dispersed systems synergize rather strongly to give a pronounced additive effect with lipophiles like BHA. Thus, at the present time, if one desires natural antioxidants for consumer acceptance, alpha tocopherol, eugenol or rosemary extract, possibly reinforced with ascorbyl palmitate (but not the free acid), are good choices. Synergism of the natural antioxidants with synthetic lipophiles like BHA and BHT can greatly reduce the needed concentrations of these synthetics.

It should be emphasized, however, that such characteristics as the high volatility of BHA or BHT, or vulnerability to heat and alkaline conditions (reducing carry-through of the short-chain substituted hydroquinones and gallates in baking) must be considered. Formulation and processing conditions may affect these stability traits also, as in the beneficial volatility of some lipophiles like BHA or eugenol in seldom-opened packaged goods, or loss of volatile antioxidants in freeze-drying.

REFERENCES

1. Porter, W.L. 1980. Recent trends in food applications of antioxidants. In Autoxidation in Food and Biological Systems, M.G. Simic and M. Karel (eds.). Plenum Press, N.Y., pp. 295-365.
2. Porter, W.L., Black, E.B. and Drolet, A.M. 1989. Use of polyamide oxidative fluorescence test on lipid emulsions: contrast in relative effectiveness of antioxidants in bulk versus dispersed systems. *J. Agric. and Food Chem.* 37, 615-624.
3. Porter, W.L., 1991. Paradoxical behavior of antioxidants in food and biological systems. In Antioxidants - Chemical, Physiological, Nutritional and Toxicological Aspects. Proceedings of The International Conference on Antioxidants convened by the Food and Nutrition Council and the Environmental Health and Safety Council of the American Health Foundation, Tarrytown, N. Y., Oct.8-10, 1991. Gary Williams (ed.). Princeton Scientific Publishers, Inc. Princeton, N.J.
4. Cort, W.M. 1974. Antioxidant activity of tocopherols, ascorbyl palmitate and ascorbic acid and their mode of action. *J. Am. Oil Chem. Soc.* 51, 321-325.
5. Thompson, J.W. and Sherwin, E.R. 1966. Investigation of antioxidants for polyunsaturated edible oils. *J. Am. Oil Chem. Soc.* 43, 683-686.
6. Sherwin, E.R. and Thompson, J.W. 1967. Tertiary - butylhydroquinone - an antioxidant for fats and oils and fat-containing foods. *Food Technol.* 21, 106-110.
7. Bishov, S.J. and Henick, A.S. 1975. Antioxidant effect of protein hydrolysates in freeze-dried model systems. Synergistic action with a series of phenolic antioxidants. *J. Food Sci.* 40, 345-348.
8. Porter, W.L., Levasseur, L.A. and Henick, A.S. 1977. Evaluation of some natural and synthetic phenolic antioxidants in linoleic acid monolayers on silica. *J. Food Sci.* 42, 1533-1535.
9. Porter, W.L., Henick, A.S., Murphy, F., Colgan, R., and Porfert, G. 1978. Autoxidation and effects of pro- and antioxidants in lyophilized red blood cell membranes. *Lipids* 13, 137-146.
10. Corliss, G.A. and Dugan, L.R., Jr. 1970. Phospholipid oxidation in emulsions. *Lipids* 5, 846-853.
11. Kaschnitz, R.M. and Hatafi, Y. 1975. Lipid oxidation in biological membranes. Electron transfer proteins as initiators of lipid oxidation. *Arch. Biochem. Biophys.* 171, 292-304.
12. Gutteridge, J.M.C. 1977. The measurement of malondialdehyde in peroxidized ox-brain phospholipid liposomes. *Anal. Biochem. Biophys.* 82, 76-82.

PORTER & BLACK

13. Barclay, L.R.C. and Ingold, K.U. 1980. Autoxidation of a model membrane. Comparison of egg lecithin phosphatidyl choline in water and in chlorobenzene. *JAOCS* 102, 7792-7794.
14. Kornbrust, D.J. and Mavis, R.D. 1980. Relative susceptibility of microsomes from lung, heart, liver, kidney, brain and testes to lipid peroxidation: correlation with vitamin E content. *Lipids* 15, 315-322.
15. Koreh, K., Seligman, M.L. and Demopoulos, H.B. 1982. The effect of dihydroergotoxine on lipid peroxidation in vitro. *Lipids* 17, 724-726.
16. Weenen, H. and Porter, N. A. 1982. Autoxidation of model membrane systems: cooxidation of polyunsaturated lecithins with sterols, fatty acids and alpha-tocopherol. *JAOCS* 104, 5216-21.
17. Wu, G.-S., Stein, R.A. and Mead, J.F. 1982. Autoxidation of phosphatidyl choline liposomes. 17, 403-413.
18. Porter, W.L. 1981. Method for determining oxidative status of unsaturated lipids and method for evaluating antioxidant effectiveness in lipid-polypeptide layers. U.S. Patent 4,253,848, March 3, 1981.
19. Porter, W.L., Wetherby, A.M. and Kapsalis, J.G. 1980. Fluorescence test of oxidative abuse status of fats, oils and dry whole tissue. *JAOCS* 57, 187A.
20. Porter, W.L., Black, E.D., Drolet, A.M. and Kapsalis, J.G. 1983. Analytical use of fluorescence-producing reactions of lipid- and carbohydrate-derived carbonyl groups with amine end groups of polyamide powder. In "The Maillard Reaction in Foods and Nutrition," Waller, G.R. and Feather, M.S. Eds. ACS Symposium Series 215. American Chemical Society, Washington, D.C., pp.47-70.
21. Petrochemical Division, Imperial Chemical Industries, Ltd., Development Bulletin. 1974. I.C.I., Ltd., Billingham, Teeside, England, p.
22. Geissman, T.A. 1962. The Chemistry of Flavonoid Compounds; Pergamon Press, New York, N.Y.
23. Furia, T.E. and Bellanca, N. 1977. The properties and performance of Poly AO<sup>TM</sup>-79; a nonabsorbable polymeric antioxidant intended for use in foods. *JAOCS* 54, 239-244.
24. Porter, W.L., Black, E.D., Kim, Y.-K. and Hoke, L. 1986. "Development of Rapid Methods to Monitor Oxidative and Maillard (Sugar-amine) Polymerization in Energy-Dense, Encapsulated Model Systems." Technical Report, NATICK/TR-86/063, U.S. Army Natick Research, Development and Engineering Center, Natick, MA. (AD A 179 574).
25. Porter, W.L., Black, E.D. and Hoke, L. 1988. "Extension of Storage Stability in Energy-Dense Encapsulated Systems by Minimization of Lipid Oxidation." Technical Report, NATICK/TR-88/074, U.S. Army Natick Research, Development and Engineering Center, Natick, MA.



26. Sherwin, E.R. 1976. Antioxidants for vegetable oils. *J. Am. Oil Chem. Soc.* 53, 430-436.
27. Latimer, W.M. 1938. "The Oxidation States of the Elements and Their Potentials in Aqueous Solution," Prentice-Hall, Inc., New York, N.Y.
28. CRC Handbook of Chemistry and Physics. 1978. 59th Ed., West, R.C. Ed. CRC Press, Inc., West Palm Beach, Florida.
29. Daniels, D.G.H. and Martin, H.F. 1967. Antioxidants in oats. Mono-esters of caffeic and ferulic acids. *J. Sci. Food Agric.* 18, 589-595.
30. Dziedzic, S.Z. and Hudson, B.G.F. 1984. Phosphatidylethanolamine as a synergist for primary antioxidants in edible oils. *J. Am. Oil Chem. Soc.* 61, 1042-1045.
31. Abbot, J. and Waite, R. 1962. The effect of antioxidants on the keeping quality of whole milk powder. I. Flavones, gallates, butylhydroxyanisole and nordihydroguaiaretic acid, *J. Dairy Res.* 29, 55-61.
32. Simpson, T.H. and Uri, N. 1956. Hydroxyflavones as inhibitors of the aerobic oxidation of unsaturated fatty acids. *Chem. Ind. (London)* 956-957.
33. Ragnarsson, J.O. 1977. Accelerated temperature shelf life testing of antioxidants in dehydrated and intermediate moisture systems. Ph.D. Thesis. University of Minnesota. University Microfilms International, Ann Arbor, Michigan. p. 126.
34. Moore, R.N. and Bickford, W.G. 1952. A comparative evaluation of several antioxidants in edible fats. *J. Am. Oil Chem. Soc.* 29, 1-4.
35. Lea, C. H. and Ward, R.J. 1959. Relative activities of the seven tocopherols. *J. Sci. Food Agric.* 10, 537-538.
36. Wacks, W. 1949. *Biochem. Z.* 319, 561. Cited by Aaes-Jorgenson, E. 1962. Autoxidation of fatty compounds in living tissue, biological antioxidants. *In* Autoxidation and Antioxidants, Vol. II, W.O. Lundberg (ed.). Interscience Pub., N.Y. p. 1072.
37. Cillard, J. and Cillard, P. 1980. Behavior of alpha, gamma and delta tocopherols with linoleic acid in aqueous media. *J. Am. Oil Chem. Soc.* 57, 39-42.
38. Ikeda, N. and Fukuzumi, K. 1977. Synergistic Antioxidant Effects of Nucleic Acids and Tocopherols. *J. Am. Oil Chem. Soc.* 54, 360-366.
39. Castle, L. and Perkins, M.J. 1986. Inhibition kinetics of chain-breaking phenolic antioxidants in SDS micelles. Evidence that intermicellar diffusion rates may be rate-limiting for hydrophobic inhibitors such as alpha-tocopherol. *J. Am. Chem. Soc.* 108, 6381-6382.

40. Pryor, W.A., Strickland, T., and Church, D.F. 1988. Comparison of the efficiencies of several natural and synthetic antioxidants in aqueous sodium dodecyl sulfate micelle solutions. *J. Am. Chem. Soc.* 110, 2224-2229.
41. Fukuzawa, K., Tokumura, A., Ouchi, S. and Tsukatani, H. 1982. Antioxidant activities of tocopherols on  $\text{Fe}^{2+}$ -ascorbate-induced lipid peroxidation in lecithin liposomes. *Lipids* 17, 511-513.
42. Andrikopoulos, N.K., Breuschweiler, H., Felber, H. and Taeschler, C. 1991. HPLC analysis of phenolic antioxidants, tocopherols and triglycerides. *J. Am. Oil Chem. Soc.* 68, 359-364.
43. Olcott, H.S. and Einset, E. 1958. An antagonistic effect with antioxidants for unsaturated fats. *JAOCs* 35, 159-160.
44. Dugan, L.R., Jr. and Kraybill, H.R. 1956. Tocopherols as carry-through antioxidants. *JAOCs* 33, 527-528.
45. Warner, K., Frankel, E.N., Snyder, J.M. and Porter, W.L. 1986. Storage stability of soybean oil-based salad dressings: effects of antioxidants and hydrogenation. *J. Food Sci.* 51, 703-708.
46. Cort, W.M. 1982. Antioxidant properties of ascorbic acid in foods. *In* *Ascorbic Acid: Chemistry, Metabolism and Uses*, P.A. Seib and B.M. Tolbert (eds.). *Advances in Chemistry Series No. 200*, Am. Chem. Soc., Washington D.C.
47. Packer, J.E., Slater, T.F. and Willson, R.L., 1979. Direct observation of free radical interaction between vitamin E and vitamin C. *Nature* 278, 737-8.
48. Pratt, D.E. 1976. Role of flavones and related compounds in retarding lipid-oxidative flavor changes in foods. *In* *Phenolic, Sulfur and Nitrogen Compounds in Food Flavors*, Charamboulos, G. and I. Katz (eds.). *Am. Chem. Soc. Symposium Series No. 26*, ACS, Washington, D.C.
49. Sosulski, T.H. and Fleming, S.E. 1977. Chemical, functional, and nutritional properties of sunflower protein products. *J.A.O.C.S.* 54, 100A-104A.
50. Haumann, B.F. 1990. Antioxidant firms seeking products they can label as natural. *Inform (Am. Oil Chem. Soc.)* 1, 1003-1013.
51. Namiki, M. 1990. Antioxidants/antimutagens in food. *Critical Reviews in Food Science and Nutrition.* 29, 273-300. CRC Press, Boston.
52. Stocker, R., Yamamoto, Y., McDonagh, A.F., Glazer, A.N. and Ames, B. 1987. Bilirubin is an antioxidant of possible physiological importance. *Science* 235, 1043-1046.



PORTER & BLACK

53. White, A., Handler, P., Smith, E.L. and Stetten, D., Jr. 1954.  
Principles of Biochemistry, McGraw-Hill Book Company, Inc., New York.

PORTER & BLACK

ACKNOWLEDGMENT

Thanks are extended to NIPA Laboratories, Ltd., for a gift of five alkyl gallates; to Petrochemicals Division, Imperial Chemical Industries, Ltd., for a gift of Topanol 354; to Nicolo Bellanca, Dynapol, Inc., for a gift of PolyAO 79; to Eastman Chemical Products, for a gift of BHA and TBHQ; to Koppers Co., Inc., for a gift of BHT; and to Monsanto Chemical Co., for a gift of Santoquin (Ethoxyquin). The secretarial assistance of Ms. Kim Pfister is gratefully acknowledged. Thanks are due to Dr. K. Ananth Narayan, to Mr. Alan Bennett and to Ms. Marcia Lightbody for critical reviews of the manuscript.

TITLE: Stability of Beta-Galactosidase and Immobilization  
on an Ultrafiltration Membrane for the Continuous  
Processing of Low-Lactose Milk  
Andre G. Senecal, Dr., and Arthur G. Rand, Dr.

ABSTRACT: Milk has long been known as a nearly complete food, being a rich source of calcium, riboflavin, and protein. The high incidence of lactose intolerance, especially by noncaucasians, has resulted in their avoidance of milk and milk products and, therefore, they cannot benefit from the nutrients supplied by milk. The percentage of lactose intolerance is higher in the military than in the general population (35% vs 15%), a fact that has convinced the Services to seek a lactose-reduced dry milk, low in fat, as a replacement for nonfat dry milk currently used as a component of the B-Ration, T-Ration, and Pre-Positioned War Reserved Stocks.

Lactose is hydrolyzed to glucose and galactose by the enzyme beta-galactosidase. The enzyme is subject to severe competitive product inhibition by the galactose produced in a batch system and thus the process requires excessive amounts of costly enzyme for a high degree of conversion. An economical method for reducing product inhibition could be an immobilized lactase reactor modeled after the mammalian intestinal mucosa. Commercial yeast lactases were tested for stability in skim milk ultrafiltration permeate at 20, 30, and 40°C. Enzymes derived from Kluyveromyces lactis, possessing different lactase activity units, were found to be the most stable. The K. lactis enzyme with the greatest lactase activity units was immobilized on an ultrafiltration hollow fiber membrane to determine the best temperatures and flow rate for lactose hydrolysis and stability. Results indicate reactor conditions of 5 psi and 30°C with an enzyme load of 2000 mg/0.06m<sup>2</sup> to be the best tested. This reactor appeared to minimize the problem of product inhibition through continuous removal of galactose. Lactose reduction for milk products could be conducted through ultrafiltration of skim milk, followed by lactose hydrolysis of the permeate through an ultrafiltration lactase reactor.

BIOGRAPHY OF PRESENTER: Andre G. Senecal

PRESENT ASSIGNMENT: Food Technologist, Food Engineering Directorate

PAST EXPERIENCE: Graduate Research Assistant, University of Rhode Island.

DEGREES HELD: B.A., Assumption College, M.S. Long Island University, Ph.D. University of Rhode Island.

Stability of Beta-Galactosidase and Immobilization  
on an Ultrafiltration Membrane for the Continuous  
Processing of Low-Lactose Milk

Andre G. Senecal, Dr.  
U.S. Army Natick RD&E  
Natick, MA 01760

Arthur G. Rand, Dr.  
University of Rhode Island  
Kingston, RI 02881

INTRODUCTION

The principal carbohydrate in animal milk is lactose. It is hydrolyzed by the enzyme  $\beta$ -galactosidase (lactase) to form glucose and galactose. Lactase is located in the small intestine and plays an important role in infant nutrition. Most adult populations are lactose intolerant because of insufficient quantities of lactase in their small intestine. These individuals tend to avoid milk because of the risk of serious discomfort. Caucasians are the exception, especially those from Northern European descent (Montgomery et al. 1991). The development of commercial lactase ( $\beta$ -galactosidase) has stimulated production of products that are lactose-reduced. The enzyme is able to hydrolyze lactose into the monosaccharides, glucose and galactose, which are readily absorbed by the small intestine. Lactose-intolerant individuals are now able to benefit from the nutrients supplied from milk. This reduces the danger of low-intake levels of calcium, phosphorus, vitamin D and riboflavin (Rand, 1981). The United States Armed Forces have expressed a need for a low-fat, dry milk that is lactose reduced. The percentage of lactose-intolerant individuals in the military is much greater than it is for the general American population due to the higher ratio of noncaucasians present.

There are a variety of commercial lactase enzymes available for use in food. These enzymes are derived from yeast and mold. The yeast lactases are heat labile (Mahoney and Whitaker, 1977; Guy and Bingham, 1978; Mahoney and Wilder, 1988; Mahoney and Wilder, 1989) and have optimum activity in the neutral pH range, which is typical of milk and whey permeate. Mold lactases are more heat stable (Rand and Linklater, 1973), but have an optimum activity in the acidic range. Enzymes derived from different sources have demonstrated dissimilar properties due to variations in enzyme-substrate affinity (Jacobson-Pivarnik and Rand, 1984; Garg et al. 1989). Temperature and optimum pH have been found to vary depending on the source and even the particular commercial preparation (Gekas and Lopez-Leiva, 1985).

The objective of this study was twofold. The first part was to determine the stability of commercial lactase enzyme preparations in skim milk ultrafiltration permeate at varying storage temperatures. The results would determine which sources of lactase would be best suited for batch operations under fixed conditions and establish the potential for continuous use in an immobilized reactor. The second aspect was to establish conditions of hydrolysis and stability for the localized enzyme membrane reactor in the hydrolysis of lactose from milk.

Studies have established the stabilizing effect of various substrates on lactase. Milk and whey have been found to increase the stability of *Kluyveromyces lactis* (Dahlqvist et al. 1977) *Kluyveromyces fragilis* (Mahoney and Adumchuck, 1980) *Kluyveromyces marxianus* (Mahoney and Wilder, 1988) and *Escherichia coli* (Mahoney and Wilder, 1989). The increased stability was attributed to the stabilizing properties of the casein and whey proteins. Mahoney and Adumchuck (1980) also observed that lactase activity was controlled by the ionic environment.

Product inhibition has represented a major disadvantage to batch-type processing. Large quantities of expensive enzymes have been required to increase percent lactose hydrolysis in the process. Reduction of galactose during lactose hydrolysis would greatly increase enzyme efficiency. Finnie (1980) tested a coupled enzyme system ( $\beta$ -galactosidase together with  $\beta$ -D-galactose dehydrogenase) as a means of removing galactose from the reactor through enzymatic conversion.

The simplest method would be to remove the product as it was being produced (Rand, 1981). A continuous process reactor utilizing immobilized enzymes would achieve this goal. Studies to immobilize the enzyme on various supports were reviewed by Shukla (1975). These systems suffered from enzyme instability attributed to enzyme denaturation and leakage. Coughlin and Charles (1980) concluded that tubular reactors containing catalyst appeared to be the best choice for large-scale hydrolysis of lactose from milk and whey. Senecal (1991) found that *K. lactis* lactase was an enzyme source with potential for long-term continuous use in milk.

An attractive alternative method of enzyme immobilization is ultrafiltration (UF). These "membrane bioreactors" take advantage of the differences in size between the enzyme and the product (Cheryan and Mehaia, 1986). The method commonly used is the continuous-stirred tank reactor (CSTR). The enzyme is recirculated with the substrate in the UF mode (Roger, et al. 1978; Huffman-Reichenbach and Harper, 1982; Cheryan and Mehaia, 1986). Another method involves entrapping the lactase enzyme in the shell side of a hollow fiber membrane and hydrolyzing the substrate in the recycle mode (Breslau and Kilcullen, 1975; Huffman-Reichenbach and Harper, 1982). Disadvantages are excessive enzyme leakage unless covalently bonded to the membrane.



A membrane lactase reactor, modelled after the mammalian small intestine, has been developed by localizing Kluyveromyces lactis on the lumen side of a hollow fiber in a pressure-induced flow regime (Maculan, 1979). The reactor reduced product inhibition through removal of galactose. At the same time, lactose was fed into the reactor maintaining high concentration levels near the enzyme. Mahoney and Wilder (1989) demonstrated the stabilizing effect of high lactose concentration on lactase from Escherichia coli. Problems associated with enzyme leakage were easily solved by proper selection of membrane porosity. A disadvantage was that the enzyme was severely denatured by contact with the polysulfone membrane material. This was resolved by loading bovine serum albumin ahead of the enzyme. The protein formed a protective bed that doubled the half-life of the enzyme reactor.

The membrane reactor operates in the single pass mode. Therefore, the membrane chosen should be permeable to the substrate employed to avoid changes in flux. Milk would be an unsuitable substrate for this system because of the presence of high molecular weight compounds. However, milk UF permeate composed of low molecular weight compounds could be a feasible substrate. An interesting approach would employ a hollow fiber membrane with a small enough pore size to retain proteins inherent in the milk UF permeate. This would result in utilization of the substrate's own protein material as a protective layer against lactase denaturation by the membrane material. All the studies involving enzyme "immobilization" in hollow fiber membranes employed buffered lactose solutions as the substrate. These systems were important for establishing operating conditions but had little application to industry. Research utilizing an UF food substrate would determine the possibility of applying the reactor industrially and could easily be adapted to membrane processing of milk.

## MATERIALS AND METHODS

### Materials

Maxilact LX 5000 (KL5000) yeast lactase derived from Kluyveromyces lactis was donated by Gist-Brocades USA Inc. (Charlotte, NC). Lactozyme 3000 L (KF3000) yeast lactase from Kluyveromyces fragilis was furnished by Novo Laboratories (Danbury, CT). Neutral lactase 8000 (KL8000) from K. lactis was provided by Biocon (US) Inc. (Lexington, KY). Neutral lactase (NLCP) derived from Candida pseudotropicalis was provided by Pfizer Inc. (Milwaukee, WI). Lactase YL "Amano" (YLCS) from Candida sp. was supplied by Amano International Enzyme Co., Inc. (Troy, VA). Low-heat nonfat dry milk (NDM) was purchased from Land O'Lakes Inc. (Minneapolis, MN). Skim milk was bought through the University of Rhode Island Dining Services (Kingston, RI). All other chemicals were reagent grade. Reverse



osmosis/deionized (RO/DI) purified water was used throughout the study.

#### Measurement of Enzyme Activity

Lactase activity units (LAU) for the commercial enzymes were assayed in NDM according to the procedure of Jacober-Pivarnik and Rand (1984) with a modification. The enzyme concentrations were prepared in a 0.1 M potassium phosphate buffer, pH 6.5, in place of distilled deionized water or 0.1 M imidazole-HCl buffer. Glucose production was measured in mg% with a YSI Model 23A Glucose Analyzer (Yellow Springs Instrument Co., Yellow Springs, OH). LAU were calculated from the micromoles of glucose produced per minute per milligram of enzyme.

#### Production of Skim Milk Ultrafiltration Permeate

Skim milk ultrafiltration permeate (SMUFP) was produced through the ultrafiltration (UF) of skim milk with a Lab 5 Hollow Fiber Membrane system (Romicon Inc., Woburn, MA). The process was conducted in a recycle batch operation with an inlet pressure of 25 psi and an outlet pressure of 5 psi. The hollow fiber membrane cartridge was a PM50 with a nominal molecular weight cutoff of 50,000 daltons and an area of 5 ft<sup>2</sup>. The skim milk was preheated to 40°C by passing through the system's heat exchanger, with permeate ports closed. Once temperature was reached, the system was maintained at 40°C throughout the operation. The SMUFP constituted 80% of the original skim milk. The permeate to be used with the UF lactase bioreactor was stored at 4°C with 0.1 % potassium sorbate added as a bacterial retardant.

#### Substrate Composition

The composition of skim milk and SMUFP was determined by the analytical section of the Food Engineering Directorate of the United States Army Natick Research, Development and Engineering Center (Natick, MA). Percent lactose present in the substrates was determined using a YSI Model 27 Industrial Analyzer (Yellow Springs Instrument Co., Yellow Springs, OH). Table 1 lists the composition of skim milk and whey permeate.

Table 1. Composition of skim milk and skim milk UF permeate

| Substrate | pH  | Protein | Lactose | Ca  | P   | K   | Mg |
|-----------|-----|---------|---------|-----|-----|-----|----|
| Skim milk | 6.6 | 3.3     | 5.1     | 131 | 105 | 158 | 12 |
| SMUFP     | 6.5 | 0.5     | 5.4     | 34  | 43  | 149 | 9  |

Metal ions are expressed in mg/100 grams.

### Enzyme Substrate Preparation

All glassware and handling equipment were sterilized to minimize bacterial contamination. SMUFP was added in 84 mL aliquots to culture bottles in a laminar flow hood. A single crystal of thymol, a bactericide, was added to each bottle to delay the onset of the natural bacterial loads present in the substrates and enzymes. Commercial enzymes were added aseptically to the bottles in 1000 mg equivalents. The densities of the liquid lactase were determined and the 1000 mg amount added by pipet. The enzyme-substrate preparations were placed in water baths at temperatures of 20, 30 and 40°C. Controls for each substrate, without enzyme addition, were used to monitor the effect of thymol in resisting bacterial contamination. This was accomplished by periodically monitoring the pH of the samples.

### Assay Procedure for Enzyme Stability

Enzyme-substrate preparations were assayed initially and periodically for IAU. The assay procedure was similar to the method used in the initial screening of the enzymes in NDM with modifications. A 0.5 mL aliquot of the enzyme-substrate was added to 2.5 mL of reconstituted NDM. Another 0.5 mL aliquot was added to a second tube containing 2.5 mL of 0.1 M potassium phosphate buffer, pH 6.5. The buffer was used to monitor the background quantities of glucose present in each preparation, attributed to the initial presence of lactose in each substrate. The amount of enzyme assayed in each tube was equal to 5.95 mg/mL. The enzymes were assayed periodically until they had lost at least 50% of their initial activity. Stability determinations were conducted in duplicate. The half-life for each condition was read directly from the percent remaining activity curve.

### Effect of Increasing Enzyme Concentration on Stability

The lactase enzymes that displayed activity units considerably lower than the *K. lactis* derived enzymes, from the NDM assay, had their protein concentrations increased for additional stability studies in SMUFP at 20 and 30°C. Protein concentrations tested were 2700 mg KF3000, 3700 mg NLCP and 3700 mg YLCS. These enzyme concentrations were derived from the difference in IAU between these lactase and LK8000 (initially assayed as 5600 IAU).

### Localized Enzyme UF Reactor

A schematic of the localized enzyme UF reactor is presented in Figure 1. Enzyme immobilization was conducted with an Amicon CH-4 Hollow Fiber Cartridge Adapter (Amicon Corp., Lexington, MA). A H1P30 hollow fiber membrane was used in the study. The membrane, composed of polysulfone, had a surface area of 0.06 m<sup>2</sup> and a nominal molecular weight cutoff of

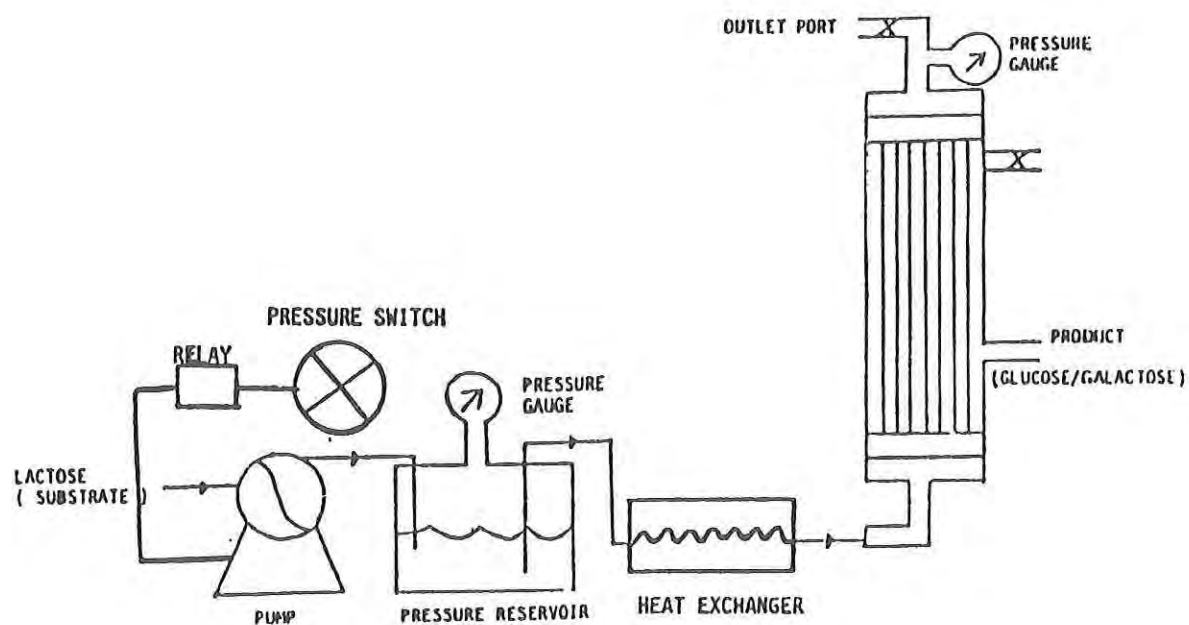


Figure 1. Ultrafiltration Enzyme Bioreactor

30,000 daltons. The pressure of the system was preserved with a Bio Fiber Pressure Vessel and Bio Fiber Pump Module (Bio-Rad Laboratories, Richmond, CA). Pressure was controlled through a pressure switch (United Electronic Controls Co., Watertown, MA) and a relay control (Wilkins-Anderson Co., Chicago, IL). Temperature for the enzyme reactor was controlled by placing the cartridge above the water level in a covered Tecam Water Bath (Techne, Inc., Princeton, NJ). The substrate was kept at 2-4°C in ice. The substrate was preheated with a Parker Dual Heat Exchanger (King-Gage Engineering Corp., Natick, MA) prior to entrance into the reactor. The temperature of the heat exchanger was controlled by a Forma Scientific Water Bath and Circulator Model 2067 (Forma Scientific Inc., Marietta, OH).

#### Operation of Localized Enzyme UF Reactor

A 200 mL quantity of SMUFP was pumped into the pressure vessel reservoir and loaded onto the lumen side of the membrane at 10 psi. This deposited a protective protein bed that separated the enzyme from the membrane material. Lactase derived from *K. lactis* was dispersed into 100 mL of SMUFP and pumped into the lumen at 10 psi with the retentate port closed and the permeate port open. This was followed by the SMUFP, which was pumped continuously through the reactor at the desired temperature and pressure.

#### Enzyme Assay

The enzyme solution (1000 mg/100 mL of substrate) was assayed for activity units prior to loading the reactor, and upon recovery from the reactor and completion of the run. Lactase activity units (IAU) were determined in NDM according to the method for the enzyme stability in SMUFP.

#### Reactor Assay

The hydrolyzed permeate was collected periodically and monitored for glucose production per hour, pH, and system flux. The glucose produced was expressed as mg/hr at maximum steady state. The permeate was assayed for lactase activity to check if enzyme leakage had occurred through the membrane.

### RESULTS AND DISCUSSION

#### Activity Units of Commercial Yeast Lactases

The IAU for the commercial yeast lactases assayed in NDM and orthonitrophenol- $\beta$ -D-galactosidase (ONPG) (Manufacturer's Product

Specification) are listed in Table 2. The data revealed appreciable differences in activity for enzymes derived from *K. fragilis*, *C. pseudotropicalis* and *C. sp.* in the two test substrates. The *K. lactis* lactases displayed similar activities in both substrates. Therefore, these results demonstrated the importance of comparing commercial enzymes, since they do not always have the same activity in all substrates.

Table 2. Activity units of commercial yeast lactases in NDM and ONPG

| Lactase | IAU* |        | % Activity |
|---------|------|--------|------------|
|         | NDM  | ONPG** |            |
| KL5000  | 5300 | 5000   | 106        |
| KL8000  | 8400 | 8000   | 105        |
| KF3000  | 1900 | 3000   | 63         |
| NLCP    | 1400 | 2750   | 51         |
| YLCS    | 1400 | 2500   | 56         |

\* IAU are per gram of enzyme per mL.

\*\* As reported by the manufacturer.

#### Effect of Temperature on Stability of Lactases in SMUFP

The stability of the yeast lactases, expressed in half-lives, in SMUFP at 20, 30 and 40°C is presented in Table 3. The *K. lactis* derived lactases (KL8000 & KL5000) demonstrated analogous stabilities at 20 and 30°C. At 40°C KL8000 was two to three times more stable. The greater stability at 40°C may have been attributed to the enzyme having higher activity units. KF3000 exhibited similar stabilities to the *K. lactis* lactases at 20 and 30°C. However, at 40°C the enzyme was denatured within the first hour. The lactases taken from *Candida* were slightly less stable at 30°C and lost activity within the first hour at 40°C.

Table 3. Effect of temperature on lactase half-life in SMUFP

| Lactase | 20°C | 30°C | 40°C |
|---------|------|------|------|
| KL5000  | 55   | 15   | 5    |
| KL8000  | 62   | 17   | 14   |
| KF3000  | 82   | 14   | <1   |
| NLCP    | 67   | 11   | <1   |
| YLCS    | 43   | 10   | <1   |

Half-life is expressed in hours.

Enzyme concentration is 11.9 mg/mL substrate.

Substrate pH is another environmental factor that affects enzyme stability. Each commercial yeast lactase has an optimum pH range for enzyme activity. At pH's outside this range, activity and stability are severely impaired. Differences in lactase half-lives at 20°C were controlled by the progressive spoilage of each enzyme/substrate mixture. Stabilities for the different commercial lactases reflected changes to a



pH below their optimum range of activity. At 30°C, enzymes derived from Kluyveromyces might have attained greater half-life values if spoilage could have been delayed. The Candida-derived enzymes lost their stabilities due to effects of temperature. Activity was found to decrease rapidly below pH 5.9 for K. lactis derived lactases (Guy and Bingham, 1978) and pH 5.5 for K. fragilis derived lactases (Wendorff and Amundson, 1971; Mahoney and Whitaker, 1977). Dahlqvist et al. (1977) observed that stability in milk for K. lactis declined rapidly if bacterial growth occurred in milk. Since SMUFP was processed at 40°C, this temperature exposure might have resulted in increased bacterial load, thus reducing the useful shelf life. Thymol used as a bactericide worked well at 40°C, but not at the lower test temperatures. This was probably due to lack of thymol solubility at 20 and 30°C.

#### Effect of Enzyme Concentration

Lactase enzymes that displayed considerable differences from KL8000 in IAU per mg of enzyme were increased to determine the effects of enzyme concentration on stability. The concentrations were increased 2.7x for KF3000, 3.7x for NLCP and 3.7x for YLCS. At 30°C there was a 1 hr increase in enzyme half-life for all three lactases. On the other hand, exposure at 20°C resulted in a reduction in enzyme half-life. KF3000 displayed comparatively no changes in enzyme stability at either 20 or 30°C for enzyme concentrations of 11.9 mg/mL or 32.1 mg/mL. Increasing enzyme concentrations 3.7x resulted in stability reductions of 21% for NLCP and 14% for YLCS at 20°C. It appeared that the Candida derived lactases were more sensitive to increased enzyme concentrations at 20°C. The higher concentrations of enzyme might have increased the hydrolysis rate enough to reduce the stabilizing effect of lactose or these enzymes are more sensitive to increased galactose inhibition. The effect was probably more apparent at 20°C than 30°C because of the much greater exposure time of the enzymes to changes in substrate composition.

K. marxianus derived lactases had very little change in stability in milk at 45°C with a 30-fold increase in lactase concentration (Mahoney and Wilder, 1988). On the other hand, an increase in enzyme concentration for E. coli in milk at 60°C caused a decrease in the lactase's half-life (Mahoney and Wilder, 1989). It is believed that the half-life fell as the result of an increase in hydrolysis. The lactose concentration was reduced, minimizing the combined stabilizing effect of casein and lactose.

#### Stability of K. lactis in a Localized Enzyme UF Reactor

The effects of glucose production vs flux at 20, 30 and 40°C in a localized lactase UF reactor are shown in Table 4. The flux and mg glucose produced per minute varied considerably with changes in temperature. However, mg percent glucose and percent lactose hydrolysis were similar at all three temperatures.



Table 4. Influence of temperature on flow rate and glucose production in UF lactase bioreactors

| Temperature | Mg% Glucose | Mg Glucose/H | Flux* | %Hydrolysis |
|-------------|-------------|--------------|-------|-------------|
| 20°C        | 2342        | 411          | 0.3   | 41.5        |
| 30°C        | 2404        | 911          | 0.6   | 44.1        |
| 40°C        | 2087        | 1470         | 1.2   | 38.1        |

All bioreactors were operated with 1000 mg of lactase and a pressure controlled flow of 2.5 psi.

The values are an average over 6 h of operation for each bioreactor.

\* Flux is in L/m<sup>2</sup>/h

Temperature had a profound effect on the lactase UF reactor. Increasing the temperature 10°C resulted in a rise in flux and glucose production. Reactor half-lives were estimated at approximately 47 h at 20°C, 13 h at 30°C and 11 h at 40°C. The 30°C reactor demonstrated the best ratio of glucose production to flux and seems to give the best combination of activity and stability. The 20°C reactor displayed the greatest stability. However, the reactor required approximately 12-14 h of operation to achieve maximum conditions. Loss of enzyme stability at 20°C correlated with an increase in flux and may be attributed to denaturation by the membrane material. At 30°C, the enzyme was probably denatured by the reactor temperature over time (Senecal, 1992) or by bacterial contamination.

#### Effect of Pressure on Flux and Glucose Production

Figures 2 and 3 show the effect of increasing the operating pressure from 2.5 to 5 psi on glucose production and flux. The increase in pressure from 2.5 to 5 psi appeared to have increased and stabilized the concentration polarization layer. Glucose production was increased 159% and remained relatively constant for the first 6 h of operation. However, by 20 h the activity of the reactor had declined by 75%. Flux was increased 268%. However, this did not have a significant effect on the enzyme stability in the UF lactase reactor. The half-life of the reactor was estimated to be 15-16 h. This represented a slight increase from the 13 h found at 2.5 psi and was attributed to the quicker removal of galactose from the system. Maculan (1979) indicated that this type of reactor could reduce competitive inhibition through increased flow rates.

#### Effect of Enzyme Concentration

Figures 2 and 3 show the effect of enzyme concentration on glucose production and flux at 5 psi in the UF membrane reactor. Linear regression correlation coefficients for glucose production at 5 psi indicated that the 1000 mg (.995) and 2000 mg (.885) reactors displayed similar tendencies over time. However, the actual plot of each reactor

# GLUCOSE PRODUCTION IN UF BIOREACTORS

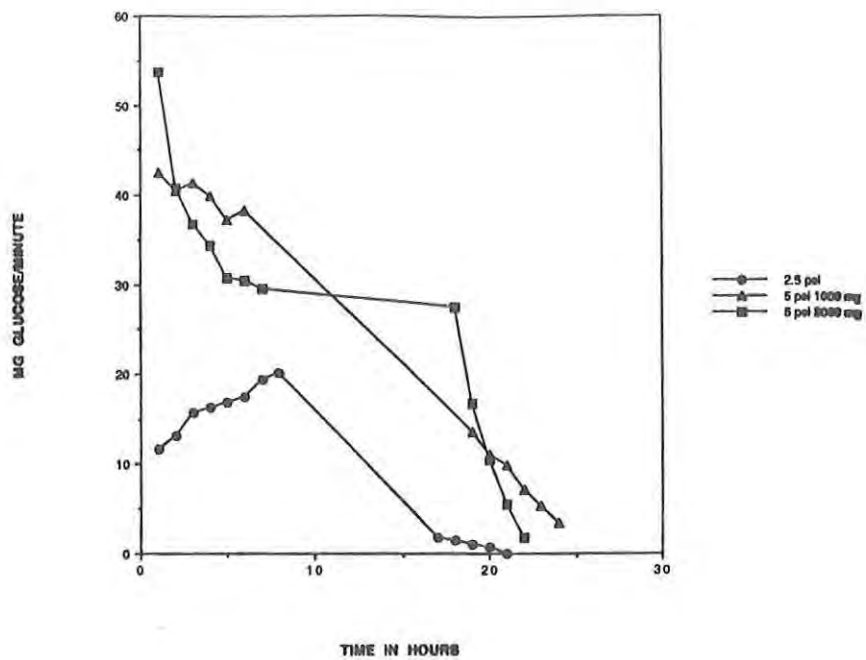


Figure 2. Effect of pressure and enzyme concentration on glucose production for skim milk UF permeate in a lactase UF membrane bioreactor at 30°C.

# FLUX IN UF BIOREACTORS

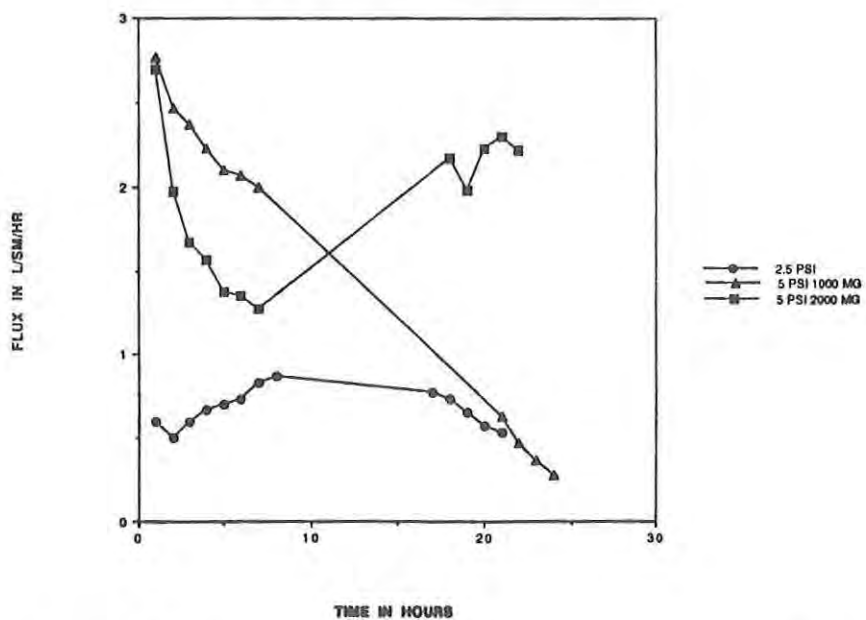


Figure 3. Effect of pressure and enzyme concentration on flux for skim milk UF permeate in a lactase UF membrane bioreactor at 30°C.

showed that they had considerable operating differences. The 1000 mg enzyme reactor (1x) displayed a linear reduction in glucose production and flux over time. This never occurred in the 2000 mg lactase reactor (2x). Initially, the 2x reactor performed similarly to the 1x reactor. However, unlike the 1x reactor, flux eventually increased in the 2x reactor. This increased flux resulted in the 2x reactor sustaining glucose production at an almost steady state for about 14 h of operation. This was the only reactor tested that displayed steady state glucose production for a period of time. Protein analysis of the permeate established that 18.7% more nitrogen containing material was penetrating the UF membrane. This was probably due to protein hydrolysis by protease enzymes. Commercial lactase enzymes have been shown to contain protease (Mahoney and Wilder, 1989). Increasing enzyme concentration might have resulted in an increase of protease enzymes, which had a reducing effect on the concentration polarization layer over time.

Doubling the enzyme concentration increased the stability of the lactase UF reactor. The reactor had a half-life of approximately 19 h. This was approximately 20% greater than the 1000 mg reactor. Percent lactose hydrolysis during the first 6 h of operation was increased 8%. This was equivalent to the conversion rates displayed in the 2.5 psi reactors over the same periods of operation.

#### CONCLUSION

There are two important factors identified in the present study that demonstrate the importance of choosing the yeast-derived lactase to fit the processing situation. First, the stability of commercial lactases is dependent on the yeast source from which the enzyme was derived. Secondly, the enzyme concentration has little effect on increasing lactase stability. Lactases derived from *K. lactis* have the greater overall thermostability of all the commercial yeast-derived enzymes. The other yeast-derived lactases were completely denatured within 2 h at 40°C and increasing their enzyme concentration did not extend their half-lives. The KL8000 lactase derived from *K. lactis* was immobilized on a UF membrane bioreactor. The bioreactor that operates at 5 psi and 30°C with an enzyme concentration of 2000 mg combines the highest levels of glucose production and stability. This bioreactor demonstrates the potential for utilization in a continuous process for the reduction of lactose in milk.

REFERENCES

- Breslau, B.R. and Kilcullen, B.M. 1975. Hollow fiber enzymatic reactors: An engineering approach. 3rd Int. Conf. on Enzyme Eng., August 3-8, Portland, OR.
- Cheryan, M. 1986. "Ultrafiltration Handbook." Technomic Publishing Co., Inc., Lancaster, PA.
- Cheryan, M. and Mehaia, M.A. 1986. Membrane bioreactors. In "Membrane Separations In Biotechnology," Ed. McGregor, W.C. p. 255. Marcel Dekker, Inc., New York, NY.
- Coughlin, R.W. and Charles, M. 1980. Applications of lactase and immobilized lactase. In "Immobilized Enzymes For Food Processing," Ed. Pitcher, W.H. p. 153. CRC Press, Inc., Boca Raton, FL.
- Dahlqvist, A., Asp, N.-G., Burvall, A, and Rausing, H. 1977. Hydrolysis of lactose in milk and whey with minute amounts of lactase. Journal of Dairy Research 44: 541.
- Finnie, K.J. 1980. Continuous processing of low lactose milk to minimize lactase product inhibition. Master of Science thesis, University of Rhode Island, Kingston, RI.
- Garg, S.K., Dutta, S.M., and Agrawal, S. 1989. Microbial B-galactosidase: Production, properties and industrial applications - a review. Indian Journal of Dairy Science 42(2): 251.
- Guy, E.J. and Bingham, E.W. 1978. Process of  $\beta$ -galactosidase of *Saccharomyces lactis* in milk and milk products. Journal of Dairy Science 61:147
- Huffman-Reichenbach, L.M. and Harper, J. 1982. Beta-galactosidase retention by hollow fiber membranes. Journal of Dairy Science 65: 887.
- Jacober-Pivarnik, L.F. and Rand, A.G. 1984. Use of a milk assay to evaluate the effects of potassium on commercial yeast lactases. Journal of Food Science 49: 435.
- Maculan, T.P. 1979. Ultrafiltration membrane immobilization of lactase and the processing of low lactose milk. Master of Sciences thesis, University of Rhode Island, Kingston, RI.
- Mahoney, R.R. and Adumchuck, C. 1980. Effect of milk constituents on the hydrolysis of lactose from *Kluyveromyces fragilis*. Journal of Food Science 45: 962.

- Mahoney, R.R. and Whitaker, J.R. 1977. Stability and enzymatic properties of B-galactosidase from *Kluyveromyces fragilis*. *Journal of Food Biochemistry* 1: 327.
- Mahoney, R.R. and Wilder, T. 1988. Thermostability of yeast lactase (*Kluyveromyces marxianus*) in milk. *Journal of Dairy Research* 55: 423.
- Mahoney, R.R. and Wilder, T. 1989. Stabilization of lactase (*Escherichia coli* by milk components and related compounds. *Journal of Food Science* 54(4): 899.
- Montgomery, R.K., Buller, H.A., Rings, E.H.H., and Grand, R.J. 1991. Lactose intolerance and genetic regulation of intestinal lactase-phlorizin hydrolase. *FASEB* 5: 2824.
- Rand, A.G. 1981. Enzyme technology and the development of lactose-hydrolyzed milk. In "Lactose Digestion: Clinical and Nutritional Implications," Eds. Paige, D.M. and Bayless, T.M. p. 219. Johns Hopkins University Press, Baltimore, MD.
- Rand, A.G. and Linklater, P.M. 1973. The use of enzymes for the reduction of lactose levels in milk products. *Australian Journal of Dairy Technology* 28: 63.
- Roger, L., Maubois, J.L., Thapon, J.L., and Brule, G. 1978. Hydrolyse du lactose contenu dans l'ultrafiltrat de lait ou de lactosérum en réacteur enzymatique à membrane. *Annals Nutritionnelle Alimentaire* 32: 657.
- Senecal Jr., A. G., 1991. Ph.D. Thesis, University of Rhode Island.
- Senecal Jr., A. G. and Rand, A. G., Stability of commercial yeast lactases in skim milk and skim milk ultrafiltration permeate. To be presented at the Institute of Food Technologists Annual Meeting and Expo (1992).
- Shukla, T.P. 1975. Beta-Galactosidase Technology: A solution of the lactose problem. *CRC Critical Reviews in Food Technology*: 325.
- Wendorff, W.L. and Amundson, C.H. 1971. Characterization of beta-galactosidase from *Saccharomyces fragilis*. *Journal of Milk and Food Technology* 34(6): 300.





KIM, et al.

**TITLE:** Structural Investigation of the Intrinsic Chemical Markers Formed in Aseptically Processed Particulate Foods  
Hie-Joon Kim, Dr., Irwin A. Taub, Dr., Michelle J. Richardson, Ms., Walter Yeomans, Mr., and Kenneth Kustin, Dr.

**ABSTRACT:** The research on intrinsic chemical markers was undertaken to find a long sought objective method for validating that a pathogenic microorganism in the center of a particulate food received a sufficient heat treatment to ensure its destruction. Such a method would facilitate approval of new thermal processing techniques and would enable food processors to provide a commercially sterile product without compromising nutrition and quality.

The chemical structure of the three intrinsic chemical markers found in aseptically processed particulate foods has been investigated. D-fructose was identified as the precursor for two markers, M-1 and M-3. M-1 is observed in heated meats, fruits, and vegetables. M-3 is observed primarily in heated fruits. M-1 and M-3 were purified from heated orange extract by anion exclusion chromatography and analyzed by gas chromatography-mass spectrometry (GC-MS). M-1 has a molecular weight of 144 and a unique fragmentation pattern that matches the library spectrum of 2,3-dihydro-3,5-dihydroxy-6-methyl-4(H)-pyran-4-one (DHDHMP). Its molecular weight was also confirmed by thermospray liquid chromatography-mass spectrometry (LC-MS), and its UV absorption maximum matches the published value of 298 nm for DHDHMP. The formation of DHDHMP proceeds either by dehydration of D-fructose or by the Maillard reaction involving D-glucose and amines through the 2,3-enediol and methyl dicarbonyl intermediates. GC-MS analysis of M-3 produced a mass spectrum that matches the library spectrum of 5-hydroxymethylfurfural (HMF). M-3 and authentic HMF show the same UV absorption spectrum and the same retention time on the anion exclusion chromatographic column. The formation of M-2, a small molecule of about 200-dalton molecular weight observed primarily in heated meats, involves both the proteins in the meat and a small water-soluble molecule.

These results along with previous kinetic characterization put this Thermal Process Validation (TPV) method on a firm physical chemical basis. Its use with new technologies ensures that high quality, shelf-stable packaged rations can be provided to troops in the field.

**BIOGRAPHY OF PRESENTER:** Hie-Joon Kim

**PRESENT ASSIGNMENT:** Senior Research Chemist, Food Engineering Directorate, 1985-1992.

**PAST EXPERIENCE:** Research Associate, Harvard Medical School; Postdoctoral Associate, MIT.

**DEGREES HELD:** B.S., Seoul National University, 1970; M.S., University of Chicago, 1974; Ph.D., University of Chicago, 1977.

KIM, et al.

Structural Investigation of the Intrinsic Chemical Markers  
Formed in Aseptically Processed Particulate Foods

Hie-Joon Kim, Dr., Irwin A. Taub, Dr., Michelle J. Richardson, Ms.  
Food Engineering Directorate  
U.S. Army Natick RD&E Center  
Natick, MA 01760-5018

Walter Yeomans, Mr.  
Soldier Science Directorate  
U.S. Army Natick RD&E Center  
Natick, MA 01760-5020

Kenneth Kustin, Dr.  
Department of Chemistry  
Brandeis University  
Waltham, MA 02154

INTRODUCTION

In the new thermal processes where food particulates are sterilized under flowing conditions either with the scraped surface heat exchanger or by ohmic heating, it is not practical to monitor the temperature-time profile within the particulate and thus prove sterility at the cold spot of a moving particulate. For this reason, the Food and Drug Administration (FDA) has not approved the aseptic processing for low-acid foods containing particulates.<sup>1</sup> In the past, several authors reported attempts to demonstrate sterility of foods by monitoring destruction of compounds commonly present in foods.<sup>2-4</sup> Since only a small fraction of such compounds are destroyed under normal thermal processing conditions, such an approach suffers from experimental uncertainties involved in measuring small changes from a high baseline concentration.

In the new approach undertaken here, the concentration of compounds not present in unheated foods but produced upon heating (intrinsic chemical markers) is correlated with the reduction in the population of test microorganisms, such as *B. stearothermophilus*.<sup>5</sup> The key feature of the correlation is that the decadic reduction in the bacterial population, i.e.,  $\log(N_0/N)$  where  $N_0$  is the initial population and  $N$  is the survivor population, is proportional to the marker concentration expressed as  $M/M_0$  where  $M$  is the observed marker concentration and  $M_0$  is the limiting value of  $M$ . This feature makes the chemical markers extremely useful for validating thermal processes.<sup>6</sup>

Recently, we identified three compounds that appear to be useful intrinsic chemical markers with regard to their easy detectability and appropriate kinetic parameters, such as the rate constants and the

KIM, et al.

activation energies.<sup>5</sup> One of the markers, M-1, was observed in heated meats, vegetables, and fruits. A second compound, M-2, was observed primarily in heated meats, such as beef, pork, and chicken. A third compound, M-3, was observed in heated fruits. Since these are compounds not initially present in foods at appreciable concentrations, it becomes necessary to determine the chemical identity of the markers as well as the precursors.

The chemistry of marker formation from precursors is also important because we need to understand how the marker formation depends on the chemical environment (such as pH, ionic strength, water activity, etc.) and the precursor concentration in order to judiciously use the markers for thermal process validation. In this paper we outline approaches taken and techniques used for obtaining structural information about the three chemical markers and their precursors.

#### MATERIALS AND METHODS

##### Anion Exclusion Chromatography-Photodiode Array Detection (AEC-PAD)

Aqueous extract from heated foods was filtered and injected into an anion exclusion chromatography (AEC) system. Alltech Model 440 metal-free pump delivered 10 mM sulfuric acid eluant at a 1.0 mL/min flow rate. A Wescan (Deerfield, IL) anion exclusion column (sulfonated polystyrene/divinylbenzene, 7.8x100 mm) and a Waters (Milford, MA) Model 990 photodiode array detector (PAD) were used. The UV spectra of eluting compounds were collected every six seconds and stored in a computer for spectral analysis, chromatographic analysis, and three-dimensional or contour display. When necessary, the marker compounds were collected immediately after the UV flow cell for further instrumental analyses.

##### Gel Filtration Chromatography

Gel filtration chromatography was performed on an open column (2x30 cm) using Bio-Gel P-2 (Richmond, CA; molecular weight cut-off, 2,000). Approximately 3-mL fractions were collected using a Gilson fraction collector. Collected fractions were analyzed for the markers by the above AEC-PAD system.

##### Gas Chromatography-Mass Spectrometry (GC-MS)

Purified markers were injected into the GC-MS system, which consisted of a Finnigan model 9610 gas chromatograph and a Finnigan model 4500 mass spectrometer. The GC column was a 60 m DB-5 with 0.32 mm inner diameter. An JNCOS data system and a 31331 spectra library were used. The column temperature was increased from 60°C to 200°C at a 10°C/min rate. The injector temperature was 150°C and the detector temperature was 200°C. A flame ionization detector was also used with a Hewlett-Packard model 5890 gas chromatograph.

### Liquid Chromatography-Mass Spectrometry (LC-MS)

The parent molecular weight of the marker, M-1, was also determined by thermospray LC-MS by Dr. Robert Rosen at the Center for Advanced Food Technology, Rutgers University. The instrument used was a Vestec Model 201 mass spectrometer operated in the positive ion discharge mode. The samples were introduced directly into the system without an LC column.

### RESULTS & DISCUSSION

Fig. 1 shows contour diagrams for water-soluble compounds in control beef and heated beef separated on an anion exclusion chromatographic column and detected by a photodiode array detector. The heated beef shows two compounds that were not present in unheated beef. One compound, M-1, is eluted with 4.0 min retention time and has a UV absorption maximum of 298 nm. Another compound, M-2, is eluted with 5.8 min retention time and has a UV absorption maximum of 285 nm. M-1 was observed from a variety of food categories (meats, vegetables, fruits, extruded products and bread crust) and seemed to be the most useful marker. Therefore, initially most efforts were directed to determination of the precursor and the chemical structure of this compound.

#### Precursor for M-1 and M-3

In gel filtration chromatography smaller molecules penetrate the crosslinked network of the gel matrix more easily and are retained longer than larger molecules. Therefore, this method can be used to establish the molecular weight relationship between the precursor and the product in a simple reaction. When heated orange extract was run on a gel filtration column (Bio Gel P-2) and each fraction analyzed for M-1 by the AEC-PAD system, M-1 was found around fraction 24, which corresponded to a molecular weight of about 150 daltons (Fig. 2). To determine its precursor, unheated orange extract was separated on the same gel filtration column, the collected fractions were heated, and each heated fraction was analyzed for M-1. M-1 was observed in the heated fraction 21 (molecular weight, about 200). Several candidate precursor compounds (glucose, fructose, ascorbic acid, thiamin, sucrose, etc.) were heated in solution, and M-1 was produced only when D-fructose was heated (Fig. 3). Authentic D-fructose (molecular weight, 180) was eluted in fraction 21 under the same gel filtration conditions. Thus, it appears that D-fructose in the orange extract (fraction 21) is converted to a smaller marker molecule (M-1, fraction 24) upon heating. A similar relationship was also observed in vegetables and meats.

When either the D-fructose solution or the orange extract was heated, another compound was observed by the AEC-PAD system. This compound turned out to be a useful marker as well and was named M-3. M-3 has a retention time of 7.5 min and UV absorption maxima of 285 nm and 230 nm (Fig. 3). M-3 was found in fraction 26 after gel filtration separation of the heated



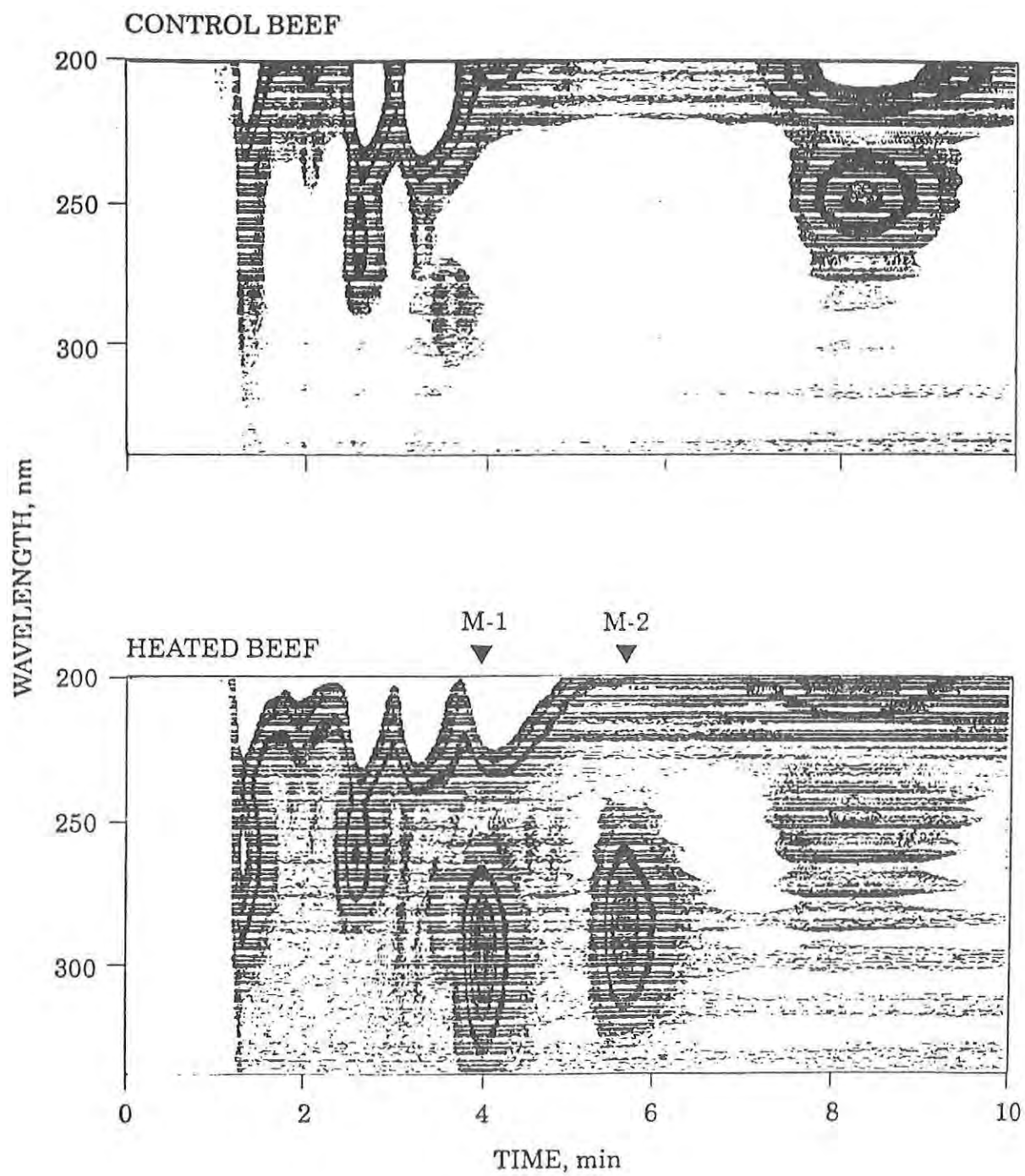


Fig. 1 Contour diagram for control and heated beef showing production of M-1 and M-2.

## GEL FILTRATION CHROMATOGRAPHY

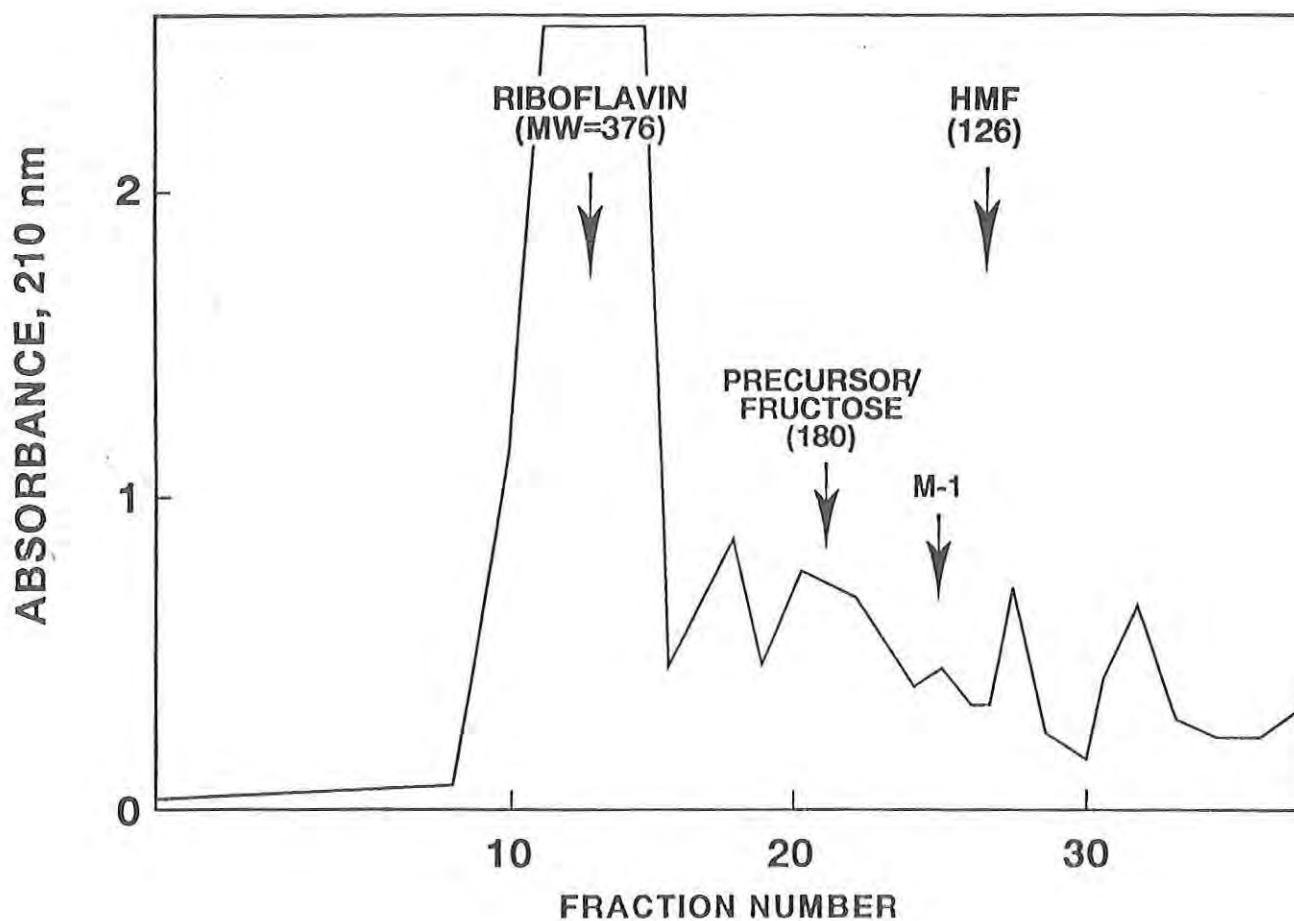


Fig. 2 Gel filtration chromatographic separation of the precursor (fraction 21) and M-1 (fraction 24) from orange extract. 5-Hydroxymethylfurfural (M-3) is eluted at fraction 26.



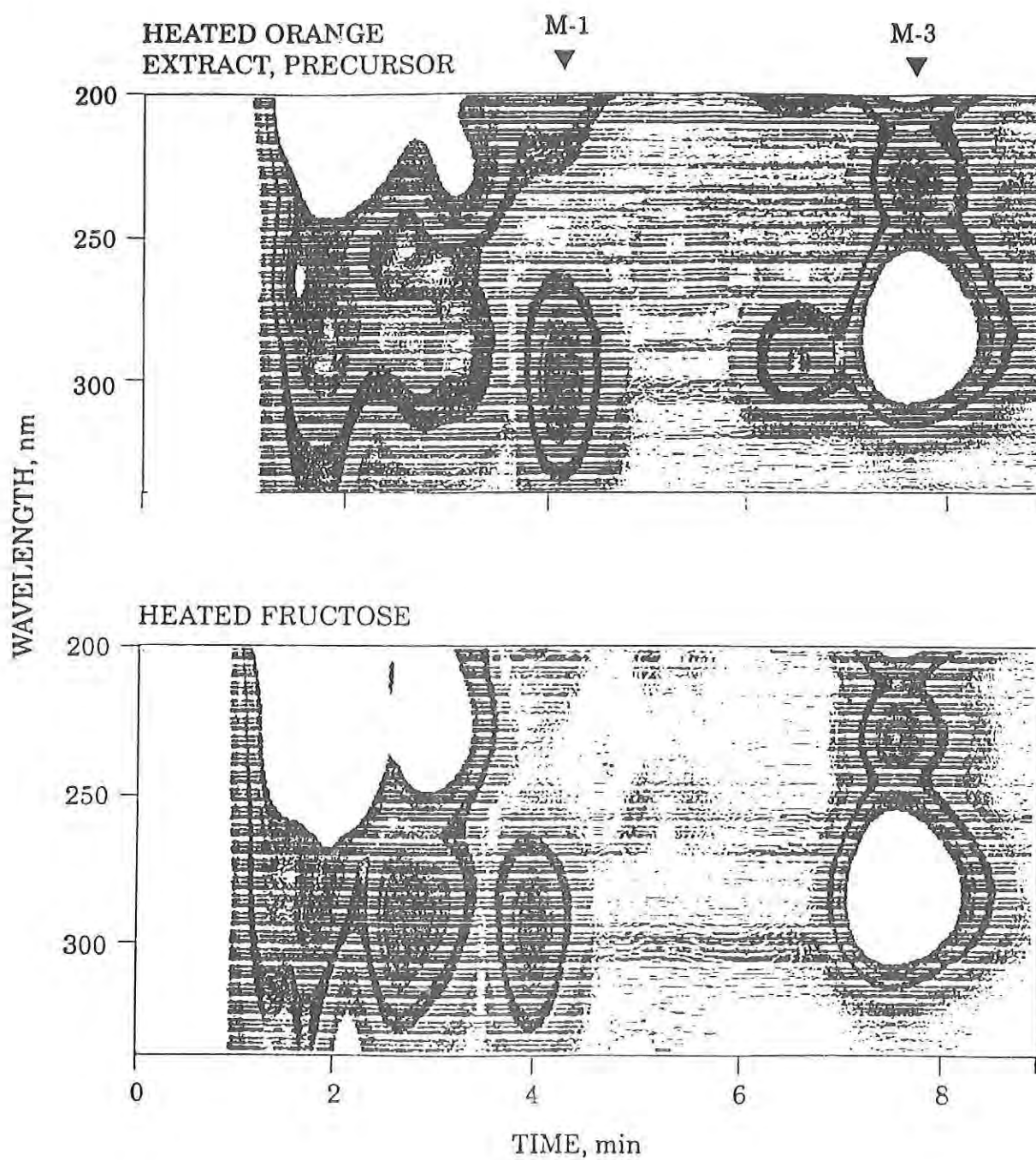


Fig. 3 Contour diagrams showing production of M-1 and M-3 upon heating an orange extract containing the precursor and a solution of D-fructose.

KIM, et al.

orange extract. Therefore, M-3 appears to be even smaller than M-1. M-3 was also produced upon heating D-glucose even though the yield was lower than from D-fructose.

M-1 is 2,3-dihydro-3,5-dihydroxy-6-methyl-(4H)-pyran-4-one (DHDHMP)

In order to purify M-1 and M-3 in large quantities, an orange extract containing added D-fructose (10% by weight) was heated in a sealed vial for 60 min at 130°C. The heated extract was passed through a disposable C<sub>18</sub> cartridge to remove dark brown pigments and then injected into the AEC-PAD system through a 100 µL loop. The eluted portion corresponding to M-1 was collected and evaporated in a desiccator. The remaining material was dissolved in methanol and analyzed by GC-MS. An electron impact spectrum was obtained that matches a published spectrum of 2,3-dihydro-3,5-dihydroxy-6-methyl-(4H)-4-one (Fig. 4, top).<sup>7</sup> A parent molecular weight of 144 was also observed in the mass spectrum.

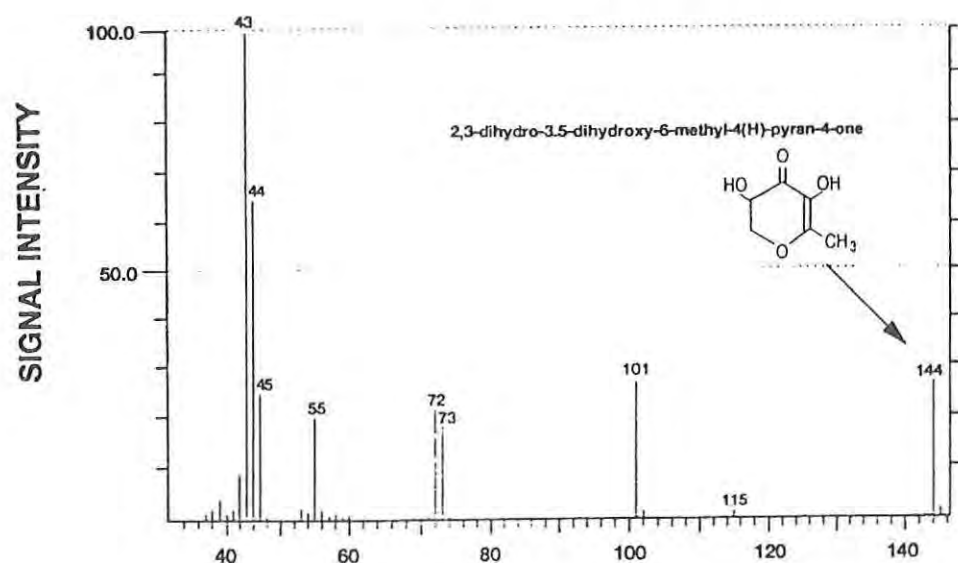
Analysis of the M-1 sample by thermospray LC-MS in the positive ion discharge mode showed (M+H)<sup>+</sup> with a m/e value of 145 as the major species (Fig. 5; Dr. R. Rosen, personal communication). This result confirms that the molecular weight of M-1 determined by GC-MS is correct.

The UV absorption maximum of 298 nm for M-1 (Fig. 1 and Fig. 3) was also reported for DHDHMP prepared by acid-catalyzed dehydration of D-fructose.<sup>8</sup>

Additional information about the structure of M-1 was obtained by a high resolution nuclear magnetic resonance (NMR) experiment. A 600 MHz NMR spectrum (Fig. 6) (courtesy of Dr. M. Kang of Glaxo, Inc.) clearly shows a lack of proton resonance associated with a carboxylic group (around 12 ppm), an aldehyde group (around 10 ppm), or an aromatic ring structure (around 7.5 ppm). This observation is consistent with the structure of DHDHMP. The hyperfine structure in the 1-5 ppm region is believed to be due to two hydroxyl protons, a methyl proton, and three protons bonded to the pyranone ring.

M-1 is formed either by removal of two moles of water from D-fructose<sup>8</sup> or through a more complex mechanism shown in Fig. 7, which involves aldohexose, such as D-glucose, and amines. Initially, a mole of water is removed and an Amadori compound is formed through the Maillard reaction. The Amadori compound is then converted to a 2,3-enediol compound, which is converted after removal of an amine into the pyranose form through methyl dicarbonyl intermediates. The pyranose is converted to DHDHMP upon removal of water.<sup>9</sup> The formation of M-1 is probably through the former mechanism involving the removal of water from fructose in fruits and vegetables and through the latter mechanism involving the Maillard reaction in meats rich in glucose, proteins and amino acids.

## GC-MS ANALYSIS OF M-1



## GC-MS ANALYSIS OF M-3

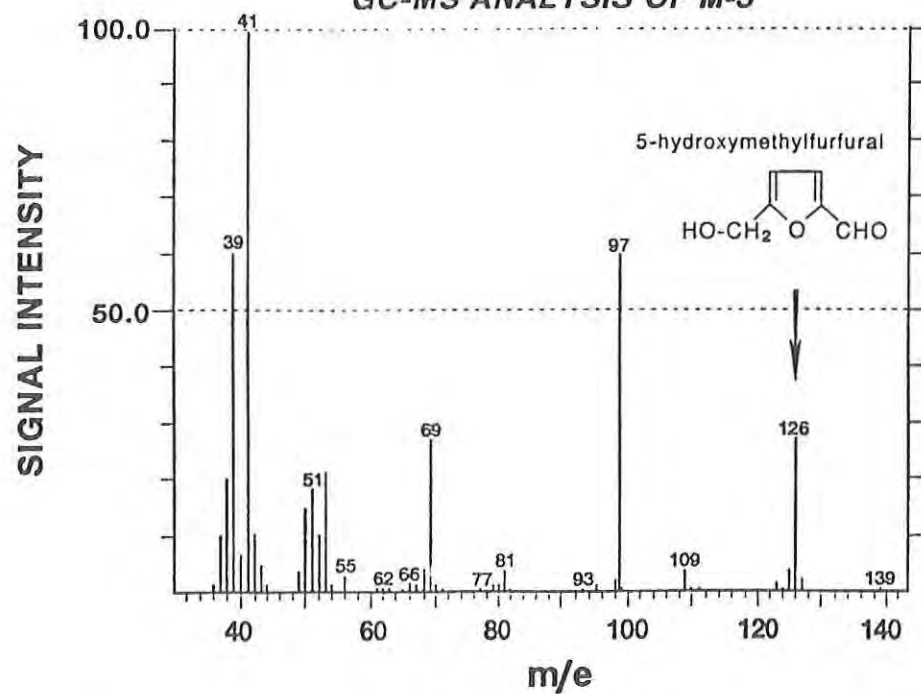


Fig. 4 Electron impact mass spectra of M-1 and M-3 obtained by GC-MS analysis.

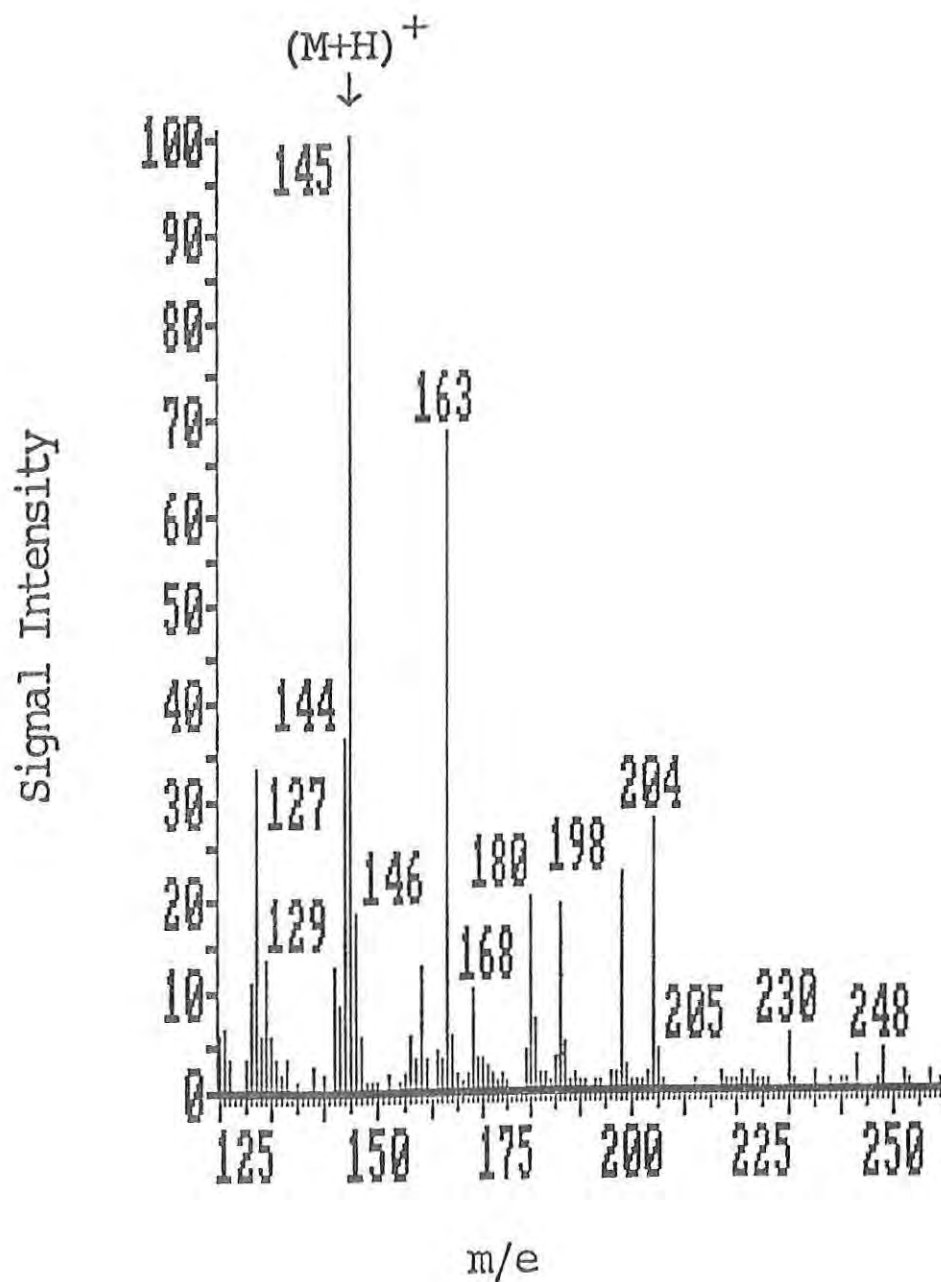


Fig. 5 Mass spectrum for M-1 obtained by thermospray LC-MS showing  $(M+H)^+$  at 145.

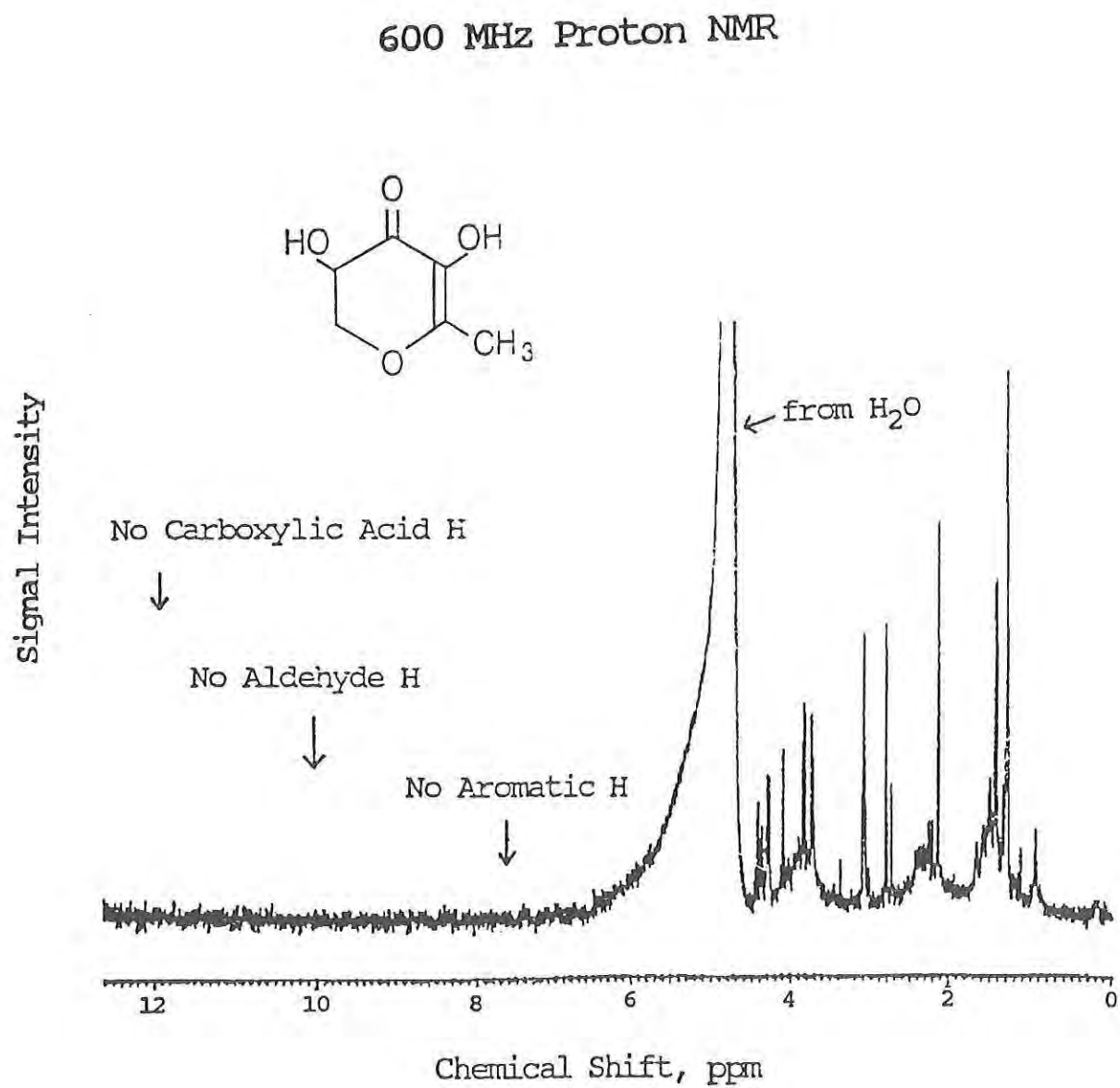


Fig. 6 600 MHz high resolution NMR spectrum of M-1

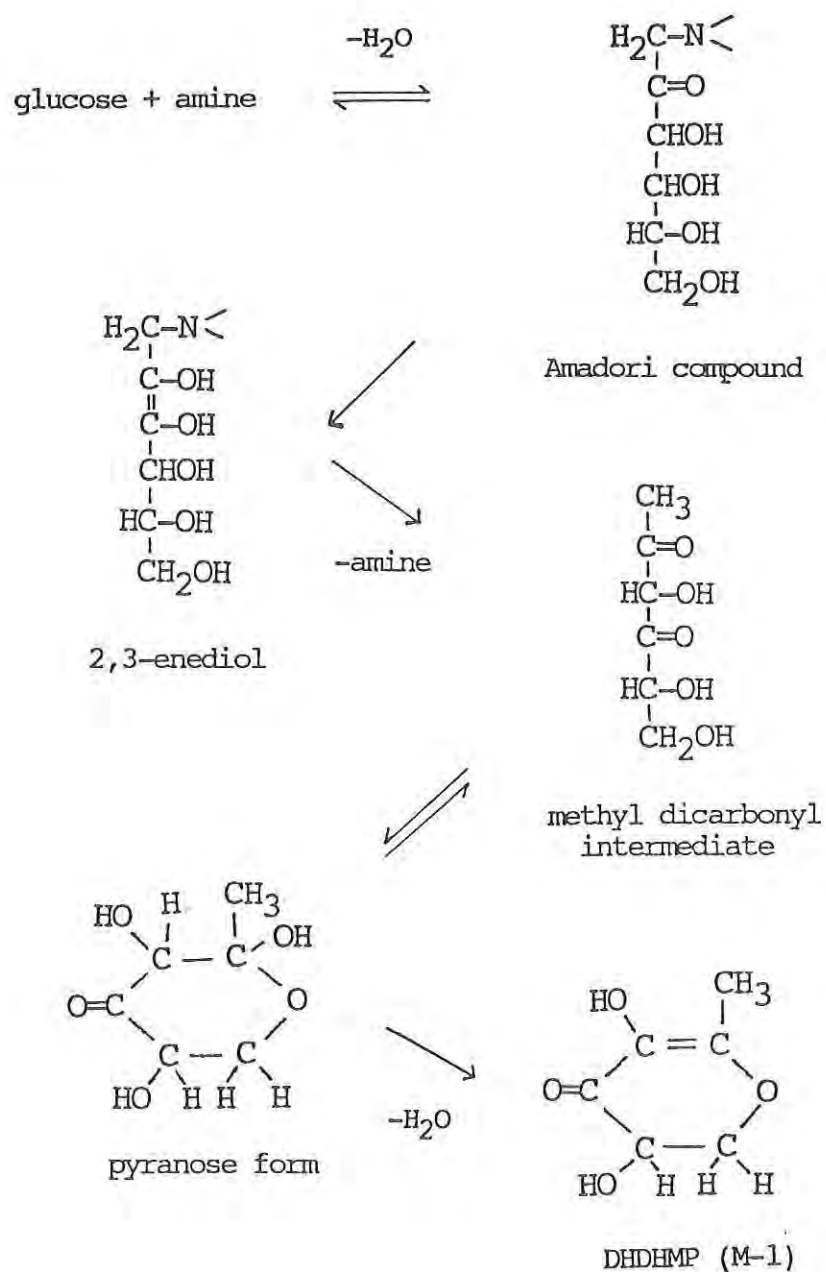


Fig. 7 Reaction mechanism for formation of M-1 through the Maillard reaction pathway.



Kim, et al.

#### M-3 is 5-hydroxymethylfurfural (HMF)

As described above for the preparation of M-1, M-3 was purified from heated orange extract. Subsequent GC-MS analysis positively established M-3 to be HMF, based on the electron impact mass spectrum obtained (Fig. 4, bottom). A parent molecular weight of 126 was also observed. This observation is consistent with the fact that, in the gel filtration separation, M-3 is eluted (fraction 26) after M-1, which has the higher molecular weight. Authentic HMF was also eluted in fraction 26. When both HMF and M-3, collected from a separation shown in Fig. 3, were injected into the AEC-PAD system, identical spectrochromatograms were obtained with a 7.5 min retention time and a unique spectrum with absorption maxima at 230 nm and 285 nm. As shown in the contour diagram in Fig. 3, the absorption at 285 nm was more intense than that at 230 nm. It has been pointed out that a molecule containing a carbonyl group attached to a linear conjugated chain can have more than one electronic transition, one usually more intense than the other.<sup>10</sup>

#### Protein is Involved in M-2 Formation

M-2 was observed primarily in meats. It is an important marker for aseptic processing, because meats represent the most important group of particulates in thermally processed foods. Since it was observed almost exclusively in heated meats, we suspected that proteins might be involved in the formation of M-2. It turned out that proteins are actually involved as demonstrated below.

Meat was homogenized with five-fold excess water and gently heated at about 70°C until proteins were precipitated. The heated meat extract was centrifuged and the precipitate was separated from the supernatant. A clear filtrate containing water-soluble components from the meat was obtained by filtration of the supernatant through a 0.4  $\mu$ m membrane filter. When the filtrate was heated alone for 30 min at 130°C, no M-2 was formed. When the precipitate was heated with an equal weight of water, very little M-2 was formed. However, when the precipitate was heated with an equal weight of the filtrate, M-2 was obtained at a high yield (Fig. 8). This result clearly shows that the formation of M-2 involves a water-soluble component and a component in the precipitate.

In order to further demonstrate that proteins are involved, the filtrate was heated with pure proteins such as bovine serum albumin (BSA) and lysozyme. As expected, M-2 was observed with both BSA and lysozyme. M-2 was not produced when an aqueous solution of BSA or lysozyme alone was heated. The precursor for M-2 in the filtrate appears to be a small molecule (150-200 dalton). The nature of the precursor is unknown at present. M-2 appears to have a molecular weight of approximately 200, based on the gel filtration experiment. It appears that a small water-soluble molecule in the meat reacts with a side group of large protein molecules followed by a detachment to form M-2. The chemical

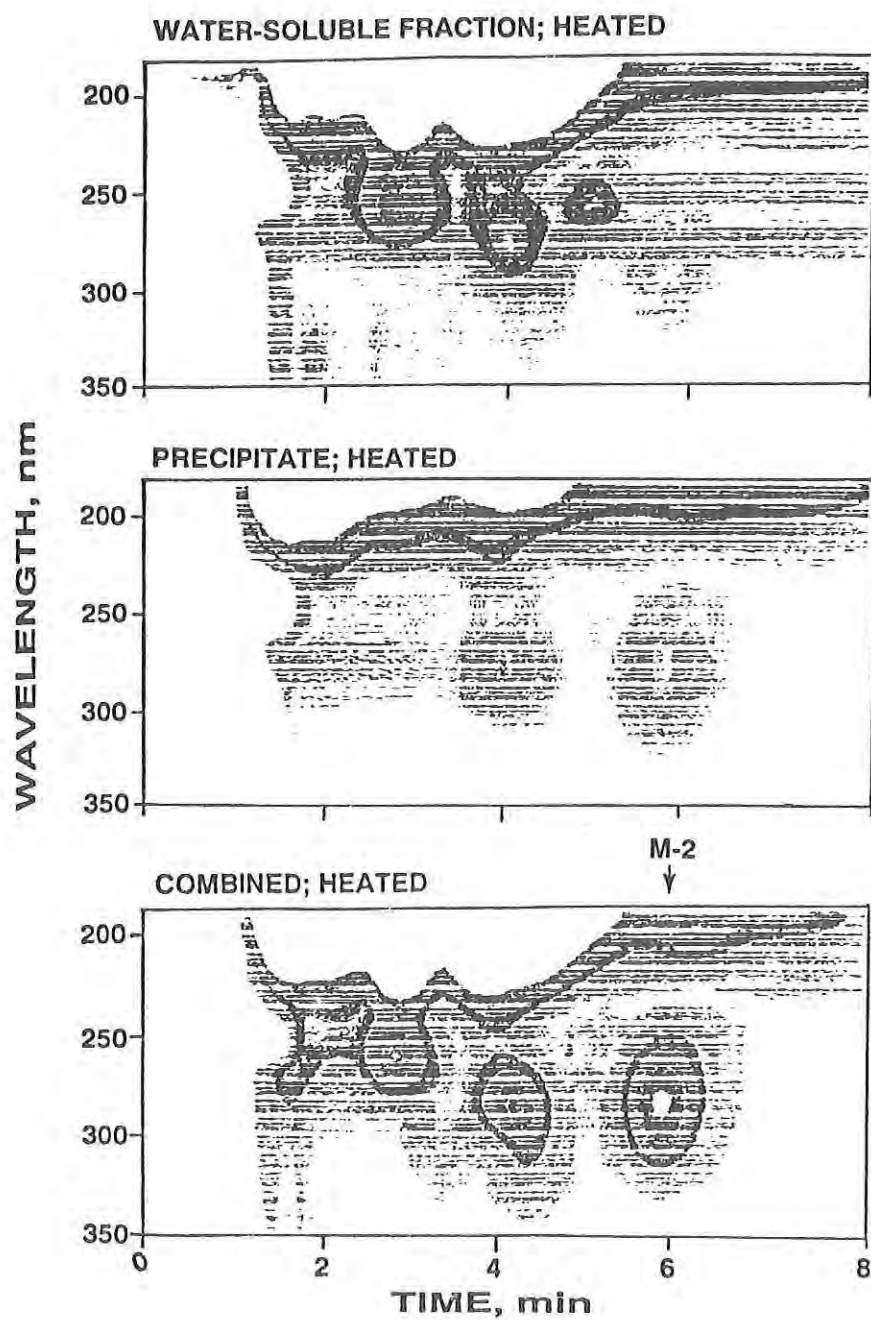


Fig. 8 Contour diagrams showing the involvement of both the water-soluble fraction and the precipitated protein in the formation of M-2

KIM, et al.

structure of M-2 is under investigation and, once known, it will shed light on the mechanism for this intriguing reaction.

#### CONCLUSION

The structural characterization of the markers put the Thermal Process Validation method on a firm physical chemical ground. The existence of different reaction mechanisms for M-1 suggests that one needs to identify the mechanism in different types of foods and use the appropriate rate constants and activation energies when using the mathematical model for the Thermal Process Validation. Its use with new technologies, such as ohmic heating, ensures that high quality, shelf-stable packaged rations can be provided to troops in the field.

#### REFERENCES

1. Dignan, D.M., Berry, M.R., Pflug, I.J., and Gardine, T.D., Food Technol. 43(3), 118 (1989).
2. Mulley, E.A., Stumbo, C.R., and Hunting, W.M., J. Food Sci., 40, 993 (1975).
3. Rao, M.A., Lee, C.Y., Katz, J., and Cooley, H.J., J. Food Sci., 46, 636 (1981).
4. Berry, M.F., Singh, R.K., and Nelson, P.E., J. Food Sci. 55, 502 (1990).
5. Kim, H.-J. and Taub, I.A., Food Technol. to be published (1992).
6. Kim, H.-J., Taub, I.A., Richardson, M., Kustin, K., and Ross, E., Activ. Rept. R&D Associates. in press (1992).
7. Mills, F.D., Weisleder, D., and Hodge, J.E., Tetrahedron Letters, 15, 1243 (1970).
8. Shaw, P.E., Tatum, J.H., and Berry, R.E., Carbohydr. Res. 5, 266 (1967).
9. Hodge, J.E. and Osman, E.M., "Principles of Food Science" edited by O.R. Fennema, p. 84, Marcel Dekker, 1976.
10. Singh, B., Dean, G.R., and Cantor, S.M., J. Am. Chem. Soc. 70, 517 (1948).



**TITLE: Determining the Influence of Moisture and Humectants on the Staling of Long Shelf-Life Bread Using Dynamic Mechanical Analyzer and Nuclear Magnetic Resonance**

Pavinee Chinachoti, Dr., Yang Kou, Mr., and Linnea M. Hallberg, Ms.

**ABSTRACT:** The glassy-rubbery state of bread polymers has been proposed as a key factor contributing to staling. Glassy-rubbery states of bread components as measured by Dynamic Mechanical Analyzer (DMA) in meal-ready-to-eat (MRE) bread exhibit three thermal transitions: two moisture dependent and one moisture independent. The moisture-dependent transition at -70°C range was a result of the humectants added. The other moisture-dependent transition showed a rapid drop in  $E'$  (by one to two orders of magnitude) corresponding with a  $\tan\delta$  peak at about -12°C. At lower moisture content, however, the glass-transition temperature ( $T_g$ ) increased to 150°C at 2 % moisture; the values agreed with  $T_g$  reported for starch and gluten. This  $T_g$  has some relationship with the presence of unfrozen water detected by a Differential Scanning Calorimeter (DSC). Over storage, the MRE bread gave a significant decrease in the  $\tan\delta$  peak height but the  $T_g$  temperature remained relatively unchanged, indicating no maturation of the polymer network over time. In contrast, a white pan bread showed only one moisture-dependent  $T_g$  and, over storage, there was a dynamic change in  $T_g$ . Not only did the transition temperature increase to a higher temperature but also there was an emergence of new  $T_g$ 's. The development of these multiple transitions indicated that water was not uniformly distributed among different domains. Since this bread suffered some significant moisture loss, the  $T_g$  for these domains all increased to a temperature much higher than room temperature, reaching 60°C after a 1 month storage at 25°C. Therefore, firming of white bread during staling is, at least in part, a result of an increased  $T_g$ .

<sup>17</sup>O NMR water mobility measurement showed that there was some decrease in the water  $T_2$  relaxation time over storage of humectant-treated breads, indicating some water redistribution. Sorbitol and glycerol affected such redistribution very differently. While glycerol gave a relative greater decrease in  $T_2$  of the mobile water, the amount of (relatively) immobile water remained unchanged. Sorbitol, however, showed the opposite. This indicates a different ability of humectants to monitor the redistribution (and plasticization mediating ability) of water. Breads with glycerol were softer as the amount of mobile water remained unchanged, while sorbitol-treated bread turned harder, probably due to a decreasing amount of mobile water over time.

**BIOGRAPHY OF PRESENTER:** Pavinee Chinachoti

**PRESENT ASSIGNMENT:** Assistant Professor, Univ. of Massachusetts.

**DEGREE HELD:** B.S. Biology, Mahidol Univ. Bangkok, Thailand; M.S. & Ph.D. Food Science, University of Illinois, Urbana-Champaign.

CHINACHOTI, et al.

Determining the Influence of Moisture and Humectants  
on the Staling of Long Shelf-Life Bread  
Using Dynamic Mechanical Analyzer and Nuclear Magnetic Resonance

Pavinee Chinachoti, Dr., Yang Kou, Mr., and Linnea M. Hallberg\*, Ms.

University of Massachusetts-Amherst, Amherst, MA 01003

\* U.S. Army Natick Research, Development and Engineering Center  
Natick, MA 01760-5018

#### INTRODUCTION

The freshness of shelf-stable, "meal-ready-to-eat" (MRE) bread is preserved by controlling water activity  $a_w$ , pH, oxygen content, and initial microbial load (1,2). Although the bread is microbiologically safe, physical and chemical changes can still occur during a shelf-life of up to three years. Normally, breads are prone to staling, which involves a considerable deterioration of flavor, texture and color characteristics of a fresh bread.

Back in 1902, starch retrogradation (recrystallization) was proposed to be the predominant factor in the staling of bread (3). Now, after a century of research, starch retrogradation is still considered to be one of the key factors contributing to staling (4-8). Other factors include changes in gluten functionality (6,7), moisture migration/redistribution (9-11), and, recently, the glassy-rubbery state of bread polymers (12).

Today, many believe that the recrystallization of starch is aided by water-mediated plasticization (13,14). Willhoft (15) proposed that this water is released from the denatured gluten which slowly decreases its "water holding capacity." He claimed that up to 30% of the water migrated from gluten to starch in 120 hours at room temperature. Others reported the opposite, water migrating from starch to gluten (16,17). Recently, there has been a considerable interest in the dynamic state of water in



CHINACHOTI, et al.

bread, and the role of bound and free water is hypothesized to be an important factor in the staling process (18).

The water-mediated plasticization of components in the firming of bread is related to changes in the molecular motion of polymer chains. The glassy/rubbery state and its transition temperature ( $T_g$ ) has been described to play a key role (12). The  $T_g$  responsible for mechanical firmness of bread, namely the "effective" network  $T_g$ , has been described as changing during staling resulting in texture firming of bread. Freshly baked bread has been proposed to give the effective  $T_g$  at subzero temperature; during staling  $T_g$  tends to increase to well above room temperature, reaching 60°C in a completely staled bread and indicating network maturation in aging bread (12).

With water as a mediator of plasticization,  $T_g$  of bread polymers has been reported to decrease from about 160°C to close to room temperature upon increasing moisture content from approximately 0 to 20% (18,19). Because most bread staling experiments involve some degree of moisture loss from the crumb, the increase in  $T_g$  during staling mentioned above could be partly influenced by the decreasing moisture content. MRE bread allows us to study bread staling for up to three years of storage with no moisture loss from its hermetically sealed pouch. The "effective"  $T_g$  can thus be measured and any maturation of the network can be observed with no artifact of moisture loss. Therefore, the objective of this work is to apply Dynamic Mechanical Analysis to determine glass transitions in MRE bread and to identify the "effective"  $T_g$  as a function of moisture content and storage time.

Nuclear magnetic resonance (NMR) and differential scanning calorimetry (DSC) have been used to study water molecular mobility and unfreezeable water in bread, respectively. Wynne-Jones and Blanshard (14) found a significant increase in unfreezeable water with storage time. Proton spin-spin relaxation time ( $T_2$ ) was found to decrease with time and thus it was concluded that the changes in the physical state of water occurred primarily in the amylopectin fraction (9,14). Recently, it has been suggested that the freezable water in the amorphous matrix migrated to the crystalline hydrate of B-type wheat starch (12). Here the water became unfrozen upon cooling to subzero temperature.

$^{17}\text{O}$  NMR has recently been suggested to be the best nuclei to study water in that it is not subjected to errors normally anticipated in  $^1\text{H}$  and  $^2\text{H}$  nuclei, including 1) cross relaxation between protons of the water and the matrix, and 2) exchange of  $^2\text{H}$  on water with  $^1\text{H}$  of the matrix (20-23). Recent work has shown that  $T_2$  relaxation time and the signal intensity using  $^{17}\text{O}$  NMR can yield valuable information about water in liquid and semisolid food model systems (24).

In this work,  $^{17}\text{O}$  NMR is applied to study water mobility by measuring the  $T_2$  relaxation time and the signal intensity in bread upon storage. We compared the behavior of surfactants and humectants used in bread in order to relate them to amylopectin crystallization. (Surfactants retard amylopectin crystallization and humectants are water 'binders'.)

## MATERIALS AND METHODS

### Thermal Transition Study

#### Materials

The breads used in this study were a standard white bread (SWB) and a long shelf life MRE bread. The MRE Breads are a straight dough product that are hermetically sealed in a trilaminate polyethylene-aluminum foil-polyester pouch with controlled atmosphere and moisture ( $< 1.6\% \text{ O}_2$  and  $< 0.89$  water activity at  $25^\circ\text{C}$ ). The standard white bread was made fresh in our lab via a straight dough method (25). The long shelf-life, MRE bread was made according to the procedure specified in Military Specification (26). The formula for SWB includes 57.47% flour, 34.48% water, 3.02% shortening, 2.73% sugar, 0.86% salt, 0.29% calcium propionate, 0.11% potassium sorbate, and 0.11% active dry yeast. The formula for MRE bread includes 50.28% flour, 28.96% water, 8.50% shortening, 6.34% glycerol, 2.25% yeast, 1.29% salt, 1.00% sucrose ester, 0.50% gum arabic, 0.50% xanthan gum, 0.25% calcium sulfate, 0.10% sorbic acid, and 0.03% cream flavor.

#### Methods

The effect of moisture and storage time on thermal transitions will be studied. Various moisture contents were obtained by hydration or desorption from the original moisture. The hydrated samples were prepared by placing the compressed and cut bread bar described below in a desiccator above pure water for 1, 2 and 15 hours. The desorbed samples were prepared by dehydrating in a vacuum oven at room temperature and 30 in Hg vacuum for time periods of 15 min, 2 hrs and 24 hrs. The final moisture contents were 28.8%, 24.5%, 22.6%, 17.0%, 13.4%, 8.5% and 2.6% total weight basis. The storage time studied was done by storing the MRE and SWB breads at  $22^\circ\text{C}$  for up to three years. The SWB sample was stored in double polyethylene bags and some moisture loss was observed.

#### DMA Analysis

All samples were uniformly sliced to a thickness of 10 mm, the crust removed, and then the crumb compressed to a 2 mm thickness using a Carver press with 300 lb per sq in pressure. This pressure was found optimum to obtain a uniform thickness of 2 mm with no porous structure remaining. The resulting pressed bread was cut with a die into a 50 mm x 12 mm rectangle. Uniform geometry of the sample was critical so as to prevent variation. The resulting bars were of  $0.10 \pm 0.001 \text{ g/cm}^3$  density.

The bread bars were placed in the DMA (Seiko Instruments International, Model DMS110, Torrance, CA). The sample was cooled to  $-80^\circ\text{C}$  and then heated to  $200^\circ\text{C}$  at a rate of  $2^\circ\text{C/min}$ . A three point bending head was used and the stress was applied at 1, 2, 5, 10, 20 Hz frequencies. Our data show the  $T_g$  values to vary within 2.4% experimental error.

## Water Study

### Materials

Standard white breads as above were prepared with varying surfactants and humectants. Surfactants were added at 0.5% flour basis. These included sodium stearyl-2-lactylate (SSL, Patco Products, Kansas City, MO), mono- and di-glycerides (Dimodan<sup>R</sup>, Grindsted Products, Inc., Kansas City, MO), and sucrose esters (SE1170, Mitsubishi Kasei Food Corp., Tokyo Japan). Humectants (glycerol and sorbitol) were applied at 5% (flour basis) concentration.

The moisture contents of the bread crumb were  $0.557 \pm 0.012$ ,  $0.537 \pm 0.007$ , and  $0.513 \pm 0.008$  g of water/g of solids for the control, sorbitol-treated, and glycerol-treated bread, respectively. There was no significant difference in moisture content among the various surfactant treatments for breads with the same humectant treatment. The value of  $a_w$  for the humectant-free fresh bread was 0.97, and that for all humectant treated fresh breads was 0.93.

All bread samples were also enriched in oxygen-17 by placing a small portion above a saturated solution of potassium nitrate made with oxygen-17 enriched water to achieve an  $a_w$  of 0.93. The bread was left in the 0.93  $a_w$  chamber for 12 h at 25°C, after which time-weighted samples were placed in NMR tubes and sealed. The samples were kept at room temperature throughout the study. In some cases moisture content was determined before and after the aging study. At most, the humectant-treated samples lost 2% of their moisture.

### NMR Measurements.

The  $^{17}\text{O}$  NMR spectra at 40.67 MHz were recorded on a Varian XL-300 broad band spectrometer retrofitted with a VXR-4000 computer system. A spectral width of 20,000 Hz and a 15- $\mu\text{s}$  pulse (corresponding to a flip angle of 79°C) were used to obtain the spectra. Maximum sensitivity was obtained by using a short acquisition time (0.02 s) and a large number of repetitive accumulations (4000-60,000). Acoustic ringing was found to distort the baseline in most samples; hence, to avoid this problem, a 150- $\mu\text{s}$  delay (dead time) between the pulse and the acquisition was introduced to suppress the rolling baseline effect. Proton decoupling was used during acquisition, but the samples were not spun. In fact, neither of these was found to have any significant effect on the spectra.

It is difficult to observe signals with relaxation times less than 150- $\mu\text{s}$  with the Varian XL-300, and there is a possibility that a broad component of the spectrum may be lost. Consequently, some of the samples were submitted to  $^{17}\text{O}$  NMR analysis at 28.7 MHz using an IBM 200-AF spectrometer with IBM Solids Accessory (dead time of ca. 15  $\mu\text{s}$ ). Using similar acquisition times and numbers of accumulations, there was no large difference in the  $T_2$  values obtained on both instruments, the largest being 6%. Magic angle spinning (MAS) had no effect on the  $^{17}\text{O}$  spectrum. The signal from every sample was a simple Lorentzian line,

regardless of which instrument was used.

Since no signals were observed in the range  $15 \mu s < T_2 < 150 \mu s$ , the water in the bread samples falls into two distinct categories. That with  $T_2 > 150 \mu s$  cannot be detected with either instrument. As an operational definition, we take this to be "bound" water. The transverse relaxation time was obtained by measuring the line width of the  $^{17}O$  peak in the NMR spectra and using the standard formula for  $T_2$ ,  $1/\pi \Delta\nu$ , where  $\Delta\nu$  is the line width at half-height.

Table 1.  $^{17}O$  NMR Transverse Relaxation Times ( $T_2$ ) for Sorbitol-Treated Breads with Four Surfactant Treatments

| bread                    | <u>Transverse relaxation time ( ms )</u> |        |
|--------------------------|--|--------|
|                          | 200-AF                                   | XL-300 |
| standard (no surfactant) | 0.259                                    | 0.253  |
| with SSL                 | 0.241                                    | 0.239  |
| with SE                  | 0.220                                    | 0.233  |
| with Dimodan             | 0.245                                    | 0.241  |

<sup>a</sup>All samples were obtained from 1 day of storage. Spectra were at 20°C using both IBM 200-AF and Varian XL-300 spectrometers.

The amount of detectable water was monitored using the absolute integrated signal of the NMR spectra (24). The volume of the samples was always less than 1.2 mL. Liquid water was used as an external standard for all measurements. The  $^{17}O$  intensities are self-consistent for each sample. They give a valid comparison of detectable water as each sample ages. The parameters define detectable water as that fraction which relaxes slower than ca. 150  $\mu s$ , a figure which is determined by the dead time.

Duplicate measurements of  $T_2$  on a single sample showed an average variation of 2%. Duplicate samples were examined in some cases. Here the average variation was 4%, which reflects small differences in sample preparation and handling.

#### DSC Measurements

To observe the degree of unfreezable water and amylopectin crystallization during bread staling, the degree of endothermic melting was measured over storage time. The endotherms were obtained using a Perkin-Elmer DSC (DSC<sub>2</sub> Perkin-Elmer Corp., Norwalk, CT). A 10-mg bread sample was weighed and placed in a hermetically sealed pan and heated from -100°C to 160°C at a rate of 10°C/min. An empty pan was used as the



CHINACHOTI, et al.

reference. The degree of ice and amylopectin melting was measured from the endothermic peak area at ca.  $-10^{\circ}\text{C}$  to  $-20^{\circ}\text{C}$ , and  $70^{\circ}\text{C}$ , respectively.

## RESULTS

### Thermal Transitions

#### MRE versus Standard White Bread

The  $\tan \delta$ ,  $E'$  and  $E''$  of fresh standard and MRE breads are plotted against temperature in Fig. 1. The resulting  $E'$  and  $E''$  started from relatively high values and sharply dropped at approximately  $-2.5^{\circ}\text{C}$ , and  $-11.0^{\circ}\text{C}$  for the white and MRE breads, respectively. At these same temperatures, the  $\tan \delta$  values (ratio between  $E'$  and  $E''$ ) rose to a peak and then sharply dropped. This phenomena can be due either to a first order transition (melt) or a second order (glass transition). To the left of the main transition ( $T_1$ ), there appears to be another small and broad transition at approximately  $-70^{\circ}\text{C}$ , indicated by a shoulder in  $\tan \delta$  accompanied by a slight drop in  $E'$ . This  $T_2$  transition seemed to be quite noticeable in the MRE bread ( $T_2$ , Fig. 1b) and almost undetectable in the white bread (Fig. 1a). In addition, the MRE bread showed another strong shoulder in  $\tan \delta$  to the right of the main transition peak ( $T_3$ , Fig. 1b) where the white bread did not (Fig. 1a).

The sharp single  $\tan \delta$  peak in the standard white bread (SWB) at  $-2.5^{\circ}\text{C}$  (Fig. 1a) indicated that there was one transition occurring. On the other hand, the presence of shoulders of  $\tan \delta$  found in the MRE bread indicated that there were two additional transitions detectable under these conditions.  $\tan \delta$  at various frequencies illustrated in Fig. 1, showed that the temperature shifted to a higher value at a higher frequency.

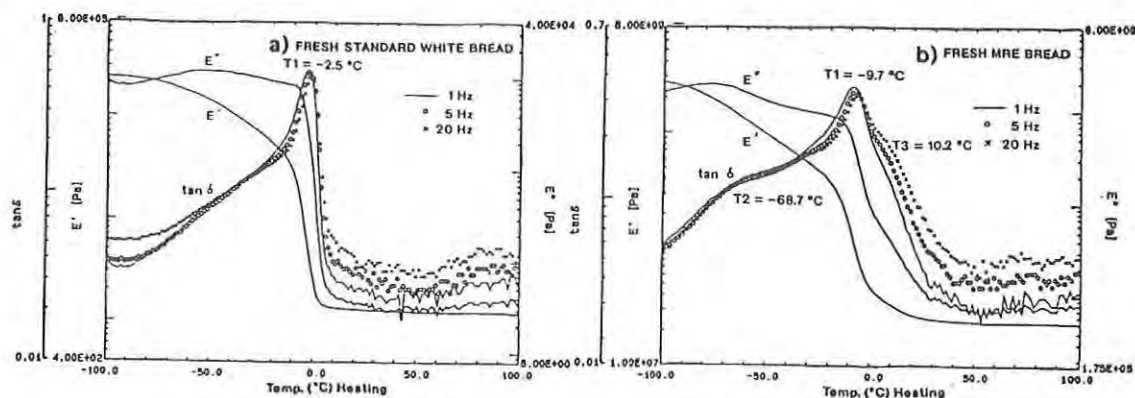


Figure 1. DMA Thermograms of fresh standard white (a) and MRE breads (b).  $\tan \delta$  at 1, 5, and 20 Hz is represented by —,  $\circ$ , and  $\times$ , respectively.

The main thermal transitions (T1) in white bread ( $-2.5^{\circ}\text{C}$ ) and in MRE bread ( $-9.7^{\circ}\text{C}$ ) were found to occur simultaneously with ice melting. DSC scans of these samples (Fig. 2) showed a corresponding endothermic melting of ice. The endotherm  $T_0$  (initial temperature) was at  $-10.1 \pm 0.4^{\circ}\text{C}$  for the case of SWB and at  $-18.3 \pm 0.2^{\circ}\text{C}$  for the case of MRE bread. In addition to melting of ice, there was a shift in the DSC baseline after the ice melting process was completed. This resulted in a relatively lower baseline to the right of the endothermic curve (Fig. 2). This is reasonable since ice and liquid water are different in specific heat and thus melting of ice would result in an increased heat capacity in the sample, resulting in an endothermic shift in baseline. It needs to be mentioned here also that there was a possibility that, once melted, the frozen water was able to plasticize bread polymers. Thus an instantaneous plasticization and a glass transition of the polymers is highly possible; this would contribute to the change in heat capacity. The significance is yet to be determined.

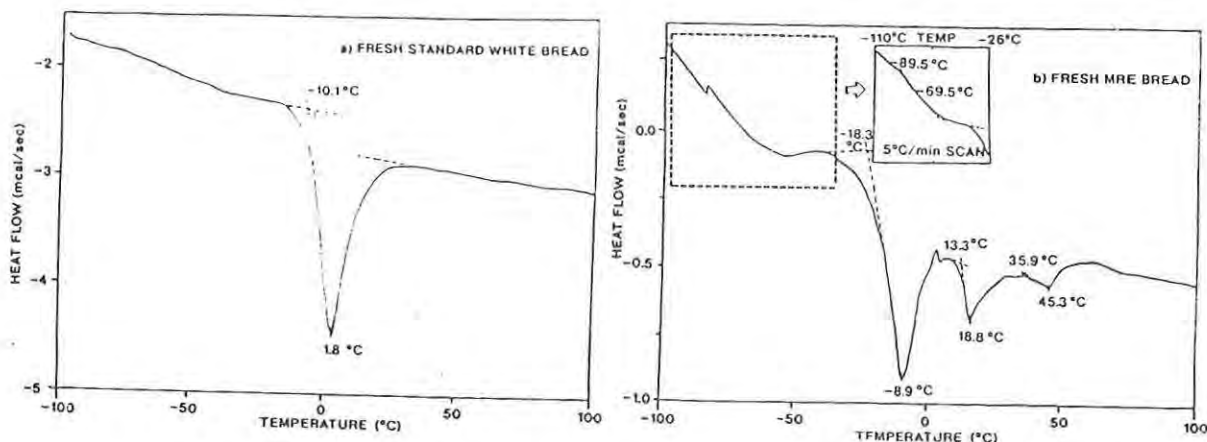


Figure 2. DSC thermograms of fresh standard white bread (a) and of fresh MRE bread (b). Samples were heated from  $-100^{\circ}\text{C}$  to  $100^{\circ}\text{C}$  at  $10^{\circ}\text{C/min}$  in hermetically sealed pan.

Also indicated in Fig. 2 is a DSC result at  $-110^{\circ}\text{C}$  to  $-26^{\circ}\text{C}$  range showing a baseline shift (more evident when the  $5^{\circ}\text{C/min}$  scan rate was used, see Fig. 2), indicating a glass transition process. Thus, the T2 transition in Fig 1b was confirmed to be a glass transition. This was due to the presence of glycerol in MRE bread. This glass transition (T2) was not found in SWB because of the lack of glycerol (Fig. 1a, 2a).



## Comparison of Moisture Content

The effect of moisture on the three thermal transitions in MRE bread as determined by DMA, is shown in Fig. 3. As the moisture content increased from 2%, the main transition (T1) temperature decreased from 150°C drastically and levelled off at some subzero temperature (-23°C). The T2 transition at approximately -70°C was observed only at moisture 17.0% and above; T2 temperature decreased with increasing moisture. And lastly, the T3 transition was at a constant range of temperature (8-14°C) regardless of moisture constant. Note that T3 is not ice melting since its peak temperature is above the melting point of ice. It is clear in Fig. 3 that there are three distinct transitions in fresh MRE bread, two moisture-dependent transitions (T1 and T2) and one moisture-independent transition (T3).

The T1 transition occurred within the reported range of Tg for gluten and starch (19,12,27). The T2 transition is a glass transition as confirmed by DSC (Fig. 2b). Such low Tg temperature and moisture dependency indicated that it was most likely to be contributed by water-soluble solutes, glycerol in this case (see formula for MRE bread). Glycerol has been reported to show a glass transition temperature of -65°C (28). This coincided with the values obtained from DSC,  $-69.5 \pm 1.3^\circ\text{C}$ . White bread contained no glycerol and thus gave no T2 transition. The moisture independency of the third transition (T3, Fig. 3) indicated that T3 was due to water-immiscible components. These could include shortening and hydrophobic domains of bread components. The absence of T3 transition in the fresh standard white bread (Fig. 1a) was partly due to the relatively small amount of shortening added. The DSC (Fig. 2b) confirmed that there were two endothermic melting processes at temperatures above zero. One of these fell in the temperature range corresponding to T3 indicated by the DMA results (Fig 1b).

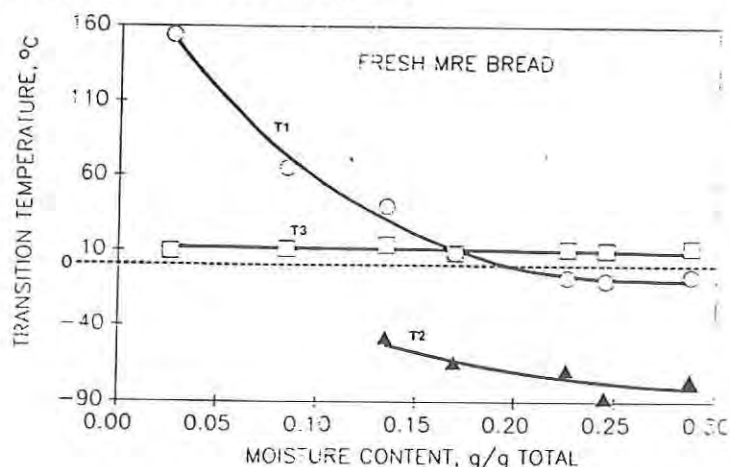


Figure 3. Thermal transition temperatures of fresh MRE bread as a function of moisture content.

## Storage Time

MRE bread samples stored at room temperature for up to three years gave thermograms as illustrated in Fig. 4. In Fig. 4, the fresh sample showed a sharp T1 transition at a  $\tan \delta$  peak temperature of  $-9.7^\circ\text{C}$ , with a very small right shoulder. As the bread aged for three months, the T1 transition became much less prominent (from 0.45  $\tan \delta$  for fresh bread to 0.25  $\tan \delta$  for three month old bread), and thus the right shoulder (T3) became more observable. However, there were no significant changes in either T1 or T3 temperatures with storage time.

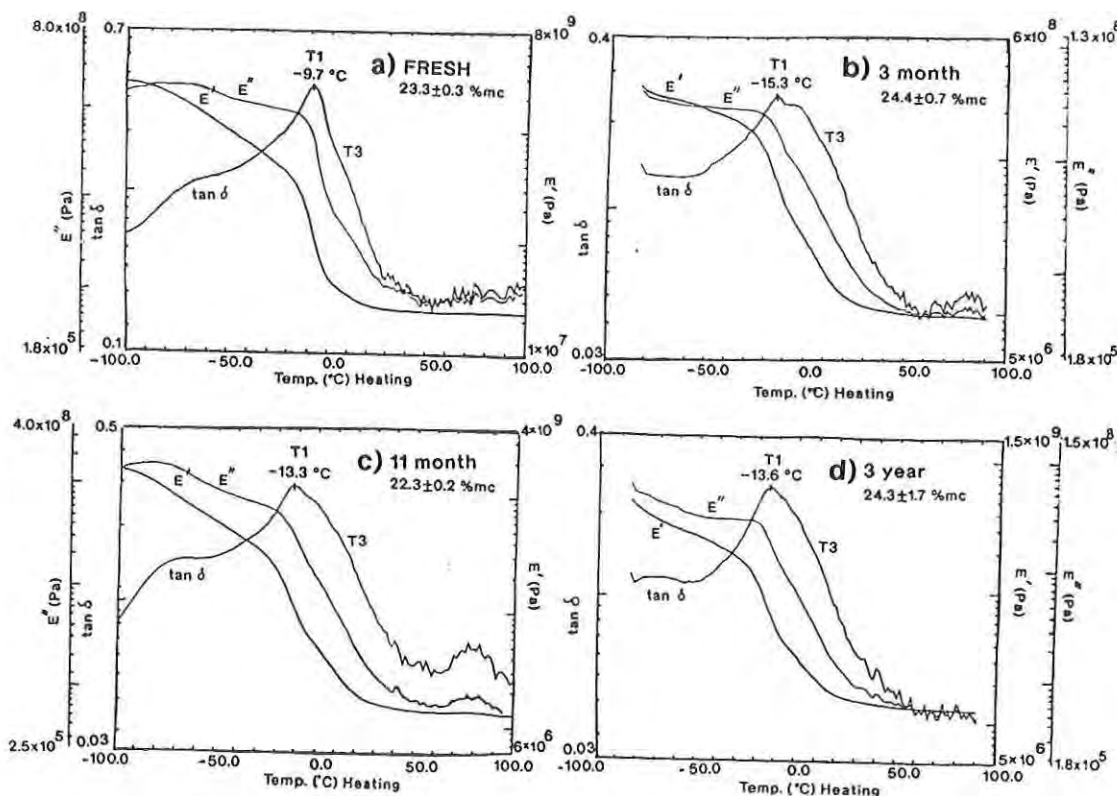


Figure 4. DMA Thermograms of MRE breads stored in hermetically sealed pouch at room temperature for various periods up to 3 years.

In the 3 month and 11 month old samples (Fig. 4), some DMA data showed what could be identified as a small peak in  $\tan \delta$  at  $60^\circ\text{C}$ - $90^\circ\text{C}$  temperature range. However, the  $E'$  and  $E''$  values did not considerably change. It is

possible that this might be an evidence of some small melting process of retrograded starch. No such evidence was found in the three year sample, however.

According to Slade and Levine (12), a maturation process of the polymer network occurred during bread staling leading to another glass transition ("effective  $T_g$ ") at some higher temperature (max.  $60^\circ\text{C}$ ). Our data in Fig. 4 indicated no development of such "effective  $T_g$ " transition over time. In addition the sample firmness as measured by the stress-strain curve (Instron data, not shown) was found to increase only slightly during the first three months and then leveled off for the rest of the storage period. Over the three-year period, the sample remained relatively soft and acceptable, unlike staled bread. This finding agreed with the fact that there was no evidence of a mature network formation in MRE bread during storage.

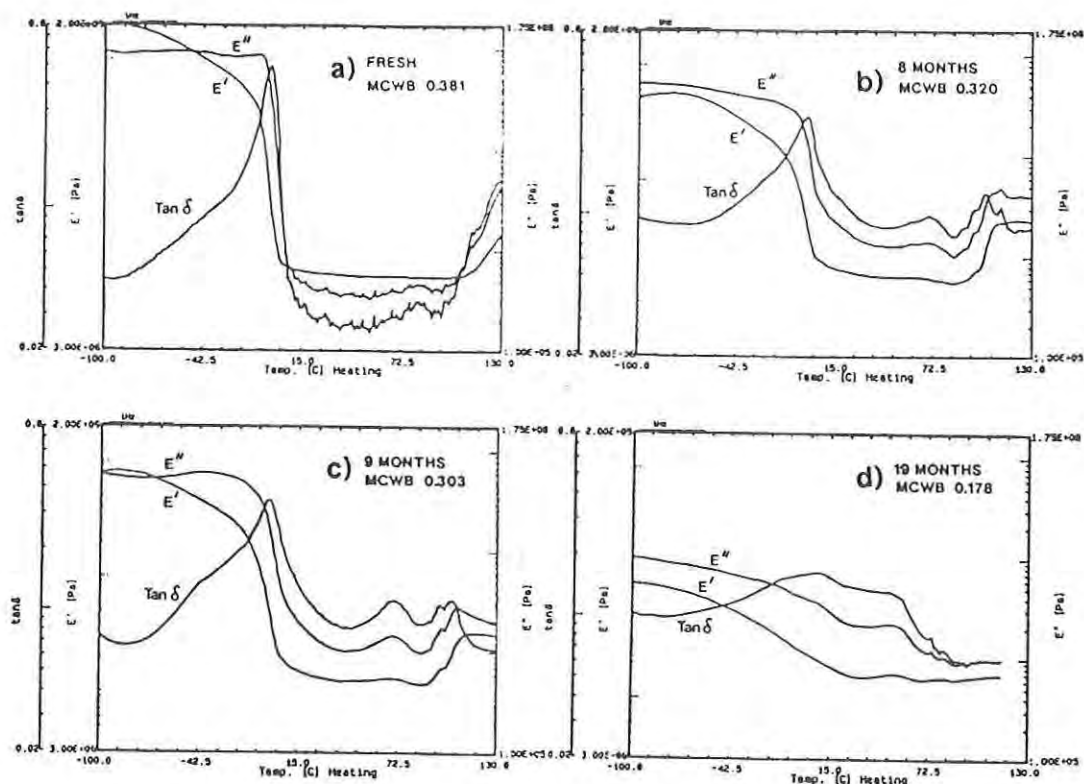


Figure 5. DMA Thermograms of SWB breads stored at room temperature.

CHINACHOTI, et al.

SWB thermograms by DMA gave a more drastic change in the magnitude of the T1 transition in the temperature range between -2.5°C and 2.5°C temperature range (Fig. 5) confirmed by the DSC results for ice melting (Table 2).

Table 2. DMA and DSC Thermogram for MRE and SWB Breads

| <u>MRE BREAD</u>        |       |                               |                     |             |        |
|-------------------------|-------|-------------------------------|---------------------|-------------|--------|
| STORAGE<br>TIME<br>(mo) | mcwb  | DMA                           | % UNFROZEN<br>WATER | DSC         |        |
|                         |       | Transitions Tg2 at 1 Hz<br>°C |                     | ICE MELTING |        |
|                         |       |                               |                     | To(°C)      | Tp(°C) |
| 0                       | 0.230 | -11.35±1.25                   | 74.50               | -23.03      | -12.20 |
| 3                       | 0.250 | -15.25±2.05                   | 81.10               | -28.08      | -17.58 |
| 5                       | 0.230 | -13.25±0.95                   | 87.65               | -25.04      | -17.14 |
| 11                      | 0.225 | -13.55±1.45                   | 78.00               | -22.71      | -13.33 |
| 36                      | 0.261 | -13.55±1.45                   | 81.70               | -26.38      | -17.80 |

| <u>WHITE PAN BREAD</u>  |       |                               |                     |             |             |
|-------------------------|-------|-------------------------------|---------------------|-------------|-------------|
| STORAGE<br>TIME<br>(mo) | mcwb  | DMA                           | % UNFROZEN<br>WATER | DSC         |             |
|                         |       | Transitions Tg2 at 1 Hz<br>°C |                     | ICE MELTING |             |
|                         |       |                               |                     | To(°C)      | Tp(°C)      |
| 0                       | 0.381 | -2.5±0.0                      | 62.69               | -10.08±0.40 | 1.78±0.16   |
| 7                       | 0.328 | -1.6±1.3, 89.0±1.5            | 76.05±2.93          | -12.65±0.02 | -5.49±0.23  |
| 8                       | 0.320 | -1.9, 70.6                    | 78.40±0.07          | -12.74±1.20 | -5.88±0.87  |
| 9                       | 0.303 | 0, 72.9                       | 87.14               | -13.54      | -7.36       |
| 19                      | 0.178 | 1.55±4.45, 49.0               | 95.74±0.21          | -19.05±0.43 | -12.11±0.09 |

In addition, there was an emergence of another transition at 49°C to 89°C temperature range during aging of bread (Fig. 5). This was in contrast to the DMA results for aging MRE bread. While the two breads were different in composition, they were aged under different moisture conditions; MRE bread in hermetically sealed pouch experienced no significant moisture loss while SWB lost more than 50% of its original moisture. This could be a factor related to the higher temperature transition. However, this transition temperature failed to correlate to moisture content but rather its relative amplitude seemed to increase with

CHINACHOTI, et al.

storage time (Fig. 5). It is hypothesized that amylopectin crystallization could be responsible. (Melting temperature for amylopectin crystals and this DMA transition fell within the same range of temperature.) How much this factor contributes to the mechanical firmness of the bread is yet to be determined.

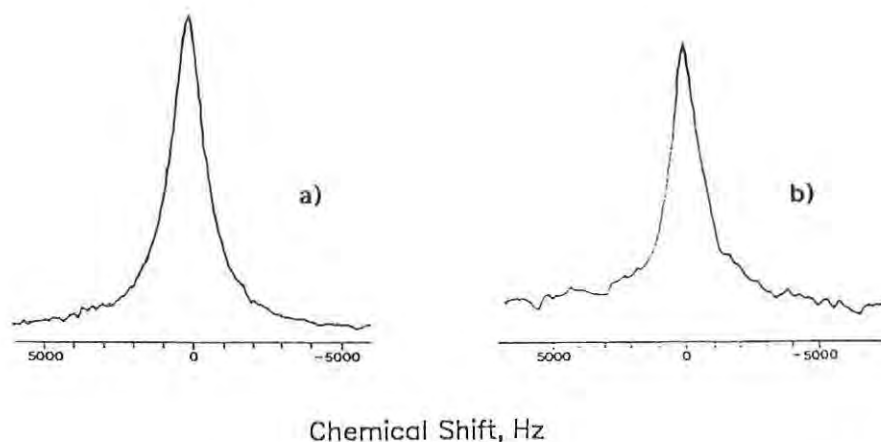


Figure 6. Fourier transformed  $^{17}\text{O}$  NMR for  $^{17}\text{O}$  enriched bread measured under a) the high field Varian XL-300 and b) the solid state IBM 200-AF spectrometers.

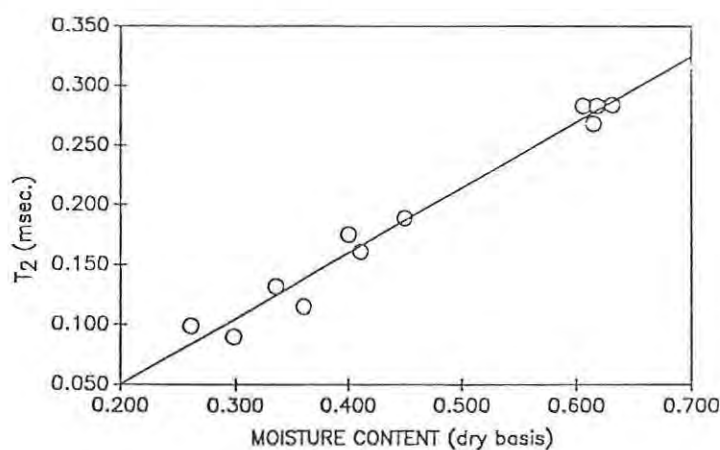


Figure 7.  $^{17}\text{O}$  NMR relaxation time ( $T_2$ ) for water in a fresh control (humectant-, surfactant-free) bread of various moisture contents.

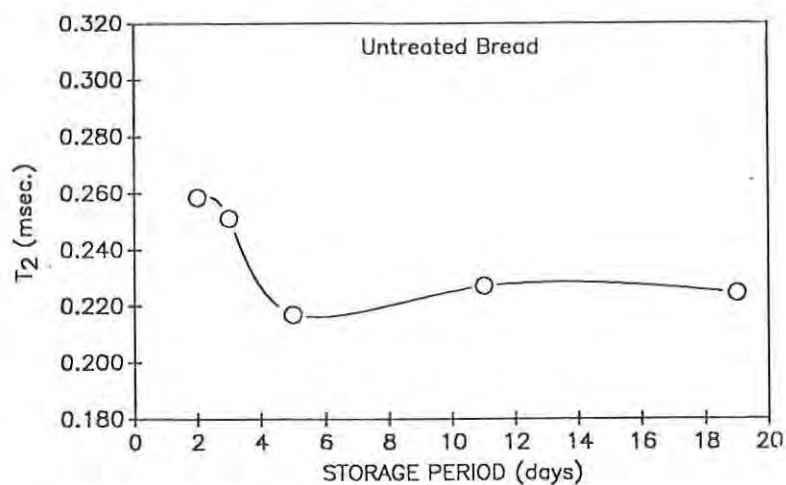


Figure 8. Changes in  $^{17}\text{O}$  NMR relaxation time ( $T_2$ ) for water in the control (humectant-, surfactant-free) bread during storage at room temperature.

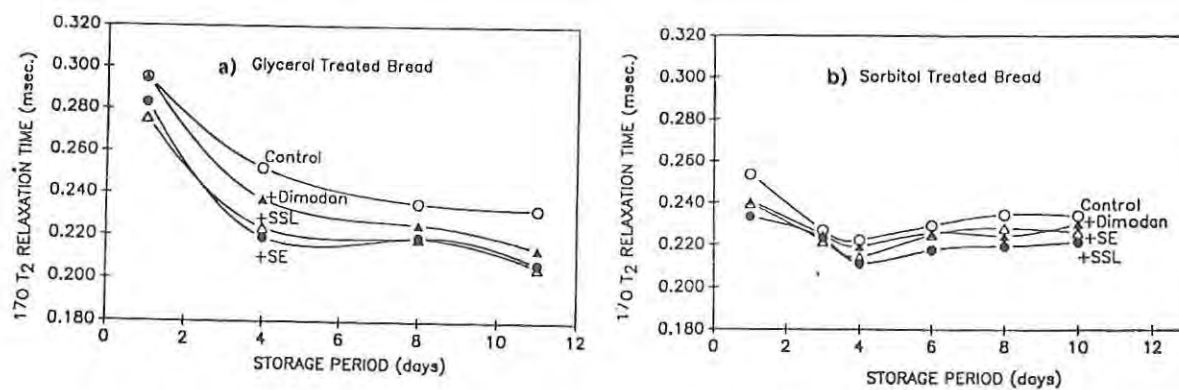


Figure 9. Changes in  $^{17}\text{O}$  NMR relaxation time ( $T_2$ ) for water in bread during storage. Bread treated with 5% glycerol (a) and sorbitol (b).



## Water Studies

Untreated Bread.  $^{17}\text{O}$  NMR spectra are shown in Fig. 6. The  $T_2$  of a sample of untreated bread (no added surfactants or humectants) is plotted against moisture content in Figure 7. Within the moisture range studied (0.25-0.65 g of water/g of solids),  $T_2$  increased linearly with moisture content ( $r = 0.988$ ). Figures 8 and 9 show that  $T_2$  of the water decreased rapidly during the first 3-4 days of storage and remained relatively constant at ca. 0.22 ms afterward up to 19 days of storage. The sharp decrease in  $T_2$  early in storage is presumed to be due to physicochemical processes accompanying staling. The two humectants did affect  $T_2$  differently; the glycerol-treated sample showed a significantly higher  $T_2$  at day 1 as compared with the bread treated with sorbitol, for all surfactant treatments. Over the full storage period,  $T_2$  for both cases decreased to nearly the same level (0.22-0.24 ms) at day 11.

Figure 10 shows the change in the amount of NMR-detectable water (i.e., integrated signal intensity) in the bread samples with time. In all cases the signal intensity decreased or remained unchanged. Glycerol-treated samples (Figure 10a) showed very little loss over the 15-day period; indeed, the loss is negligible within experimental error. The sorbitol-treated samples (Figure 10b) showed a real loss of signal, and the loss is nearly the same for all surfactants. All of the samples lost ca. 22% of the signal intensity during the first 4-6 days, and it remained essentially constant thereafter. Since the samples were sealed throughout the experiment, the loss could not be due to simple evaporation beyond a small amount of moisture lost to the headspace.

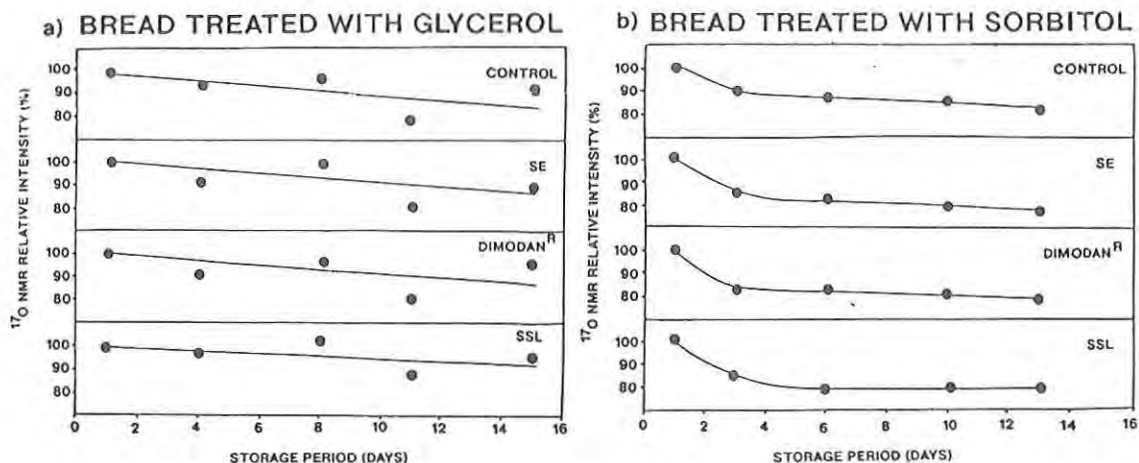


Figure 10.  $^{17}\text{O}$  NMR relative intensity as plotted against storage time for breads treated with glycerol (a) and sorbitol (b).

Bread samples untreated and treated with 0.5% (flour basis) monoglycerides (Dimodan, SSL, and sucrose ester) all showed a decrease in  $T_2$  on aging. In glycerol-treated bread (Figure 9a), the water mobility as determined by  $T_2$  appears to have the following trend: no surfactant Dimodan sucrose ester SSL, although the differences are not great.

Varying the surfactant had very little effect on the behavior of the signal intensity with time. Figure 10a shows that there is essentially no change in signal intensity with time for all of the glycerol-treated samples whether they contained a surfactant or not. The sorbitol-treated samples (Figure 10b) did exhibit a drop in intensity during the first 4-6 days of storage, but the curves for all four samples have the same shape within experimental error.

Amylopectin Crystallization. The DSC results for bread treated with surfactants and humectants are shown in Table 3. The enthalpy of melting shows that added surfactants had some inhibitory effect on the amylopectin crystallization as expected. The data shown here, 7 days after baking, support the report by others (Krog et al. 8) previously suggesting that amylopectin crystallization plays a key role in bread staling.

Our untreated bread samples lost 5% of their moisture during storage. According to the data in Figure 7, a 5% moisture loss would cause a change of 0.015 ms in  $T_2$  on average. This 5% loss is about one third of the total change in  $T_2$  on staling and is consistent with the observation of Leung et al. (10), who noted that in their samples "the decrease in moisture content would account for less than 40% of the reduction in relaxation time". Our breads with humectants showed even less than 2% moisture loss, which supports this conclusion. It has been proposed that the decrease in water mobility was due to the incorporation of the water molecules (probably released from gluten upon stabilizing) into the starch crystalline structure that developed upon staling (10,12,14).

The  $T_2$  values observed in this work range from 0.200 to 0.300 ms. These values are indicative of water that is less mobile than the pure liquid but which is not tightly held in a crystal lattice. The correlation time for molecular rotation of a water molecule in the liquid is  $2.5 \times 10^{-12}$  s (29), while the  $T_2$  values observed here lead to an average time of  $70 \times 10^{-12}$  s. The water of crystallization of amylopectin should be essentially rigid. It would not be detected by our spectrometer, because of the extreme quadrupolar broadening of  $^{17}\text{O}$  in rigid solids (30). Therefore, we conclude that the decrease in  $T_2$  shown in Figure 9 is mainly due to water not incorporated in the amylopectin crystals. The water of crystallization is firmly bound, and it does not exchange with the observed water rapidly enough to affect its NMR spectrum.

It should be noted that there could have been some water in the amorphous regions that was so "tightly bound" that it did not exchange rapidly with other water. Thus, during the process of  $^{17}\text{O}$  enrichment,

this water was not exchanged, and thus it was not detected due to (1) its low  $^{17}\text{O}$  population and (2) its very low  $T_2$ .

Since only mobile water can be observed in the NMR experiment, it is impossible to ascertain whether any of this water became bound during staling such that its signal could not be observed. This process would show up as a drop in the integrated signal intensity during staling. For the most part, the loss of intensity was small. Within experimental error, varying the surfactant had no effect on the degree of signal loss. Even the samples containing no surfactant did not differ significantly from the others. This is surprising since surfactants are known to retard bread staling, which is believed to be greatly influenced by the degree of water "binding" (31,32). Moreover, an independent study in this laboratory demonstrated that surfactants inhibit the amylopectin crystallization during staling (32). In this work DSC was used to measure the amount of crystallized amylopectin after 7 days of aging. The relevant data are presented in Table 3. Similar results have also been obtained by Krog et al. (8).

Table 3. DSC Endothermic Enthalpy of Melting of Crystalline Amylopectin for Breads Stored at 22°C for 7 days

| sample             | enthalpy ( $\Delta H$ ) |                   |
|--------------------|-------------------------|-------------------|
|                    | cal/g of sample         | cal/g of starch   |
| control            | 0.227 $\pm$ 0.015       | 0.600 $\pm$ 0.024 |
| surfactant treated |                         |                   |
| Dimodan            | 0.180 $\pm$ 0.012       | 0.480 $\pm$ 0.023 |
| SSL                | 0.170 $\pm$ 0.27        | 0.449 $\pm$ 0.057 |
| sucrose ester      | 0.160 $\pm$ 0.028       | 0.443 $\pm$ 0.047 |
| humectant treated  |                         |                   |
| glycerol           | 0.205 $\pm$ 0.021       | 0.455 $\pm$ 0.046 |
| sorbitol           | 0.153 $\pm$ 0.021       | 0.347 $\pm$ 0.046 |

If the drop in  $T_2$  and signal intensity during storage were due to amylopectin crystallization, the samples with less crystallization (i.e., samples with added surfactant) should have shown a smaller decrease in  $T_2$  and/or signal intensity as compared to samples without surfactant. However, this was not the case; within experimental error, the surfactant-treated samples behaved the same as the controls which contained humectant only. Consequently, the redistribution of water during staling is most likely related to the amorphous regions (amylopectin, gluten, and amylose) and/or the crystalline amylose. However, amylose crystallizes immediately after baking, and thus it does not play a role in the staling process (4,6).

There was a curious difference in behavior between the glycerol- and sorbitol-treated samples. The glycerol-treated bread showed a larger drop in  $T_2$ , while the sorbitol-treated material had the larger drop in signal intensity (Figures 9 and 10). The cause of this inverse relationship

CHINACHOTI, et al.

cannot be known until we have a better understanding of the processes taking place in the amorphous region during staling.

### CONCLUSION

DMA has been found sensitive to phase transitions detected by a combination of a decrease in  $E'$  and  $E''$  a peak in  $\tan \delta$  as the bread sample approached the transition temperature. The transition found in fresh white bread was identified as ice melting that occurred simultaneously with a change in heat capacity. In MRE bread, in addition to the ice melting transition, the presence of glycerol was found to be responsible for the low temperature  $T_g$  transition ( $-70^\circ\text{C}$  range). As the moisture content decreased  $T_l$  increased, reaching a value of  $160^\circ\text{C}$  at 2% moisture. An MRE bread storage study revealed that the transition temperatures remained relatively unchanged throughout the three-year storage. No significant evidence was found of network maturation upon storage of MRE bread because the moisture was retained in the bread. In contrast, there was evidence of a thermal transition at  $50^\circ\text{C}$  in SWB bread (where significant moisture loss was found), a possible evidence of retrograded starch or a transition of a network matrix.

Unfreezable water did not change significantly in MRE bread while that for SWB increased with storage time, showing some correlation with the decreasing moisture content.

The water we observed under NMR is a mobile fraction which is presumably in an amorphous region. The  $T_2$  decreased by 20-30% during staling. This could not have been caused by moisture loss, since the samples were sealed. Furthermore, it could have not been caused by fast exchange with water of crystallization; otherwise, there would have been a much larger drop in  $T_2$  during the crystallization process.

We found no correlation between the amylopectin crystallization and either  $T_2$  or signal intensity during staling. Addition of antistaling surfactants, which inhibit amylopectin crystallization, did not significantly affect either  $T_2$  or the signal intensity. Therefore, we propose that the effects observed here are not caused by amylopectin crystallization but are more likely due to changes that take place within the amorphous region.



#### REFERENCES

1. Hallberg, L. M., Yang, T. C. S., and Taub, I. A., 1990. Optimization of Functional Ingredients in a Low Water Activity Bread using Response Surface Methodology in Proceedings of the Third Natick Science Symposium. M. L. Herz and T. A. Sklarsky eds. Technical Report NATICK/TR-90/039, U.S. Army Natick RD & E Center, Natick, MA.
2. Powers, E. M. and Berkowitz, D., 1990. Efficacy of an Oxygen Scavenger to Modify the Atmosphere and Prevent Mold Growth on Meal, Ready-to-Eat Pouched Bread, *J. Food Protection* 53:767
3. Lindet, L. *Bull. Soc. Chim. Fr.* 1902, 27, 634.
4. Schoch, T. J.; French, D. Studies on bread staling. I. The role of starch. *Cereal Chem.* 1947, 24, 231.
5. D'Appolonia, B. L.; Morad, M. M. Bread staling. *Cereal Chem.* 1981, 58, 186.
6. Maga, J. A. Bread staling. *CRC Crit. Rev. Food Technol.* 1975, 8, 443.
7. Kulp, K.; Ponte, P. G., Jr. Staling of white pan bread: fundamental causes. *CRC Crit. Rev. Food Sci. Nutr.* 1981, 15, 1.
8. Krog, N.; Olesen, S. K.; Toernaes, H.; Joensson, T. Retrodegradation of the starch fraction in wheat bread. *Cereal Foods World* 1989, 34, 281.
9. Leung, H. K. Structure and properties of water. *Cereal Foods World* 1981, 26, 350.
10. Leung, H.K., Magnuson, J. A., Bruinsma, B. L. Water binding of wheat flour doughs and breads as studied by deuterium relaxation. *J. Food Sci.* 1983, 48, 95.
11. Cesari, L. de. *Sci. Technol. Aliment.* 1974, 4, 139.
12. Slade, L.; Levine, H. Beyond water activity: Recent advances based on an alternative approach to the assessment of food quality and safety. *Crit. Rev. Food Sci. Nutr.* 1991, in press.
13. Lechert, H. T. Water binding on starch: NMR studies on native and gelatinized starch. In *Water Activity: Influences on Food Quality*; Rockland, R. B., Stewart, G. F., Eds.; Academic Press: New York, 1981.
14. Wynne-Jones, S.; Blanshard, J.M.V. Hydration studies of wheat starch amylopectin, amylose gels and bread by proton magnetic resonance. *Carbohydr. Polym.* 1986, 6, 289.
15. Willhoft, E. M. A. Mechanism and theory of staling of bread and baked goods, and associated changes in textural properties. *J. Texture Stud.* 1973. 4, 191.
16. Clusky, J. E.; Taylor, N. W.; Senti, F. R. Relation of the rigidity of flour, starch, and gluten gels to bread staling. *Cereal Chem.* 1959, 36, 236.
17. Zobel, H. F. Review of bread staling. *Baker's Dig.* 1973, 47, 52.
18. Zeleznak, K. J. and Hoseney, R. C., 1987. The Glass Transition in Starch. *Cereal Chem.* 64:121.

CHINACHOTI, et al.

19. Hoseney, R. C.; Zeleznak, K. and Lai C. S. 1986. Wheat gluten: a glassy polymer. *Cereal Chem.* 63:285.
20. Edzes, H. T.; Samulski, E. T. The nature of cross relaxation effects in the protein NMR spin-lattice relaxation of water in biological systems: Hydrated collagen and muscle. *J. Magn. Reson.* 1978, 31, 207.
21. Richardson, S. J.; Steinberg, M. P. Applications of nuclear magnetic resonance. In *Water Activity: Theory and Applications to Food*; Rockland, L. B., Beuchat, L. R., Eds.; Dekker: New York, 1987.
22. Shirley, W. M.; Bryant, R. G. Proton-nuclear spin relaxation and molecular dynamics in the lysozyme-water system. *J. Am. Chem. Soc.* 1982, 104, 2910.
23. Kakalis, L. T.; Baianu, I. C. Oxygen-17 and deuterium nuclear magnetic resonance relaxation studies of lysozyme hydration in solution: field dispersion, concentration, pH/pD, and protein activity dependences. *Arch. Biochem. Biophys.* 1988, 267, 829.
24. Chinachoti, P.; Stengle, T. R. Water mobility in starch/sucrose systems: an oxygen-17 NMR study. *J. Food Sci.* 1990, 55, 1732.
25. Nussinovitch, A., Steffens, M. S. and Chinachoti, P. 1991. Exponential Model of the Compressive Stress-Strain Relationships of Bread. *Lebensm-Wiss. u-Technol.* 24:323.
26. Anon. 1989. Military Specification: Pouch Bread, for Meal-Ready-to-Eat, #B-44360. Government Printing Office; U.S. Army Natick RD & E Center, Natick MA.
27. Morris, V. J. 1990. Starch gelation and Retrogradation Trends in Food Science and Tech. 1:2.
28. Levine, H. and Slade, L. 1988. Non-equilibrium melting of native granular starch: Part I. Temperature location of the glass transition associated with gelatinization of A-type cereal starches. *Carbohydr. Polym.* 8:183.
29. Glasel, J. A. Nuclear magnetic resonance studies on water and ice. In *Water, A Comprehensive Treatise*; Franks, F., Ed.; Plenum Press: New York, 1972; Vol. 1.
30. Cohen, M. H.; Reif, F. Quadrupole effects in nuclear magnetic resonance studies of solids. In *Solid State Physics*; Seitz, F., Turnbull, D., Eds.; Academic Press: New York, 1957; Vol. 5.
31. Bushuk, W.; Mehrota, V. K. Studies of water binding by differential thermal analysis. II. Dough studies using the melting mode. *Cereal Chem.* 1977a, 54, 320.
32. Bushuk, W.; Mehrota, V. K. Studies of water binding by differential thermal analysis. III. Bread studies using the melting mode. *Cereal Chem.* 1977b, 54, 326.



BARRETT, et al.

TITLE: Fourier and Fractal Analysis for the Textural Characterization of Porous Foods

Ann Barrett, Dr., Mark Normand, Mr., Micha Peleg, Dr.,  
Edward Ross, Dr.

ABSTRACT:

Porous foods, such as extruded, baked, or foamed products, have highly complex 3-dimensional cellular structures--and correspondingly complex textural properties. The structure of these materials cannot adequately be described by a single parameter and must be evaluated statistically and with regard to distributions of cell sizes. Similarly, the "texture" of porous foods, particularly that of "crunchy" snack-type products, is not a single attribute, but a property associated with deformation of many individual cell wall components. Most important, the texture of these foods has a time-dependent quality that results from the progressive fracture or failure of the cells.

The perception of "crunchiness" arises during chewing from the sequential breakage of subsections in a product: the food does not fail all at once. Correspondingly, stress-strain curves of brittle porous foods (or other foamed materials) under compression have complicated "jagged" patterns caused by the sequential fracture of cell components. The frequency and magnitude of peaks in the compression curves are a function of the material tested and are indicative of the texture of the product.

The characterization of such foods in this study involved the use of two mathematical techniques, the Fast Fourier Transform and fractal analysis, to quantitatively describe the jagged pattern of compression curves in porous foods. The Fourier Transform was used to analyze the frequencies of fracture and fractal analysis was used to describe the overall ruggedness of compression curves. These techniques have made it possible to determine textural differences in products, especially starch-based foods, that arise from formulation and storage conditions. Examples relating to the influence of water activity will be discussed.

BIOGRAPHY: Ann Barrett

PRESENT ASSIGNMENT: Project Officer of Model for Food Structure and Functionality, Chemical Engineer, Food Engineering Directorate; employed at Natick RD&E Center for seven years.

PAST EXPERIENCE: Process Engineer, Brady Enterprises, Inc.

DEGREES HELD: B.A. Chemistry, Williams College; M.S. Food Engineering, University of Massachusetts, Ph.D., Food Engineering, University of Massachusetts.

Fourier and Fractal Analysis for the Textural Characterization  
of Porous Foods

Ann Barrett, Dr.  
U.S. Army Natick Research, Development and Engineering Center  
Natick, MA 01760

Mark Normand, Mr.  
Micha Peleg, Dr.  
University of Massachusetts  
Amherst, MA 01003

Edward Ross, Dr.  
Worcester Polytech Institute  
Worcester, MA 01602

INTRODUCTION

Porous foods often have complex textural and mechanical properties that arise from their cellularity and their tendency to fail in a sequential, progressive manner; the individual structural components of these materials (cells and cell walls) largely determine the behavior of samples during either mechanical compression or chewing.

The compressive force-deformation and corresponding stress-strain relationships of many cellular food and nonfood materials are composed of three distinct regions (Gibson and Ashby, 1988): a nearly linear increase in stress with strain, prior to irreversible deformation of the material; a plateau region in which stress remains at approximately a constant level, indicating buckling or fracturing of cell wall components; and a second sharp increase in stress, produced by densification of the material. Brittle cellular materials are distinguished from plastic substances by an extreme jaggedness superimposed upon the stress-strain curves: cell walls in brittle materials fracture rather than buckle, and the plateau region in compression curves for these samples shows rapidly oscillating stress levels. This ruggedness, and specifically the frequency of oscillations in the stress-strain functions has rarely been characterized; however, quantification of the specific deformation mechanism could help describe important textural attributes particular to brittle, cellular foods—especially qualities such as "crunchiness".

Analytical techniques are available for the evaluation of oscillating data in general and for the description of "shapes" of functions. One commonly used tool for frequency analysis is the Fast Fourier Transform (Ramirez, 1985), or FFT. The FFT converts the original relationship into a power spectrum of frequencies, and thus indicates repetitive occurrences in the data. The transform expresses a function by the Fourier series (Kreyszig, 1972)

$$f(x) = a_0 + \sum_{n=1}^n [a_n \cos(nx) + b_n \sin(nx)]$$

where  $a$  and  $b$  are constants and  $n$  is frequency; the sum of the squares of  $a$  and  $b$  (i.e.,  $a^2 + b^2$ ) at each frequency  $n$  is defined as the power corresponding to that frequency. Plots of power vs. frequency, known as

power spectra, are thus transforms of the original function of the variable  $x$  to a new function dependent on frequency. Significant frequencies in these plots are indicated and easily identified by a large power magnitude, or peak, in the function.

Application of the FFT to force-deformation data yields a power spectrum in which the frequency axis can have units of reciprocal length ( $\text{mm}^{-1}$ ), obtained by dividing the original scale ( $\text{sec}^{-1}$ ) by the compression velocity ( $\text{mm/sec}$ ). A frequency scale in length units is useful in that frequencies of fracturing can then be interpreted in terms of cellular dimensions.

A second method for assessing the overall roughness of relationships is fractal analysis. Mathematical techniques have been used to describe the ruggedness of three-dimensional objects or two-dimensional images (Peleg et al., 1984) and also computer generated x-y functions (Normand and Peleg, 1988). Such real-world objects are not truly fractal, since they have finite dimensions and do not repeat at all length scales; however, they can yield a "fractal dimension" through numerical techniques that is characteristic of the overall tortuosity of the object. The fractal dimension is determined by the slope of the Richardson plot (Mandelbrot, 1983), which is obtained through a blanket algorithm (Peleg et al., 1984 and Normand and Peleg, 1988). This algorithm is based upon iteratively "coating" the investigated image with successive blanket layers, according to rules specified by the algorithm, and is particularly suited to digitized computer data. The fractal dimension yields less specific information than does the power spectrum in that it is affected both by the frequency and amplitude of oscillations in the original data; however, this technique has the advantage of providing a single number that can be used as a descriptive index for a particular type of compression curve.

The objectives of this work were to use the Fast Fourier Transform and fractal analysis to describe the force-deformation relationships of extrudates, and to evaluate the effectiveness of these methods for identifying different kinds of failure mechanisms. In particular, these techniques were used to determine differences in samples that had various degrees of plasticity effected by equilibration at a range of relative humidity levels.

#### MATERIALS AND METHODS

Extrudates were produced using a Werner & Pfleiderer ZSK-30 twin screw extruder using a 4 mm round die. Two lots were produced, one from pure corn meal and one from a corn-rice-sugar blend (44:44:12, respectively). These formulations were selected so that two distinct types of structures would be obtained--a highly expanded, large-celled product from corn meal, and a finer-celled, softer product from the multicomponent formula. For

each experiment the initial moisture content was 15%, the temperature profile 38-38-116-116-138-138°C and the screw speed 400 RPM. The solids feed rate was 27 kg/h for corn meal and 20 kg/h for the multicomponent formula (which necessitated a lower feed rate due to excessive torque values).

The extrudates were dried at 45°C for 5 min and cut into cube-shaped pieces approximately 1 cm in size. The samples were equilibrated 72 hours at ambient temperature at three different relative humidity levels using desiccators containing saturated solutions of LiCl (11% RH),  $K_2CO_3$  (43% RH) and NaCl (75% RH) (Greenspan, 1977).

The specimens were measured using a caliper and compressed using an Instron Universal Testing Machine (model 1000) to 50% deformation at a rate of 10 mm/min. Each sample was cut and positioned so that compression took place in a direction parallel to the direction of extrusion. Voltage output, corresponding to force, was measured at 0.1 s intervals. Data in the form of voltage vs. time and stress vs. strain were stored automatically in a Macintosh II computer.

The cell size distributions of extrudates were measured using an Olympus Cue-2 image analyzer according to the procedure described by Barrett and Ross (1990). Sample characteristics are listed in Table 1.

Table 1. Physical Characteristics of Extrudates

| Extrudate      | <u>Radial Cross Section</u> |                     | <u>Axial Cross Section</u> |                     |
|----------------|-----------------------------|---------------------|----------------------------|---------------------|
|                | Mean<br>Cell Area           | Median<br>Cell Area | Mean<br>Cell Area          | Median<br>Cell Area |
| Corn           | 19 mm <sup>2</sup>          | 12 mm <sup>2</sup>  | 14 mm <sup>2</sup>         | 10 mm <sup>2</sup>  |
| Multicomponent | 4.5 mm <sup>2</sup>         | 3.0 mm <sup>2</sup> | 4.4 mm <sup>2</sup>        | 2.4 mm <sup>2</sup> |

The compression curves were first fitted to 3-term and 4-term polynomial models and the residuals of the models used in analyses. Use of residuals rather than raw data served to eliminate the overall upward trend of the relationships and to isolate only the jaggedness of the curves. Two modeling techniques for voltage data were employed: model 1 used a truncated data file in which the first 100 points (the linear elastic region) had been eliminated and Model 2 used the entire data range. Truncated data were used to obtain power spectra, both models were used and compared in fractal analysis and residuals from these models normalized by dividing them by the model value.



BARRETT, et al.

Power spectra of voltage residuals were obtained using a Fast Fourier Algorithm provided by Systat Co., Evanston IL. Fractal dimensions were calculated using the blanket algorithm and the procedure described by Normand and Peleg (1988). The blanket algorithm iteratively added to the residuals by the formula

$$X_{e+1}(i) = \max\{X_e(i)+1, \max[X_e(i-1), X_e(i+1)]\}$$

in which  $X(i)$  was the thickness of the blanket at location  $i$  and iteration  $e$ . Effectively, the depth of the blanket at any particular point during any iteration was proportional to the difference in height between that point and its neighboring point: the greater this distance the thicker the blanket laid down. The Blanket algorithm was used to construct Richardson-type plots of log "line length" vs. log "half thickness" in which the line length was equal to the blanket area divided by its thickness. The slope of the Richardson plot is indicative of the roughness of the original image. Since the blanket area decreases with each iteration, as the image is "smoothed", the Richardson plot has a negative slope, the magnitude of which depends on the irregularity of the original function. The fractal dimension of the original object obtained through the blanket algorithm is defined as  $[1 - \text{the slope of the Richardson plot}]$ ; the fractal dimension is a positive quantity with a lower limit of 1.0 (for perfectly smooth images). Linear regression was used to determine the slopes of the Richardson plots and to calculate the fractal dimension of the voltage residuals.

Both Fourier and fractal procedures were performed in triplicate.

## RESULTS AND DISCUSSION

Typical stress-strain functions of the extrudates equilibrated under the three levels of relative humidity are shown in figures 1 (corn samples) and 2 (multicomponent extrudates). The effect of relative humidity on the compressive behavior of the samples is evident in the shift from brittleness at the low humidity level to plasticity at the high humidity level: curves obtained from 73% RH samples are quite smooth whereas curves obtained from 11% RH samples are extremely jagged with large and frequent oscillations in stress. Equilibration at the intermediate humidity level gave different results for the corn and multicomponent samples, in that the compression curves for pure corn samples retained a certain level of roughness while those for the multicomponent samples were smooth and similar to those of the high RH samples. Evidently, the sugar-containing samples were more sensitive to moisture than were the pure corn extrudates and consequently lost their brittleness at a relatively lower humidity level. Figure 3 shows the difference in ruggedness for residuals of representative low and high humidity compression curves for corn samples.

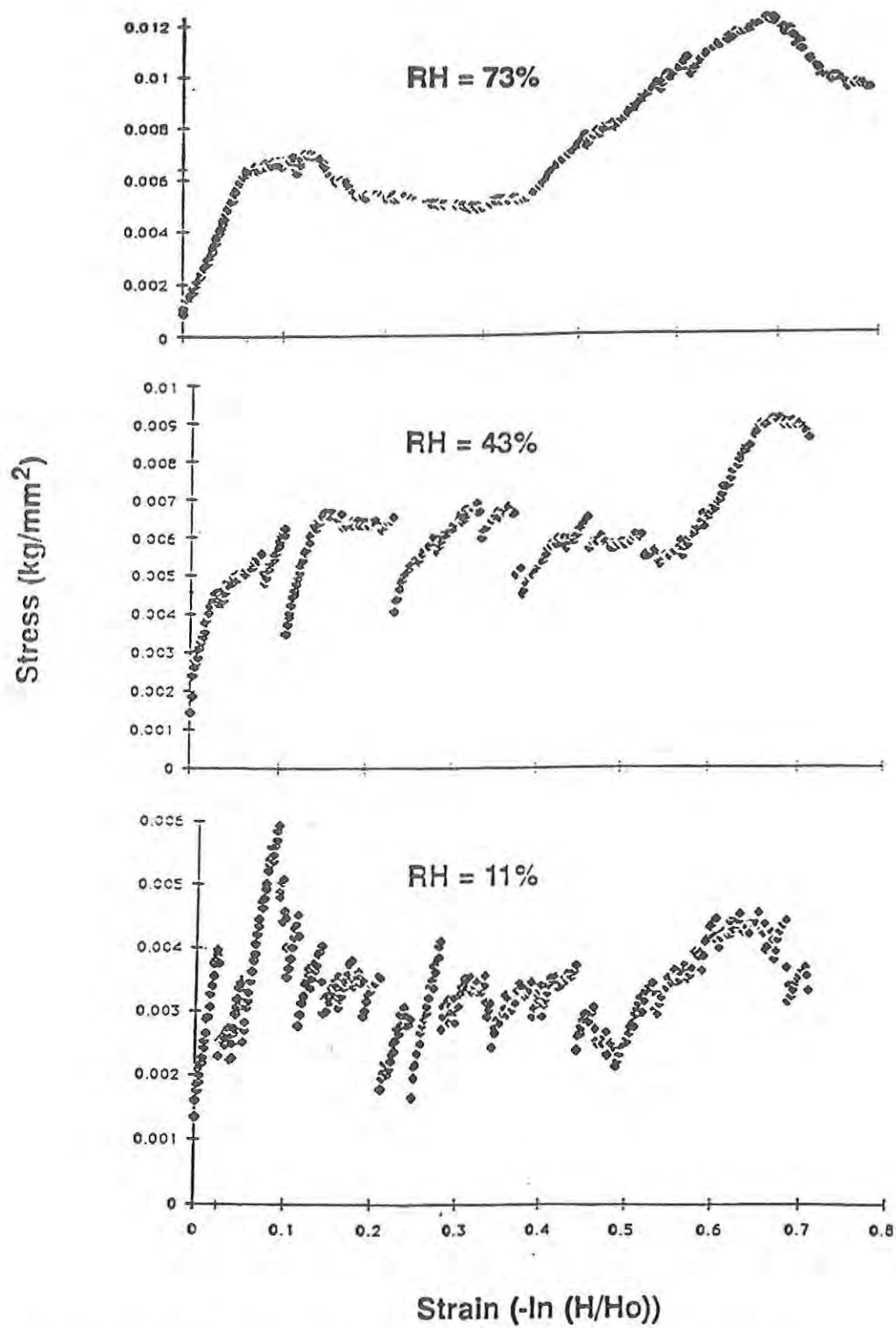


FIGURE 1: Representative Compression Curves, Corn Extrudates



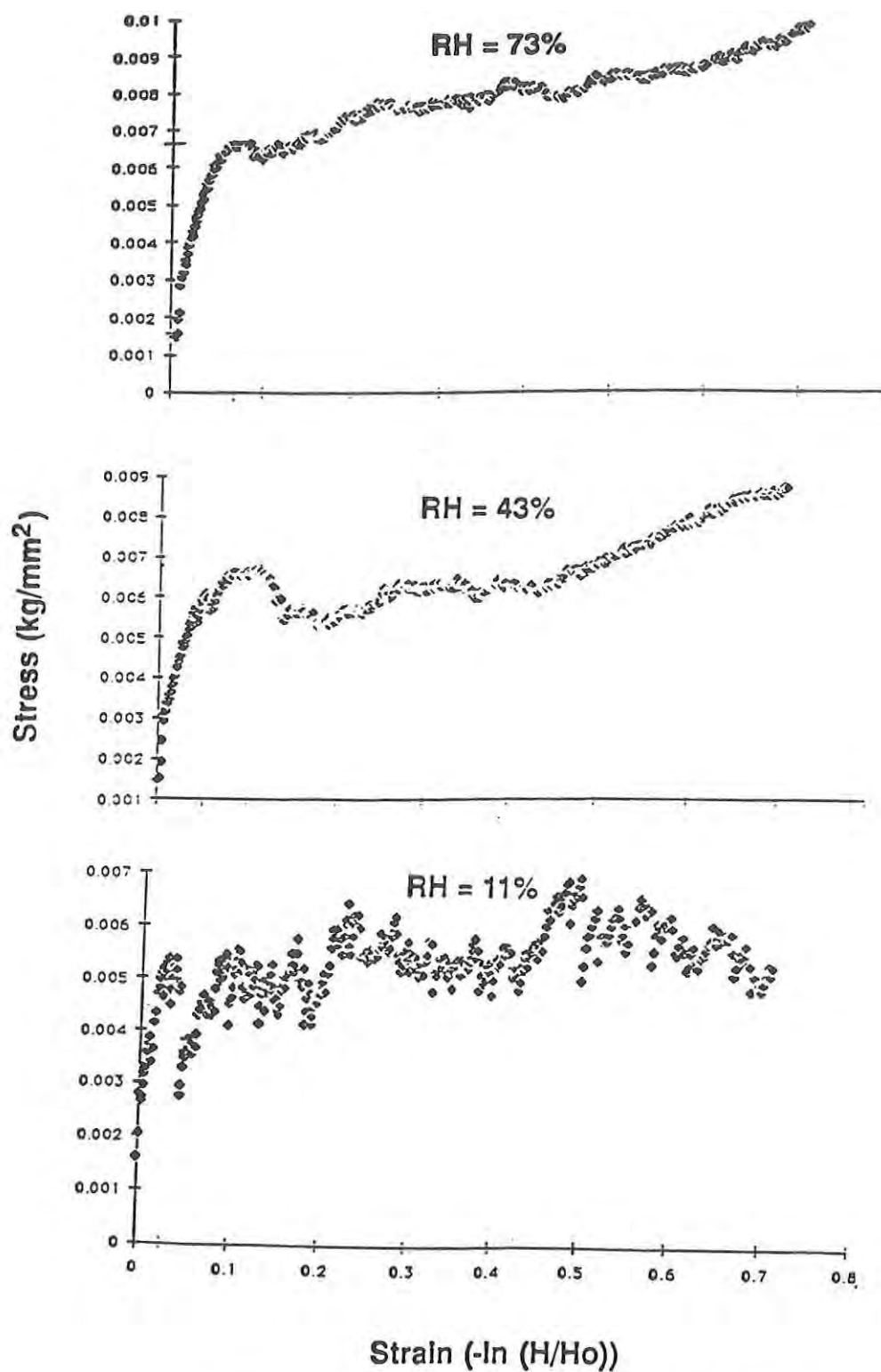


FIGURE 2: Representative Compression Curves, Multicomponent Extrudates

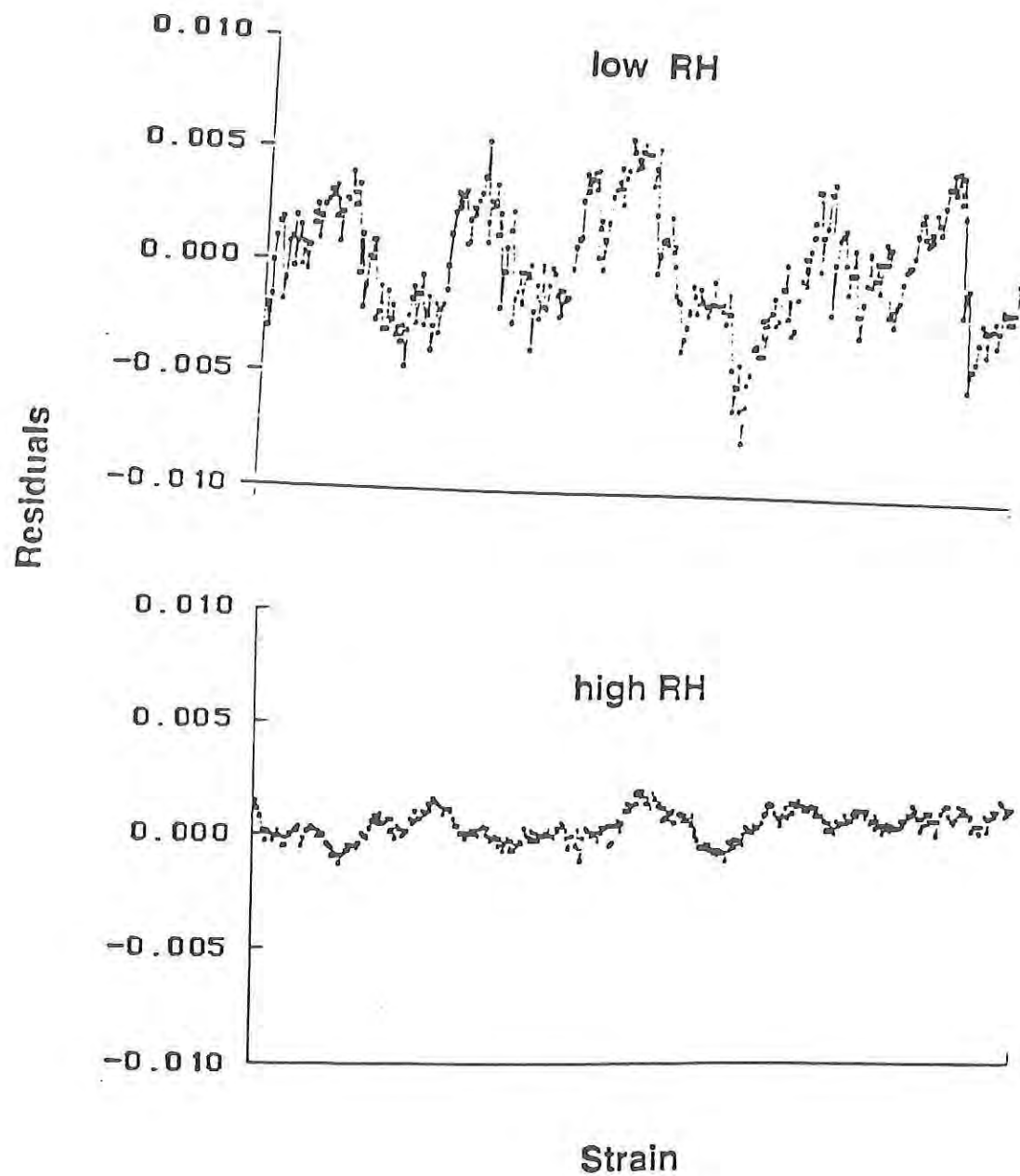


FIGURE 3 : Representative Residuals From Modeling Compression Curves

Results of the Fourier Transform

Representative power spectra of the 2 extrudates are shown in Figures 4 and 5, and their features summarized in Table 2.

Table 2. Characteristics of Power Spectra

| Extrudate      | RH (%) | <u>Upper Limit of Frequency Range<sup>a</sup></u> |                      |
|----------------|--------|---|----------------------|
|                |        | Mean ( $\text{mm}^{-1}$ )                         | COV <sup>b</sup> (%) |
| Corn           | 11     | 8   | 9                    |
|                | 43     | 9   | 58                   |
|                | 75     | 2.8   | 36                   |
| Multicomponent | 11     | 5   | 35                   |
|                | 43     | 1.5   | 44                   |
|                | 75     | 1.5   | 29                   |

<sup>a</sup> Intensity > 0.0025

<sup>b</sup> Coefficient of Variation [(standard deviation/mean) x 100]

All spectra had large peaks at frequencies of up to  $2\text{--}3\text{ mm}^{-1}$  that corresponded to the failure of major structural components. Spectra from low humidity compression curves, however, were characterized by additional peaks at much higher frequencies and shorter lengths, on the order of  $6\text{--}15\text{ mm}^{-1}$ , which reflect the fragmentation of cell wall components. In both extrudates, equilibration at higher moisture conditions reduced the incidence of high frequency peaks and eliminated them at 75% RH. Again, the spectra for the two samples equilibrated at 43% RH differ the most in that those for the multicomponent extrudates have few high frequency peaks due to increased hygroscopicity of these samples.

Since each specimen had a unique cellular structure, each power spectrum was a unique signature that could not be reproduced exactly. However, the general form of spectra for sample replicates could be easily recognized by the distribution and magnitude of the peaks. In particular, the power spectra distinguished between degrees of plasticity that were effected by storage conditions.

Results of Fractal Analysis

Examples of typical Richardson plots of normalized residuals

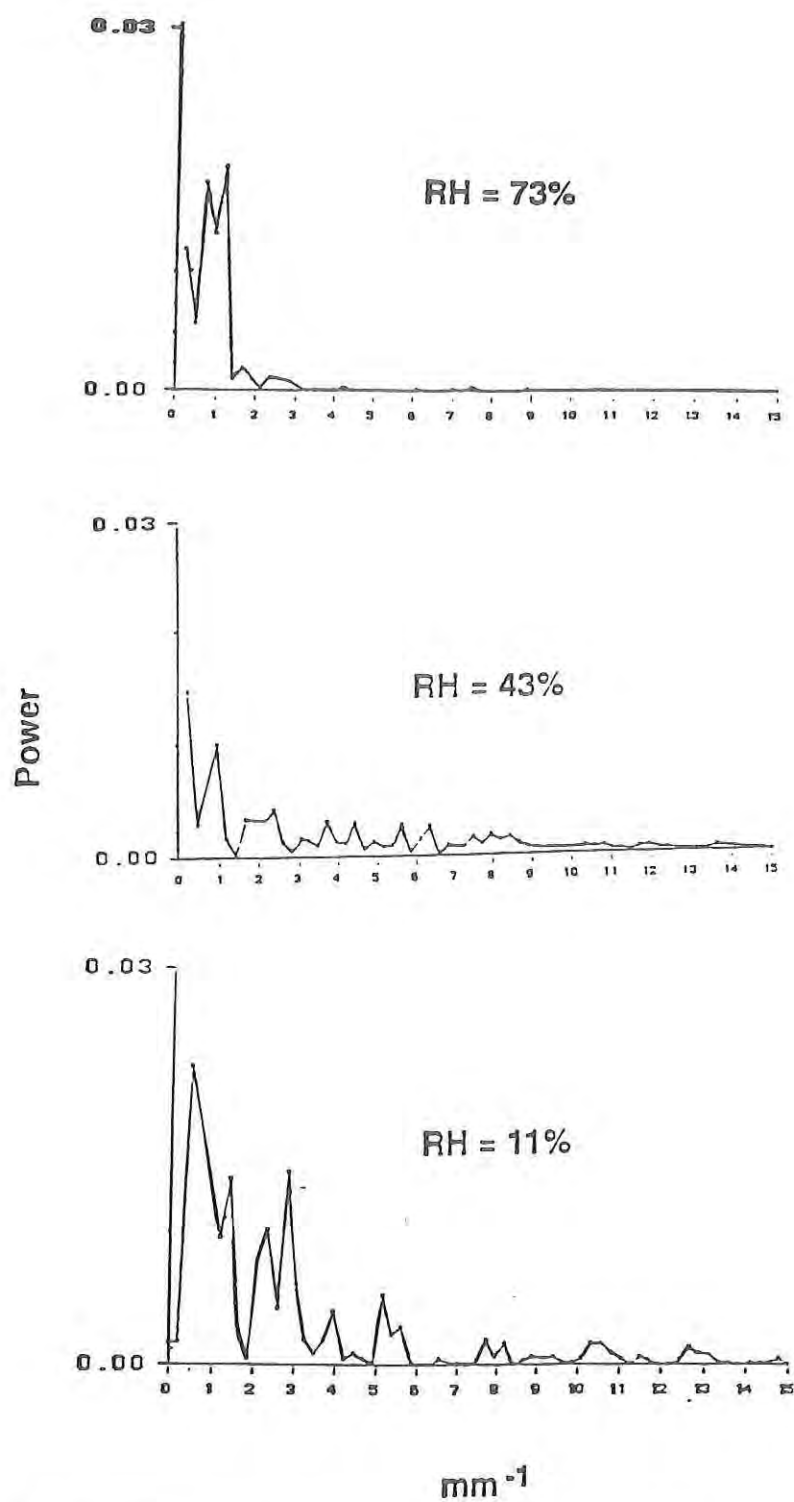


FIGURE 4 : Representative Power Spectra, Corn Extrudates

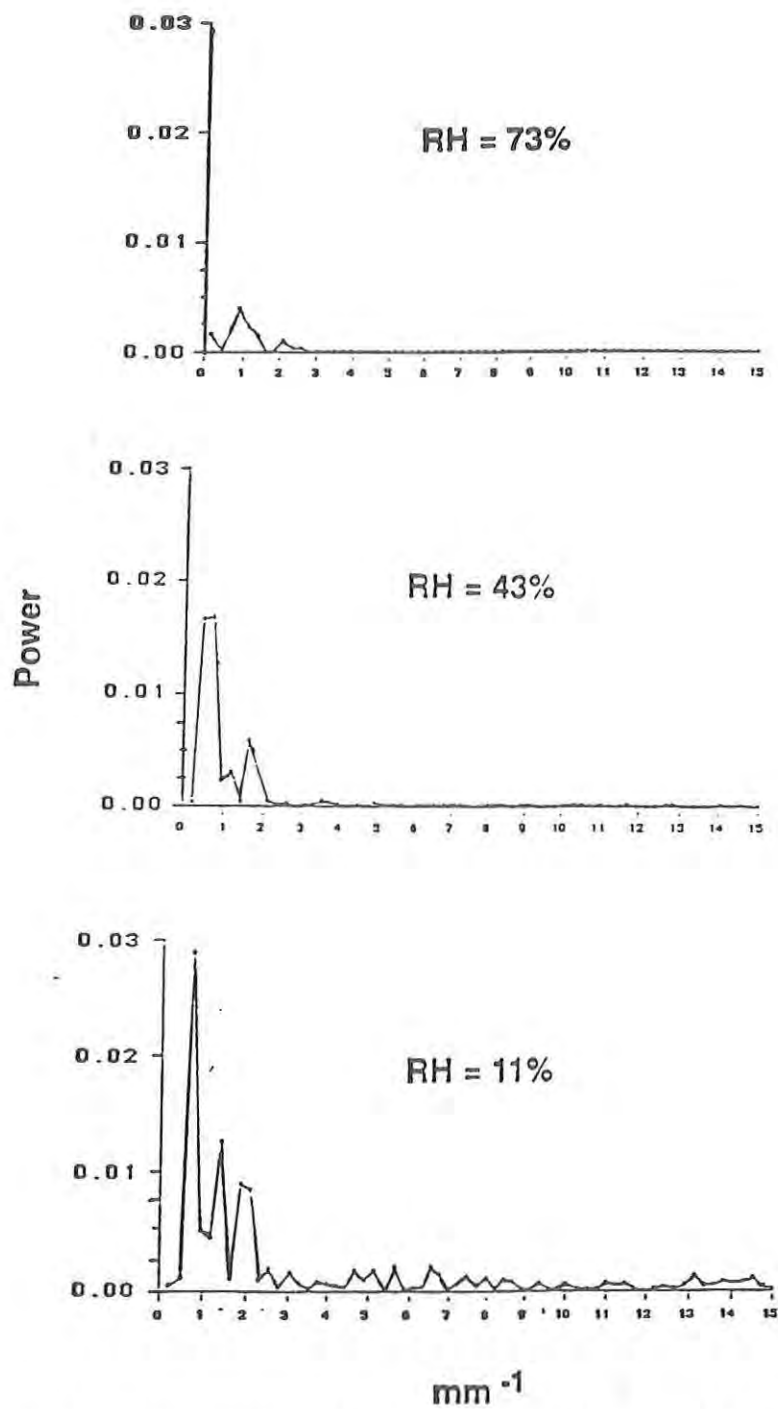


FIGURE 5 : Representative Power Spectra, Multicomponent Extrudates

BARRETT, et al.

constructed using the blanket algorithm are shown in Figures 6 and 7. Calculated fractal dimensions are shown in Table 3.

Table 3: Fractal Dimensions of Compression Curves

| Extrudate      | RH (%) | Fractal Dimension<br>Model 1 |                      | Fractal Dimension<br>Model 2 |                      |
|----------------|--------|------------------------------|----------------------|------------------------------|----------------------|
|                |        | Mean                         | COV <sup>a</sup> (%) | Mean                         | COV <sup>a</sup> (%) |
| Corn           | 11     | 1.44                         | 1.0                  | 1.45                         | 0.3                  |
|                | 43     | 1.27                         | 2.0                  | 1.26                         | 3.3                  |
|                | 75     | 1.17                         | 2.0                  | 1.14                         | 2.2                  |
| Multicomponent | 11     | 1.44                         | 1.0                  | 1.46                         | 0.6                  |
|                | 43     | 1.17                         | 2.8                  | 1.17                         | 0.7                  |
|                | 75     | 1.09                         | 0.9                  | 1.15                         | 2.6                  |

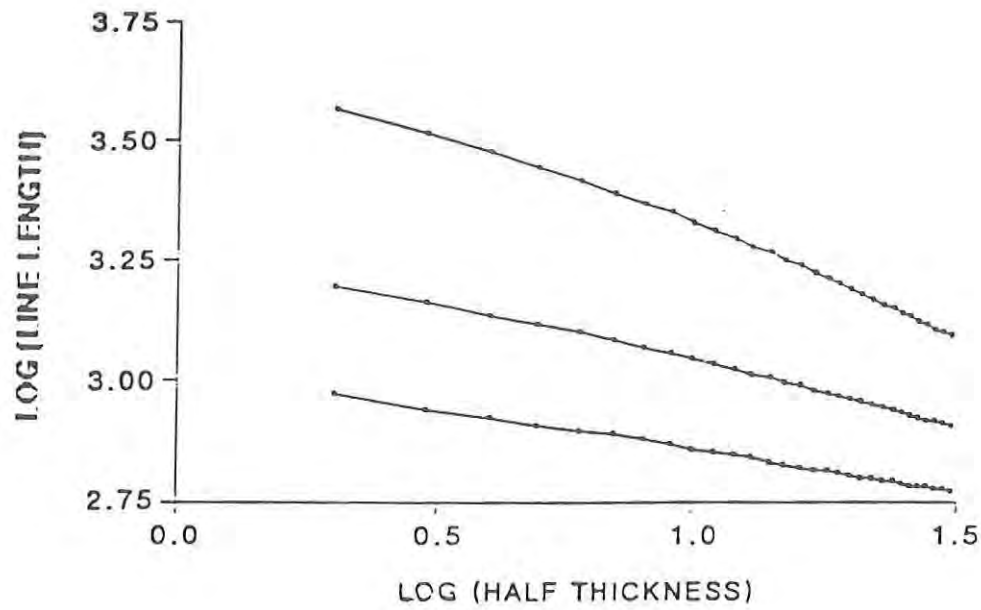
<sup>a</sup> Coefficient of Variation [(Standard deviation/mean) x 100]

The figures demonstrate that the procedure was sensitive to the original function and yielded functions with different slopes. The Richardson plots obtained from compression curves of the low humidity extrudates, which had more jagged stress-strain relationships, had higher negative slopes than did those constructed from higher humidity samples. The effect of storage conditions was clearly manifest in the computed fractal dimensions which varied from approximately 1.4 for the brittle curves to 1.1 for the high humidity curves. The absolute magnitude of the fractal dimension was largely independent of the model used for fitting the data, showing that the technique is sensitive to the form of the original function despite the exact method used to process the data.

Interpretation of the fractal dimension in terms of structural or textural features is similar to that for the power spectra: samples collapsing in abrupt, high frequency fractures yield higher values than do samples that fail in a more continuous, plastic mode. Fractal analysis has the advantage of yielding one number that can conveniently be used to describe deformation behavior. However, the fractal dimension is sensitive to the magnitude as well as the frequency of oscillations and is an overall measure of roughness--and does not provide any information about specific frequencies occurring in the data, as does Fourier analysis.



# MODEL 1



# MODEL 2

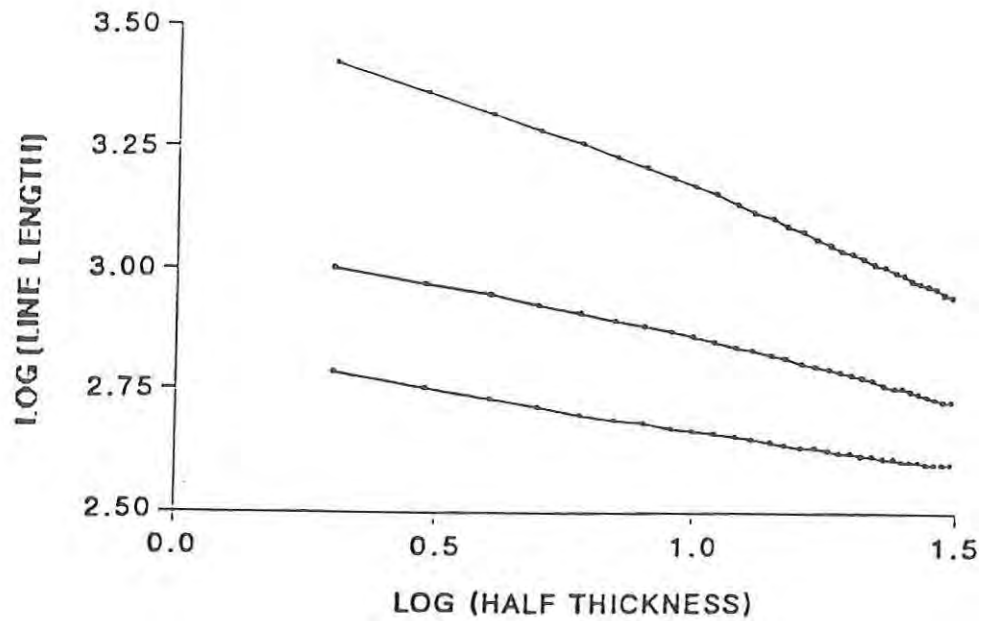
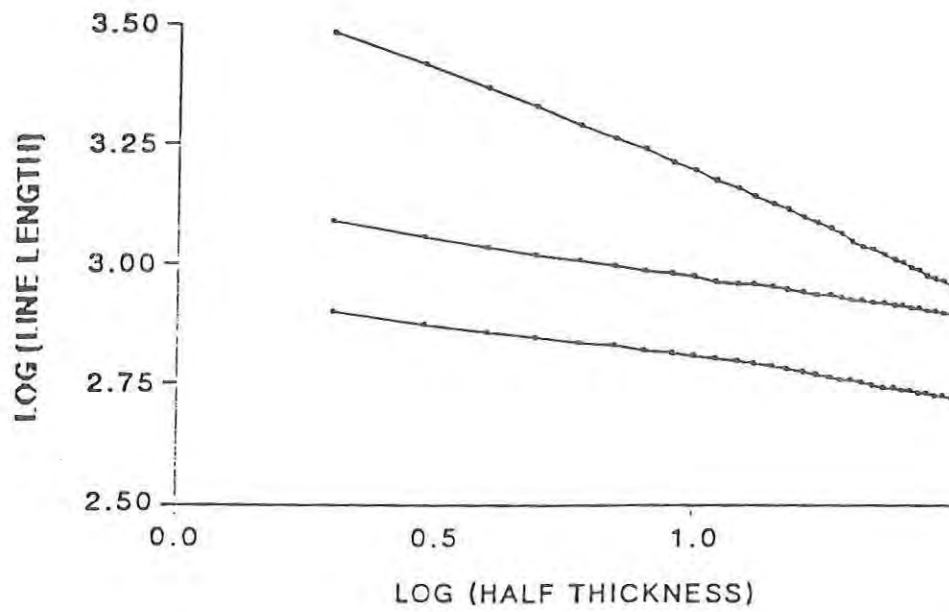


FIGURE 6 : Representative Blanket Plots, Corn Extrudates

MODEL 1



MODEL 2

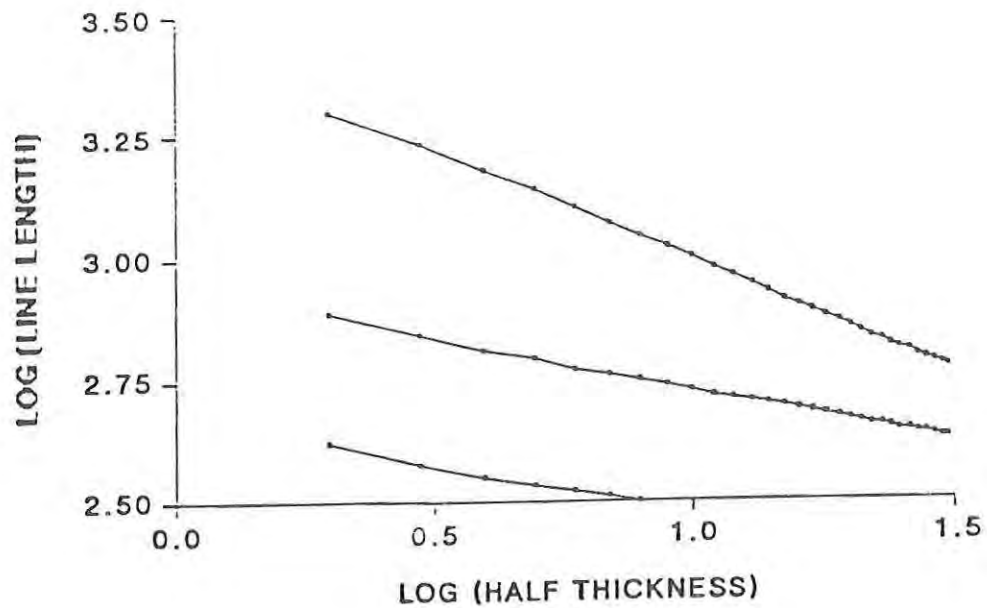


FIGURE 7 : Representative Blanket Plots, Multicomponent Extrudates

BARRETT, et al.

### CONCLUSIONS

Fourier and fractal analysis are useful techniques for analysis of the time-dependent deformation behavior of foods. These methods potentially provide a more complete indication of food texture than do single-parameter measurements since they describe the progressive structural failure that is perceived during chewing. The FFT and blanket algorithm are particularly applicable to the analysis of "crunchy" or "crisp" foods and offer a means of characterizing the complex textural properties of these products. These analytical techniques also offer the possibility of further research into fundamental relationships between the failure behavior, sensory properties, and physical characteristics of brittle foods.

### REFERENCES

- Barrett, A.H. and Ross, E. 1990. J. Food Sci. 55: 1378
- Gibson, L.J. and Ashby, M.L. 1988. Cellular Solids: Structure and Properties. Pergamon Press, Oxford.
- Greenspan, L. 1977. J. Research Nat'l Bureau of Standards. 81A:89.
- Kreyszig, E. 1972. Advanced Engineering Mathematics, 3rd ed. Wiley & Sons, New York.
- Mandelbrot, B.B., 1983. The Fractal Geometry of Nature. W.H. Freeman & Co., New York.
- Normand, M.D. and Peleg, M. 1988. Powder Technology. 54:255.
- Peleg, S., Naor, J., Hartley, R. and Avnir, D. 1984. Transactions on Pattern Analysis and Machine Intelligence. PAM 1-6:518.
- Ramirez, R. 1985. The FFT: Fundamentals and Concepts. Prentice-Hall, Englewood Cliffs, NJ.



ROSS, et al.

TITLE: Kinetic Model for Predicting Bacterial Destruction  
from Intrinsic Chemical Marker Formation in Thermally  
Processed Foods

Edward Ross, Dr., Hie-Joon Kim, Dr., Irwin A. Taub, Dr.,  
Kenneth Kustin, Dr., Edgar Shattuck, Mr.

ABSTRACT:

A mathematical model was developed that predicts bacterial destruction in particulate and whole meat foods based on the kinetic behavior during food processing of a bacterium and of one or more intrinsic chemical markers. The destruction of the bacterium is assumed to follow a first-order rate law and to obey Arrhenius kinetics. The temperature-time profile during processing is taken to follow a symmetric, quadratic behavior in an inverse temperature description. This form of thermal pulse leads to exact formulas for the dependence of the rate-functions on time, which in turn lead to relationships between bacterial destruction and marker formation. Using kinetic data on the thermal sensitivity of Clostridium botulinum and B. stearothermophilus and the thermal formation of marker M-1, it was possible to show that a wide dynamic range of bacterial destruction and associated F-values can be covered for nonisothermal conditions appropriate to aseptic processing. Measurements of the marker concentrations, consequently, allow one to predict the extent of bacterial destruction. With one marker, some collateral information on pulse width and/or maximum pulse temperature is needed; with two or more markers, no other information is needed. Simulations suggest that the predictions are good in most cases. Experimental validation of the model has been obtained by using ham cubes of different sizes containing an alginate bead inoculated with B. stearothermophilus and by measuring the yields of markers M-1 in each and every cube. The model should satisfy the requirement for ensuring that a microorganism at the center of the fastest moving particulate would have received a sterilizing heat treatment.

BIOGRAPHY OF PRESENTER: Edward Ross

PRESENT ASSIGNMENT: Professor, Department of Mathematics,  
Worcester Polytech Institute, Worcester, MA.

PAST EXPERIENCE: Staff Mathematician, U.S. Army Natick Research &  
Development Command.

DEGREES HELD: B.S., Webb Inst. Naval Archit., 1945; M.S., Brown  
University, 1949; Ph.D., Brown University, 1954.

ROSS, et al.

Kinetic Model for Predicting Bacterial Destruction from Intrinsic  
Chemical Marker Formation in Thermally Processed Foods

Edward Ross, Dr.,  
Department of Mathematics  
Worcester Polytech Institute  
Worcester, MA 01602

Hie-Joon Kim, Dr., Irwin A. Taub, Dr.,  
Food Engineering Directorate  
U.S. Army Natick RD&E Center  
Natick, MA 01760-5018

Kenneth Kustin, Dr.,  
Department of Chemistry  
Brandeis University  
Waltham, MA 02154

Edgar Shattuck, Mr.  
Soldier Science Directorate  
U.S. Army Natick RD&E Center  
Natick, MA 01760-5020

INTRODUCTION

The safety of an operational ration component made shelf-stable by thermoprocessing must be validated to the satisfaction of regulatory agencies, the Food and Drug Administration (FDA) and the United States Department of Agriculture (USDA). For conventional thermoprocessing involving batch loads of sealed containers in retorts, the validation is based on temperature measurements at the slowest heating point in the food, which can be converted into a factor corresponding to the number of log cycles of pathogenic Clostridium botulinum destroyed. The minimum required destruction is 12 log cycles. For the new thermoprocessing technologies in which particulate foods flow continuously through the processing system until aseptically packaged in sterile containers and for which no temperature measurement can be made, validation would require the cumbersome use of a tester microorganism imbedded in the food and the subsequent determination of the level of destruction attained. Conceptually, if a chemical entity is produced in the food that correlates well with bacterial destruction, it should be possible to use the food itself as an indicator of the thermal history at the center of the fastest moving particulate, and thereby provide the validation required. As the following will show, such intrinsic chemical markers have been found, the yield of which, when combined with a mathematical model correlating bacterial destruction to marker formation, can be used to validate the sterility of aseptically processed particulates.



#### MARKER DETECTION AND CHARACTERIZATION

One such marker detected in broccoli is shown in a three-dimensional representation in Fig. 1. It was obtained by extracting the heat-processed broccoli with an aqueous solution and then injecting the extract into an anion exclusion chromatographic column. As a consequence, the extracted components are separated into a distinctive order of elution

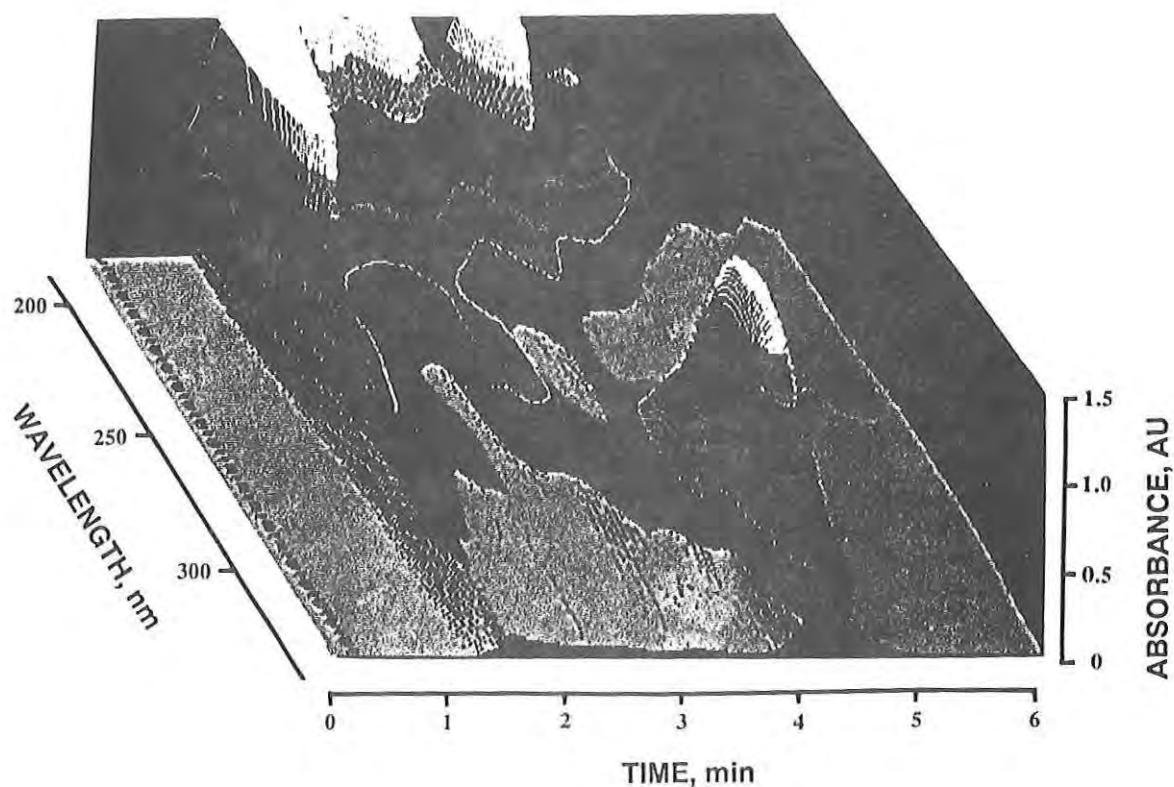


Fig. 1 Three-dimensional representation of a spectrochromatogram for partially purified marker, M-1, obtained from heated broccoli

and pass through a photodiode array detector. The detector takes an optical absorption spectrum of the eluted components every two seconds, the wavelength ranging in this case from 200 to 350 nm. This representation then defines a time-wavelength domain in the X-Y plane; the intensity of the absorption appears in the Z direction. The elution of the marker, M-1 in this case, occurs at 4.2 min, and the peak of its optical absorption spectrum is at 298 nm; both elution time and peak wavelength characterize the marker.

A two-dimensional representation, namely a contour map, is shown in Fig. 2 for chicken samples. The upper portion is for a chicken sample aseptically processed (Cherry-Burrell, Louisville, KY) at 268°F and a 1,100 lb/h flow rate. In the time-wavelength domain out to 8 minutes, there are no peaks of interest. The lower portion is for a chicken sample processed at a higher temperature (280°F) and a lower flow rate (500 lb/h). Under this high temperature-time condition, marker M-1 appears at 4.2 min, with a 298 nm absorption maximum, and another marker, M-2, that is specifically associated with meats, appears at 5.8 min, with an absorption maximum of 285 nm.

Markers are also be found in fruits. If an extract of orange juice is heated, M-1 and another compound, M-3, eluting at 7.5 min, appear. Experiments have been done to show that the precursor of M-1 and M-3 is fructose. The identities of M-1 and M-3 have been established using combined gas chromatography and mass spectrometry (GC/MS). The mass spectrum of M-1 shows that it has a molecular weight of 144 and a cracking pattern that matches what exists in the literature for 2,3-dihydro-3,5-dihydroxy-6-methyl-4(H)-pyran-4-one.<sup>1</sup> M-3 is 5-hydroxymethylfurfural (molecular weight of 126). The identity of M-2 is not yet positively established.

To use these markers in demonstrating sterility, their kinetic characteristics must be known precisely. These were determined for M-1 by taking a broccoli extract, heating it at 121°C (250°F), and tracking the isothermal formation of M-1; it rises quite rapidly at the beginning then begins to trail off, eventually reaching a plateau or limiting value (Fig. 3). Since there appears to be a limit to the amount of the precursor that can convert to the marker, that plateau is defined as the limiting marker yield at time infinity, or  $M_{\infty}$ .

A plot of the logarithm of the marker yield as a function of time gives a straight line, indicating that this conversion is a first-order process. If the formation is tracked at several different temperatures and if the logarithm of the observed rate constants is plotted against reciprocal temperature, a straight line is also obtained, indicating that the formation of this marker follows Arrhenius kinetics. The activation energy for the reaction can be obtained from the slope of this plot, which for M-1 is 23.7 kilocalories per mole.

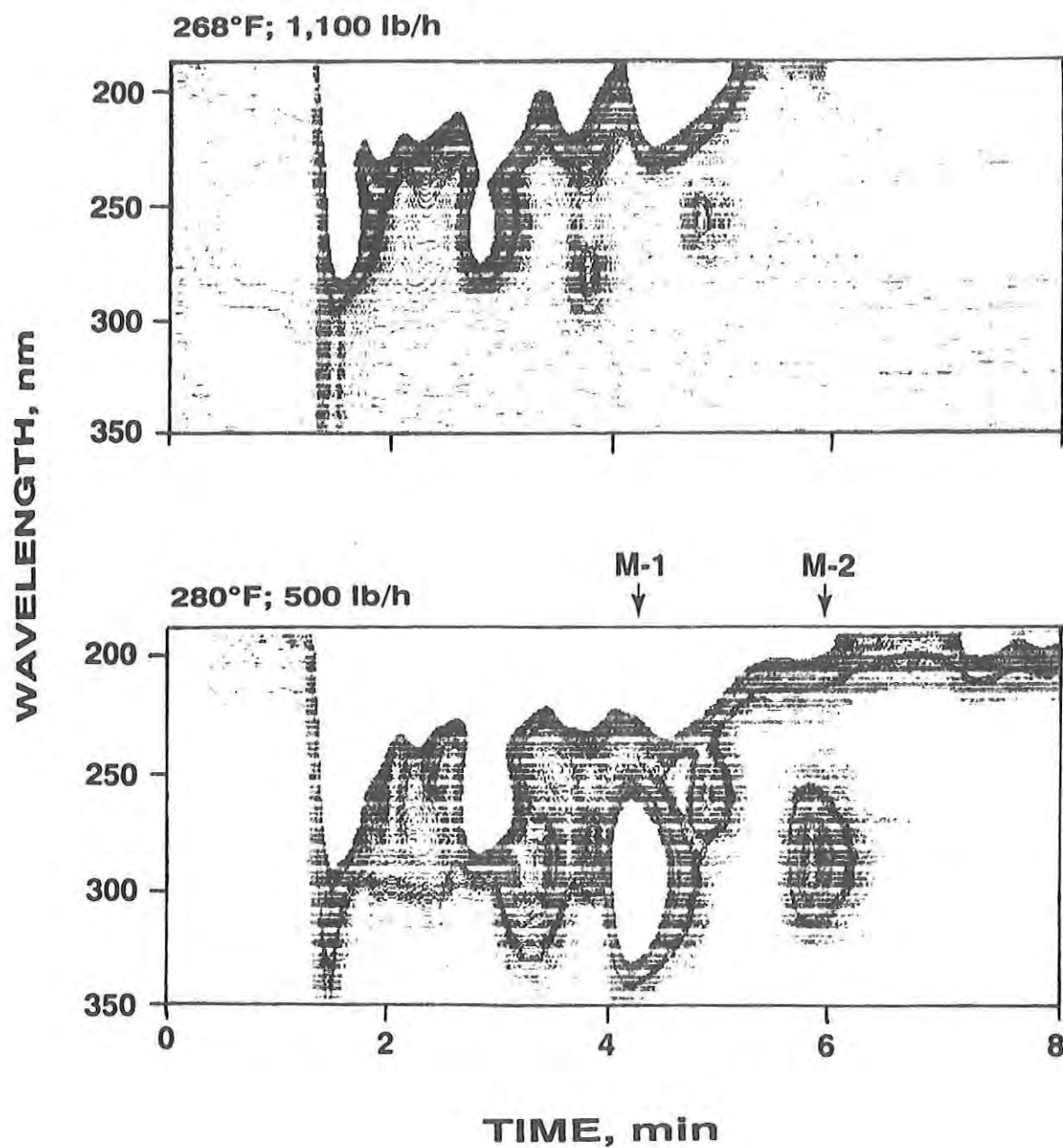


Fig. 2 Contour diagram for aseptically processed chicken samples showing formation of two markers, M-1 and M-2, under the high temperature-time condition

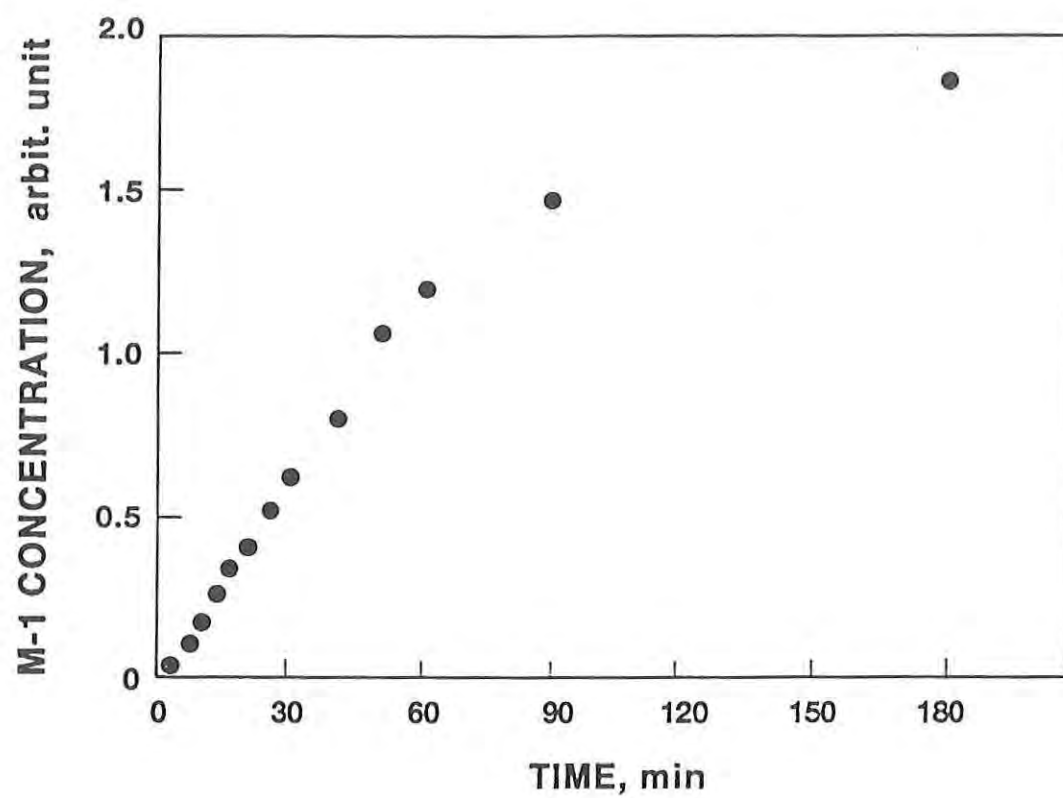


Fig. 3 Kinetic plot for isothermal formation of M-1 in broccoli at 121°C

# MODEL RELATING BACTERIAL DESTRUCTION TO MARKER FORMATION

To use this information in a practical way requires that we mathematically relate the destruction of food-contaminating bacteria to the formation of intrinsic markers in the same system.<sup>2</sup> To understand the relationship, three points are emphasized. Firstly, the precursor of the marker and the bacterium of interest can be considered to be collocated and, therefore, experience the same thermal exposure. Secondly, since both kinetic processes are first-order, we need only consider the fraction of convertible precursor converted to the marker, namely  $M/M_{00}$ , and the fraction of the total bacterial population remaining at any time, namely  $N/N_0$ . And, thirdly, since the rates of bacterial destruction and marker are temperature-dependent, the time-temperature profile influences these processes and the cumulative effects must be found by integrating over this profile. The final predictive equation relates  $\log N_0/N$  to  $(M/M_{00})$  and involves several key kinetic parameters and the peak temperature in the profile. The derivation of the model is outlined briefly, but will be detailed elsewhere.

$N(t)$ , the number of microorganisms remaining at time,  $t$ , behaves as a first-order process, and so

$$N(t_e) = N_0 e^{-\sigma(t_e)} \quad (1)$$

$$\sigma(t_e) = \int_0^{t_e} k[T(t)] dt = \ln[N_0/N(t_e)]. \quad (2)$$

$k$ , the rate constant, depends on absolute temperature,  $T$ , and so on  $t$ .  $N = N_0$  at  $t = 0$ . The dependence of the rate constant on temperature is assumed to be given by the Arrhenius relationship

$$k[T(t)] = k_0 e^{[-E_a/(R T(t))]},$$

where  $E_a$  is the activation energy,  $R$  the universal gas constant, and  $k_0$  the pre-exponential or frequency factor.

These relations are put in dimensionless form by introducing a reference temperature,  $T_r$ , and defining

$$E = E_a/(R T_r) \quad (3)$$

$$x = T_r/T - 1 \quad \text{or} \quad T = T_r/(1 + x). \quad (4)$$

ROSS, et al.

$E$  is dimensionless activation energy, and  $x$  is a dimensionless inverse transformation of  $T$ , i.e.,  $x$  decreases as  $T$  increases. Then

$$E_a/(RT) = [E_a/(RT_r)] [T_r/T] = E(1+x),$$

and the Arrhenius relationship and Eqns (3) and (4) lead to

$$k = k_r e^{-Ex}, \quad k_r = k_0 e^{-E}. \quad (5)$$

Equation (5) implies that  $k_r$  is the rate constant at the temperature,  $T_r$ . In dimensionless terms, Eqns (1) and (2) become

$$\sigma(t_e) = k_r F(t_e) \quad (6)$$

$$F(t_e) = \int_0^{t_e} e^{-Ex(t)} dt. \quad (7)$$

$M(t)$ , the marker concentration at any time,  $t$ , is assumed to obey first-order formation kinetics, and so

$$M(t_e) = M_{\infty} \{1 - e^{-\alpha(t_e)}\}, \text{ where}$$

$$\alpha(t_e) = \int_0^{t_e} k_m [T(t)] dt = -\ln[1 - M(t_e)/M_{\infty}]. \quad (8)$$

$M_{\infty}$  is the limiting marker concentration attained at maximum conversion of the precursor, and  $k_m$  is the rate constant for marker formation. The rate constant is also assumed to follow the Arrhenius relationship with activation energy  $E_{am}$  and pre-exponential constant  $k_{m0}$ . The dimensionless transformation of  $T$  for  $M$  is the same for  $N$ .  $k_{mr}$  is the rate constant when  $T = T_r$ , and

$$E_m = E_{am}/(R T_r).$$

By analogy with the formulas for  $N$ , we obtain from Eqn (7)

$$\begin{aligned} k_m &= k_{mr} e^{-E_m x}; \quad k_{mr} = k_{m0} e^{-E_m} \\ \alpha(t_e) &= k_{mr} F_m(t_e) \end{aligned} \quad (9)$$



$$F_m(t_e) = \int_0^{t_e} e^{-E_m x(t)} dt. \quad (10)$$

If the temperature pulse is quadratic in  $t$ , then we can calculate  $F(t_e)$  exactly. The pulse is taken as symmetric with duration  $t_e = 2 t_p$ , and the transformation of  $T$  into  $x$  gives

$$x(t) = x_p + (x_o - x_p) [(t-t_p)/t_p]^2.$$

$x$  is parabolic, starting and ending with  $x = x_o$ ; the peak temperature (minimum  $x$ ) is attained for  $x = x_p$  when  $t = t_p$ . Inserting this pulse-form in Eqn (7) gives

$$F(t_e) = t_e (C/g) \operatorname{erf}(g) e^{-Ex_p}, \text{ where}$$

$$C = \sqrt{\pi}/2, \quad g = \sqrt{E(x_o - x_p)}.$$

It is usual that  $g > 1.4$ , in which case  $\operatorname{erf}(g)$  is nearly 1,<sup>3</sup> so

$$F(t_e) = (C/g) t_e e^{-Ex_p}.$$

The estimates of  $\sigma(t_e)$  and  $\alpha(t_e)$  are found by combining Eqns (6) through (10) to obtain

$$\sigma(t_e) = k_r (C/g) t_e e^{-Ex_p} \quad (11)$$

$$g = \sqrt{E(x_o - x_p)}$$

$$\alpha(t_e) = k_{rm} (C/g_m) t_e e^{-E_m x_p} \quad (12)$$

$$g_m = \sqrt{E_m(x_o - x_p)}.$$

Dividing Eqns (11) and (12) we find

$$\sigma/\alpha = (k_r/k_{rm}) \sqrt{E_m/E} e^{[(E_m - E)x_p]}. \quad (13)$$

If  $x_p$  is known, Eqn (13) allows the calculation of  $\sigma$  from measurements of  $\alpha$ . If  $x_p$  is not known, it can be found from measurements on two (or more) different markers, designated by subscripts  $m$  and  $q$ . Both markers receive the same temperature-pulse as the microorganism, and so obey the same formulas except for parameter-values. If  $Q$  is the concentration of the extra marker and  $Q_\infty$  its limiting concentration,

ROSS, et al.

$$\begin{aligned}\alpha_q &= -\ln[1 - (Q/Q_\infty)] \\ &= k_{qr}(C/g)t_e e^{-E_q x_p} \\ g_q &= \sqrt{E_q(x_o - x_p)}\end{aligned}\quad (14)$$

Eqs (12) and (14) can be solved for  $x_p$ ,

$$x_p = \ln\{(\alpha_m/\alpha_q)(k_{qr}/k_{mr})\sqrt{(E_m/E_q)}\}/(E_q - E_m), \quad (15)$$

and  $\sigma$  can then be found from Eqn (13).

To illustrate these calculations, they are performed for two microorganisms, Clostridium botulinum ( $k_r=10.96 \text{ min}^{-1}$ ,  $E = 88.5$ ) and B. stearothermophilus ( $k_r=1.1515 \text{ min}^{-1}$ ,  $E = 73.3$ ), using  $T_r = 394.1^\circ \text{ K}$  and  $R = 1.987 \text{ cal/mol/(deg K)}$ . The M-1 marker has  $k_r = .0151 \text{ min}^{-1}$ ,  $E = 30.3$ . For Clostridium botulinum and the marker, and for B. stearothermophilus and the marker, Eqn (13) leads to

$$\begin{aligned}\log_{10}(N_o/N) &= 184.4 e^{-58.2x_p}[-\ln\{1-(M/M_\infty)\}] \\ \log_{10}(N_o/N) &= 21.29 e^{-43.0x_p}[-\ln\{1-(M/M_\infty)\}],\end{aligned}$$

respectively. These relations are graphed in Figs. 4 and 5 for various peak temperatures. Fig. 4 shows that marker measurements at  $250^\circ\text{F}$  in the range  $0 < M/M_\infty < .15$  furnish estimates of  $N_o/N$  in the range  $0 < \log_{10}(N_o/N) < 30$  for Clostridium botulinum. The marker is easily measurable in this range, and the log cycle reduction in the microorganism can be calculated to demonstrate that the food had been adequately processed to assure safety.

#### EXPERIMENTAL TEST OF THE MODEL

The validity of the model can be tested using microbiological data from a simulated aseptic processing procedure. Spores of the thermophilic bacterium, B. stearothermophilus, are embedded in alginate beads,<sup>4</sup> placed at the center of a particulate food, and subjected to a thermal pulse. Surviving bacteria are counted and their decadic reduction is related to the marker concentration determined in the vicinity of the bacteria.

These microbiological experiments have several limitations. Firstly, there is a limit to the number of spores (approximately 10 million) that can be loaded at the center of the food particulate. Secondly, the size of the alginate beads is difficult to reproduce, and these beads are cured before being exposed to high temperature. Therefore, the initial bacterial counts vary significantly, by as much as 100%. Thirdly, since

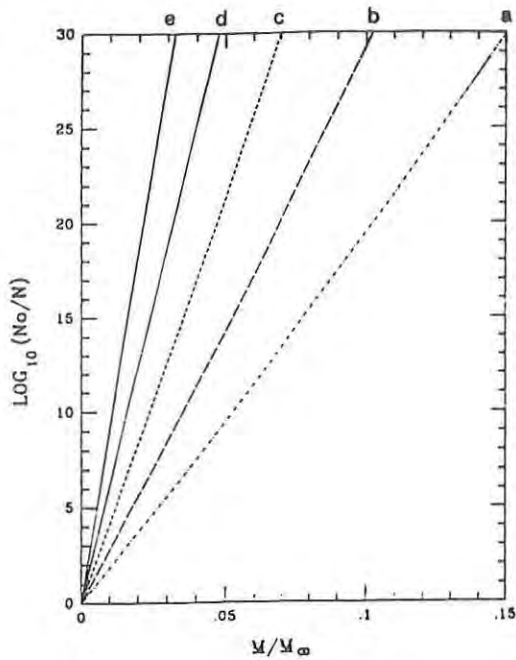


Fig. 4 Relation between  $\text{Log}_{10}(N_0/N)$  for C. botulinum and  $M/M_0$  at several peak temperatures:

- (a) - - - - , 250°F
- (b) — — — , 255°F
- (c) - - - - , 260°F
- (d) ····· , 265°F
- (e) — — — , 270°F.

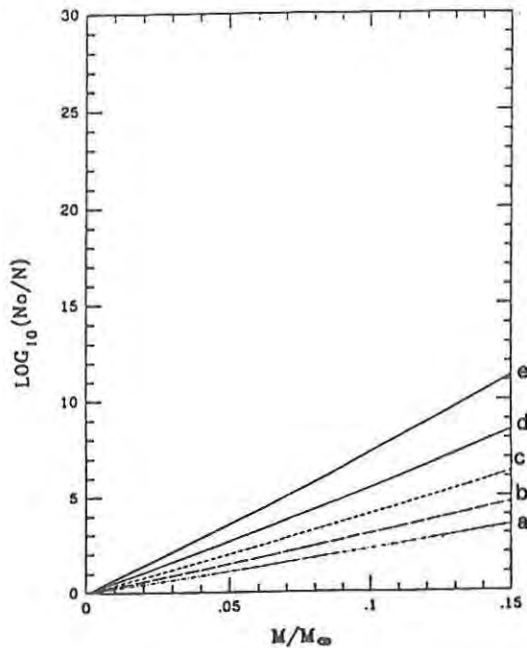


Fig. 5 Relation between  $\text{Log}_{10}(N_0/N)$  for B. Stearothermophilus and  $M/M_0$  at several peak temperatures:

- (a) - - - - , 250°F
- (b) — — — , 255°F
- (c) - - - - , 260°F
- (d) ····· , 265°F
- (e) — — — , 270°F.

ROSS, et al.

the spores are diluted while harvesting and culturing, it is difficult to count reliably less than 10 colony forming units related to the surviving spores. As a result, six decadic reduction in B. stearothermophilus is the maximum reduction one can hope to observe.

Despite these limitations, encouraging preliminary results were obtained. Alginate beads containing approximately  $8 \times 10^6$  spores were placed at the center of ham cubes of different sizes (1", 3/4", and 1/2"). Ten ham cubes of the same size were heated in a chamber with pressurized steam until 131°C was reached at the center, as measured by a thermocouple in one of the ham cubes. As expected, it took much longer for the larger cube to reach the same temperature at the center. For example, it took 1.5 min for the center temperature of a 1/2" cube to increase from 100°C to 131°C; the same temperature increase took 6 min for a 1" cube. The temperature profile was a good approximation of a quadratic function. When the final temperature was reached, the chamber was rapidly evacuated and the center temperature dropped to about 100°C instantly. The alginate bead was recovered and the surviving spore population was measured. The ham cubes were cut into three portions (surface, intermediate, and center). The marker, M-1, was extracted with five-fold excess water and its concentration was determined by anion exclusion chromatography with photodiode array detection. The ham sample was also heated in an oven at 131°C until a plateau value was obtained.

In the 1/2" ham cube, M-1 was observed at a low concentration corresponding to a  $M/M_0$  value of approximately 0.05. The survivor population varied considerably; however, a decadic reduction of approximately one was observed on the average as shown in Fig. 6. A much higher value of  $M/M_0$ , about 0.21, was observed from the center of the 3/4" cube. About 3.5 decadic reduction was observed from the 3/4" cube. The model described above predicts a linear relationship between  $\log N_0/N$  and  $M/M_0$ . The experimental results are consistent with the prediction of the model. A higher value of 0.43 was observed for  $M/M_0$  in 1" ham cubes. The linear relationship predicts about seven decadic reduction and no bacterial survivor was observed, consistent with the marker yield.

In the 1" ham cube, a gradient in the marker concentration was observed decreasing from the surface to the center. The gradient is consistent with the direction of the heat transfer from the surface to the center.

The test shows that the model correctly described the form of the relationship between bacterial destruction and marker formation. Additional experiments are underway using a more suitable temperature range and more precise microbial counting technique to refine further this test.

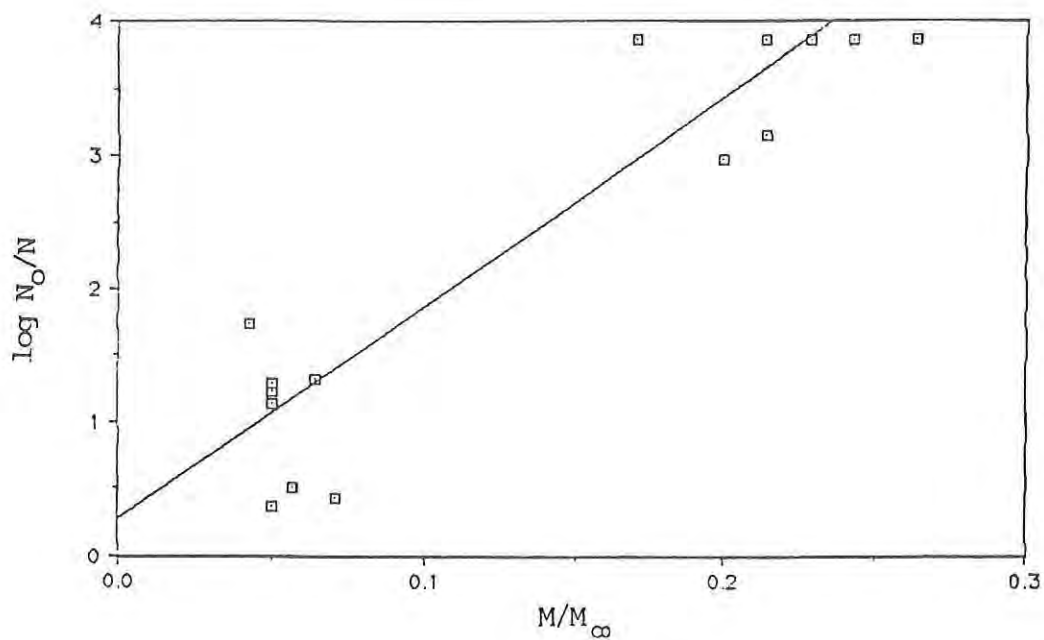


Fig. 6 A plot of decadic reduction of B. stearrowthermophilus vs.  $M/M_\infty$  at the center of 1/2" ham cubes (lower left) and 3/4" cubes (upper right) showing a linear relationship

#### CONCLUSION

The model developed and the test results obtained indicate that the markers could be used to validate the sterility of aseptically processed particulates. It should be possible to calculate the decadic reduction that would have been attained in microbial contaminants in the largest particulate moving at the fastest speed based on the marker yield. Some refinement in the technique and confirmation of key kinetic parameters are needed and are being made to achieve the precision desired. The approach is sensitive, being able to demonstrate a wide range of bacterial destruction with the accessible range of marker detection. It is also possible to determine the heat distribution within the particulate, by cutting up the particulate and analyzing for the marker in any section from the surface to the center. The residence time distribution of particulates in aseptic processing systems can be determined as well. The marker approach can be used in general to demonstrate that the process is safe and, in particular, to gain approval for aseptic processing of particulates.

#### REFERENCES

1. Mills, F.D., Weisleder, D., and Hodge, J.E., Tetrahedron Letters. 15, 1243 (1970).
2. Toledo, R.T. and Chang, S.-Y., Food Technol. 44(2), 72 (1990).
3. Abramowitz, M. and Stegun, I. A., Handbook of Mathematical Functions, US National Bureau of Standards, US Printing Office, Washington, DC., 1964.
4. Brown, K.L., Ayres, C.A., Gaze, J.E., and Newman, M.E., Food Microbiol. 1, 187 (1984).



PISCITELLE

TITLE: Bifurcation Analysis of Divergence and  
Flutter of an Aerodynamic Decelerator  
Louis J. Piscitelle, Dr.

ABSTRACT: A new mathematical model is developed and analyzed to determine the qualitative behavior of a decelerator during the initial opening phase. Currently, all models of canopy opening are valid only once the canopy has begun to inflate and has some assumed shape. The ability to determine the appropriate initial shape would greatly enhance these models. A set of elastodynamic equations for a simplified canopy model is nonlinearly coupled to a model for the relative velocity between a cylinder and the flow past it. Previous work used a linear model for the fluid structure interaction. The new model presented in this paper uses a nonlinear interaction model. The resultant nonlinear partial differential equation is expanded in terms of a complete set of eigenfunctions. The result is an infinite set of coupled ordinary differential equations in time. This set is then truncated to obtain various sets of "low-dimensional" models. These low dimensional models are investigated to determine the stability of the canopy with respect to the fluid's velocity, the line tension and the drag coefficients. Using dynamical system theory, the two-dimensional system corresponding to the smallest nonlinear model is shown to undergo a Hopf bifurcation.

BIOGRAPHY OF PRESENTER: Louis J. Piscitelle

PRESENT ASSIGNMENT: Research Mechanical Engineer at the U.S. Army Natick Research, Development and Engineering Center, Natick, MA

PAST EXPERIENCE: Research Mechanical Engineer at Stowe Woodward Co. for two and one half years; prior to which, Combustion Engineering Co. for two years.

DEGREES HELD: BS and MS in Mechanical Engineering, Worcester Polytechnic Institute, Ph.D in Mathematics, Northeastern University

## PISCITELLE

### BIFURCATION ANALYSIS OF DIVERGENCE AND FLUTTER OF AN AERODYNAMIC DECELERATOR

Louis J. Piscitelle, Dr.  
Aero-Mechanical Engineering Directorate  
U.S. Army Natick Research, Development and Engineering Center  
Natick, MA 01760

#### Introduction

The prediction of a circular decelerator's behavior during the initial phase of the opening process is an important technical barrier for the Airdrop community. As a parachute is expected to open successfully at higher speeds and lower altitudes, the ability to predict the stability of the initial interaction between the decelerator and the flow field becomes crucial. A stability analysis of a mathematically rigorous model for this process would predict which conditions would result in various types of stable and unstable behavior. If under certain conditions, the unstable behavior caused the parachute to exhibit oscillations of increasing amplitude, a fabric failure might occur before the parachute could open. If the conditions of deployment resulted in a sustained oscillation of bounded amplitude, it is not known how the opening would be affected. The conjecture is that this global motion might prevent the failure known as "squidding," where the parachute never begins to inflate. Conditions may also be such that the canopy assumes a stable deflected shape. In any of these cases, the analysis would provide details about the shape of the canopy just prior to the inflation process. Currently, all models of the opening process (Steeves, 1986, 1989; Ross, 1970, 1971; Ludtke, 1986; Purvis, 1982; Reddy, 1974; Heinrich and Jamison, 1966) are applicable only after the decelerator has attained some assumed initial shape. Since this assumed shape is determined by the behavior of the decelerator during the initial phase of the opening process, an understanding of a decelerator's behavior just prior to the inflation phase is of fundamental value.

The subject of this paper is the development of a mathematical model of a canopy's behavior just after the canopy is extracted. This model requires the development of a partial differential equation (PDE), which governs the interaction of the canopy with the flow field. The derived model could be analyzed using dynamical system theory to determine the stability of the canopy as a function of the values of various physical parameters (e.g., airspeed and line tension).

## PISCITELLE

### Literature Review

There are numerous models in the open literature for the interaction of a flexible structure with a flow field; for an overview see Dowell, 1975, 1980; Bisplinghoff and Ashley, 1962. Typically, these models were created to analyze the aerodynamic flutter problem of a structure in a supersonic flow field. While the fluid structure interaction is easier to model using this assumption, most Army airdrops are performed at subsonic speeds. Thus, these models are not directly applicable to the decelerator problem. Work has been published for problems where a pipe either conveys fluid or is in a flow field (Paidoussis and Issid, 1974; Thompson and Lunn, 1981; Paidoussis, 1966). These models were either not applicable, such as those for pipes conveying fluid, or too restrictive, such as the linear models of Paidoussis, 1966. Hence, the development of an applicable model was essential.

The application of dynamical system theory to aerodynamic stability problems is not new. For a good mathematical introduction to dynamical systems see Guckenheimer and Holmes, 1983; for an introduction from an engineering viewpoint see Thompson and Stewart, 1986. In fact, the supersonic flutter problem has been examined in some detail (Holmes and Marsden, 1978; Dowell, 1966, 1980; Marsden and Hughes, 1983). The stability of pipes conveying fluid has also been examined by Holmes, 1977. The idea is to use dynamical system techniques to find the "essential generic models" from the full system of PDEs (Holmes, 1977; Holmes and Rand, 1976).

### Definitions

Under certain conditions, i.e. wind load, line tension, the decelerator may attain a specific shape and remain that way until inflation begins. This would indicate stability. Sometimes, when the conditions are changed, a dramatic change in the behavior of the decelerator occurs. The new state may be one in which the decelerator is oscillating steadily with bounded amplitude (flutter, or sustained flutter), one in which the amplitudes of the oscillation grow without bound (divergent flutter), one in which the oscillations are chaotic, or one in which the tube is displaced to a new equilibrium position (divergence). The definitions used here for flutter and divergence are in accordance with nonlinear theory and differ from the definitions of divergence and flutter for linear theory (in which divergence is defined as a zero frequency displacement that grows without bound and flutter is defined as an oscillatory motion whose amplitude grows without bound). This rapid change as a function of the

## PISCITELLE

value of a given parameter or parameters is termed a bifurcation.

### Dynamical System Theory

The advantage to applying dynamical system theory in the study of these complicated physical problems is that the parameter values for which qualitative changes in decelerator behavior occur may be determined by looking at a set of equations, which are much simpler than the original PDE. This simpler set, or reduced set, of equations is easier to analyze, both mathematically and numerically, yet still contains all the information required to describe the bifurcation phenomena. In general, the reduced set of equations is a finite system of nonlinear ordinary differential equations (ODEs) in time. This set of ODEs is called a low-dimensional model because it contains a small number (one, two or perhaps four) of ODEs as opposed to the original PDE, which was infinite dimensional. There are a number of techniques for making the reduction (Holmes, 1977; Guckenheimer and Holmes, 1983; Carr, 1981). One technique is to expand each of the PDE's variables as an infinite series of appropriate space functions with time-dependent coefficients, substitute the series into the original PDE and truncate the system to a finite number of ODEs in time. Another technique is to determine if a center manifold exists for the PDE. This would also reduce the PDE to a finite set of ODEs in the variables which were changing slowly in time on the center manifold. The local bifurcation behavior is then described by the set of ODEs which govern the dynamics on this usually low-dimensional space (see Marsden and McCracken, 1976; Henry, 1981; Guckenheimer and Holmes, 1983; Carr, 1981).

### Scope

The scope of this paper is limited to narrow tubes with simple supports on each end. This model was chosen because of the parachute's shape and attachments during the initial extraction phase. Typically, the parachute has one end attached to the payload and is extracted by another parachute attached at the opposite end. While the extracting parachute can not perfectly fix the top of the extracted parachute, films of actual parachute deployments show that the assumption of a simple support is not unreasonable as a first approximation. In addition, prior to opening, the canopy appears to assume a tube-like shape. The PDE derived in this report is not restricted to the assumption of simply supported end conditions. Other supports (such as fixed-free) may be used and the appropriate set of ODEs would be derived based



## PISCITELLE

upon a slightly different eigenfunction expansion. The tubes are assumed to be viscoelastic and may have a general cross-section. The flow field is parallel to the initial (at rest) axis of the tube and a nonlinear fluid-solid interaction model is derived. The extension of the fluid-solid interaction model to include nonlinear terms, while important for subsonic flows, has not been derived previously because the effect is small for supersonic flows (see Holmes, 1977).

The section titled Physical Model contains the basic assumptions used in developing the PDE that describes the uninflated decelerator and its interaction with the external flow field. This section also develops the extension of the fluid-solid interaction model to include nonlinear terms. A complete PDE is then presented and compared to models already published, which serve as special cases of this more general model.

The section titled Derivation of Low-Dimensional Models begins with the PDE derived in the previous section and determines a set of eigenfunctions for the nonlinear problem. Each of the PDE's variables is then expanded as an infinite series (with time-dependent coefficients) in these eigenfunctions. The substitution of these series representations into the original PDE and the use of standard, albeit tedious, calculations yields an infinite system of coupled nonlinear ODEs. Truncation of this system at various levels gives a sequence of low-dimensional models, which are examined in the next section.

The Results and Discussion section presents the models developed and the results of the stability analysis along with phase plane plots for the lowest dimensional model. This section examines and compares the results to those found by previous authors for similar systems of equations and also describes the numerical software used.

The Conclusions are the salient findings of the paper. The implications of these findings to the initial opening problem of a decelerator are then discussed.

The Recommendations outline a set of theoretical and experimental studies for the future. The course of action presented is based upon the results obtained in the current investigation and number of new approaches and extensions, which the author believes could prove fruitful.

## PISCITELLE

### Physical Model

The decelerator is modelled as a long thin tube, with mass per unit length  $m$ , which is simply supported at each end. The tube is immersed in a fluid which is flowing with a free stream velocity  $U$  parallel to the initial (undeformed) axis of the tube. The tube may also be subject to an initial axial load,  $T_0$ , applied at the right support by displacing the right support.

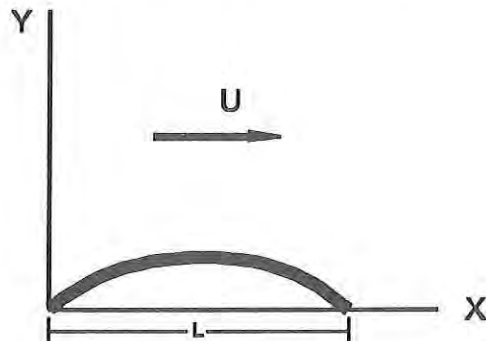


Figure 1. Simply Supported Tube in Axial Fluid Flow.

The boundary conditions are chosen to model the attachment of the decelerator to the payload at one end and to the extraction chute at the other end. The boundary conditions wherein both ends are fixed or one end is fixed with the other free may also be used.

Thus far the geometrical model is the same as that used by Paidoussis, 1966 to construct a linear equation of motion for the flexible cylinder. At this point, the assumptions used to construct the nonlinear model analyzed in this report are described.



## PISCITELLE

The material is assumed to be viscoelastic and to obey the Kelvin-Voight model as was assumed by Holmes, 1977 and Paidoussis and Issid, 1974. Thus, the stress strain law for the material is

$$\sigma = Ee + \eta \dot{e} , \quad (1)$$

where  $\sigma$  = stress,  $E$  = Young's modulus,  $\eta$  = coefficient of viscosity,

$$e = \text{strain, and } (\dot{\phantom{x}}) \equiv \frac{\partial (\phantom{x})}{\partial t} .$$

The study is also limited to motions which result in small strains in the tube. Under these assumptions (see Holmes, 1977), the axial extension,  $w(x)$ , induced by the lateral deflection  $y(x)$  is given by

$$w(x) = \frac{1}{2} \int_0^L (y'(x))^2 dx \quad (2)$$

$$\text{where } (\phantom{x})' \equiv \frac{\partial (\phantom{x})}{\partial x} .$$

Expression 4 and Equation 5 are used to modify the linear model of Paidoussis, 1966. The resulting PDE is structurally nonlinear.

Before writing down the PDE for the motion of the tube, the extension of the fluid-structure interaction model will be derived. Assuming small lateral motions for the tube, Paidoussis, 1966 used the result of Lighthill, 1960 for the resultant relative velocity,  $v(x,t)$ , between the tube and the flow.  $V(x,t)$  then has the form (see Lighthill, 1960)

$$v(x,t) = \dot{y} + U y' . \quad (3)$$

## PISCITELLE

By letting  $M$  be the virtual mass of the fluid for a unit length of tube, Paidoussis, 1966 shows that the resultant lateral force on the tube may be expressed as

$$\left( \left[ \frac{\partial}{\partial t} + U \left[ \frac{\partial}{\partial x} \right] \right) (M v(x, t)) \right). \quad (4)$$

In addition, Paidoussis, 1966 assumed that there were viscous forces acting on the tube and using the results of Taylor, 1952 for long inclined tubes with turbulent boundary layers obtained

$$F_N = \frac{1}{2} \rho D U^2 (C_{D_p} \sin^2(i) + C_f \sin(i)) \quad (5)$$

for the viscous normal force per unit length of tube.

Paidoussis, 1966 also obtained

$$\begin{aligned} F_L &= \frac{1}{2} \rho D U^2 C_f \cos(i) \\ \text{Where } i &= \arcsin\left(\frac{v}{U}\right) \end{aligned} \quad (6)$$

for the viscous longitudinal force per unit length of tube. In equations 5 and 6,  $D$  is the tube diameter,  $\rho$  is the density of the incompressible fluid,  $C_{D_p}$  is coefficient of form drag for a cylinder in cross flow and  $C_f$  is the coefficient of friction drag. Paidoussis, 1966 implicitly assumes that  $v \ll U$  which implies that  $\sin(i) \gg \sin^2(i)$  and  $\cos(i) = 1$ .

## PISCITELLE

Thus, Paidoussis, 1966 obtains

$$\begin{aligned} & \text{and} \quad F_N \approx \frac{1}{2} \rho D U^2 \sin(i) \\ & \quad F_L \approx \frac{1}{2} \rho U^2 C_f . \end{aligned} \quad (7a,b)$$

Equations 7a and 7b represent the linearization by Paidoussis, 1966.

Equations 7a and 7b are first order approximations to the drag experienced by the tube. In order to derive a better approximation, it is necessary to more closely examine equation 5 and the geometry of interaction of the tube with the flow field. Equation 5 was chosen by Taylor 1952 as a likely candidate for the variation of normal force with tube angle. This was estimated based upon a curve fitted to laminar flow data in which sine squared worked well. The difficulty with equation 5 is that the sine squared term leads to terms in the PDE which are even in  $y$ . This is not physical. The same data has been fitted well by the author using sine cubed for the nonlinear extension and this leads to physically meaningful terms for the PDE, i.e. terms which are odd in  $y$ .

The new drag equation may be written as

$$F_N = \frac{1}{2} \rho D U^2 (C_{D_p} \sin^3(i) + C_f \sin(i)) \quad (8)$$

Including the effect of the tube's velocity in the  $y$  direction on both the magnitude and direction of the total fluid velocity relative to the tube, the resultant velocity and direction angle relative to the tube are

$$\begin{aligned} & (U^2 + (\dot{y})^2) \\ & \text{and} \quad (\arctan(y') + \arctan(\frac{\dot{y}}{U}) , \end{aligned} \quad (9a,b)$$

respectively.

## PISCITELLE

Substituting expressions 9a,b into equation 8, expanding in a Taylor series and retaining the first set of higher order terms, the normal drag force may be written as

$$F_N = \frac{1}{2} \rho D C_f [U^2 y' + U \dot{y}] + \frac{1}{2} \rho D [U^2 (C_{D_p} - \frac{1}{2} C_f) (y')^3 + U (3 C_{D_p} - \frac{1}{2} C_f) (y')^2 \dot{y}] \quad (9c)$$

The longitudinal drag force is the one used by Paidoussis, 1966, equation 7b.

Using equations 2, 3, 4, 7b, 8, and 9a-c, the equation of motion may be written as (see Paidoussis, 1966; Holmes, 1977)

$$\begin{aligned} \alpha \ddot{y}'''' + y'''' + [u^2 (1 - \frac{1}{2} \zeta C_T (\frac{1}{2} - x)) - \Gamma - \kappa \int_0^1 (y')^2 dx - \sigma \int_0^1 y' \dot{y}' dx] y'' \\ + 2\beta^{1/2} u \dot{y}' + \zeta C_T u^2 y' + \frac{1}{2} \beta^{1/2} \zeta C_T u \dot{y} \\ + \ddot{y} + \frac{1}{2} \zeta u^2 C_T (R - \frac{1}{2}) (y')^3 + \frac{1}{2} C_T \beta^{1/2} \zeta u (3R - \frac{1}{2}) (y')^2 \dot{y} = 0 \quad . \quad (10) \end{aligned}$$

The boundary conditions for equation 10 are

$$y = y'' = 0 \quad \text{at} \quad x = 0, 1 \quad . \quad (11a,b)$$

# PISCITELLE

Equation 10 is in dimensionless form. The nondimensional variables are defined as

$$\begin{aligned}\bar{x} &= x/L, & \bar{y} &= y/L, & \tau &= \frac{t}{L^2} \left( \frac{EI}{m+M} \right)^{1/2}, & \beta &= \frac{M}{m+M}, \\ \Gamma &= \frac{T_o L^2}{EI}, & \zeta &= \frac{L}{D}, & u &= UL \left( \frac{M}{EI} \right)^{1/2}, & \kappa &= \frac{AL^2}{2I}, \\ \alpha &= \frac{\eta}{L^2} \left( \frac{I}{E(m+M)} \right)^{1/2}, & \sigma &= \frac{\eta A}{(EI(m+M))^{1/2}}, \\ c_T &= \frac{D^2}{M} \rho C_f, & R &= \frac{C_{D_p}}{C_f},\end{aligned}\tag{12a-1}$$

where A is the cross-sectional area of the tube, I is the cross-sectional moment of inertia of the tube, and all other terms are as define previously. In equation 10, the bars have

been dropped from the x and y variables and  $(\cdot) \equiv \frac{\partial(\cdot)}{\partial \tau}$  for

convenience. If only the linear terms in equation 10 are retained, the resulting equation is equivalent to the linear PDE examined by Paidoussis, 1966. If the last two nonlinear terms on the left hand side (LHS) of equation 10 are eliminated, the resulting equation is similar to that derived in Holmes, 1977.

Based on physical reasoning, the ranges of the parameters defined in equations 12a -1 are restricted. One sets the structural damping parameters  $\alpha, \sigma > 0$ , and fixes  $\beta, \kappa > 0$ .

Also, it is typically assumed (see Holmes, 1977) that viscous damping terms such as  $c_T$  are fixed at some positive value.

This then leaves the nondimensional tension  $\Gamma$  (which may be either positive, negative or zero) and the nondimensional fluid velocity  $u \geq 0$ , as the parameters which may be varied.

## PISCITELLE

Hence, equation 10 would represent a two-parameter family of PDEs with the so-called control parameters (see Holmes, 1977; Holmes and Marsden, 1978; Guckenheimer and Holmes, 1983)

$$\bar{\mu} = (u, \Gamma) \in \mathbb{R}^2.$$

This choice of control parameters is a function of the particular physical problem being analyzed. In the system of equations examined in this report, equations 10 and 12a,b, the ratio of drag coefficients  $R$  is a new parameter, which may be varied in conjunction with the previously mentioned tension and velocity parameters. Thus, one may consider equation 10 as a three-parameter family with  $\bar{v} = (u, \Gamma, R) \in \mathbb{R}^3$ .



## PISCITELLE

### Derivation of Low-Dimensional Models

The equilibrium states may be found by setting all time derivatives to zero in equation 10. The resulting ODE is

$$y'''' + [u^2(1 - \frac{1}{2}\zeta c_T(\frac{1}{2} - x)) - \Gamma - \kappa \int_0^1 (y')^2 dx] y'' + \zeta c_T u^2 y' + \frac{1}{2} c_T u^2 \zeta (R - \frac{1}{2}) (y')^3 = 0 \quad (13)$$

with the boundary conditions given by equations 11a, b.

Following Holmes, 1977, it is observed that for  $c_T = 0$ , equation 13 reduces to a nonlinear equation examined by Reiss, 1969. This representation will allow one to extract a complete set of eigenfunctions for the equation 13 by solving for the eigenfunctions of the linearized ODE

$$w_j'''' + \lambda_j w_j'' = 0, \quad (14)$$

$$|w_j'| = \frac{(u^2 - \Gamma - \lambda_j)}{\kappa}.$$

For simple supports, equations 11a, b, the resulting eigenfunctions are  $w_j(x) = a_j \sin(j\pi x)$ . Thus, using Galerkin averaging (see Dowell, 1966; Holmes, 1977) and the eigenfunctions from equation 14, let

$$y_n(x, \tau) = \sum_{j=1}^n r_j(\tau) w_j(x). \quad (15)$$

The  $r_j$ 's are time dependent functions to be determined. Of course, the use of equation 15 assumes that the series approximation for  $y_n$  converges to  $y$  as  $n \rightarrow \infty$ .

# PISCITELLE

Now, substitute equation 15 into equation 10 (and note that as expected the boundary conditions given by equations 11a, b are satisfied because equation 15 is a linear combination of functions, each of which satisfies these boundary conditions) to obtain

$$\begin{aligned}
 & \alpha \sum_{j=1}^n w_j''' \dot{x}_j + \sum_{j=1}^n w_j''' r_j + [u^2(1 - \frac{1}{2}\zeta c_T(\frac{1}{2} - x)) - \Gamma] \sum_{j=1}^n w_j' r_j \\
 & + 2\beta^{1/2}u \sum_{j=1}^n w_j \dot{x}_j + \zeta c_T u^2 \sum_{j=1}^n w_j r_j + \frac{1}{2}\beta^{1/2}\zeta c_T u \sum_{j=1}^n w_j \dot{x}_j \\
 & + \sum_{j=1}^n w_j \ddot{x}_j - [\kappa \int_0^1 (\sum_{k=1}^n w_k r_k)^2 dx] \sum_{j=1}^n w_j' r_j \\
 & - [\sigma \int_0^1 (\sum_{k=1}^n w_k r_k) (\sum_{k=1}^n w_k \dot{x}_k) dx] \sum_{j=1}^n w_j' r_j \\
 & + \frac{1}{2}\zeta c_T u^2 (R - \frac{1}{2}) (\sum_{j=1}^n w_j r_j)^3 \\
 & + \frac{1}{2}c_T \zeta \beta^{1/2} u (3R - \frac{1}{2}) (\sum_{k=1}^n w_k r_k)^2 (\sum_{k=1}^n w_k \dot{x}_k) = 0 .
 \end{aligned} \tag{16}$$

The Galerkin procedure then requires that equation 16 be multiplied by  $w_s(x)$  and integrated from  $x = 0$  to  $x = 1$ . The resulting equation is then reduced using the standard orthonormality relationships. The result is a set of  $n$  second order ODE in the coefficients  $r_s(\tau)$ .

By truncating the series at  $n = 1$ , and 2, two low dimensional models are developed. They are

for  $n = 1$ :

$$\begin{aligned}
 & \ddot{x}_1 + A_1 \dot{x}_1 + B_1 r_1 + \kappa \frac{\pi^4}{2} r_1^3 \\
 & + \sigma \frac{\pi^4}{2} r_1^2 \dot{x}_1 + \frac{\pi^2 c_T u \zeta \beta^{1/2} (3R - \frac{1}{2})}{8} r_1^2 \dot{x}_1 = 0 ,
 \end{aligned} \tag{17}$$

# PISCITELLE

for  $n = 2$ :

$$\begin{aligned}
 \ddot{r}_1 + A_1 \dot{r}_1 + B_1 r_1 + \frac{8}{9} \zeta C_T u^2 r_2 - \frac{16}{3} \beta^{1/2} u \dot{r}_2 \\
 + \kappa \pi^4 \left[ \frac{1}{2} r_1^2 + 2 r_2^2 \right] r_1 + \sigma \frac{\pi^4}{2} [r_1 \dot{r}_1 + r_2 \dot{r}_2] r_1 \\
 + \pi^2 \zeta C_T u^2 \left( R - \frac{1}{2} \right) \left[ \frac{4}{5} r_1^2 r_2 - \frac{144}{35} r_2^3 \right] \\
 + \pi^2 C_T \zeta \beta^{1/2} u \left( 3R - \frac{1}{2} \right) [\dot{r}_1 r_2^2 + \frac{1}{8} r_1^2 \dot{r}_1] = 0 \quad ,
 \end{aligned} \tag{18a}$$

$$\begin{aligned}
 \ddot{r}_2 + A_2 \dot{r}_2 + B_2 r_2 + \frac{32}{9} \zeta C_T u^2 r_1 - \frac{16}{3} \beta^{1/2} u \dot{r}_1 \\
 + \kappa \pi^4 [2 r_1^2 + 8 r_2^2] r_2 + \sigma \frac{\pi^4}{2} [4 r_1 \dot{r}_1 + 16 r_2 \dot{r}_2] r_2 \\
 + \pi^2 \zeta C_T u^2 \left( R - \frac{1}{2} \right) \left[ \frac{176}{35} r_1 r_2^2 + \frac{4}{5} r_1^3 \right] \\
 + \pi^2 C_T \zeta \beta^{1/2} u \left( 3R - \frac{1}{2} \right) \left[ \frac{1}{2} r_2^2 \dot{r}_2 + \frac{1}{4} r_1^2 \dot{r}_2 \right] = 0 \quad .
 \end{aligned} \tag{18b}$$

In equations 17, and 18a,b the coefficients  $A_s$  and  $B_s$  are defined as

$$A_s = \pi^4 s^4 \left[ \alpha + \frac{1}{2} \beta^{1/2} \zeta C_T u \right] \tag{19a,b}$$

$$B_s = \pi^4 s^4 + [\Gamma - u^2] \pi^2 s^2 \quad .$$

## PISCITELLE

Any one of the systems given by equations 17 or 18a,b may be written as a first order ODE on  $\mathbb{R}^{2n}$ . For example, equation 17 may be put in the form

$$\dot{x} = A_\mu x + N(x) \quad ; \quad x(0) = x_0 \in \mathbb{R}^2, \quad (20a-e)$$

where

$$x = \begin{pmatrix} x_1 \\ \dot{x}_1 \end{pmatrix}, \quad A_\mu = \begin{pmatrix} 0 & 1 \\ -B_1 & -A_1 \end{pmatrix}$$

and

$$N(x) = \begin{pmatrix} 0 \\ -\frac{\kappa\pi^4}{2}x_1^3 - \frac{\sigma\pi^4}{2}x_1^2x_2 - \frac{\pi^2\beta^{1/2}c_T u\zeta(3R-\frac{1}{2})}{8}x_1^2x_2 \end{pmatrix}.$$

Clearly, for a given set of initial conditions, equations 20a-e may be numerically integrated using standard techniques. In fact, all of the low-dimensional models may be put in the form of equations 20a-e with the only change being that the entries in equation 20d become matrices of order  $n \times n$ . Holmes, 1977 points out that the accuracy with which the numerical solutions to any particular low-dimensional model agree with the solution to the PDE is dependent upon the speed of convergence as the number of modes goes to infinity. Dowell, 1966 showed that for similar systems  $n = 4$  or  $6$  was a good approximation. This (see Holmes, 1977) is probably due to a concentration of the energy at the low frequencies. Following Holmes, 1977, as the current report is primarily concerned with the qualitative behavior of solutions, the assumption is made that the convergence is rapid enough for the low-dimensional models to be physically reasonable. This assumption will have to be examined later in this research, either analytically or experimentally.

## PISCITELLE

### Results and Discussion

This section describes the use of dynamical system theory to investigate the bifurcation behavior of the low dimensional model given by equation 20a-e. It also describes the software which is used to provide the phase plane plots and compute the stable and unstable manifolds associated with the equilibrium points.

As stated previously, one may consider equation 20a-e as a three-parameter family with  $\bar{v} = (u, \Gamma, R) \in \mathbb{R}^3$ . Equation 20a-e has equilibrium points given by

$$\begin{aligned} x_2 &= 0, \\ \frac{\kappa\pi^4}{2}x_1^3 + B_1x_1 &= 0. \end{aligned} \quad (21)$$

Equation 21 agrees with the results obtained by Holmes, 1977. They are reproduced here for comparison. If  $B_1 > 0$ , then  $(0,0)$  is a unique fixed point and it is a sink, see figure 2. This means that the undeflected shape is stable. If  $B_1 < 0$ , there exist three equilibrium points given by  $(0,0)$  and

$(\pm\sqrt{-2B_1/\kappa\pi^4}, 0)$ . The tube is now unstable since the center fixed point is a saddle and, for  $R$  large enough, the other two are sinks as shown in figure 3 (see Holmes, 1977). Note also that The change in sign of  $B_1$  from positive to negative takes place when  $\Gamma - u^2 = -\pi^2$ , (this is the Euler buckling mode).

For the case where  $R < R_{cr}$  (where  $R_{cr}$  is the critical value above which the results agree with Holmes, 1977), different results are obtained. For  $B_1 > 0$  there still exists a unique fixed point at  $(x_1, x_2) = (0,0)$ . For  $B_1 < 0$  and  $R > R_{cr}$ , the structure is identical to that found by Holmes, 1977 and there are three equilibrium points, one saddle and two sinks, see figure 4. If however,  $R$  is reduced to a value below  $R_{cr}$  then the two sinks become sources and a pair of limit cycles is born, see figure 5. Physically, these limit cycles correspond to the canopy oscillating about either one of the displaced positions, i.e., fluttering.

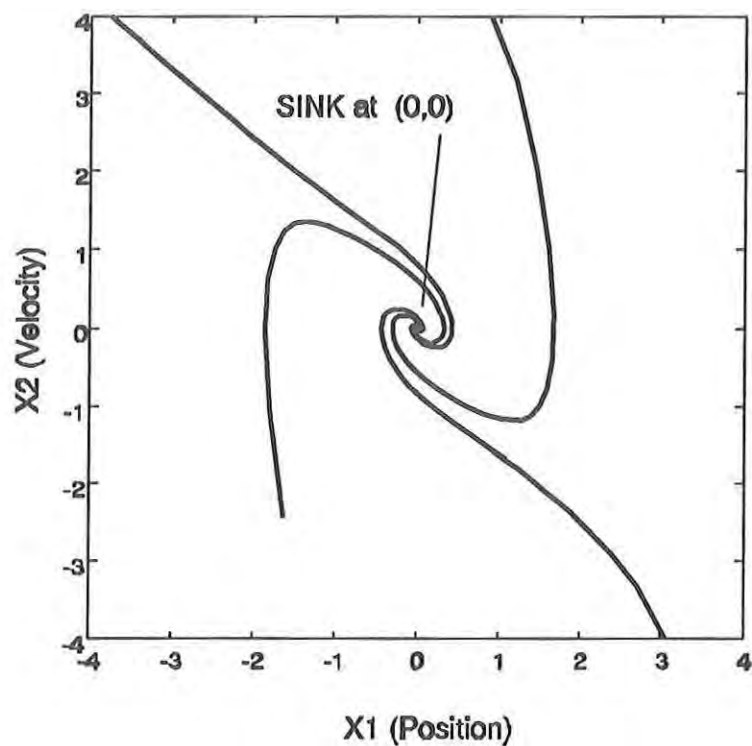


Figure 2. Holmes' One Mode Model with  $B_1 > 0$ .

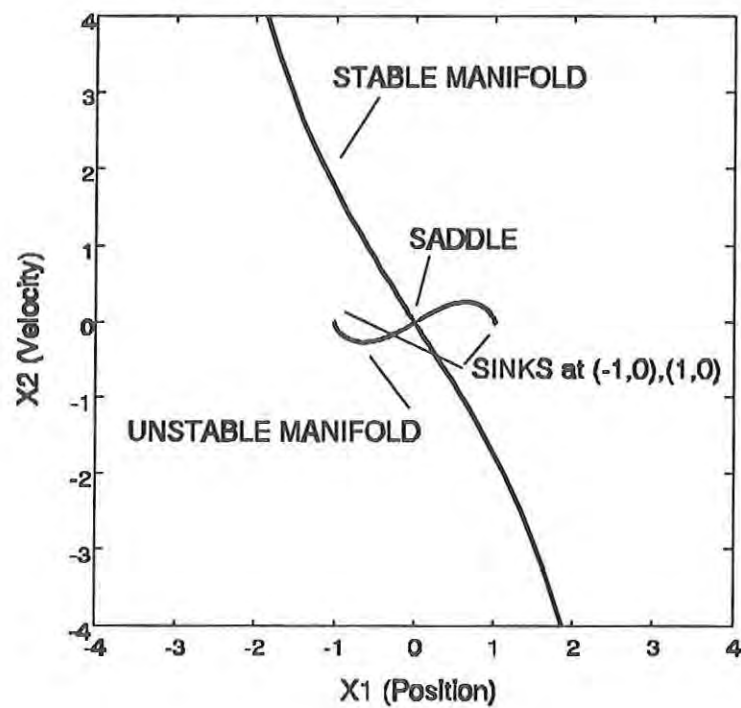


Figure 3. Holmes' One Mode Model with  $B_1 < 0$ .



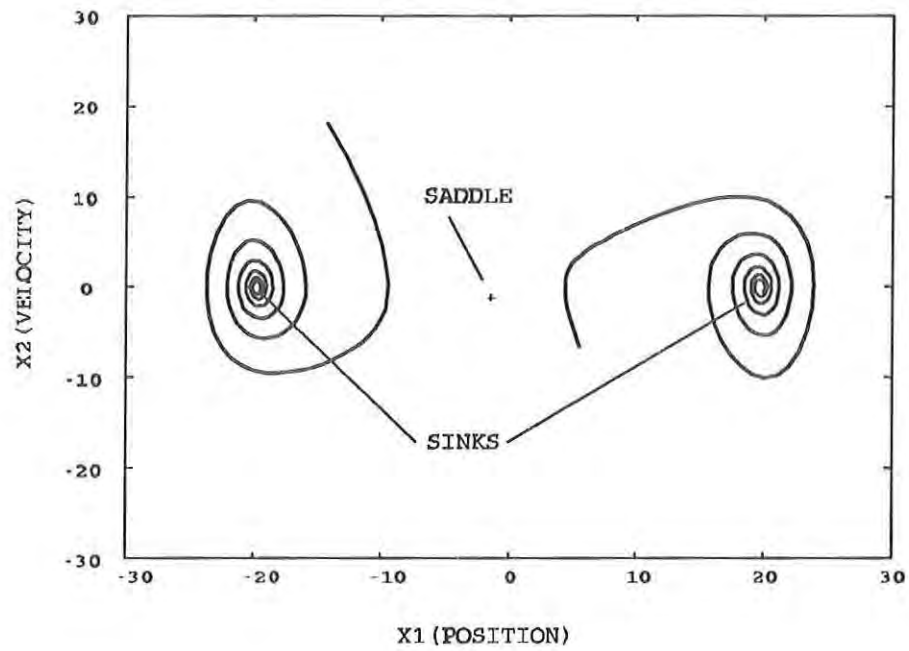


Figure 4. New One Mode Model with  $B_1 < 0$  and  $R > R_{cr}$ .

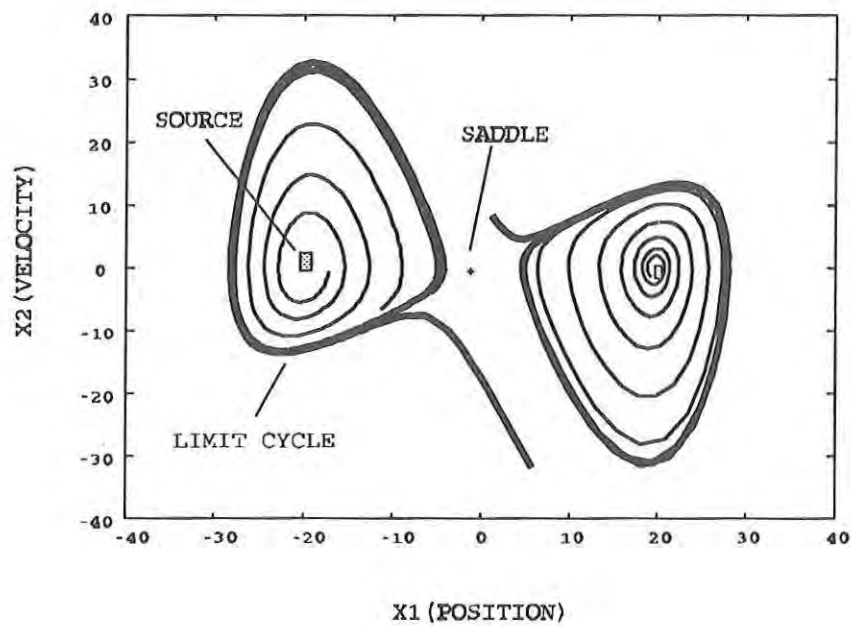


Figure 5. New One Mode Model with  $B_1 < 0$  and  $R < R_{cr}$ .

## PISCITELLE

At this point, the dynamical system software used to examine the low-dimensional model is described. The specific software is "kaos<sup>(TM)</sup> Dynamical System Toolkit with Interactive Graphic Interface" and was developed by J. Guckenheimer and S. Kim. The package is a collection of numerical and graphical routines which are quite helpful in computing equilibrium points, stable and unstable manifolds and other dynamical system phenomena, such as limit cycles. The program runs on a SUN SPARC<sup>(TM)</sup> workstation and is easy to compile and easy to use. (For a detailed description of the package see J. Guckenheimer and S. Kim; 1990.) Figure 6 is an example of the display produced on screen for the user.

The program allows the users to examine the behavior of their own system of equations in a interactive mode. The graphical output is supplemented by data written to a file. These data may include locations in phase space of equilibrium points, types of fixed points (i.e., saddles, sinks, sources) and eigenvalues and eigendirections for the stable and unstable manifolds. The toolkit also computes time series and allows users to construct Poincare maps. The user may also choose a particular integration algorithm.

The program was obtained free of charge by anonymous ftp. The package contained detailed instructions and appropriate Makefiles to enable one to build a working version on their machine in a very short period of time. For someone well versed in dynamical system theory, this toolkit can greatly reduce the routine calculations one previously had to perform and can provide visualization capability with little or no effort.

# PISCITELLE

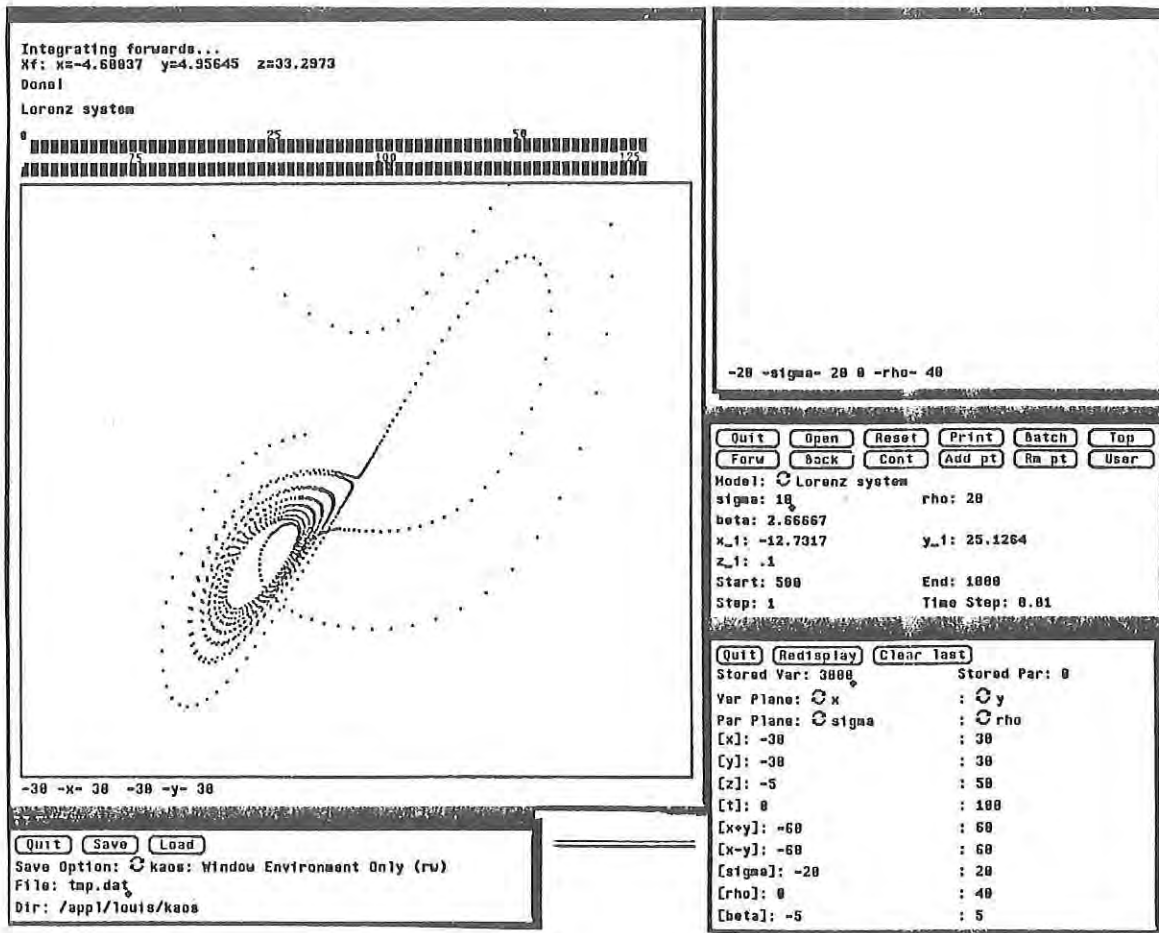


Figure 6. Typical SUN Display of KAOS.

Concluding Remarks

A new nonlinear partial differential equation is derived to model the behavior of a simply supported tube immersed in a viscous fluid flowing parallel to the support axis. The new model extends the linear fluid-structure interaction model used by Holmes, 1977 and Paidoussis, 1966. Using this model, a sequence of low-dimensional models is constructed. Each finite dimensional model is a set of time-dependent nonlinear ODEs.

Analysis of the smallest low dimensional model shows that the extension of the linear fluid-structure interaction model to include nonlinear effects results in a low-dimensional model capable of predicting the dynamics of flutter in a canopy. Previously (see Holmes, 1977), the undeflected shape could be made to become unstable by a suitable choice of parameters. In the model examined in this report, the undeflected shape can also become unstable and may evolve to either a displaced static position or an oscillatory motion about a displaced position, i.e., flutter. This is a new result for a model of such low dimension.

## **PISCITELLE**

### **Recommendations**

The results presented in this report are preliminary. Only the smallest low-dimensional model was examined and it is well known (see Holmes, 1977) that the larger models, which allow modal coupling, can also present interesting behavior, such as flutter. It is therefore recommended that the two-mode and four-mode models be analyzed.

The low-dimensional models were derived using the assumption that the series representation for each variable converged to the true solution sufficiently rapidly for a small number of terms to yield good results. It is recommended that the actual PDE be examined using center manifold theory to produce a low-dimensional model and that it be compared to the set of models produced in this report. The PDE should also be directly integrated for specific parameter values and the results compared with the predictions of the low-dimensional models.

Finally, the value of any model is determined by its ability to predict. Therefore, experimental work should be performed to verify that the qualitative behavior predicted by the model agrees with the behavior observed in the laboratory.

## PISCITELLE

### References

- BISPLINGHOFF, R. L. and H. ASHLEY, 1962. *Principles of Aeroelasticity*, John Wiley and Sons, New York.
- CARR, J., 1981. *Applications of Centre Manifold Theory*, Applied Math. Sci. Vol. 35, Springer-Verlag, New York.
- DOWELL, E. H., 1966. Nonlinear Oscillations of a Fluttering Plate, *AIAA Journal* 4;7:1267-1275.
- 1975. *Aeroelasticity of Plates and Shells*, Leyden: Noordhoff International Publishing.
- 1980. *New Approaches in Nonlinear Problems in Dynamics*, Philadelpha: SIAM. Nonlinear Aeroelasticity.
- GUCKENHEIMER, J. and P. HOLMES, 1983. *Nonlinear Oscillations, Dynamical Systems, and Bifurcations of Vector Fields*, Applied Math. Sci. Vol. 42, Springer-Verlag, New York.
- GUCKENHEIMER, J. and S. KIM, 1990. *Kaos Dynamical System Toolkit with Interactive Graphics Interface*, DRAFT Report, Math. Dept., Cornell Univ., Ithaca, New York.
- HEINRICH, H. G. and L. R. JAMISON, 1966. Parachute Stress Analysis During Inflation and at Steady State, *J. Aircraft* 3;1: 52-58.
- HENRY, D., 1981. *Geometric Theory of Semilinear Parabolic Equations*, Springer Lecture Notes in Math., No. 840, Springer-Verlag, New York.
- HOLMES, P., 1977. Bifurcations to Divergence and Flutter in Flow-Induced Oscillations: A Finite Dimensional Analysis, *J. Sound Vib.* 53;4:471-503.
- HOLMES, P. and J. MARSDEN, 1983. Bifurcation to Divergence and Flutter in Flow Induced Oscillations; an Infinite Dimensional Analysis, *Automatica* 14:367-384.
- HOLMES, P. and D. A. RAND, 1976. Identification of Vibrating Systems by Generic Modelling, With an Application to Flutter, *Inst. of Sound and Vib. Research Technical Report No. 79*.
- LIGHTHILL, M. J., 1960. Note on the Swimming of Slender Fish, *J. Fluid Mech.* 9:305-317.
- LUDTKE, W. P., 1986. Notes on a Generic Parachute Opening Force Analysis, Naval Surface Weapons Center Technical Report NSWC TR 86-142.
- MARSDEN, J. and T. HUGHES, 1983. *Mathematical Foundations of Elasticity*, Prentice-Hall, Inc., Englewood Cliffs, NJ.



## PISCITELLE

MARSDEN, J. and M. McCracken, 1976. *The Hopf Bifurcation and Its Applications*, Applied Math. Sci. Vol. 19, Springer-Verlag, New York.

PAIDOUSSIS, M. P., 1966. Dynamics of Flexible Slender Cylinders in Axial Flow: I-Theory, *J. Fluid Mech.* 26: 717-736.

PAIDOUSSIS, M. P. and N. T. Issid, 1974. Dynamic Stability of Pipes Conveying Fluid, *J. Sound Vib.* 33: 267-294.

PURVIS, J. W., 1982. Theoretical Analysis of Parachute Inflation Including Fluid Kinetics, *J. Aircraft* 19;4: 290-296.

REDDY, K. R., 1974. Unsteady Vortex Flow Past an Inflating, Decelerating Wedge, *J. Aircraft* 11;7: 427-429.

REISS, E. L., 1969. in *Bifurcation Theory and Non-Linear Eigenvalue Problems* (J. B. Keller and S. Antman, Editors), Column buckling--an elementary example of bifurcation. New York: Benjamin.

ROSS, E. W., 1970. Approximate Analysis of a Flat, Circular Parachute in Steady Descent, *J. Aircraft* 27;3: 266-271.

----- 1971. A General Theory of Parachute Opening, U.S. Army Natick RD&E Center Technical Report TR-71-32-OSD.

STEEVES, E. C., 1986. Analysis of Decelerators Behavior Using Computational Fluid Dynamics, *Proc. AIAA 10th Aerodynamic Decelerator and Balloon Tech. Conf.*, Albuquerque, NM.

----- 1989. Analysis of Decelerators in Motion Using Computational Fluid Dynamics, *Proc. AIAA 10th Aerodynamic Decelerator and Balloon Tech. Conf.*, Cocoa Beach, FL.

TAYLOR, G. I., 1952. *Proc. Roy. Soc. A*;214: 158.

THOMPSON, J. M. T. and T. S. LUNN, 1981. Static Elastica Formulations of a Pipe Conveying Fluid, *J. Sound Vib.* 77:127-132.

THOMPSON, J. M. T. and H. B. STEWART, 1986. *Nonlinear Dynamics and Chaos*, John Wiley and Sons, New York.



STEIN

TITLE: An Investigation of Parachute Aerodynamic Characteristics Using  
Computational Fluid Dynamics  
Keith R. Stein, Mr.

ABSTRACT: In parachute research, the transient canopy inflation process is a difficult and important problem. The complexity of this process arises largely from the fact that the flow field is dependent on the canopy shape, which is itself dependent on the flow field. The state of the art is presently incapable of adequately modeling the pressure and stress distributions on a canopy during the opening process. Thus, there is a need to improve our present capability in predicting parachute behavior computationally.

Obtaining solutions to the governing equations of fluid dynamics is a great challenge. The governing equations, or Navier-Stokes equations, consist of a set of nonlinear, partial differential equations which must be solved in time and space. Until recent years, solving the complete Navier-Stokes equations for complex fluid dynamics problems was impossible. For this reason, parachute aerodynamics has been a science that has been predominantly experimental in nature. However, experimental fluid dynamics cannot provide information about an entire flow field. Instead, experimental fluid dynamics focuses on a small portion of the flow field. For this reason alone, the solution of the complete Navier-Stokes equations for the flow field about an aerodynamic decelerator would be very valuable.

Advances in computers and computational methods have made the use of computational fluid dynamics (CFD) possible for more complex fluid dynamics problems. These computations provide information about the entire flow field (i.e., pressure distributions, velocities, etc.) about a decelerator. This paper will present results from a study on the behavior of aerodynamic decelerators using CFD. First, the effect of the vent size on the performance of a fully inflated annular decelerator were investigated and will be presented. Secondly, predicted time-variant behavior for deforming aerodynamic decelerators will be presented. With continued advances in computers and computational methods, the next step is to model computationally the inflation process for an entire parachute system.

BIOGRAPHY OF PRESENTER: Keith R. Stein

PRESENT ASSIGNMENT: Aerospace Engineer, Engineering Technology Division,  
Aero-Mechanical Engineering Directorate, U.S. Army Natick RD&E Center

DEGREES HELD: B.A. in Physics, Bethel College, St. Paul, Minnesota. M.S. in  
Aerospace Engineering, University of Minnesota.

An Investigation of Parachute Aerodynamic Characteristics  
Using Computational Fluid Dynamics

Keith R. Stein

U.S. Army Natick Research, Development and Engineering Center  
Natick, MA 01760-5017

INTRODUCTION

The United States Army requires future airdrop systems to operate at lower altitudes and higher speeds than those of current parachutes. In order to meet these requirements, it is necessary to understand details about the pressure and velocity fields that are difficult to obtain through empirical approaches. Advances in recent years in computers and computational methods have made the use of computational fluid dynamics (CFD) for parachutes possible for these detailed flow field studies.

Obtaining solutions to the governing equations of fluid dynamics is a great challenge. The governing equations, or Navier-Stokes equations, consist of a set of nonlinear, partial differential equations which must be solved in time and space. Until recent years, solving the complete Navier-Stokes equations for complex fluid dynamics problems was impossible. For this reason, parachute aerodynamics has been a science that has been predominantly experimental in nature. However, experimental fluid dynamics cannot provide information about an entire flow field. Instead, experimental fluid dynamics focuses on a small portion of the flow field. For this reason alone, the solution of the complete Navier-Stokes equations for the flow field about an aerodynamic decelerator would be very valuable.

Advances in computers and computational methods have made the use of computational fluid dynamics (CFD) possible for more complex fluid dynamics problems. These computations provide information about the entire flow field (i.e., pressure distributions, velocities, etc.) about a decelerator. This paper will present results from a study on the behavior of aerodynamic decelerators using CFD. First, the effect of the vent size on the performance of a fully inflated annular decelerator was investigated and will be presented along with related experimental data from a recent wind tunnel test. Secondly, predicted time-variant behavior for deforming aerodynamic decelerators will be presented.

STEIN

## APPROACH

### Annular Decelerator Flow Behavior

Initial research at the U.S. Army Natick Research, Development and Engineering Center using CFD to study the aerodynamic characteristics of decelerators was conducted by Dr. Steeves at the Engineering Technology Division of the Aero-Mechanical Engineering Directorate (AMED/ETD). Steeves adapted the "SALE" CFD code, from Los Alamos National Laboratory, to solve the flow characteristics for desired decelerator shapes [1,2,3]. The efforts of Steeves laid the groundwork for a study on annular parachutes using CFD [4].

The annular parachute is known for its high drag performance and is characterized by the large vent in its center. The drag coefficient for annular parachutes based on the canopy surface area is the highest of all known parachutes [5]. It is this drag efficiency for annular parachutes that was the motivation for a study to determine the shape of annular decelerators for optimum drag performance.

### Wind Tunnel Tests of Annular Decelerator

Although CFD computations have been made for various annular decelerators, until recently data did not exist on annular decelerators that could verify or refute the computational results. In September of 1991, experiments were conducted at a U.S. Army Aviation Systems Command (AVSCOM) wind tunnel at the NASA Ames Research Center in order to obtain data on annular decelerators, which would be used to measure the accuracy of the CFD predictions.

The wind tunnel model was a rigid and axisymmetric annular decelerator that was 20 inches in diameter. The model was constructed out of plastic from a mold and several models of identical geometries were fabricated to meet different test needs. One model was instrumented with a row of differential pressure sensors in order to get experimental data on the pressure distribution. This model was supported in the wind tunnel by a force balance, which allowed measurements of the drag experienced by the decelerator. A second model was uninstrumented and was used to gain information on the velocity flow field by utilizing experimental flow visualization techniques. The information obtained in the pressure and drag experiments was quantitative in nature, whereas the velocity information was more qualitative. However, the information obtained in both experiments developed a new level of confidence in the CFD predictions, which allowed the work to progress to the more difficult modeling of the opening problem.



## STEIN

### Deforming Decelerators

The time-variant aerodynamic characteristics associated with the opening of a parachute are extremely complex to model. The complexity of the process arises largely from the fact that the flow field is dependent on the canopy shape, which is itself dependent on the flow field. Thus, in order to predict accurately opening behavior, the equations defining fluid and structural behavior cannot be modeled independently but must be coupled together. Dr. Steeves is leading an effort to couple the fluid-structure interaction during the opening process. In addition to the work of Steeves, additional efforts are in progress to model the structural and fluid properties independently. Richard Benney of AMED/ETD is conducting research on the structural behavior of parachutes in order to model opening characteristics associated with defined pressures. Also, an effort is underway to model the aerodynamic characteristics associated with defined openings. Initial results on the CFD modeling of deforming decelerators will be presented.

### SALE CFD CODE

The SALE (Simplified Arbitrary Lagrangian-Eulerian) FORTRAN code, developed at Los Alamos National Laboratories, is being adapted to solve the Navier-Stokes equations about aerodynamic decelerator shapes [3]. SALE uses a finite difference algorithm to solve the time-dependent two-dimensional Navier-Stokes equation and the mass and internal energy equations. The fluid pressure is determined from an equation of state. It should be noted that velocities are defined at the nodes of the computational grid, whereas pressures are defined at cell centers. The finite difference algorithm of SALE allows the use of nonuniform computational grids, made up of quadrilateral cells, allowing the grid to be deformed to treat the curved surfaces of the decelerator. SALE also has the option of solving the nonlinear Navier-Stokes equations for two-dimensional planar or axisymmetric coordinates. SALE uses the arbitrary Lagrangian-Eulerian (ALE) grid rezoning method, which allows the grid to be adjusted with time. This rezoning method can be useful for solving flows about decelerators in motion or for inflation problems.

### Governing Equations

The problems reported assumed an axisymmetric computational domain and incompressible flow. The Navier-Stokes equations are solved in time ( $t$ ) and in the cylindrical coordinate space ( $r, z$ ). The primary variables are the radial velocity component ( $v_r$ ), the axial velocity component ( $v_z$ ), pressure ( $p$ ), and internal energy ( $I$ ). Additional terms in the Navier-Stokes equations are the fluid density ( $\rho$ ) and the fluid viscosity ( $\mu$ ). The equations are reduced to the following form:



## STEIN

### Conservation of Momentum-

$$\rho \left( \frac{\partial v_r}{\partial t} + v_r \frac{\partial v_r}{\partial r} + v_z \frac{\partial v_r}{\partial z} \right) = -\frac{\partial p}{\partial r} + \mu \left[ \frac{\partial}{\partial r} \left( \frac{1}{r} \frac{\partial}{\partial r} (r v_r) \right) + \frac{\partial^2 v_r}{\partial z^2} \right] \quad (1)$$

$$\rho \left( \frac{\partial v_z}{\partial t} + v_r \frac{\partial v_z}{\partial r} + v_z \frac{\partial v_z}{\partial z} \right) = -\frac{\partial p}{\partial z} + \mu \left[ \frac{1}{r} \frac{\partial}{\partial r} \left( r \frac{\partial v_z}{\partial r} \right) + \frac{\partial^2 v_z}{\partial z^2} \right] \quad (2)$$

### Conservation of Mass-

$$\frac{\partial r v_r}{\partial r} + r \frac{\partial v_z}{\partial z} = 0 \quad (3)$$

### Conservation of Energy-

$$\rho \left( \frac{\partial I}{\partial t} + v_r \frac{\partial I}{\partial r} + v_z \frac{\partial I}{\partial z} \right) = \mu \left[ 2 \left( \frac{\partial v_r}{\partial r} \right)^2 + \left( \frac{\partial v_r}{\partial z} + \frac{\partial v_z}{\partial r} \right)^2 + 2 \frac{v_r^2}{r^2} + 2 \left( \frac{\partial v_z}{\partial z} \right)^2 \right] \quad (4)$$

### Initial and Boundary Conditions

For the problems addressed, the flow fields are solved from an Eulerian viewpoint and thus the decelerators are fixed in space. The decelerator is assumed to have a nonporous, no-slip surface. Thus, the decelerator surface is defined by a single row of grid points with no fluid velocities at the surface (Figure 2). The flow field is impulsively started at time  $t=0$ . This instantaneously started flow is modeled by initially defining the surface velocities to be zero and all other nodal velocities to be  $V_\infty$ , where  $V_\infty$  is the free-stream velocity entering the computational grid. The Navier-Stokes equations are solved in time. After each time step the boundary conditions are imposed for the decelerator surface as well as for the outer boundaries of the computational grid. Surface velocities are set to zero. Boundary conditions for the four outer boundaries of the computational grid must also be imposed. For an axisymmetric flow, the normal component of velocity along the centerline must be set to zero. For the outer boundary parallel to the flow, a free-slip boundary condition is imposed by setting the normal components of velocity to zero. The velocity at the inflow boundary is set to  $V_\infty$  and the outflow velocity is scaled in order to satisfy conservation of mass within the computational domain.

### Drag Coefficient

Drag is not computed directly from the Navier-Stokes equations, but is determined by

## STEIN

integrating the pressure and viscous forces over the decelerator surface. In the problems addressed, computations indicate that the viscous contributions to the overall drag are negligible when compared to the pressure contributions. Thus, the overall drag can be defined as follows:

$$D = \sum_{i=1}^{n-1} (p_{i, \text{lower}} - p_{i, \text{upper}}) \Delta A_i \quad (5)$$

where

- $n$  = Number of nodes defining the decelerator surface
- $p_i$  = Pressures on the upper and lower surfaces between nodes  $i$  and  $i+1$
- $\Delta A_i = \pi(x_{i+1}^2 - x_i^2)$
- $x_i$  = x-coordinate value for node  $i$

The drag coefficient ( $C_D$ ) is a measure of the drag efficiency of the decelerator and is defined as follows:

$$C_D = \frac{2D}{\rho V_\infty^2 S} \quad (6)$$

where

- $\rho$  = fluid density
- $S$  = projected area of decelerator ( $\pi R_{\text{outer}}^2$ )

It should be noted that the defined drag coefficient is based on the overall drag. Thus, during transient behavior, the drag coefficient has an added mass term which is related to an additional force experienced by the decelerator due to the acceleration of surrounding air. The defined drag coefficient reduces to the steady-state drag coefficient after the flow becomes fully developed [6].

## RESULTS

### Annular Decelerator

Experimental data of Hoerner have demonstrated that a circular disk does not lose significant drag upon adding a small hole to its center [7]. Experimental data obtained at a Reynolds number of  $10^5$  indicate that it is only after the radius of the vent exceeds 25 percent of the outer radius that drag begins to decrease noticeably (Figure 1). This behavior for the vented disk is a good indication that annular decelerators would be efficient in drag performance. CFD computations indicate that there is a non-zero, optimum drag value for the vent size of an annular decelerator with cambered cross sections.

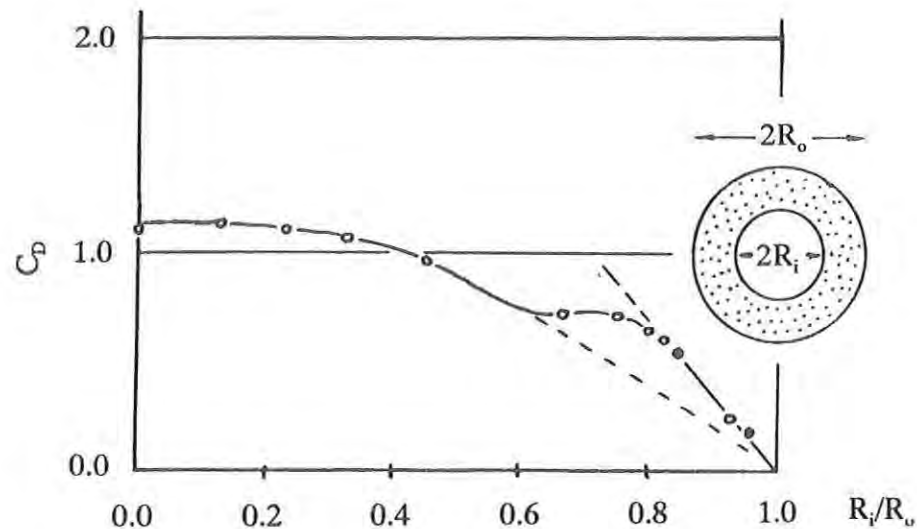


Figure 1: Drag Coefficient of Vented Disks at a Reynolds Number of  $10^5$  as Reported in Reference 7.

In order to investigate the influence of the vent size on the drag performance of an annular decelerator a series of CFD computations were made on a specific annular cross section with various vent sizes. The Reynolds number based on the width of the decelerator cross section ( $R = \rho V_\infty W / \mu$ ) was equal to  $10^5$  for all calculations. Figure 2 shows the computational grid for the case in which the vent radius is 50 percent of the outer radius ( $R_i/R_o = 0.5$ ). Computed velocity and pressure flow fields are shown in Figure 3. Values for the drag coefficient were determined for  $R_i/R_o = 0.0$  to  $R_i/R_o = 0.64$  and are shown in Figure 4. Computational results predicted optimum drag performance when  $R_i/R_o = 0.25$ .

#### Wind Tunnel

The objective of the wind tunnel testing conducted at the NASA Ames Research Center on the annular decelerator model was to obtain data which could be used to measure the accuracy of CFD predictions in AMED/ETD using the SALE code. The testing was divided into two parts. First, experiments were conducted in order to obtain data on the differential pressure distribution and on the total drag experienced by the decelerator model over airspeeds ranging from 0-150 ft/s. The setup for the pressure and drag tests is shown in Figure 5. Three pressure sensors were damaged beyond repair and thus the pressure distribution was limited to the four functioning sensors. The experimental pressure data for an airspeed of 150 ft/s and the CFD predicted pressure distribution are shown in Figure 6. The measured differential pressures compared favorably with predicted values. Drag data

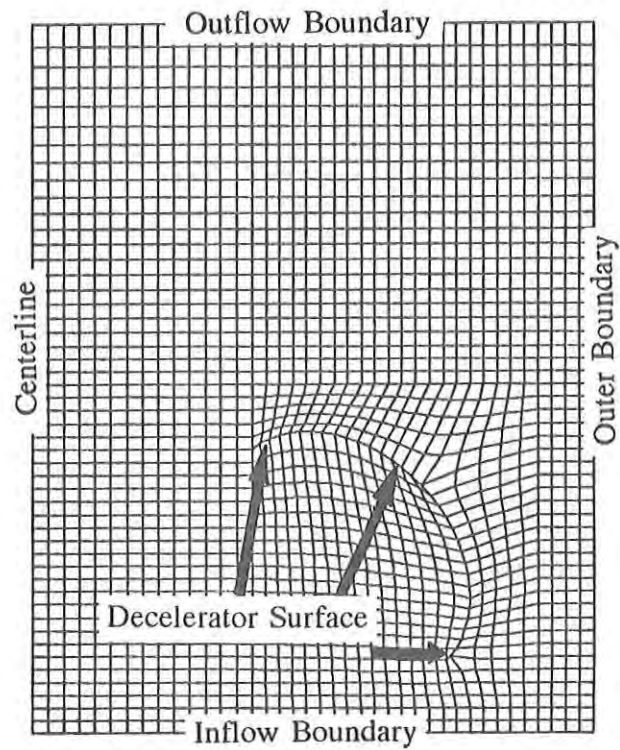


Figure 2: CFD Grid for Annular Decelerator with  $R_i/R_o=0.5$

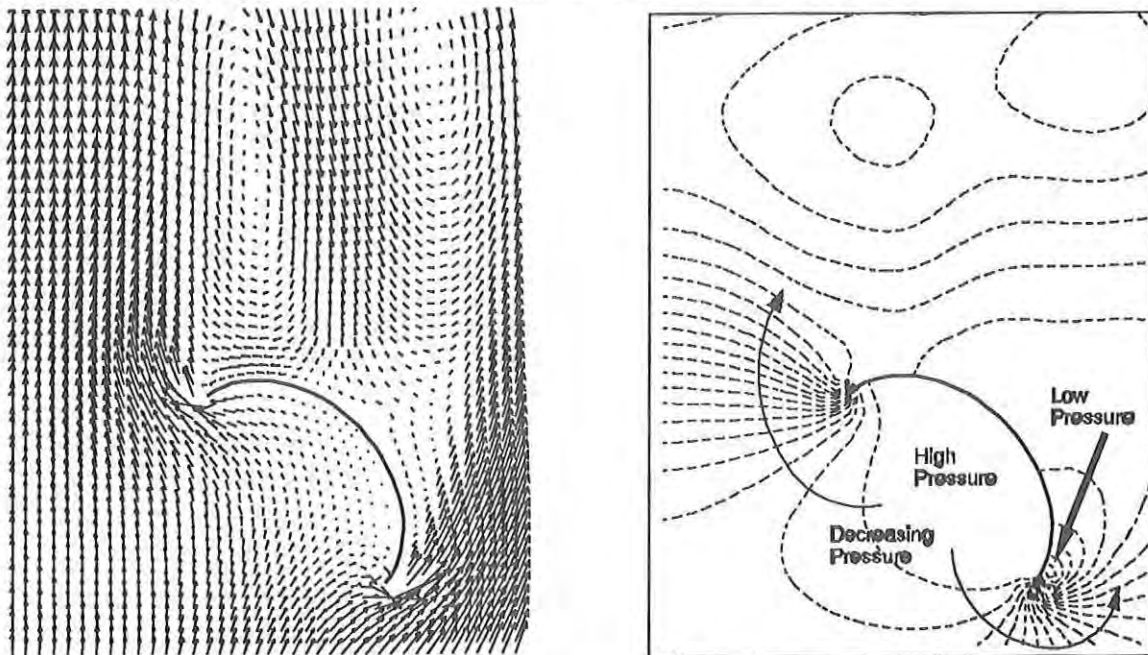


Figure 3: Predicted Velocity and Pressure Fields for Annular Decelerator with  $R_i/R_o=0.5$  at a Reynolds Number of  $10^5$

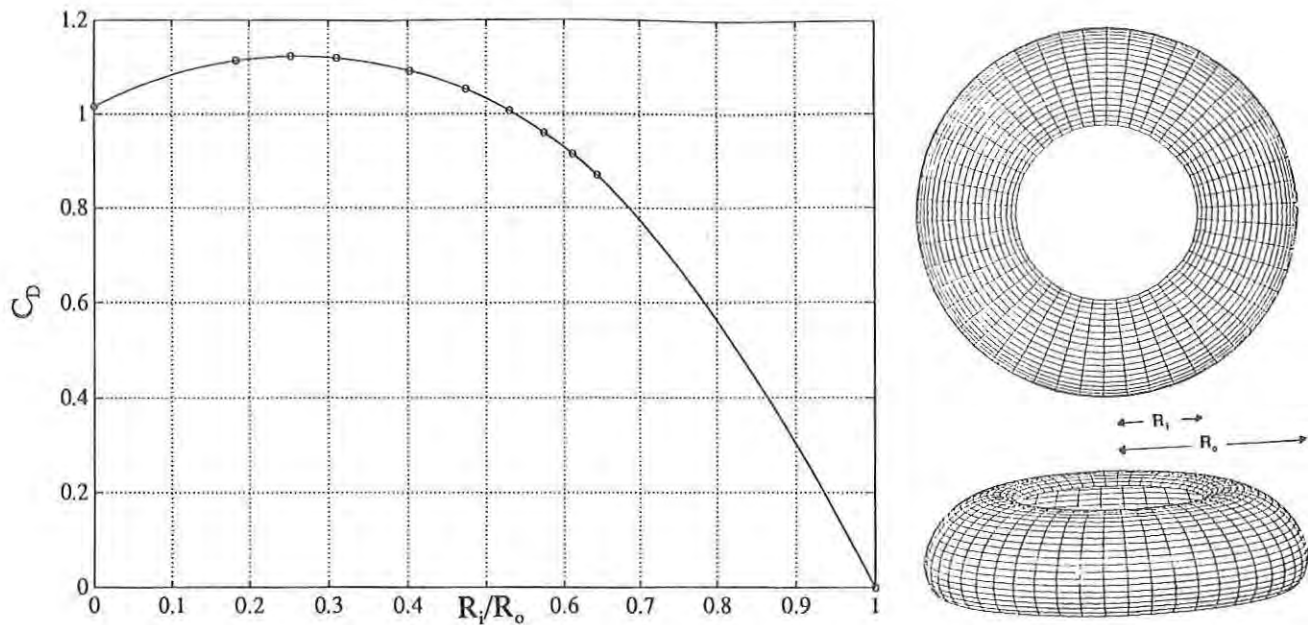


Figure 4: Influence of the Vent Size of an Annular Decelerator on Drag Performance (Reynolds Number =  $10^5$ )

were obtained from direct measurements from a balance which supported the model in the tunnel. In addition to the balance data, drag information was obtained by assuming a linear pressure distribution and then fitting the pressure data to the assumed linear distribution. Drag coefficients were determined from both the balance data and the pressure sensor data and are compared with the CFD predicted drag coefficient in Figure 7 (CFD  $\rightarrow C_D = 0.97$ ). The discrepancy between the drag coefficient from the force balance and from the assumed pressure distribution is roughly 3-5 percent over most of the range of airspeeds. This is most likely attributed to errors due to the assumed linear pressure distribution. At the lower airspeeds, the difference in the two drag coefficients is much larger. The majority of the deviation probably results from difficulties in maintaining steady and accurate tunnel airspeeds at the low speeds. Also, the zero readings for the force balance and pressure sensors would have larger contributions to the total error at the low airspeeds.

The second part of the wind tunnel testing consisted of flow visualization, which provided qualitative information on the characteristics of the velocity flow field about the annular decelerator model. The airflow patterns about the annular decelerator were visualized using a Class IV argon laser and theatrical smoke. The smoke was released from the wind tunnel settling chamber so that it flowed over the decelerator model. The laser beam was swept at a high frequency within a desired plane surrounding the model. Thus, only the flow behavior in the plane of the laser light sheet was visualized. Information was obtained about





Figure 5: Wind Tunnel Test Setup Used to Obtain Pressure and Drag Data

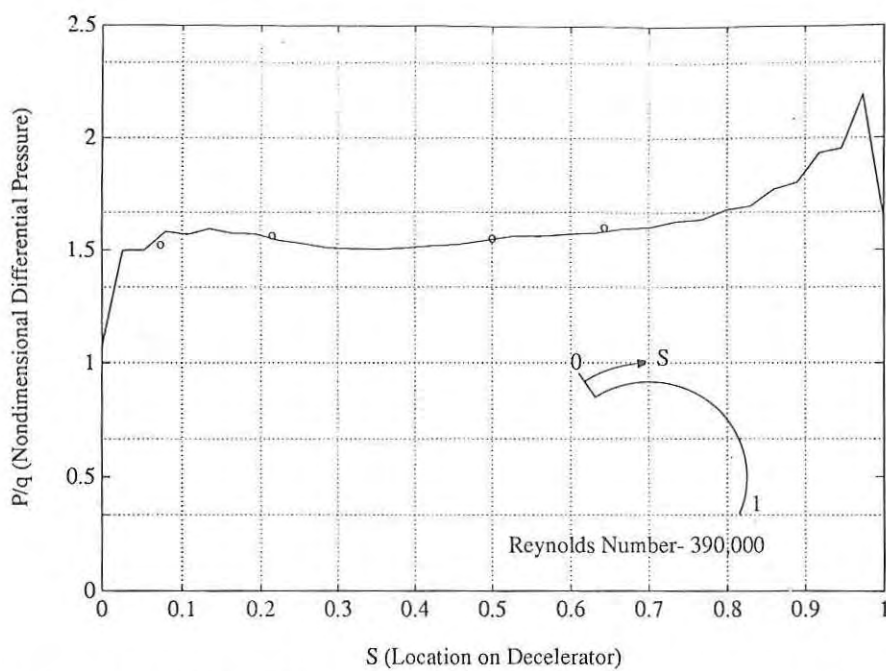


Figure 6: CFD and Experimental Differential Pressure Distribution on the Annular Decelerator Model



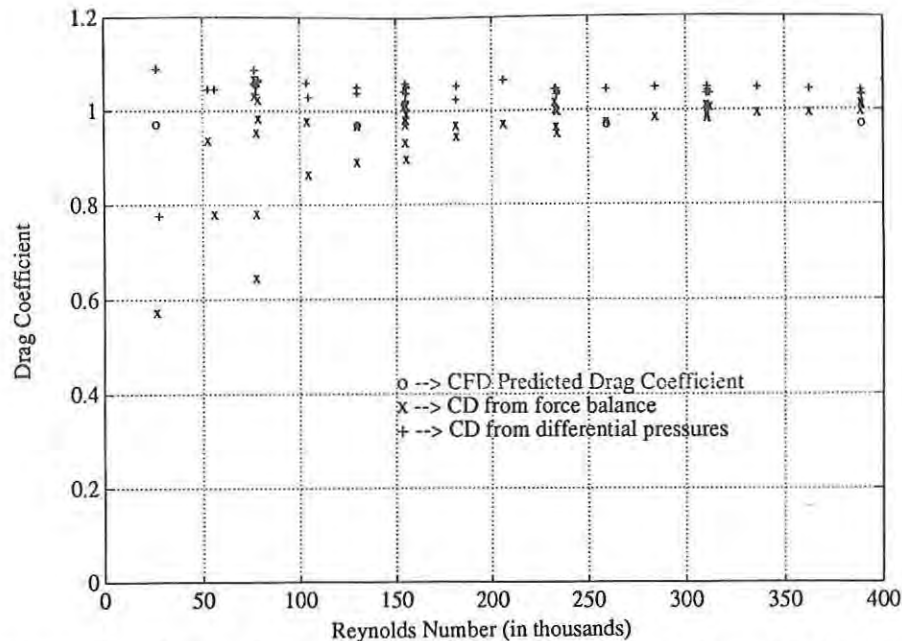


Figure 7: Comparison of Experimental and CFD Values for the Drag Coefficient of the Annular Decelerator over a Range of Reynolds Numbers

the wake size and flow patterns associated with the decelerator model at a Reynolds number ranging from 26,000 to 130,000 (10-50 ft/s). Flow visualization information was obtained on videotape in various planes surrounding the annular decelerator model. Figures 8a and 8b are a comparison between the experimental flow field and the computational flow field for the plane that bisects the annular decelerator.

#### Deforming Decelerators

In order to model the fluid-structure interaction associated with the parachute opening problem, several complexities must be addressed. One complexity connected to the opening problem is the CFD modeling of the flow around decelerators that deform with time. The manner in which the decelerator deforms must be physically realistic. This is required because the specified opening behavior is not determined by the flow behavior but is specified, and thus the nodes defining the decelerator surface are forced to move unnaturally with respect to time. The conservation of momentum equations (1-2) contain time derivatives of the velocity components, or second derivatives with respect to position. Thus, Navier-Stokes solutions for any opening curve with nodal accelerations ( $d^2r/dt^2$  and  $d^2z/dt^2$ ) that are not continuous will result in drag histories that are not continuous. In order to obtain drag histories that are continuous and smooth, the opening curve must be continuous to the third time derivative. Decelerator shapes that deform in some arbitrary way result in flow

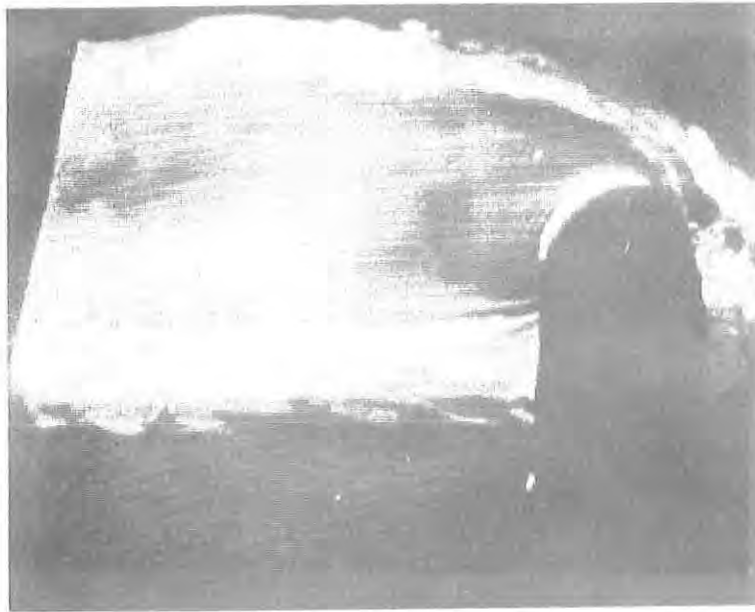


Figure 8a: Experimental Visualization of the Velocity Flow Field in the Plane Bisecting the Annular Decelerator Model at a Reynolds Number of 130,000

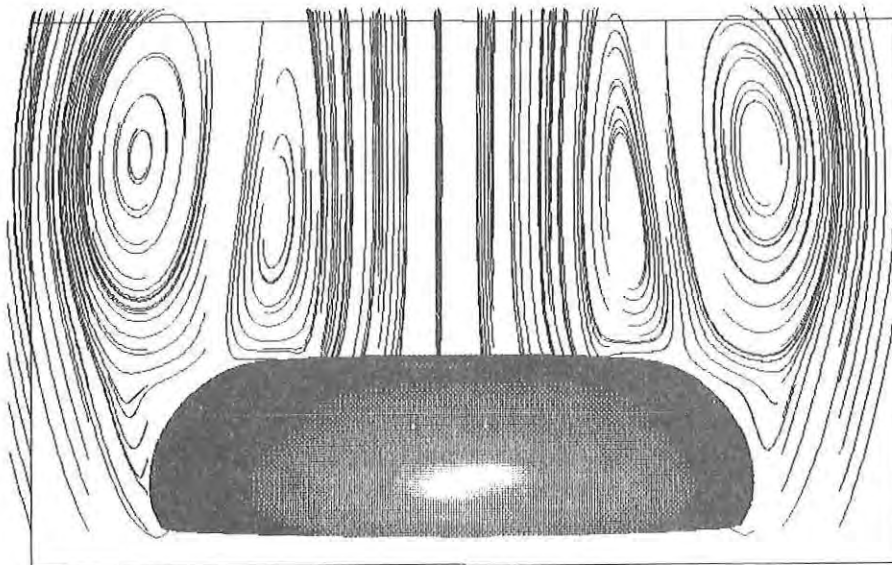


Figure 8b: Visualization of CFD Velocity Field in the Plane Bisecting the Annular Decelerator at a Reynolds Number of 130,000

characteristics and drag histories which are nonphysical. A set of computations was made for a ellipsoid-shaped decelerator that was deformed with three different degrees of smoothness. Figure 9 shows the time curves for the position of the node defining the outer radius of the decelerator and for the drag coefficient. The curves demonstrate that the predicted drag history will not be smooth unless the third derivative of the nodal positions is also smooth.

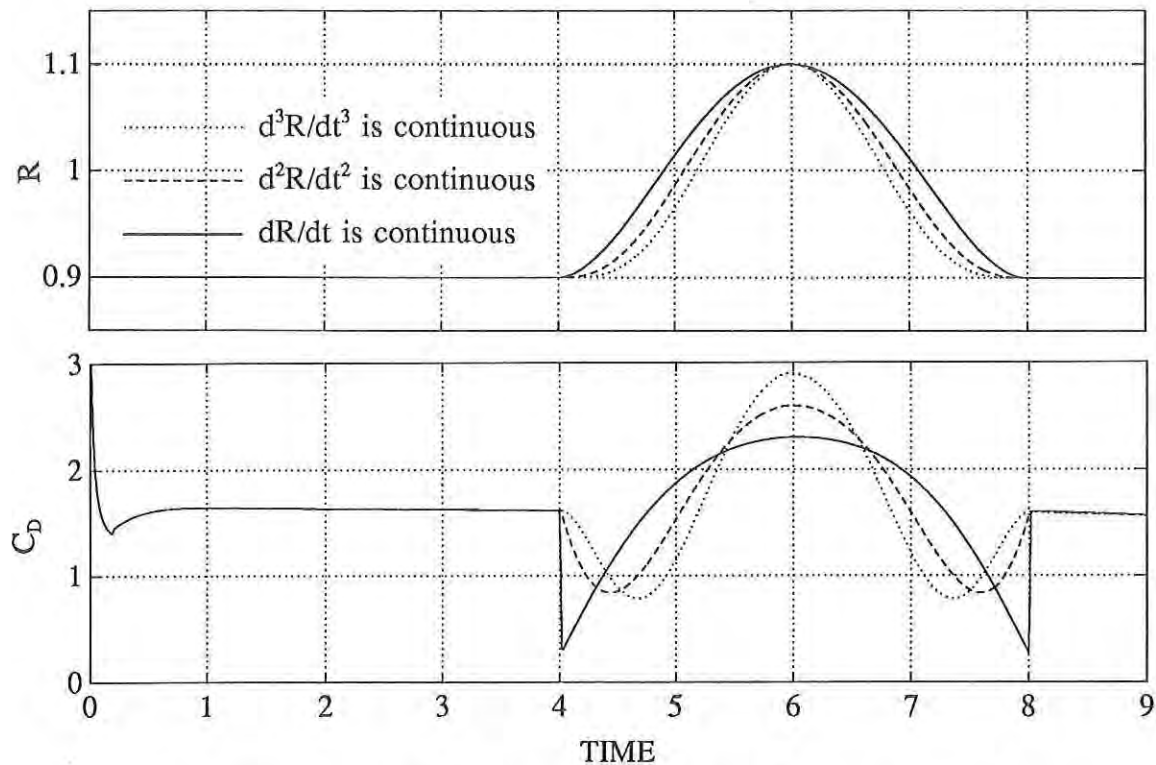


Figure 9: Position of the Outermost Node for Various Opening Curves and the Associated Drag History

A second case was investigated using an opening model developed by Berndt and DeWeese [8]. Initial and final decelerator shapes were established from the stated model and the projected diameter of the decelerator was allowed to grow 37 percent during the opening process. Each decelerator surface node moved from initial to final position by a hyperbolic tangent (tanh) curve. Properties of the tanh curve allowed the opening to be smooth to all derivatives and also allowed the vast majority of the opening to occur over any desired time period. Drag histories for three different opening rates were computed. Figure 10 shows the initial and final decelerator shape, the opening curves for the outermost node, and the associated drag histories for each case.

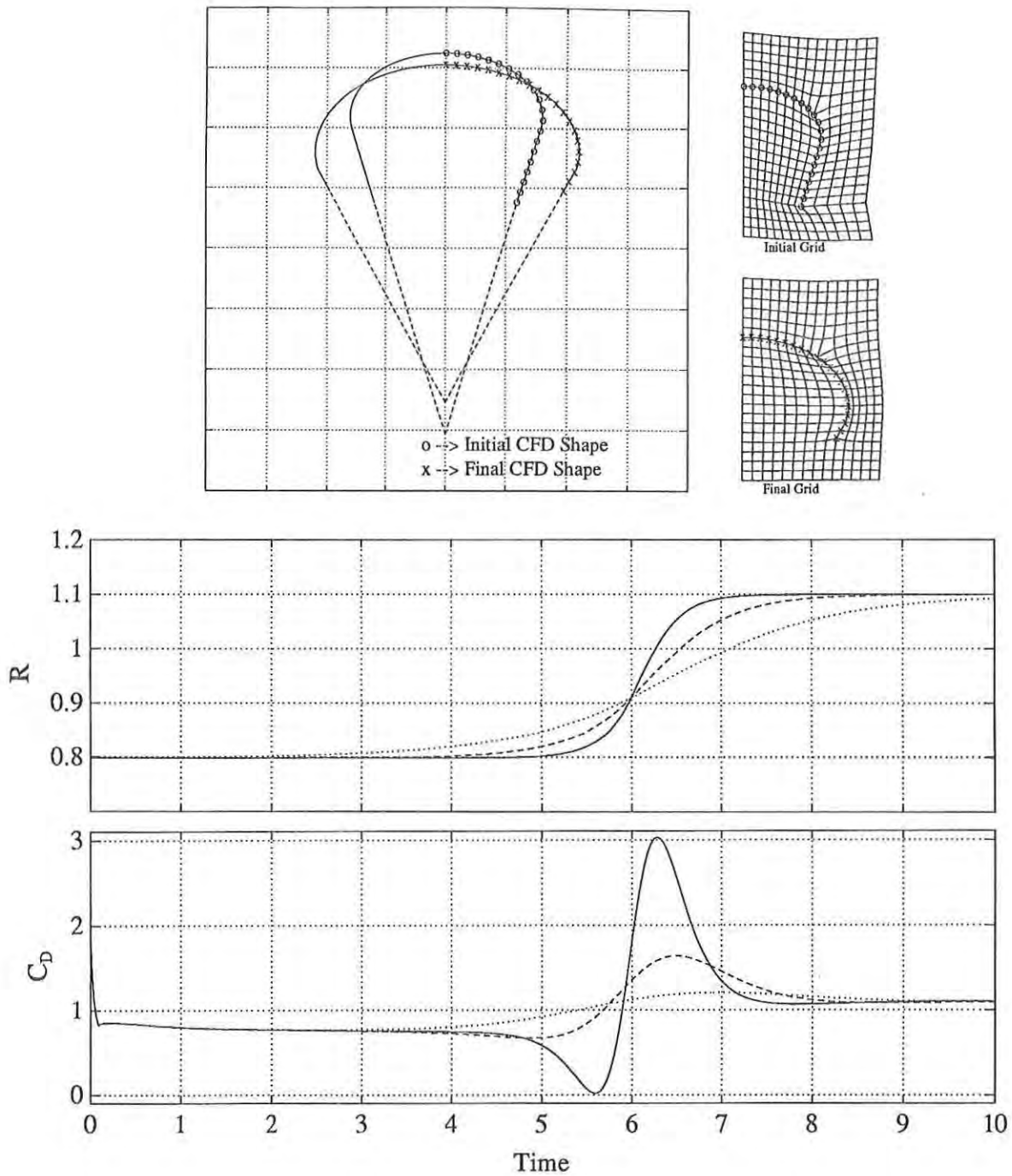


Figure 10: Initial and Final Shape for Deforming Decelerator using the Berndt and DeWeese Opening Model (reference 7) and Position of Outermost Node for Various Opening Rates and Associated Drag Histories

STEIN

## CONCLUSIONS AND FUTURE EFFORTS

CFD modeling for decelerator problems at the U.S. Army Natick Research, Development, and Engineering Center has progressed from steady-state modeling to modeling opening behavior. Predicted steady-state flow characteristics for annular decelerators have been presented and compared with wind tunnel data. Comparisons between predicted and experimental flow characteristics are encouraging and increase the level of confidence in the CFD model.

Initial efforts in modeling the flow properties about deforming decelerator shapes have been presented. The work presented is a step towards modeling the opening problem. In reality, an opening parachute has much larger deformations than the deformations that were presented and is free-falling in space. More importantly, a true opening has a coupling between the fluid behavior of air and the structural behavior of the canopy. Several of the complexities in modeling the opening problem are currently being addressed. With continued progress in computers and computational methods, it should be possible in the future to model computationally the behaviors associated with the parachute opening process.

## REFERENCES

1. Steeves, Earl C. "Prediction of Decelerator Behavior Using Computational Fluid Dynamics." *Proceedings of AIAA 9th Aerodynamic Decelerator and Balloon Technology Conference*. Albuquerque, NM. October 7-9, 1986.
2. Steeves, Earl C. "Analysis of Decelerators in Motion Using Computational Fluid Dynamics." *Proceedings of AIAA 10th Aerodynamic Decelerator and Balloon Technology Conference*. Cocoa Beach, FL. April 18-20. 1989.
3. Amsden, A.A., Ruppel, H.M., and Hirt, C.V. "SALE: A Simplified ALE Computer Program for Fluid Flow at All Speeds." Los Alamos Scientific Laboratory Report No. LA-8095. 1980.
4. Stein, Keith. "Computations of the Flow Characteristics of Aerodynamic Decelerators Using Computational Fluid Dynamics." *Proceedings of AIAA 11th Aerodynamic Decelerator Systems Technology Conference*. San Diego, CA. April 9-11, 1991.
5. Knacke, Theo W. "Parachute Recovery Systems Design Manual." Naval Weapons Center Technical Report No. NWC-TP-6575. China Lake. 1991.

## STEIN

6. Sarpkaya, Turgut. "Methods of Analysis for Flow Around Parachute Canopies." *Proceedings of AIAA 11th Aerodynamic Decelerator Systems Technology Conference*. San Diego, CA. April 9-11, 1991.
7. Hoerner, Sighard F. *Fluid Dynamic Drag*. Published by the author, 1965.
8. Berndt, R.J. and DeWeese, J.H. "Filling Time Prediction Approach for Solid Cloth Type Parachute Canopies." *Proceedings of AIAA Aerodynamic Deceleration Systems Conference*. Houston, TX. September 1966.



FOSSEY, et al.

TITLE: Molecular Modeling Studies on Silk Peptides  
Stephen A. Fossey, Mr., George Nemethy, Dr., Kenneth Gibson,  
Dr., David L. Kaplan, Dr., Harold Scheraga, Dr.

ABSTRACT: Computational energy calculations on model polypeptide sequences of the crystalline domains of Bombyx mori (silkworm) silk are presented. The morphologies of the two crystalline forms of silk, known as silk I and silk II, were investigated. The structure of silk II has been well understood since the 1950s. Silk I has remained poorly understood because it is a metastable state and readily converts to the silk II form. As a result of these calculations, a new model for the silk I form has been proposed. The geometry and energetics of the silk I/silk II transition have also been investigated. The detailed molecular model will provide a basis for understanding fiber and film formation and properties of silk polymers.

BIOGRAPHY OF PRESENTER: Stephen A. Fossey  
PRESENT ASSIGNMENT: Materials Research Engineer, Biotechnology  
Division, Soldier Science Directorate, US Army Natick Research,  
Development and Engineering Center, Natick, MA 01760-5020  
DEGREES HELD: MS, BS Chemical Engineering, University of Lowell

FOSSEY, et al.

Molecular Modeling Studies on Silk Peptides  
Stephen A. Fossey, Mr., George Nemethy\*, Dr.,  
Kenneth D. Gibson\*, Dr., David L. Kaplan, Dr.,  
and Harold A. Scheraga\*, Dr.

U.S. Army Natick Research, Development and Engineering Center  
Kansas Street, Natick, Massachusetts 01760-5020

\*Baker Laboratory of Chemistry, Cornell University,  
Ithaca, New York 14853-1301

## INTRODUCTION

Silk-like proteins are being considered for such uses as high-performance fibers<sup>1</sup> and enzyme-immobilizing substrates.<sup>2</sup> Knowledge of the structure of silk (in particular, the metastable silk I form) is critical for understanding the formation and processing of such materials. There is evidence to suggest the silk I chain conformation is the same as that of the liquid crystal state<sup>3,4</sup> and the average chain conformation in the noncrystalline domains. We present here the results of conformational energy computations to establish structural models for silk. Conformational energy calculations provide a very useful tool for the detailed modeling of the structures of fibrous proteins.<sup>5</sup> Conformational energy calculations on representative model polypeptides have been used successfully to elucidate the structure of collagen.<sup>5,6</sup>

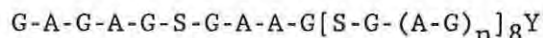
There is an extensive literature on the chemical composition, morphology, and physical properties of silk, excellent reviews of which can be found in Refs. 7 and 8. Because of the presumed prevalence of beta sheets in silk, and because they are an important structural motif in globular proteins<sup>9</sup> and at the interfaces of oligomeric proteins<sup>10</sup> the structure and packing of beta sheets are relevant to study of silk fibroin.

Silk fibroin is a block copolypeptide of crystalline domains characterized by a Gly-X repeat where X is Ala or Ser, and of less crystalline domains in which the Gly-X repeat is common but which contains a higher fraction of residues with large side chains.<sup>7</sup> The crystalline domains of *B. mori* can exist in one of two different morphologies. The more stable one is known as silk II.<sup>11,12</sup> A detailed structural model for silk II was first proposed by Marsh et al.<sup>13</sup> and refined by Fraser et al.<sup>14,15</sup> Its basic feature, a packing of antiparallel, beta-pleated sheets, is generally accepted.<sup>16</sup> A parallel-chain model for silk II was proposed by Lim and Steinberg<sup>16</sup> based on molecular model construction,

but they did not present a quantitative comparison of the model with experimental data. The less stable form, silk<sup>7,11</sup> however, has remained poorly understood. Attempts to induce orientation of its polymer chains for studies by x-ray or electron diffraction tend to cause the silk I form to convert to the more stable silk II form. Silk I can be obtained by letting the contents of the silk gland dry undisturbed.<sup>14</sup> If the contents of the gland are mechanically sheared or rolled, as in spinning, the silk II form is obtained.<sup>14</sup>

Experimental studies of silk I have consisted primarily of powder x-ray diffraction<sup>11,12,17,18</sup> electron diffraction<sup>17</sup>, and solid state <sup>13</sup>C-NMR spectroscopy.<sup>18-22</sup> From these studies, it has not been possible to define a unique structure for silk I. Attempts to determine a structure were based on model building and comparison of the predictions of these models with experimental data. A number of models have been proposed, including the "crankshaft" model<sup>17</sup> and a loose fourfold helix.<sup>23</sup>

The repeating sequence unit of the crystalline fraction of B. mori silk fibroin is<sup>24</sup>



where n is usually 2 and averages to 2. Poly(L-Ala Gly) has often been used as a model for the crystalline fraction of B. mori silk fibroin since the two crystalline forms of poly(L-Ala-Gly) have been shown to be isomorphous with the two crystalline forms of silk. The present calculations have been carried out on beta-sheets of poly(L-Ala-Gly). In a later paper<sup>25</sup>, we will report the results of calculations relating to the structure of beta-sheets of poly(Gly-L-Ser-Gly-L-Ala-Gly-L-Ala).

#### METHODS

The calculations were carried out by using the ECEPP/2 (Empirical Conformational Energy Program for Peptides) algorithm<sup>26-28</sup> on the IBM 3090-600E supercomputer at the Cornell National Supercomputer Facility. These calculations differ from those previously reported on single beta-sheets<sup>28-33</sup> and stacked beta-sheets<sup>34</sup> in that an analytical expression for the derivative of the potential energy with respect to the rigid body variables for individual chains has been included here.<sup>4</sup> The routine SUMSL (Secant Unconstrained Minimization Solver)<sup>35</sup> was used for energy minimization.

#### Starting Conformations

Single Sheets. In all cases, beta-sheets consisting of five strands of six residues each were used. Each chain was either Ac-(L-Ala-Gly)<sub>3</sub>-NHMe or Ac-(Gly-L-Ala)<sub>3</sub>-NHMe, as indicated below. The side chains of residues along a beta strand project alternately either above or below the plane of a beta-sheet.<sup>36</sup> Therefore, in a poly(L-Ala-Gly) strand, all Ala side chains point to the same side. There are then two ways in

which adjacent strands can be related, the methyl side chains of the alanine residues in these strands can point to either the same side or to opposite sides of the beta-sheet. The sheets in which methyl groups of adjacent strands point to opposite sides of the sheet are referred to as "out of register." Those in which all methyl groups point to the same side of the sheet are referred to as "in register."

Both parallel and antiparallel, beta-sheets were considered. In parallel sheets, the Ac-(Ala-Gly)<sub>3</sub>-NHMe sequence was used for every strand of in-register sheets, while Ac-(Ala-Gly)<sub>3</sub>-NHMe and Ac-(Gly-Ala)<sub>3</sub>-NHMe sequences alternated in neighboring strands of the out-of-register sheets. In antiparallel sheets, the Ac-(Ala-Gly)<sub>3</sub>-NHMe and Ac-(Gly-Ala)<sub>3</sub>-NHMe sequences alternated for neighboring strands of in-register sheets, while out-of-register sheets were composed of Ac-(Ala-Gly)<sub>3</sub>-NHMe strands.

The conformational energy of each of the four possible types of sheets was minimized from eleven starting values of the dihedral angles. The dihedral angles were chosen at 10° intervals over the range of psi values 80° to 180°; phi=-psi. This selection covers the entire range of nontwisted chains in the extended region of the phi-psi map.<sup>29,32</sup> Initially, the dihedral angles of every residue in every chain were equal. During energy minimization all dihedral angles (24 per strand), as well as the six rigid-body variables for each chain, were allowed to vary; thus, there were 144 variables in each minimization. SUMSL was called repeatedly until the total energy changed by less than 10-3 kcal/mol.

Some energy minimizations of antiparallel, out-of-register sheets resulted in a sheet in which most of the alanine residues had dihedral angles near (phi,psi)=(-80°, 150°) and most of the glycine residues dihedral angles near (phi,psi)=(-150°, 80°). Therefore, a twelfth starting point was chosen for all out-of-register antiparallel structures, viz., a sheet with all alanine residues starting at (phi,psi)=(-80°, 150°) and all glycine residues starting at (phi,psi)=(-150°, 80°). Minimization from this new starting point gave a more regular and lower energy structure for out-of-register sheets than the minimization mentioned above in this paragraph.

Stacked Sheets. Three identical sheets were used as the starting point in all computations, except for one, viz., the one giving rise to the orthorhombic out-of-register structure, as described in Results. Two orientations of adjacent sheets were used for in-register structures, with either (a) the Ala sides facing each other and the Gly sides facing each other, or (b) the Gly sides facing the Ala sides. The two sides of out-of-register sheets are the same; therefore, only one orientation is possible. In each starting structure, the dihedral angles of all residues of a given type were assigned the same value. The use of more regular sheets, with the same dihedral angles for each kind of residue, allowed the sheets to be placed closer to each other initially. This resulted in faster minimization and improved convergence. The values of the starting dihedral angles were chosen to be the same as those in one of the starting points for single beta-sheets. A starting point was chosen that lies near



one of the single-sheet minima. The energy minimizations of stacked sheets were carried out by first minimizing the energy with respect to the rigid-body variables. Then all variables (including the rigid body variables) were allowed to change during energy minimization.

#### Determination of the Unit Cell

For the polypeptides considered here, the b axis is usually taken along the strand, the a axis is perpendicular to the strand in the sheet, and the c axis is in the direction between sheets. The dimensions of a unit cell correspond to the distance between repeating units in each direction, viz., two residues (Ala-Gly) along the b axis and two adjacent chains in the sheet along the a axis. In the direction of sheet packing (c axis), the repeating unit contains two adjacent sheets for most structures discussed here, with one exception: in the structure referred to later as monoclinic, the repeating unit along the c axis contains only one sheet instead of two, because strands in adjacent sheets are identical.

### RESULTS

#### Conformational Energies of Single Beta-Sheets

All energy-minimized single-sheet structures had a right-handed twist, as found previously.<sup>29,34</sup> For each of the four types of sheets, energy minima were found in the C and E regions<sup>37</sup> of the phi-psi map. All of those minima that were located in the C region had dihedral angles of approximately  $(\phi, \psi) = (-80^\circ, 80^\circ)$  for every residue and all minima located in the E region occurred approximately at  $(\phi, \psi) = (-150^\circ, 150^\circ)$  for every residue. In addition to these two minima, the out-of-register arrangement for an antiparallel sheet gave a third minimum with a different conformation, in which most of the alanyl residues adopted dihedral angles near  $(\phi, \psi) = (-80^\circ, 150^\circ)$  and most of the glycyl residues adopted dihedral angles near  $(\phi, \psi) = (-150^\circ, 80^\circ)$ . The components of the conformational energy and the characteristic repeats of each single sheet minimum are shown in Table 1. For both the in-register and out-of-register single sheets, the minima in the C region are clearly of lower energy. From the intra- and interchain components of the energy, it can be seen that the minima in the C region are favored because of a much lower intrachain energy. This lower intrachain energy is the result of the formation of a bent intrachain hydrogen bond in the C conformation, while interstrand hydrogen bonds are also retained.<sup>30,31</sup> The minima in the C region show poor agreement with the crystal lattice repeats found experimentally for the two crystalline forms of poly(L-Ala-Gly). The disagreement disappears, however, when the energy of three stacked sheets is considered, as discussed below.

Table 1. Conformational Energies (kcal/mol) of Single Sheets

| Descriptor(a,b,c) | Total  | Inter-Strand | Intra-Strand | Repeat Distance            |        |
|-------------------|--------|--------------|--------------|----------------------------|--------|
|                   |        |              |              | Along Chain Direction (nm) | Across |
| E, A, IR          | -73.4  | -121.3       | 47.9         | 0.713                      | 0.480  |
| C, A, IR          | -91.1  | -108.0       | 16.9         | 0.566                      | 0.459  |
| E, P, IR          | -43.1  | -90.9        | 47.8         | 0.715                      | 0.460  |
| C, P, IR          | -91.9  | -107.7       | 15.7         | 0.563                      | 0.456  |
| E, A, OR          | -76.8  | -128.4       | 51.7         | 0.708                      | 0.459  |
| C, A, OR          | -104.8 | -115.5       | 10.6         | 0.566                      | 0.460  |
| FD, A, OR         | -79.9  | -133.6       | 53.8         | 0.645                      | 0.449  |
| E, P, OR          | -72.1  | -125.8       | 53.7         | 0.716                      | 0.448  |
| C, P, OR          | -90.2  | -105.4       | 15.2         | 0.567                      | 0.483  |

a The letter code of Zimmerman et al.(37) is used FD indicates conformations near  $(\phi, \psi) = (-80^\circ, 150^\circ)$  for Ala,  $(\phi, \psi) = (-150^\circ, 80^\circ)$  for Gly. For the other structures, the letter code pertains to the conformational states of *both* Ala and Gly

b A: antiparallel sheet; P: parallel sheet.

c IR: in-register sheet; OR: out-of-register sheet.

### Conformational Energies of Three Stacked Beta-Sheets

Table 2 lists the conformational energy contributions for stacked beta-sheets. The C-region minima are not listed because their total energy is much higher, by at least 300 kcal/mol (i.e., at least about 3 kcal/mol per residue). Although the isolated sheets with C conformations contain short interstrand hydrogen bonds, in addition to the bent intrachain hydrogen bonds, as mentioned above,<sup>30,31</sup> many of these interstrand hydrogen bonds are weakened or broken when the energies of the stacked sheets are minimized.

Table 2. Conformational Energies(kcal/mol) of Three Stacked Sheets

| Number | Description (a,b,c) | Total | intra-strand | inter-strand (d) | inter-sheet |
|--------|---------------------|-------|--------------|------------------|-------------|
| 1e     | E, A, IR            | -481  | 164          | -297             | -348        |
| 2f     | E, A, IR            | -437  | 152          | -338             | -251        |
| 3      | E, P, IR            | -420  | 153          | -390             | -183        |
| 4      | E, A, OR            | -299  | 152          | -334             | -117        |
| 5g     | FD, A, OR           | -394  | 177          | -337             | -184        |
| 6h     | FD, A, OR           | -388  | 191          | -189             | -390        |
| 7      | E, P, OR            | -260  | 155          | -226             | -189        |

a-c See corresponding footnotes of Table 1. d Sum of interstrand energies between strands of the same sheet. e Figure 2. f Unlike the other in-register structures, these sheets have Gly faces stacked against Ala faces of adjacent sheets. g Orthorhombic structure, Figure 1. h Monoclinic structure, Figure 2.



The computed lowest energy structure is formed by antiparallel beta-sheets with in-register chains and residues in the E conformational state (line 1 in Table 2). As discussed below, this structure is essentially identical with the model that had been proposed by Marsh et al.,<sup>13</sup> and its unit cell parameters agree with the observed values for silk II and the silk II-like structure of poly(L-Ala-Gly).

The lowest energy out-of-register structure is composed of antiparallel sheets in which the residues adopt the dihedral angles alternating near  $(\phi, \psi) = (-80^\circ, 150^\circ)$  for Ala and near  $(\phi, \psi) = (-150^\circ, 80^\circ)$  for Gly (Figure 1). These dihedral angles correspond to right-handed and left-handed twisting of sheets,<sup>9</sup> respectively, with approximately equal magnitudes of the twist. Their alternation results in a twofold axial repeat, with no net twist of the sheets. This structure can exist in two modifications with slightly different packing arrangements that differ in total energy by only 6 kcal/mol or  $<0.1$  kcal/mol per residue (lines 5 and 6 in Table 2).

The higher energy modification of the out-of-register structure (line 6 of Table 2) has a monoclinic unit cell (Figure 2). The dihedral angles of the orthorhombic and monoclinic modifications are very close to each other, differing on the average by less than  $2^\circ$ . The unit cell dimensions in the plane of the sheets (axes a and b) are within 0.01 nm of each other. Because of the change in the intersheet packing, however, the lengths of the c axes differ in the two structures. The length of the c axis in the monoclinic structure is 0.595 nm, inclined at the unit cell angle  $\beta = 106.6^\circ$ , i.e., the distance between second nearest-neighbor sheets is 1.190 nm, measured along the c axis, in contrast to the corresponding c axis length of 1.126 nm in the orthorhombic structure. The unit cell geometry in the monoclinic structure, on the other hand, results in a perpendicular separation of 1.14 nm between second-neighbor sheets, which is only slightly higher than the 1.126 nm distance in the orthorhombic structure. The  $c = 1.126$  nm unit cell dimension of the orthorhombic structure agrees better with observed x-ray data, as shown below. For these reasons, and because of the difference in energies, we propose the orthorhombic modification as the model for silk I, as discussed below.

The energy of the in-register silk II structure (line 1 of Table 2) is 8 kcal/mol lower than that of the proposed out-of-register silk I structure (line 5 of Table 2), i.e., it is lower by almost 1 kcal/mol per residue. This explains why silk II is more stable than silk I, as observed. On the other hand, the energy difference is sufficiently small, so that silk I can exist as a less stable form.

Comparing Tables 1 and 2, it can be seen that the order of the energy minima is different for single and for stacked sheets. Two differences, described below, are of particular note.

First, if one considers only conformational states E and FD, the differences in the total energy are dominated in both cases by the interstrand component, but the intersheet energy may also make a large

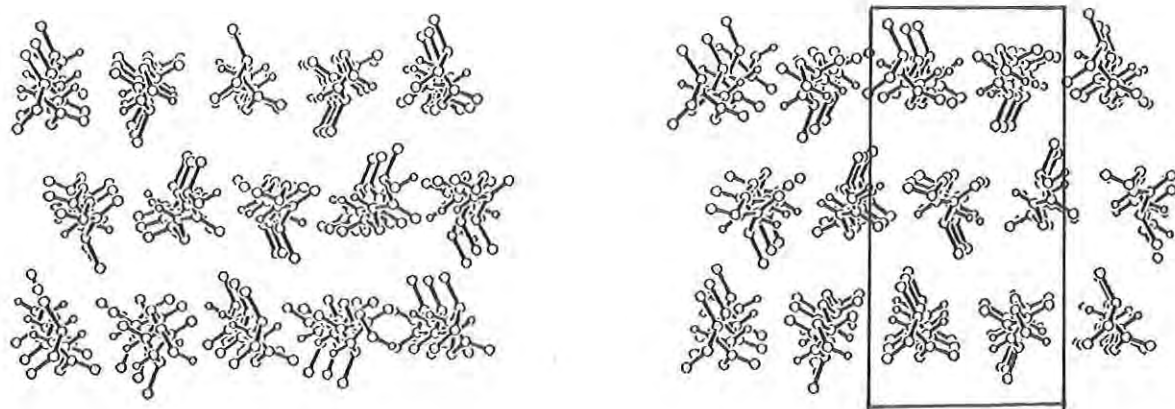


**Figure 1.** Stereo view of computed model for the proposed structure of silk I. Three stacked antiparallel beta-sheets consisting of Ac-(Ala-Gly)<sub>3</sub>-NHMe strands are shown in an orthorhombic unit cell. The strands in the sheets have out-of-register orientation. The structure is viewed along the direction of the polypeptide chains. The sheets are perpendicular to the plane of the drawing. Hydrogen bonds within each sheet (not shown) are horizontal.

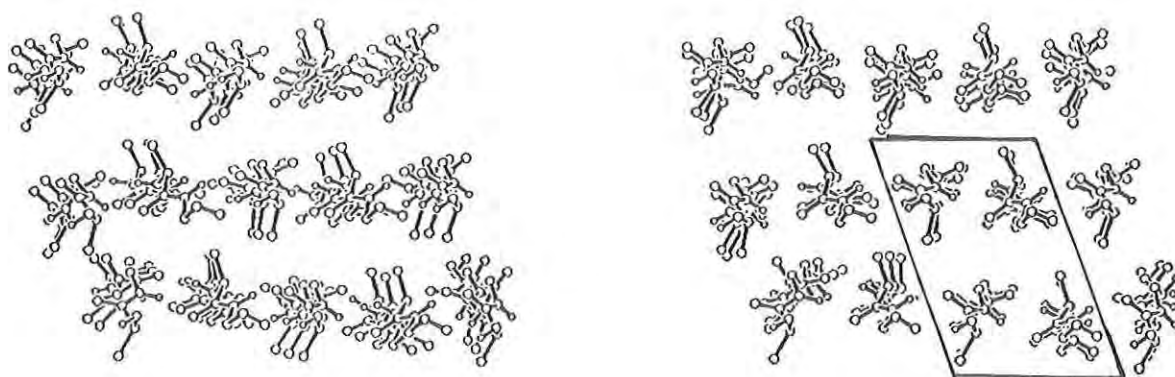


**Figure 2.** Stereo view of computed model for an alternative form of the proposed structure of silk I. Three stacked antiparallel beta-sheets consisting of Ac-(Ala-Gly)<sub>3</sub>-NHMe strands are shown in a monoclinic unit cell. The strands in the sheets have out-of-register orientation. The structure is viewed along the direction of the polypeptide chains. The sheets are perpendicular to the plane of the drawing. Hydrogen bonds within each sheet (not shown) are horizontal.

contribution in some structures. In the single sheet, out-of-register chains are favored over in-register ones in the E conformation by the interstrand energy, because the strands can be packed more closely, allowing an interchain spacing of 0.46 nm (as compared to 0.48 nm for in-register antiparallel sheets). On the other hand, for stacked sheets, an antiparallel in-register sheet with an E conformation (line 1 of Table 2) has the lowest energy. It is favored over out-of-register sheets, because the low intersheet energy, arising from interactions of two Gly faces in contact with each other and of two Ala faces in contact with each other, more than compensates for the less favorable intrasheet chain-chain interactions. This is seen by a comparison of lines 1 and 2 of Table 2, where it is indicated that the stacking of like faces in contact (line 1) is highly favored by over 100 kcal/mol in intersheet energy over the arrangement in which the Gly faces pack against Ala faces (line 2).

Secondly, conformational states FD and E have nearly the same total energy in antiparallel out-of-register single sheets (Table 1), but the FD state allows better stacking, as indicated by the much more favorable intersheet energies (cf. line 4 with lines 5 and 6 of Table 2).

The calculated coordinates have been deposited with the Brookhaven Protein Data Bank.

## DISCUSSION

### Comparison with Crystal Structures

The lowest energy structures for both in-register and out-of-register forms are discussed below. The in-register antiparallel form corresponds to a beta-pleated sheet (with a structure similar to silk II),<sup>12</sup> and we propose, based on a comparison with x-ray and electron diffraction data as well as the calculated density, that the out-of-register antiparallel sheet should serve as a model for silk I.

### Poly(L-Alanine-Glycine), Silk I Form

We propose a new model for the silk I form of poly(L-alanine-glycine) and, by inference, for the crystal structure of silk I. The structure, shown in Figure 1, is a hydrogen-bonded antiparallel sheet in which the alanyl residues adopt dihedral angles near  $(\phi, \psi) = (-80^\circ, 150^\circ)$  and the glycyI residues adopt dihedral angles near  $(\phi, \psi) = (-150^\circ, 80^\circ)$  (Table 3). Since the proposed structure is composed of out-of-register sheets, the methyl side chains of alanyl residues in adjacent strands point to opposite sides of the sheet. The side-chain distribution in the out-of-register sheet is thus symmetrical, in contrast to the in-register silk II form, which has all alanyl residues on one side and all glycyI residues on the other. The sheets in both forms are stacked such that the strands of adjacent sheets are offset laterally (i.e., horizontally in Figure 2) by one half the interstrand distance.<sup>14</sup>

The unit cell is orthorhombic with  $a = 0.894$  nm,  $b = 0.646$  nm,  $c = 1.126$  nm. The  $a$  dimension is twice the interstrand distance, the  $b$  dimension is the repeat for two residues along the chain, and the  $c$

Table 3. Average Dihedral Angles and Hydrogen-Bond Parameters for the Calculated Structures

| Conformational State(a,b)        | Silk I Form<br>(Orthorhombic) |      | Silk I Form<br>(Monoclinic) |      | Silk II Form |      | Poly(L-Ala)<br>(Observed) |
|----------------------------------|-------------------------------|------|-----------------------------|------|--------------|------|---------------------------|
|                                  | Ala                           | Gly  | Ala                         | Gly  | Ala          | Gly  |                           |
|                                  | F                             | D    | F                           | D    | E            | E    |                           |
| phi (deg)                        | -80                           | -150 | -82                         | -150 | -150         | -152 |                           |
| SD                               | 1.9                           | 1.5  | 10.8                        | 7.9  | 3.6          | 3.5  |                           |
| psi (deg)                        | 148                           | 80   | 146                         | 78   | 149          | 148  |                           |
| SD                               | 1.4                           | 1.3  | 9.2                         | 14.8 | 4.3          | 5.4  |                           |
| omega (deg)                      | 180                           | 178  | -179                        | 179  | 179          | -177 |                           |
| SD                               | 1.6                           | 1.8  | 3.3                         | 2.7  | 1.5          | 1.9  |                           |
| H . . . O H-bond length (Å)      | 1.95                          |      | 1.98                        |      | 1.96         |      | 1.90(c)                   |
| SD                               | 0.034                         |      | 0.113                       |      | 0.077        |      |                           |
| N—H . . . O H-bond angle (deg)   | 154                           |      | 154                         |      | 154          |      | 154(d)                    |
| C = O . . . H H-bond angle (deg) | 134                           |      | 133                         |      | 156          |      | 158(d)                    |
| Out-of-plane bending (deg)       | 39                            |      | 40                          |      | 19           |      |                           |

a Reference 37. b The alternation of residue conformational states F and D along the chain is denoted in this paper as state FD. c Calculated here from the data of Arnott et al. d Calculated by Chou et al.<sup>29</sup> from the data of Arnott et al.<sup>39</sup> e Angles of the O H vector with respect to the C = O plane of the peptide group.

dimension is twice the intersheet distance. The observed spacings reported by Lotz and Keith<sup>17</sup> are consistent with this unit cell, as shown in Table 4.

The hydrogen bonds in the proposed orthorhombic structure are of normal length, with an average H...O distance of 0.195 nm. The average N-H...O angle of 154° is close to those in observed antiparallel beta-sheets of globular proteins,<sup>40</sup> viz. 160°-10°, and it is very similar to the value of 164° reported<sup>39</sup> for beta-poly(L-Ala). The average C = O...H angle is 134°, which is less than the 158° reported for beta polyalanine. The out-of-plane component of the C = O...H angle is 39°, which is considerably larger than the median of the absolute value of the out-of-plane angle, 15°, in antiparallel, beta-sheets.<sup>40</sup> However, in small molecules there is considerable variation in the C = O...H angle, with large out-of-plane angles being common. In fact, the preferred C = O...H angle is 135° in many crystals of small molecules, which are free to adopt the most advantageous geometry.<sup>40</sup> The hydrogen bonds formed in the proposed structure are thus somewhat different from those in a beta pleated sheet, but they appear to be reasonable, in comparison with hydrogen bonds observed in organic crystals.<sup>40</sup>

Table 4. Observed and Calculated Spacings for the Silk I Form of Poly(L-Ala-Gly) and Silk I

| Poly(L-Ala-Gly) in<br>the Silk I Form(a) |           | Silk I(b)    |           | calculated<br>structure<br>spacing (nm) |
|--|-----------|--------------|-----------|---|
| spacing(nm)                              | intensity | spacing (nm) | intensity |   |
| 0.780                                    | w-d       | —            | —         |   |
| 0.721                                    | s         | 0.729        | m         | 0.700                                   |
| 0.560                                    | w-d       | 0.561        | w         | 0.563                                   |
| 0.486                                    | w-d       | —            | —         |   |
| 0.449                                    | vs        | 0.450        | s         | 0.447                                   |
| 0.420                                    | w-d       | —            | —         |   |
| 0.394                                    | ms        | 0.402        | w         | 0.375                                   |
| 0.360                                    | ms        | 0.362        | m         |   |
| 0.316                                    | ms-vd     | 0.315        | m         | 0.323                                   |
| 0.272                                    | w-d       | 0.273        | w         | 0.282                                   |
| 0.240                                    | ms-vd     | 0.244        | mw        |   |
| 0.225                                    | vw-d      | 0.224        | vw        | 0.225                                   |
| 0.207                                    | vw-d      | —            | —         |   |

a Reference 17.

b Reference 18.

c Abbreviations used: w, weak; d, diffuse; s, strong; vs, very strong; ms, medium-strong; vw, very weak; vd, very diffuse.(17)



The x-ray diffraction results of Asakura et al.<sup>18</sup> for silk I and Lotz and Keith<sup>18</sup> for the silk I form of poly(L-Ala-Gly) are shown in Table 4, in comparison with the characteristic repeat distances from the proposed structure. From x-ray or electron diffraction, two lattice dimensions are characteristic of the silk I form;<sup>18</sup> in a third, the repeat is less certain. We assign the strong observed reflection at 0.45 nm to the interstrand distance. The average interstrand spacing in our model is 0.447 nm. The computed fiber axis repeat is 0.646 nm for two residues or 0.323 nm per residue, close to the observed 0.316 nm reflection. A spacing of 0.700 nm in our model corresponds to a strong reflection indexed as 101. This spacing is closest to the observed 0.721 nm spacing for poly(L-Ala-Gly). Thus, most of the observed reflections, especially the strong ones, can be indexed in a consistent manner, using the model proposed here, as shown in Table 4.

The calculated density of the overall structure is 1.30 g/cm<sup>3</sup> while Lotz and Keith<sup>18</sup> report that the density of wet crystals of poly(L-Ala-Gly) in the silk I form is 1.33 g/cm<sup>3</sup>, and when corrected by them for water content, 1.25 g/cm<sup>3</sup>.

A number of models for silk I have been proposed earlier. In the "crankshaft model" of Lotz and Keith,<sup>17</sup> the alanyl residues are in a beta conformation and the glycyl residues in a left-handed alpha-helical conformation. The resulting unit cell has the dimensions  $a = 0.472$  nm,  $b = 0.96$  nm, and  $c = 1.44$  nm. A fiber axis repeat of an integer multiple of 0.32 nm has been proposed by Lotz and Keith.<sup>17</sup> Using the crankshaft model, they assigned to the length of the unit cell the value of 0.96 nm, i.e., four residues per chain axis repeat. In the model proposed here,  $b = 0.646$  nm, i.e., an average axial rise of 0.323 nm per residue accounts well for this reflection.

We have also calculated the conformational energy of three sheets of five strands of the antiparallel crankshaft structure proposed by Lotz and Colonna Cesari.<sup>8</sup> The total energy was -365 kcal/mol, which is considerably higher than the values computed for our model (Table 2). The structure proposed by Lotz and Keith<sup>17</sup> and the one presented here are alternative models for silk I, because both are consistent with the fiber x-ray diffraction data. We prefer the present model because it has the lower conformational energy.

Several other models have been proposed, based on x-ray diffraction and NMR data, in which the chains adopt various helical conformations.<sup>41-44</sup> It has been shown for several models<sup>8,16,17,41-43</sup> by conformational energy computations that their strand conformations correspond to relatively low-energy conformations of an isolated poly(L-Ala-Gly) chain. Most of these models lead to less consistent assignments of the available experimental diffraction data with regard to the translational repeat than those of the present model.



On the basis of  $^{13}\text{C}$ -NMR observations on silk I and the form of poly(L-Ala-Gly) that is like silk I, Saito et al. suggested that the hydrogen bonds are perpendicular to the fiber axis.<sup>23</sup> They also conclude, however, that the Ala residues in silk I cannot be in a beta-sheet conformation as in the crankshaft model. Brack and Spach<sup>45</sup> observed IR spectra that correspond to neither an alpha nor a beta form. Some of the amide A, I, and II absorption bands were doubled, implying two hydrogen-bond geometries. They concluded, on the basis of the IR spectra, x-ray diffraction, and other experiments, that the repeating conformational unit is a dipeptide. Our proposed model accounts for both sets of observations.<sup>23,45</sup>

### CONCLUSIONS

A model for silk I and the silk I form of poly(L-alanine-glycine) has been proposed, based on conformational energy calculations. The computed silk model provides very good agreement with the available experimental data, because it can account for most spacings in the observed fiber x-ray diffraction pattern of silk I and of the corresponding form of poly(L-Ala-Gly). The alanyl residues adopt a right-handed sheet-like conformation and the glycyl residues a left-handed sheet-like conformation in the proposed structure. The dimensions of its orthorhombic unit cell are  $a = 0.894$  nm,  $b = 0.646$  nm, and  $c = 1.126$  nm. The proposed silk I model may also represent the structure of the liquid crystal phase recently described by Kerkam et al.,<sup>47</sup> who showed that concentrated silk fibroin solutions formed nematic liquid crystals. Silk fibroin, when in the gland, is a concentrated solution, and when it is allowed to dry undisturbed, is found to be in the silk I form;<sup>7</sup> therefore, it is likely that the liquid crystalline structures also consist of silk I. Our computations are now being extended<sup>25</sup> to real sequences,<sup>24</sup> containing Ser residues in addition to Gly and Ala.

We thank J. A. Grant and M. J. Dudek for helpful advice during this work, and A. Zagari for helpful comments on the manuscript. This work was supported by research grants from the National Institute of General Medical Sciences (GM 14312) and the National Institute on Aging (AG-00322) of the National Institutes of Health, U.S. Public Health Service, and from the National Science Foundation (DMB84-01811). Support was also provided by the Cornell University Biotechnology Center. The computations were carried out using the Cornell National Supercomputer Facility, a resource of the Center for Theory and Simulation in Science and Engineering at Cornell University, which is funded in part by the National Science Foundation, New York State, the IBM Corporation, and members of its Corporate Research Institute.

# REFERENCES

1. Lombardi, S. J., Fossey, S. A. & Kaplan, D. K. (1990) Proceedings of the American Society for Composites - Fifth Technical Conference.
2. Demura, M. & Asakura, T. (1989) *Biotech. and Bioeng.* 33, 598-603.
3. Asakura, T. (1986) *Makromol. Chem., Rapid Commun.* 7,755-759.
4. Fossey, S. A., Nemethy, G., Gibson, K. D., and Scheraga, H. A. (1991) *Biopolymers* 31,1529-1541.
5. Scheraga, H. A. & Nemethy, G. (1991) in *Molecules in Natural Biosciences-Encomium for Linus Pauling*, In press.
6. Nemethy, G. & Scheraga, H. A. (1989) *Bull. Inst. Chem. Res. Univ. Kyoto* 66, 398-408.
7. Fraser, R. D. B. & MacRae, T. P. (1973) in *Conformation in Fibrous Proteins and Related Synthetic Polypeptides*, Academic Press, New York, 1973, chap. 13.
8. Lotz, B. & Colonna-Cesari, F. (1979) *Biochimie* 61, 205-214.
9. Chou, K. C., Nemethy, G. & Scheraga, H. A. (1990) *Accts. Chem. Res.* 23,134-141.
10. Miller, S. (1989) *Protein Eng.* 3, 77-83.
11. Kratky, O., Schauenstein, E. & Sekora, A. (1950) *Nature* 165, 319-320.
12. Kratky, O. (1956) *Trans. Faraday Soc.* 52, 558-570.
13. Marsh, R. E., Corey, R. B. & Pauling, L. (1955) *Biochem. Biophys. Acta* 16, 1-34.
14. Fraser, R. D. B., MacRae, T. P., Stewart, F. H. C. & Suzuki, E. (1965) *J. Mol. Biol.* 11, 706-712.
15. Fraser, R. D. B., MacRae, T. P. & Stewart, F. H. C. (1966) *J. Mol. Biol.* 19, 580-582.
16. Lim, V. I. & Steinberg, S. V. (1981) *FEBS Lett.* 131, 203-207.
17. Lotz, B. & Keith, H. D. (1971) *J. Mol. Biol.* 61, 201-215.
18. Asakura, T., Kuzuhara, A., Tabeta, R. & Saito, H. (1985) *Macromolecules* 18, 1841-1845.
19. Kricheldorf, H. R., Muller, D. & Ziegler, K. I (1983) *Polymer Bull.* 9, 284-291.

20. Saito, H., Tabeta, R., Kuzuhara, A. & Asakura, T. (1986) Bull. Chem. Soc. Japan 59, 3383-3387.
21. Asakura, T., Yoshimizu, H. & Yoshizawa, F. (1988) Macromolecules 21, 2038-2041.
22. Ishida, M., Asakura, T., Yokoi, M. & Saito, H. (1990) Macromolecules 23, 88-94.
23. Saito, H., Tabeta, R., Asakura, T., Iwanaga, Y., Shoji, A., Ozaki, T. & Ando, I. (1984) Macromolecules 17, 1405-1412.
24. Strydom, D. J., Haylett, T. & Stead, R. H. (1977) Biochem. Biophys. Res. Comm. 79, 932-938.
25. Fossey, S. A., Nemethy, G. & Scheraga, H. A., in preparation.
26. Momany, F. A., McGuire, R. F., Burgess, A. W. & Scheraga, H. A. (1975) J. Phys. Chem. 79, 2361-2381.
27. Nemethy, G., Pottle, M. S. & Scheraga, H. A. (1983) J. Phys. Chem. 87, 1883-1887.
28. Sippl, M. J., Nemethy, G. & Scheraga, H. A. (1984) J. Phys. Chem. 88, 6231-6233.
29. Chou, K.-C., Pottle, M., Nemethy, G., Ueda, Y. & Scheraga, H. A. (1982) J. Mol. Biol. 162, 89-112.
30. Chou, K.-C. & Scheraga, H. A. (1982) Proc. Natl. Acad. Sci., U.S.A. 79, 7047-7051.
31. Chou, K.-C., Nemethy, G. & Scheraga, H. A. (1983) J. Mol. Biol. 168, 389-407.
32. Chou, K.-C., Nemethy, G. & Scheraga, H. A. (1983) Biochemistry 22, 6213-6221.
33. Chou, K.-C., Nemethy, G., Rumsey, S., Tuttle, R. W. & Scheraga, H. A. (1985) J. Mol. Biol. 186, 591-609.
34. Chou, K.-C., Nemethy, G., Rumsey, S., Tuttle, R. W. & Scheraga, H. A. (1986) J. Mol. Biol. 188, 641-649.
35. Gay, D. M. (1983) ACM Trans. Math. Software 9, 503-512.
36. Pauling, L. & Corey, R. B. (1953) Proc. Natl. Acad. Sci., U.S.A. 39, 253-256.
37. Zimmerman, S. S., Pottle, M. S., Nemethy, G. & Scheraga, H. A. (1977) Macromolecules 10, 1-9.

38. Colonna-Cesari, F., Premilat, S. & Lotz, B. (1975) J. Mol. Biol. 95, 71-82.
39. Arnott, S., Dover, S. D. & Elliot, A. (1967) J. Mol. Biol. 30, 201-208.
40. Baker, E. N. & Hubbard, R. E. (1984) Prog. Biophys. Mol. Biol. 44, 97-179.
41. Konishi, T. & Kurokawa, M. (1968) Sen-i Gakkaishi 24, 550-554.
42. Asakura, T. & Yamaguchi, T. (1987) J. Seric. Sci. Jpn. 56, 300-304.
43. Ichimura, S. & Okuyama, K. (1989) Polym. Prep. Jpn. 38, E48,.
44. Oka, M., Baba, Y., Kagemoto, A. & Nakajima, A. (1990) Polym. J. (Jpn.) 22, 416-425.
45. Brack, A. & Spach, G. (1972) Biopolymers 11, 563-586.
46. Lotz, B., Brack, A. & Spach, G. (1974) J. Mol. Biol. 87, 193-203.
47. Kerkam, K., Viney, C., Kaplan, D. & Lombardi, S. (1991) Nature 349, 596-598.

MAYER, et al.

TITLE: Biodegradable Polymers for Packaging

Jean M. Mayer, Ms., Joseph E. McCassie, Mr.,  
Derek H. Ball, Dr., Robert E. Stote, Mr., James R.  
Wright, Sgt., Ashley E. Shupe, Sgt., Peter J.  
Stenhouse, Mr., Paul A. Dell, Mr., Mark J. Hepfinger, Mr.,  
Elizabeth A. Costa, Ms., Elwyn T. Reese, Dr., and David L. Kaplan, Dr.

ABSTRACT: Natural and derivatized polysaccharide and polyester polymers, selected blends and laminates are being investigated for biodegradable packaging applications. Films are produced from these polymer formulations by solvent casting or extrusion techniques and are evaluated for physical and mechanical properties such as tensile strength, ultimate elongation, oxygen permeability and moisture vapor transmission rate. Biodegradation kinetics in marine and soil environments are determined using accelerated laboratory test systems currently under development. Results indicate that fillers such as starch or pullulan can provide improved oxygen permeability resistance over many conventional plastics, while outer layers comprised of bacterial polyesters or synthetically produced polycaprolactone can improve moisture stability and flexibility. Packaging comprising these materials is completely biodegradable in both marine and soil environments.

BIOGRAPHY OF PRESENTER: Jean M. Mayer

PRESENT ASSIGNMENT: Research Microbiologist, Biotechnology  
Division, SSD

DEGREES HELD: B.S., Providence College, 1980

MAYER, et al.

### Biodegradable Polymers for Packaging

Jean M. Mayer, Ms., Joseph E. McCassie, Mr., Derek H. Ball, Dr., Robert E. Stote, Mr., James R. Wright, Sgt., Ashley E. Shupe, Sgt., Peter J. Stenhouse, Dr., Paul A. Dell, Mr., Mark J. Hepfinger, Mr., Elizabeth A. Costa, Ms., Elwyn T. Reese, Dr., and David L. Kaplan, Dr.

U. S. Army Natick Research, Development and Engineering Center  
Kansas Street, Natick, MA 01760-5020

### INTRODUCTION

The use of plastic packaging during the 20<sup>th</sup> century has greatly improved food safety, quality, and storage stability. Environmental concerns over the impact of plastics, in general, and plastic packaging in particular, have received much attention in the last decade. Whereas plastic stability during use has been viewed as an asset, its continued nondegradability upon disposal is considered by many to be deleterious.

A survey conducted in 1984<sup>2</sup>, showed that approximately one third of all municipal solid waste consists of packaging materials; 11.5% of which is plastic packaging by weight. The Armed Services utilize a tremendous amount of plastic packaging. A 1990 report to Congress<sup>5</sup>, identified 3559 disposable plastic items not related to food that are registered in the Federal Catalog System, the two most costly categories being bags and sacks (54.8%) and medical equipment and supplies (25.1%). A survey of Navy shipboard wastes conducted on the USS O'Bannon in 1988 showed that 45.7% of the plastic waste was generated in the foodservice area. In the past, shipboard wastes, including plastics, have been thrown overboard. This has resulted in the accumulation of litter on beaches and death of thousands of sea mammals, birds and fish due to entrapment or ingestion.

Concern over this problem resulted in the ratification of an international treaty called the MARPOL treaty, which will prohibit the overboard disposal of plastics from any vessel after 1993. The Navy, in trying to comply with the treaty, has attempted to store all waste plastics onboard ship, but has had great difficulty holding food-contaminated plastics for more than three days due to odor problems and potential health hazard concerns.

Edible food coatings made from biopolymers could improve storage stability and reduce food-contaminated plastic waste, which would permit longer onboard storage of plastics. Biodegradable plastic substitutes, if proven to be functional and safe as packaging, as well as biodegradable and nontoxic in the marine environment, could be disposed of in the ocean with pulped food and paper wastes.



The Army must maintain a large inventory of shelf-stable rations, which has resulted in the requirement for multilaminate packaging. The Meal-Ready-to-Eat (MRE), for example, is packaged in triple laminate retortable pouches comprised of polypropylene, foil, polyethylene terephthalate (PET) and adhesives. This pouch is not recyclable nor degradable if buried in soil. Although not mandated by any legislation, the Army is actively pursuing the development of biodegradable packaging which would meet safety and performance criteria.

This paper discusses biodegradable film production, derivatization, and evaluation of physical, mechanical and biological properties for edible coating and biodegradable outer packaging applications. Polymers under evaluation include four polysaccharides, pullulan, starch, chitosan and cellulose, two polymeric alcohols, polyvinyl alcohol (PVOH) and ethylene vinyl alcohol (EVOH) and two polyesters, polycaprolactone (PCL) and polyhydroxybutyrate/polyhydroxyvalerate (PHBV). Structures are presented in Figures 1 and 2.

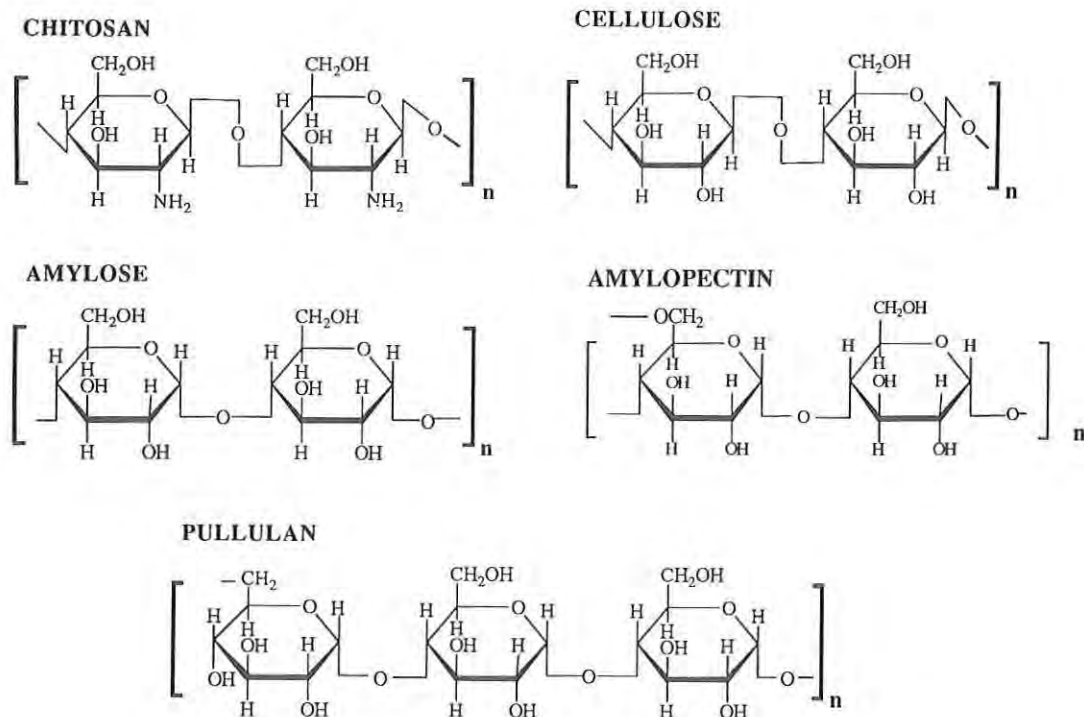


Figure 1. Structures of biodegradable polysaccharides

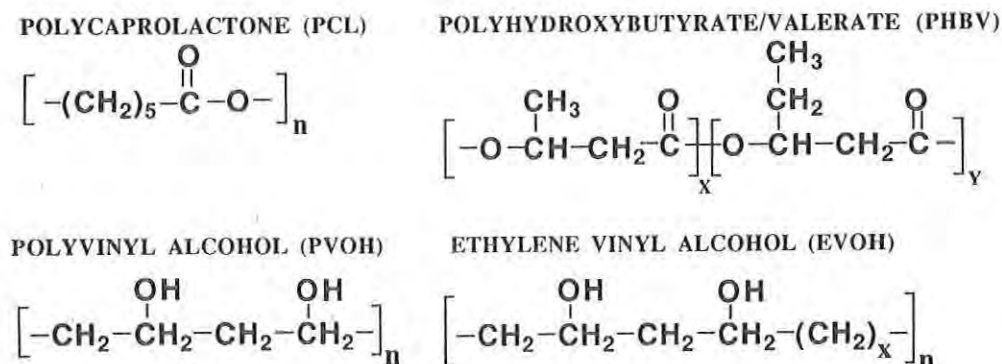


Figure 2. Structures of biodegradable polyesters (PCL and PHBV) and polymeric alcohols (PVOH and EVOH)

#### MATERIALS AND METHODS

**Solvent Cast Film Production.** Pullulan (Hayashibara Laboratories, Okayama, Japan) and polyvinyl alcohol (Sigma Chemical Company, St. Louis, MO) films were cast from water solution onto plexiglass plates with teflon gaskets and dried overnight at 40°C. Chitosan (Protan Laboratories, Redmond, WA) was cast in a similar manner from 2% acetic acid solution. PHBV (Imperial Chemical Industries, Billingham, UK) was first Soxhlet extracted with chloroform and filtered prior to casting onto a glass plate and evaporated at room temperature in a hood.

**Starch Blend Blown Film Production.** Starch/PVOH blown film was produced by combining 200 g starch (Best Foods, Englewood Cliffs, NJ), 200 g PVOH (Sigma Chemical Co. St. Louis, MO) and 20 g talc (J. T. Baker Co., Phillipsburg, NJ) and mixing these ingredients into a solution containing 160 mL distilled water and 32 g glycerol (Fisher Scientific, Pittsburg, PA). In the first trial, three different molecular weight ranges of PVOH were used, 30-70 K, 70-100 K and 124-186 K (determined by low angle laser light scattering). The formulations were processed using a Brabender 42 mm counter-rotating twin screw mixer (TSM) fitted with a blown film die (2.54 cm I.D. with a 0.05 cm gap). The extrusion system contained three heated zones, two on the twin screw and one at the die. The formulations were hand fed into the extruder and temperatures and extruder speed adjusted until smooth melted blends exited the blown film die. The molten tube of polymer was then taken up through rollers and internal and external air supplies were used to blow and cool the film, respectively.

Pullulan Derivatization. 6-chloro-6-deoxy-pullulan was prepared by treatment of pullulan in dimethylformamide with methanesulfonyl/chloride<sup>1</sup>. Treatment of this derivative with alkali resulted in intermolecular cyclization and the formation of 3,6-anhydro-pullulan. The reaction of 6-chloro-6-deoxy-pullulan with sodium azide in boiling water gave 6-azido-6-deoxy-pullulan. All structures were confirmed by <sup>13</sup>C NMR spectroscopy.

Enzymatic Hydrolysis of Pullulan. The enzymes were generously donated by the investigators who first prepared them (Table 1), except for the isopullulanase. This we prepared from the same *Aspergillus niger* strain (QM 386) used by Sakano et al.<sup>6</sup> The crude enzyme was purified by absorption on bentonite. Activity of the enzymes was determined as described previously.<sup>4</sup> A typical assay contained pullulan (3 mg) and enzyme in 0.05 M acetate buffer at optimum pH (Table 1). Incubation was for 30 minutes at 40°C. For resistant substrates, the amount of enzyme was increased and the incubation period prolonged. Reducing sugars were determined by the dinitrosalicylic acid method.

Table 1. Sources of Pullulanases

| Enzyme                        | pH Optimum   | Dominant Product | Enzyme Source                             | Reference                        |
|-------------------------------|--------------|------------------|---|----------------------------------|
| Glucamylase<br>EC 3.2.1.3     | 5.0          | Glucose          | <i>Aspergillus niger</i><br>(Diazyme 455) | Miles Laboratory                 |
| Pullulanase<br>EC 3.2.1.41    | 6.0<br>(7.0) | Maltotriose      | <i>Aerobacter aerogenes</i>               | Bender & Wallenfels <sup>7</sup> |
| Neopullulanase<br>EC 3.2.1.-  | 6.0          | Panose           | <i>Bacillus subtilis</i>                  | Kuriki et al. <sup>8</sup>       |
| Isopullulanase<br>EC 3.2.1.57 | 3.5          | Isopanose        | <i>Aspergillus niger</i>                  | Reese (this paper)               |

Note: The activity (mg reducing sugar/h/mg enzyme) of these preparations varied from 0.8 (glucamylase) to 26 (neopullulanase) when determined under our conditions of assay. The  $K_M$  values for the endo-pullulanase on pullulan are about 1 mg/mL; for the exo-pullulanase (glucamylase) about 150 mg/mL (lit. values).

Chitosan Crosslinking. Crosslinked chitosan was synthesized by reaction with epichlorohydrin under alkaline conditions.<sup>3</sup> A chitosan film was first cast from a 2% acetic acid solution. A solution containing epichlorohydrin and enough sodium hydroxide to neutralize the acetic acid and catalyze the reaction was poured over the chitosan film and heated at 40°C until dry. The film was then washed in water and dried under tension to prevent wrinkling.

Physical Testing of Films. Film thickness (required for tensile strength calculations) was determined with a micrometer (E.J. Cady & Co., Chicago, IL) and tensile strength at break and ultimate elongation was determined by ASTM standard D 882-90 using a Model 4201 tensile strength tester (Instron Co., Canton, MA).

Simulated Marine Biodegradation Testing. Laboratory-accelerated marine water and sediment studies were conducted in 76-liter aquaria maintained at 30°C under controlled fluorescent lighting conditions, 12 hours on and 12 hours off. Standard, artificial marine water consisted of a mixture of salts (Aquarium Systems, Mentor, OH) diluted with distilled water to simulate the concentration and proportion of the major and minor mineral components of the ocean. The marine water was aerated and replenished continuously with fresh artificial brine at the rate of 15% volume per week. Marine organisms were collected by filtration of approximately 76 liters of marine water through a 0.45  $\mu$  capsule filter (Gelman Sciences, Ann Arbor, MI) using a hand pump. The organisms were eluted off the filters by placing the filters in the aquaria overnight. Triplicate 2.5 cm X 7.5 cm test specimens were retained in fiberglass sample holders for both water and sediment exposure. Specimens were supported vertically for water exposure and horizontally for sediment exposure. A schematic of the system is presented in Figure 3.

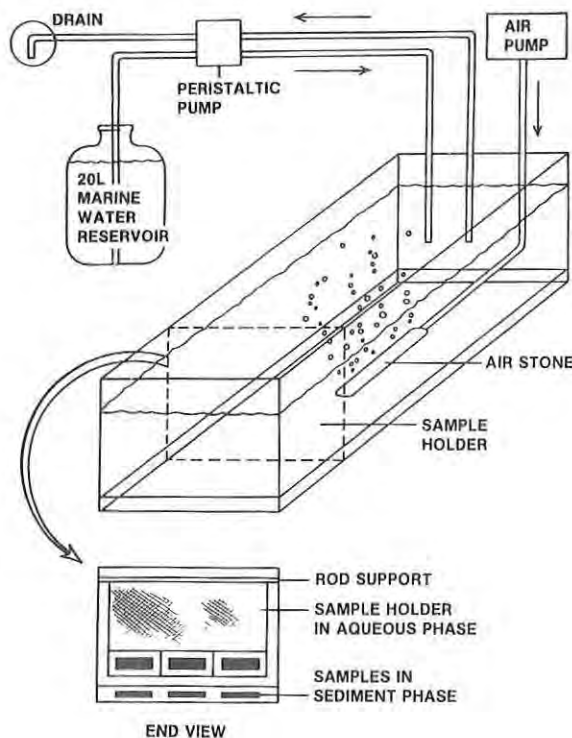


Figure 3. Schematic of the simulated marine biodegradation test system

Simulated Soil Biodegradation Testing. Laboratory-accelerated soil degradation studies were conducted in microbially active soil beds stored in an environmental chamber maintained at 30°C and 95% relative humidity. Triplicate 2.5 cm X 7.5 cm specimens were buried horizontally in soil composed of top soil, sand and decomposed manure or leaf mold in equal parts. Prior to use, the soil was composted for a minimum of three months to develop a natural microbial population. The soil was standardized to a pH of 6.5 to 7.5 and a moisture content of 20 to 30%. Sample holders were not used for soil biodegradation experiments to ensure maximum specimen contact with the soil.

Biodegradation Sample Characterization. After exposure, triplicate polymer film samples were washed, dried overnight in a 70°C oven and conditioned to a constant weight in a desiccator. Weight changes are reported per surface area to account for differences in sample thickness.

## RESULTS AND DISCUSSION

Starch/PVOH blown film production. The molecular weight of PVOH in the formulations used to blow film affected the conditions required to extrude the material. As Table 2 indicates, the lowest molecular weight PVOH could be extruded at lower temperatures and higher extrusion speeds, presumably due to its lower viscosity. Higher temperatures and lower speeds were required for the higher molecular weight PVOH formulations. It was also found that pressure at the die was critical to extrudability. When a tubular die with a much larger die gap was used (0.95 cm versus 0.05 cm), the starch/PVOH formulations did not melt and film could not be blown. Future studies will determine what die gap range is necessary to produce blown film from starch/PVOH blends.

Table 2. Extrusion Conditions Used to Produce Starch/PVOH Blown Film

| Sample <sup>1</sup> | Extrusion<br>Speed (rpm) | Extrusion<br>Temperature °C |        |        | Melt<br>Temp (°C) | Pressure<br>(psi) |
|---------------------|--------------------------|-----------------------------|--------|--------|-------------------|-------------------|
|                     |                          | Zone 1                      | Zone 2 | Zone 3 |                   |                   |
| 30-70K MW PVOH      | 60                       | 95                          | 95     | 100    | 105               | 200               |
| 70-100K MW PVOH     | 50                       | 105                         | 105    | 110    | 113               | 200               |
| 124-186K MW PVOH    | 50                       | 95                          | 115    | 120    | 125               | 200               |

<sup>1</sup>Samples contain starch, glycerol, water and talc as described in materials and methods.



**Crosslinked Chitosan.** The proposed mechanism of chitosan crosslinking is presented in Figure 4. The base catalyzes epoxide ring scission, which then reacts with the amine groups between two different monomers in the chitosan. The mechanical properties of chitosan films as a function of epichlorohydrin crosslinking agent content are presented in Table 3. The tensile strength at break improves with increased epichlorohydrin content up to 12.5% (mol/mol) and then decreases. This decrease seems to be due to brittleness of the highly crosslinked film.

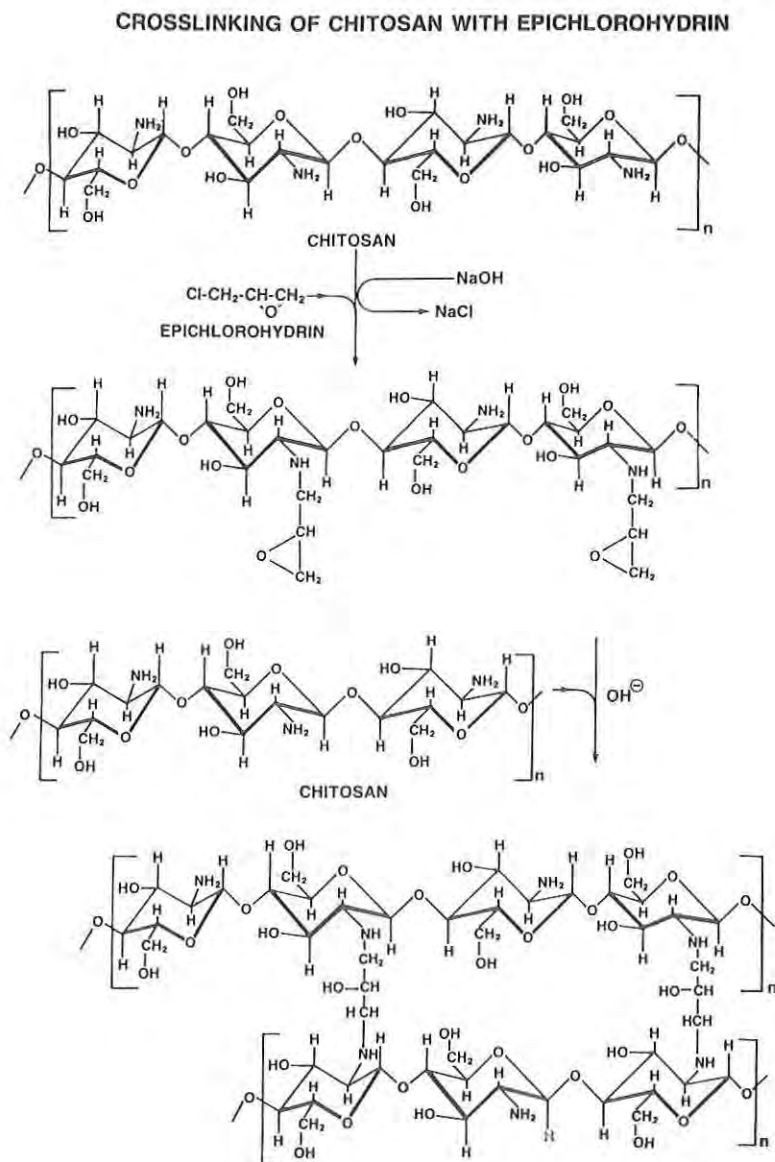


Figure 4. Proposed mechanism of chitosan crosslinking with epichlorohydrin



Table 3. Physical Properties of Chitosan and Crosslinked Chitosan Films<sup>a</sup>

| Film Composition                            | Thickness (mm) | Elongation (%)   | Tensile Strength (mPa) |
|---|----------------|------------------|------------------------|
| Chitosan <sup>b</sup>                       | 0.035 ± 0.008  | 2.9 ± 1.0        | 51.0 ± 11.3            |
| Crosslinked Chitosan, 6% Epichlorohydrin    | 0.036 ± 0.005  | 11.8 ± 4.1       | 57.8 ± 12.1            |
| Crosslinked Chitosan, 12.5% Epichlorohydrin | 0.041 ± 0.008  | --- <sup>c</sup> | 125.4 ± 32.1           |
| Crosslinked Chitosan, 25% Epichlorohydrin   | 0.057 ± 0.013  | 16.0 ± 9.8       | 75.6 ± 13.0            |

<sup>a</sup>N=5<sup>b</sup>Protan Laboratories Inc., Redmond, Washington<sup>c</sup>No Data

Physical properties of films. Physical properties of extruded, cast or commercial biodegradable films are presented in Table 4. Data on polypropylene and polyethylene terephthalate, two nonbiodegradable plastics, are included for comparison, since they are often used in packaging. The oxygen permeability results show that the biodegradable polymers, with the exceptions of polycaprolactone and cellophane, are good oxygen barriers. The moisture barrier properties for the biodegradable polymers are poor, however, except for PHBV. Crosslinked chitosan is the only biopolymer with high tensile strength while PCL and the starch/PVOH blend have good elongation properties.

Table 4. Physical Properties of Plastic Films<sup>1</sup>

| PROPERTY | TENSILE<br>STRENGTH (mPa) | ELONGATION<br>AT BREAK | MVTR <sup>2</sup><br>(g/m <sup>2</sup> /24h) | O <sub>2</sub> PERMEABILITY<br>(cc/m <sup>2</sup> /24h) |
|----------|---------------------------|------------------------|--|---|
| PP       | 20-60                     | 300-800                | 3-12   | 1000-2500   |
| PET      | 170-225                   | 70-300                 | 20-30  | 40-50   |
| CEL      | 50-125                    | 15-30                  | >950   | 40-70   |
| PUL      | 35-50                     | 1-4                    | --- <sup>3</sup>                             | 0.5-1.5   |
| CHIT     | 40-160                    | 1.5-3                  | >950   | 1.5-10  |
| PHBV     | 15-25                     | 13-70                  | 40   | 1-5   |
| PCL      | 28-40                     | 600-1000               | >950   | 116   |
| ST/PVOH  | 5-30                      | 50-300                 | ND <sup>4</sup>                              | 1.1   |

<sup>1</sup>PP - polypropylene (nonoriented); PET - polyethylene terephthalate; CEL - cellophane; PUL - Pullulan; CHIT - Chitosan; PHVB - polyhydroxybutyrate/polyhydroxyvalerate; PCL - polycaprolactone; ST - starch; PVOH - polyvinyl alcohol

<sup>2</sup>MVTR = moisture vapor transmission rate

<sup>3</sup>Cannot be determined since polymer is water soluble

<sup>4</sup>No Data

Pullulan derivatization and enzymatic hydrolysis. Chlorination at C-6 produced a derivative with reduced water solubility; however, upon acidifying to pH 2.6, a clear solution was formed. Azido-pullulan solutions were slightly colored and little precipitation occurred. Enzyme susceptibility studies of C-6 modified pullulans are presented in Table 5. Results show that 6-azido pullulan was the only derivative that appreciably hydrolyzed, in this case, by isopullulanase. Isopullulanase hydrolysis is predictable since this endo-enzyme acts at a cleavage site where the reducing sugar is unchanged from that of the parent compound (Figure 5). This does not explain the lack of hydrolysis of chloro-pullulan by isopullulanase, unless steric hinderance plays a role. Future studies will examine how degree of substitution affects the enzymatic hydrolysis and water stability of 6-chloro- and 6-azido-substituted pullulan and starch.

Table 5. Susceptibility of C-6 Modified Pullulans to Enzymatic Hydrolysis.

| Enzyme         | pullulan | Hydrolysis rates (relative)* |                   |                  |
|----------------|----------|------------------------------|-------------------|------------------|
|                |          | 3,6-anhydro-pullulan         | 6-chloro-pullulan | 6-azido-pullulan |
| Glucamylase    | 100      | 0                            | 0.03              | 0.05             |
| Pullulanase    | 100      | 0                            | 0.01              | 0.03             |
| Neopullulanase | 100      | 0                            | 0.02              | 0.01             |
| Isopullulanase | 100      | 0                            | 0                 | 23.0             |

\*Hydrolysis at rates less than one ten thousandth that of pullulan are assigned a "0" value.

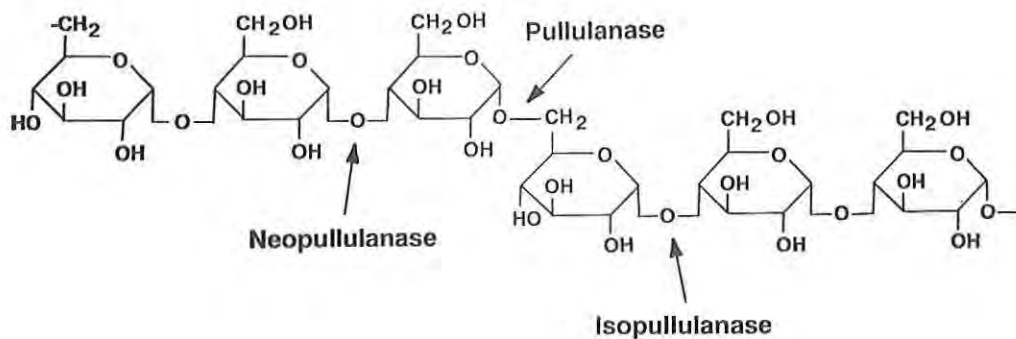


Figure 5. Hydrolysis sites for pullulanase, neopullulanase and isopullulanase

Biodegradation studies. Marine and soil biodegradation results are presented in Figures 6-8. Results were graphed as a function of weight loss/surface area versus time. If biodegradation rate is viewed as the slope of the lines in the graph, PHBV appears to be the most biodegradable, even when compared to paper, which is currently allowed to be disposed from ships. Polypropylene, the negative control, did not lose weight in any environment, under any conditions. Many of the materials used in testing such as cellophane and PCL were completely lost before the end of the testing period. More data and more meaningful results would be obtained if thicker samples were used. This will be a goal of future studies, so that reliable slopes can be determined and used to rank the biodegradation rates of various compounds under these standard conditions. While the use of weight loss/surface area equalizes differences between thick and thin samples when hydrophobic polymers such as PHBV are tested (unpublished results), it has yet to be determined if this equalization applies to hydrophilic materials. This will be determined in future studies. The biodegradation tests will be further standardized by selection of defined natural populations, which degrade a variety of polymer types, and creation of synthetically formulated, reproducible marine sediment to eliminate variation due to obtaining natural sediments at different geographic locations.

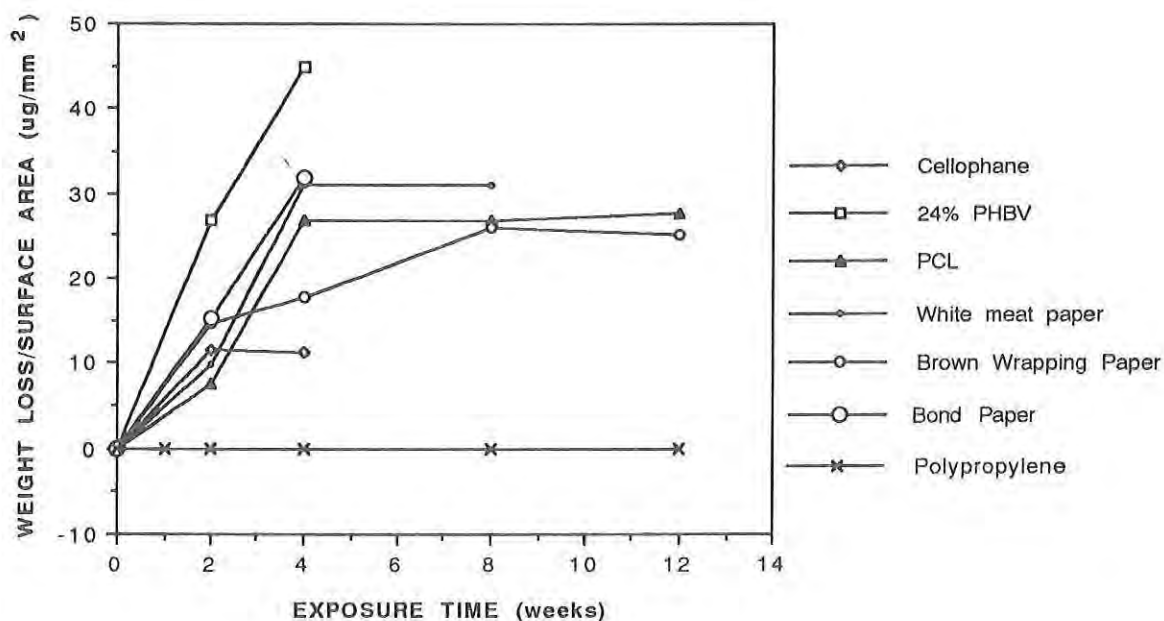


Figure 6. Polymer film biodegradation in simulated marine water test system

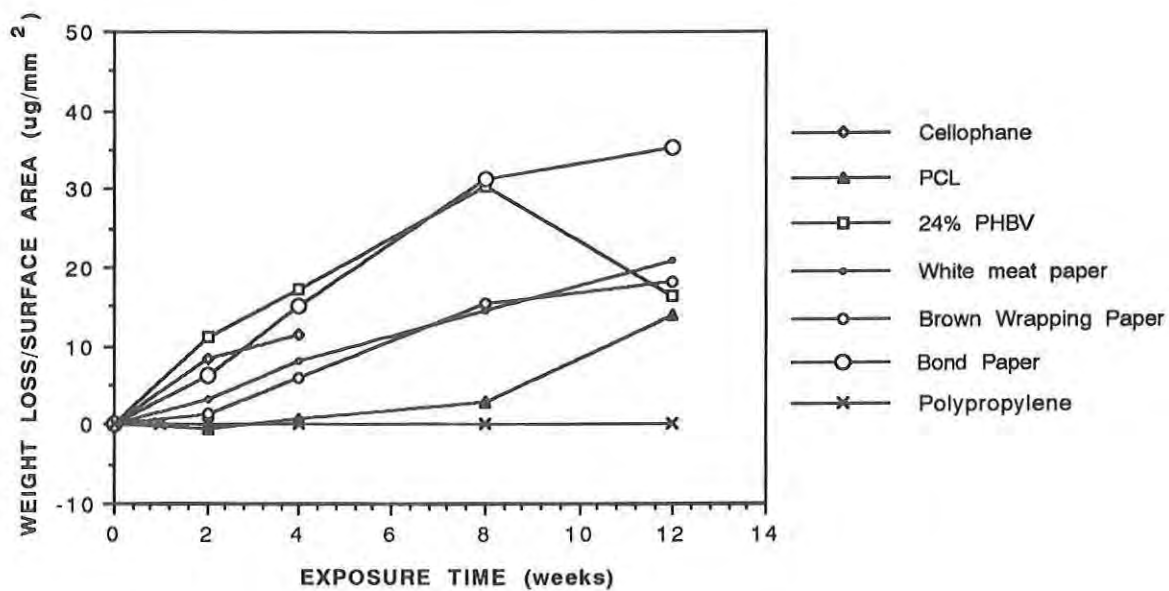


Figure 7. Polymer film biodegradation in simulated marine sediment test system

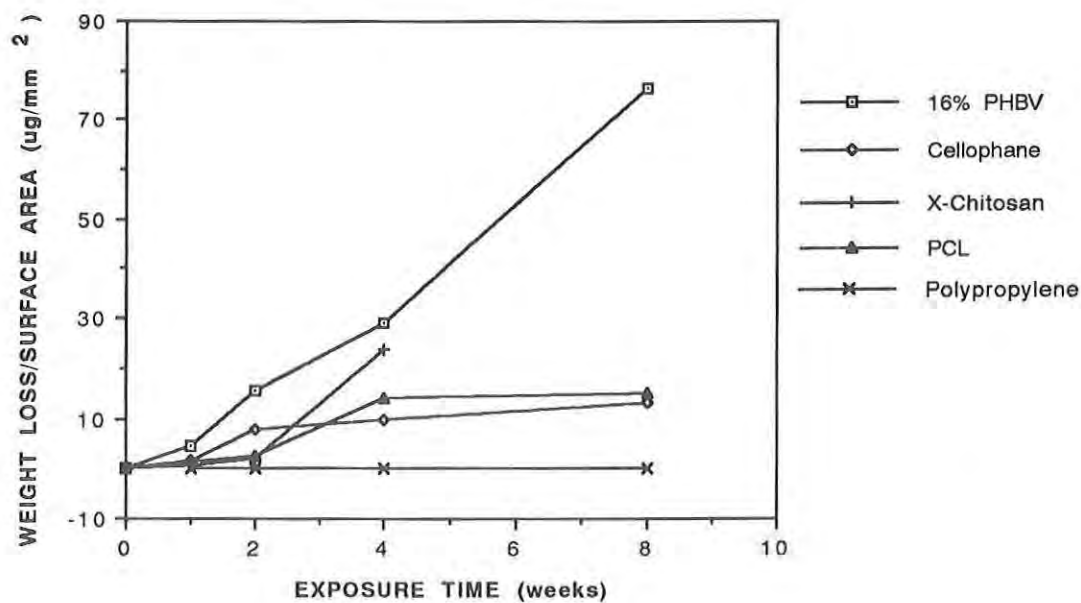


Figure 8. Polymer film biodegradation in soil test system

## CONCLUSIONS

It appears that a combination of biopolymers, in blend or laminate form, will be necessary to produce packaging with required performance characteristics. Moisture stability is a critical area to address. Lamination of flexible, high oxygen barrier biopolymers with PHBV may provide film with good overall performance characteristics. A compatibilizer will be necessary, however, because good oxygen barriers are usually hydrophilic polymers, while PHBV is hydrophobic. An alternative approach is to partially derivatize hydrophilic polymers such as starch or pullulan to produce water stable products, but care must be taken not to affect oxygen barrier properties or biodegradability.

## REFERENCES

1. EVANS, M. E., L. Long and F. W. Parrish. 1968. Reaction of Carbohydrates with Methylsulfonyl Chloride in N,N-dimethylformamide. J. Org. Chem. 33:107401976.
2. JOHNSON, R. 10 June 1987. An SPI Overview of Degradable Plastics. "Proceedings of Symposium on Degradable Plastics, The Society of the Plastics Industry Inc.," Washington, D.C. pp.6-13.
3. MAYER, J. M. and D. L. Kaplan. 1991. Method of Forming a Crosslinked Chitosan Polymer and Product Thereof. U.S. Patent 5,025,293.
4. REESE, E. T., A. Maguire and F. W. Parrish. 1968. Glucosides and Exo-glucanases. Can. J. Biochem. 46:25-33.
5. Report to Congress by Under Secretary of Defense (Aquisition). March 1990. "Degradable Plastic Items Used by Department of Defense."
6. SAKANO, Y., M. Higuchi and T. Kobayashi. 1972. Pullulan 4-glucanohydrolase from Aspergillus niger. Arch. Biochem. Biophys. 153:180-187.
7. BENDER, H. and K. Wallenfels. 1961. Pullulan II specific breakdown by a bacterial enzyme. Biochem. Z. 334:79-95.
8. KURIKI, T., S. Okada and T. Imanaka. 1988. New type of pullulanase. J. Bacteriol. 170:1554-1559.



SAMUELSON, et al.

TITLE: Dynamic Optical Camouflage Systems Based on Orientated Streptavidin Conjugated Phycoerythrin Protein in Monolayers

Lynne Samuelson, Dr., Pascal Miller, Dr., Dianne Galotti, Ms.,  
Rupmoni Sarma, Ms., Kenneth Marx, Dr., Jayant Kumar, Dr.,  
Sukant Tripathy, Dr., and David Kaplan, Dr.

ABSTRACT: New methodology for the two-dimensional ordering of a photodynamic protein system using the Langmuir-Blodgett technique is presented. Specific and nonspecific surface recognition of biotin on biotinylated monolayers by streptavidin and avidin conjugated phycoerythrin were investigated. Pressure-area isotherms displayed a biotin-streptavidin/avidin complex-dependent increase in surface pressure at expanded areas indicating protein adsorption. Spectral characterizations of thin films confirmed the presence of protein. Spectral studies, photoconductivity studies and immobilization and orientation studies with other photodynamic protein systems are continuing. The research provides the basis for a dynamic optical camouflage system, which will be capable of responding and changing with different environmental inputs. The extension of this technology to any biotin or avidin/streptavidin derivatized protein system is expected to lead to the fabrication of ultrathin, ordered, protein molecular assemblies with potential bioelectronic, optical and protein structure research applications.

BIOGRAPHY OF PRESENTER: Lynne A. Samuelson

PRESENT ASSIGNMENT: Biotechnology Division, Soldier Science Directorate, US Army Natick Research, Development and Engineering Center, Natick, MA and Visiting Scientist, Department of Chemistry, University of Lowell, Lowell, MA

DEGREES HELD: Ph.D., University of Lowell

Dynamic Optical Camouflage Systems Based on Oriented Streptavidin Conjugated  
Phycoerythrin Protein in Monolayers

Lynne A. Samuelson, Dr.<sup>\*</sup> Pascal Miller, Dr., Dianne M. Galotti, Ms.,  
Rupmoni Sarma, Ms., Kenneth A. Marx, Dr., Jayant Kumar, Dr.,  
Sukant K. Tripathy, Dr. and David L. Kaplan, Dr.<sup>\*</sup>

University of Massachusetts-Lowell,  
Lowell, Massachusetts 01854

<sup>\*</sup> U.S. Army Natick Research, Development and Engineering Center  
Natick, Massachusetts 01760

Introduction

The Langmuir-Blodgett (LB) technique has been used extensively in the past as a method to simultaneously orient and couple various organic surfactant materials to electronic and optical substrates for an extensive number of molecular device applications. Recently, there has been a great interest in extending this methodology to incorporate biological materials into these assemblies. The end purpose is to elicit the desired inherent, intelligent materials properties which nature has evolved and fine-tune them to serve in many biomedical research and biotechnology applications. In addition, such integrated assemblies should simultaneously provide unique biomimetic or simple environments for the study of protein structure. The LB technique has recently found much utility in this area as it allows both the orientation and spatial organization of protein assemblies at the molecular level into unique biomimetic environments (1).

Our research has involved the development of a novel methodology which incorporates and couples a highly pigmented, water soluble phycobiliprotein, phycoerythrin, into biomimetic LB monolayer films. The objective was to utilize the inherent light harvesting properties of this photodynamic protein for signal transduction in photonic devices employing dynamic optical mimic or contrast strategies. Such systems could be made capable of sensing a background image and translating it into a signal, which could then cause emission of a similar or contrasting image to the recorded background. The use of light-transducing proteins as active components of photonic devices, such as spatial light modulators and optically bistable devices based on bacteriorhodopsin, has recently been

reported to have performance levels competitive with commercially available devices (2,3,4). The phycobiliproteins represent another important class of photodynamic proteins and are expected to support applications similar to those demonstrated with bacteriorhodopsin.

Phycoerythrin is the outermost phycobiliprotein of the phycobilisome "Light Harvesting System" found in red and blue-green algae. Phycobilisomes are organized in membrane assemblies for maximum energy transfer (greater than 90% efficiency) and are composed of a series of phycobiliproteins; phycoerythrin (PE), phycocyanin (PC) and allophycocyanin (AP) and the final acceptor, chlorophyll (5,6,7). Phycoerythrin is the most highly pigmented phycobiliprotein and is characteristically fluorescent, with a very large Stoke's shift of 81 nm (495 nm excitation and 576 emission). In addition, the molecular environment of the chromophores and time-resolved fluorescence properties of this much studied antennae pigment are reasonably well understood (8,9). These unique optical properties in conjunction with the protein's stability and its ability to function efficiently in low light level situations, suggest promising new biomedical research, biotechnology and biosensor applications.

Phycoerythrin, however, is a large, bulky, water-soluble protein which alone will not form monolayer films using the Langmuir-Blodgett technique. Therefore, a modification of the LB technique was required which would serve to anchor the proteins to the monolayer. One recent approach has been to utilize the highly specific recognition of biotin on the trough subphase surface of biotinylated LB lipid monolayers by the proteins streptavidin and avidin (10). It was demonstrated that the proteins avidin and streptavidin form oriented two-dimensional protein domains (11) in LB monolayers. Avidin and streptavidin are tetramer proteins which possess four identical biotin binding sites that each have a high specificity for binding biotin functionalities. The binding affinity of biotin to these tetramer proteins is well known and once formed the complex is essentially irreversible with a stability comparable to that of a covalent bond (12,13). This specific binding affinity has already been employed in several biomedical research and biotechnology applications (14) and has recently been used to fabricate piezoelectric and electrochemical biosensors based on assembly on metallic surfaces for detection of a viral strand of DNA (15).

We describe here research directed toward the two-dimensional ordering and incorporation of the highly pigmented phycoerythrin protein using the LB technique. Biotinylated lipid monolayer films were first prepared at the air-water interface. Streptavidin- or avidin-conjugated phycoerythrin was then injected under the monolayers and incubated to allow for adsorption of the protein complex to the monolayer. Protein binding to the monolayer was observed through pressure-area isotherms and fluorescence spectroscopy. The role of specific versus nonspecific binding mechanisms in the conjugated protein systems was investigated. Using various controls, we have demonstrated that a specific biotin-streptavidin interaction is responsible for the protein binding, while both nonspecific and specific binding mechanisms occur with the biotin-

avidin complex. An extension of these studies has involved the utilization of the multiple biotin binding sites on the tetramer proteins to demonstrate a cassette type of attachment methodology for the incorporation of any biomolecular system which can be derivatized with biotin or avidin/streptavidin. This involved first binding streptavidin only to the biotinylated monolayer, followed by adsorption of biotinylated phycoerythrin and then similar characterization.

## Methods and Materials

The biotinylated phospholipid, N-(biotinoyl)dipalmitoyl-L- $\alpha$ -phosphatidylethanolamine, triethylammonium salt (B-DPPE), R-Phycoerythrin biotin conjugate (B-PE), avidin (egg white) and streptavidin (St) were purchased from Molecular Probes (Eugene, Oregon) and used as received. Dipalmitoyl-L- $\alpha$ -phosphatidylethanolamine, triethylammonium salt (DPPE), was purchased from Avanti Polar Lipids (Pelham, Alabama) and was used as received. The unconjugated phycoerythrin (PE) and avidin (Av-PE), and streptavidin conjugated R-Phycoerythrin (St-PE), proteins were purchased from Biomeda Corporation (Foster City, California) and were used as received. The B-DPPE and DPPE spreading solutions were prepared as 0.5 mM solutions in Aldrich HPLC chloroform. The subphase was composed of an aqueous solution of 0.1 mM sodium phosphate, 0.1 M NaCl, at pH 6.8. The water in all cases was purified by a Milli-Q water filtration system, Millipore, with a resistivity greater than 18 M $\Omega$ /cm. The avidin, streptavidin, B-PE, Av-PE and St-PE proteins were diluted in the buffered subphase before addition to the trough.

Monolayer studies were carried out on Lauda MCW Filmwaag troughs with a surface area of approximately 930 cm<sup>2</sup>. For each pressure-area isotherm, the lipid was spread from a 0.5 mM chloroform solution and 0.1 mg of the protein in 5 ml of the buffered subphase was injected under the spread film and then left to incubate for 2 hours at 30° C. In the case of the B-PE, 0.1 mg of the B-PE was injected under the B-DPPE after the two hour tetramer protein incubation period and allowed to incubate for two more hours before compression. Compression was then carried out at a speed of approximately 2 mm<sup>2</sup>/min until collapse of the film was observed. For transfer studies, the lipid was spread, followed by protein introduction and incubation in the expanded state for 2 hours and then compressed to an annealing surface pressure of approximately 15 mN/m for deposition. Monolayer films were then transferred onto glass solid supports, with transfer ratios ranging from 100 to 150 %, for fluorescence spectroscopy.

Fluorescence spectra were obtained using an argon ion laser (coherent, Innova 90E), with 10 mW laser power as the pumped light source as shown schematically in Figure 1. The chosen wavelength of excitation was 496.5 nm, which is close to the absorption peak of the native protein and the emission was scanned from 500 to 700 nm. The laser beam was collimated with a cylindrical lens and the illuminated area of the sample was imaged



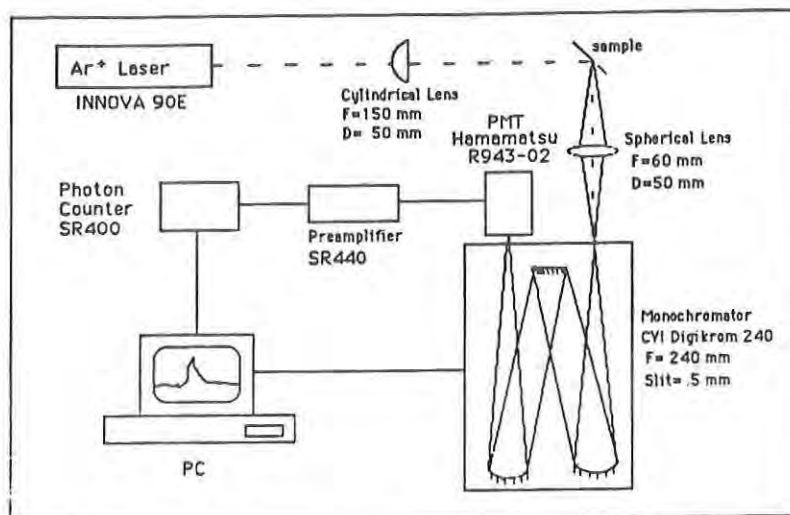


Figure 1. Schematic of Fluorescence Setup.

with a 1 x 1 ratio, onto the entrance slit of the monochromator. A 500  $\mu\text{m}$  slit width of the monochromator provided a 6  $\text{\AA}$  spectral resolution. The signal was detected with a photomultiplier tube (PMT), cooled to  $-20^\circ\text{C}$ , and then sent to a photon counter, with an integration time of 1 second. Background correction for the glass solid support was performed.

## Results and Discussion

Pressure-area isotherms of the protein-injected monolayers may be compared to that of the pure phospholipid to establish the attachment of the proteins to the monolayer films subsequent to incubation. Figure 2 shows the structure of the biotinylated phospholipid (B-DPPE), and the pressure-area isotherms of B-DPPE and protein-injected B-DPPE (PE, Av-PE and St-PE). As shown, all four isotherms give a relatively steep slope after 15 mN/m which corresponds to an area per lipid molecule of approximately 100  $\text{\AA}^2$  prior to film collapse. It is interesting to note that for the injected Av-PE or St-PE monolayers, a significant increase in surface pressure of the lipid in the gas-expanded phase was observed. This suggests that the conjugated protein systems are interacting with the biotinylated lipid and causing an expansion of the B-DPPE monolayer. Upon further compression, the lipids and/or bound protein conjugates begin to preferentially orient and the isotherms overlap that of the pure B-DPPE. This indicates that the bulky protein systems may be reorienting down into the aqueous subphase, thus not causing any expansion of the monolayer at higher surface pressure. A schematic illustrating the possible spatial organization and reorientation of these materials during monolayer

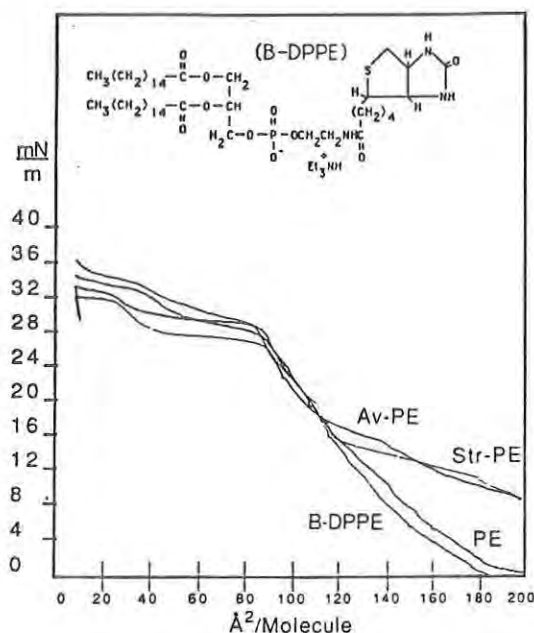


Figure 2. Isotherms of B-DPPE and Protein Injected B-DPPE (PE, Av-PE and St-PE).

compression is shown in figure 3.

In contrast to the St-PE and Av-PE conjugates, the unconjugated PE injected monolayer displayed very little change in the Figure 2 isotherm in comparison to the pure B-DPPE. Since the PE does not have any tetramer protein bound to it, this further supports the idea

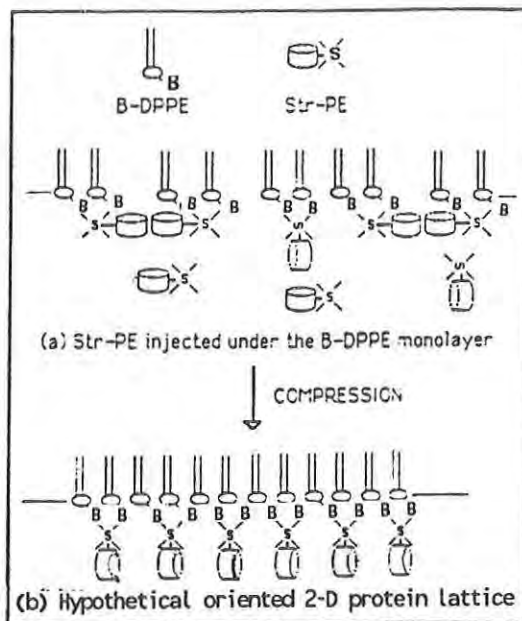


Figure 3. Idealized Schematic of the Two-Dimensional Ordering of Derivatized Protein Monolayers onto a Biotinylated Lipid LB Film.



that the biotin binding sites of the avidin and streptavidin tetramer proteins are responsible for adsorption. However, the question is raised as to whether the protein adsorption proceeds through an entirely specific (biotin-avidin or -streptavidin) mechanism or both specific and nonspecific binding mechanisms. Fluorescence spectroscopy was used to address this issue and confirm the presence of bound protein to the monolayer films.

The fluorescence spectra of a B-DPPE monolayer with St-PE, a B-DPPE monolayer with PE and a monolayer of DPPE (not biotinylated) with St-PE are compared in Figure 4. Therefore, each control was missing one component of the biotin-tetramer protein complex. As shown, the B-DPPE/St-PE monolayer gives a strong emission at 576 nm which corresponds to the fluorescence spectrum of the native phycoerythrin monolayer. In comparison, the unconjugated phycoerythrin monolayer shows no fluorescence signal at 576 nm suggesting that the streptavidin is, in fact, necessary for binding of the phycoerythrin to the monolayer. In addition, the monolayer where St-PE was injected under a monolayer of the parent lipid (DPPE) containing no biotin showed no fluorescence emission at 576 nm, providing further evidence that the biotin-streptavidin complexation is essential in the protein-binding mechanism. Films of Av-PE bound to a monolayer of B-DPPE exhibited similar fluorescence properties (data not shown). Spontaneous adsorption of protein onto the bare clean glass surface was also ruled out through fluorescence spectroscopy (16).

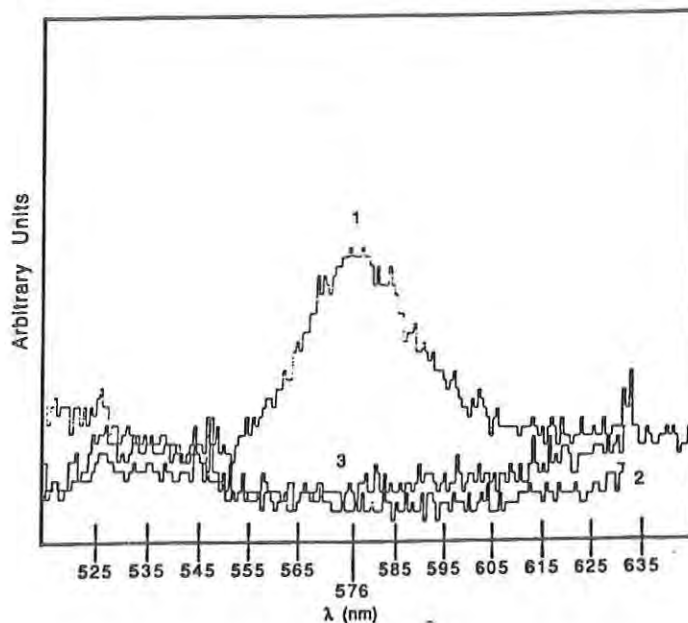


Figure 4. Fluorescence Spectra of Protein-Adsorbed LB Films: 1, B-DPPE + St-PE; 2, B-DPPE + PE; 3, DPPE + St-PE.

A question is raised, however, as to whether the protein adsorption to the monolayer proceeds entirely through the specific biotin-streptavidin or avidin mechanism or also includes nonspecific binding mechanisms. To address this issue, similar studies were carried out with the Av-PE injected monolayer protein system. The structure of avidin is post translationally modified by surface carbohydrate residues and known to complex to the biotin lipid monolayer by both specific and nonspecific (carbohydrate and electrostatic) binding mechanisms (17). Streptavidin, however, is not chemically modified by carbohydrate, and binds by what appears to be only the specific mechanism (10).

The fluorescence spectra in figure 5 summarize and support these binding mechanisms as a direct comparison is made of the fluorescence of B-DPPE monolayers with the three phycobiliprotein systems, Av-PE, St-PE and PE. As shown, the Av-PE injected monolayer gives a strong emission at 576 nm, which indicates binding of the protein to the monolayer. This emission however, is observed to be considerably stronger in comparison to that of the St-PE monolayer. Such a difference in intensity would be expected if both specific and nonspecific binding of the avidin conjugated protein system to the monolayer was occurring. Evidence to support the nonspecific binding of the Av-PE electrostatic-based complex was obtained when NaCl was added to the aqueous subphase (18). A decrease in emission intensity at 576 nm from the NaCl containing subphase (results not shown) demonstrates that charge-charge interactions contributing to the nonspecific adsorption of avidin are occurring and may be decreased with the addition of NaCl (10).

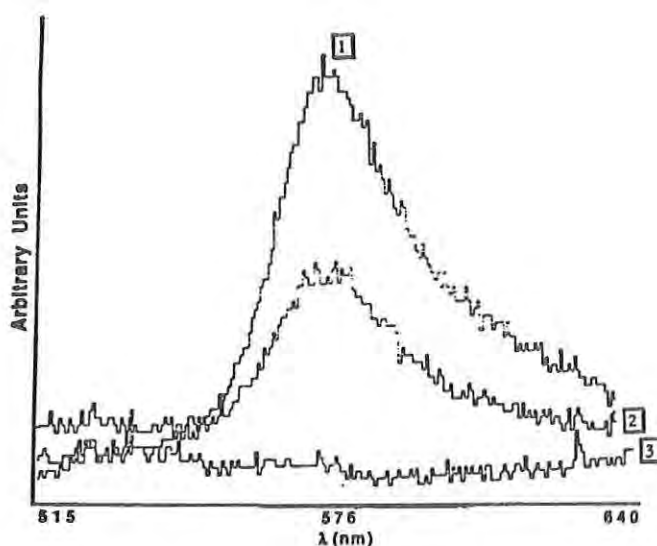


Figure 5. Fluorescence Spectra of Protein-Adsorbed LB Films: 1, B-DPPE + Av-PE; 2, B-DPPE + St-PE; 3, B-DPPE + PE.

These results demonstrated for the first time the formation of monomolecular films of the photodynamic phycobiliprotein, phycoerythrin. However, it is of interest to employ the versatility inherent in the multiple biotin binding sites of the tetramer proteins for the incorporation and organization of various interacting biomolecules for biomimetic studies. Therefore, a cassette type of attachment methodology was investigated which involved first binding streptavidin only to the biotinylated monolayer, followed by adsorption of biotinylated-phycoerythrin (B-PE). A comparison of the pressure-area isotherms of B-DPPE, B-DPPE/streptavidin, B-DPPE/B-PE and B-DPPE/streptavidin/B-PE are given in figure 6. These isotherms differ from our previous conjugated protein system (St-PE) results, in that there is an increase in area throughout the majority of the compression cycle, not just in the expanded phase, for the B-DPPE/streptavidin and B-DPPE/St/B-PE. This continuous expansion suggests that the streptavidin and B-PE are interacting with the monolayer film but do not reorient upon compression in the same manner as the St-PE system.

A possible explanation for this may be that the streptavidin alone is considerably smaller in size than the conjugated St-PE system, and thus upon exposure to the B-DPPE monolayer the streptavidin is more mobile and able to position itself for complexation completely saturating the biotin functionalities in the monolayers. When the bulkier B-PE is injected, it subsequently searches out the free biotin binding sites which are already positioned in the expanded monolayer. The protein interaction with the monolayer is then enhanced and results in an even more significant increase in area during the compression cycle, as observed. Thus it appears that the bulkiness of the protein initially interacting with the monolayer plays a significant role in the monolayer formation. In the case of the

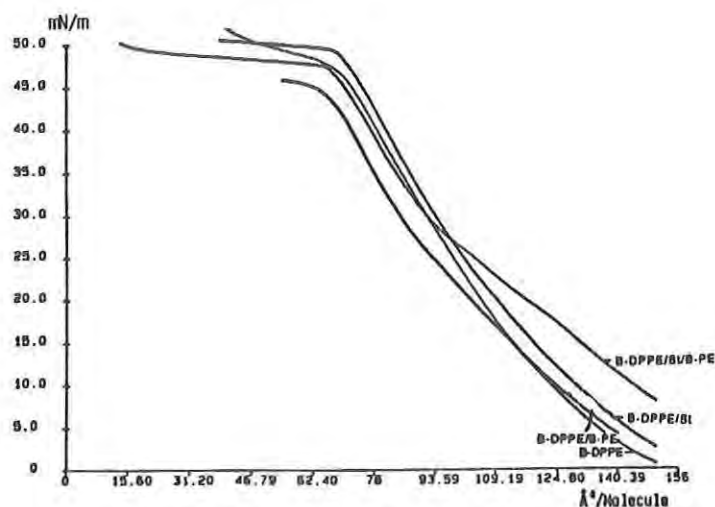


Figure 6. Isotherms of B-DPPE, B-DPPE/B-PE, B-DPPE/St, B-DPPE/St/B-PE.

B-PE-only injected monolayer, it is interesting to note that little or no expansion is observed in comparison to the streptavidin-injected monolayers. This again suggests that it is the streptavidin-biotin complexation which is responsible for protein binding.

To confirm the binding of the B-PE to the monolayer, fluorescence spectroscopy was again carried out on transferred samples. Figure 7 shows the fluorescence spectrum of a monolayer of B-DPPE, to which streptavidin and B-PE were sequentially injected. As shown, the B-DPPE/St/B-PE monolayer gives a distinct emission peak at 576 nm. This is direct evidence of complexation of the biotinylated phycoerythrin to the monolayer and supports the cassette attachment methodology. Glass slides which were vertically passed through the subphase only were used as controls. These samples gave no fluorescence signal at 576 nm ruling out spontaneous nonspecific adsorption of protein to the clean glass surface. Figure 8 gives a comparison of the monolayer fluorescence versus that of a buckled film. As expected, the fluorescence intensity from the collapsed monolayer is much greater than that of the true monolayer. This is further evidence that the phycoerythrin is incorporated into the entire monolayer film (19).

One of the next steps in this research is to utilize this highly selective protein attachment methodology for the organization and immobilization of specific protein systems into intelligent material architectures. Here, one could make use of the naturally occurring redox reactions, electron mediation of pH changes that occur with various photodynamic protein systems such as bacteriorhodopsin and phycobiliproteins. Scattered incident radiation from the environment for example may be sensed and subsequently used to evoke a color, electronic, or optical change. Hierarchical arrangement of photodynamic proteins

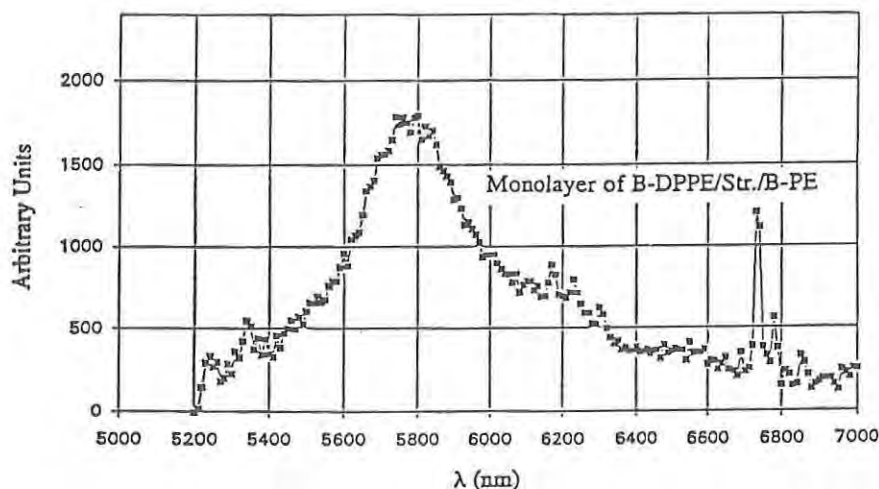


Figure 7. Fluorescence Spectrum of a Monolayer of B-DPPE/Streptavidin/B-PE.

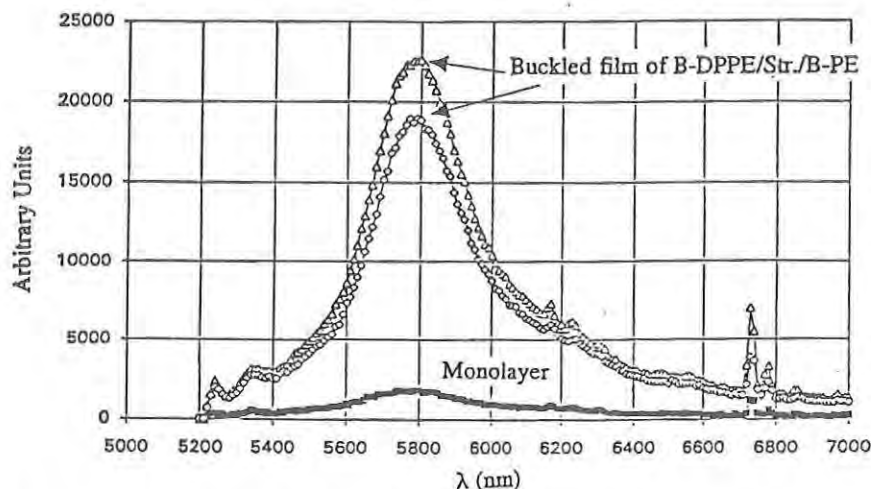


Figure 8. Fluorescence Spectra of a Monolayer and Buckled Film of B-DPPE/St/B-PE.

using the cassette approach may be utilized to realize the optimum signal transduction. Appropriately designed microelectrode interfaces and sensing systems may be embedded underneath the protein arrays. Mimicking the extremely efficient energy transfer mechanism of the phycobilisome by preparing multilayer arrays sequentially composed of phycoerythrin, phycocyanin, and allophycocyanin should also be possible.

## Conclusion

It has been shown that the photodynamic "antennae" protein phycoerythrin when conjugated to either of the tetramer proteins streptavidin or avidin will bind to a biotinylated phospholipid monolayer at the air-water interface. Fluorescence measurements of transferred monolayers confirm the presence of phycoerythrin and provide evidence that the avidin-conjugated system may bind by both specific and nonspecific mechanisms, while the streptavidin systems bind via only a specific mechanism. An extension of these studies has involved demonstration of a cassette attachment methodology through the sequential binding of streptavidin and biotinylated phycoerythrin to the biotinylated monolayers. These results establish a general approach for the monolayer assembly of any biomolecular system, which may be derivatized with biotin or avidin/streptavidin such as photodynamic protein assemblies, enzymes, antibodies, and genetic probes. The multiple binding sites on the tetramer proteins should allow for the incorporation of multiple interacting biomolecules such that ultrathin dynamic optical camouflage and biosensor devices may be designed and fabricated.



1. Reichert, W.M.; Bruckner, C.J.; and Joseph, J. *Thin solid Films* **1987**, 152, 345.
2. Birge, R.R. *Annu. Rev. Phys. Chem.* **1990**, 41, 683.
3. Sosken, M.S.; Taranenko, V.B. *Proceedings of the Conference on Lasers and Electro-Optics*, Anaheim, CA **1990**.
4. Birge, R.R. *Bull. Am. Phys. Soc.* **1991**, 36 (No. 3), 441.
5. Gantt, E. *Bioscience* **1975**, 25 (12), 781.
6. Gantt, E. *Annu. Rev. Plant Physiol.* **1981**, 32, 327.
7. Glazer, A.N. *Annu. Rev. Biophys. Biophys. Chem.* **1985**, 14, 47.
8. Holzwarth, A. *Q. Rev. Biophys.* **1989**, 22 (No. 3), 239.
9. Schirmer, T.; Huber, R.; Schneider, M.; Bode, W.; Miller, M.; Hackert, M.L. *J. Mol. Biol.* **1986**, 188, 651.
10. Blankenburg, R.; Meller, P.; Ringsdorf, P.; Salesse, C. *Biochemistry* **1989**, 28 (No. 20), 8214.
11. Darst, S.A.; Ahlers, M.; Meller, P.H.; Kubalek, E.W.; Blankenburg, R.; Ribi, H.O.; Ringsdorf, H.; Kornberg, R.D.; *Biophys. J.* **1991**, 59 (2), 387.
12. Green N.M.; *Adv. Protein Chem.* **1975**, 29, 85.
13. Weber, P.C.; Ohlendorf, P.C.; Wendoloski, J.J.; Salemme, F.R. *Science* **1989**, 243, 85.
14. Wilchek, M.; Bayer, E.A. *Trends in Biochem. Sci.* **1989**, 14, 408.
15. Ebersole, R.C.; Miller, J.A.; Moran, J.R.; Ward, M.D. *J. Am. Chem. Soc.* **1990**, 112, 3239.
16. Samuelson, L.A.; Miller, P.; Galotti, D.M.; Marx, K.A.; Kumar, J.; Tripathy, S.K.; Kaplan, D.L. In *Proteins-Structure, Dynamics and Design*, Renugopalakrishnan, V.; Carey, P.R.; Smith, I.C.P.; Huang, S.G.; Storer, A.C. (ed) **1991**, ESCOM, Leiden, The Netherlands, 160.
17. Gimlick, R.K.; Giese, R.W. *J. Biol. Chem.* **1988**, 263, 210.
18. Samuelson, L.A.; Miller, P.; Galotti, D.M.; Marx, K.A.; Kumar, J.; Tripathy, S.K.; Kaplan, D.L. *Langmuir* **1992**, 8, 604.
19. Samuelson, L.A.; Yang, Y.; Marx, K.A.; Kumar, J.; Tripathy, S.K.; Kaplan, D.L. *Biomimetics*, **In Press**.



KEITH, et al.

TITLE: Characterization of Mollusc Shell Matrix Proteins--  
Development of a Model for Biomimetic Ceramics  
Julia Keith, Mrs., Scott Stockwell, Dr., Derek Ball, Dr.,  
Kelly Napier, MAJ, Wayne Muller, Mr.

ABSTRACT: The production of calcium carbonate shells by molluscs involves a control over crystal morphology, size, density, and orientation at the molecular level that is presently unattainable in conventional ceramics. The organic portion of the shell makes up less than 1% by weight of the total structure, but is believed to be the source of this control. However, little is known about the nature of this material. Shell matrix from Mytilus edulis, the blue mussel, was isolated and separated into soluble and insoluble fractions. These fractions were then separated using Sodium Dodecylsulfate-Polyacrimide Gel Electrophoresis (SDS-PAGE) and High Performance Liquid Chromatography (HPLC) into discrete molecular weight proteins and evaluated for amino acid composition, N-terminal sequence, calcium binding and effects on crystallization of  $\text{CaCO}_3$  from solution, in order to determine which proteins might be important elements in the design of a biomimetic system. The results of these analyses were used in the development of a synthetic model using Langmuir monolayer techniques to mimic the natural system. Characterization of the products of this synthetic system will further the development of a model for biomimetic ceramics.

BIOGRAPHY OF PRESENTER: Julia Keith

PRESENT ASSIGNMENT: Biotechnology Division, Soldier Science  
Directorate, US Army Natick Research, Development and Engineering Center,  
Natick, MA 01760-5020

DEGREES HELD: BS Biology; BS Chemistry; Presently enrolled in MA  
Chemistry, Boston University

## Characterization of Mollusc Shell Matrix Proteins--Development of a Model for Biomimetic Ceramics

Julia Keith, Mrs., Scott Stockwell, Dr., Derek Ball, Dr., Kelly Napier, MAJ,  
Wayne Muller, Mr., Biotechnology Division, US Army Natick RD&E Center,  
Natick, MA 01760-5020

### Introduction

The formation of molluscan shell structures, composites containing calcium carbonate, involves control over crystal morphology, size, density, and orientation at the molecular level that is at present unattainable synthetically. The organic portion of most mollusc shells, consisting of 0.1 to 5 % by weight of the total structure [19], is postulated to be the source of this control [24,28,54,55]. Tight control over design at the molecular level is important in the development of new high-performance materials, especially ceramics. It may be possible to obtain this level of control by modeling or mimicking the natural system. In order to successfully mimic a system researchers must first understand its essential components. This work is an examination of the organic portion of the shell of the blue mussel (*Mytilus edulis*) with a view toward applying the molecular level control of the natural system to the formation of conventional and novel ceramic precursors.

A review of the literature shows a variety of compositions and functionalities assigned to this organic portion, termed the matrix, including proteins; specifically, proteoglycans [52], phenyloxidase crosslinked proteins [16], and phosphoproteins [36,40,41], as well as polysaccharides, such as chitin [20,34], sulfated mucopolysaccharides [14,38], neutral and amino sugars [4,13,19], and lipids [4]. Characterization of the matrix composition varies with species of mollusc [19,24,33,46] and methodology [23]. Past attempts to characterize this organic matrix have focused on a soluble proteinaceous fraction with acidic functionality that inhibits crystallization [37,44,46], isolated mainly from *Mercenaria mercenaria*, *Crassostrea virginica*, or *Mytilus californianus* [13,24,46].

*M. edulis* was chosen for investigation in part because of the complexity of the shell, which consists of an inner nacreous layer of aragonite, a pallial

calcitic layer, and an outer prismatic layer of calcite [10,17,18,21]. It was believed that this level of structural complexity would lead to a better understanding of the complexity of control attributed to these organic matrices.

This investigation analyzed the organic components and purified individual proteins from the matrix. Analysis of the protein and polysaccharide portions of this organic matrix has revealed many components, including several proteins of discrete molecular weight, amino acid composition and glycosylation pattern. The proteins were analyzed for amino acid content, glycosylation, N-terminal sequence, and calcium binding affinity using microanalytical techniques. It was hoped that these data would contribute to an understanding of the relationships between protein structure and mineral binding function. This correlation will be further clarified once sequence data on the isolated proteins is completed. Furthering the complexity of the matrix and its interactions was the absence of a polysaccharide component (chitin) generally inferred to be present.

The natural system was then modeled, using a monolayer of stearic acid over a saturated  $\text{CaCO}_3$  subphase, in an attempt to ascertain the degree of control possible over crystallization in a simple *in vitro* system. The preliminary results suggest that such control may be possible.

## Materials and Methods

### Matrix Purification

Live specimens of *M. edulis* were collected locally (Marshfield, MA), maintained in seawater and processed within 24 hours of collection. Soft tissue was removed, the shells were scrubbed with 5% NaOH to remove the periostracum and any adhering organisms and then lightly crushed in a mortar and pestle. The crushed shell was ground to a fine powder in a freezer mill under liquid nitrogen and stored at  $-70^\circ\text{C}$ .

Two methods were used for extraction of the matrix. Initially, extraction was carried out over three days by stirring 40 g of powdered shell at  $4^\circ\text{C}$  in 2 liters of buffer modified from Butler [7] that contained per liter: 382.2 g guanidine-HCl; 95 g ethylenediamine tetraacetic acid (EDTA); 13.12 g 6-aminohexanoic acid; 0.78 g benzamidine-HCl; 0.17 g phenylmethylsulfonyl fluoride and 3 mg aprotinin. The protease inhibitor aprotinin replaced the soybean trypsin inhibitor and pepstatin in Butler's [7] extraction, and the EDTA concentration was reduced from 0.5M to 0.25M to help maintain solubility of the material. Higher yields of protein were observed when the permanent reducing agent sodium iodoacetate was added at 0.018 g/liter after the method of Butler, but proteins isolated under these conditions were

unsuitable for characterization dependent on charge or isoelectric point because of the irreversible replacement of sulfhydryl groups with acetate groups. Therefore, the sodium iodoacetate was used only for certain preparations. Two liters of solution can be used to process 40 g of powdered shell in two to three days.

The extract was centrifuged at 10,000 rpm for 20 minutes to separate the soluble matrix (supernatant) from the insoluble matrix (pellet). Following the methodology of Sikes and Wheeler [37], the supernatant was filtered through a Mini-Tan<sup>TM</sup> (Millipore, Milford, MA) tangential flow membrane cassette with a molecular weight cutoff of 10 kilodaltons (kDa) and concentrated with the same apparatus to a volume of 100 mL by recycling the retentate. The preparation is dialyzed against Milli-Q<sup>TM</sup> water (Millipore, Milford, MA) and lyophilized. For complete removal of EDTA for calcium binding assays, the lyophilized sample was redissolved in 10 mL of Milli-Q<sup>TM</sup> water, dialyzed and lyophilized with a final yield of about 40 mg from 40 g of shell. This process rendered some of the previously soluble material insoluble.

The second extraction procedure, as described by Furlong and Humbert [15], was adopted because of its simplicity. Although the resulting material is the same (as confirmed by gel electrophoresis), it was much easier to work with, eliminating many of the purification steps subsequent to extraction. In this procedure, 30 grams of powdered shell were added to 1 L of 5% acetic acid in a vacuum flask with stirring at room temperature. Vacuum was applied to remove CO<sub>2</sub> and push the equilibrium toward demineralization. After two to three days, the mixture was centrifuged as in the EDTA procedure above and the pellet resolubilized in Milli-Q<sup>TM</sup> water. Any material which did not redissolve in the water was considered insoluble matrix. No protein was present in the supernatant as determined by modified Lowry assay [35].

### Matrix Characterization

Protein content of the purified soluble matrix material was determined by Lowry assay with a deoxycholate trichloroacetic acid precipitation [35]. Protein content of purified insoluble matrix material was determined by elemental carbon, hydrogen, and nitrogen analysis performed by Oneida Research Services (Whitesboro, NY).

Polyacrylamide gel electrophoresis and Western blotting to PVDF membranes were performed on a Novex<sup>TM</sup> Gel Electrophoresis system (Novel Experimental Technology, Encinitas, CA), with Novex<sup>TM</sup> Tris-Gly and Tricine buffers and gradient gels. In an attempt to identify calcium binding proteins, SDS-PAGE gels were also stained with Stains-all (1-ethyl-2-(3-[1-



ethylnaphtho(1,2-d)-thiazolin-2-ylidene]-2-methylpropenyl)naphtho(1,2-d)-thiazolium bromide) (Sigma Chemical Co, St. Louis, MO) [9], or with Alcian blue (Sigma Chemical Co, St. Louis, MO) to identify phosphoproteins [8].

Amino acid analysis of the purified matrix as well as protein bands purified by PAGE was performed by derivatization after hydrolysis and reverse phase HPLC using the Waters Pico-Tag™ method (Waters, Division of Millipore, Milford, MA). Analysis of the individual protein bands transferred to PVDF membranes was by the method of LeGendre and Matsudaira [25], modified by Robert Sherwood of the Analytical and Synthesis Facility at Cornell University, while the standard manufacturer's protocols [12] were used for the total soluble and insoluble matrix proteins. Controls consisting of a section of membrane without protein were run with each sample to correct for background.

Glycosylation of purified matrix proteins was determined by microanalysis by gas liquid chromatography (GLC), based on the method of Chaplin [11]. 20  $\mu$ L of 0.001 M mesoinositol was added to <1 mg of material, either shell powder, purified matrices or protein bands excised from PVDF membranes, and the mixtures dried over  $P_2O_5$  in an aspirated vacuum chamber. Three percent methanolic hydrogen chloride, 150  $\mu$ L, was added and the mixtures were stirred magnetically and heated at 70°C overnight in a Reacti-Therm Heating/Stirring Module in vials capped with Teflon-lined septa. T-butanol, 30  $\mu$ L, was added to each vial and volatiles were removed with a stream of oxygen-free nitrogen at room temperature. To ensure complete N-acetylation of any amino sugars present, re-N-acetylation was carried out by addition of methanol, 150  $\mu$ L; pyridine, 15  $\mu$ L; and acetic anhydride, 15  $\mu$ L. After 15 minutes at room temperature, volatiles were again removed with oxygen-free nitrogen. Tri-Sil Z (Pierce Chemical Co., Rockford, IL) (100  $\mu$ L) was added to each vial and the mixtures were stirred for one hour at room temperature. Controls consisted of known glycoproteins and PVDF membrane.

Gas liquid chromatographic analysis was performed on a Hewlett Packard (Andover, MA) gas chromatograph, Model 5880A, equipped with a flame-ionization detector and a J&W Scientific (Rancho Cordova, CA) fused silica capillary column, 30m x 0.26mm i.d.: liquid phase DB1 (equivalent to SE 30), film thickness 0.1  $\mu$ m.

### Calcium Binding

Calcium binding was assayed using a modification of a procedure from Maruyama et al. [31]. Proteins purified from the matrix were solubilized and blotted onto nitrocellulose and dried at room temperature. The nitrocellulose was washed for one hour in 60 mM KCl, 5 mM  $MgCl_2$  and 10 mM imidazole-

HCl (pH 6.8). The membrane was washed for 15 minutes in the same buffer containing 5 mM  $^{45}\text{Ca}^{2+}$  and rinsed with 50% EtOH. After drying, the membrane was placed in a film cassette with X-ray film and exposed for 24 to 48 hours before developing. Phosvitin (Sigma Chemical Co, St Louis, MO), an eggshell protein, was used as a positive control and aprotinin (Sigma Chemical Co, St. Louis, MO), a protease inhibitor, as the negative control. Relative affinity for calcium in comparison to phosvitin was determined by densitometric scan of the developed film with a Pharmacia-LKB Ultrascan XL scanning laser densitometer (Pharmacia LKB, Uppsala, Sweden).

### Model System

$\text{CaCO}_3$  was crystallized under Langmuir monolayers of stearic acid according to the methodology of Mann, et al. [30]. A Lauda film balance, model D (Brinkmann Instruments, Westbury, NY) with temperature control was used to create solid-phase monolayers of stearic acid over supersaturated calcium carbonate (10 mM) at 20, 30 and 35°C. The monolayers and any attached crystals were transferred onto quartz slides, with control slides made from sampling portions of the same trough, which did not support a monolayer. SEM micrographs were taken of random portions of the slides at the U.S. Army Materials Technology Laboratory in Watertown, MA and crystal types present in the photographs were counted using a 6200 point grid.

### Results and Discussion

Table 1. Elemental Analysis of Insoluble Matrix.

| Sample #                 | % carbon | % hydrogen | % nitrogen |
|--------------------------|----------|------------|------------|
| 1                        | 41.64    | 5.65       | 17.23      |
| 2                        | 41.44    | 5.59       | 17.24      |
| Total protein (average)* |          | high: 107% | low: 91%   |

\* Based on conversion of nitrogen x 6.25% for high value, 5.30% for low [3]. These values cover most proteins, including structural proteins like silk and collagen.

Total protein is calculated by using an average value of 6.25% nitrogen for protein, which can vary with amino acid content, explaining why total protein is greater than unity.

Total soluble protein content of the shell is 0.3-0.5% by weight when determined by Lowry assay. Although the values from the Lowry assays were used in subsequent purification steps, visual inspection of gel staining suggested that the Lowry determination of soluble protein content may be low.



Lower values can be accounted for by the fact some proteins have a differential response to the assay [35]. The precipitation step allows the Lowry assay to be used in the presence of EDTA and other interfering substances [35], but can reduce recovery by half (Sigma procedure #P 5656). Insoluble material, determined to be 100% protein by elemental analysis (Table 1), accounts for 2-5% of the shell by weight; together, the soluble and insoluble proteins make up about 3-5% of the shell.

The soluble protein portion of the matrix has four major protein components and several minor protein components. The four major protein components were identified by SDS PAGE; in the absence of reducing agents they run at about 200 kDa, 95 kDa, 32 kDa and 21 kDa (Figure 1). Adding 2-mercaptoethanol to the sample buffer eliminates the 200 kDa band, greatly intensifies the 95 kDa band, and eliminates shadow bands on either side of the 21 kDa band. This suggests that the 200 kDa protein may consist of two subunits of the 95 kDa protein. The elimination of the shadow bands on either side of the 21 kDa band by reducing agent also suggests that these two bands are conformational isomers of the major band at 21 kDa.



Figure 1. Tricine SDS 10-20% gradient gel, 125 volts, 90 minutes, 6  $\mu$ g protein loaded per lane, stained with Coomassie Blue. Lanes 1,8,14 are Rainbow™ molecular weight markers (Amersham, Arlington Heights, IL), sizes as indicated; lanes 2-7 are run in the presence of 8% 2-mercaptoethanol.

Amino acid analysis of the soluble proteins is reported in Table 2. The lower molecular weight proteins have similar compositions with an abundance of Gly, Glx and Ser residues. The composition of the total soluble matrix (Table 3) is over 40% small side chain amino acids (Gly, Ala, Ser), with another 20% Asx and Glx. The amino acid composition of the 95 kDa protein is significantly different from the 32 and 21 kDa proteins, containing 46% Asx

KEITH, et al.

and Glx residues.

Table 2. Amino acid composition of individual proteins from the mussel soluble matrix and comparison with sea urchin matrix.

| amino acid | 95kDa | 32 kDa | 21 kDa | 50 kDa protein from sea urchin |
|------------|-------|--------|--------|--------------------------------|
| Gly        | 1.0   | 17.7   | 24.2   | 8.0                            |
| Glx        | 18.8  | 13.3   | 6.1    | 12.9                           |
| Ser        | 6.0   | 12.1   | 9.9    | 5.4                            |
| Asx        | 18.5  | 9.5    | 8.2    | 15.4                           |
| Ala        | 11.9  | 6.2    | 8.6    | 8.9                            |
| Leu        | 8.9   | 5.4    | 7.7    | 2.9                            |
| Arg        | 7.0   | 4.9    | 3.9    | 4.7                            |
| Val        | 4.3   | 4.8    | 4.3    | 11.4                           |
| Lys        | 5.3   | 4.7    | 4.1    | 1.1                            |
| Pro        | 3.4   | 4.5    | 5.0    | 7.4                            |
| Thr        | 3.9   | 4.4    | 4.3    | 4.5                            |
| Ile        | 3.8   | 3.1    | 3.8    | 3.6                            |
| Phe        | 1.3   | 2.7    | 4.0    | 2.5                            |
| His        | 1.3   | 2.3    | 1.1    | <1.0                           |
| Tyr*       | 2.2   | 2.0    | 3.5    | 1.6                            |
| Met*       | 3.1   | 1.6    | <1.0   | 2.5                            |
| Cys*       | <1.0  | <1.0   | <1.0   | 1.4                            |
| Trp**      | -     | -      | -      | 6.3                            |

\*Indicates amino acids most sensitive to PVDF membrane procedure.

\*\*Amino acid not detected by Pico-Tag™ analysis.

Figures given are mole %, not adjusting for Trp, which cannot be detected by Pico-Tag™ analysis. Sea urchin figures are from the actual gene sequence [39].

Amino acid analyses of some fractions of the molluscan matrix have been reported. These include analyses of *Mercenaria mercenaria*, *Mytilus californianus*, *M. edulis*, *M. veridus*, *Protothaca grata*, *Sanguinolaria nuttalli*, *Tagelus californianus* and *Tivella argentina* [19]; *Campeloma decisum*, *Littorina irrorata*, *Nassarius obsoletus*, *Pila virens*, *Polinices duplucatus*, *Pomacea paludosa* and *Thais floridana* [32,33]; *Mercenaria mercenaria* [13]; *Crassostrea irredescens*, *C. virginica*, *Mercenaria mercenaria*, and *Nautilus pompilius* [46]; *Neotrigonia margaritacea* and *Scabrotrigonia thoracica* [47]; *Nautilus repertus* [45]; *Crassostrea gigas* [22]; and *C. virginica* [54]. None of these analyses is of individual proteins, such as those reported here.

The composition of the total soluble matrix (Table 3) bears some similarity to the spicule matrix from *Strongylocentrus purpuratus* [5], especially in the percentages of Gly, Ala, Ser, Asx, and Glx, which make up 60% of the two matrix fractions. The amino acid composition of the 95 kDa protein suggests that it may be the acidic fraction often referred to in the literature as having an influence on crystallization [1,2,6,44]. Some researchers report difficulty in staining these types of acidic proteins [45]; however, when poor staining was observed in the current study, it was often attributable to insufficient protein concentration. Butler et al. [8] was able to stain acidic rat glycoproteins with Coomassie blue and Weiner et al. [48] had earlier reported staining of *Mytilus* proteins with Coomassie blue. Comparison of the 95 kDa protein with the 50 kDa protein from sea urchin spicules sequenced by Sucov et al. [39] (Table 2) shows similar amounts of Glx, Asx and Ala; the only significant differences between them are the percentages of Val and Gly residues.

Table 3. Comparison of amino acid compositions of matrix with other proteins.

| amino acid | Insoluble matrix | Spider dragline silk* | Sea urchin spicule matrix** | Soluble matrix |
|------------|------------------|-----------------------|-----------------------------|----------------|
| Gly        | 27.8             | 37.1                  | 21.3                        | 20.5           |
| Ala        | 26.1             | 21.1                  | 8.3                         | 11.6           |
| Ser        | 10.9             | 4.5                   | 12.5                        | 9.3            |
| Asx        | 10.6             | 2.5                   | 11.0                        | 13.0           |
| Leu        | 4.9              | 3.8                   | 4.2                         | 5.2            |
| Glx        | 3.5              | 9.2                   | 12.1                        | 7.5            |
| Arg        | 2.6              | 7.6                   | 2.3                         | 4.4            |
| Lys        | 2.5              | <1.0                  | 3.3                         | 5.2            |
| Val        | 1.9              | 2.9                   | 1.3                         | 2.5            |
| Ile        | 1.6              | <1.0                  | 2.5                         | 5.2            |
| Thr        | 1.3              | 1.7                   | 4.4                         | 2.8            |
| Pro        | 1.0              | 4.3                   | 4.5                         | 3.4            |
| Met        | <1.0             | <1.0                  | <1.0                        | 1.1            |
| His        | <1.0             | -                     | 3.7                         | 3.2            |
| Cys        | <1.0             | <1.0                  | 2.9                         | <1.0           |

Figures given are mole %, not adjusting for Trp, which cannot be detected by Pico-Tag analysis.

\* from *Nephila clavipes* [27].

\*\* from *Strongylocentrotus purpuratus* [5].

Extraction of the insoluble portion of the matrix by grinding, boiling and subsequent centrifugation yields more soluble material of the same amino acid

composition and calcium binding affinity as that described above for the original soluble matrix. Some of the matrix remains insoluble even after these additional treatments. The amino acid composition of the insoluble matrix (Table 3) indicates a predominance of Gly, Ala, and Ser residues (65%), which is characteristic of silk structures. Comparison of the amino acid composition of the insoluble matrix to spider dragline silk indicates strong similarities (Table 3). This composition is also in good agreement, taking into account differences in methodology, with that reported by Hare and Abelson [19] for insoluble *M. edulis* matrix. A beta-sheet structure has been suggested as a key scaffolding element in the organic matrix of the shell based on X-ray diffraction analysis [49,50], and the composition of the mussel shell insoluble matrix reported here supports this hypothesis.

No chitin has been detected in this insoluble material by hydrolysis and gas chromatographic analysis for N-acetyl glucosamine. No glucosamine or N-acetyl glucosamine residues, which would indicate the presence of chitin or chitosan, were found during GLC analysis of the insoluble material and of powdered shell, further supporting the elemental analysis determination that the matrix is composed almost completely of protein. This contradicts the common assertion that chitin is omnipresent in molluscan organic matrixes [28].

Of the four primary soluble bands purified, only the 95 kDa protein is glycosylated, containing N-acetyl glucosamine and glucose, in a ratio of 1:7. Alcian blue staining revealed no evidence for phosphorylated proteins. None of the proteins isolated is a periostracal protein. This was precluded by removal of the outer shell layer during preparation of the shell material for purification of matrix. In addition, a control preparation of periostracum scraped from the outer shell revealed two protein bands that do not correspond to any of the proteins purified above (Figure 2) and the amino acid composition of the isolated proteins bears no resemblance to that reported for periostracin [42].

Both total soluble matrix and total insoluble matrix bind calcium under the assay conditions studied in a weight ratio equal to phosvitin. To confirm that the calcium binding observed was not an artifact created by residual EDTA in the matrix preparations, a problem noted by others [43,54], both EDTA and GLC analysis were used as controls. GLC was able to detect an EDTA adduct when EDTA remained in matrix preparations, and the protein components which bound calcium were shown to be free of EDTA by this method. Matrix components isolated by the acetic acid method behave the same in the assays as those prepared by the guanidine-EDTA method, further supporting the conclusion that calcium binding observed was attributable to protein and not residual EDTA.

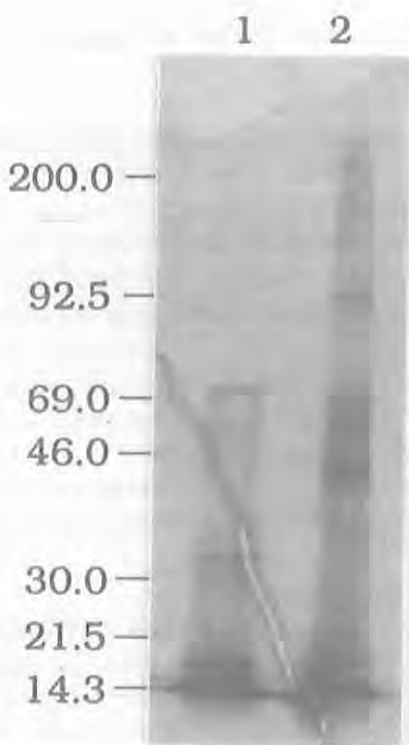


Figure 2. Tris-Glycine SDS reducing 8-16% gradient gel, 125 volts, 90 minutes, stained with Coomassie blue. Lane 1 is 2  $\mu$ g periostracal prep, lane 2 is 2  $\mu$ g soluble matrix.

The 95, 32, and 21 kDa bands gave a positive (blue) response to differential staining of calcium binding proteins with Stains-all, while all of the proteins used as molecular weight markers gave a negative (pink) response. The 200 kDa band did not stain at all with Stains-all, but did stain with Coomassie Blue.

Both total soluble matrix and total insoluble matrix bind calcium under the assay conditions studied. This fact suggests that calcium binding is not limited to anionic proteins and may involve an ionotropy, a change in affinity for calcium resulting from already bound calcium carbonate, as suggested by Sikes and Wheeler [36]. It should be noted that the assay used characterizes calcium affinity of proteins immobilized on membranes, which may be different from calcium affinity of protein free in solution [54] and does not incorporate any interactions with other macromolecules that may be present *in vivo*. This immobilization assay may still be more representative of *in vivo* conditions than free solution measurements if it is immobilized protein which



initiates crystallization, as suggested by Linde et al. [26]. Aside from differences in free solution versus immobilization conditions for the assay, subtle changes in protein conformation under the assay conditions could also impact on calcium binding affinity.

The findings that both the acidic soluble matrix proteins and the more neutral insoluble matrix proteins bind calcium, despite differences in amino acid composition and functionality, and that chitin is not present in the *M. edulis* matrix, indicate that the *in vivo* conditions may be more complex than suggested by models of matrix-mediated crystallization, which assign calcium interaction to the acidic macromolecules and structural support to a chitin-based polysaccharide coupled to a silk-like protein component [51,52]. Further research on the structural, temporal and molecular recognition issues associated with the matrix macromolecules may reveal that more complex interactions, such as between several organic components, may be required to mediate controlled crystal growth in molluscan shells. This level of understanding may be required before biomimetic approaches to this process can be fully realized.

In the model system, the stearic acid monolayer was used to mimic acidic functionality (COO<sup>-</sup> groups) with a defined spacing (24 Å<sup>2</sup> in a fully compressed monolayer). This is comparable to a protein with acidic functionality complexed with a beta-sheet protein, which may be what is happening in the natural system. Mann et al. [30] had shown that such a model system could selectively nucleate vaterite, the thermodynamically favored polymorph of calcium carbonate, over calcite and aragonite, the kinetically favored polymorphs. In addition, a change in concentration can shift the equilibrium to calcite, but unlike natural calcite, the calcite nucleated in such a system consists of discrete crystals nucleated off the same face [29].



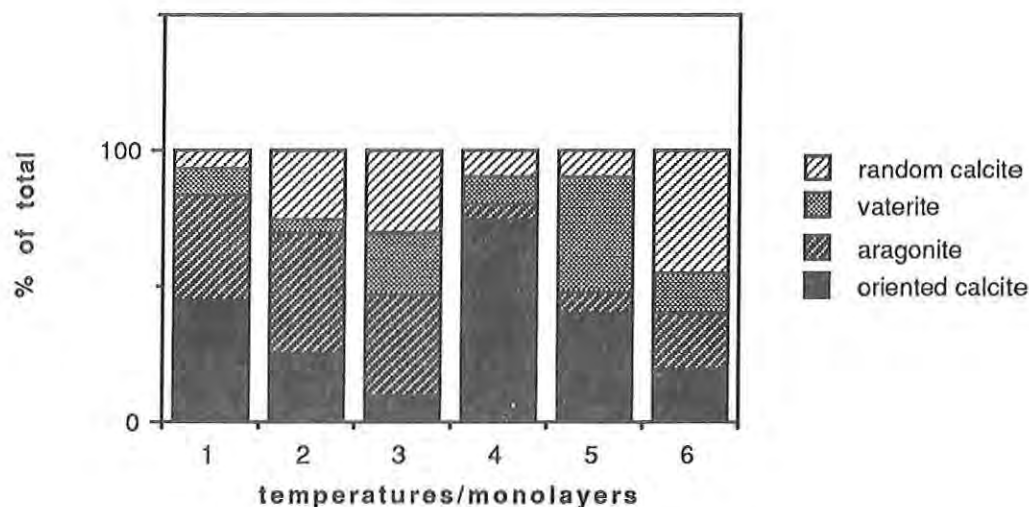


Figure 3. Percentage of calcium carbonate polymorphs present in model systems. 1=20°C no monolayer, 2= 30°C no monolayer, 3=35°C no monolayer, 4= 20°C monolayer, 5=30°C monolayer, 6= 35°C monolayer breaking down (see text).

To determine the strength of this selective crystallization, the present study varied the temperature of the nucleation event. Higher temperature should favor the nucleation of aragonite over calcite or vaterite, but the monolayer was able to shift the equilibrium toward ordered calcite and vaterite (Figure 3) except at the highest temperatures, where collapse of the monolayer was indicated by the pressure-area isotherm. This implies a temperature limitation, that of the breakdown of a given surfactant molecule, on any monolayer system used to mimic natural crystallization. However, the ability of the monolayer to influence crystallization even under strong kinetic pressure suggests that biomimetic crystallization as a route to new ceramics may be possible.

#### Literature Cited

1. Addadi, L. and Weiner, S. (1985), Interactions between acidic proteins and crystals: stereochemical requirements in biomineralization, *Proc. Natl. Acad. Sci. USA*, 82, 4110-4114.
2. Addadi, L. and Weiner, S. (1986), Interactions between acidic macromolecules and structured crystal surfaces: stereochemistry and biomineralization, *Mol. Cryst. Liq. Crystal*, 13, 305-322.
3. Agricultural Research Service (1963), *Composition of Foods, Handbook 8*, USDA,

KEITH, et al.

Washington, DC, USA.

4. Beedham, G.E. (1958), Observations on the non-calcareous component of the shell of the Lamellibranchia, *Quart. J. Microsc. Sci.*, 99, 341-357.
5. Benson, S.C., Benson, N.C., and Wilt, F. (1986), The organic matrix of the skeletal spicule of sea urchin embryos, *J. Cell Biol.*, 102, 1878-1886.
6. Berman, A., Addadi, L., and Weiner, S., (1988), Interactions of sea urchin skeleton macromolecules with growing calcite crystals-a study of intracrystalline proteins, *Nature*, 331, 546-548.
7. Butler, W.T. (1987), Dentin-specific proteins, In Cunningham, L.W. (ed.), *Methods in Enzymology* Vol 145, pp. 290-303, Academic Press.
8. Butler, W.T., Bhowan, M., Dimuzio, M.T., and Linde, A. (1981) Noncollagenous Proteins of Dentin. Isolation and partial characterization of rat dentin proteins and proteoglycans using a three-step preparative method, *Coll. Res.*, 1, 187-199.
9. Campbell, K.P., MacLennan, D.H., and Jorgensen, A.O. (1983), Staining of the  $Ca^{2+}$ -binding proteins, calsequestrin, calmodulin, troponin C and S-100, with the cationic carbocyanine dye "Stains-all", *J. Biol. Chem.*, 258, 11267-11273.
10. Carriker, M. R. (1978), Ultrastructural analysis of dissolution of shell of the bivalve *Mytilus edulis* by the accessory boring organ of the gastropod *Urosalpinx cinerea*, *Mar. Biol.*, 48, 105-134.
11. Chaplin, M. F. (1982), A rapid and sensitive method for the analysis of carbohydrate components in glycoproteins using gas-liquid chromatography, *Anal. Biochem*, 123, 336-341.
12. Cohen, S.A., Meys, M., and Tarvin, T.L. (1989), The Pico-Tag™ method, A manual of advanced techniques for amino acid analysis, Waters Division of Millipore, Milford, MA USA.
13. Crenshaw, M.A. (1972), The soluble matrix from *Mercenaria mercenaria* shell, *Biom mineralization*, 6, 6-11.
14. Crenshaw, M.A., and Ristedt, H. (1976), The histochemical localization of reactive groups in septal nacre from *Nautilus pompilus* L., In Watabe, N., and Wilbur, K.M. (eds), *The Mechanisms of Mineralization in the Invertebrates and Plants* pp. 355-367, University of South Carolina Press.
15. Furlong, C. E., and Humbert, R. (1992) Design of protein-producing bioreactors for self-assembling systems, *Mat. Res. Soc. Symp. Proc.*, in press.
16. Gordon, J., and Carriker, M.R. (1980), Sclerotized protein in the shell matrix of a bivalve mollusc, *Mar. Biol.*, 57, 251-260.
17. Gregoire, C. (1961), Structure of the conchiolin cases of the prisms in *Mytilus edulis* linne, *J. Biophys. Biochem. Cytol.*, 9, 395-400.
18. Gregoire, C.L. (1972), Structure of the molluscan shell, In Florkin, M., and Scheer, B. T.

KEITH, et al.

(eds), Chemical Zoology, Vol 7, pp. 45-102, Academic Press.

19. Hare, P.E., and Abelson, P.H. (1965), Amino acid composition of some calcified proteins, Carnegie Institution Yearbook, 64, 223-232.

20. Jeuniaux, C. (1963), Chitine et Chitinolyse, Masson, Paris, France.

21. Kennedy, W.J., Taylor, J.D., and Hall, A. (1969), Environmental and biological controls on bivalve shell mineralogy, Biol. Rev., 44, 499-530.

22. Krampitz, G., Drolshagen, H., Hausle, J., and Hof-Irmscher, K. (1983a), Organic matrices of mollusc shells, In Westbroek, P. and de Jong, E.W. (eds) Biomineralization and Biological Metal Accumulation, pp. 231-247, D. Reidel Publishing Co, Dordrecht, Holland.

23. Krampitz, G., Drolshagen, H., and Hotta, S. (1983b), Simultaneous binding of calcium and bicarbonate by conchiolin of oyster shells, Experientia, 39, 1104-1105.

24. Krampitz, G., Engels, J., and Cazaux, C. (1976), Biochemical studies on water-soluble proteins and related components of gastropod shells, In Watabe, N., and Wilbur, K.M. (eds) The Mechanisms of Mineralization in Invertebrates and Plants, pp. 155-173, University of South Carolina Press.

25. LeGendre, N. and Matsudaira, P. (1988), Direct Protein Microsequencing from Immobilized-P Transfer Membrane, Biotechniques, 6 (2), 154-159.

26. Linde, A., Lussi, A., and Crenshaw, M.A. (1989) Mineral induction by immobilized polyanionic proteins, Calcif. Tissue Int., 44, 286-295.

27. Lombardi, S., and Kaplan, D. (1990), The amino acid composition of major ampullate gland silk (dragline) of *Nephila clavipes* (Araneae, Tetragnathidae), J. Arachnol., 18, 297-306.

28. Lowenstam, H. A. and Weiner, S. (1989), On Biomineralization, Oxford University Press, New York, NY.

29. Mann, S., Heywood, B.R., Didymus, J.M., Rajam, S., Wade, V.J., and Walker, J.B.A. (1990), Biomineralization: New routes to crystal engineering, Mat. Res. Soc. Symp. Proc., 174, 25-37.

30. Mann, S., Heywood, B. R., Rajam, S., and Birchall, J. D. (1988), Controlled crystallization of CaCO<sub>3</sub> under stearic acid monolayers, Nature, 334, 692-695.

31. Maruyama, K., Mikawa, T., and Ebashi, S. (1984), Detection of calcium binding proteins by <sup>45</sup>Ca autoradiography on nitrocellulose membrane after sodium dodecyl sulfate gel electrophoresis, J. Biochem, 95, 511-519.

32. Meenakshi, V. R., Blackwelder, P. L., Hare, P. E., Wilbur, K. M., and Watabe, N. (1975), Studies on shell regeneration I. Matrix and mineral composition of the normal and regenerated shell of *Pomacea paludosa*, Comp. Biochem. Physiol., 50A, 347-351.

33. Meenakshi, V. R., Hare, P. E., and Wilbur, K. M. (1971), Amino acids of the organic matrix of neogastropod shells, Comp. Biochem. Physiol., 40B, 1037-1043.

KEITH, et al.

34. Peters, W. (1972), Occurrence of chitin in mollusca, *Comp. Biochem. Biophysiol.*, 41B, 541-550.
35. Peterson, G.L. (1977), A simplification of the protein assay method of Lowry et al. which is more generally applicable, *Anal. Biochem.*, 83, 346-356.
36. Sikes, C.S., and Wheeler, A.P. (1983), A systematic approach to some fundamental questions of calcium carbonate calcification, In Westbroek, P., and DeJong, E. W. (eds) *Biom mineralization and Biological Metal Accumulation*, pp. 285-289, D. Reidel, Dordrecht, Holland.
37. Sikes, C. S., and Wheeler, A. P. (1988b), Regulators of biomineralization, *Chemtech*, Oct., 620-626.
38. Simkiss, K. (1965), The organic matrix of the oyster shell, *Comp. Biochem. Physiol.*, 16, 427-435.
39. Sucov, H.M., Benson, S., Robinson, J.J., Britten, R.J., Wilt, F., and Davidson, E.H. (1987), A lineage-specific gene encoding a major matrix protein of the sea urchin embryo spicule, *Dev. Biol.*, 120, 507-519.
40. Swift, D. M., Sikes, C. S., and Wheeler, A. P. (1986) Analysis and function of organic matrix from sea urchin tests, *J. Exp. Zool.*, 240, 65-73.
41. Veis, D. J., Albinder, T.M., Clohisy, J., Rahima, M., Sabsay, B., and Veis, A. (1986), Matrix proteins of the teeth of the sea urchin *Lytechinus variegatus*, *J. Exp. Zool.*, 240, 35-46.
42. Waite, J. H., Saleuddin, A.S.M., and Andersen, S.O. (1979), Periostracin-a soluble precursor of sclerotized periostracum in *Mytilus edulis* L., *J. Comp. Physiol.*, 130, 301-307.
43. Weiner, S. (1979), Aspartic acid-rich proteins: major components of the soluble organic matrix of mollusk shells, *Calcif. Tissue Int.*, 29, 163-167.
44. Weiner, S. (1981), Repeating amino acid sequences in the soluble protein of mollusk shell organic matrices: their involvement in crystal formation, In Veis, A. (ed) *The Chemistry and Biology of Mineralized Connective Tissues*, pp. 517-521, Elsevier North Holland, Inc.
45. Weiner, S. (1982), Separation of acidic proteins from mineralized tissues by reversed-phase high performance liquid chromatography, *J. Chrom.*, 245, 148-154.
46. Weiner, S., and Hood, L. (1975), Soluble protein of the organic matrix of mollusc shells: A potential template for shell formation, *Science*, 190, 987-989.
47. Weiner, S., Lowenstam, H.A., and Hood, L. (1976) Characterization of 80-million-year-old mollusk shell proteins, *Proc. Natl. Acad. Sci. USA*, 73:8, 2541-2545.
48. Weiner, S., Lowenstam, H.A., and Hood, L. (1977), Discrete molecular weight components of the organic matrices of mollusc shells, *J. Exp. Mar. Biol. Ecol.*, 30, 45-51.
49. Weiner, S., and Traub, W. (1980), X-ray diffraction study of the insoluble organic matrix

KEITH, et al.

of mollusc shells, FEBS Letters, 111(2), 311-316.

50. Weiner, S., and Traub, W. (1981), Organic-matrix-mineral relationships in mollusk-shell nacreous layers, In Balaban, M., Sussman, J.L., Traub, W. and Yonath, A. (eds) Structural Aspects of Recognition and Assembly in Biological Macromolecules, pp. 467-482, Balaban ISS.

51. Weiner, S., and Traub, W. (1984) Macromolecules in mollusc shells and their functions in biomineralization, Phil. Trans. R. Soc. London Ser. B, 304, 421-438.

52. Weiner, S., Traub, W., Lowenstam, H.A. (1983) Organic matrix in calcified exoskeltons, In Westbroek, P., and deJong, E.W., (eds) Biomineralization and Biological Metal Accumulation, pp. 205-224, D. Reidel Publishing Co., Dordrecht, Holland.

53. Wheeler, A. P., Rusenko, K. W., George, J. W., and Sikes, C. S. (1987) Evaluation of calcium binding by molluscan shell organic matrix and its relevance to biomineralization, Com. Biochem. Physiol., 87B (4), 953-960.

54. Wheeler, A. P., and Sikes, C. S. (1989), Matrix-crystal interaction in  $\text{CaCO}_3$  biomineralization, In Mann, S, Webb, J., and Williams, R. P. (eds) Biomineralization Chemical and Biochemical Perspectives, pp. 95-132, VCH Publishers, New York, NY.

55. Wilbur, K. (1964), Shell formation and regeneration, In Wilbur, K.M., and Yonge, C.M. (eds) Physiology of Mollusca, Vol I, pp. 243-282, Academic Press, New York, NY.

